Department of Computer Science
University of Oxford

In Silico Modelling of Tumour-Induced Angiogenesis

Author:

Anthony J. Connor

Academic Supervisors:

Prof. Helen M. Byrne

Dr. Jonathan Cooper

Prof. Philip K. Maini

Dr. Steve McKeever

Industrial Supervisors:

Dr. Tom Quaiser

Dr. Eliezer Shochat

Thesis submitted to The University of Oxford for the degree of Doctor of Philosophy

May, 2016

In Silico Modelling of Tumour-Induced Angiogenesis

Anthony J Connor

Keble College

Submitted for Doctor of Philosophy

Michaelmas Term 2014

Angiogenesis, the process by which new vessels form from existing ones, is a key event in the development of a large and malignant vascularised tumour. A rapid expansion in *in vivo* and *in vitro* angiogenesis research in recent years has led to increased knowledge about the processes underlying angiogenesis and to promising steps forward in the development of anti-angiogenic therapies for the treatment of various cancers. However, substantial gaps in knowledge persist and the development of effective treatments remains a major challenge.

In this thesis we study tumour-induced angiogenesis within the context of a highly controllable experimental environment: the cornea micropocket assay. Using a multidisciplinary approach that combines experiments, image processing and analysis, and mathematical and computational modelling, we aim to provide mechanistic insight into the action of two angiogenic factors which are known to play central roles during tumour-induced angiogenesis: vascular endothelial growth factor A (VEGF-A) and basic fibroblast growth factor (bFGF). Image analysis techniques are used to extract quantitative data, which are both spatially and temporally resolved, from experimental images. These data are then used to develop and parametrise mathematical models describing the evolution of the corneal vasculature in response to both VEGF-A and bFGF.

The first models developed in this thesis are one-dimensional continuum models of angiogenesis in which VEGF-A and/or bFGF are released from a pellet implanted into a mouse cornea. We also use an object-oriented framework, designed to facilitate the re-use and extensibility of hybrid multiscale models of angiogenesis and vascular tumour growth, to develop a complementary three-dimensional hybrid model of the same system. The hybrid model incorporates a new non-local cell sensing model which facilitates the formation of well-perfused and functional vascular networks in three dimensions.

The continuum models are used to assess the utility of the cornea micropocket assay as a quantitative assay for angiogenesis, to characterise proposed synergies between VEGF-A and bFGF, and to generate experimentally testable predictions regarding the effect of anti-VEGF-A therapies on bFGF-induced angiogenesis. Meanwhile, the hybrid model is used to provide context for the comparison that is drawn between the continuum models and the data, to study the relative distributions of perfused and unperfused vessels in the evolving neovasculature, and to investigate the impact of tip cell sensing dysregulation on the angiogenic response in the cornea.

We have found that by exploiting a close link with quantitative data we have been able to extend the predictive and hypothesis-testing capabilities of our models. As such, this thesis demonstrates the potential for integrating mathematical modelling with image analysis techniques to increase insight into the mechanisms underlying angiogenesis.

Acknowledgements

The list of people that I would like to thank for helping me through the PhD process is long. Nevertheless, it is easy to know where to start. To my academic supervisors, Helen, Philip and Jonathan, I am sincerely grateful to you for your guidance, patience, support, vision and expertise over the last few years. A big thank you is also owed to my industrial supervisors, Tom and Eliezer. Your keen insights have been crucial in guiding me through my PhD project and your finesse has helped to institute a valuable relationship with the industrial scientists at Roche Diagnostics GmbH (Roche). I would also like to thank Steve McKeever, Alexander Manta and Josef Scheiber, who supervised me during my first year of research. I owe another thank you to Steve, in particular, for the opportunity to continue to collaborate on numerous papers following his departure from Oxford to Uppsala.

Next, I would like to thank all of the scientists at Roche, Penzberg, for making me feel so welcome during my visits there, and for the numerous illuminating conversations and feedback. I am particularly indebted to Erica Lorenzon, Frank Herting, Stefan Hoert and Markus Thomas, who performed the experiments and provided the images on which the work in this thesis draws. Thank you also to Vicente Grau and Franziska Mech for their invaluable feedback regarding the image processing work contained in this thesis, and thank you to Radek Nowak who initiated the image processing work during his Doctoral Training Centre short project.

I am grateful for the financial support of the Engineering and Physical Sciences Research Council (EPSRC), the Systems Approaches to Biomedical Sciences Industrial Doctorate Centre (SABS-IDC) and Roche. Thanks also to the administrative staff at the Doctoral Training Centre and Department of Computer Science, who have been instrumental in helping my PhD experience run as smoothly as possible.

Thank you to those in the Computational Biology group - Tom, Gary, Anna, Kylie, Lorenz, Raf, Sara, Mandeep, Sam, Joe and Ozzy, to name a few - who have made my time in the Department of Computer Science an enjoyable one and provided many a sanity-preserving distraction. Thanks, in particular, to Tom and Gary whose guidance, experience and reassurance helped to keep me on an even keel on more than one occasion. Thanks also to Alex and James from Maths for your guidance and comforting words. To those many others from Keble College MCR - for starters: Sameer, Chris, Dan, Tatiana, Hannah, Ricklef, Jayati, John, Ross, Tom, Bob and Tania - you helped to make my graduate experience an unforgettable one.

Finally, I would like to say a heart-felt thank you to my parents, my brother, Sam, and to Michelle for their boundless love, support and encouragement, without which this work would not have been possible.

Contents

List of Abbreviations

Here we provide a list of abbreviations used to denote various biological entities throughout this thesis. Most of these abbreviations are introduced formally in Chapter 2.

AF	Angiogenic factor
aFGF	Acidic fibroblast growth factor (also FGF-1)
Ang-1/2	Angiopoietin-1/2
bFGF	Basic fibroblast growth factor (also FGF-2)
Dll-4	Delta-like-4
EC	Endothelial cell
ECM	Extra-cellular matrix
EGF	Epidermal growth factor
FGF-1-5	Fibroblast growth factor-1-5
FGFR-1-4	Fibroblast growth factor receptor-1-4
HAEC	Human aortic endothelial cell
HIF-1α	Hypoxia inducible factor-1α
HSPG	Heparan sulphate proteoglycan
HUVEC	Human umbilical vein endothelial cell
MMP	Matrix metalloproteinases
NRP-1/2	Neuropilin-1/2
PDGF-B	Platelet-derived growth factor B
PDGFR-β	Platelet-derived growth factor receptor β
PlGF	Placental growth factor
RTK	Receptor tyrosine kinase
TAF	Tumour angiogenic factor
TGF-β	Transforming growth factor β
Tie-1/2	Tyrosine kinase with immunoglobulin-like and EGF-like domains 1/2 (binds Angiopoietins)
uPA	Urokinase type plasminogen activator
VEGF-A -E	Vascular endothelial growth factor A - E (VEGF-A also VPF - vascular permeability factor)
VEGFR-1	Vascular endothelial growth factor receptor 1 (also Flt-1)
VEGFR-2	Vascular endothelial growth factor receptor 2 (also Flk-1 or KDR)

Technical Terminology

Here we briefly distinguish a number of important modelling concepts.

Parameter estimation. Mathematical models can contain anything from one to hundreds of parameters - adjustable variables which determine quantitatively how a model behaves (Peirce 2008). Parameter values are often estimated from (or derived from) published experimental data. Such literature-derived parameter values (and values of parameters not available in the literature) are often tuned manually until model outputs agree (qualitatively or quantitatively) with experimental observations (Peirce 2008). Parameter values can also be derived more rigorously by fitting the model to quantitative experimental data (see **Parameter fitting**).

Parameter fitting concerns estimating model parameters from quantitative experimental data using automated minimisation, or optimisation, techniques. The parameters that are most likely to describe the data can be found using maximum likelihood estimation, which aims to minimise the weighted sum of squared residuals (WSSR) between the model output and experimental measurements. The parameter set returned by an algorithm which minimises the WSSR is that fitting the data best. See Quaiser (2012) for further details.

Parameter sensitivity analysis involves systematically adjusting the values of parameters to discern the effect that such changes have on model outputs. Such analyses can either be local, where parameter values are adjusted one at a time about a single point in parameter space, or global, where multidimensional parameter space is explored more broadly.

Parameter identifiability concerns whether the parameter set which generates the solution to a given parameter fitting (optimisation) problem can be uniquely identified (either locally or globally) (Little *et al.* 2010). Parameter identifiability analysis can also provide insight into what new experiments are required, and what new data should be acquired, so that model parameters may be fully constrained (uniquely identifiable with respect to the available data) (Quaiser *et al.* 2011).

Model prediction. A prediction is generally a statement about something which will happen given a particular set of specific conditions. Sometimes predictions can be made about what has happened in the past in order for a given set of circumstances to have come about. Mathematical and computational models are often used to describe the past and future behaviour of a system. Predictions can be quantitative or qualitative and, in some cases, a prediction may comprise a set of probabilistic outcomes.

Model validation involves establishing how accurately a model represents reality (Cooper *et al.* 2014). After a model has been parametrised, model inputs should be perturbed to make a prediction. The prediction should be compared with qualitative or quantitative experimental observations to confirm its accuracy. Comparison of model predictions against quantitative experimental observations offers a more rigorous validation than comparisons against qualitative experimental observations. Importantly, model validation requires that independent data sets be used for model construction (and parametrisation) and validation (Peirce 2008).

Model verification involves establishing how accurately one's software implements an underlying model (Cooper *et al.* 2014). That is, verification is the process of confirming that model equations are accurately implemented and that outputs from the implementation of a model match those that are expected from the model given a particular set of inputs (Peirce 2008).

CHAPTER 1

Introduction

Angiogenesis is the process by which new vessels form from existing vasculature. As well as being key to successful wound healing and the healthy development of embryos, angiogenesis is prevalent in many pathological conditions, including obesity, asthma, AIDS and cancer (Carmeliet 2005). Thus, identifying its principal characteristics and understanding the mechanisms that regulate angiogenesis are important avenues of research, as is determining how angiogenesis is dysregulated in diseased tissues.

Typically, until tumours reach a critical size of around two millimetres in diameter, tumour cells obtain the nutrients they need for growth and proliferation via diffusion from the nearby existing vasculature. However, to grow past this critical size, a tumour must undergo a period of sustained angiogenesis. Once vascularised, a tumour has increased access to nutrients and thus may invade further and grow faster than was possible in its earlier avascular stage. The tumour vasculature also provides a mechanism by which cancer cells may escape from the primary tumour and form metastases in other organs. Thus, the onset of angiogenesis marks the transition of a tumour from something which is relatively harmless to something which is potentially fatal.

The concept of targeting angiogenesis to inhibit tumour growth was first proposed in the 1970s (Folkman *et al.* 1971). Since then, tumour angiogenesis has developed into a mature research area. Dedicated wet-lab research has increased our knowledge of the associated cellular processes, leading to the identification of key molecular regulators of angiogenesis, such as vascular endothelial growth factor A (VEGF-A), and to exciting advances in the development of anti-angiogenic cancer therapies. Most notably, in 2004, bevacizumab, an antibody which inhibits VEGF-A, was approved for combination use with chemotherapy to treat metastatic colon cancer. Since 2004, bevacizumab has been approved for the treatment of other cancers and several more anti-angiogenesis drugs have been approved, a number of which exclusively target the VEGF-A pathway. Regrettably, however, most anti-angiogenic therapies have failed to live up to the promise shown in pre-clinical trials; such therapies typically prolong the survival of responsive patients by only a few months (Carmeliet and Jain 2011). Most patients seemingly quickly acquire resistance to anti-VEGF-A therapies whilst others do not respond at all. Additionally, the cost and potential side-effects from chronic use of these drugs are significant issues. These findings have stimulated research into the development of more effective ways of combining anti-angiogenic drugs with traditional cancer therapies and the search for more efficacious anti-angiogenic drugs. In particular, efforts are being devoted to developing combination therapies which target both VEGF-A and other molecular signals which promote angiogenesis in cancer, for example, basic fibroblast growth factor (bFGF). It is hoped that targeting these pathways as well as VEGF-A may help overcome resistance to current anti-angiogenic therapies.

It is widely believed that developing a fuller, quantitative understanding of the mechanisms that regulate angiogenesis may have a critical role to play in improving cancer treatment (Jain 2003). Recent *in vitro* and *in vivo* experiments have begun to reveal details of the cellular and sub-cellular events leading to angiogenesis. However, to fully understand such a complex process, experimental techniques should be supplemented with mathematical and computational (or *in silico*) models. Such models can be used to generate testable hypotheses about the biomechanical and biochemical mechanisms underlying angiogenesis, providing a means by which to bridge biological theory and experiments. In this way, they may enhance our understanding of angiogenesis and guide the development of novel or improved anti-angiogenic treatment strategies for cancer. *In silico* models may also form an important element within pre-clinical drug studies by helping to determine preliminary details such as toxicity, pharmacokinetics and efficacy. Moreover, by allowing researchers to refine hypotheses and develop more accurate experimental procedures before embarking on *in vivo* or *in vitro* experiments, *in silico* models may help to reduce costs and boost research efficiency (Trisilowati and Mallet 2012).

To address the many complex phenomena associated with tumour-induced angiogenesis, an eclectic array of mathematical models has been developed over the last three decades. The earliest models used a continuum approach (Balding and McElwain 1985; Byrne and Chaplain 1995). They were formulated in a 1-D Cartesian geometry and focused on a small number of model variables, such as vessels, cells and chemicals. The development and analysis of such models provided a solid base for the development of more complex models, which treat the underlying biochemistry and vascular components in greater detail. In combination with the boom in the availability of biological data at ever smaller scales, it is the increase in available computational resources over the last two decades that has accelerated the development of more detailed models of tumour-induced angiogenesis. Increasingly the trend in tumour-induced angiogenesis model development has been towards integrating continuum descriptions of molecular species with discrete representations of cells and vessels in multiple dimensions. These *hybrid* models allow the vasculature to be represented as a heterogeneous structure with a well-defined topology, upon which detailed models of blood flow and drug delivery can be layered. Developing models of biological systems is difficult however. To be practically useful, models should be well parametrised and, if possible, validated. And, crucially, if we are to achieve a more quantitative understanding of cancer then it is important that we begin to develop methods to rigorously compare simulated and experimental results. This will allow us to develop and parametrise models so that they not only "look like" experiments, but quantitatively agree with them.

To develop models which are quantitative, it is important to study vascular growth in simple systems which are amenable to quantitative analysis and are not subject to as many confounding factors as are present inside a tumour. This approach mirrors that taken by experimentalists who study angiogenesis in simple and controllable assays, such as the cornea micropocket assay, as a starting point to understanding the mechanisms regulating angiogenesis in cancer. Following this approach, the emphasis of model development in this thesis will be on angiogenesis in the cornea.

1.1. Thesis aims and structure

The main focus of this thesis is to integrate quantitative experimental data, which depict the spatiotemporal evolution of a vascular network, with techniques for mathematically modelling tumour-induced angiogenesis. In so doing, we aim to close the gap between angiogenesis observed in the wet-lab and simulated *in silico*. Our principal motivation is that, if the types of spatiotemporal models discussed in this thesis are ever to be translated into widespread clinical use, then they need to be rigorously compared against experimental data. We move a step closer towards this goal by demonstrating that our models are able to quantitatively reproduce dynamic, spatially-resolved data on reasonable time, length and vascular density scales when physically realistic parameter values are employed. We develop new models of angiogenesis which will provide the building blocks for starting to address questions which are currently at the forefront of angiogenesis research (e.g. what biological mechanisms are responsible for resistance to anti-VEGF-A therapies?). At the same time, we ensure that the models we develop are grounded, as far as possible, in experimental data. In the following we describe the structure of this thesis. Figure 1.1 also illustrates how the main results chapters in this thesis interrelate.

This thesis begins, in Chapter 2, with a review of the biology which is fundamental to tumour

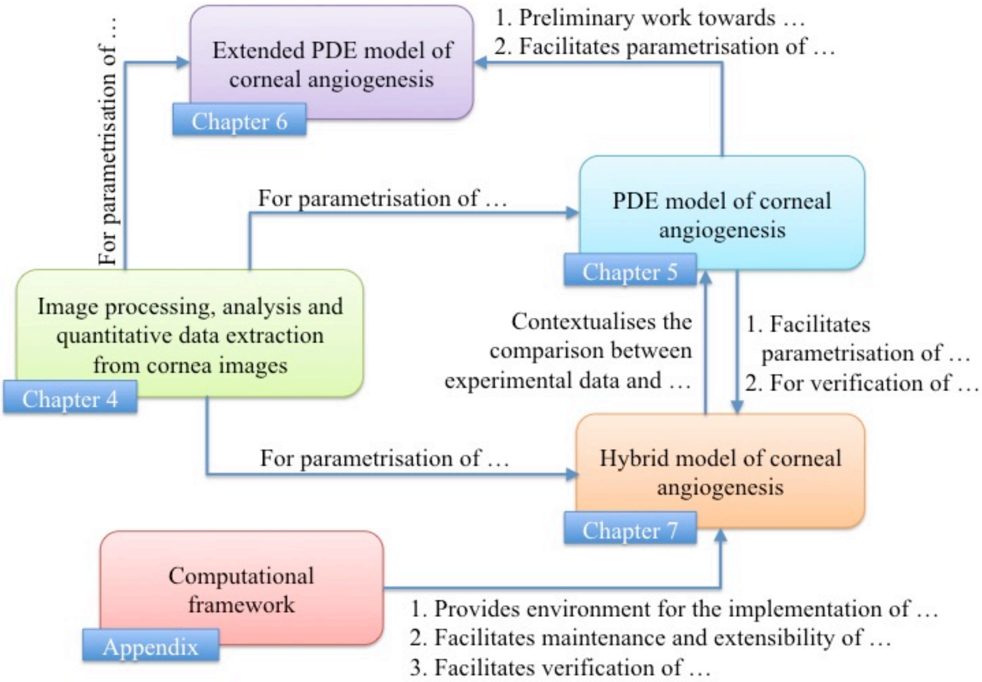

Figure 1.1.: Schematic summarising how the results chapters within this thesis (Chapters 4-7) interrelate. Chapter 4 is the pillar on which the thesis is based as, through image analysis, we extract the data which need to be explained. This chapter feeds into Chapters 5 and 6, which develop and extend, respectively, continuum models of corneal angiogenesis, and into Chapter 7, where we build a hybrid model of corneal angiogenesis. The hybrid model is implemented inside an object-oriented modelling framework which is described in Appendix C. PDE: partial differential equation.

angiogenesis. We explain how anti-angiogenic drugs combine with chemotherapeutic agents to improve cancer treatment outcomes and also introduce the mouse cornea micropocket assay, on which the mathematical models of angiogenesis developed in this thesis are based. In Chapter 3 we review existing models of angiogenesis and vascular tumour growth, drawing particular attention to those models which provide a basis for the work in this thesis.

Image analysis provides an avenue through which quantitative links can be made between experimental assays and spatially-resolved, tissue scale mathematical models of angiogenesis. Detailed images of the vasculature both inside tumours and in experimental assays such as the cornea micropocket assay are now becoming available, and imaging techniques have advanced to the stage where we can begin to (semi-)automatically extract vascular networks from those images with some reliability. In Chapter 4 we review and quantitatively compare several state-of-the-art vascular segmentation algorithms in order to determine which algorithm is best suited to extract data from a series of images of corneal angiogenesis. The images we analyse were captured on days three and five of cornea micropocket assay experiments performed at Roche Diagnostics GmbH, Penzberg (henceforth abbreviated to Roche). In these experiments, angiogenesis was stimulated by the administration of either VEGF-A or bFGF, angiogenic factors (AFs) known to play central roles during intra-tumoural angiogenesis. Our analysis provides us with quantitative estimates for how the vascular density in the cornea evolves in space and time in response to VEGF-A and bFGF when administered in isolation. The data extracted from the images are not sufficient to identify all of the parameters contained in the models developed in this thesis. Thus, we do not fit our models to the data by minimising, for example, the root mean squared error. Instead we establish parameter values by a thorough review of the experimental literature and subsequent manual fine-tuning until our model outputs are quantitatively consistent with the data.

Our first mathematical modelling approach is introduced in Chapter 5 and follows that initially introduced by Balding and McElwain (1985) and then extended by Byrne and Chaplain (1995). These models were originally developed to establish qualitative agreement with experimental data, incorporating essential phenomena such as chemotaxis (movement in response to gradients in an AF), and focused on the action of a single generic tumour angiogenic factor (TAF). In light of the recent advances in imaging technology and imaging processing techniques which can yield quantitative spatiotemporal data, we aim to parametrise such mathematical models against our data, with the intention of extending their predictive and hypothesis-testing capabilities. The 1-D continuum model which we develop is based on the model of corneal angiogenesis presented by Byrne and Chaplain (1995). The model is parametrised against the VEGF-A data and then, making minor changes, against the bFGF data. The model is first used to perform a local parameter sensitivity analysis, providing insight into the limitations of the cornea assay as a quantitative assay for angiogenesis. Then the model is extended to include important tip cell-extracellular matrix (ECM) interactions and we study the effect that including such interactions has on model predictions of anti-angiogenic therapies. Finally, the model is simplified and refit to the data and a brief comparison is drawn between the simplified and more complex models.

Building on the models developed in Chapter 5, in Chapter 6 we develop a 1-D model of corneal angiogenesis in which vascular growth occurs in response to VEGF-A and bFGF simultaneously. In contrast to the models developed in the previous chapter, this model incorporates cross-talk between VEGF-A and bFGF. The model is once again parametrised against the data presented in Chapter 4, after which we use the model to generate experimentally testable predictions regarding the response of the corneal vasculature when exposed to bFGF and VEGF-A in combination, and the effect of anti-VEGF-A therapies on bFGF-induced angiogenesis.

Chapter 7 is devoted to the development of hybrid models of tumour-induced angiogenesis. Here, we initially adapt and extend the model of VEGF-A-induced angiogenesis implemented by Perfahl *et al.* (2011), principally by incorporating a biologically motivated model of cell sensing which facilitates the formation of well perfused vascular networks in three dimensions. The model is again parametrised against the experimental data introduced in Chapter 4. However, the discrete treatment of the model vasculature and its 3-D formulation here mean that more rigorous comparisons may be drawn between simulation results and experimental data. A major advantage of treating vessels discretely is the ability to calculate flow through the vascular network and thus discriminate between perfused and unperfused vessels. Thus, we use the hybrid model to study the distributions of perfused and unperfused vessels in the evolving vasculature. Additionally we investigate the effect that dysregulation in the cell sensing model has on the angiogenic response. We also use the 3-D simulations to estimate how accurately one might expect the vascular density extracted from our 2-D images to resemble the *in vivo* vascular density. This renders explicit the comparison that we draw between the continuum models developed in Chapters 5 and 6 and the experimental data. Finally, as in Chapter 5, we extend our hybrid model to include key tip cell-ECM interactions and study the effect that including such interactions has on model predictions regarding the effect of anti-angiogenic therapies.

Our hybrid models are implemented in an object-oriented modelling framework which aims to facilitate the development and extension of hybrid models of angiogenesis and vascular tumour growth. The framework is presented in Appendix C where we outline how we have adopted object-orientation to encourage code understandability and model extensibility, and to facilitate the rigorous testing of model code.

We conclude in Chapter 8 by summarising our findings and discussing possible directions for further research.

CHAPTER 2

Review of Biology: Angiogenesis and Tumour Growth

2.1. Overview

All types of cancer emerge as a result of dynamic changes to the genome contained within cells. At the phenotypic level these genomic changes manifest themselves as selectively advantageous cellular capabilities, and it is the successive accumulation of these capabilities that drives the transformation of normal cells into the highly malignant ones which characterise late-stage tumours. Currently, eight acquired functional capabilities have been identified which allow cancer cells to survive, proliferate and re-distribute themselves beyond normal means. These include the ability to promote sustained angiogenesis and the ability to invade neighbouring tissues and form metastases[1]. These functional capabilities have been labelled the “hallmarks of cancer” and are described in detail by Hanahan and Weinberg (2011).

The genomic and phenotypic changes which occur at the sub-cellular and cell levels drive a tumour through two successive growth phases: avascular and vascular growth. During the avascular phase, the tumour receives nutrients via diffusion and, as a result, is limited in size. To grow beyond this size tumours must obtain their own blood supply. They may envelop existing vessels in a process known as co-option (Holash 1999) or they may stimulate the growth of new blood vessels, principally via sprouting angiogenesis, which forms the focus of this thesis.

In a tumour, sprouting angiogenesis is initiated when it grows so large that parts of the tumour become deprived of sufficient levels of oxygen (and other nutrients, such as glucose). In such hypoxic conditions some tumour cells enter a quiescent state and others die. Experimental evidence suggests that some tumour cells respond to hypoxic conditions by secreting AFs, such as VEGF-A (Shweiki *et al.* 1995), which diffuse through the surrounding tissue and, upon reaching a blood vessel, trigger a cascade of events which result in the formation of new vessel sprouts

---

[1] The further six capabilities have been identified as: self-sufficiency in growth signals, insensitivity to growth-inhibitory signals, evasion of programmed cell death (apoptosis), limitless replicative potential (immortality), reprogramming of energy metabolism and evading immune destruction. A further two enabling characteristics have also been identified, genome instability and mutation, and tumour promoting inflammation, which make possible the acquisition of these functional capabilities.

which subsequently migrate towards the source of the AFs. As they grow, sprouts may connect with each other, or with existing vessels, to form closed loops. Within such loops, after lumen formation, blood may begin to flow. This increases the tumour's nutrient supply, allowing it to continue growing and to invade the adjacent healthy tissue. Once vascularised, a tumour may grow more rapidly than was possible in its diffusion-limited, avascular stage. A vascularised tumour also has a network by which its cells may be transported to other parts of the host where they may establish secondary tumours. Therefore, the process by which a tumour becomes vascularised marks its transition from a phase in which it is relatively harmless to one in which it is potentially fatal (Folkman *et al.* 1971).

Other methods also exist by which tumours manipulate their own blood supply. For example, during vasculogenic mimicry, networks of tubes which are rich in ECM, but lack endothelial cells (ECs), which line normal vessels, may develop (Maniotis *et al.* 1999). These tubes can support the flow of red blood cells. Alternatively, bone-marrow derived endothelial progenitor cells may be recruited to a tumour to form new vessels (Roskoski 2007) via a process termed postnatal vasculogenesis. Cancer cells may also insert themselves into the walls of vessels via a process known as mosaic vessel formation (Chang *et al.* 2000). These processes will not be addressed in this thesis; they are mentioned here mainly to provide some context.

In the remainder of this chapter we will discuss in further detail aspects of the biology underlying tumour-induced angiogenesis. We will focus on sprouting angiogenesis, outlining the key molecular and cellular players which are believed to take part in this process.

2.2. The structure of blood vessels in normal tissues

During normal development, the coordinated and tightly regulated interaction of many cell types and biomolecular signals eventually results in the formation of organised and well-perfused vascular networks, within which ECs are bound to each other via adherens junctions (Dejana *et al.* 2009). The ECs, known as phalanx cells (Carmeliet and Jain 2011), are maintained in a quiescent state by a host of mechanical and chemical signals. They form a monolayer along continuous hollow tubular structures, which are covered by a *basement membrane*. Within and external to this basement membrane lie additional cells, known as mural cells. In the microvasculature, these cells are mainly pericytes, which release cell-survival signals, such as VEGF-A, and other factors such as angiopoietin-1 (Ang-1), which maintain ECs in a quiescent and stable state (Carmeliet and Jain 2011). In larger vessels, additional layers and more cell-types, such as vascular smooth muscle cells, may be present. Quiescent vessels which have a “normal” level of pericyte coverage are known as *mature* and the hollow structure inside a vessel is the *lumen.* The lumen enables mature vessels to efficiently transport blood, and the vital nutrients it carries, to tissues.

2.3. Angiogenesis

Angiogenesis is the process by which new blood vessels form from existing ones. This contrasts vasculogenesis (occurring mainly in development) in which individual ECs self-assemble into a primitive network (Carmeliet 2000). There are several distinct types of angiogenesis: sprouting angiogenesis, where ECs migrate through, and proliferate within, the ECM (Folkman *et al.* 1971); intussusceptive angiogenesis (Djonov *et al.* 2000), which involves a single vessel splitting into two in the absence of EC proliferation; and looping angiogenesis (Peebo 2008; Kilarski *et al.* 2009), involving neovascularisation by the translocation of blood vessels due to biomechanical forces. Each type of angiogenesis may be initiated in different physiological conditions and each process may occur concurrently within a given tissue.

In this thesis we focus on sprouting angiogenesis since this is thought to be dominant in cancer (Hlushchuk *et al.* 2011). However, in the following we will also review intussusceptive angiogenesis due to its observed role in the tumour vasculature’s response to anti-angiogenic therapies.

2.3.1. Sprouting angiogenesis

As noted above, in general, and in the absence of any pathological condition, blood vessels in adult humans usually reside in a mature, inactive state. They are enclosed within a sheath of mural cells, such as pericytes, and are maintained in a quiescent state through exposure to high levels of Ang-1 (Augustin *et al.* 2009). However, exposure to AFs, such as VEGF-A and bFGF, can destabilise vessels, prior to vascular growth. Briefly, in non-pathological conditions, such as wound healing, the binding of VEGF-A to cell surface receptors on the ECs lining vessels induces the production and release of angiopoietin-2 (Ang-2) (Hegen *et al.* 2004). This protein is commonly referred to as a vessel destabiliser and its over-expression leads to further activation of ECs and the detachment of mural cells from the mature vessel. The ECs produce proteases, including matrix metalloproteinases (MMPs), which degrade the basement membrane, allowing the ECs to escape the parent vessel and invade the surrounding ECM. Locally, VEGF-A stimulates a single EC to become a *tip cell.* These tip cells, which do not proliferate, continuously extend and retract filopodia to explore their local environment (Gerhardt 2003). This allows the tip cells to sense and migrate up spatial gradients of AFs, including VEGF-A. Other ECs, known as *stalk cells*, trail behind the migrating tip cell, proliferating at a rate which ensures that a contiguous border is maintained between the tip cell and its parent vessel, and allowing the sprout to form a lumen (De Smet *et al.* 2009). To form a fully functional and perfused vascular loop, tip cells must connect with other sprouts or existing vessels, in a process known as anastomosis. The ECs which make up the body of the immature sprout release platelet-derived growth factor-B (PDGF-B), which stimulates the proliferation of pericytes and their migration towards the immature vessel (Gaengel *et al.* 2009)[2]. Together, pericytes and ECs eventually produce a new basement membrane, providing structural support for the newly formed vessel. As noted in Section 2.2, recruited pericytes also secrete Ang-1. Eventually, the local concentration of Ang-1 increases until it overcomes the destabilising effect of Ang-2. After Ang-1 has again regained dominance over Ang-2 and pericytes have established coverage, the new capillary stabilises and the ECs return to their phalanx-like, quiescent states (Augustin *et al.* 2009). Other factors, such as transforming growth factor beta (TGF-β), are also known to be involved in the maturation of vessel sprouts (Ramsauer and D'Amore 2002). The main events which occur during non-pathogenic sprouting angiogenesis are depicted in Figure 2.1, meanwhile, Figure 2.2 summarises some of the main molecular interactions in angiogenesis. We elaborate further on the interactions and molecules in this figure in Sections 2.4-2.6.

Although the major players and events in intra-tumoural angiogenesis are largely the same as those described above for non-pathological angiogenesis, an imbalance of pro-angiogenic factors and inhibitors in a tumour has a profound effect on the evolving vasculature. This imbalance causes tumour-associated vessels to be highly tortuous, immature and, more generally, to lack the well-defined structure of their normal peers. As a consequence, tumour-associated vessels are usually leaky and prone to collapse under the pressure of the growing tumour. Moreover, these structural defects often lead to inefficient delivery of nutrients to tumours, which contributes to the hypoxia which is experienced even by vascularised tumours (Jain 2001). For a more comprehensive review of the structure of tumour-associated microvessels see Goel *et al.* (2011).

2.3.2. Intussusceptive angiogenesis

While sprouting angiogenesis usually occurs in response to AFs, intussusceptive angogenesis, or"non-sprouting" angiogenesis, appears to be mediated predominantly by mechanical stimuli,

---

[2] Furthermore, if the vessel is destined to become larger, smooth muscle cells may be recruited (Tomanek and Schatteman 2000).

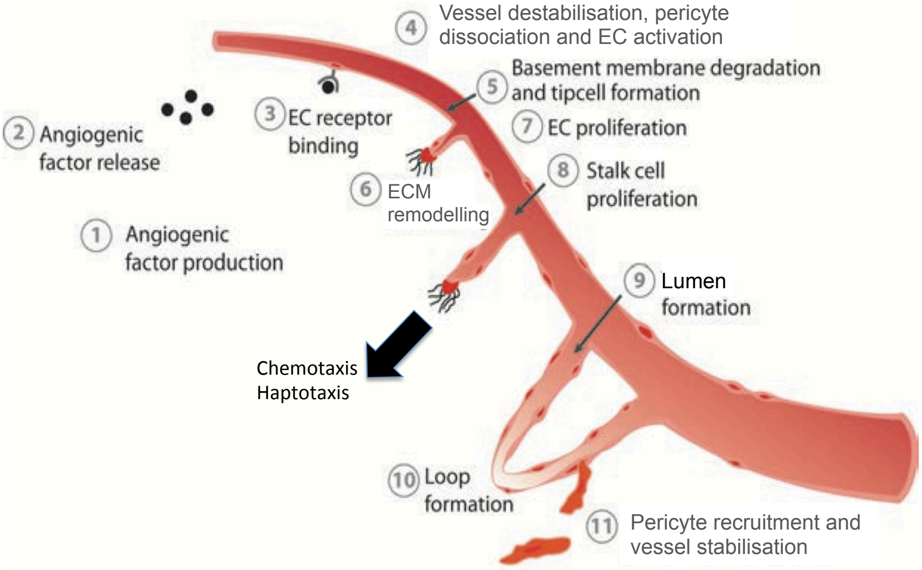

Figure 2.1.: Simple schematic summarising the major processes in sprouting angiogenesis. Adapted with permission from Peebo (2008). See main text for details.

such as the levels of shear stress due to blood flow (Styp-Rekowska *et al.* 2011). Intussusceptive angiogenesis is accomplished through intraluminal growth (Hlushchuk *et al.* 2008). That is, ECs on opposite sides of the affected vessel project protrusions transluminally. When these protrusions meet they form an EC bilayer. Perforation of this bilayer then leads to the formation of a transluminal pillar, which is subsequently invaded by pericytes and fibroblasts which deposit a layer of collagen to stabilise the pillar (Burri *et al.* 2004).

Intussusceptive angiogenesis is faster than sprouting angiogenesis, typically occurring within a couple of hours. It is also more economical energetically since ECs do not need to proliferate and degradation of the basement membrane is not required. Thus, the structure of the vessels remains intact and the permeability of vessels changes less dramatically (Burri *et al.* 2004). One advantage that sprouting angiogensis has over intussusceptive angiogenesis is its ability to propagate vascular growth across gaps in vascular networks. Meanwhile intussusceptive angiogenesis merely results in a local increase of vascular density (and vascular exchange surface area). Other, shear stress mediated processes, which are closely related to intussusceptive angiogenesis, may also result in vessel regression or vessel branching angle remodelling, as detailed by Burri *et al.* (2004). We briefly return to the role of intussusceptive angiogenesis in cancer in Section 2.7.

2.3.3. A note on post-angiogenic vascular remodelling

Intussusceptive angiogenesis may perform a significant role in the structural remodelling of a vascular network which occurs after new vascular growth. New vessels which are redundant may

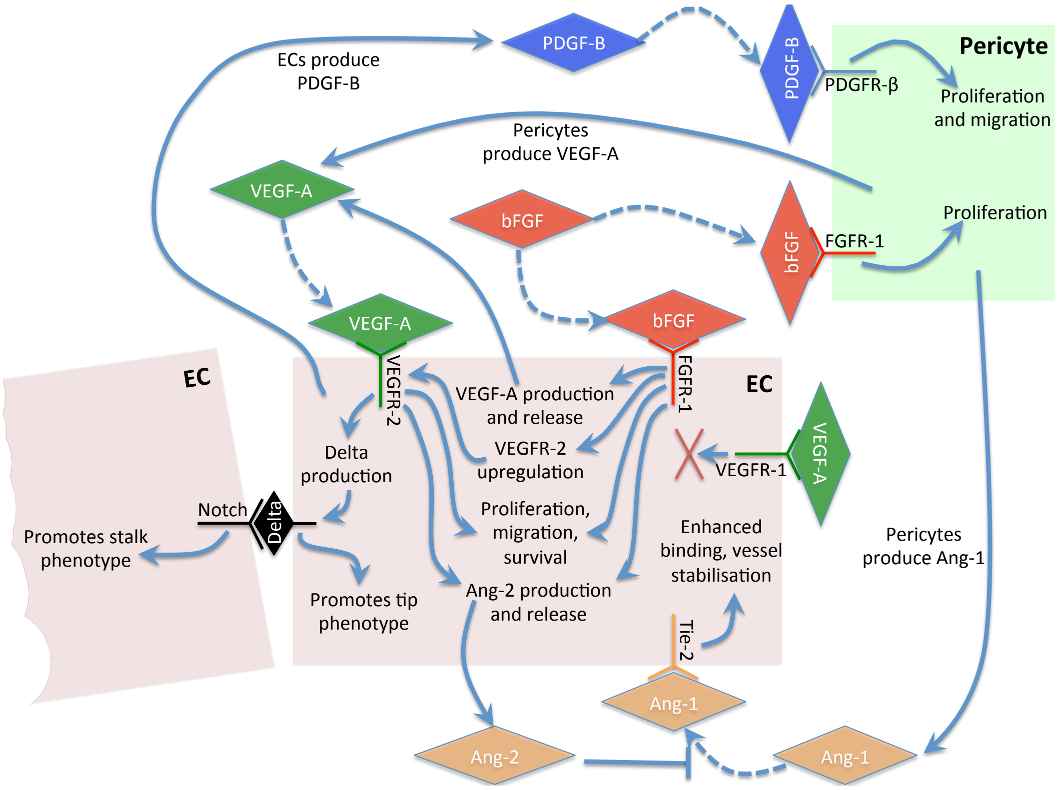

Figure 2.2.: Summary of interactions between important factors involved in sprouting angiogenesis. See main text for details.

also eventually be pruned from the network. Such remodelling processes are important to ensure that the vasculature in normal tissues is able to efficiently and effectively transport nutrients to a given region. However, the efficient and effective transport of blood to vascularised regions does not depend purely on the presence or absence of vasculature. As important as the processes which ensure the presence of adequate numbers of vessels, are those processes which control the diameter and thus the flow of blood through those vessels.

In healthy tissues the diameter of vessels is tightly regulated by various mechanisms to ensure that flow is well-distributed through the often heterogeneous vascular network. These mechanisms, discussed in detail by Pries *et al.* (2010), inhibit the formation of vascular shunts, whereby short paths through the vascular network become enlarged and flow bypasses the longer pathways. In particular, the prevention of vascular shunting appears to require signal propagation against the direction of flow to instruct feeding vessels that flow is required in a particular downstream region of the network[3]. Such upstream signals may be propagated through gap junctions[4].

In tumours, vascular shunting is often observed, indicating that the mechanisms underlying

---

[3] Furthermore, it appears that the upstream signal must only ever be able to travel upstream and not be able to re-enter the network in a downstream direction.

[4] Gap junctions are intercellular channels which connect the cytoplasm of neighbouring cells.

vessel diameter control in tumours may be dysregulated. In particular, it has been suggested that the ability to propagate an effective upstream signal is likely to be dysregulated in tumours (Pries *et al.* 2010). Vascular shunting and ineffective use of the tumour vasculature are also thought to contribute to the hypoxia experienced by vascularised tumours.

2.4. The role of VEGF-A in sprouting angiogenesis

The VEGF family of growth factors has six members: VEGF-A, -B, -C, -D, -E and placental growth factor (PlGF). VEGF-A, also known as vascular permeability factor (VPF), is thought to be the most important growth factor associated with tumour angiogenesis. Alternative splicing of the gene encoding for VEGF-A results in different isoforms, with masses in the range $34 - 45\,\text{kDa}$. The three most common isoforms in humans (in descending order) are VEGF-A_{165}, VEGF-A_{189} and VEGF-A_{121} (Roskoski 2007). VEGF-A_{165} and VEGF-A_{189} both bind to heparin (present on the surface of cells and in the ECM) with increasing affinity, to the extent that VEGF-A_{189} is almost entirely sequestered by the ECM. Meanwhile VEGF-A_{121} lacks the heparin-binding domain present in VEGF-A_{165} and VEGF-A_{189} and so is freely diffusible. Each isoform is differentially angiogenically potent, where the loss of the heparin binding domain has been linked to a significant loss in the mitogenic activity of VEGF-A (Keyt *et al.* 1996).

Critical in intra-tumoural angiogenesis is the fact that VEGF-A expression and secretion is upregulated in cells which are hypoxic. Briefly, in normoxic conditions, oxygen promotes the hydroxylation of hypoxia inducible factor (HIF-1α), leading to its eventual proteosomal degradation (see Roskoski, 2007, for more details). However, under hypoxic conditions, the rate of hydroxylation falls, leading to decreased degradation and thus the accumulation of intracellular HIF-1α. Such increases in HIF-1α upregulate the transcription of VEGF-A which is subsequently released by the hypoxic cell. Several other growth factors are known to upregulate VEGF-A expression and release. These include bFGF, PDGF-B, TGF-β and epidermal growth factor (EGF). Additionally, VEGF-A may also be mobilised from the ECM when it is degraded.

VEGF-A binds to several transmembrane receptor tyrosine kinases (RTKs), including VEGF receptor 1 (VEGFR-1) - also known as Flt-1 - and VEGF receptor 2 (VEGFR-2) - also known as Flk-1 or KDR - which are predominantly found on ECs. VEGF-A binding to VEGFR-1 or -2 induces receptor dimerisation, leading to autophosphorylation of the tyrosine residues located in the cytoplasmic domain. The phosphorylated tyrosine residues either enhance receptor catalytic activity or provide docking sites for downstream signalling proteins (Hubbard 1999). While the precise function of VEGF-A/VEGFR-1 binding in ECs is still under debate it appears to have no direct proliferative or structural effects on ECs (Waltenberger *et al.* 1994). It has been suggested that VEGFR-1 acts as a decoy receptor, whose presence potentiates VEGF-A/VEGFR-2 binding (Park *et al.* 1994). However, VEGFR-1 is likely to be important in other scenarios. For example, activation of VEGFR-1 by VEGF-B in ECs has been linked to increased expression of urokinase type plasminogen activator (uPA) and plasminogen activator inhibitor-1, which are involved in ECM degradation and cell migration (Olofsson *et al.* 1998).

VEGFR-2 has an affinity for VEGF-A which is approximately 8 times lower than that of VEGFR-1 (Waltenberger *et al.* 1994). Nevertheless, presently VEGF-A/VEGFR-2 interactions appear to be the most important regulators of sprouting angiogenesis, particularly under hypoxia, as observed in tumour growth. Activation of VEGFR-2 by VEGF-A results in mitogenic, chemotactic and pro-survival signals. In addition, VEGF-A increases vascular permeability via VEGFR-2 signalling. VEGF-A (all isoforms except VEGF-A_{121}) also interacts with a family of receptors known as neuropilins, NRP-1 and NRP-2. When co-expressed with VEGFR-2 the NRPs appear to enhance VEGFR-2-mediated signal transduction (see Ferrara *et al.*, 2003, and references therein). Becker (2005) also suggests a key role for NRP-1 in mediating vascular permeability in response to VEGF-A. VEGF-A also binds to heparan sulphate proteoglycans (HSPGs) on the surface of cells which act as co-receptors.

VEGF-A was first discovered because of its notable effect on vascular permeability (Senger *et al.* 1983) and is now thought to play a major role in inflammation and other pathologies (Ferrara *et al.* 2003). Increased permeability can result in a large influx of water and other macromolecules, including fibrinogen and other clotting proteins, from the vasculature into the interstitial space (Bates and Harper 2002). The associated deposition of fibrin (formed from fibrinogen) in the tumour stroma can cause water retention (contributing to the increase in interstitial pressure observed in tumours), and provides an environment conducive to EC migration. Vascular permeability is enhanced at concentrations of less than 1 nM of VEGF-A and has an effect 50000 times that of histamine (see Dvorak, 2002, and references therein).

VEGF-A directly stimulates EC division and migration. To facilitate migration VEGF-A also stimulates the production of proteins such as MMPs and uPA. Furthermore, VEGF-A is a known survival factor for ECs *in vitro* and *in vivo* (Benjamin *et al.* 1999; Gerber *et al.* 1998); ECs exposed to VEGF-A upregulate the production of proteins such as Bcl-2 (Gerber *et al.* 1998), which prevents apoptosis. VEGF-A also promotes Ang-2 production (Hegen 2004) which contributes to the induction of vessel dematuration. In summary, VEGF-A and its receptors (in particular VEGFR-2) appear to stimulate all essential EC behaviours required for angiogenesis, promoting EC survival, proliferation and migration. It also increases vascular permeability and facilitates ECM remodelling via the production of downstream factors. A more comprehensive review on the role of VEGF-A in angiogenesis is provided by Roskoski (2007).

2.5. The role of bFGF in sprouting angiogenesis

Fibroblast growth factor (FGF) was first extracted from the bovine pituitary and was shown to stimulate division of mouse embryo fibroblast cells (Gospodarowicz 1974). Since then, 22 structurally similar molecules have been identified, varying in mass between 17 and 34 kDa. FGF-1, -2, -4, and -5 are known to possess angiogenic properties (Lieu *et al.* 2011). In fact, it has been suggested that FGF-1 - or acidic fibroblast growth factor (aFGF) - and FGF-2 - or bFGF - may be more potent AFs than VEGF-A or PDGF-B (Cao *et al.* 2003). Both normal and cancerous cell lines express bFGF (Presta *et al.* 1986; Presta *et al.* 2005), as do inflammatory cells. The production and release of FGFs from cells is triggered by shear stress, hypoxia, cell damage and a number of chemicals (see Presta *et al.*, 2005, and references therein). FGFs may also be mobilised from the ECM when it is degraded.

FGFs, in general, act by binding to FGF receptors (FGFR-1-4) on cell surfaces (Lieu *et al.* 2011). Their binding to HSPGs also helps to sequester and stabilise FGF molecules (Lieu *et al.* 2011). Whilst the precise mechanisms of FGF-FGFR signalling remain unknown, it is thought that the formation of FGF-FGFR-HSPG complex dimers and receptor endocytosis have a strong influence on signalling (Murakami and Sakurai 2012). See Presta *et al.* (2005) for an in-depth discussion on the intricacies of FGF binding kinetics and internalisation.

Primarily FGFs, such as aFGF and bFGF, interact with FGFR-1 on ECs, promoting proliferation, migration, protease production and tubular morphogenesis (Javerzat *et al.* 2002) and, through more complex interactions, FGFs (in particular bFGF) are believed to play a role in vessel maturation (Lieu *et al.* 2011; Murakami and Sakurai 2012) and EC survival (Cao *et al.* 2003). FGFs may also influence vascular permeability (Presta *et al.* 2005).

The cross-talk between FGFs and other AFs has been well documented. In particular, bFGF stimulates the expression of VEGF-A in ECs. Experiments by Seghezzi *et al.* (1998) suggest that upon exposure to bFGF, ECs upregulate the production and release of VEGF-A. Additionally, the systemic administration of a VEGF-A antibody had a profound negative effect on bFGF-induced angiogenesis in the cornea micropocket assay (Section 2.9.1). The authors therefore suggest that VEGF-A is an important autocrine mediator of bFGF-induced angiogenesis. In an *in vitro* EC proliferation assay, the addition of an anti-VEGF-A antibody to bFGF-treated human aortic endothelial cells (HAECs) and human umbilical vein endothelial cells (HUVECs) reduced proliferation by 50% and 100% respectively. Thus, Seghezzi *et al.* further suggest that VEGF-A is an important downstream mediator of bFGF-induced mitogenic activity. bFGF may also stimulate the production of VEGF-A in stromal cells (Claffey *et al.* 2001; Tsunoda *et al.* 2007). Additionally, bFGF appears to upregulate the VEGFR-2 expression in ECs (Murakami *et al.* 2011). By contrast, VEGF-A-induced angiogenesis appears to be less affected by FGF signalling inhibition (Presta *et al.* 2005). However, Murakami *et al.* (2011) suggest that basal FGF-signalling may be needed to maintain VEGFR-2 expression.

There is also evidence that EC exposure to bFGF increases expression of Ang-2 (Hegen 2004; Fujii and Kuwano 2010), and thus may indirectly influence vessel dematuration, as in VEGF-A-induced angiogenesis (Sections 2.3.1 and 2.4). bFGF may also collaborate with PDGF-BB[5] to promote the formation of stable and mature vasculature. Cao *et al.* (2003) study the induction of corneal angiogenesis upon exposure to VEGF-A, PDGF-BB and bFGF. Applied individually, VEGF-A, PDGF-BB and bFGF induced modest angiogenic responses. Meanwhile, a marked synergy was evident when bFGF and PDGF-BB were combined; bFGF and PDGF-BB together promoted the growth of mature vasculature which remained stable for over a year. The addition of VEGF-A and bFGF in combination and PDGF-BB and VEGF-A in combination did not result in the formation of stable and mature vasculature. PDGF-BB is produced by immature ECs and induces the recruitment and division of pericyte cells when it binds to PDGF receptor-β (PDGFR-β) receptors on their surface. bFGF appears to increase PDGFR levels on ECs (Nissen *et al.* 2007) and on pericytes (Kano *et al.* 2005). bFGF also potentiates pericyte migration in response to PDGF-BB through other mechnisms (see Murakami and Simons, 2008, and references therein). Independent of PDGF-BB, bFGF appears to stimulate the proliferation of pericytes as well as ECs (Kano *et al.* 2005). Contrasting the results of Cao *et al.*, Kano *et al.* (2005) found that stimulation of angiogenesis in the Matrigel plug assay by bFGF and VEGF-A produces more mature vessels than stimulation by either factor in isolation. Kano *et al.* (2005) suggest that VEGF-A may promote PDGF-BB expression in ECs, while bFGF increases PDGFR-β in mural cells. Thus, bFGF and VEGF-A may act synergystically by enhancing

---

[5] PDGF is actually a dimeric glycoprotein. There are four PDGF ligands, PDGF-A to PDGF-D. PDGF-BB denotes a homodimer between two PDGF-B ligands.

PDGF-BB-PDGFR-β signalling and thus promoting vessel maturation. In this assay, the addition of exogenous PDGF-BB disrupted the formation of mature vessels. The authors suggest that this disruption is due to exogenous PDGF-BB overwhelming the PDGF-BB-gradient established by immature ECs, leading to ineffective migration of pericytes towards immature vessels. bFGF also appears to interact with cell-cell adhesion molecules which may contribute to vessel maturation and dematuration (Presta *et al.* 2005; Murakami and Sakurai 2012).

2.6. Other factors involved in angiogenesis

In this section we review other important factors involved in sprouting angiogenesis, some of which have already been mentioned in the discussion above.

The angiopoietins, Ang-1 and Ang-2, have been mentioned earlier in this chapter within the context of vessel maturation and dematuration. Ang-1 and -2 both bind to Tie-2 receptors (tyrosine kinases with immunoglobulin-like and EGF-like domains) which are specific to ECs. Experimental evidence suggests that Ang-1 plays a major role in ensuring vascular integrity and preventing leakage (Thurston *et al.* 2000). It is expressed by both tumour cells and mural cells, and in normal vessels Ang-1/Tie-2 signalling maintains vessels in a quiescent state by maintaining EC-EC and EC-basement membrane interactions, and inhibiting apoptosis. In the presence of VEGF-A and other pro-angiogenic factors, sprouting ECs release Ang-2, which antagonistically binds Tie-2. This results in mural cell detachment, increases in vascular permeability and permits sprout formation. In the presence of VEGF-A or other pro-angiogenic factors, Ang-2 facilitates EC sprouting and angiogenesis. However, in the absence of VEGF-A, excessive Ang-2 results in vascular regression. Ang-2, indeed, appears to be required for both angiogenic sprouting and vascular regression (Gale *et al.* 2002). It has also been suggested that Ang-2 may activate Tie-2 in some circumstances (Gale *et al.* 2002; Daly *et al.* 2006).

Delta/Notch signalling influences many processes during vascular development. Of particular interest here is its role in tip cell selection during sprouting angiogenesis. Since both Delta ligands and Notch receptors are membrane bound, Delta/Notch signalling requires direct cell-cell interactions. In response to binding of a Delta ligand, such as Delta-like-4 (Dll-4), the extracellular portion of Notch detaches and is endocytosed by the cell from which the Dll-4 ligand originated. The intracellular portion of Notch is eventually transported to the nucleus of the signal receiving cell, where it upregulates the expression of Notch and downregulates Dll-4 (Phng and Gerhardt 2009). This also modifies the expression of other proteins, such as the VEGFR RTKs. In response to VEGF-A/VEGFR-2 binding, ECs upregulate their expression of Dll-4. Adjacent ECs then compete for tip cell position via Delta/Notch signalling, where the EC which produces more Dll-4 than its neighbour eventually becomes the tip cell. In ECs, the cell receiving the Notch signal responds, in part, by decreasing VEGFR-2 expression and increasing VEGFR-1 expression, providing a negative feedback which reinforces the roles of tip and stalk. The assignment of tip or stalk phenotype to an EC is not fixed however; EC fates are subject to change as cells meet new neighbours. See Phng and Gerhardt (2009) for further discussion regarding the effects of Delta and Notch on EC fate and behaviour.

The ECM also plays an important role in sprouting angiogenesis. The major components of the ECM include collagen, fibrillin, fibronectin, laminin and proteoglycans. The basement membranes which surround mature vessels are a specialised form of the ECM, containing mainly laminins, type IV collagen and HSPGs (Mantzaris *et al.* 2004). Several anti-angiogenic molecules, such as endostatin, are sequestered by the ECM (Rundhaug 2005) and, since ECs are usually quiescent while enclosed by a basement membrane, it is thought that the primary signals transmitted from the basement membrane to ECs in normal, mature vessels inhibit proliferation, and promote quiescence and appropriate cell-cell adhesion (Kalluri 2003). However, as noted above, AFs such as VEGF-A and FGF bind to HSPGs. Thus, the ECM is a reservoir of both pro- and anti-angiogenic factors, which may be released when it undergoes proteolytic degradation. It is thought that MMPs, acting alone or with other enzymes, degrade most of the components of the ECM (Ebrahem *et al.* 2010). In cancer, MMPs are produced by the tumour, the stroma and the vasculature. The ECM and, in particular, the basement membrane provide mechanical support for vessel walls. Meanwhile remodelling of the ECM can promote cell migration and proliferation. In addition to matrix bound VEGF-A and FGF, a number of other ECM molecules, including collagen and fibronectin, promote EC survival, growth, migration, and/or tube formation, and thus have pro-angiogenic properties (see Sottile, 2004, and references therein). A comprehensive review of the role of the ECM and MMPs in angiogenesis is provided by Rundhaug (2005).

2.7. Anti-angiogenic chemotherapy and vascular normalisation theory

Conventional chemotherapeutic agents can be divided into two main categories: cell-cycle specific and non-cell-cycle specific. Non-cell-cycle specific drugs act at several or all phases of the cell cycle, whereas cell-cycle specific drugs act only during specific cell cycle phases (Morgan 2003). Although some chemotherapeutic drugs are being developed which target proteins that are over-expressed in cancer cells, most chemotherapeutic agents are indiscriminately cytotoxic, meaning that they kill normal cells and cancerous cells. In particular, cell-cycle specific drugs, whilst particularly effective against rapidly dividing cancerous cells, also seriously affect normal cells which divide rapidly. This results in some of the most common side-effects of traditional chemotherapy: immunosuppression, inflammation of the digestive tract and hair loss.

Since most cytotoxic drugs are administered to cancer patients intravenously, their delivery to tumours, and thus their efficacy, depends on the vasculature around those tumours. In patients receiving conventional systemic chemotherapy, abnormal features of tumour-associated vasculature present a significant barrier to the delivery and efficacy of the intravenously administered cytotoxic drugs (Jain 2001). However, in preclinical studies, an increase in the perfusion of tumours and the overall efficacy of cytotoxic drugs was observed when they were administered with anti-angiogenic drugs, such as bevacizumab (Dickson *et al.* 2007). The rationale behind this combination treatment is that, following administration of an anti-angiogenic drug, immature blood vessels in the tumour vasculature are pruned, blood vessel tortuosity and dilation decrease, and other structural changes occur which cause the tumour vasculature to more closely resemble normal vessels (Goel *et al.* 2011). Overall the tumour vessels post anti-angiogenic treatment have decreased permeability, increased pericyte coverage and overall better perfusion. While this change is transient, it opens up a *window of opportunity* in which drug delivery to tumours may be improved, as has been the conclusion of various clinical trials (see Goel *et al.*, 2011, for a review). By increasing the delivery of chemotherapeutic drugs to a tumour, anti-angiogenic treatments aim to increase the effect of those drugs on tumour growth. With an effective anti-angiogenic treatment, the dose of the chemotherapeutic agent and hence its side-effects could be reduced.

Another consequence of anti-angiogenic therapy is the switch in modes of angiogenesis in and around the tumour from sprouting angiogenesis to intussusceptive angiogenesis (Hlushchuk *et al.* 2011). The onset of intussusceptive angiogenesis appears to contribute to the transient normalisation of the tumour vasculature and thus to the increased availablility of oxygen and drugs to the tumour. The vasculature which remains post anti-angiogenic treatment is more mature and thus more resistant to further anti-angiogenic treatment. Such adaptive mechanisms may contribute to the observed resistance to anti-angiogenic therapies, discussed further in Section 2.8. For a more comprehensive review of intussusceptive angiogenesis and its role in cancer, see Hlushchuk *et al.* (2011).

2.8. Resistance to anti-VEGF-A therapies

Due to VEGF-A's central role in intra-tumoural angiogenesis, initially anti-angiogenic therapies focused on suppressing the VEGF-A/VEGFR-2 pathway. As a result bevacizumab, an antibody which binds VEGF-A, has been approved by the US FDA for use with chemotherapy to treat various cancer types. Since bevacizumab was first approved several other anti-angiogenic agents, principally targeting VEGF-A/VEGFR-2, have been approved for cancer treatment. Currently, combination treatments of chemotherapy with bevacizumab typically prolong the survival of responsive patients by a few months (Carmeliet and Jain 2011). While this may provide precious time to a family affected by cancer, the efficacy of such anti-angiogenic treatments in patients has been underwhelming. Some patients do not respond to anti-VEGF-A therapies and others quickly acquire resistance to such therapies. Moreover, it is a concern that anti-angiogenic treatments may cause some cancer cells to become more aggressive and malignant (Ebos *et al.* 2009).

The prevailing hypothesis is that tumours may adapt to the presence of angiogenesis inhibitors in ways which allow them to continue growing as if unhindered (Bergers and Hanahan 2008). It is thought that a tumour may acquire resistance to anti-VEGF-A therapies in a number of ways. For instance: tumour cells, aggravated by increased hypoxia, may upregulate the production of other pro-angiogenic factors, such as FGF, ephrins and PlGF, resulting in the activation of alternative angiogenic pathways; vascular progenitor cells and pro-angiogenic monocytes may be recruited from the bone-marrow, leading to vessel formation in the absence of VEGF-A; or, tumour cells may become increasingly invasive in order to escape hypoxic regions. For individuals who fail to respond to anti-angiogenic treatment, pre-existing redundancy in activated angiogenic pathways may negate the effect of single-target anti-angiogenic treatments, like bevacizumab. Furthermore, unpredictable excessive vascular pruning in some individuals (and in some tumour types) may actually decrease the delivery of therapeutic agents to the site of a tumour. Other methods of acquired or intrinsic resistance to anti-angiogenic therapies have also been postulated: see Bergers and Hanahan (2008) and Moserle *et al.* (2014) for more details.

To combat this complex and adaptive phenomenon, combination therapies are now being developed. For instance, there has been a focus on developing combination therapies which target both VEGF-A and FGF pathways (Allen *et al.* 2011), and VEGF-A and Ang-2 pathways (Kienast *et al.* 2013). Such combination therapies show promise and are likely to be the focus of much future study.

2.9. Experimental angiogenesis assays

Evidently, angiogenesis is an intricate process which integrates phenomena acting over numerous biological scales and involves many cell types and chemical signalling factors. Moreover, the process becomes even more complex when viewed within the context of a growing tumour, where an imbalance between the tumour's need for energy and the complementary secretion of various AFs can result in pathological vessel formation. Thus, to gain a foothold into understanding the processes underlying angiogenesis and to perform preliminary assessments of the efficacy of anti-angiogenic drugs, simpler and more controllable experimental assays are often used.

Two types of experimental assays are widely used to study angiogenesis and assess the efficacy of anti-angiogenic drugs: *in vitro* assays and *in vivo* assays. Traditionally, *in vitro* assays have been used to determine the behaviour of isolated ECs. They have been used to study cell proliferation, migration and network formation, amongst other things (Staton *et al.* 2009). These assays provide reproducible and controllable environments in which to study elements of the angiogenic process. However, they fail to incorporate the remodelling and stabilisation that occurs once blood begins to flow through the new vasculature (Rogers *et al.* 2007). In order to comprehensively model angiogenesis and incorporate this important feature, whole animal *in vivo* assays are needed. These assays range from angiogenesis in the zebrafish embryo (Rubinstein 2003) and the chick embryo chorioallantoic membrane (Nguyen *et al.* 1994) to angiogenesis in the avascular cornea of the rodent eye (Koch *et al.* 1992). Since the cornea assay forms the focus of work in this thesis, we discuss it in more detail below. Staton *et al.* (2009) should be consulted for a critical review of other assays.

2.9.1. The mouse cornea micropocket assay

The rodent eye angiogenesis assay has undergone significant evolution over the last few decades. In early experiments, non-specific angiogenic stimuli, tumour fragments, were inserted into the stroma of rabbit corneas in order to induce neovascularisation (Gimbrone *et al.* 1974). Later models substituted the tumour fragments for slow-release pellets containing known quantities of, first, semi-purified growth factors from tumour cells and, later, purified specific angiogenic growth factors, such as bFGF and VEGF-A. As more advanced and effective slow-release pellets became available, the transition was made from larger rodents (rabbits and rats) to the smaller, less expensive and more genetically tractable mouse (Kenyon *et al.* 1996; Rogers *et al.* 2007).

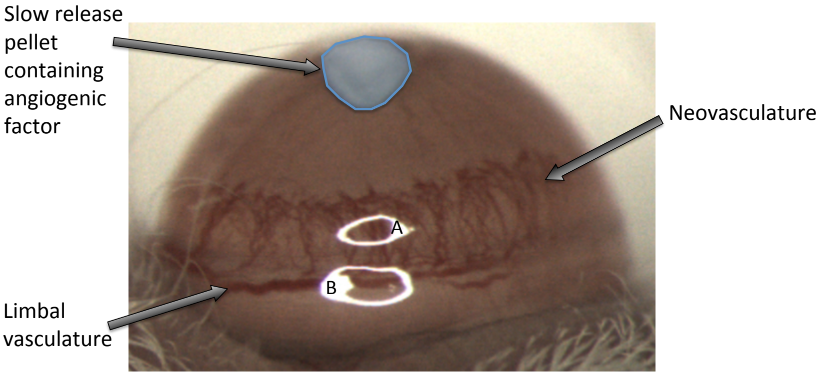

Figure 2.3.: Schematic of the mouse corneal micropocket assay. A pellet containing an AF is placed inside a surgically created micropocket. The subsequent release of AF from the pellet, diffusion through the corneal stroma, and uptake by ECs induces vessel growth from the limbal vessels towards the pellet. A and B are artefacts due to camera lighting. Image courtesy of Erica Lorenzon (Roche, Penzberg).

At present, this assay typically involves the insertion of an AF-containing, slow-release pellet into the stromal layer of a mouse cornea. The cornea is composed of five discrete layers. The two layers which constitute the largest portion of the cornea are the epithelium and the stromal layer which, in mice, are approximately 50 μm and 100 μm thick, respectively (Zhang *et al.* 1996; Song *et al.* 2003). In this assay, extreme care is required in order to make an initial, vertical, partial incision into the stroma. This initial incision is extended perpendicular to the stromal layer boundaries to create a pocket. The pellet is then placed on top of the cornea and slid inside the pocket. Pellets containing VEGF-A are typically placed approximately 1 mm from the limbal vessels (Rogers *et al.* 2007), a set of vessels encircling the cornea with a circumference of approximately 9.6 mm in mice. However, the exact concentrations of AF, the dimensions of pellets and the distance that they should be placed from the limbal vessels are generally optimised on an experiment-by-experiment basis.

Whilst their composition often varies, pellets usually contain a mixture of a slow-release polymer, for example Hydron or polyhydroxyethylmethacrylate (poly-HEMA); sucralfate, which acts to stabilise large growth factors or to maintain bulk and texture for pellets containing smaller molecules which do not require stabilisation; and the AF itself. Figure 2.3 summarises the experimental model set-up. After insertion, the AF is slowly released into the surrounding stroma and then diffuses throughout the entire corneal area. Upon reaching the limbal vessels, the AF stimulates the sprouting of new vessels which grow towards the pellet over the following days. This phenomenon is observed over a period of approximately one week, after which the angiogenic effect of the AF is recorded, usually by measuring the circumferential neovascularisation and the maximal vessel length, or the area of neovascularisation.

The visibility and normally avascular nature of the cornea provide distinct advantages over other *in vivo* angiogenesis assays and, as such, cornea-based experiments often form an integral part of pre-clinical drug trials. The approach is often used by research institutions, including Roche, to confirm the potency of AFs and the efficacy of candidate anti-angiogenic drugs (Thomas *et al.* 2013). Additionally, the cornea assay has been used to investigate potential synergies between combinations of AFs (Cao *et al.* 2003). In fact, it has been estimated that more than one third of our basic knowledge concerning the formation of blood vessels originates from corneal models (Chen *et al.* 2011).

2.10. Discussion

Angiogenesis is a complex process which operates over multiple biological time and length scales and involves many different cell types and chemical species. It is a key and inevitable event in the development of large and malignant vascularised tumours. The recent expansion in angiogenesis research has increased knowledge about the processes underlying angiogenesis and stimulated the development of promising anti-angiogenic therapies for cancer treatment. However, substantial gaps in knowledge persist and the development of effective treatments against pathological angiogenesis in diseases like cancer remains a major challenge.

Due to its complex, multiscale nature, developing a quantitative understanding of angiogenesis, which is required for the development of effective therapies, necessitates the use of mathematical and computational approaches. Mathematical models represent an inexpensive, complementary approach to *in vivo* and *in vitro* experiments, providing a method by which to bridge biological theory and experiments. They can be used to both test and generate biological hypotheses and therefore may help guide future wet-lab research. In the longer term, mathematical models may be used to reduce the number of animals used in pre-clinical drug trials.

The primary objective of this thesis is to develop a mathematical and computational toolset which may help us understand the complex biology that underlies tumour angiogenesis. In the next chapter we will review mathematical models which have already provided insight into angiogenesis. Some of these models will provide a basis for the models that we will develop later in the thesis. Our work will focus on *in silico* models of angiogenesis in the cornea, which itself is used as an *in vivo* model of intra-tumoural vascular growth. We will focus on angiogenesis occurring in response to VEGF-A and bFGF only. Some of the biological processes outlined in this chapter will be incorporated explicitly into our models (to varying degrees of complexity) while others will be accounted for implicitly or, indeed, entirely neglected. The material covered in this chapter provides appropriate context for our modelling work, as well as demonstrating that intra-tumoural angiogenesis is a fertile ground for future mathematical modelling endeavours.

CHAPTER 3

Review of Mathematical Models of Angiogenesis and Tumour Growth

3.1. Overview

As noted in Chapter 1, the use of mathematical models to provide insight into various aspects of tumour growth began to gain traction several decades ago. Since then, as our knowledge of cancer biology has expanded through dedicated experimental research in the wet-lab, and as our understanding of cancer as a complex and multiscale system has evolved, so have the mathematical approaches used to model this system.

In this thesis we will focus on developing mathematical models which to varying extents emphasise the spatial structure of the vasculature associated with a tumour. As such, in this chapter we review two pertinent approaches which have been used to study the mechanisms underlying tumour-induced angiogenesis and vascular tumour growth: continuum and discrete (or hybrid) approaches. First, we consider continuum modelling methodologies as a basis for the development of our own continuum models of angiogenesis in the mouse cornea micropocket assay (presented in Chapters 5 and 6). Secondly, we turn our attention to discrete and hybrid modelling approaches. We review a number of hybrid models of angiogenesis in the cornea and several notable families of hybrid multiscale models of vascular tumour growth. One such family of models, developed by Alarćon and co-workers (Alarcón *et al.* 2003; Alarcón *et al.* 2005; Alarcón *et al.* 2006; Betteridge *et al.* 2006; Owen *et al.* 2009; Perfahl *et al.* 2011), has motivated us to build an object-oriented computational framework in which such models may be implemented and easily extended. This computational framework is presented in Appendix C. The models of Alarćon and co-workers also provide the basis for the development of our own hybrid model of corneal angiogenesis, presented in Chapter 7.

For brevity, details of the mathematics that underpin the model implementations are not repeated here; more comprehensive descriptions may be found in the original papers and in extensive reviews (Mantzaris *et al.* 2004; Peirce 2008; Qutub *et al.* 2009; Scianna *et al.* 2013).

3.2. Continuum modelling methodologies

Continuum models of angiogenesis and cancer are generally founded on the laws of conservation of mass and mass action. They typically describe a tissue in terms of averaged densities of cells, vessels and molecules, and may comprise systems of ordinary differential equations (ODEs) or partial differential equations (PDEs). In this work we will focus on spatially-resolved, PDE approaches to modelling angiogenesis.

Advection-reaction-diffusion PDE models describe the spatiotemporal evolution of concentrations of molecular species and cell densities. Such models are based on the law of mass conservation which assumes that for each model species, a_i, the following balance holds true:

$$\left(\begin{array}{c}\text{rate of accumulation}\\ \text{of species } \mathsf{a_i}\\ \text{inside control volume}\end{array}\right) = \left(\begin{array}{c}\text{net flux of } \mathsf{a_i}\\ \text{into control volume}\end{array}\right) + \left(\begin{array}{c}\text{net production}\\ \text{rate of } \mathsf{a_i} \text{ within}\\ \text{control volume}\end{array}\right). \tag{3.1}$$

In mathematical terms, a continuum model of the type described by (3.1) is defined in general by the following set of equations:

$$\begin{aligned}
\frac{\partial \rho_1}{\partial t} &= -\nabla \cdot \mathbf{J}_1 + g_1(\rho_1 ... \rho_n, a_1 ... a_m), && (3.2)\\
&\vdots \\
\frac{\partial \rho_n}{\partial t} &= -\nabla \cdot \mathbf{J}_n + g_n(\rho_1 ... \rho_n, a_1 ... a_m), && (3.3)\\
\frac{\partial a_1}{\partial t} &= D_1 \nabla^2 a_1 + f_1(\rho_1 ... \rho_n, a_1 ... a_m), && (3.4)\\
&\vdots \\
\frac{\partial a_m}{\partial t} &= D_m \nabla^2 a_m + f_m(\rho_1 ... \rho_n, a_1 ... a_m), && (3.5)
\end{aligned}$$

where $\rho_i(\mathbf{x}, t)$ $(i = 1...n)$ are the densities of vessels or cellular species, such as ECs or pericytes, $a_j(\mathbf{x}, t)$ $(j = 1...m)$ are the concentrations of (diffusible) molecular species, D_j $(j = 1...m)$ are the assumed constant diffusion coefficients for each molecular species and g_i $(i = 1...n)$, f_j $(j = 1...m)$ represent the net source terms for each species. The fluxes, $\mathbf{J}_i$ $(i = 1...n)$, typically contain terms associated with random motion, chemotaxis (directed motion in response to a chemical stimulus) and haptotaxis (directed motion usually up a gradient of cellular adhesion sites or substrate-bound chemoattractants), such as:

$$\mathbf{J}_i = \underbrace{-\mu_i \nabla \rho_i}_{\text{random motility}} + \underbrace{\chi_c \rho_i \nabla c}_{\text{chemotaxis}} + \underbrace{\chi_h \rho_i \nabla h}_{\text{haptotaxis}}, \tag{3.6}$$

where μ_i is the random motility coefficient, χ_c is the chemotaxis coefficient, and χ_h is the haptotaxis coefficient, all of which may be constant or dependent on local chemical concentrations. c is the concentration of a chemoattractant and h, here, we suppose is the concentration of some component of the ECM (e.g. fibronectin).

Continuum mathematical models of angiogenesis date back to Deakin (1976), who published a model in which ECs migrated in response to a generic TAF, leading to capillary loop formation. A decade later Balding and McElwain (1985) conceived a model of angiogenesis in the cornea which was based on an earlier model of fungal growth (Edelstein 1982). Balding and McElwain's model contained equations of the form (3.2)-(3.5). An attractive feature of their model was that it distinguished between tip cells and stalk cells. It is formulated on a semi-infinite 1-D Cartesian geometry with PDEs for the density of tip cells, capillary sprouts and a generic TAF. Crucially, capillary sprout density is assumed to increase in response to the migration of tip cells only, in an approach which is now known as the snail-trail approach (see Section 3.2.1 for more details).

Chaplain and Stuart (1993) developed the model of Balding and McElwain, including additional sink terms to model TAF uptake by ECs and posing the model on a finite domain. However, Chaplain and Stuart (1993) did not distinguish tip cells and stalk cells, instead modelling the vasculature as a population of generic ECs. Later, Byrne and Chaplain (1995) combined ideas from the models of Balding and McElwain (1985) and Chaplain and Stuart (1993), adopting the snail-trail approach to model vascular growth, posing the model on a finite domain and incorporating terms to model TAF uptake by ECs. Following Byrne and Chaplain's model there was a rapid increase in the rate of development of subsequent mathematical models of angiogenesis, many of which have incorporated a variant of the snail-trail approach. For example, Pettet *et al.* (1996a; 1996b) used the same approach to model angiogenesis in wound healing, incorporating additional equations for fibroblast density, ECM density and oxygen concentration. Other similar models of angiogenesis in wound healing have also been developed (Byrne *et al.* 2000; Gaffney *et al.* 2002; Schugart *et al.* 2008), meanwhile Panovska *et al.* (2007) adapted the model of Byrne and Chaplain (1995) to model vascular tumour growth. Such models, while unable to reproduce the detailed morphology of the developing vasculature, exhibit many of the characteristic features of angiogenesis and can predict the behaviour of quantities such as vessel and tip cell densities and the rate of vascular growth.

The continuum models of angiogenesis mentioned above do not do justice to the many and varied continuum models which have been published. Noteworthy are the models of Swanson and co-workers (see Hawkins-Daarud *et al.*, 2013, and references therein), which have been applied to the growth and treatment of gliomas, given patient specific data and patient specific geometries. The variety of continuum models of angiogenesis is testament to the extensibility of the general framework set out in (3.2)-(3.5). For an exhaustive review of continuum models of angiogenesis see Scianna *et al.* (2013).

In Chapters 5 and 6 we adapt and extend Byrne and Chaplain's model of angiogenesis in the cornea. Thus, in the remainder of this section we review this model in more detail.

3.2.1. Byrne and Chaplain's model of corneal angiogenesis

Byrne and Chaplain (1995) developed a continuum model of corneal angiogenesis which describes the spatiotemporal evolution of tip cells and vessel sprouts in response to a generic TAF released from a tumour implanted into the cornea. The governing equations were of the form (3.2)-(3.5), where a 1-D Cartesian geometry was assumed. In this model tip cells move by a combination of chemotaxis and random motion. While vessel sprouts are assumed to be static, their production is related to how tip cells move. More specifically, as a tip cell migrates it is assumed to leave behind it a trail of stalk cells, which form the body of a sprout. This is the snail-trail approach. The main assumption is that the length of vessels produced in a control volume per unit time is proportional to the number of tip cells leaving that control volume per unit time (see Figure 3.1).

Tip cells are produced in two ways. Primarily, tips form from the body of vessel sprouts when stimulated by the presence of a TAF. Byrne and Chaplain also postulate the existence of a secondary sprouting mechanism in which tip cells are assumed to proliferate in high concentrations of the generic TAF. Such a secondary mechanism was introduced to phenomenologically account for the formation of the brush border (Muthukkaruppan *et al.* 1982), characterised by a dense distribution of vessels at the leading front of the vasculature. Capillary sprouts are assumed to regress at a constant rate, and tip cells are annihilated when they anastomose with vessels (tip-to-tip anastomosis and tip death are neglected). Finally, the boundary at $x = 0$ is identified with the edge of a tumour and is assumed to continuously release a TAF into the cornea. The TAF is taken up by tip cells and decays naturally as it diffuses towards the limbus (at $x = L$), at

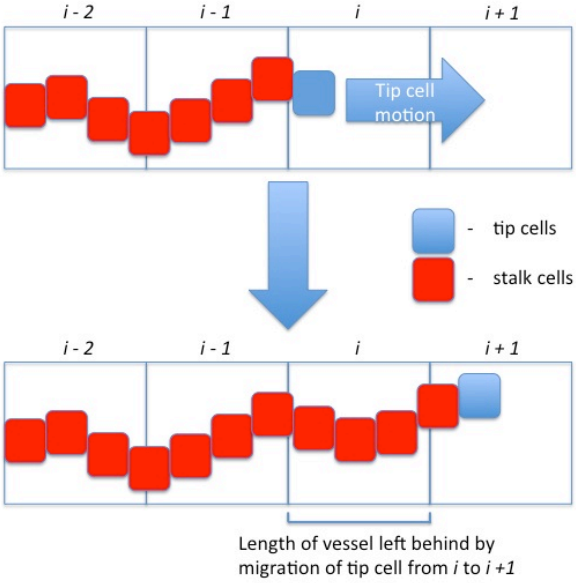

Figure 3.1.: Schematic of the *snail-trail* approach. As a tip cell moves from one location to the next it leaves in its wake a length of vessel.

which the concentration of the TAF is assumed to be equal to zero.

In summary, the dimensionless equations for tip cell density, $n(x,t)$, measured in units of number of tips per unit area in the cross-sectional plane perpendicular to front propagation, vessel density, $\rho(x,t)$, measured in units of length per unit cross-sectional area, and the TAF concentration, $a(x,t)$, measured in units of mean concentration per unit of cross-sectional area, are as follows:

$$\frac{\partial n}{\partial t} = \frac{\partial}{\partial x}\left(\underbrace{\mu\frac{\partial n}{\partial x}}_{\text{random motion}} - \underbrace{\chi n\frac{\partial a}{\partial x}}_{\text{chemotaxis}}\right) + \underbrace{\alpha_0\rho a}_{\substack{\text{primary}\\ \text{sprouting}\\ \text{mechanism}}} + \underbrace{\alpha_1 H(a-\hat{a})na}_{\text{tip cell proliferation}} - \underbrace{\beta n\rho}_{\substack{\text{tip}-\text{vessel}\\ \text{anastomosis}}}, \tag{3.7}$$

$$\frac{\partial \rho}{\partial t} = \underbrace{\mu\frac{\partial n}{\partial x} - \chi n\frac{\partial a}{\partial x}}_{\text{snail}-\text{trail}} - \underbrace{\gamma\rho}_{\text{regression}}, \tag{3.8}$$

$$\frac{\partial a}{\partial t} = \underbrace{\frac{\partial^2 a}{\partial x^2}}_{\text{diffusion}} - \underbrace{\lambda a}_{\text{natural decay}} - \underbrace{\alpha_1 H(a-\hat{a})na}_{\text{uptake by tip cells}}. \tag{3.9}$$

These equations are subject to the boundary conditions

$$\rho(1,t) = \rho_{min} + (1-\rho_{min})e^{-kt}, \quad n(0,t)=0, \quad n(1,t) = n_L e^{-kt}, \tag{3.10}$$

$$a(0,t) = 1, \quad a(1,t) = 0,$$

and the initial conditions

$$\rho(x,0) \;=\; \delta(1), \quad n(x,0) = n_L\delta(1), \quad a(x,0) = \delta(0), \tag{3.11}$$

where $\delta(a) = 1$ for $x = a$ and $\delta(a) = 0$ for $x \neq a$. In (3.7) and (3.9), $H(...)$ is the Heaviside step function. A list of model parameters and their descriptions is provided in Table 3.1. We remark that the snail-trail vessel growth term in (3.8) is given by $-\,J_n = \mu\frac{\partial n}{\partial x} - \chi n\frac{\partial a}{\partial x}$.

Byrne and Chaplain apply boundary conditions (see Equation 3.10) at the limbus, in which the concentration of tip cells (and vessels) there decay exponentially in time. These boundary conditions elegantly sidestep the onset of angiogenesis in the cornea but offer no explanation why tip cell production at the limbus ceases a short time after angiogenesis is initiated. Additionally, the concentration of tip cells at the tumour boundary is fixed at zero, limiting the model's validity to the time before the migrating front of tip cells reaches the tumour.

To gain insight into the phenomena involved in their model, Byrne and Chaplain developed a caricature model by making several simplifications to (3.7)-(3.11). Firstly, since both numerical results and dimensional analysis suggested that the TAF rapidly relaxes to its steady state, the authors considered the TAF distribution to be at steady state. Then, by neglecting TAF consumption by tip cells they obtained an analytic expression for the steady state profile of a which decouples from the other model species:

$$a(x) = \frac{\sinh\left(\sqrt{\lambda}\,(1-x)\right)}{\sinh\left(\sqrt{\lambda}\right)}. \tag{3.12}$$

In order to proceed, a further simplification was made; in (3.7) and (3.8) the random motility of tips, μ, was set to zero. Using the method of characteristics to construct analytical expressions for tip cells and sprouts, the authors showed that the ability of the vasculature to successfully reach the tumour is governed by the balance between the 'proliferative parameter grouping' $\frac{\alpha_1}{\chi}$ and several 'death' parameters, including $\hat{a}$ and $\frac{\beta}{\gamma}$. Moreover, their analysis predicts that the tip cell wave-speed is given by

$$\frac{dx}{dt} = \chi\frac{da}{dx} = -\frac{\chi\sqrt{\lambda}\cosh\left(\sqrt{\lambda}\,(1-x)\right)}{\sinh\left(\sqrt{\lambda}\right)}, \tag{3.13}$$

Parameter	Description
μ	Tip cell random motility coefficient.
χ	Tip cell chemotaxis coefficient.
α_0	Primary tip sprouting rate.
α_1	Rate of tip proliferation.
β	Anastomosis rate.
$\hat{a}$	Concentration of TAF above which tip proliferation is activated.
γ	Rate of vessel regression.
λ	Natural decay rate for TAF.
ρ_{min}	Minimum density of vasculature at the limbus.
n_L	Initial concentration of tip cells at the limbus.
k	Rate at which tip and vessel densities decay to zero at the limbus.

Table 3.1.: Description of model parameters for the Byrne and Chaplain (1995) model of corneal angiogenesis.

which, given appropriate estimates for the chemotactic sensitivity, χ, produces results which are qualitatively consistent with experimental measurements, showing tip velocities increasing as the vascular front approaches the tumour boundary.

To provide context for their analytical investigations Byrne and Chaplain also simulated their model numerically. Through numerical simulation the authors were able to show that the model correctly predicts: i) the qualitative effect of increasing the TAF decay rate on corneal vascularisation; ii) the localisation of increased vessel density behind a moving front of vessel tip cells; and iii) a pronounced brush-border effect (Muthukkaruppan *et al.* 1982), given the presence of some secondary tip cell proliferation mechanism.

3.2.1.1. Summarising comments

Byrne and Chaplain's model was developed with simplicity in mind to permit in-depth analysis and to establish qualitative agreement with experimental results. For example, linear kinetic terms were used to model tip cell creation in response to the TAF. Although unlikely to be biologically realistic, such linear terms render the governing equations more analytically tractable than, for example, Michaelis-Menten reaction kinetic terms. There is much scope for adapting and extending the model and making it more compatible with what is now known about the biology underlying angiogenesis. Some such model extensions have been proposed in other models for various applications. More recently, an in-depth analysis of the snail-trail term in (3.8) reveals that the associated rate of vessel production may more realistically be captured by assuming that the rate of vessel production is proportional to the absolute value of tip cell flux, $|J_{tip}|$, rather than $-J_{tip}$ (Spill *et al.* 2014).

It is unclear whether, in such 1-D models of corneal angiogenesis, Cartesian or cylindrical co-ordinates are more appropriate. If the tumour (or other source of AF) is placed centrally in the cornea, cylindrical co-ordinates may be more appropriate. Cylindrically symmetric geometries have been used in models of angiogenesis in wound healing (see, for example, Byrne *et al.*, 2000). However, if the source of AF is not placed centrally (as in this thesis) symmetry is broken. Preliminary investigations performed by the candidate using the model of Byrne and Chaplain (1995) showed that if cylindrical symmetry is assumed then the simulation results are similar to those obtained for a Cartesian geometry if appropriate changes in parameter values are made.

3.3. Discrete and hybrid modelling approaches

Continuum models are typically only valid when they describe the average behaviour of large numbers of individuals. As the number of individuals in a population decreases, the validity of the continuum model becomes compromised. In such situations, the behaviour of individuals must be modelled explicitly. Unlike continuum models, discrete models in which cells and vessels are treated as individuals can accommodate highly heterogeneous structures. They permit the inclusion of subcellular, cell-cell and cell-microenvironmental interactions. Moreover, they allow for direct, quantitative comparison of simulated vascular networks with experimental data. However, as these models become increasingly detailed, their simulation becomes increasingly computationally expensive. At present, this limits models of this type to relatively small numbers of cells and short time-scales.

Individual cells and vessels may be modelled using either on- or off-lattice techniques. On-lattice models constrain individual entities to lie on a regular lattice, whereas off-lattice models allow continuous movement through space. Most discrete models of angiogenesis and cancer to date are on-lattice models; they are typically easier to implement than their off-lattice counterparts but they restrict the directions in which a cell, for example, may move, and the ways in which cells may communicate with their neighbours. Examples of on-lattice approaches that have been used to model tumour growth and angiogenesis include cellular automata (Owen *et al.* 2009) and cellular Potts models (Shirinifard *et al.* 2009). Meanwhile, off-lattice models may be either vertex-based (Walter 2009) or cell-centre based (Jeon *et al.* 2010). See Rejniak and Anderson (2010) for a review of these discrete modelling techniques as they relate to tumour growth.

Many discrete models may more accurately be termed *hybrid* models. This is because some biological phenomena are incorporated using discrete techniques whilst others are incorporated using a continuum approach. Many hybrid models of intra-tumoural angiogenesis treat cells and vessels as discrete entities and associate with them sub-cellular models which dictate cell/vessel behaviour in response to microenvironmental cues (Owen *et al.* 2009; Welter *et al.* 2009). The sub-cellular models may be, for example, stochastic (Bartha and Rieger 2006) or based on deterministic ODEs (Alarcón *et al.* 2005; Owen *et al.* 2011). Moreover, cells and vessels may interact with each other directly or indirectly via tissue-scale chemical (Stephanou *et al.* 2006; Owen *et al.* 2009) or mechanical fields, e.g. interstitial pressure (Soltani and Chen 2013), which are modelled in the continuum, using PDEs.

Given the complex and multiscale nature of cancer, to generate quantitative results and to uncover novel cross-scale biological mechanisms, it is often argued that multiscale modelling approaches are needed (Deisboeck *et al.* 2011). Hybrid models are ideally suited to multiscale modelling applications. And, although these models are unlikely to bridge all scales, hybrid models can span several scales both above and below the fundamental unit of the cell (Rejniak and Anderson 2010).

Many hybrid models of vascular tumour growth and angiogenesis have been developed in an attempt to better understand how a tumour interacts with its macro- and micro-environment, both of which influence its growth and response to treatment. We now briefly review several notable multiscale hybrid models of angiogenesis and vascular tumour growth.

3.3.1. Hybrid multiscale models of angiogenesis

We partition our review into two sections. First, we review several hybrid models of corneal angiogenesis. Secondly, we review several notable families of hybrid models of vascular tumour growth, focusing on their general structure. By extracting the main features and components of these models, we are able to understand what sub-models and components should be incorporated into a computational framework for simulating multiscale models of angiogenesis and vascular tumour growth. We include within this review the work of Alarcón and co-workers, whose models form the basis for the object-orientated modelling framework presented in Appendix C.

3.3.1.1. Hybrid models of corneal angiogenesis

One of the first discrete models of angiogenesis was that of Stokes and Lauffenburger (1991). They modelled the sprouting, growth and anastomosis of vessels in a two-dimensional Cartesian domain and assumed that the path of each new vessel could be determined solely by the behaviour of a tip cell, which migrates with velocity $\mathbf{v_i}$. The velocity of each tip cell, $\mathbf{v}_i$, evolves according to a stochastic ODE:

$$\underbrace{d\mathbf{v}_i(t)}_{\text{change in velocity}} = \underbrace{-\beta\mathbf{v}_i(t)dt}_{\text{resistance to motion}} + \underbrace{\sqrt{\alpha}\,d\mathbf{W}_i(t)}_{\text{random motion}} + \underbrace{\kappa\nabla a\sin\left|\frac{\phi_i}{2}\right|dt}_{\text{chemotactic bias}}, \tag{3.14}$$

where β is a decay rate of the current velocity, α dictates how random the motion of a tip cell is, κ is the chemotactic responsiveness, ∇a is the gradient of the chemoattractant, $a(x,y)$, and ϕ_i is the angle between the direction of tip migration and that of the source of the chemoattractant (see Figure 3.2). $\mathbf{W}_i$ is a Wiener process, a continuous-time stochastic process with zero mean and variance dt, that accounts for the randomness associated with tip cell motion. Notably, the tip cell velocity is not affected by mechanical attachment to other cells in the sprout, which it is assumed are deposited directly behind the path of the tip cell. Thus, it is principally the behaviour of the tip cell which affects the growth of each sprout. This approach may be viewed as a discrete version of the snail-trail model of vascular growth proposed by Balding and McElwain (1985). By incorporating appropriate rules for sprouting and anastomosis the authors generated discrete vascular networks which are similar to those seen *in vivo*. By prescribing a fixed chemotactic gradient, the authors showed that a moderate chemotactic response was required to stimulate directed growth towards the source of the chemoattractant, and that a significant degree of random motility was required to ensure anastomosis formation. The model predicts that in the absence of a chemotactic stimulus, random motion, in combination with sprouting which is initially biased towards the source of chemoattractant, is not sufficient to drive directed growth.

Another breakthrough in modelling angiogenesis, the so-called discrete-continuous approach, was presented by Anderson and Chaplain (1998). They developed a model in which tip cells perform a biased random walk up gradients of a TAF and fibronectin. To develop their discrete model of tip cell motion they first consider a reaction-diffusion model of EC motility, which incorporates random motion, chemotaxis and haptotaxis. The governing equations for the density of ECs, n, the concentration of TAF, c, and the concentration of fibronectin, f, are given by:

$$\frac{\partial n}{\partial t} = \underbrace{D_n\nabla^2 n}_{\text{randommotility}} - \underbrace{\nabla.\left(\chi(c)n\nabla c\right)}_{\text{chemotaxis}} - \underbrace{\nabla.(\rho_0 n\nabla f)}_{\text{haptotaxis}}, \tag{3.15}$$

$$\frac{\partial f}{\partial t} = \underbrace{\omega n}_{\text{production}} - \underbrace{\mu n f}_{\text{uptake}}, \tag{3.16}$$

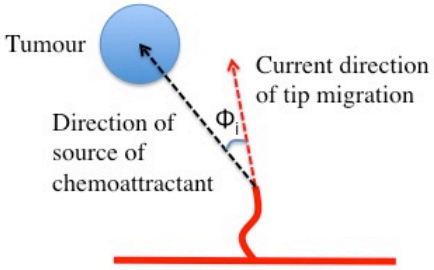

Figure 3.2.: Diagram showing the angle ϕ_i, as defined by Stokes and Lauffenburger (1991). ϕ_i is the angle between the direction of tip migration and that of the tumour.

$$\frac{\partial c}{\partial t} = -\underbrace{\lambda nc}_{\text{uptake}} . \tag{3.17}$$

Here, D_n is the random motility coefficient of tip cells, $\chi(c)$ is the chemotactic coefficient, ρ_0 is the haptotactic coefficient, ω and μ represent production and uptake rates of fibronectin, respectively, and λ is the uptake rate of the TAF. Anderson and Chaplain then discretised (3.15)-(3.17), using standard finite-difference methods. That is, they decomposed the two-dimensional domain upon which the model is based into a regular grid, or lattice, with distance h between lattice sites. The lattice sites (x, y) are then given by $x = lh$, $y = mh$, where $l, m \in \mathbf{Z}^+$. Time, t, is also discretised in increments of length k such that $t = qk$, where $q \in \mathbf{Z}^+$. Using the standard five-point finite-difference stencil (Strikwerda 2004) results in a discretised equation for the ECs of the form:

$$n_{l,m}^{q+1} = n_{l,m}^{q} P_0 + n_{l+1,m}^{q} P_1 + n_{l-1,m}^{q} P_2 + n_{l,m+1}^{q} P_3 + n_{l,m-1}^{q} P_4, \tag{3.18}$$

where the functions P_0, ..., P_4 depend on the fibronectin and TAF concentrations near the lattice site, (l, m). At each time step, P_0, ..., P_4 are interpreted as being proportional to the probabilities that a tip cell at (x, y), or (l, m), on the discrete lattice remains where it is (P_0), or moves left (P_1), right (P_2), up (P_3), or down (P_4). As in Stokes and Lauffenburger (1991), a key assumption made by Anderson and Chaplain is that it is the motion of the tip cell which governs the evolution of the entire sprout. As a tip cell moves, it deposits behind it a vessel segment. When coupled to simple discrete rules for vessel branching and anastomosis, the tip cell movement model presented by Anderson and Chaplain generates vascular networks qualitatively similar to those seen in cornea experiments. The method adopted by Anderson and Chaplain, which may be considered to be an extended type of cellular automaton model, is easily extendible to consider vascular growth in 3-D (for example, see Stephanou *et al.*, 2005). Such lattice-based methods may also be extended to consider diagonal tip cell motion, which gives rise to vascular networks which are more verisimilitudinous.

Tong and Yuan (2001) developed the first hybrid model to investigate how the concentrations of AFs and growth of the vascular networks influence each other; earlier angiogenesis models assumed the concentration of AFs to be fixed (Stokes and Lauffenburger 1991; Anderson and Chaplain 1998). Their model was based on experimental work by Kenyon *et al.* (1996) and Polverini *et al.* (1991) in which bFGF was released from a pellet into the cornea. For simplicity, the authors assumed that the concentration of free bFGF in the pellet remained at a small, constant value throughout their simulations. Tong and Yuan approximated the cornea to be a flat circular disc, located centrally on a square model domain. The model incorporated the diffusion of bFGF, natural decay and uptake by ECs, the formation of vessel sprouts and their subsequent growth and anastomosis. The authors adopted a snail-trail based circular random walk model for tip cell migration, where the random element was used to implicitly account for dynamic changes in the structure of the ECM near the tip of a migrating sprout. While the model reproduced the experimentally observed brush border effect, the tip migration speeds observed in experiments and generated neovasculature only on the inferior limbus, discrepancies were observed in the timing of the onset of angiogenesis. These discrepancies were attributed to sprouting occurring instantaneously after exposure to bFGF; in practice, sprouting is not instantaneous. While an improvement over existing models, the biological accuracy of the model was relatively weak and several key aspects of vascular remodelling were neglected; in general, linear reaction-kinetic and exponential activation terms were used throughout and structural adaptation, pruning and maturation of vessels were neglected.

In 2008, Tong and Yuan revisited their corneal angiogenesis model, making several significant improvements (Tong and Yuan 2008b). Their 2008 model represents the best attempt to model accurately how a TAF distribution responds to the presence of ECs and, to the best of our knowledge, is the only model of angiogenesis to consider explicitly the dynamic binding and release of a TAF from pellets, such as those used in modern cornea micropocket assay experiments. Additionally, although the authors maintained the circular random walk framework for vascular growth, Michaelis-Menten type reaction kinetics were used to model activation levels of ECs, allowing for a more biologically motivated parametrisation. The authors used this model to simulate the growth dynamics of corneal vascular networks and the spatial and temporal distribution of bFGF, which could not be measured experimentally. The dose response of angiogenesis to bFGF was simulated and compared with complementary *in vivo* experiments. They analysed experimental images at a single time-point, exploiting a semi-automatic method for segmenting vascular networks (Thackray and Nelson 1993), and compared the location of the vascular front and total vessel length in experiments and simulations with some success. Through simulation, the authors concluded that the accurate coupling between diffusion and cellular uptake of a TAF is critical for determining the structures of vascular networks. They also identified a mechanism for self-adaptive regulation which may help to maintain the structural stability of vascular networks; the uptake of bFGF by ECs could lead to rapid clearance of bFGF from vascularised regions, so that the advancing vascular front would form an effective barrier against the transport of bFGF and contribute to the formation of a brush border. Despite its many successes, this model neglects the effects of blood flow on vascular remodelling and structural adaptation.

More recently, Jackson and Zheng formulated two models to study the roles of EC proliferation, elongation and migration in corneal angiogenesis and to investigate the effect of alternative therapies on vascular growth. Their cell-based model (Jackson and Zheng 2010) integrates a mechanical model of cell elongation with a biochemical model for maturation, regulated by local concentrations of Ang-1 and Ang-2. They simulate the growth and maturation of capillary sprouts in the rat cornea where angiogenesis is stimulated by the presence of VEGF-A, released from a region of cauterised tissue. As in Tong and Yuan (2008b), Jackson and Zheng view the cornea as a flat, 2-D circular disc and, for simplicity, maintain VEGF-A at a constant concentration inside the cauterised lesion. The model contains a visco-elastic spring model for ECs inside a sprout and individual sprouts were considered to be composed of ECs of two different phenotypes: tip cells and stalk cells. The tip cells migrate in response to a chemotactic force, and are able to drag the trailing sprout a small distance, which is limited by the elasticity of cells. If a new stalk cell is born or if a new stalk cell is added to the growing sprout from the parent vessel, the tip cell can drag the sprout further forwards but only by a finite distance. In this way, this model explicitly accounts for the effect of stalk cell proliferation and migration on sprout growth, ensuring that sprouts can only extend by a limited amount in the absence of proliferation.

Maturation is included in this model following the approach developed by Plank *et al.* (2004). The explicit cell-level representation of vessels, combined with this mechanistic model of maturation, allowed the authors to investigate where in growing sprouts proliferation was most likely to occur. Their results indicated that maturation combined with the bioavailability of VEGF-A can explain why cells at the leading edge of growing sprouts proliferate more rapidly than cells behind them. This result is consistent with experiments in which proliferation was localised to the leading edge of developing sprouts (Sholley *et al.* 1984). The authors also accounted for the effects of X-ray irradiation, Ang-2 inhibition and extracellular anisotropy on sprout morphology and extension speed.

As an extension to their cell-based model of sprout growth, Jackson and Zheng also developed a continuum visco-elastic model of sprout extension (Zheng *et al.* 2013). They consider the growth and maturation of individual sprouts of zero width on a square 2-D geometry, where sprout formation, chemotaxis and blood flow are ignored. In contrast to their previous work, all components of growing sprouts (cells included) are modelled as continuously varying densities along the length of a sprout. This allows for greater model flexibility and the inclusion of additional biochemical mechanisms within the model at minimal computational cost. An important new feature of this model is that immature vessels regress if VEGF-A levels are too low. This allows the authors to study vessel regression in response to the application of both individual and combination therapies.

In Zheng *et al.* (2013), the effect of VEGF-A and Ang-1 and Ang-2 on EC proliferation, migration and maturation is considered, as is the effect of PDGF-B on the proliferation and migration of pericytes, which are explicitly included in this model. Although some simplifications are made, this model arguably represents one of the best efforts thus far to incorporate mechanistically the combined effect of most of the key molecular players in a model of VEGF-A-induced sprout growth. The model demonstrates: i) the importance of competition between Ang-1 and Ang-2 in forming an angiogenic switch; ii) that the maturation process, modulated by pericytes and angiopoietins, is critical to vessel normalisation and may explain the resistance of developing vasculature to anti-VEGF-A therapy; and iii) that combined anti-pericyte and anti-VEGF-A therapy causes greater vessel regression over anti-VEGF-A therapy alone. In order to advance this model of sprout growth, it could be integrated with models for branching, chemotaxis, and blood flow (see Pries *et al.*, 1990; 1994; 1998).

3.3.1.2. Hybrid models of tumour-induced angiogenesis

McDougall and co-workers have developed an array of hybrid cellular automaton models of tumour-induced angiongenesis (McDougall *et al.* 2002; Stephanou *et al.* 2005; McDougall *et al.*

2006; Stephanou *et al.* 2006). They model vascular growth in response to a generic TAF concentration field both in 2-D (McDougall *et al.* 2002; McDougall *et al.* 2006; Stephanou *et al.* 2006) and in 3-D (Stephanou *et al.* 2005) using the snail-trail based discrete-continuous model of angiogenesis originally developed by Anderson and Chaplain (1998). The models were used to show how structural abnormalities of a tumour's vasculature may hinder the delivery of blood-borne drugs to large regions of a tumour. Early versions of this model considered vessels with a fixed radius, and blood was considered to be a Newtonian fluid. In later models, vessel radii were modelled dynamically and non-Newtonian blood flow was incorporated by employing the structural adaptation algorithm pioneered by Pries *et al.* (1990; 1994; 1998). The models were subsequently adapted to incorporate shear stress dependent branching and the mediation of vessel growth by ECM proteolysis by specific enzymes produced by ECs (Stephanou *et al.* 2006). It could be argued that the main drawback of this set of models is that the tumour is not explicitly represented. Instead, the lower boundary of the model domain is identified with the invasive edge of a tumour and acts as a source of generic TAF. However, more recently, Macklin *et al.* (2008) addressed this issue by coupling the discrete model of vasculature in McDougall *et al.* (2006) to a continuum model of solid tumour growth, developed by Macklin and Lowengrub (2008). This coupling allows the effect of an oncotic mechanical pressure, generated by the proliferating and invading tumour, on the native vasculature to be studied. It was assumed that this pressure would cause vessels to constrict and would also affect nutrient extravasation. This provided a novel method by which to couple tumour invasion with the evolving neovasculature, and specifically to investigate the phenomenon of vessel occlusion and collapse due to the pressures exerted by a growing tumour.

McDougall and co-workers adapted their models of tumour-induced angiogenesis to study angiogenesis in the developing murine retina (Watson *et al.* 2012) and in wound healing (Machado *et al.* 2011). Their numerical simulations of the retina, in particular, are visually stunning, bearing remarkable resemblance to *in vivo* networks in the retina, and in both cases significant efforts were made to parametrise the models against quantitative experimental data. For example, in Watson *et al.* (2012), the authors were able to demonstrate good agreement between their model and data which detailed the locations of migrating fronts of tip cells and astrocytes over time.

Alarcón *et al.* (2003; 2005) were among the first to develop models that systematically couple phenomena relating to vascular tumour growth that act on different time and length scales. Using a hybrid cellular automaton framework and a 2-D domain, they develop models which couple vascular remodelling, blood flow, and nutrient and VEGF-A diffusion through the ECM, with the cellular and sub-cellular dynamics of normal and cancerous cells. In their preliminary models, the vasculature was viewed as a static hexagonal network. Such hexagonal vessel networks have been observed, for example, in the avian yolk sac (Honda and Yoshizato 1997). The structural adaptation algorithm of Pries *et al.* (1990; 1994; 1998), was used to model non-Newtonian blood flow and radial adaptation in the vascular network. Alarcón *et al.* initially used these models to illustrate the profound effect that blood flow has on the growth of normal and cancerous cell colonies. However, their basic framework has since been extended to include additional phenomena. For instance, vessel co-option and maturation and the effect of combination anti-angiogenic drugs and chemotherapy on the growth of a tumour were investigated in Alarcón *et al.* (2006). Meanwhile, tumour and normal cell movement was introduced by Betteridge *et al.* (2006). Betteridge *et al.* also allowed multiple cells to occupy each lattice site, so that contact inhibition of proliferation could be investigated. More significantly, Owen *et al.* (2009) allowed the morphology of the vascular network to evolve by explicitly including a model of vessel regression and a discrete snail-trail based reaction-diffusion model of angiogenesis. The model of vascular growth adopted by Owen *et al.* is similar to that of Anderson and Chaplain (1998), however, Owen *et al.* neglect haptotaxis and allow for diagonal tip-cell movement. More recently, Perfahl *et al.* (2011) incorporated these elements into a 3-D model of vascular tumour growth, and used the model to investigate the influence of boundary conditions and domain size on simulation results. Within this family of models, different sub-cellular models of the cell cycle have been adopted (Alarcón *et al.* 2003; Alarcón *et al.* 2005; Owen *et al.* 2011), and the vascular structural adaptation algorithm has been modified, most notably to account for the fact that cancerous and normal vasculature differ considerably in both structure and function (Alarcón *et al.* 2006). Figure 3.3 summarises the major components which are included in models of this type.

Bartha and co-workers (Bartha and Rieger 2006; Lee *et al.* 2006; Welter *et al.* 2008; Welter *et al.* 2009) developed a hybrid cellular automaton model to study the growth dynamics of cancer cells in response to blood-borne nutrients and the evolution of tumour vasculature in response to a TAF released from cancerous cells. Their models illustrate the transformation of regular vasculature in normal tissues into highly heterogeneous vascular networks by incorporating tumour growth, cell death, vessel co-option, angiogenesis and vessel collapse. They show that microvascular density, once thought to be an important prognostic indicator, does not necessarily

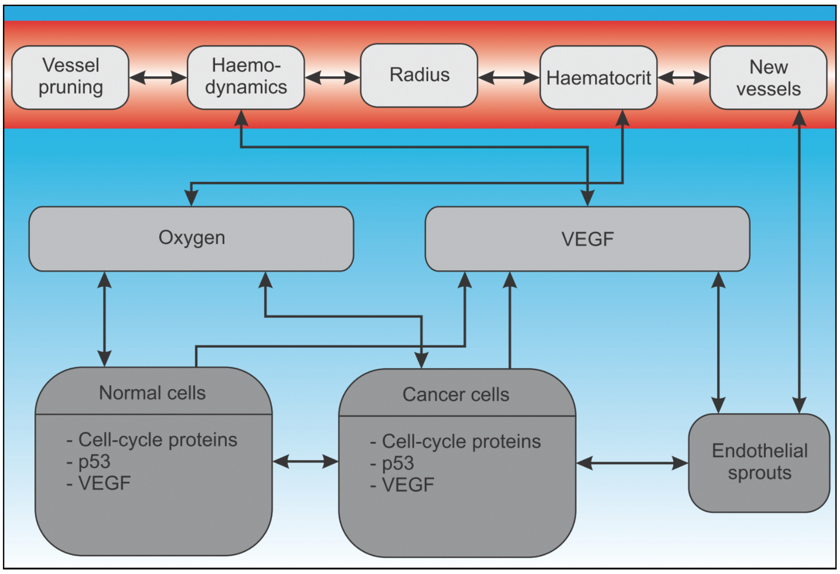

Figure 3.3.: This figure, reproduced from Perfahl *et al.* (2011), shows the major modelling components used within the Alarcón *et al.* family of models. Connections between components denote that those components are coupled in some way. Components and couplings are described in detail in the original paper.

determine the speed of tumour progression. Furthermore, they are able to generate vascular networks with similar fractal geometries to those found in tumours by assuming stochastic removal of vessels inside the tumour via vessel collapse and regression. The first two models in this series consider the evolution of a vascular tumour on a square lattice in 2-D (Bartha and Rieger 2006) and 3-D (Lee *et al.* 2006) while later models, presented in Welter *et al.* (2008; 2009) consider growth on a hexagonal lattice, incorporating, amongst other things, Pries *et al.*'s (1990; 1994; 1998) algorithm for adaptation of vessel radii. The authors also analyse how the complex topology of a tumour's vasculature affects the distribution of a blood-borne drug to a tumour using the same technique as was used by McDougall *et al.*. Several features of this family of models are rather simple. However, by modelling various biological phenomena in a coupled way, the authors were able to produce results which qualitatively agree with what is observed experimentally.

Many other hybrid models of vascular tumour growth exist. For example, Zheng *et al.* (2005) designed a hybrid model to study highly invasive tumour types such as gliomas. The tumour tissue was treated as a viscous fluid and angiogenesis was again modelled using the hybrid model of Anderson and Chaplain (1998). Extending work by Zheng *et al.* (2005), Frieboes *et al.* (2007) coupled a lattice-free model of angiogenesis (originally developed by Plank and Sleeman, 2004) to a continuum model of tumour tissue growth.

3.4. Discussion

Many different mathematical models of angiogenesis and vascular tumour growth have been developed. Early continuum models were idealised to permit mathematical analysis and to establish qualitative agreement with experimental results. These models laid a solid foundation on which more complex models have been developed to account for details of the biochemistry associated with tumour angiogenesis. Increasingly, the trend in angiogenesis model development has been towards that of hybrid models which aim to provide insight into cross-scale biological mechanisms and may also provide insight into tumour-associated phenomena in which structural heterogeneities in the vasculature are thought to be important.

Until recently spatially-resolved mathematical models of angiogenesis and vascular tumour growth have largely been developed without comparison to quantitative experimental data for parametrisation or validation. However, if we are to move towards a more quantitative understanding of cancer then we must develop techniques to rigorously compare simulated and experimental results. Additionally, the models must include pertinent up-to-date knowledge, and be developed in a way which allows them to provide insight into new therapeutic strategies that are being developed.

Recent mathematical modelling efforts, such as that of Tong and Yuan (2008b) and Watson *et al.* (2012), which aim to link quantitative experimental data with simulation results in simple model systems, underline the potential for integrating mathematical modelling with image analysis techniques to increase insight into the phenomena underlying angiogenesis. In Chapter 4, we will review and compare existing image analysis techniques which may be used to extract quantitative vascular network data from experimental images. We use one such algorithm to extract quantitative spatiotemporal data from novel images of corneal angiogenesis, in which vascular growth occurs in response to either VEGF-A_{165} or bFGF. These data will be used for the parametrisation of models developed later in this thesis.

CHAPTER 4

Analysis of Experimental Images

4.1. Overview

The development of mathematical models and their subsequent parametrisation and validation rely heavily on experimental information. Such information is firstly required to guide model development and to establish the likely range of values of model parameters. Secondly, experimental information is needed for comparison with the results of model simulations. Such information may involve qualitative descriptions of expected behaviours or quantitative data. It is generally accepted that the more reliable, quantitative information we are able to utilise to construct and validate models, the better (Bentley *et al.* 2013). By improving the rigour with which our model simulations are compared to experimental data we aim to increase our confidence in these models and to generate quantitative predictions that motivate the design of further experiments.

In this chapter we focus on the acquisition of quantitative vascular growth data from experimental images of corneal angiogenesis using automated and semi-automated methods. Such automated methods aim to reduce the subjectivity associated with vessel identification from images and provide a faster way to identify vessels than manual image annotation. In Section 4.2, we introduce the images taken from cornea micropocket assay experiments carried out by our industrial collaborators at Roche, Penzberg. In Section 4.3, we survey and compare existing state-of-the-art imaging techniques used to extract vessel networks from images. We modify one such imaging technique and show that it out performs all other algorithms examined here when applied to images of retinal vasculature. We then use this technique to extract dynamic and spatially resolved data from the cornea images (Section 4.4). These quantitative data guide the development and parametrisation of the models presented in Chapters 5, 6 and 7. Finally, in Section 4.5 we discuss the results presented in this chapter and their significance within a mathematical modelling context.

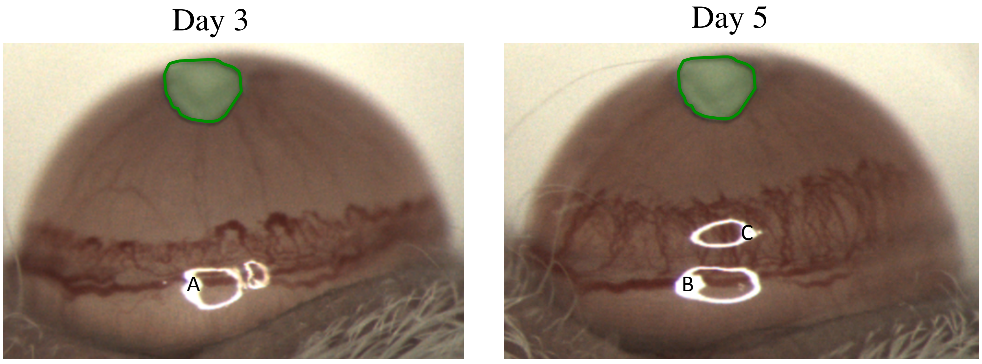

Figure 4.1.: Representative images from cornea micropocket assay experiments where a pellet soaked with 300 ng of VEGF-A_{165} was placed ~ 1 mm away from the limbal vessels inside the cornea of a mouse. Left: day 3 image. Right: day 5 image. The pellet is highlighted in green in each image. A, B and C are artefacts due to camera lighting. Images courtesy of Erica Lorenzon (Roche, Penzberg).

4.2. Experimental images

Our images come from cornea micropocket assay experiments (Chapter 2) performed at Roche, Penzberg. Nylon pellets (Nylaflo®, Pall corporation, Michigan) of radius 0.3 mm and thickness 0.06 mm are incubated in an AF and implanted into the cornea. We consider pellets that initially contain either 300 ng of VEGF-A_{165} or 15 ng of bFGF. We focus on VEGF-A_{165} because it has been shown to be the dominant VEGF-A isoform in normal vascular development (see Chung and Ferrara, 2011, and references therein) and on bFGF because of its role in tumour-induced angiogenesis (Presta *et al.* 2005; Murakami and Simons 2008).

Pellets are placed approximately 1 mm away from the anterior portion of the limbal vessels (Kienast *et al.* 2013; Thomas *et al.* 2013) and images of the neovascular growth are captured on days three and five after implantation. Figure 4.1 shows representative images from VEGF-A_{165} experiments. Colour-based segmentation algorithms are used to estimate the percentage area of the cornea occupied by the neovasculature on day five. This metric is assumed to be representative of the strength of the angiogenic response of the limbal vessels to a given AF. However, it does not give a truly quantitative estimate for the vascular density in the cornea, which is more useful for comparing experimental results with model simulations. Moreover, colour-based segmentation methods are typically unable to extract the details of individual vessels in images, which are required to estimate vascular density and to extract spatially resolved data. To extract such details more sophisticated image processing algorithms are needed. In the next section, we compare several such algorithms.

4.3. Review of state-of-the-art vessel enhancement algorithms

The detection of blood vessels has received a lot of attention from the image processing community and many established semi-automated and automated techniques now exist which aim to distinguish vessels, vessel networks and other network-like structures from the background of an image (see Kirbas and Quek, 2004, and Dehkordi *et al.*, 2011, for comprehensive reviews of existing image processing techniques). The short review presented below introduces several state-of-the-art image processing techniques for vessel extraction.

Dehkordi *et al.* (2011) divide image processing methods for vessel identification into two categories:

1. Vessel enhancement methods.
2. Vessel segmentation methods.

We focus on vessel enhancement methods, which aim not to identify vessels directly but to make vessel-like structures stand out from the background of an image. The purpose of this processing step is, then, to improve the accuracy of a subsequent segmentation step, where segmentation corresponds to the binary classification of pixels into those belonging to vessels or not.

4.3.1. The Gaussian matched filter

The matched filter approach is a template-matching algorithm, whose success relies on the assumption that vessels have a predictable intensity profile. An acceptable assumption may be, for example, that the cross-sectional intensity profile of a vessel is approximately Gaussian. Figure 4.2 shows the cross-sectional grayscale intensity profiles of three vessels of varying width from one of our experimental images. The graphs show the cross-sectional intensity profile at various points along the length of a vessel (blue dashed lines) as well as the average intensity profile across all cross-sections (green lines). A Gaussian curve of the form

$$f(x) = A \left(1 - k\, exp\left(-\frac{(x-\mu)^2}{2\sigma^2}\right)\right) \tag{4.1}$$

has been fitted (with respect to the parameters A, k, μ and σ) to each average intensity profile and is shown in each plot by a red line. The figure indicates that, for our images, a Gaussian intensity profile is likely to be appropriate, particularly for larger vessels which contrast well with the background. It should be noted that Gaussian intensity profiles are not always the most appropriate matched filter for vessel identification. For example, in images where central

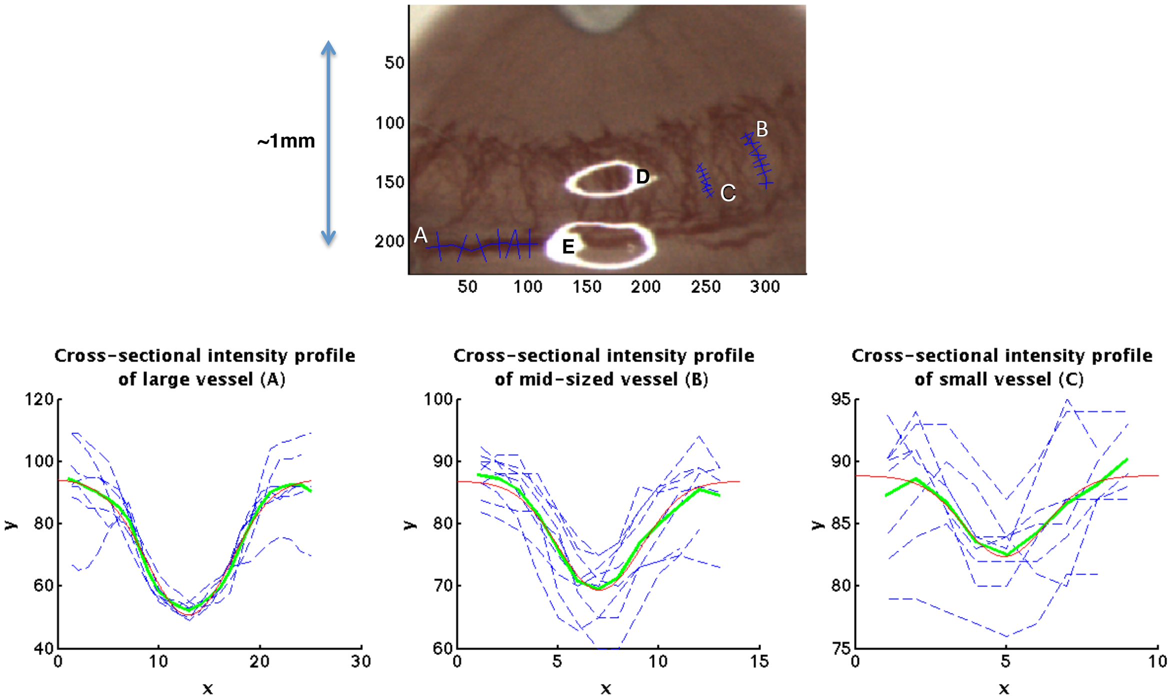

Figure 4.2.: The cross-sectional intensity profiles of three vessels, A, B and C, are shown at a number of locations along that vessel's length (blue dashed lines). The average intensity profiles for each vessel are shown in green and a fitted Gaussian curve is shown in red. D and E are artefacts due to the camera lighting. Note the difference in scales between the three plots.

regions of large surface vessels reflect lots of light the Gaussian profile assumption is not valid and alternative matched intensity profiles must be sought (Wang *et al.* 2007; Wu *et al.* 2006; Vermeer *et al.* 2004; Lowell *et al.* 2004).

The matched filter approach was first introduced by Chaudhuri *et al.* (1989) who, motivated by the types of intensity profiles shown in Figure 4.2, assumed a Gaussian shape for the cross-sectional intensity profile of vessels. The filter is extended to two dimensions by assuming that vessels usually have small curvatures and can therefore be approximated by small piecewise linear segments. Thus, the matched filter kernel may be expressed as

$$k(x,y) = -exp\left(-\frac{x^2}{2\sigma^2}\right) \quad \forall \quad |y| \le \frac{L}{2}, \tag{4.2}$$

where L is the length over which the vessel is assumed to have a fixed orientation[1]. Taking $L > 1$ reduces the response of the filter to noise while smaller values of L permit strong matched filter responses for more tortuous vessels. Since vessels may appear in any orientation, the

---

[1] In image processing, a *kernel* is a small matrix used to manipulate or extract information from an image. For example, a kernel can be used to blur or sharpen an image. Kernels accomplish their tasks through convolution with an image.

filter is rotated through all possible angles ($0 \leq \theta \leq \pi$) to produce a bank of filters, k_i, of fixed size. A number of independent investigations have concluded that an angular resolution of 15^o, corresponding to 12 filters, provides an adequate level of accuracy for vessel detection (Chaudhuri *et al.* 1989; Al-Rawi *et al.* 2007).

To limit the size of the matched filters, the Gaussian curves, which have infinitely long tails, are truncated at $\pm T$ pixels. Furthermore, the kernel is modified by subtracting the mean value of $k(x, y)$ so that when the kernel is applied to a pixel belonging to a background of constant intensity, with zero mean additive noise, the response will be zero. Thus, we have

$$k_i^{'}(x, y) = k_i(x, y) - \frac{1}{a} \sum_{x,y} k_i(x, y), \tag{4.3}$$

where a is the number of elements in the discrete implementation of the filter.

The vessel enhancement algorithm proceeds by convolving each matched filter kernel, k_i, with the image to produce an array of matched filter responses, M_i. The final matched filter response, M, is obtained by retaining the maximal matched filter response over all orientations for each pixel, i.e. $M(x, y) = \max_i M_i(x, y)$. Chaudhuri *et al.* (1989) fixed the parameters σ, T and L to be 2, 6 and 9 pixels, respectively. σ was chosen to match the medium-sized vessels in the images considered by the authors and it was concluded that $T = 3\sigma$ pixels provided a sufficiently accurate representation of the Gaussian curve. Meanwhile, the authors found that taking $L = 9$ pixels provided good reduction in noise whilst allowing reasonable enhancement for even the most tortuous vessels.

Using these default parameter values, it has been suggested that the Gaussian matched filter method performs poorly when compared with other vessel identification techniques. However, Al-Rawi *et al.* (2007) performed a search of the parameter space (σ, L, T) in an attempt to optimise the Gaussian matched filter method. They found that vessels in the DRIVE database images (see Section 4.3.4 and Staal *et al.*, 2004, for further details) were identified most accurately when the parameters $(\sigma, L, T) = (1.9 \text{ pixels}, 10.8 \text{ pixels}, 8 \text{ pixels})$ were used. They also investigated the use of a two-stage Gaussian matched filter where two banks of filters with parameters $(\sigma_1, L_1, T_1) = (1.9 \text{ pixels}, 10.8 \text{ pixels}, 8 \text{ pixels})$ and $(\sigma_2, L_2, T_2) = (1.9 \text{ pixels}, 7.6 \text{ pixels}, 8 \text{ pixels})$ were used in parallel and the maximum matched filter response of all 24 filters was retained. Using an optimised Gaussian matched filter and the two-stage Gaussian matched filter, Al-Rawi *et al.* found that, for images in the DRIVE database, the matched filter approach is comparable in performance to other well-known, high-performance vessel identification procedures when coupled to an appropriate thresholding algorithm[2], with the two-stage approach outperforming the single-stage one by a small margin.

The matched filter approach can be improved by considering an extended bank of Gaussian matched filters of varying σ and orientation. Extending the library to include filters of varying σ is justified by the expected dependence of filter response on the vessel width. In particular, by including filters of smaller width we increase the matched filter response to smaller vessels and thus increase the likelihood that these vessels will be identified in a subsequent segmentation step. We investigate the effect of using such an extended library of filters in Section 4.3.4.

4.3.2. The Frangi / vesselness filter

Another popular approach to vessel enhancement is to use multiscale Hessian-based operators. One such method which adopts this approach is the Frangi filter (Frangi *et al.* 1998). Like the matched filter approach, the Frangi filter aims to identify pixels which belong to tubular structures or, more precisely, elongated ellipses. This property of a pixel is determined by calculating and analysing the Hessian matrix at different image scales.

To introduce this method we define I_σ as the representation of an image, I, at scale σ; this is the convolution of the image with a Gaussian kernel with standard deviation, σ. Such a convolution suppresses the finer scale details of an image. Now, the Taylor expansion of I_σ about a point $\mathbf{x_0}$ supplies

$$I_\sigma(\mathbf{x_0} + \mathbf{dx_0}) \approx I_\sigma(\mathbf{x_0}) + \mathbf{dx_0^T} \nabla I_\sigma(\mathbf{x_0}) + \frac{1}{2}\mathbf{dx_0^T} H_\sigma(\mathbf{x_0})\mathbf{dx_0},$$

where ∇ is the gradient operator and $H_\sigma(\mathbf{x_0})$ is the real symmetric Hessian matrix, defined by the tensor of second order partial derivatives of I_σ at $\mathbf{x_0}$. In 2D, one can interpret the eigenvectors of the Hessian matrix as the principal axes of an ellipse, each having length equal to the eigenvector's corresponding (real) eigenvalue[3]. This ellipse describes how the intensity of the image changes locally along the two orthonormal directions given by the eigenvectors of the matrix and thus describes the likely local shape of the object to which the pixel belongs. By convention the eigenvalues, $\lambda_{i,\sigma}$ for $i = \{1, 2\}$, are ordered such that $|\lambda_{1,\sigma}| \leq |\lambda_{2,\sigma}|$, with small eigenvalues

---

[2] A thresholding algorithm is an image segmentation technique which classifies pixels based on some value associated with those pixels. Pixels with an associated value greater than some threshold are then distinguished from pixels with an associated value less than (or equal to) that threshold.

[3] A more precise description of the geometric interpretation of the Hessian matrix is given in Frangi *et al.* (1998).

indicating small variations in intensity directed along the corresponding eigenvector. Since we anticipate vessels to have a reasonably uniform intensity along their length, if a pixel belongs to a vessel then its smallest associated eigenvalue will correspond to the eigenvector pointing along the vessel's length. The other eigenvalue, corresponding to the eigenvector orientated in the direction of the ideal vessel's cross-section, where the intensity varies more rapidly, will be larger in magnitude. Thus, pixels which have large eigenvalue ratios $\frac{|\lambda_{2,\sigma}|}{|\lambda_{1,\sigma}|}$ are likely to correspond to elongated structures, like vessels.

To describe the likelihood that a particular pixel belongs to a vessel, Frangi defined a vesselness function, which, for vessels which appear darker than their background, has the form

$$V_\sigma(x_0) \quad = \quad \begin{cases} 0 & \text{for } \lambda_{2,\sigma} < 0 \\ e^{-\frac{\lambda_{\sigma,1}^2}{2\beta^2\lambda_{\sigma,2}^2}}\left(1 - e^{-\frac{\lambda_{\sigma,1}^2+\lambda_{\sigma,2}^2}{2c^2}}\right) & \text{otherwise,} \end{cases} \tag{4.4}$$

where β and c are thresholds determining the sensitivity of the vesselness measure. The first component in (4.4) ensures that V_σ is minimised for blob-like structures and the second component gives a measure of the relative brightness or darkness of the candidate structure at $\mathbf{x_0}$ and enables well-defined structures to be differentiated from background noise.

The final vesselness score for each pixel is calculated as the maximum vesselness across all scales. That is:

$$V(\mathbf{x_0}) = \max_{\sigma\in\Sigma} \; V_\sigma(\mathbf{x_0}), \tag{4.5}$$

where Σ is the set of all image scales.

4.3.3. The PCT-vesselness filter

The enhancement algorithms discussed thus far are based on the intensity profiles of vessels. As such they may not perform well when used to detect small vessels which contrast poorly against the background of an image. Equally, vessel detection methods which rely on calculating the gradient of an image may have difficulties locating vessels which have low contrast. To address these issues, Obara *et al.* (2012) proposed a brightness- and contrast-independent method for curvilinear structure identification based on the concept of phase congruency, a detailed explanation of which can be found in Kovesi (1999; 2000; 2003). For convenience, we summarise how the phase congruency of an image is calculated.

Phase congruency based feature detectors assume that features are located at points where the Fourier components of the image are maximally in phase. According to Kovesi (2000), for a 1-D signal, $f(x)$, the phase congruency may be calculated using

$$PC_{1D}(x) = \frac{\sum\limits_n W(x)\left[A_n(x)\left(\cos(\phi_n(x) - \bar{\phi}(x)) - \left|\sin(\phi_n(x) - \bar{\phi}(x))\right|\right) - T\right]^+}{\sum\limits_n A_n(x) + \epsilon}.$$

Here, $A_n(x)$ are the amplitudes of the Fourier components of the signal, $\phi_n(x)$ are the phase angles and $\bar{\phi}(x)$ is the amplitude weighted mean local phase angle of all the Fourier terms at the point x. The expression, $\sum\limits_n A_n(x)\left[\cos(\phi_n(x) - \bar{\phi}(x)) - \left|\sin(\phi_n(x) - \bar{\phi}(x))\right|\right]$, is a measure of the local energy, $E(x)$, and the weighting function, $W(x)$, is a sigmoid which adjusts for the frequency response spread. $W(x)$ has the form

$$W(x) = \frac{1}{1 + e^{\gamma(c - s(x))}}, \tag{4.6}$$

where

$$s(x) = \frac{1}{N}\frac{\sum\limits_n A_n(x)}{A_{max} + \epsilon}. \tag{4.7}$$

In (4.6), c is the cut-off value of the filter response spread, below which phase congruency values are penalised, and γ is a constant which dictates the steepness of the cut-off. The brackets, $[]^+$, indicate a function which is equal to itself if positive and equal to zero if negative. T is the estimated noise threshold, introduced by Kovesi to compensate for noise in an image. A full explanation of how the noise threshold may be estimated is provided in Kovesi (2000). Finally, ϵ is a small positive constant which prevents division by zero and N is the number of scales under consideration.

Kovesi extends the concept of phase congruency to two dimensions by measuring the phase congruency along several different orientations and then summing over all orientations. So, for a 2-D image, $I(x, y)$, we have:

$$PC_{2D}(\mathbf{x}) = \frac{\sum\limits_o\sum\limits_n W_o(\mathbf{x})\left(A_{n,o}(\mathbf{x})\left(\cos(\phi_{n,o}(\mathbf{x}) - \bar{\phi}_o(\mathbf{x})) - \left|\sin(\phi_{n,o}(\mathbf{x}) - \bar{\phi}_o(\mathbf{x}))\right|\right) - T_o\right)^+}{\sum\limits_o\sum\limits_n A_{n,o}(\mathbf{x}) \ + \ \epsilon},$$

where o denotes the orientation index. In summary, at each point on a 2-D image, an energy, $E(x, y)$, is calculated at a number of different orientations. Each energy is weighted, compensated for noise and then the energies are summed together. This sum is then normalised by the sum of all Fourier amplitudes over all scales and orientations. The subtleties involved in deriving this measure of the phase congruency of a 2-D image are described in Kovesi (2000).

Obara *et al.* proposed the phase congruency tensor (PCT) as an alternative to the Hessian matrix for representing local features (Obara *et al.* 2012). For an image, $I(x, y)$, for a set of scales $\{s\}$ and phase congruency measures, $PC_o(\mathrm{x})$, in various orientations, the PCT is given by

$$T_{PC} = \sum_{o} PC_o(\mathbf{x}) \left(\mathbf{n}_o \mathbf{n}_o^T - \alpha \mathbb{I} \right),$$

where $\mathbf{n_o}$ is the unit vector in the direction of the orientation ($[\cos(\theta(o), \sin(\theta(o))]^T$) and, for an image of dimension two, $\alpha = 1$. $\mathbb{I}$ is the identity matrix. Eigenanalysis of this tensor may then be applied in the same way as for the Hessian matrix to determine a measure of the likelihood that a vessel is located at a particular position (see Equation 4.4).

4.3.4. Comparison of vessel enhancement algorithms

In this section, the vessel enhancement algorithms, presented above, are compared by applying them to a set of 20 retina images from the DRIVE database (Staal *et al.* 2004). The database contains 40 RGB images randomly selected from a diabetic retinopathy screening program in The Netherlands. The images have been partitioned into a set of 20 training images and 20 test images. The vasculature in each training image has been manually identified by a single human observer, while the vasculature in each test image has been manually identified by two independent observers. Thus, effective ground truth segmentations of the vasculature are available. Figure 4.3 shows an example image from the DRIVE database and the two accompanying manual segmentations. In our analysis, we compare candidate segmentations against the test set segmentations prepared by *observer 2* since this observer appears to have taken more care to annotate the smallest visible vessels. The database administrators have also made available image masks which identify the field of view (FOV) of the camera with which each image was captured. While the performances of image processing algorithms are sensitive to the types of images to which they are applied, the images in the DRIVE database are similar enough to our own to provide us with an idea about the likely performance of the algorithms when applied to our own images. The rationale for using the DRIVE database images as a test bed is that the accompanying manual annotations provide us with an opportunity to benchmark

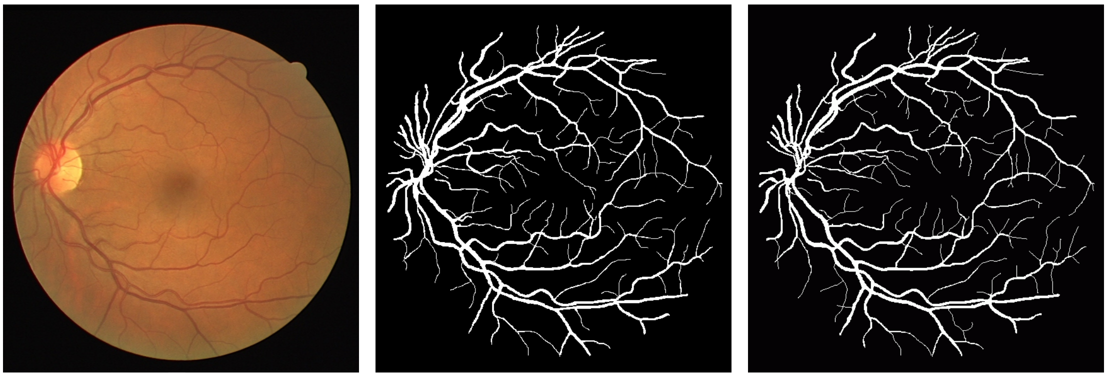

(a) Original image. **(b)** Observer 1 mask. **(c)** Observer 2 mask.

Figure 4.3.: Image 1 (test set) from the DRIVE image database and corresponding manually segmented vessel masks.

the algorithms against one-another quantitatively.

The performance of the algorithms depend on the parameters used in each algorithm. Here, we seek to compare:

1. **The Gaussian matched filter approach** using an implementation adapted from that provided by Chanwimaluang[4] with
    a) the original Chaudhuri *et al.* (1989) parametrisation.
    b) the single- and two-stage Al-Rawi *et al.* (2007) parametrisations.
    c) our own single- and two-stage parametrisations. Here, we extend the methods employed by Al-Rawi *et al.* (2007) by creating a further extended bank of matched filters in which the width of the filter, σ, is varied between 0.5 and 2 pixels in steps of 0.1. As we vary σ, T is also varied such that $T = 4\lceil\sigma\rceil$ pixels, consistent with Al-Rawi *et al.*'s parametrisation. For both the single and two-stage filters we use the same values for L as Al-Rawi *et al.* (2007).
2. **The Vesselness filter approach** using an implementation by Schrijver and Kroon[5] with
    a) their default parametrisation.
    b) the parametrisation provided by Obara *et al.* (2012).
3. **The PCT-Vesselness filter approach** using an implementation provided by Obara with parameters adapted from Obara *et al.* (2012). We change k, the number of standard deviations of the noise energy beyond the mean at which the noise threshold point is set, from 2 to 5, but keep all other parameters at their default values. The value for k was

---

[4] `http://www.vcipl.okstate.edu/localentropy.htm`.

[5] `http://www.mathworks.com/matlabcentral/fileexchange/24409-hessian-based-frangi-vesselness-filter`.

tuned manually to provide improved segmentation of the vasculature in the DRIVE images.

To compare the vessel enhancement algorithms we apply each vessel enhancement filter to a grayscale version of each image from the test set in the DRIVE database. Grayscale images are obtained by using the MATLAB function *rgb2gray*[6]. Vessel enhancement algorithms are often applied to the green channel of RGB images since this provides good contrast for red vessels against a background image. However, during preliminary investigations we found very little improvement in segmentation quality when using the green channel as opposed to a grayscale image (significant improvements were evident when using the green channel or grayscale images over the blue or red channel images). For each image, the application of a given vessel enhancement algorithm outputs a filtered grayscale image in which pixels take a continuous floating point value, which we normalise to between 0 and 255. Pixels with higher associated values are more likely to belong to a vessel. To compare the results of a given enhancement procedure with the ground truth segmentation available via the DRIVE database, a threshold must be applied to the enhanced images to produce a candidate vessel segmentation mask. After thresholding, the candidate segmentation mask is compared to the ground truth segmentation on a pixel-by-pixel basis and the number of true positive (TP), false positive (FP), false negative (FN) and true negative (TN) pixels are recorded. This process is summarised in Figure 4.4 for a single image and single threshold level. Only pixels which fall inside the FOV, as defined by the associated image mask provided in the DRIVE database, are compared.

For each of the 20 images in the test data set, and for each vessel enhancement algorithm, we vary the threshold value applied between 0 and 255 in increments of 0.25 and record the resulting confusion matrix values (TP, FP, FN, TN). From the confusion matrices we calculate the specificity, sensitivity and overall accuracy of the candidate segmentation masks produced for each image and at each threshold as follows:

$$\text{specificity} = \frac{\mathrm{TN}}{\mathrm{TN}+\mathrm{FP}} \tag{4.9}$$

$$\text{sensitivity} = \frac{\mathrm{TP}}{\mathrm{TP}+\mathrm{FN}} \tag{4.10}$$

$$\text{overall accuracy} = \frac{\mathrm{TP}+\mathrm{TN}}{\mathrm{TN}+\mathrm{FP}+\mathrm{TP}+\mathrm{FN}} \tag{4.11}$$

---

[6] This function converts RGB pixel values to grayscale ones by calculating a weighted average of the R, G and B components:

$$0.2989 \times R + 0.5870 \times G + 0.1140 \times B. \tag{4.8}$$

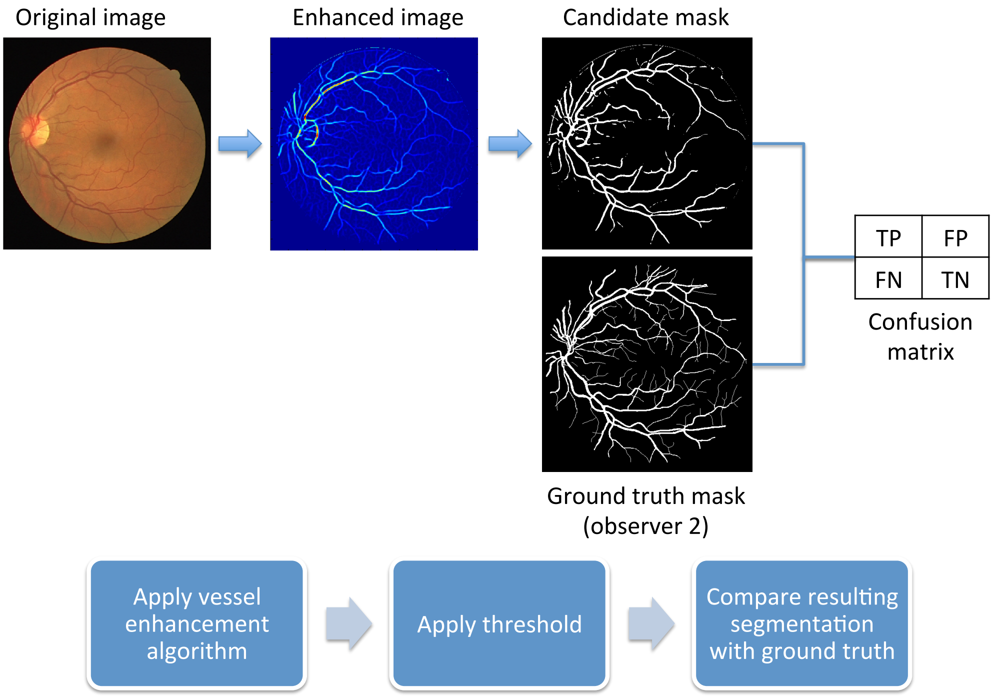

Figure 4.4.: Work flow for vessel enhancement algorithm performance evaluation. See main text for details.

Finally, we compare the performance of the vessel enhancement algorithms using two metrics, derived from the specificity, sensitivity and overall accuracy:

1. **Average maximal overall accuracy of segmentations, Z.**

   For a given vessel enhancement algorithm, and for each image, i, the threshold level which produces the most accurate segmentation (as calculated using Equation 4.11) is identified. The maximal accuracy for that image, Z_i, is recorded. Z is then given by $\frac{1}{n}\sum_{i=1}^{n} Z_i$, with $n = 20$ in our case.

2. **Area under the receiver operating curve, A_{ROC}.**

   A receiver operating curve (ROC) plots the true positive rate (sensitivity) vs the false positive rate (1 - specificity). For classifiers such as ours, which yield continuous scores and must be thresholded in order to produce a binary classification, different threshold levels produce different points in ROC-space. For a given vessel enhancement algorithm, and for each image threshold level, we calculate the average specificity and sensitivity of the segmentations across all 20 images. For each vessel enhancement algorithm, the average specificities and sensitivities at each threshold level are used to plot a ROC, known as a threshold-averaged ROC (Fawcett 2004). The area under the ROC for each algorithm is then calculated. The higher the area under the ROC, the more effective the algorithm at

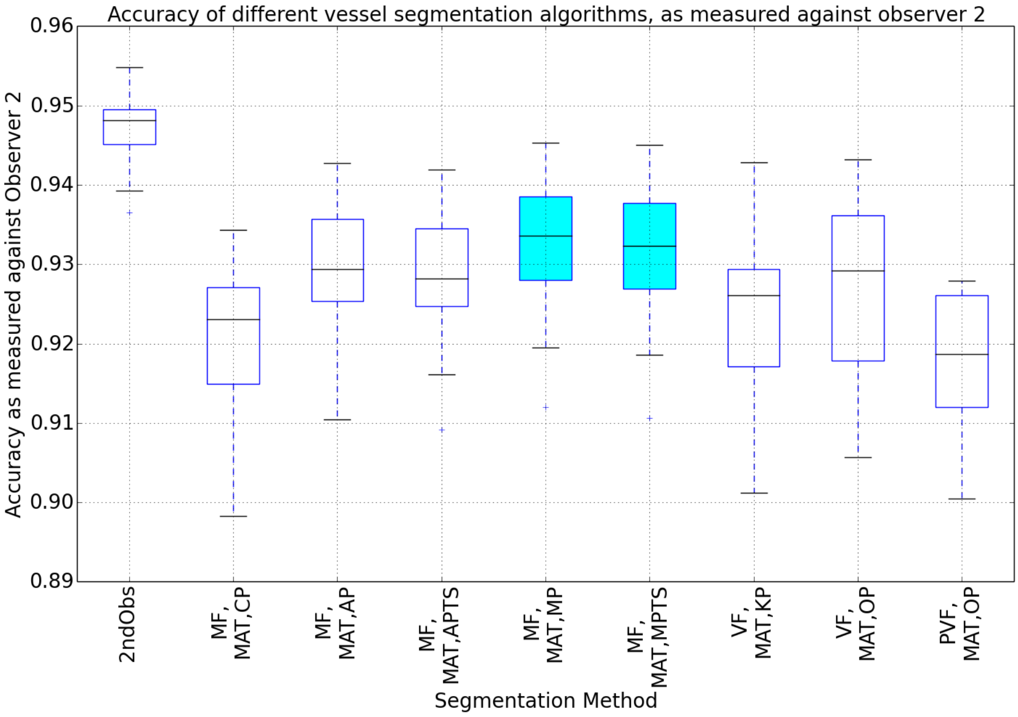

Figure 4.5.: Box and whiskers plot showing the accuracy of state-of-the-art vessel segmentation algorithms as measured against observer 2. Here, enhanced images have been thresholded at the level which produces the most accurate segmentations. 2ndObs - *observer 1* manual segmentations from DRIVE database; MF - matched filter; VF - vesselness filter; PVF - PCT vesselness filter; MAT - maximum accuracy thresholding; CP - Chaudhuri parametrisation; AP - single-stage Al-Rawi parametrisation; APTS - two-stage Al-Rawi parametrisation; MP - our single-stage parametrisation (highlighted); MPTS - our two-stage parametrisation (highlighted); KP - Kroon and Schriver parametrisation; OP - Obara parametrisation.

identifying vessel-like structures. An area of 1 means perfect vessel detection and an area of 0.5 means that the algorithm performs as well as if vessel pixels were selected at random.

Presented in Figure 4.5 is a box plot summarising the maximum segmentation accuracy achievable for each enhancement algorithm and for each image. Meanwhile, Figure 4.6 shows the threshold-averaged ROC plots for each vessel enhancement algorithm. Table 4.1 shows the Z and A_{ROC} values for each enhancement algorithm together with the average specificity and sensitivity of each algorithm when thresholding is performed at the level which results in the highest accuracy segmentation. Figure 4.5 and Table 4.1 allow us to compare the performance of computer generated segmentations against that of a second independent human observer (*observer 1*). It is immediately apparent that a second human observer outperforms all automated methods analysed here. However, all vessel enhancement algorithms, when combined with an appropriate segmentation algorithm, have the potential to perform comparably with a second human observer.

To put into context the fact that the vesselness filter, when parametrised according to Obara *et al.* (2012), has the highest *average specificity at max accuracy* across all tested algorithms (see Table 4.1), we note that the sensitivity and specificity metrics are not informative as to the performance of a classifier when viewed in isolation. An illustrative example follows. A classifier may have a specificity of 1 since it correctly identifies all negative instances. However, this says nothing about how successful the classifier is at identifying positive instances; the classifier may even identify all instances as negative (and thus have a sensitivity of 0).

Our results suggest that the Gaussian matched filter approach, even when the original Chaudhuri *et al.* (1989) parametrisation is used, performs comparably with other state-of-the-art vessel enhancement algorithms. The optimised parameter sets introduced by Al-Rawi *et al.* (2007) provide modest improvements to the segmentation of the vasculature and by extending the bank of Gaussian matched filters to include filters in which the width of the Gaussian varies we have been able to further improve the accuracy of the Gaussian matched filter approach. Our analysis shows minimal difference in accuracy for single- and two-stage Gaussian matched filter methods, however, our single-stage filter appears to perform marginally better than its two-stage counterpart. Meanwhile, the results for the single- and two-stage Gaussian matched filters, parametrised according to Al-Rawi *et al.*, are less clear. Our analysis shows that whilst the two-stage Al-Rawi *et al.* filter outperforms the single-stage filter in terms of their A_{ROC} scores, the single-stage outperforms the two-stage in terms of their Z scores. While this is contrary to Al-Rawi *et al.*'s original analysis, the discrepancy may be due to subtle differences in the way that the algorithms were compared by Al-Rawi *et al.*

Both the vesselness and PCT-vesselness filters show promise with regards to retinal vessel identification. Here, however, the two filters are outperformed by the Gaussian matched filter approaches. It is likely that the performances of these filters could be vastly improved by optimising the algorithms with respect to the parameter values used. However, optimising the filters for the DRIVE retina images is unlikely to prove useful when attempting to use the filters to extract data from our set of corneal angiogenesis images, which were taken under different lighting conditions and are subject to different sources of noise. Further, there is no guarantee that the parameters used in the vesselness and PCT-vesselness filters here will perform as well when tested against our cornea images. By contrast, an important advantage of the Gaussian matched filter approach is its relative simplicity and intuitiveness. In particular, the parameters used in the Gaussian matched filter approach are likely to work equally well for our cornea images

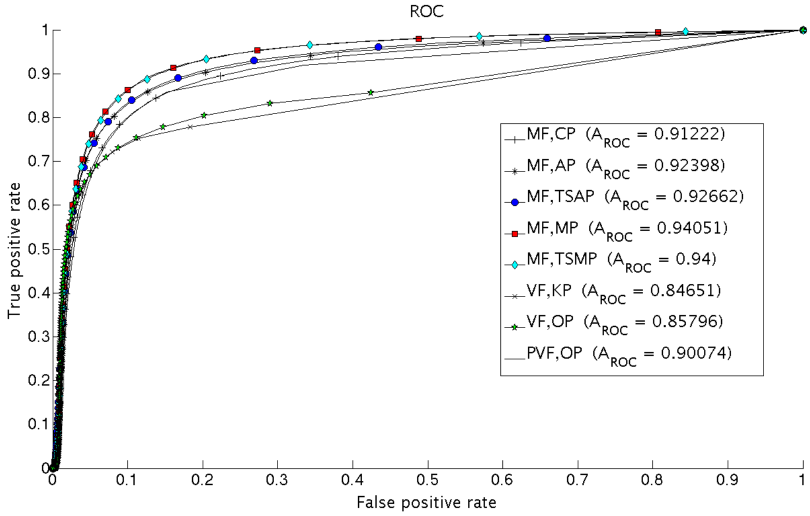

Figure 4.6.: Reciever operating curve (ROC) analysis for vessel enhancement algorithms as compared against observer 2. The area under each curve, A_{ROC}, is included here for convenience. Acronyms are as defined in Figure 4.5.

Enhancement method	Parameters	Z	Average sensitivity at max accuracy	Average specificity at max accuracy	A_{ROC}
Second observer	N/A	0.9473	0.8066	0.9674	-
Gaussian Matched Filter	(Chaudhuri *et al.* 1989)	0.9206	0.6045	0.9644	0.9122
Gaussian Matched Filter	(Al-Rawi *et al.* 2007) Single-stage filter	0.9291	0.6451	0.9683	0.9240
Gaussian Matched Filter	(Al-Rawi *et al.* 2007) Two-stage filter	0.9282	0.6458	0.9672	0.9266
Gaussian Matched Filter	Our single-stage parameters	0.9319	0.6833	0.9661	0.9405
Gaussian Matched Filter	Our two-stage parameters	0.9310	0.6821	0.9653	0.9400
Vesselness Filter	Schriver and Kroon[5]	0.9239	0.5984	0.9694	0.8470
Vesselness Filter	(Obara *et al.* 2012)	0.9269	0.5823	0.9751	0.8580
PCT Vesselness Filter	Adapted from (Obara *et al.* 2012)	0.9175	0.6017	0.9612	0.9007

Table 4.1.: Summary performance results of tested vessel enhancement algorithms. The results of our two original adaptations of the Gaussian matched filter are highlighted in blue. Also highlighted in red are the results for each performance metric which are maximal taken over the tested algorithms, i.e. excluding the second human observer.

since the vessels are of a similar size and shape to those in the DRIVE retinal images. Indeed, initial experiments on sample regions of cornea images indicated that the Gaussian matched filter is more effective at identifying vessels in our images than either the vesselness or PCT-vesselness filters, as presently parametrised. Figure 4.7 shows the results of vessel enhancement and subsequent segmentation in a small portion of a corneal image. We compare the single-stage

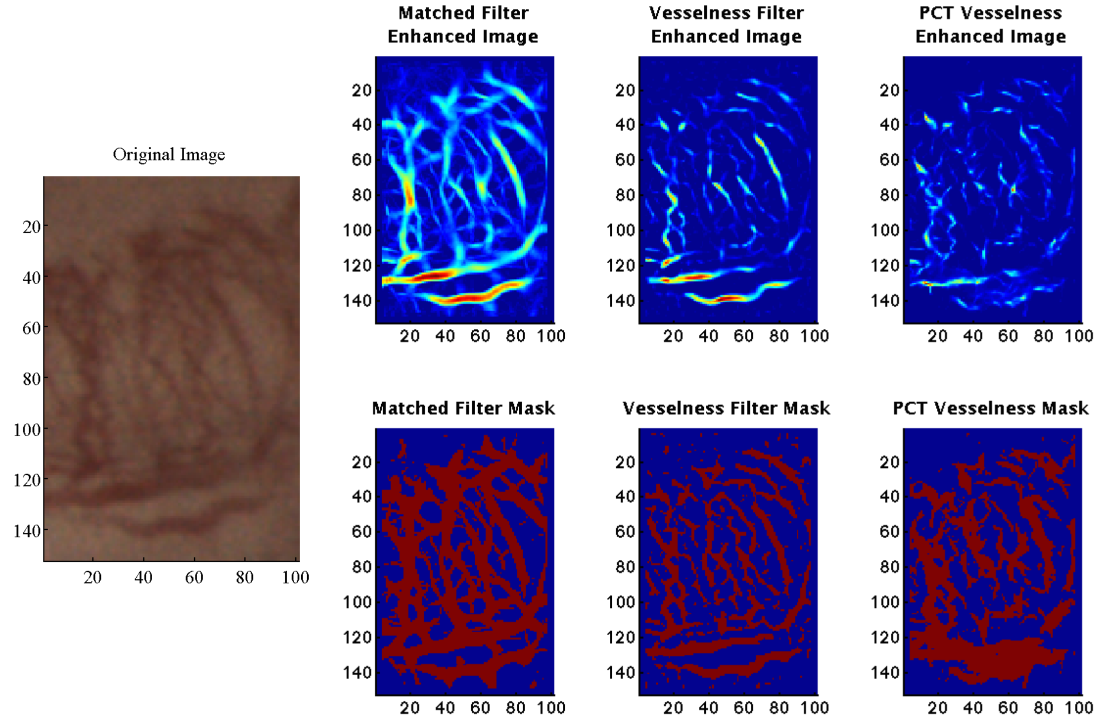

Figure 4.7.: Comparison of vessel enhancement algorithm results on a small portion of a cornea image. See main text for details.

Gaussian matched filter, using our parameters; the vesselness filter, using parameters provided by Obara *et al.* (2012); and the PCT-vesselness filter. We see that the PCT-vesselness filter, as presently parametrised, is relatively ineffective at identifying vessels in our cornea images. On the other hand, the vesselness filter performs reasonably well, typically identifying the main body of vessels in the image but occasionally undersegmenting them, particularly at vessel intersections. Meanwhile, the Gaussian matched filter, while suffering slightly from oversegmentation, is effective at identifying even the thinnest and most poorly contrasted vessels.

A potential weakness of the analysis presented in this section is that it may favour algorithms that delineate large branches very accurately, even if they miss some very thin ones. Further analysis, for example, which analyses the number and location of branches may provide further insight into the performance of the algorithms and could contribute towards future work. However, due to its simplicity and overall performance in the investigations described in this section we use an extended Gaussian matched filter approach to identify vessels in the cornea images provided by Roche.

4.4. Semi-automated vessel segmentation in cornea micropocket images

In this section we present the series of steps used to extract vascular network structures from cornea images. We were provided with images from 15 experiments in which pellets containing 300 ng of VEGF-A_{165} were implanted into the corneas of mice, and 15 in which 15 ng of bFGF was used. Six and five pairs of images, respectively, were rejected from the VEGF-A_{165} and bFGF image sets due to poor quality at one or both time-points. The process of vascular network extraction is subdivided into a series of semi-automated procedures which we partition into pre-processing, enhancement, post-processing and segmentation steps and describe below (see also Figure 4.8). For simplicity, in our analysis we neglect the effect of the curvature of the eye.

i) **Pre-processing**

To obtain a scale for the images we assume that each mouse has a spherical eye of radius 1.53 mm, as suggested by Rogers *et al.* (2007) and confirmed by measurements made at Roche, Penzberg. We fit a circle to a selection of ten points placed manually around the circumference of the exposed portion of the eye and measure the radius of that circle in terms of pixels. This allows us to estimate the scale (number of pixels per mm) for each image.

The image is manually cropped to a rectangular region which identifies the central portion of the cornea in which the vasculature is most in focus and therefore most amenable to segmentation. The cropped image is then rotated (usually by a few degrees) in order to align the limbal vessel(s) with the horizontal axis of the image. At this point the closest distance between the pellet and the limbal vessels is measured. In this way, we obtain an estimate for the distance between the pellet and the limbal vessels.

ii) **Enhancement**

The vasculature in each image is enhanced using the Gaussian matched filter approach outlined in the previous section. We use an extended array of Gaussian matched filters in which $L = 11$ pixels, $\sigma = \{0.5,\ 0.6\ ...\ 1.9,\ 2\}$ pixels and $T = 4\lceil\sigma\rceil$ pixels.

iii) **Post-processing**

We refine our region of interest (ROI) to the area in which the vascular growth is localised by drawing around it manually. This reduces the risk of spurious signals appearing in the matched filter response due to background noise in the region between the neovasculature and the pellet. We also eliminate saturated regions from each image by thresholding

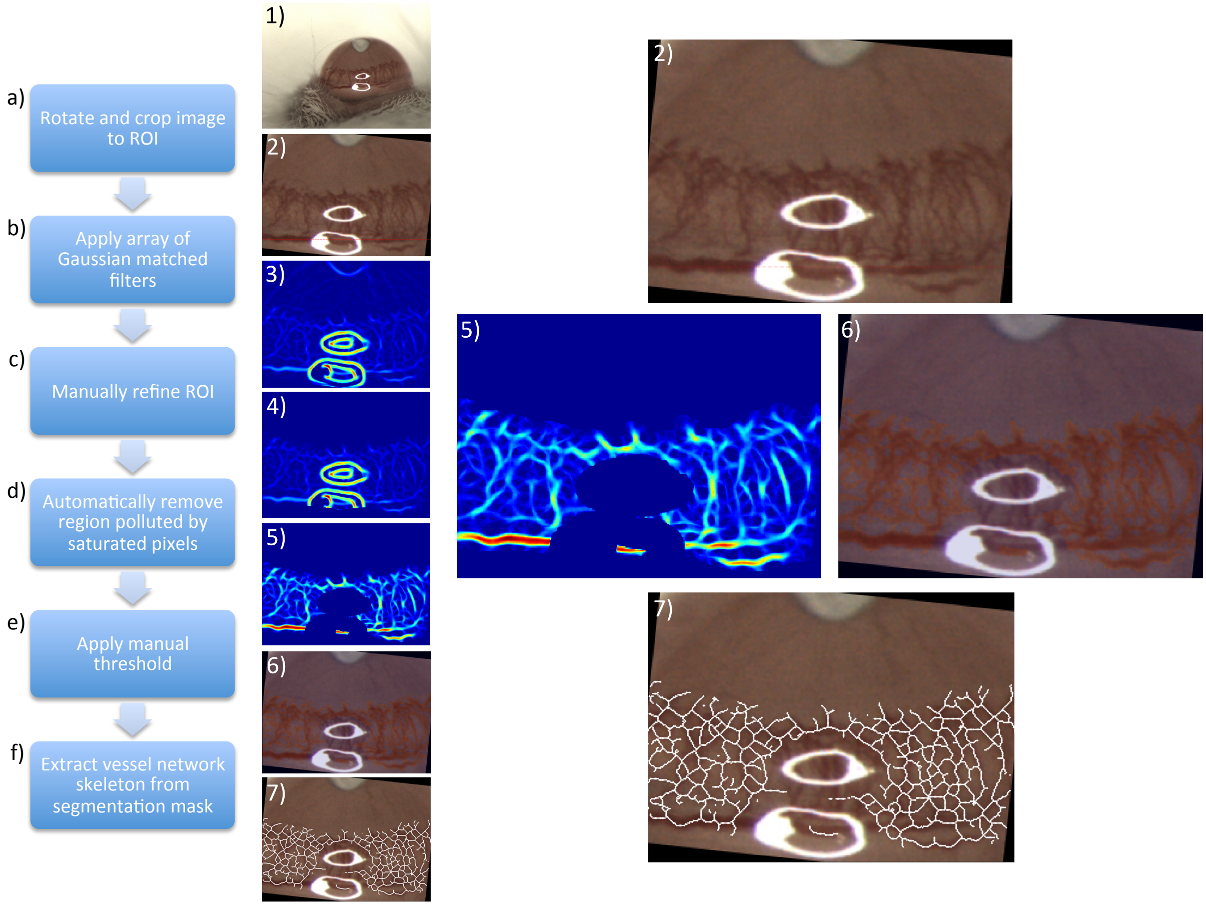

Figure 4.8.: Work flow for vessel extraction from cornea micropocket assay images. See main text for details.

a Hue-Saturation-Value (HSV) representation of the image according to each pixel's associated V-value.

After refining the ROI, the pixel values in the enhanced image are renormalised such that pixels which are most likely to correspond to a vessel are given a value of 255 and pixels which are least likely to correspond to a vessel are given a value of zero. Figure 4.8 (image 5) shows an example of a finalised enhanced image resulting from this process.

iv) **Segmentation**

To segment the vasculature from the background we apply a threshold to the enhanced image. An automated thresholding procedure, known as local entropy thresholding, provides an initial segmentation of the vascular network (Chanwimaluang and Fan 2003)[7]. The initial threshold level is tuned by eye in order to improve the accuracy of the network segmentation, where possible.

After thresholding, we apply a thinning procedure, via MATLAB's *bwmorph* function,

---

[7] We use an implementation for the local entropy thresholding algorithm as provided by Chanwimaluang and Fan at `http://www.vcipl.okstate.edu/localentropy.htm`.

to reveal the back-bone, or skeleton, of the vascular network. This skeleton provides an approximate but reasonably comprehensive indication of the locations of the centre-lines of the vessels. An example network skeleton is illustrated in Figure 4.8 (image 7).

In the models developed in this thesis (in Chapters 5 and 6, in particular) the vascular density is averaged in the directions perpendicular to that in which the vascular front is moving on average (from the limbus to the pellet). Thus, to compare model simulations with the experimental data, we perform a similar averaging here; using our skeletonised networks, we count the number of identified vessels along each plane perpendicular to the direction in which vascular growth occurs on average, i.e. we count vessels along the x-direction in our images. We use these vessel counts to estimate the average vascular density, measured in metres of vessel per metre cubed, at all locations between the pellet and limbus. In our calculation of vascular density, we assume that the corneal stroma has a thickness of approximately $100\,\mu$m as suggested by Zhang *et al.* (1996) and Song *et al.* (2003). These data are used to produce a plot, or a vascular density profile, which describes how the vascular density varies on average across each cornea image, moving from the limbal vessels towards the pellet. This process is fully automated.

We extracted the vascular density profiles from all the viable images. For each set of experiments the vascular density profiles were concatenated and averaged so that we could evaluate the average neovascular response of the corneal vasculature to each AF at their respective doses. The resulting average vascular density profiles are presented in Figure 4.9. In Figures 4.10 and 4.11 we also present the data extracted from each individual experiment. Figure 4.10 shows vascular density profiles from individual experiments, whilst Figure 4.11 shows the distributions of two summary statistics extracted from the individual profiles: the maximum amplitude of the vascular density profile (disregarding the limbal vasculature); and the location of the vascular front, defined as the location at which the vascular density becomes half-maximal[8]. To test whether the summary statistics extracted from VEGF-A$_{165}$ and bFGF experiments are significantly different we use the MATLAB function *ttest2* to perform the two-sample t-test, assuming that the two samples come from normal distributions with unknown and unequal variances. Using this statistical test, our image analysis reveals that while the vasculature travels further towards bFGF pellets than VEGF-A$_{165}$ pellets, the mean density of newly vascularised regions is transiently greater when VEGF-A$_{165}$ pellets are used. That is, day 3 maximum densities for VEGF-A$_{165}$ experiments were significantly greater than those for bFGF experiments ($p < 0.01$), while day 5 maximum

---

[8] Maximum amplitudes and front locations of experimental vascular density profiles were estimated by fitting a smoothing spline to the noisy vascular density profiles from individual experiments.

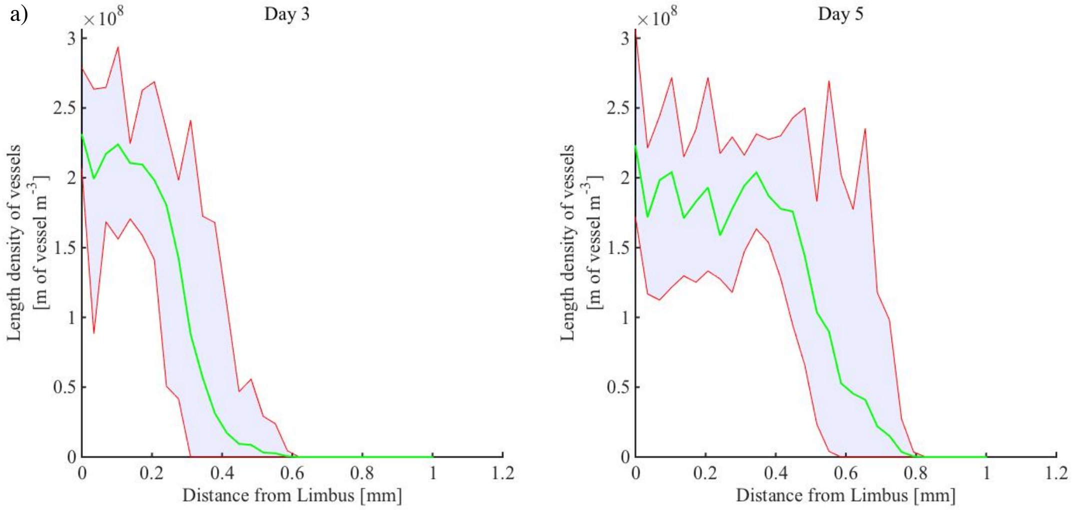

(a) 300 ng VEGF-A_{165} data.

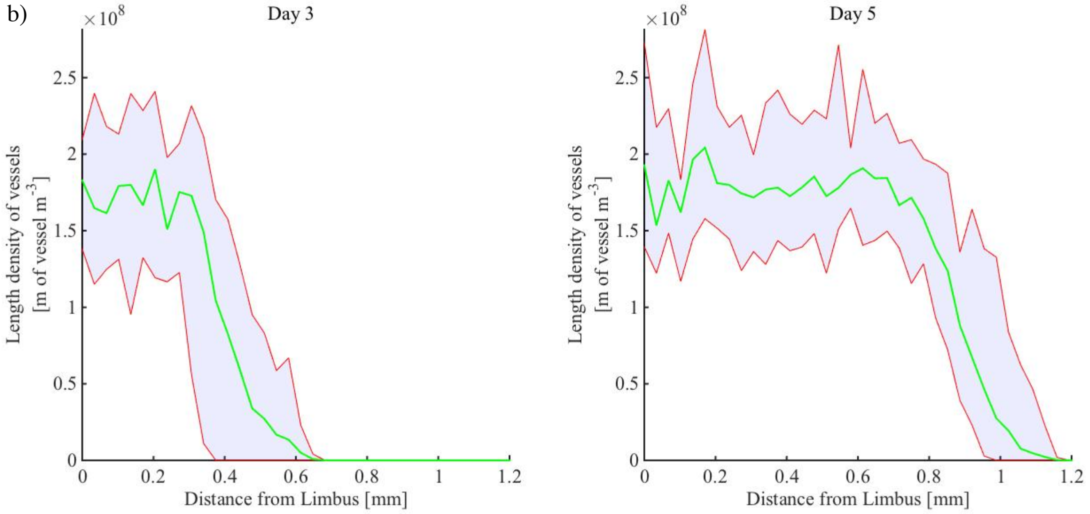

(b) 15 ng bFGF data.

Figure 4.9.: Vascular density profiles obtained from the semi-automated segmentation of cornea images. The mean vessel density profile is shown in green. The shaded region indicates the range of vessel densities at each location across all experiments.

densities were not significantly different.

While there is clear inter-individual variability in the angiogenic response for both VEGF-A_{165} and bFGF experiments, for simplicity, in this thesis we will use the averaged spatially-resolved and dynamic data presented in Figure 4.9 to parametrise our models. This is reasonable since, although the average vascular density profiles do not capture the sharp gradient at the vascular front present in some individual traces, they do appear to be representative of some of the other individual traces which have a less steep gradient. In Chapter 8 we also propose an alternative approach which could be used to parametrise our models, and which aims to take into account

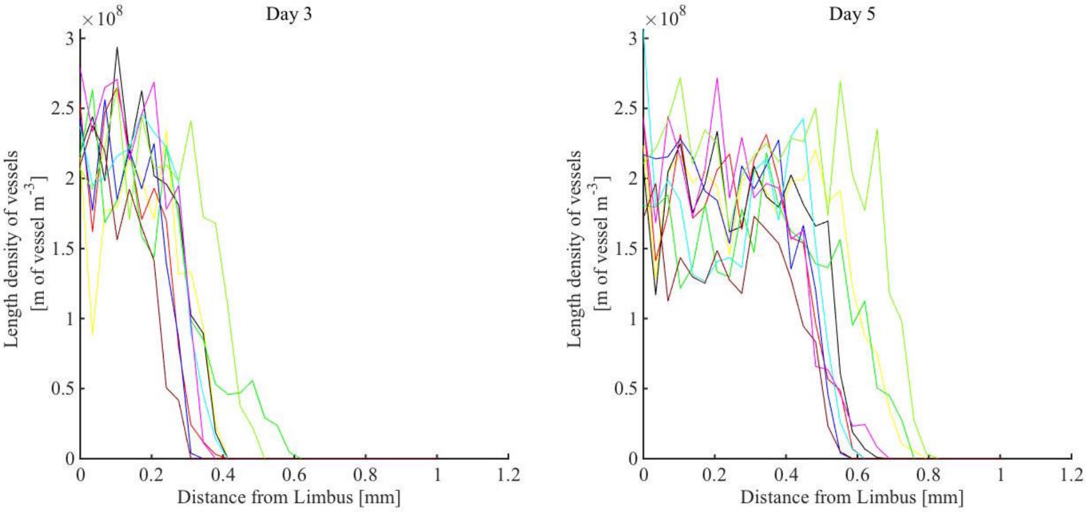

(a) 300 ng VEGF-A$_{165}$ data.

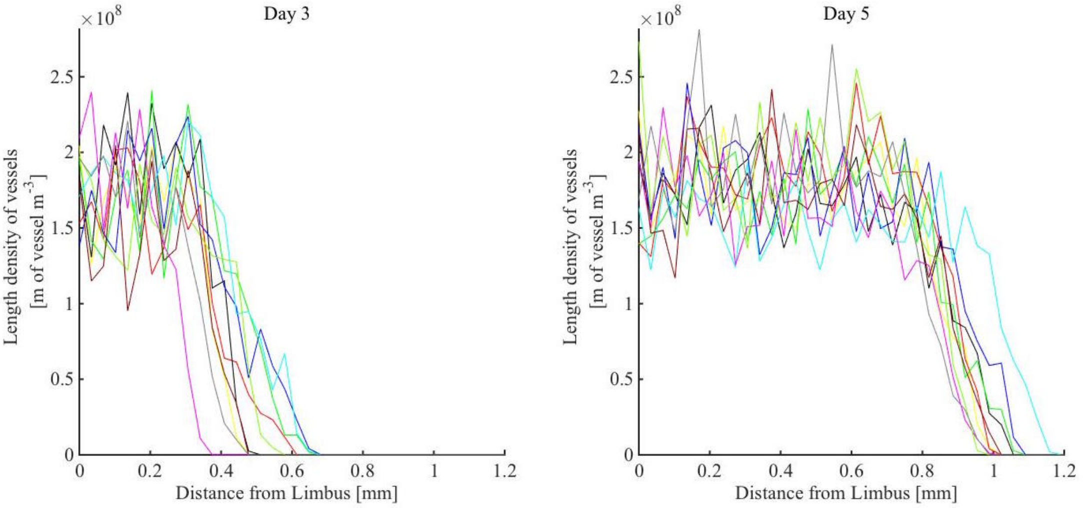

(b) 15 ng bFGF data.

Figure 4.10.: Vascular density profiles obtained from the semi-automated segmentation of cornea images. Individual traces are shown.

inter-individual variability.

The images used to generate the vascular density profiles in Figure 4.9 are hosted on figshare (`http://dx.doi.org/10.6084/m9.figshare.1176779`), where MATLAB code for efficient reproduction of the figure is also available (`http://dx.doi.org/10.6084/m9.figshare.1205083`).

4.5. Discussion

Using a set of hand-labelled retinal images from the DRIVE database we have compared various state-of-the-art algorithms designed to enhance vascular network structures in images. We have modified a well-established vessel enhancement algorithm, the Gaussian matched filter

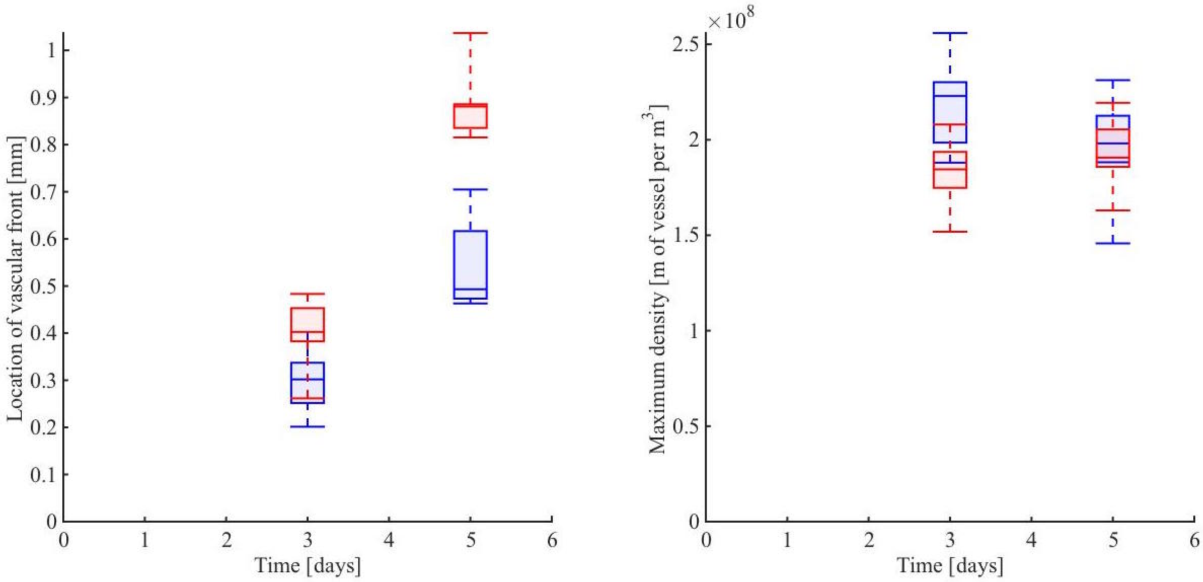

Figure 4.11.: Summary statistics estimated from experimental data are compared for VEGF-A$_{165}$-induced angiogenesis (blue) and bFGF-induced angiogenesis (red). First, second and third quartile with maxima and minima are shown.

(Chaudhuri *et al.* 1989; Al-Rawi *et al.* 2007), in order to improve its effectiveness at detecting vessels with a range of diameters. The Gaussian matched filter's proven efficacy in identifying retinal vasculature, combined with its relative simplicity and intuitiveness, indicated that it would be suitable for extracting vessels from experimental images, for which no ground truth masks are available. In particular, the Gaussian matched filter method does not require its parameters to be carefully tuned for specific applications.

We have integrated our adaptation of the Gaussian matched filter method for vessel enhancement into a series of supervised processes which aim to identify individual vessels in a set of images captured during cornea micropocket assay experiments at Roche, Penzberg. In so doing we have developed a semi-automated process which is relatively high-throughput and, thus, scalable to large numbers of images. Furthermore, by using computer-aided techniques to assist in the identification of vasculature in our images we reduce some of the subjectivity associated with the manual identification and annotation of vessels by humans. The data extracted from the images and presented in this chapter will be used to parametrise the models presented in Chapters 5, 6 and 7, and for comparison with model simulations.

Our image analysis offers several advantages over the analysis currently performed by Roche. Their colour-based image processing can provide insight into the extent of neovascular growth and also the area of neovascularisation at the end-point of experiments (day 5). While the area of neovascularisation at the end-point of experiments may be a good proxy for the strength of the neovascular response to a given growth factor, it does not provide a reliable estimate for the neovascular density. By contrast, our analysis provides us with an estimate for the vascular density, how it is distributed, and the extent of the neovascularisation. This extra quantitative information which we extract from the images then allows us to better estimate model parameters. To illustrate this point further, consider the following. If our models were fit only to the extent of neovascularisation, the spatial profile of the vascular density could take any shape as long as it extended the correct distance towards the pellet. See, for example, Figure 4.12 in which three artificially generated vessel density profiles are presented, each of which extend the same distance towards the pellet, but which all have very different density profiles. In a mathematical modelling context, each of these profiles would correspond to a different set of model parameters and, by using only the location of the vascular front to guide model parametrisation, it is not possible to discriminate between these parametrisations. Differentiating between the three parametrisations requires more information. In summary, then, by estimating the vessel density and showing how that density varies in space and evolves in time, our analysis provides a more detailed description of angiogenesis, allowing us to better constrain model parameter values.

Manual inspection reveals that the resulting segmentations of the vascular networks from our cornea images appear to be reasonably accurate; most vessels, including the thinnest and most poorly contrasted ones, are identified and false positive results are relatively infrequent. Future work could entail confirming the accuracy of our segmentations by manually annotating a few cornea images.

We believe our images to be of an appropriate type and quality to provide quantitative estimates for vascular densities in the cornea. Most reliably, our analysis allows us to estimate the extent of the neovascularisation towards the pellet. With regards to the extraction of further details of vascular network morphology, the images provide a 2-D projection of a 3-D structure[9]. Thus, even with perfect segmentation, the images are unlikely to be appropriate for reliably extracting the locations of anastomoses and the lengths of individual vessels, for instance. Meanwhile, the 3-D hybrid model of angiogenesis in the cornea we develop in Chapter 7 provides some insight into how accurately one may estimate the *in vivo* corneal vascular density from 2-D images, given that the neovasculature is actually a 3-D structure.

Several aspects of our analysis may limit the quality of the quantitative data which we extract. First, our data are prone to segmentation errors. A fundamental limit to the accuracy of our

---

[9] In mice, the stromal layer of the cornea is approximately 100 μm thick (Zhang *et al.* 1996; Song *et al.* 2003), while vessels in the cornea have a diameter of between ~ 10 and $\sim 20\,\mu$m.

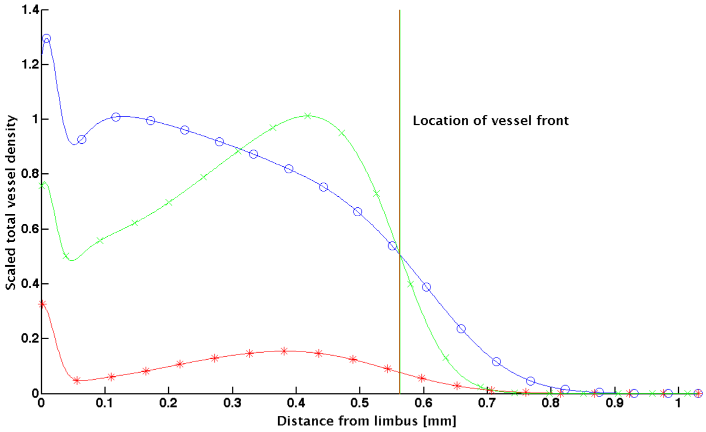

Figure 4.12.: Artificially generated vessel density profiles. The location of the front of each density profile is the same but the profiles are vastly different in shape. Here, we define the location of the vascular front as the location at which the vascular density becomes half maximal.

segmentations, and thus to the quantitative data which we have extracted, is the resolution of the available images. All of the images with which we were provided were taken from live mice. On the one hand, this provides us with two time-points for each animal throughout the period of an experiment. Since we wish to use the image-derived data to parametrise and compare to the results of dynamic mathematical models, the acquisition of dynamic data is extremely valuable. However, images taken from live mice are limited in terms of resolution due to animal movement and low camera exposure time. While post-mortem cornea extraction and vessel staining could yield better resolution images, data extracted from such images are not dynamic in nature. Such images could in principle be used to validate the quantitative data extracted from the *in vivo* images that we have processed and analysed but at this time these images are not available.

Using the radius of a mouse's eye to provide a scale for each image appears to be a reasonably reliable approach, since the distances measured between the limbal vessels and the pellet are consistent with those outlined in the experimental procedure. However, in the future a scale bar or ruler placed close to the mouse's eye would be a useful addition to images, as suggested by Cao *et al.* (2011). Further, accounting for the eye's curvature may provide modest improvements in the accuracy of our data. However, as Figure 4.13 suggests, for the region of the eye in which we are interested, ignoring the curvature is a reasonable assumption. The figure shows a typical cornea image. Superimposed onto the image is a typical ROI (blue) and a series of tissot indicatrices, or ellipses of distortion (cyan), which are tools commonly used to illustrate map projection distortion. Each ellipse depicts what a circle placed on the surface of the eye

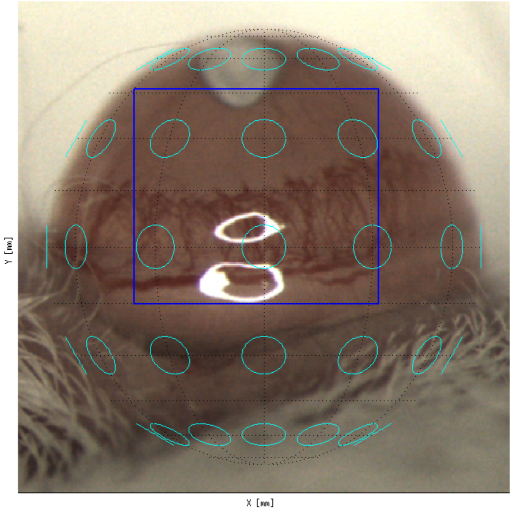

Figure 4.13.: The approximate distortion in length scales brought about by projecting a spherical eye onto a 2-D Cartesian plane is shown. A mouse eye, a sphere of radius $\sim 1.5\,\text{mm}$, is shown and a typical ROI is identified (blue box). Tissot indicatrices (cyan) have been superimposed onto the image. These ellipses approximately depict the distortion brought about by the projection of the sphere onto the image plane. For simplicity, we have assumed that the projection is orthogonal.

would look like in the image plane. For this illustration we have assumed that the projection of the eye onto the 2-D image plane is approximately orthogonal. We see that inside the ROI the distortion is relatively insignificant and that the worst distortion occurs in the top corners of the ROI. However, few vessels are ever identified in this region.

A final comment regarding the work presented in this chapter: much progress has been made on the segmentation of vasculature from images and the improvement of algorithms designed to both enhance and segment vasculature from images remains an active area of research. Furthermore, modalities for capturing more detailed and better quality images of vascular networks continue to improve. Taken together, this means that the increased availability of high quality quantitative data is likely in the near future. Such data may be utilised for mathematical model development, parametrisation and validation. As higher quality imaging modalities appear, more work is needed to merge the two complementary fields of image analysis and mathematical modelling in angiogenesis research. The successful merging of the two fields and the materialisation of quality quantitative data, which are spatially and temporally resolved, will allow for improved parametrisation of mathematical models of angiogenesis. What is more, comparing the results from mathematical models of angiogenesis to data which are quantitative will enable modellers to build trust in those models which is required so that they may gain wide-spread acceptance amongst the biological community.

CHAPTER 5

A Continuum Model of Angiogenesis in the Mouse Cornea Micropocket Assay

5.1. Overview

As discussed in Chapter 3, many mathematical models have been developed to study different aspects of angiogenesis. Recent mathematical modelling efforts have attempted to link quantitative experimental data with tissue scale simulation of angiogenesis (Tong and Yuan 2008b; Watson *et al.* 2012), underlining the potential for integrating mathematical modelling with image analysis techniques to increase insight into the mechanisms underlying angiogenesis. In this chapter, inspired by these efforts, we utilise the spatiotemporal information extracted from experimental images in Chapter 4 to parametrise deterministic, continuum models of angiogenesis based on cornea micropocket assay experiments. Our data describe how the density of the vasculature develops behind the invading front of capillary tips, thus enabling us to constrain model parameter values to a greater extent than achieved previously within the context of similar continuum models. This provides us with increased confidence in the predictions made by our mathematical models.

For convenience, we begin this chapter by recapping the important details of the experiments on which our models are based (Section 5.2). Our models specialise and extend Byrne and Chaplain's (1995) model of corneal angiogenesis (reviewed in Section 3.2.1). The model is initially extended to include important biological details such as vessel maturation and specialised by adding a model of controlled release of an AF, which ensures that the model better represents the cornea experiments for which quantitative data are available. Moreover, by extending the model to include the limbal vessels and the outward flux of the AFs at the limbus boundary explicitly, we aim to capture both the processes which lead to the onset of angiogenesis in the cornea and the cessation of tip production at the limbus after vascular growth has begun. The model is initially developed and parametrised (in Sections 5.3 and 5.4, respectively) to describe VEGF-A$_{165}$-induced angiogenesis. We then explore the behaviour of our model through numerical simulation and a parameter sensitivity analysis in Section 5.5, providing insight into the limitations of the cornea micropocket assay. In Sections 5.6-5.8, the model is adapted and re-parametrised to describe bFGF-induced angiogenesis. The model is further extended to account for tip cell-ECM interactions in Sections 5.9-5.11, where we investigate the impact that such interactions have on model predictions of anti-angiogenic therapies. Finally, in Section 5.12 a simplified version of our model is developed and also compared to the experimental data[1]. This simplified model is also able to reproduce quantitatively our experimental data. The contributions of this chapter and potential extensions are discussed in Section 5.13. Given that both our detailed and simplified models are able to reproduce quantitatively our experimental data, we also discuss the utility of developing more detailed models.

5.2. Experimental basis for the mathematical model

Our models are based on cornea micropocket experiments performed at Roche, Penzberg (see Sections 2.9.1 and 4.2). For convenience, we describe here the details which are relevant to our modelling efforts. Nylon pellets of radius 0.3 mm and thickness 0.06 mm were implanted into the cornea of mice at a distance of approximately 1 mm from the anterior portion of the limbal vessels. Images of the resulting neovascular response were captured three and five days after implantation and analysed quantitatively. We focus on experiments involving pellets that initially contained 300 ng of VEGF-A$_{165}$ or 15 ng of bFGF.

5.3. Model development: VEGF-A$_{165}$-induced angiogenesis

In this section we develop a continuum model of corneal angiogenesis, formulated in 1-D Cartesian coordinates. Figure 5.1 illustrates how our model is constructed. We assume that the position of the vascular front as it advances towards the pellet can be approximated by a straight line. Figure 5.1a provides some motivation for this assumption while a schematic of our model is presented in Figure 5.1b. By considering dependent variables which represent averages in the plane perpendicular to the average direction of tip cell motion, we restrict attention to one spatial dimension. Thus, the independent variables in our model are time, t, and space, x, where the

---

[1] The rationale for developing the detailed models first are two-fold. First, a detailed model is easier to parametrise using values from the literature since its parameters correspond more directly to experimentally measurable quantities. Second, by reducing a detailed model to a simplified version of that model, we make explicit the approximations that are made in developing such a simple model, putting it clearly in context.

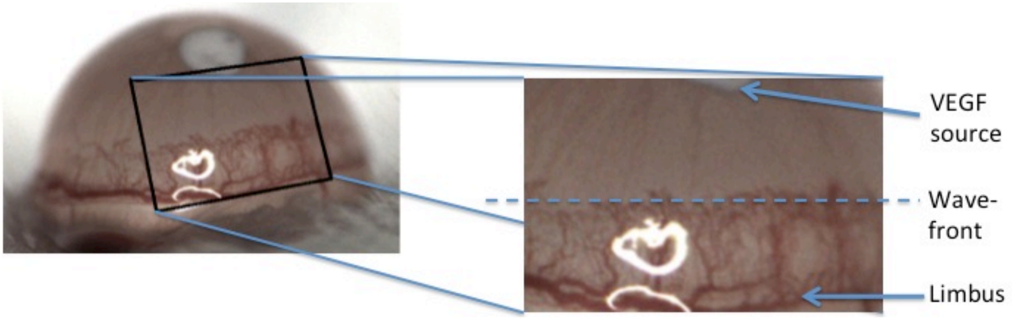

(a) The region of interest in experimental images.

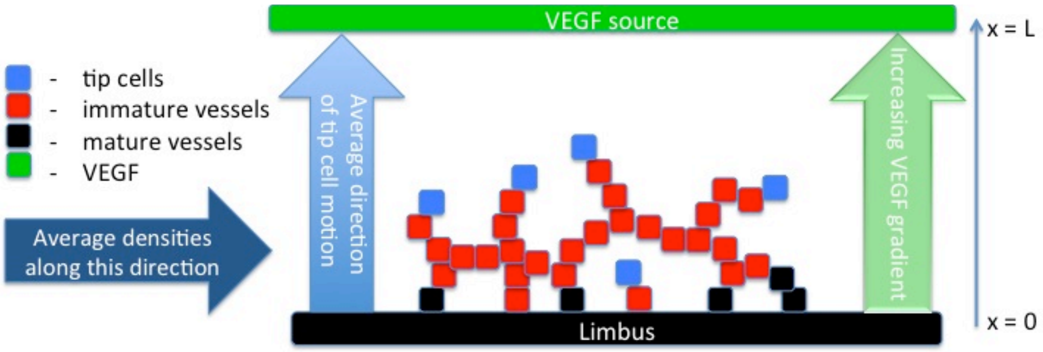

(b) Schematic of the cornea micropocket assay, on which our mathematical models are based. Tip cells are assumed to migrate (and thus vessels grow), on average, in the direction of increasing VEGF concentration, i.e. towards the pellet. For simplicity, we formulate our model in terms of dependent variables which represent quantities averaged in the plane perpendicular to the predominant direction of tip cell motion.

Figure 5.1.: Relationship between the mathematical model and the experimental system.

x-axis lies parallel to the average direction of tip cell motion, with the limbus located at $x = 0$ and the pellet at $x = L$.

Following Balding and McElwain (1985) and Byrne and Chaplain (1995), we employ the snail-trail approach to model vascular growth and, thus, consider separately the dynamics of the tip cells and stalk cells, which constitute the major part of new vessels in our model. Due to the importance of maturation in vascular development, we further decompose the vessels according to their state of maturity. A major difference between mature and immature vessels which we account for in our model is that mature vessels are self-sufficient in growth signals, whereas immature vessels are reliant on external sources of AFs (such as VEGF-A) for survival (Benjamin *et al.* 1999). We also assume that mature vessels, being stable, can not form new sprouts, whereas immature ones can. Whilst modelling vessel perfusion is an essential feature of models of vascular tumour growth, since only perfused vessels supply nutrients to tumours, in our system we focus purely on angiogenesis and do not concern ourselves with the delivery of nutrients to a tumour. Thus, we do not distinguish between perfused and unperfused vessels;

vessels in our model implicitly include both perfused and unperfused sub-populations. Initially, we consider pellets incubated with 300 ng of VEGF-A$_{165}$ only and thus develop equations for the average density of tip cells, $n(x,t)$, the average length density of immature vessels, $\rho(x,t)$, the average length density of mature vessels, $m(x,t)$, and the average concentration of VEGF-A$_{165}$, $v(x,t)$. We also model the mean concentration of VEGF-A$_{165}$ in the pellet, denoted $[V_T](t)$. A summary of the dependent variables used in this model is given in Table 5.1. In the following sections we introduce the equations governing the time-evolution of each model species.

5.3.1. Mature vessel density equation, $m(x,t)$

Vessel maturation and dematuration are complex processes involving many chemical species and multiple cell types (Chapter 2). In what follows, we take a simple approach to model these processes. We assume VEGF-A$_{165}$ binding to ECs induces vessel dematuration at a rate proportional to the fraction of bound VEGFR-2 receptors, further assuming Michaelis-Menten reaction kinetics. Meanwhile, we suppose that vessels mature at a rate proportional to the fraction of unbound VEGFR-2 receptors if, and only if, the local concentration of ECs is above some threshold, N_{min}[2]. Based on evidence presented in Hall (2006), mature vessels are viewed as immobile and stable, and only maturation and dematuration are assumed to contribute to their evolution. Combining these assumptions, the equation governing the mature vessel density, m, is given by:

$$\frac{\partial m}{\partial t} = \underbrace{-\lambda_1^v\left(\frac{v}{v+v_{\frac{1}{2}}}\right)m}_{\text{dematuration}} + \underbrace{\lambda_2^v\left(\frac{v_{\frac{1}{2}}}{v+v_{\frac{1}{2}}}\right)H\left(\nu\left(m+\rho\right)+n-N_{min}\right)\rho}_{\text{maturation}}. \tag{5.1}$$

Here, λ_1^v is the maximal rate of vessel dematuration, λ_2^v is the maximal rate of maturation and $H(...)$ is the Heaviside function. Additionally, $v_{\frac{1}{2}}$ is the concentration of VEGF-A$_{165}$ at which half of the VEGFR-2 receptors are bound and ν is the average number of ECs contained in a metre length of vessel.

In practice, mature vessels are subject to regression and other types of remodelling. For example, ECs lining vessels with low levels of blood flow experience low levels of wall shear stress and regress (Meeson *et al.* 1996; Resnick *et al.* 2003). However, since remodelling of this type

---

[2] The assumption we make implicitly here is that, for maturation to occur, there is some threshold level of PDGF-B production required in order to promote sufficient levels of pericyte proliferation and recruitment. Since we do not model PDGF-B or pericytes directly, we use EC density as a proxy for PDGF-B production and suppose that a minimum density of ECs, N_{min}, must be present locally for vessels to (re-)mature in lower concentrations of VEGF-A$_{165}$, where Ang-2 production by ECs has been reduced sufficiently.

Variable	Description	Units
$n(x,t)$	Number of tip cells per unit volume, averaged along directions perpendicular to direction of tip migration.	tip cells m^{-3}
$\rho(x,t)$	Length of immature vessels per unit volume, averaged along directions perpendicular to direction of tip migration.	m of vessel m^{-3}
$m(x,t)$	Length of mature vessels per unit volume, averaged along directions perpendicular to direction of tip migration.	m of vessel m^{-3}
$v(x,t)$	Mean molar concentration of VEGF-A$_{165}$ across cross-sectional area of cornea.	M
$[V_T]$	Mean total (bound + unbound) concentration of VEGF-A$_{165}$ inside pellet.	M

Table 5.1.: Table of dependent variables.

typically occurs over several days (Brown 2005; Owen *et al.* 2011), and because we do not account for blood flow or the wall shear stress inside individual vessels, we neglect such remodelling in our model.

5.3.2. Tip cell density equation, $n(x,t)$

VEGF-A$_{165}$ binding to immature vessels stimulates tip cell production at a rate which is assumed proportional to the local fraction of bound VEGFR-2. Tip cell migration is thought to involve two principal mechanisms: chemotaxis and haptotaxis. Following Balding and McElwain (1985) and Byrne and Chaplain (1995), we assume that chemotaxis is the dominant transport mechanism in cornea assay experiments. Thus, we neglect haptotaxis but assume that tip cells also undergo a small amount of random motion which accounts for the fact that chemotaxis is not the only mechanism at work. Tip cells are annihilated when they anastomose with vessels or other tip cells. Additionally, based on evidence suggesting that VEGF-A promotes EC survival (Benjamin *et al.* 1999), we assume that tip cells die in low VEGF-A$_{165}$ concentrations. The governing equation for tip cell density, $n(x,t)$, is then given by:

$$\frac{\partial n}{\partial t} = \frac{\partial}{\partial x}\left(\underbrace{\mu \frac{\partial n}{\partial x}}_{\text{random motion}} \underbrace{- \chi_v \, n \frac{\partial v}{\partial x}}_{\text{chemotaxis}}\right) + \underbrace{\alpha_0^v \, \rho \left(\frac{v}{v + v_{\frac{1}{2}}}\right)}_{\text{sprouting from vessels}}$$
$$- \underbrace{\beta_1 \, n \, (\rho + m)}_{\text{tip—to—vessel anastomosis}} - \underbrace{2 \, \beta_2 \, n^2}_{\text{tip—to—tip anastomosis}} \underbrace{- \gamma \, n \left(\frac{v_{\frac{1}{2}}}{v + v_{\frac{1}{2}}}\right)}_{\text{death}}, \tag{5.2}$$

where μ and χ_v are the random motility and chemotactic coefficients, respectively, α_0^v is the maximum rate of production of tip cells per length of immature vessel, β_1 is the rate of tip-to-vessel anastomosis per unit vessel length density per unit tip cell density per unit volume, β_2 is the rate of tip-to-tip anastomosis per unit tip cell density squared per unit volume and γ is the maximum rate of EC death in low VEGF-A$_{165}$ conditions. All parameters are assumed non-negative and constant.

5.3.3. Immature vessel density equation, $\rho(x,t)$

As stated earlier, we follow Balding and McElwain (1985) and Byrne and Chaplain (1995), describing the production of immature vessels using the snail-trail approach (see Figure 3.1). We also model vessel production due to the movement of tip cells in the direction purely perpendicular to the average direction of tip cell motion. More explicitly, we assume that when a tip cell is annihilated in an anastomosis event, a small length of vessel is deposited. Figure 5.2 illustrates a circumstance in which a tip cell does not migrate from one control volume to the next along the x-axis but instead forms an anastomosis with a vessel which exists inside that volume. Even though the tip cell has not moved towards the pellet, a small length of vessel has been laid down. Such cross-linking events could plausibly contribute significantly to vessel length production.

As mentioned above, we assume that the ECs associated with immature vessels rely on VEGF-A for survival. Therefore, in the absence of VEGF-A$_{165}$, immature vessels regress. By contrast, mature vessels do not rely on external sources of VEGF-A for their viability and, as a result, do not undergo regression when VEGF-A$_{165}$ is withdrawn (Benjamin *et al.* 1999). In summary, then, the immature vessel length density, $\rho(x,t)$, obeys the following PDE:

$$\begin{aligned}\frac{\partial \rho}{\partial t} = {} & \underbrace{\kappa \left| \mu \frac{\partial n}{\partial x} - \chi_v \, n \frac{\partial v}{\partial x} \right|}_{\text{snail−trail}} + \underbrace{\bar{l}_\rho \, \beta_1 \, n \, (\rho + m)^{\frac{1}{2}} + \bar{l}_n \beta_2 \, n^{\frac{5}{3}}}_{\text{vessel production due to anastomosis events}} \underbrace{- \gamma \, \rho \left(\frac{v_{\frac{1}{2}}}{v + v_{\frac{1}{2}}} \right)}_{\text{regression}} \\ & \underbrace{+ \lambda_1^v \left(\frac{v}{v + v_{\frac{1}{2}}} \right) m}_{\text{dematuration}} \underbrace{- \lambda_2^v \left(\frac{v_{\frac{1}{2}}}{v + v_{\frac{1}{2}}} \right) H\left(\nu\,(m+\rho) + n - N_{min}\right) \rho}_{\text{maturation}} .\end{aligned} \tag{5.3}$$

In (5.3) we have also included terms for vessel maturation and dematuration to ensure appropriate conservation of vessel length density between Equations (5.1) and (5.3). The constant κ quantifies the length of vessel left behind as a tip cell migrates towards the pellet. Setting $\kappa > 1$ allows us to account for some production of vessel length in the plane perpendicular to the x-axis. However, in contrast to vessel production due to anastomosis events, this requires some tip cell movement along the x-axis. We have assumed that the length of vessel laid down when a tip cell undergoes anastomosis with a vessel is proportional to the mean inter-vessel distance, $\propto \frac{1}{(\rho+m)^{\frac{1}{2}}}$. Similarly, the length of vessel laid down when two tip cells anastomose is proportional to the

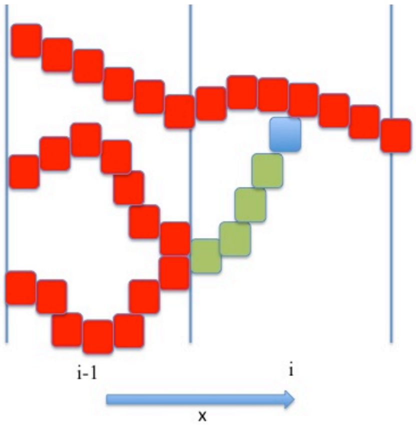

Figure 5.2.: Schematic showing the production of vessel length in a control volume which is attributable to motion purely perpendicular to the x-direction. The tip cell (blue), associated with the green vessel, moves towards another vessel and forms an anastomosis. Although the tip cell has not moved towards the pellet (at the scale we are interested in), a small length of vessel has been deposited.

mean inter-tip cell distance, $\propto \frac{1}{n^{\frac{1}{3}}}$. Here, the constants of proportionality, $\bar{l}_\rho$ and $\bar{l}_n$, are assumed to be of order unity, as explained fully in Section 5.4.

5.3.4. VEGF-A$_{165}$ concentration equation, $v(x,t)$

The VEGF-A$_{165}$ distribution in our system is assumed to depend upon diffusion through the corneal stroma, natural decay, uptake by ECs and drainage through the vasculature. Combining these assumptions, we propose the following equation for the evolution of the VEGF-A$_{165}$ distribution in our model domain:

$$\frac{\partial v}{\partial t} = \underbrace{D_v \frac{\partial^2 v}{\partial x^2}}_{\text{diffusion}} - \underbrace{\lambda_v\, v}_{\text{natural decay}} - \underbrace{2\,\pi\,\bar{R}\,P_v\,(\rho+m)\,(v-v_{blood})}_{\text{drainage through vessels}}$$

$$\underbrace{-\,K^v_{EC}\,(n+\nu\,(\rho+m))\left(\frac{v}{v+v_{\frac{1}{2}}}\right)}_{\text{uptake by ECs}}. \qquad (5.4)$$

In (5.4), D_v is the assumed constant diffusion coefficient for VEGF-A$_{165}$ in the corneal stroma and λ_v is the rate constant for natural decay. For simplicity, we assume that, P_v, the permeability of vessels to VEGF-A$_{165}$ is constant and all vessels have the same radius, $\bar{R}$. Additionally, we assume that the maximal rate at which ECs uptake VEGF-A$_{165}$ is K^v_{EC}.

The third term in (5.4) represents the rate of loss of VEGF-A$_{165}$ per unit volume due to the outward flux of VEGF-A$_{165}$ through vessel walls. We approximate vessels as cylinders and therefore assume that the surface area for VEGF-A$_{165}$ exchange per unit volume is given by

$2\,\pi\,\bar{R}\,(\rho+m)$. The flux of VEGF-A$_{165}$ crossing a vessel wall, measured in moles per unit time per unit area of vessel wall, is assumed proportional to the difference in molar concentration of VEGF-A$_{165}$ on either side of the wall, where we denote the concentration of VEGF-A$_{165}$ inside a vessel by v_{blood}. The uptake of VEGF-A$_{165}$ by ECs is described by the fourth term on the RHS of Equation (5.4). For simplicity, and since there are approximately three times as many VEGFR-2 molecules on the surface of ECs as there are VEGFR-1 (Wang *et al.* 2002), we neglect VEGF-A/VEGFR-1 binding and assume that VEGF-A$_{165}$ is taken up via VEGFR-2 binding only. The absence of a source term on the RHS of Equation (5.4) reflects our assumption that VEGF-A$_{165}$ is only released into the cornea from the pellet. Thus, the influx of VEGF-A$_{165}$ into the cornea is incorporated via a boundary condition at $x = L$, which we discuss below.

5.3.5. Initial and boundary conditions

In order to close Equations (5.1)-(5.4), it remains to prescribe appropriate boundary and initial conditions. The model is formulated on a 1-D Cartesian domain, $0 \leq x \leq L$, with a VEGF-A$_{165}$-containing pellet located at $x = L$ and limbal vessels (that border the cornea) at $x = 0$. Initially, the interior of the model domain is assumed to be devoid of vessels and VEGF-A$_{165}$. The distribution of vessels at $t = 0$ is described via a normal distribution of mature vessels, centred on $x = 0$, so that initially, inside the model domain, we have:

$$v(x,0) = 0, \quad \rho(x,0) = 0, \quad n(x,0) = 0, \quad m(x,0) = m_L\,exp\left[-\frac{x^2}{2\sigma^2}\right], \tag{5.5}$$

where m_L is the maximum vessel density at the limbus at $t = 0$ and σ describes the initial spread of vascular density.

We assume that tip cells are unable to penetrate the pellet or the limbus and, hence, impose no flux boundary conditions at $x = 0$ and $x = L$. Meanwhile, VEGF-A$_{165}$ is removed from the model domain at $x = 0$ via the limbal vasculature, the flux being proportional to the difference in concentrations of VEGF-A$_{165}$ inside the cornea, $v(0,t)$, and in the blood. Similarly, the influx of VEGF-A$_{165}$ from the pellet at $x = L$ is assumed proportional to the difference in concentrations of VEGF-A$_{165}$ inside the cornea, $v(L,t)$, and inside the pellet. Thus, we have:

$$\left.\begin{aligned} -\,\mu\,\frac{\partial n}{\partial x} + \chi^v\,n\,\frac{\partial v}{\partial x} &= 0, \\ -\,D_v\,\frac{\partial v}{\partial x} &= -P_v(v - v_{blood}), \end{aligned}\right\}\quad x = 0, \qquad \left.\begin{aligned} -\,\mu\,\frac{\partial n}{\partial x} + \chi^v\,n\,\frac{\partial v}{\partial x} &= 0, \\ -\,D_v\frac{\partial v}{\partial x} &= -k_p^v\;([V_f] - v)\,, \end{aligned}\right\}\quad x = L. \tag{5.6}$$

Here, k_p^v is an effective permeability constant, quantifying the rate of transfer of VEGF-A$_{165}$ across the cornea-pellet boundary. The PDEs (5.1) and (5.3) contain no spatial derivatives in m and ρ, respectively, and hence require no boundary conditions. The submodel which controls the evolution of the concentration of unbound VEGF-A$_{165}$ inside the pellet, $[V_f](t)$, is detailed in the next section.

5.3.6. Controlled release of VEGF-A$_{165}$ submodel

We assume that the concentration of VEGF-A$_{165}$ in the pellet is spatially uniform and that VEGF-A$_{165}$ binds reversibly to components of the pellet so that

$$[V_f] + [B] \underset{k_{on}}{\overset{k_{off}}{\rightleftharpoons}} [V_b]\,, \tag{5.7}$$

where $[V_f]$ and $[V_b]$ are the concentrations of free and bound VEGF-A$_{165}$ in the pellet, respectively, and $[B]$ is the concentration of free binding sites in the pellet. $[V_T]$, the combined concentration of bound and unbound VEGF-A$_{165}$, is given by $[V_f] + [V_b]$. While bound VEGF-A$_{165}$ is assumed not to decay, unbound VEGF-A$_{165}$ in the pellet decays at a constant rate of λ_p^v. This accounts for the fact that binding to constituents of a pellet, such as sucralfate, may stabilise VEGF-A$_{165}$ or bFGF (Section 2.9.1). Unbound VEGF-A$_{165}$ also diffuses across the cornea-pellet boundary. The molar flux passing through this boundary is given by $k_p^v\ ([V_f] - v(L,t))$, as in (5.6). We further assume that the concentration of VEGF-A$_{165}$ at all points immediately outside the pellet is uniform so that the total number of moles of VEGF-A$_{165}$ lost from the pellet through the boundary per unit time is given by $\zeta_p\, k_p^v\ ([V_f](t) - v(L,t))$, where ζ_p is the surface area of the pellet. Combining these assumptions, we suppose that the dynamics of VEGF-A$_{165}$ inside the pellet obeys the following equations:

$$\frac{d[B]}{dt} = -k_{on}\,[V_f]\,[B] + k_{off}\,[V_b]\,, \tag{5.8}$$

$$\frac{d[V_b]}{dt} = k_{on}\,[V_f]\,[B] - k_{off}\,[V_b]\,, \tag{5.9}$$

$$\frac{d[V_f]}{dt} = -k_{on}\,[V_f]\,[B] + k_{off}\,[V_b] - \lambda_p^v[V_f] - \frac{\zeta_p k_p^v}{\Omega_p}\left([V_f] - v(L,t)\right), \tag{5.10}$$

$$\frac{d[V_T]}{dt} = -\lambda_p^v[V_f] - \frac{\zeta_p k_p^v}{\Omega_p}\left([V_f] - v(L,t)\right), \tag{5.11}$$

where we have denoted the volume of the pellet by Ω_p. The total concentration of binding sites, $[B_0]$, remains constant so that $[B_0] = [B] + [V_b]$. Following Tong and Yuan (2008b), we assume that reactions (5.7) occur on time-scales that are much faster than those associated with decay and release of VEGF-A$_{165}$ from the pellet so that

$$k_{on}\,[V_f]\,[B] \approx k_{off}\,[V_b]\,. \tag{5.12}$$

Combining this assumption with the definition $[V_T] = [V_f] + [V_b]$ and further assuming that $[V_b] \ll [B]$, i.e. $[B] \approx [B_0]$, for all time, we find that

$$[V_T] = [V_f]\underbrace{\left(1 + \frac{k_{on}}{k_{off}}\,[B_0]\right)}_{\theta_v}. \tag{5.13}$$

Here, we have defined the binding constant, $\theta_v = \left(1 + \frac{k_{on}}{k_{off}}\,[B_0]\right)$, as in Tong and Yuan (2008b).

Using (5.13) to eliminate $[V_f]$ from (5.11), we arrive at the following equation for $[V_T]$:

$$\frac{d[V_T]}{dt} = -\lambda_p^v\frac{[V_T]}{\theta_v} - \frac{\zeta_p k_p^v}{\Omega_p}\left(\frac{[V_T]}{\theta_v} - v(L,t)\right). \tag{5.14}$$

Furthermore, (5.6) may now be rephrased in terms of $[V_T]$:

$$-\,D_v\frac{\partial v}{\partial x}(L,t) = -k_p^v\,\left(\frac{[V_T]}{\theta_v} - v(L,t)\right). \tag{5.15}$$

In this section, by assuming fast kinetics for VEGF-A$_{165}$ binding inside the pellet we have developed a simple model relating VEGF-A$_{165}$ dynamics inside the pellet to the VEGF-A$_{165}$ concentration inside the cornea. The resulting model allows us to investigate the effects of altering the release dynamics of VEGF-A$_{165}$ from a pellet. Additionally, we can prescribe the amount of VEGF-A$_{165}$ released into the cornea during a simulation. We denote the initial concentration of VEGF-A$_{165}$ in the pellet by $[V_T]_{init}$ so that

$$[V_T]\,(0) = [V_T]_{init}\,. \tag{5.16}$$

5.3.7. Nondimensionalisation

Before continuing we recast Equations (5.1)-(5.4) and (5.14), in terms of dimensionless variables. Using asterisks to denote dimensionless variables, we rescale distance with the approximate pellet-limbus distance, $\hat{L}$, and time with $\tau = \frac{\hat{L}^2}{D_v}$, so that

$$x^* = \frac{x}{\hat{L}} \quad \text{and} \quad t^* = \frac{t}{\tau}. \tag{5.17}$$

We rescale the dependent variables as

$$n^* = \frac{n}{n_0}, \quad \rho^* = \frac{\rho}{\rho_0}, \quad m^* = \frac{m}{\rho_0}, \quad v^* = \frac{v}{V_0} \quad \text{and} \quad [V_T]^* = \frac{[V_T]}{V_0}, \tag{5.18}$$

and introduce the following dimensionless parameters:

$$L^* = \frac{L}{\hat{L}}, \quad m_L^* = \left(\frac{m_L}{\rho_0}\right), \quad [V_T]_{init}^* = \left(\frac{[V_T]_{init}}{V_0}\right), \quad \sigma^* = \left(\frac{\sigma}{\hat{L}}\right), \quad P_v^* = \left(\frac{P_v \tau}{\hat{L}}\right), \quad \mu^* = \left(\frac{\mu}{D_v}\right),$$

$$\chi_v^* = \left(\frac{\chi_v V_0}{D_v}\right), \quad k_p^{v*} = \left(\frac{\tau k_p^v}{\hat{L}}\right), \quad \zeta_p = \left(\frac{\zeta_p}{\hat{L}^2}\right), \quad \Omega_p^* = \left(\frac{\Omega_p}{\hat{L}^3}\right), \quad \lambda_p^* = (\lambda_p \tau), \quad \theta_v^* = \theta_v,$$

$$v_{blood}^* = \left(\frac{v_{blood}^*}{V_0}\right), \quad \lambda_1^{v*} = (\lambda_1^v \tau), \quad \lambda_2^{v*} = (\lambda_2^v \tau), \quad \nu^* = \left(\frac{\nu \rho_0}{n_0}\right), \quad N_{min}^* = \left(\frac{N_{min}}{n_0}\right),$$

$$\alpha_0^{v*} = \left(\frac{\alpha_0^v \tau \rho_0}{n_0}\right), \quad \beta_1^* = (\beta_1 \tau \rho_0), \quad \beta_2^* = (\beta_2 n_0 \tau), \quad \gamma^* = (\gamma \tau), \quad \kappa^* = \left(\frac{\kappa \, n_0 \, \hat{L}}{\rho_0}\right), \quad v_{\frac{1}{2}}^* = \left(\frac{v_{\frac{1}{2}}}{V_0}\right),$$

$$\bar{R}^* = \left(\bar{R}\rho_0 L\right), \quad \lambda_v^* = (\lambda_v \tau), \quad K_{EC}^{v*} = \left(\frac{K_{EC}^v \tau n_0}{V_0}\right), \quad \bar{l_\rho}^* = \left(\frac{\bar{l}_\rho \, n_0}{\rho_0^{\frac{3}{2}}}\right), \quad \bar{l_n}^* = \left(\frac{\bar{l}_n \, n_0^{\frac{2}{3}}}{\rho_0}\right).$$

Substituting with (5.17) and (5.18) in (5.1)-(5.4) and (5.14), and exploiting the dimensionless parameters defined above, we obtain the following system of dimensionless equations (asterisks are omitted for clarity of presentation):

$$\frac{\partial m}{\partial t} = -\lambda_1^v \left(\frac{v}{v + v_{\frac{1}{2}}}\right) m + \lambda_2^v \left(\frac{v_{\frac{1}{2}}}{v + v_{\frac{1}{2}}}\right) H\left(\nu\left(m + \rho\right) + n - N_{min}\right) \rho, \tag{5.19}$$

$$\begin{aligned} \frac{\partial n}{\partial t} = {} & \frac{\partial}{\partial x}\left(\mu \, \frac{\partial n}{\partial x} - \chi_v \, n \, \frac{\partial v}{\partial x}\right) + \alpha_0^v \, \rho \, \left(\frac{v}{v + v_{\frac{1}{2}}}\right) \\ & - \beta_1 \, n \, (\rho + m) - 2 \, \beta_2 \, n^2 - \gamma \, n \, \left(\frac{v_{\frac{1}{2}}}{v + v_{\frac{1}{2}}}\right), \end{aligned} \tag{5.20}$$

$$\frac{\partial \rho}{\partial t} = \kappa \left|\mu \, \frac{\partial n}{\partial x} - \chi_v \, n \, \frac{\partial v}{\partial x}\right| - \gamma \, \rho \, \left(\frac{v_{\frac{1}{2}}}{v + v_{\frac{1}{2}}}\right) + \bar{l}_\rho \, \beta_1 \, n \, (\rho + m)^{\frac{1}{2}} + \bar{l}_n \beta_2 \, n^{\frac{5}{3}}$$

$$+ \lambda_1^v \left(\frac{v}{v + v_{\frac{1}{2}}} \right) m - \lambda_2^v \left(\frac{v_{\frac{1}{2}}}{v + v_{\frac{1}{2}}} \right) H \left(\nu \left(m + \rho \right) + n - N_{min} \right) \rho, \tag{5.21}$$

$$\begin{aligned} \frac{\partial v}{\partial t} &= D_v \frac{\partial^2 v}{\partial x^2} - \lambda_v \, v - 2 \, \pi \, \bar{R} \, P_v \, (\rho + m) \, (v - v_{blood}) \\ &\quad - K_{EC}^v \, (n + \nu \, (\rho + m)) \left(\frac{v}{v + v_{\frac{1}{2}}} \right), \end{aligned} \tag{5.22}$$

$$\frac{d[V_T]}{dt} = -\frac{\lambda_p^v}{\theta_v} [V_T] - \frac{\zeta_p k_p^v}{\Omega_p} \left(\frac{[V_T]}{\theta_v} - v(L, t) \right). \tag{5.23}$$

The initial conditions are

$$v(x,0) = 0, \; \rho(x,0) = 0, \; n(x,0) = 0, \; m(x,0) = m_L \; exp \left[-\frac{x^2}{2\sigma^2} \right], \; [V_T] \, (0) = [V_T]_{init} \, , \tag{5.24}$$

and the boundary conditions are

$$\left. \begin{aligned} &- \mu \, \frac{\partial n}{\partial x} + \chi^v \, n \, \frac{\partial v}{\partial x} = 0, \\ &- D_v \, \frac{\partial v}{\partial x} = -P_v (v - v_{blood}), \end{aligned} \right\} \quad x = 0, \qquad \left. \begin{aligned} &- \mu \, \frac{\partial n}{\partial x} + \chi^v \, n \, \frac{\partial v}{\partial x} = 0, \\ &- D_v \frac{\partial v}{\partial x} = -k_p^v \left(\frac{[V_T]}{\theta_v} - v \right), \end{aligned} \right\} \quad x = L. \tag{5.25}$$

5.4. Parameter value estimation for VEGF-A$_{165}$-induced angiogenesis

We begin our discussion of default parameter values by considering the scalings for time, distance and the dependent variables. We then discuss the values of model parameters, grouping them according to the equations in which they appear. We base our choice of parameter values on published data wherever possible; where appropriate data are not available, we use physical arguments and previous modelling efforts to estimate approximate values. In other cases parameter values are chosen such that model simulation results are in good quantitative agreement with the available experimental data, presented in Chapter 4. Table 5.2 summarises the values of the scaling factors for the independent and dependent variables used to nondimensionalise our model, while Tables 5.3 and 5.4 summarise the default parameter values and detail sources, where available.

Since pellets are placed at a distance of approximately 1 mm from the limbal vessels, this represents a natural choice for our length scale, $\hat{L}$. The time taken for VEGF-A$_{165}$ to diffuse a root mean squared distance of $\hat{L}$ in one dimension is given by $\frac{\hat{L}^2}{2D_v}$. However, following Byrne and

Chaplain (1995), to simplify our nondimensionalisation we use a time-scale of $\tau = \frac{\hat{L}^2}{D_v}$. Vessel density is scaled with the initial density of mature vessels at the limbus, m_L (see Equation (5.5)). The value for m_L is estimated by assuming that the limbal vessel density represents a single vessel running perpendicular to the x-axis. If Δ_z is the thickness of the cornea, Δ_y is the length along the limbus in which we are interested and ϕ is the tortuosity of the limbal vasculature then we can equate the total length of limbal vessels using

$$\phi\, \Delta_y = \Delta_y \Delta_z \int_{-\infty}^{\infty} m_L exp\left(\frac{-x^2}{2\sigma^2}\right)\, dx. \tag{5.26}$$

Solving and rearranging this equation, we find $m_L = \frac{\phi}{\sqrt{2\ \pi}\ \sigma\ \Delta_z}$. Assuming a value of $20\,\mu$m for σ, the initial width of the vessel density distribution, and by approximating $\phi = 1.1$ and the thickness of the cornea, $\Delta_z = 100\,\mu$m (Zhang *et al.* 1996; Song *et al.* 2003), we calculate $m_L \approx 2 \times 10^8$ m of vessel m^{-3}. Our estimate here is also in good agreement with the experimental data presented in Chapter 4. Initial numerical simulations suggested a convenient scaling factor for VEGF-A$_{165}$, V_0, to be of the same order of magnitude as $v_{\frac{1}{2}}$, the concentration of VEGF-A$_{165}$ at which EC activation is half-maximal, which corresponds to the EC50 for VEGFR-2 activation by VEGF-A$_{165}$. Following Akeson *et al.* (2010) we fix $v_{\frac{1}{2}} = 650\,$pM, which is within the range of dissociation constants for VEGF-A$_{165}$ binding to VEGFR-2 receptors on human colonic ECs reported in Wang *et al.* (2002): $600 - 700\,$pM. We fix $V_0 = 5\, v_{\frac{1}{2}} = 3.25\,$nM, since this ensures that the maximum scaled value of VEGF-A$_{165}$ inside the cornea in default simulations is $\mathcal{O}(1)$. The scaling factor for the tip cell density, $n_0 = 1 \times 10^{12}$ tips m^{-3}, is chosen such that the scaled tip cell density is $\mathcal{O}(1)$ in our default simulations.

Mature vessel density equation

Equation (5.19), for the mature vessel length density, contains four additional parameters, λ_1^v, λ_2^v, ν and N_{min} (the default value of $v_{\frac{1}{2}}$ was discussed above). The parameter ν represents the number of ECs per metre length of vessel. We estimate ν by assuming that an EC covers an area of $260\,\mu$m^2 (Tong and Yuan 2008a; Tong and Yuan 2008b), and that vessels are on average $10\,\mu$m in diameter (see discussion on page 85). Further, assuming that vessels can be approximated by cylinders, we estimate 1.2×10^5 ECs per metre of vessel length. The remaining parameters in (5.19) are difficult to estimate because the terms describing maturation and dematuration capture many complex biochemical interactions and cellular processes in a simple way. Thus,

Scaling parameter	Description	Value [units]
$\hat{L}$	Length scale. Approximate distance between limbal vessels and pellet.	0.001 [m]
τ	Time scale. Time for VEGF-A_{165} to diffuse from the pellet to limbal vessels.	3.97 [h]
V_0	Reference value for VEGF-A_{165} concentration.	3.25×10^{-9} [M]
n_0	Reference value for tip cell density.	1×10^{12} [cells m^{-3}]
ρ_0	Reference value for (mature and immature) vessel length density.	2×10^{8} [m of vessels m^{-3}]

Table 5.2.: Table of scaling parameters.

we estimate λ_1^v and λ_2^v by taking inspiration from a complex biochemical model. Zheng *et al.* (2013) consider a model of vessel maturation and dematuration which includes VEGF-A, Ang-1, Ang-2, ECs, pericytes, PDGF-B and a number of corresponding cell-surface receptors. In their model, ECs transition from an active to a quiescent state at a rate of 4.17×10^1 per μM bound Ang-1 per hour in high Ang-1 conditions. Conversely, the activation rate of quiescent ECs in high Ang-2 conditions is given by 1.25×10^2 per μM bound Ang-2 per hour. Drawing on evidence from the literature (Augustin *et al.* 2009; Gevertz and Torquato 2006; Plank *et al.* 2004), Zheng *et al.* use $10^{-3}\,\mu$M as the reference concentration of angiopoetins and $10^{-3}\,\mu$M as the reference concentration of Tie-2 receptors. Thus, for our model of maturation to be consistent with Zheng *et al.*, we expect the maximal rate of dematuration, λ_1^v, and maximal rate of maturation, λ_2^v, to take values of $\sim 0.1\,\mathrm{h}^{-1}$ and $\sim 0.01\,\mathrm{h}^{-1}$, respectively. For our simulations, we choose a default value of $\lambda_1^v = 0.08\,\mathrm{h}^{-1}$. However, for λ_2^v we use a value that is 20-fold smaller than that suggested from Zheng *et al.*'s work since this provides a good fit to our experimental data and is consistent with the observation that little maturation occurs in VEGF-A_{165}-induced corneal angiogenesis experiments (Cao *et al.* 2003). N_{min} is the local density of ECs above which we expect significant maturation to occur. We anticipate that significant maturation should begin when the vessel density is close to the initial peak of the vessel density at the limbus. Thus, we fix $N_{min} = 0.95 \times m_L \times \nu\,\mathrm{cells\,m}^{-3}$.

Tip cell density equation

The parameter μ is the random motility coefficient for tip cells. A number of experiments have been performed which allow us to estimate the random motility of individual ECs. For example, by fitting mathematical models to experiments involving epidermal wound healing *in vivo*, Sherratt and Murray (1990) estimate $\mu = 2.46 \times 10^{-11} - 3.6 \times 10^{-9}\,\mathrm{m}^2\mathrm{h}^{-1}$, while Stokes *et al.* (1991) estimate $\mu = 2.56 \pm 0.97 \times 10^{-9}\,\mathrm{m}^2\mathrm{h}^{-1}$ for individual ECs in vitro. Meanwhile, Kouvroukoglou *et al.* (2000) study individual EC migration on different surfaces and find $\mu = 3.5 \times 10^{-10} - 1.15 \times 10^{-9}\,\mathrm{m^2h^{-1}}$. However, as noted, these studies consider individual ECs and we expect tip cells to be less motile than isolated ECs due to cell-cell interactions with trailing ECs (Friedl and Gilmour 2009). In their models of corneal angiogenesis, Byrne and Chaplain (1995) approximate $\mu = 10^{-3}D_v \approx 10^{-11} - 10^{-10}\,\mathrm{m^2h^{-1}}$, as does Addison-Smith (2010). In their composite hybrid model of vascular tumour growth, Owen *et al.* (2011) use $\mu = 6 \times 10^{-11}\,\mathrm{m^2h^{-1}}$. We find that a value of $\mu = 7 \times 10^{-11}\,\mathrm{m^2h^{-1}}$ provides a good fit to our experimental data. The parameter χ_v, the chemotaxis coefficient for tip cells, quantifies the strength of the motile response of tip cells to gradients of VEGF-A$_{165}$. Stokes *et al.* (1990) use an under-agarose assay (Nelson *et al.* 1975) to estimate $\chi_v = 936 \pm 270\,\mathrm{m^2h^{-1}M^{-1}}$ for individual ECs in gradients of aFGF, where concentrations of aFGF were around $10^{-10}\,\mathrm{M}$. Again, we expect tip cells to be less motile than isolated ECs due to cell-cell interactions with trailing stalk cells. Balding and McElwain (1985) and Byrne and Chaplain (1995), guided by the experiments of Stokes *et al.* (1990), estimate $\chi_v = \frac{D_v}{V_0}$ and $\chi_v = 0.4 \times \frac{D_v}{V_0}$, respectively, to obtain results in qualitative agreement with experimental data (Muthukkaruppan *et al.* 1982). By contrast, Addison-Smith uses a smaller value $\left(\chi_v = 0.125 \times \frac{D_v}{V_0}\right)$ to provide results in qualitative agreement with an alternative set of experiments (Folkman and Klagsbrun 1975). We fix $\chi_v = 3.45\,\mathrm{m^2h^{-1}M^{-1}}$ to produce results that are consistent with our experimental data. This value is similar in magnitude to that used by Addison-Smith.

The parameters α_0^v, β_1, β_2 and γ determine the rates of production and destruction of tip cells (and immature vessels). We estimate α_0^v by assuming that the maximal rate of tip cell production is limited by the doubling time of ECs. The typical doubling time of a proliferating cell is about 20 hours, corresponding to a doubling rate of $k_{double} = 0.035\,\mathrm{h^{-1}}$. We also assume that only one in every two ECs may become a tip cell due to Delta-Notch mediated lateral inhibition (Bentley *et al.* 2009). Taking the number of ECs per metre of vessel to be $\nu = 1.2 \times 10^5$, we estimate $\alpha_0^v = 0.5 \times 0.035 \times 1.2 \times 10^5 = 2100\,\text{tips per hour per metre of vessel}$. In practice, numerical simulations reveal that slightly larger values of α_0^v give results which are in better agreement with our experimental data. Thus, we choose $\alpha_0^v = 2700\,\text{tips per hour per metre of vessel}$. Given that tip formation and vascular growth may occur in the absence of EC proliferation (Sholley *et al.* 1984), this value is still reasonable.

An order of magnitude estimate for γ, the maximal rate of vessel regression, can be obtained from results reported in Cao *et al.* (2003). They observed complete regression of

VEGF-A-induced neovasculature in cornea assay experiments within seven days after the source of VEGF-A was removed. Consistent with their observations, we fix $\gamma = 0.005\,\mathrm{h}^{-1}$ since this also provides a good fit to our experimental data. Values for β_1 and β_2, the rates of tip-to-vessel and tip-to-tip anastomosis, respectively, are difficult to estimate. We fix $\beta_1 = 0.4 \times 10^{-9}\,\mathrm{anastomosis\,events\,h^{-1}\,(m\,of\,vessel\,m^{-3})^{-1}\,(cells\,m^{-3})^{-1}\,m^{-3}}$ and $\beta_2 = 0.6 \times 10^{-14}\,\mathrm{anastomosis\,events\,h^{-1}\,(cells\,m^{-3})^{-2}\,m^{-3}}$ initially and investigate how changes in these parameter values affect simulation results in the following sections. Note that $\frac{\beta_1^*}{\beta_2^*} \approx 15$ (see Section 5.3.7), reflecting the fact that we expect tip-to-tip anastomosis events to be rarer than tip-to-vessel anastomosis events.

Immature vessel density equation

Other parameters relating to the evolution of the immature vessel density are κ, $\bar{l}_\rho$ and $\bar{l}_n$. κ quantifies the length of immature vessel produced in the plane perpendicular to the x-direction. Motion along the x-axis corresponds to $\kappa = 1$, while larger values of κ indicate increasing amounts of lateral movement. We assume initially that $\kappa = 5\,\mathrm{metre\,of\,vessel\,cell^{-1}\,m^{-1}}$. $\bar{l}_\rho$ and $\bar{l}_n$ are constants of proportionality which quantify the average inter-vessel and inter-tip cell distances, respectively. The parameter $\bar{l}_n$ is estimated by assuming that each volume of size $\frac{1}{n}\,\mathrm{m}^3$ contains one tip cell. The average distance between tip cells is then given by $\frac{1}{n^{\frac{1}{3}}}$ m, yielding a value of $\bar{l}_n = 1$. The parameter $\bar{l}_\rho$ is estimated in a similar fashion. For simplicity, we assume that all vessels are oriented parallel to the x-axis. Then, in the plane perpendicular to the x-axis, the mean inter-vessel distance is given by $\frac{1}{(\rho+m)^{\frac{1}{2}}}$ m (having assumed that each vessel occupies a square of area $\frac{1}{(\rho+m)}\,\mathrm{m}^2$ in the plane perpendicular to the x-axis).

VEGF-A$_{165}$ concentration equation

The remaining parameters for which we require estimates relate to VEGF-A$_{165}$. The parameter D_v is the diffusion coefficient for VEGF-A$_{165}$ in the cornea. By monitoring the intensity of fluorescently labelled VEGF-A$_{165}$ in Matrigel, Chen *et al.* (2006) estimate $D_v = 2.52\times10^{-7}\,\mathrm{m^2h^{-1}}$. Meanwhile, MacGabhann (2005) and Ambrosi *et al.* (2005) propose estimates of $D_v \approx 10^{-7}\,\mathrm{m^2h^{-1}}$, having used the Einstein-Stokes formula. Swabb *et al.* (1974) developed a formula based on experimental data involving solutes (not including VEGF-A$_{165}$) of molecular weights ranging from 32 Da to 69 kDa diffusing in a range of tissues (including ox corneal stroma). Using Swabb *et al.*'s formula, we obtain another estimate: $D_v = 2.1 \times 10^{-8}\,\mathrm{m^2h^{-1}}$. As default here we use

Parameter	Description	Default value and units	Non-dimensional value	Sources
$v_{\frac{1}{2}}$	Concentration of VEGF-A$_{165}$ at which VEGFR-2 receptors are half occupied.	6.5×10^{-10} [M]	0.02	(Akeson *et al.* 2010; Wang *et al.* 2002)
λ_1^v	Maximal rate of vessel dematuration.	0.08 [h^{-1}]	0.3176	(Zheng *et al.* 2013)
λ_2^v	Maximal rate of vessel maturation.	0.0005 [h^{-1}]	0.002	(Zheng *et al.* 2013)
ν	Average number of ECs contained in a metre of vessel.	1.2×10^5 [cells (m of vessel)$^{-1}$]	24	(Tong and Yuan 2008b)
N_{min}	Local density of ECs required for maturation.	$0.95 \times m_L \times \nu$ [cells m^{-3}]	22.8	-
σ	Initial width of limbal vessel density distribution.	20×10^{-6} [m]	0.02	-
m_L	Maximum density of mature vessel length density at the limbus initially.	2×10^8 [m of vessel m^{-3}]	1	-
μ	Random motility coefficient for tip cells.	7×10^{-11} [m^2 h^{-1}]	2.779×10^{-4}	(Sherratt and Murray 1990; Stokes *et al.* 1991; Kouvroukoglou *et al.* 2000; Addison-Smith 2010; Owen *et al.* 2011; Byrne and Chaplain 1995).
χ_v	Chemotaxis coefficient for tip cells.	3.45 [m^2 h^{-1} M^{-1}]	0.0445	(Stokes and Lauffenburger 1991; Stokes *et al.* 1990; Balding and McElwain 1985; Byrne and Chaplain 1995; Addison-Smith 2010).
α_0^v	Maximum rate of production of tip cells per length of vessel.	2700 [tips h^{-1} per m of vessel]	2.1438	-
β_1	Rate of tip-to-vessel anastomosis per unit vessel length density per unit tip density per unit volume.	0.4×10^{-9} [anastomosis events h^{-1} m^{-3} (m of vessels m^{-3})$^{-1}$ (cells m^{-3})$^{-1}$]	0.3176	-
β_2	Rate of tip-to-tip anastomosis per unit tip density squared per unit volume.	0.6×10^{-14} [anastomosis events h^{-1} m^{-3} (cells m^{-3})$^{-2}$]	0.0238	-
γ	Maximal rate of regression of ECs (vessels) in low VEGF-A$_{165}$.	5×10^{-3} [h^{-1}]	1.99×10^{-2}	(Cao *et al.* 2003)
κ	Parameter quantifying the length of vessel left behind in a unit volume after a tip cell moves out of that unit volume.	5 [m of vessel cells^{-1} m^{-1}]	25	-
$\bar{l}_\rho$	Constant of proportionality which quantifies the inter vessel distances.	1	0.3536	-
$\bar{l}_n$	Constant of proportionality which quantifies the inter tip cell distances.	1	0.5	-

Table 5.3.: List of parameters relating to the mature vessel density, tip cell density and immature vessel density equations, (5.19)-(5.21).

the value of D_v given by Chen *et al.* Chen *et al.* (2006) and Serini *et al.* (2003) estimate λ_v, the natural decay constant for VEGF-A$_{165}$, to be $\lambda_v = 0.8316\,\mathrm{h}^{-1}$ and $\lambda_v = 0.65\,\mathrm{h}^{-1}$, respectively, in Matrigel. As a default value, we fix $\lambda_v = 0.8\,\mathrm{h}^{-1}$.

K_{EC}^{v} is the maximum rate of reduction in molar VEGF-A$_{165}$ concentration per unit EC density due to VEGFR-2 binding. Wang *et al.* (2002) estimate the average number of VEGFR-2 receptors per cell to be approximately 230000, so that, at any time, at most $230000\,/\,N_A = 3.82 \times 10^{-19}$ moles of VEGF-A$_{165}$ can bind to VEGFR-2 receptors on an EC (where N_A is Avogadro's number). MacGabhann and Popel (2003) estimate the instantaneous internalisation rate of VEGF-A in HUVECs as $1.548\,\mathrm{h}^{-1}$ using data from Bikfalvi *et al.* (1991), and as $1.008\,\mathrm{h}^{-1}$ using data from (Wang *et al.* 2002). Thus, if VEGFR-2 receptor numbers remain constant on the surface of a cell then we expect ECs to uptake at most between $3.82 \times 10^{-19} \times 1.008 \approx 4 \times 10^{-19}$ and $3.82 \times 10^{-19} \times 1.548 \approx 6 \times 10^{-19}$ moles of VEGF-A$_{165}$ per hour. In practice, only a fraction of the VEGFR-2 receptors are ever present on the surface of the cell since others are being internalised and/or being recycled. However, since we are not modelling receptor kinetics directly we estimate $K_{EC}^{v} = 4 \times 10^{-22}\,\mathrm{moles\,h^{-1}\,cell^{-1}\,litre^{-1}\,m^{3}}$.

Fu and Shen (2003) calculate the permeability of vessels to α-lactalbumin and albumin when exposed to 1 nM VEGF-A$_{165}$. α-lactalbumin and albumin are molecules with Stokes radii of 20.1 and 35.0 Angstroms, respectively, similar to that of VEGF-A$_{165}$ (30.2 Angstroms). They find the peak permeability of vessel walls to be $6.12 \times 10^{-4}\,\mathrm{m\,h^{-1}}$ for α-lactalbumin and $1.332 \times 10^{-4}\,\mathrm{m\,h^{-1}}$ for albumin in 1 nM VEGF-A$_{165}$ and $1.98 \times 10^{-4}\,\mathrm{m\,h^{-1}}$ for α-lactalbumin and $2.448 \times 10^{-5}\,\mathrm{m\ h^{-1}}$ for albumin when VEGF-A$_{165}$ is not applied. In their review, Stefanini *et al.* (2008) conclude that vascular permeability in the presence of VEGF-A is likely to lie between $1.44 \times 10^{-6}\,\mathrm{m\,h^{-1}}$ and $1.44 \times 10^{-3}\,\mathrm{m\,h^{-1}}$ and estimate P_v to be $1.44 \times 10^{-6}\,\mathrm{m\,h^{-1}}$ in normal tissues, where levels of VEGF-A are low. We use a default value of $P_v = 3 \times 10^{-4}\,\mathrm{m\,h^{-1}}$ in our simulations. In the absence of VEGF-A, Tsai *et al.* (2009) find the average diameters of *in vivo* and histological microvessels in the murine brain to be $3.97\,\mu$m and $4.11\,\mu$m, respectively. We expect diameters to be larger than this in the presence of VEGF-A$_{165}$. On the other hand, Peebo *et al.* (2011) found the limbal vessel diameters in rats to vary between $9 - 12\,\mu$m on day 1 and $25 - 30\,\mu$m at their peak diameter in an inflammatory corneal angiogenesis experiment. Thus, we fix $\bar{R} = 5\,\mu$m for the radius of vessels. To simplify our model, we assume that VEGF-A$_{165}$ is cleared quickly from the corneal vasculature so that $v_{blood} = 0$.

In the absence of suitable experimental data, we assume $\theta_v = 50$, $k_p^v = 1.6 \times 10^{-7}\,\mathrm{m\,h^{-1}}$ and

Parameter	Description	Default value and units	Non-dimensional value	Sources
D_v	Diffusion constant for VEGF-A$_{165}$ in cornea.	2.52×10^{-7} [m^{2}h^{-1}]	1	(Chen *et al.* 2006; MacGabhann 2005; Ambrosi *et al.* 2005; Swabb *et al.* 1974).
λ_v	Natural decay constant of VEGF-A$_{165}$.	0.8 [h^{-1}]	3.176	(Serini *et al.* 2003; Chen *et al.* 2006).
K_{EC}^v	Maximum rate of reduction in molar VEGF-A$_{165}$ concentration per unit EC density due to VEGFR-2 binding.	4×10^{-22} [moles of VEGF$_{165}$ h^{-1}cell^{-1} litre^{-1} m^3]	0.4886	(Wang *et al.* 2002; MacGabhann and Popel 2003; Bikfalvi *et al.* 1991).
P_v	Permeability of corneal vasculature to VEGF-A$_{165}$.	3×10^{-4} [m h^{-1}]	1.191	(Fu and Shen 2003; Stefanini *et al.* 2008).
$\bar{R}$	Average radius of vessels in cornea.	5×10^{-6} [m]	1	(Tsai *et al.* 2009; Peebo *et al.* 2011)
v_{blood}	Concentration of VEGF-A$_{165}$ in the blood.	0 [M]	0	-
θ_v	Binding constant.	50	50	-
k_p^v	Effective permeability of the cornea-pellet boundary.	1.6×10^{-7} [m h^{-1}]	6.352×10^{-4}	-
Ω_p	Volume of pellet.	1.7×10^{-11} [m^3]	1.7×10^{-2}	Roche, Penzberg.
ζ_p	Surface area of pellet.	6.79×10^{-7} [m^2]	0.679	Roche, Penzberg.
λ_p^v	Natural decay constant of VEGF-A$_{165}$ in the pellet.	0.8 [h^{-1}]	3.176	Assume $\lambda_p = \lambda_v$.
$[V_T]_{init}$	Initial concentration of VEGF-A$_{165}$ in pellet.	3.93×10^{-4} [M]	1.2092×10^5	Roche, Penzberg.
L	Average distance of pellets from limbal vessels in VEGF-A$_{165}$ experiments.	1.04×10^{-3} [m]	1.04	Image analysis (Chapter 4)

Table 5.4.: List of parameters associated with VEGF-A$_{165}$ (see Equations (5.22) and (5.23)).

$\lambda_p^v = 0.8\,\mathrm{h}^{-1}$ since these values yield results in good agreement with our experimental data. In particular, we assume that the decay rate of free VEGF-A$_{165}$ in the pellet is the same as that in the cornea. The surface area, ζ_p, and the volume, Ω_p, of the cylindrical pellets can be calculated since their height is 0.06 mm and their radius 0.3 mm. Our default simulations involve pellets containing 300 ng of VEGF-A$_{165}$, which has a molecular weight of approximately 45 kDa. Given the volume of the pellet, we estimate the initial molar concentration of VEGF-A$_{165}$ in the pellet to be 3.93×10^{-4} M.

5.5. Numerical results: VEGF-A$_{165}$-induced angiogenesis

In this section we present results generated from numerical simulations of VEGF-A$_{165}$-induced angiogenesis in the cornea and discuss the effect of varying parameter values on these results. Equations (5.19)-(5.23) were solved using the method of lines (Hundsdorfer 2000). They were first discretised in space using central (finite) difference approximations. This reduces the model to a system of ODEs in time which we solved using MATLAB's inbuilt routine ode15s, a variable time-step, variable-order solver for stiff problems (Shampine and Reichelt 1997). We set the maximum order of the solver to one to improve numerical stability.

Figure 5.3 shows the results of model simulations when default parameter values are used (Tables 5.3 and 5.4). Typical simulations proceed as follows. Initially, VEGF-A$_{165}$ is released from the pellet causing the VEGF-A$_{165}$ concentration adjacent to it to increase rapidly until it reaches a maximum value. Thereafter, as VEGF-A$_{165}$ levels in the pellet decline, the VEGF-A$_{165}$ concentration in the cornea adjacent to it also declines. At the same time, VEGF-A$_{165}$ diffuses across the cornea towards the limbal vessels, where it stimulates vessel dematuration and the production of tip cells. The tip cells migrate via chemotaxis up spatial gradients in VEGF-A$_{165}$, towards the pellet, leaving behind them a trail of vessels. Since vessels and ECs are VEGF-A$_{165}$ sinks, continued vascular growth creates a barrier to the VEGF-A$_{165}$, preventing it from reaching the limbal vasculature. Consequently, because tip cell production depends on VEGF-A$_{165}$ levels, tip cell production at the limbus halts and is localised instead around the leading edge of the vascular front. Such behaviour is consistent with that observed by Tong and Yuan (2008b) in their computational model of bFGF-induced corneal angiogenesis and in retinal angiogenesis experiments by Gerhardt (2003). As the simulation proceeds, and VEGF-A$_{165}$ levels in the pellet dwindle, the rates of tip cell production and migration decrease. For the choice of parameter values used here, very little maturation occurs and, as the VEGF-A$_{165}$ becomes depleted, significant levels of vessel regression occur. This behaviour is consistent with that observed *in vivo* (Figure 4.9a).

Figure 5.4 shows that the model is in good agreement with data extracted from experimental images when default parameter values are used (Tables 5.3 and 5.4); model results are consistent with the experimental data in terms of the amplitude of the vascular density, the extent to which vascular growth towards the pellet has occurred and the overall shape of the vascular density profiles at both time-points of interest. Due to issues regarding parameter identifiability and the resulting ill-posed nature of the parameter fitting problem we do not attempt formally to fit the model parameters to the data. However, notably, the model can fit very well to the averaged experimental data when parameters are selected from a biologically feasible regime.

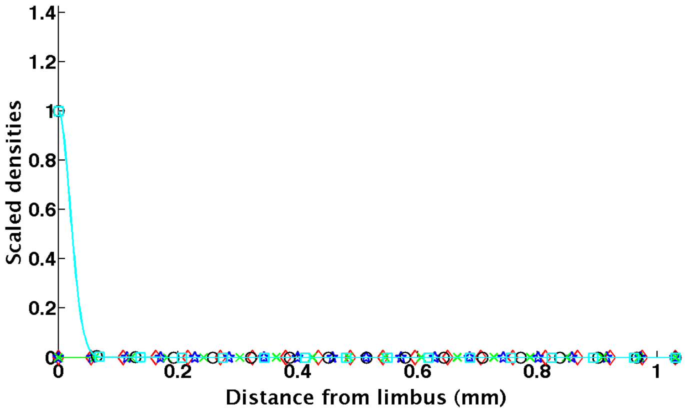

(a) Initial conditions. The cornea is initially avascular and contains no VEGF-A$_{165}$. Mature limbal vessels border the cornea.

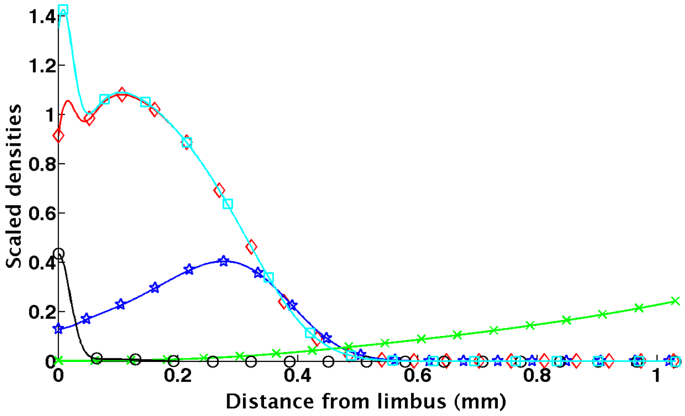

(b) Day 3 results. VEGF-A$_{165}$ is released from the pellet and diffuses towards the limbus where it stimulates vessel dematuration and tip cell production. The tip cells migrate by chemotaxis towards the pellet, leaving behind them a trail of immature vessels.

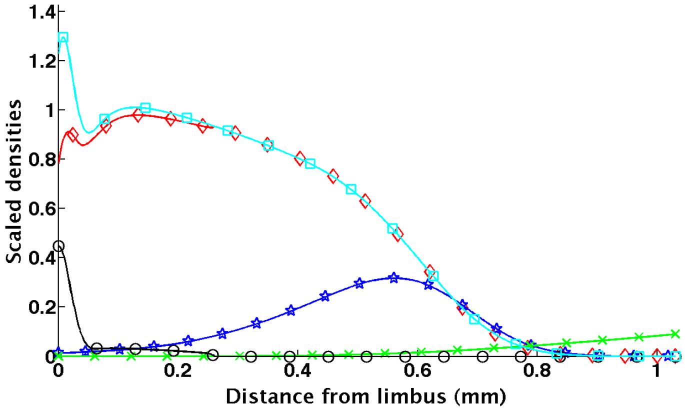

(c) Day 5 results. As VEGF-A$_{165}$ levels in the pellet decline, vascular growth slows and vessel regression occurs near the limbus.

Figure 5.3.: Results from a typical numerical simulation of our mathematical model, Equations (5.19)-(5.23), showing the angiogenic response of the limbal vessels to a VEGF-A$_{165}$ pellet implanted in the cornea. Scaled distributions of all state variables are overlaid for three time-points. Total vessel density (mature + immature): □; mature vessel density: ○; immature vessel density: ◊; tip cell density: ⋆; VEGF-A$_{165}$ concentration: ×. Parameter values are given in Tables 5.3 and 5.4.

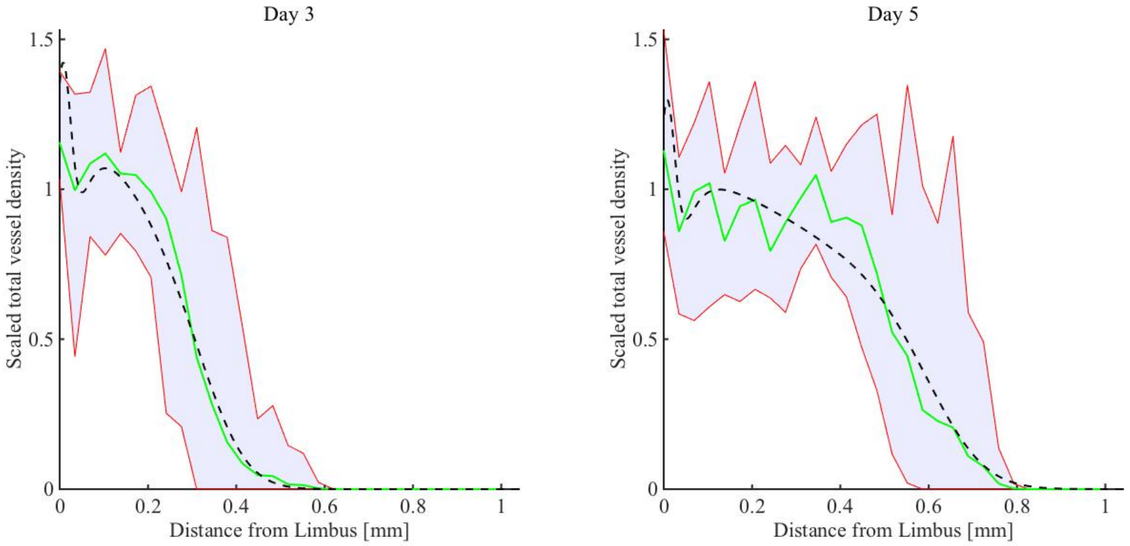

Figure 5.4.: Comparison of results from the simulation of our mathematical model, (5.19)-(5.23), with data from VEGF-A$_{165}$ experiments when default parameters (Tables 5.3 and 5.4) are used. The black dashed lines show model predictions, the solid green lines show averaged experimental data and the shaded region (bounded by solid red lines) shows the range in vessel densities across experimental data sets.

5.5.1. Numerical convergence and accuracy

The accuracy of the numerical solution is sensitive to the resolution of the time and spatial discretisations. Demonstrating that the numerical solution of a system of PDEs such as ours converges at the rate predicted by theory as the discretisation parameters (space step, Δx, and time step, Δt) are decreased is an important part of code verification (the process of ensuring that a computational model accurately solves the underlying mathematical model). An exact solution to our system of PDEs, (5.19)-(5.25), with which to compare a numerical solution is not available, thus we have computed the solution to the equations using a very fine mesh (with 3000 nodes) to use as a reference solution.

Established theory dictates that the backward-time central-space finite difference scheme that we employ to solve the system of PDEs, (5.19)-(5.25), is consistent and first-order accurate in time and second-order accurate in space. To confirm this for our implementation we successively refined the space and time steps (separately) and computed the error in the solution against our 'fine mesh' reference solution. Figures 5.5a and 5.5b show log-log convergence plots for the error

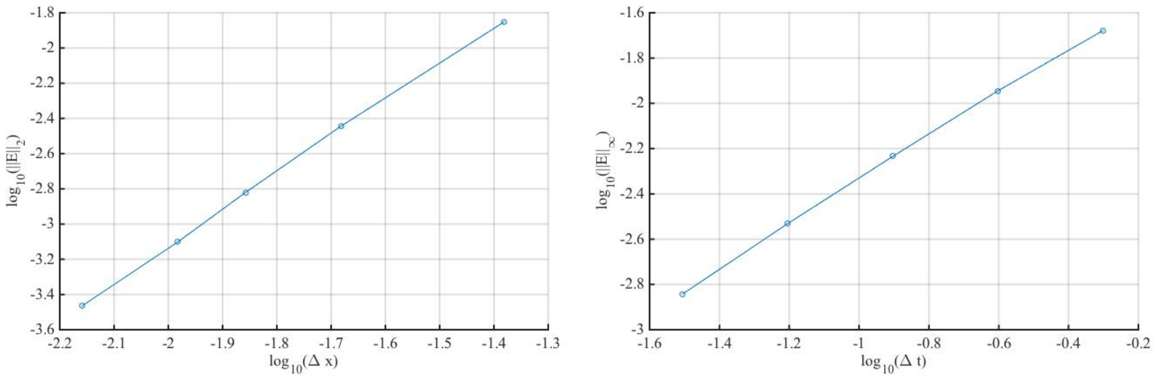

(a) Log-log plot showing the rate of convergence of the error in the solution vector on day 5 as the time step, Δx, is decreased.

(b) Log-log plot showing the rate of convergence of the error in the solution vector on day 5 as the time step, Δt, is decreased.

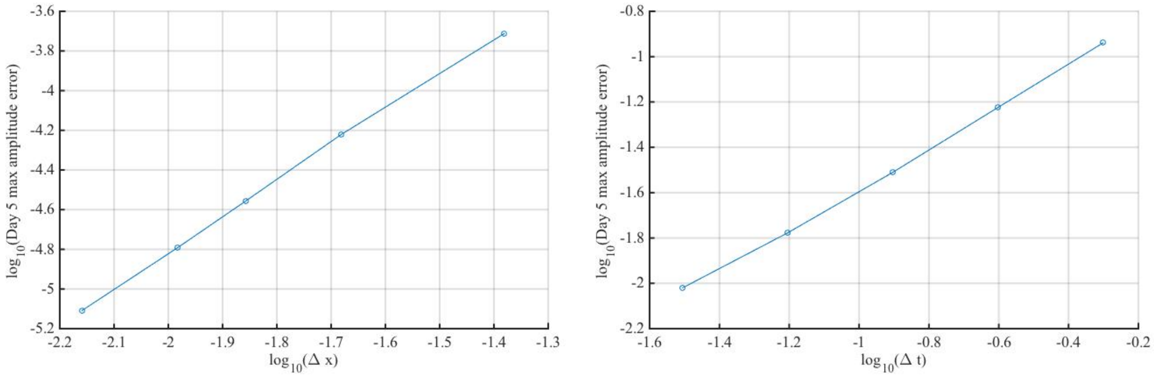

(c) Log-log plot showing the rate of convergence of the error in the maximum amplitude of the vessel density on day 5 as the spacial step size, Δx, is decreased.

(d) Log-log plot showing the rate of convergence of the error in the maximum amplitude of the vessel density on day 5 as the time step, Δt, is decreased.

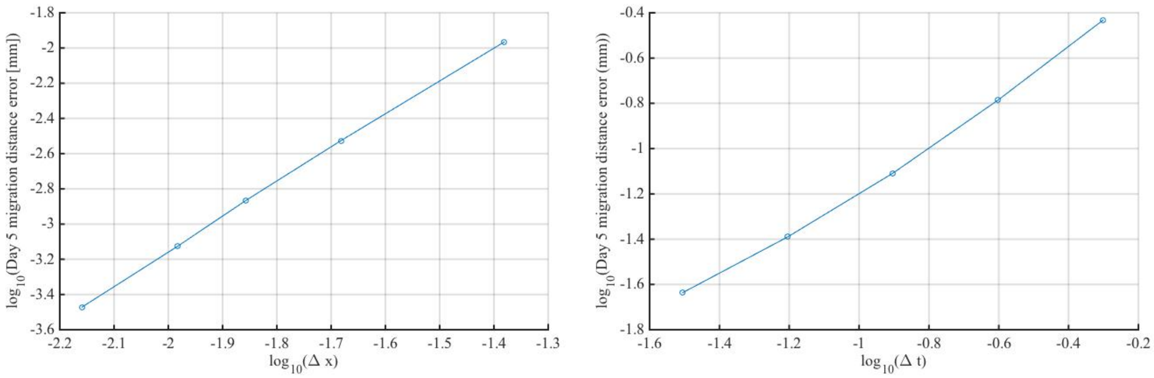

(e) Log-log plot showing the rate of convergence of the error in the location of the vascular front on day 5 as the spacial step size, Δx, is decreased.

(f) Log-log plot showing the rate of convergence of the error in the location of the vascular front on day 5 as the time step, Δt, is decreased.

Figure 5.5.: Convergence plots for the numerical solution of our model of VEGF-A$_{165}$-induced angiogenesis, Equations (5.19)-(5.25). To calculate error in the solution we compare against a 'fine-mesh' solution, as explained in the main text.

in the solution on day 5 of simulations. The error decreases as $O\left(\Delta x^2\right)$ in the L^2-norm and as

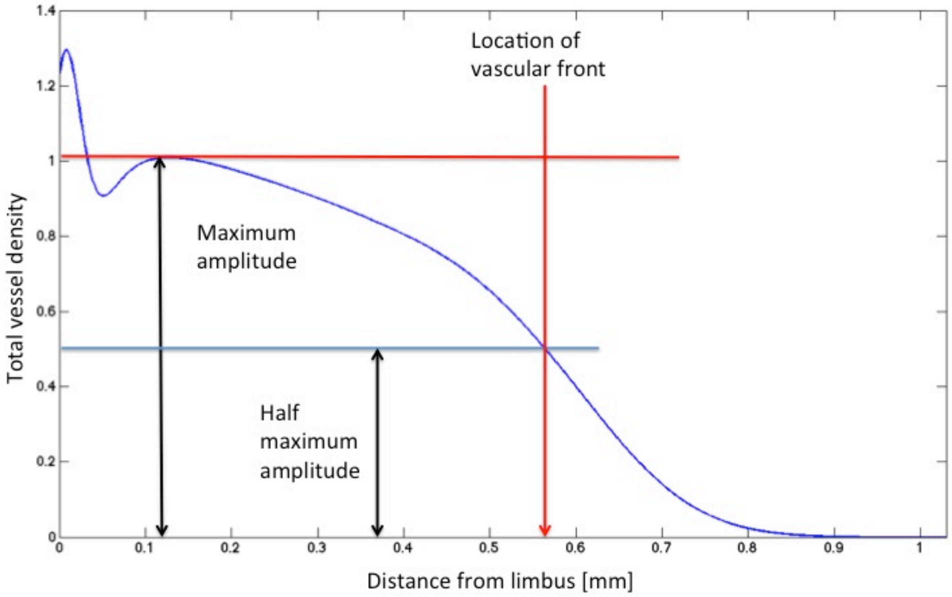

Figure 5.6.: Summary statistics for vascular density profiles. We characterise vessel density profiles using the location of the vascular front, the maximum amplitude of the neovascular wavefront and the area under the vessel density curve.

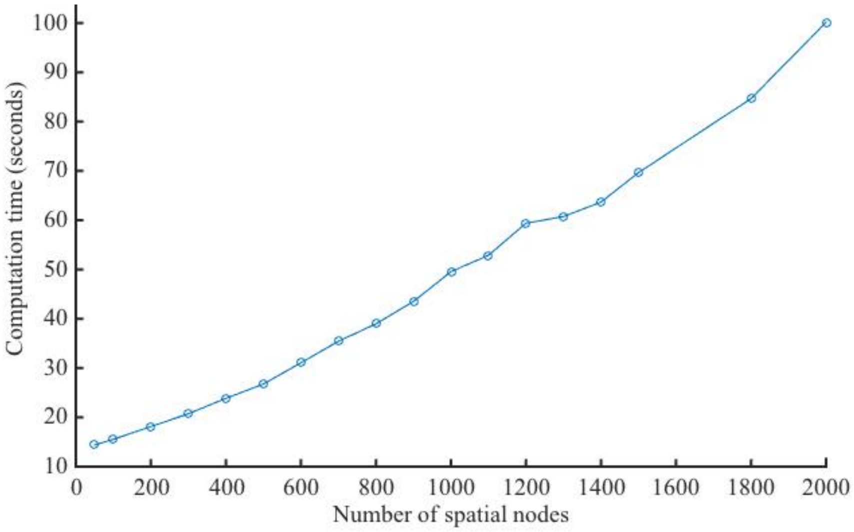

Figure 5.7.: Plot showing how the time taken to compute the numerical solution to Equations (5.19)-(5.25) changes as the number of spatial nodes increases.

$O(\Delta t)$ in the L^{∞}-norm.

To aid the analysis of our model's behaviour we define several metrics which characterise the vascular density profiles. These summary statistics are the maximum amplitude of the vascular density profile (disregarding the limbal vasculature); the location of the vascular front, defined as the location at which the vascular density becomes half-maximal; and the area under the vessel density curve, which is representative of the total length of vessels in the cornea (see Figure 5.6). As suggested in a recent white paper report (National Research Council. 2012), since these quantities will be of interest for assessing the behaviour of our model and making predictions, we have also confirmed that they converge approximately at the expected rates as the discretisation parameters are decreased ($O\left(\Delta x^2 + \Delta t\right)$). Figures 5.5c-5.5f demonstrate that the location of the vascular front and the maximum amplitude of the vascular density profile on day 5 of simulations converge at the expected rates.

For our simulations we use a spatial grid with 1000 nodes (using a variable time-step) as default since this provides a very good level of accuracy whilst producing results within reasonable time-scales. Figure 5.7 shows how the time taken to simulate an experiment of length 5 days varies with the number of spatial nodes. We also note that the use of adaptive time-step ODE solvers, such as ode15s, allows explicit control of numerical error and therefore facilitates calculation verification. In our simulations we enforce a tolerance of 1×10^{-8} on the relative error of our solutions[3].

We have further confirmed the absence of unphysical, negative values for all state variables and have compared the implementation of two independently written versions of the model codes to provide additional confidence that those codes have been written absent of errors.

5.5.2. Parameter sensitivity analysis

In this section, we use our computational model to investigate how the system responds to changes in a single parameter. As noted above, to aid our analysis we focus on the behaviour of several summary statistics which characterise the vascular density profiles (see Figure 5.6).

5.5.2.1. Local sensitivity analysis

Figure 5.8 summarises the results of our local parameter sensitivity analysis. We vary one parameter at a time, keeping all others fixed at their default values. We increase/decrease the value of each parameter by 5%, and simulate the model for each choice of parameter values. We use the simulation results to calculate a central difference approximation to the normalised sensitivities of our chosen summary statistics. For example, we calculate the normalised sensitivity of the area under the vessel density curve, A, to parameter, p as

$$\text{normalised sensitivity} = \frac{p_0}{A(p_0)} \left(\frac{\partial A}{\partial p}\right)_{\mathbf{q_0}} \approx \frac{p_0}{A(p_0)} \; \frac{A(p_0 + \Delta p_0) - A(p_0 - \Delta p_0)}{2\Delta p_0},$$

---

[3] This tolerance is provided as an optional parameter to the ode15s solver.

where the subscript, $\mathbf{q_0}$, indicates that the difference is calculated around the point $\mathbf{q_0}$ in parameter space. We present the normalised sensitivity analysis for the vascular front location (Figure 5.8a), the maximum amplitude of the vascular wavefront (Figure 5.8b) and the area under the vessel density curve (Figure 5.8c) on days 1, 3 and 5 of dimensional simulation time to illustrate how the sensitivity of the system to different parameters changes over time. Such local sensitivity analysis techniques are useful for identifying trends and also for uncovering potential weaknesses in models. That is, the analysis can help convince us that our model is behaving reasonably. For instance, if we increase the VEGF-A$_{165}$ diffusion constant, D_v, then, at each time point, the maximum amplitude of the vessel density also increases (Figure 5.8b), while the location of the vascular front decreases (Figure 5.8a). This behaviour can be explained as follows. Increases in D_v increase VEGF-A$_{165}$ levels across the model domain and decrease its spatial gradient, promoting tip cell production and reducing the chemotactic stimulus, respectively.

Our sensitivity analysis indicates which parameters may significantly influence the outcomes of our model simulations. Notably, model outputs appear to be most sensitive to changes in parameters affecting VEGF-A$_{165}$ availability (e.g. L, D_v, λ_v, θ_v, k_p^v, λ_p^v and $[V]_t^{init}$) and the response of ECs to VEGF-A$_{165}$ (e.g. χ_v and α_0^v). The model predicts, in particular, that the neoangiogenic response of the limbal vessels is highly sensitive to L, the distance between the pellet and the limbal vessels, with our simulation results being almost twice as sensitive to variations in L than to any other parameter. Figure 5.9 shows how the predicted location of the vascular front on days three and five changes as L varies. When default model parameters are used the location of the vascular front on day five is located 0.56 mm from the limbus. Varying the location of the pellet by 10 % (±0.1 mm) results in a ±25 % change in vascular front location on day five. By contrast, changes of ±10 % in $[V_T]_{init}$ result in a ±15 % change in vascular front location on day five. Thus, our sensitivity analysis suggests that variation in pellet placement may be a large source of noise in experimental results. Regardless of cellular and genetic variability, pellet (mis-)placement may, then, fundamentally limit the precision, and thus the reproducibility and repeatability, of cornea micropocket experiments. More seriously, it may significantly influence conclusions concerning the efficacy of anti-angiogenic treatments.

Inspection of Figure 5.8 reveals that small changes in the regression rate, γ, and the anastomosis rates, β_1 and β_2, do not significantly affect model outputs. However, accurate estimates for these parameters are not available from the experimental literature and varying them over larger ranges significantly affects the distributions of tip cells and vessels. Thus, next, we investigate

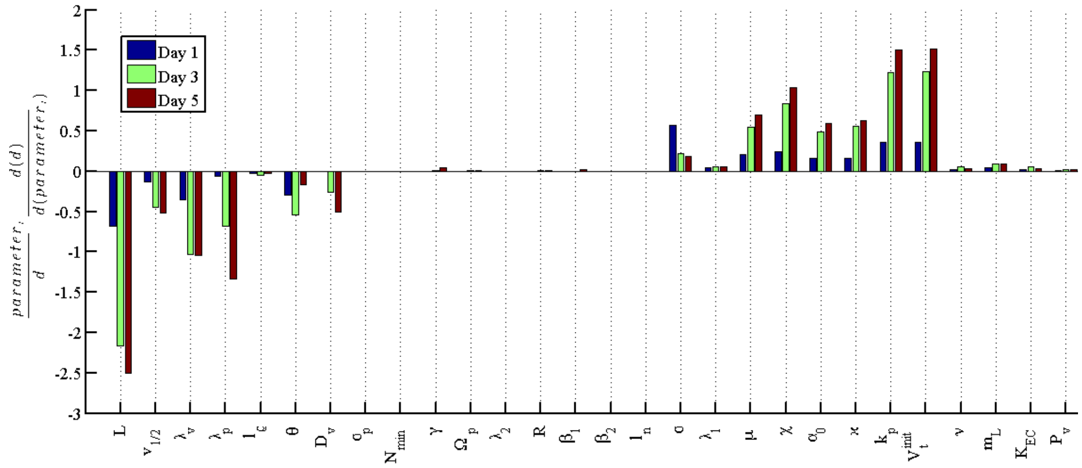

(a) Normalised sensitivity of the location of the advancing vascular wavefront, d.

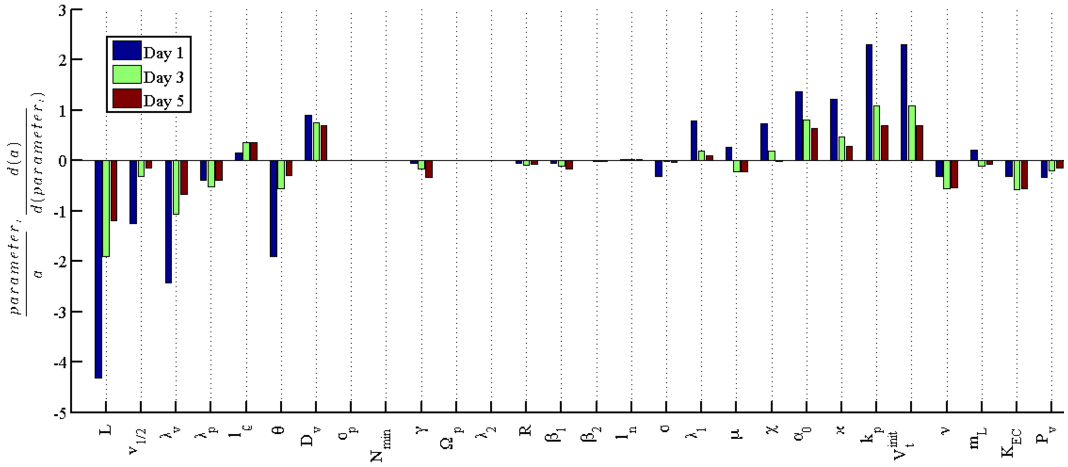

(b) Normalised sensitivity of the amplitude of the advancing vascular wavefront, a.

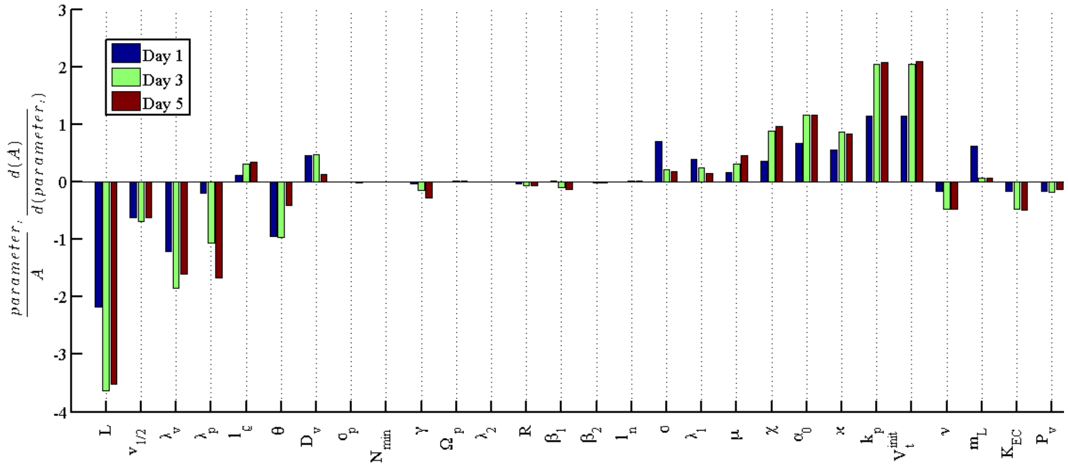

(c) Normalised sensitivity of the area under the vascular density curve, A.

Figure 5.8.: Normalised sensitivity of model output summary statistics in response to local changes in parameter values.

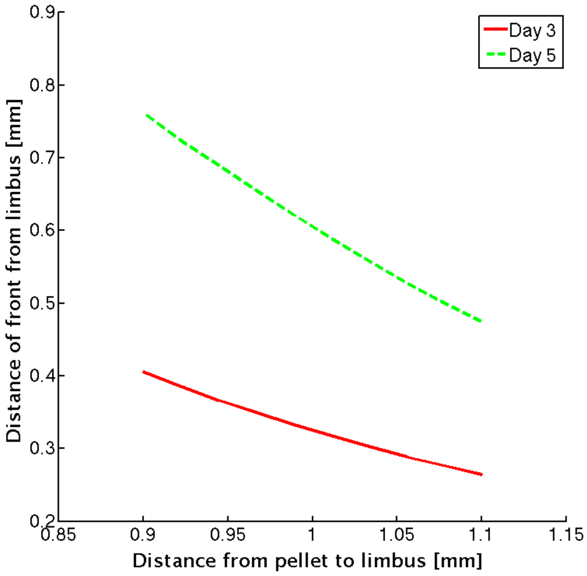

Figure 5.9.: This plot shows how the location of the vascular wavefront on days three and five predicted by the model, (5.19)-(5.23), varies with domain length, L.

the effect of changing γ, and β_1 and β_2 over a wider range of parameter values.

5.5.2.2. Varying γ

For the default parameter values, the VEGF-A$_{165}$ concentration just behind the vascular front is much smaller than the half-saturation constant of VEGFR-2 receptors, $v_{\frac{1}{2}}$. Thus, vessel regression occurs directly behind the vascular wavefront. Since γ is small, this does not markedly affect the amplitude of the vascular wavefront. However, on increasing γ, the profile of the vascular density changes (Figures 5.10 and 5.11) and there is a marked decrease in the amplitude of the vascular density at the tail of the advancing vascular front. Further, the maximum amplitude of the wavefront decreases not only because of increased regression, but also because fewer tip cells are produced.

5.5.2.3. Varying β_1 and β_2

Changes in β_1 and β_2 significantly affect the distribution of tip cells. Figures 5.12 and 5.13 show how model results change as β_1 is varied, holding $\frac{\beta_1}{\beta_2}$ and all other parameter values fixed (Tables 5.3 and 5.4). There is a range of values of β_1 (and β_2) which yield results that agree quantitatively with the experimental data, presented in Chapter 4. Figure 5.14 shows simulation results for three alternate model parametrisations, including the default parametrisation. For the two alternate parametrisations we have increased/decreased the default values of β_1 and β_2

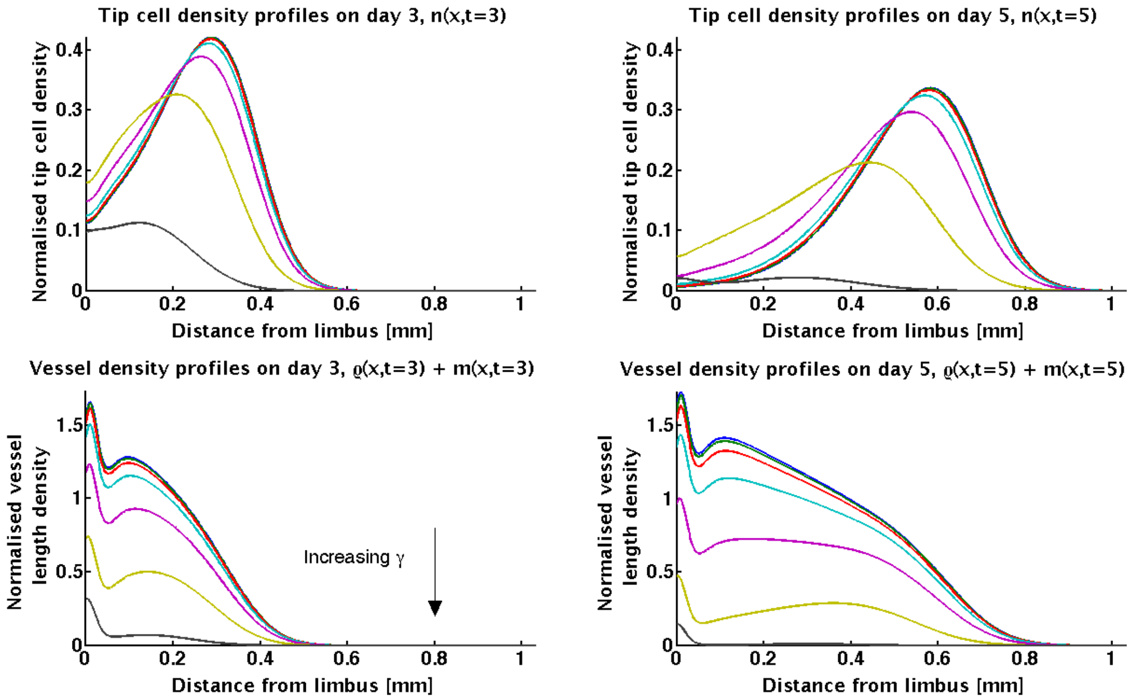

Figure 5.10.: Effect of varying the maximum regression rate, γ, on model results. As γ is increased (from $1 \times 10^{-4}\,\mathrm{h}^{-1}$ to $0.1\,\mathrm{h}^{-1}$ in six increments, evenly spaced in logspace) the amplitude of the vascular wavefront decreases and the overall shape of the vascular density profile changes. All other parameters are held fixed (Tables 5.3 and 5.4).

by ten-fold. Other parameters were then changed to ensure that the model outputs remained in good agreement with the experimental data. As before, no formal fitting of the model to the data was performed. Table 5.5 shows how the parameters have been changed in the two alternate parametrisations (only parameter values which differ from their default values are shown). Figure 5.14a confirms that each parametrisation is in good agreement with the experimental data while Figure 5.14b shows the corresponding tip cell distributions. As in Figure 5.12, where β_1 and β_2 were varied in isolation, increasing the anastomosis rates increases the extent to which tip cells are localised to the vascular wavefront. We see that, when sensible estimates for other parameters are chosen, β_1 and β_2 control the extent to which tip cells are localised to the vascular wavefront.

Together with α_0^v, the parameters β_1 and β_2 determine to a large extent the total number of tip cells in our model domain. It is instructive to consider a specific region of interest (ROI) within our model cornea, in which we can convert tip cell density into a number of tip cells. To that end, we define a ROI similar to that shown in Figure 5.1a, which is of width $\Delta y = 1\,\mathrm{mm}$ along the limbal vessels and which extends from the limbal vessels to the pellet. The total number of

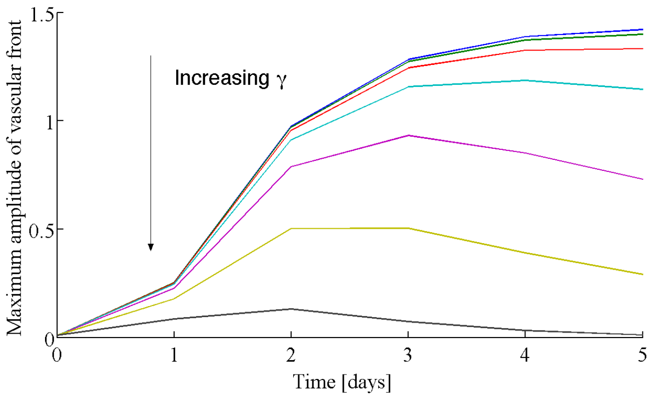

(a) Maximum amplitude of the vascular wavefront.

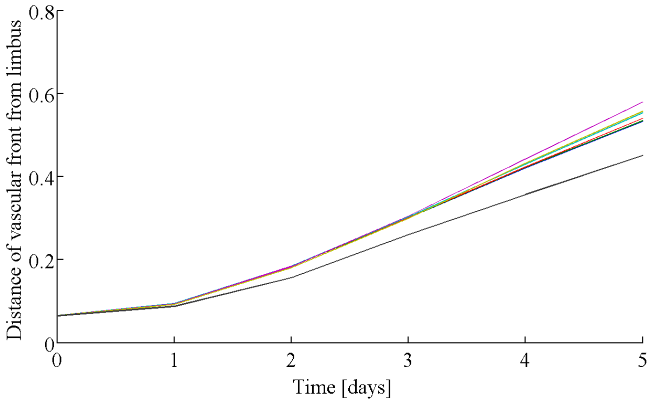

(b) Distance of the vascular wavefront from the limbus.

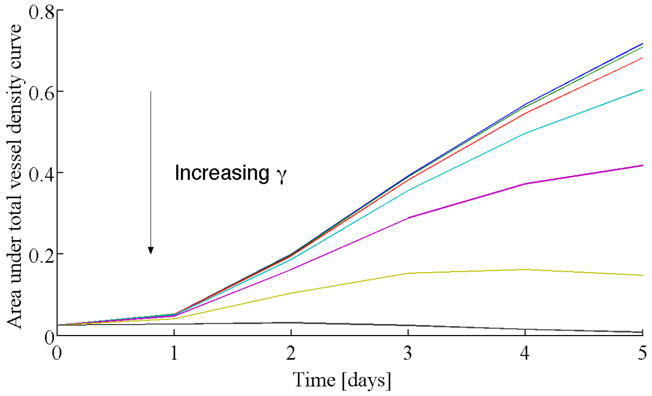

(c) Area under the total vascular density curve.

Figure 5.11.: Effect of varying the maximum regression rate, γ, on model output summary statistics. As γ is increased (from $1 \times 10^{-4}\,\mathrm{h}^{-1}$ to $0.1\,\mathrm{h}^{-1}$ in six increments, evenly spaced in logspace) the amplitude of the vascular wavefront decreases. All other parameters are held fixed (Tables 5.3 and 5.4).

tip cells, $N(t)$, in this ROI is given by

$$N(t) = \Delta_y \Delta_z \int_0^L n(x,t)\, dx, \tag{5.27}$$

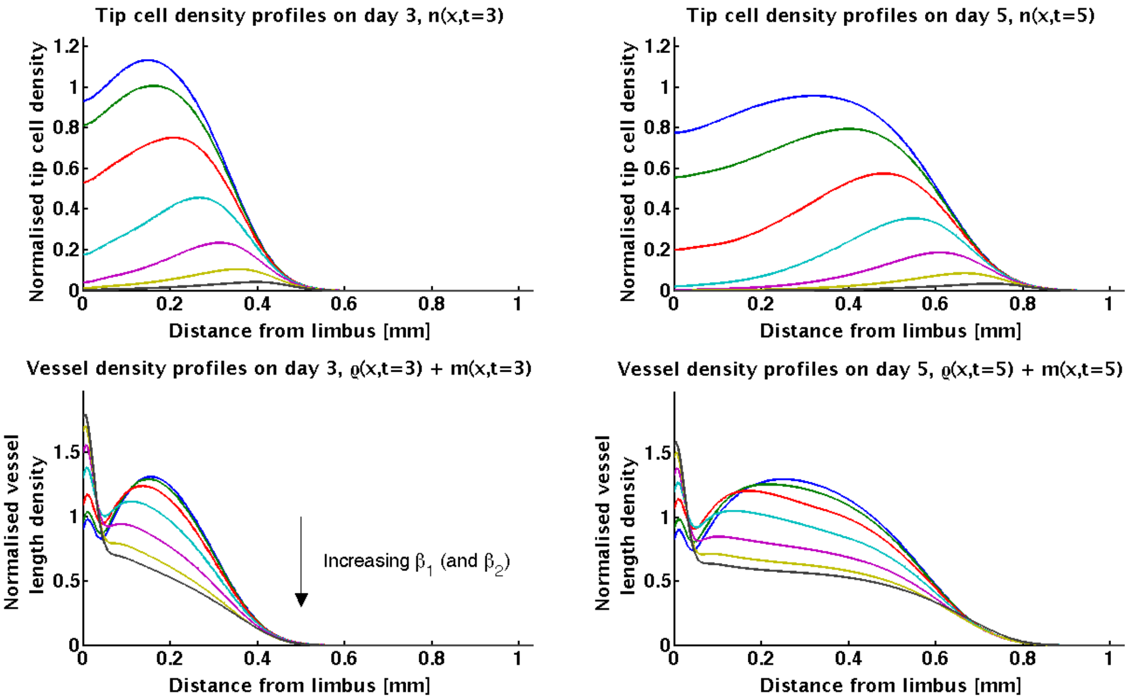

Figure 5.12.: The effect of varying β_1 and β_2 on simulation results is shown. β_1 is varied from 1×10^{-11} to 1×10^{-8} in six steps, equally spaced in logspace, holding $\frac{\beta_1}{\beta_2}$ fixed. All other parameters are held fixed (Tables 5.3 and 5.4).

since $n(x,t)$ represents the number of tip cells per unit volume, averaged along directions perpendicular to the direction of tip migration. Here we have assumed that the volume of the corneal stroma in our ROI may be approximated by a cuboid and that the thickness of the corneal stroma is $\Delta z = 100\,\mu$m (Zhang *et al.* 1996; Song *et al.* 2003). Figure 5.14c shows (unscaled) $N(t)$ for each model parametrisation (Table 5.5). Also shown in Figure 5.14c is how the total rate of anastomoses (tip-to-tip and tip-to-vessel) in our ROI changes over time. In the absence of quantitative data regarding tip cell numbers and densities, these tip cell numbers (and hence densities) and the rate at which anastomosis events occur, seem reasonable, with our model predicting anastomosis events occurring at a rate of order one per hour in our ROI. This then justifies our choice of values for β_1 and β_2. However, clearly, additional spatially-resolved data which detail the locations of tip cells in the cornea would enable further model validation and allow us to further constrain model parameters.

5.6. Adaptation to bFGF-induced angiogenesis

In this section we adapt our model of VEGF-A$_{165}$-induced angiogenesis, stated in full in Section 5.3.7, to simulate bFGF-induced angiogenesis. bFGF induces angiogenesis (both directly and

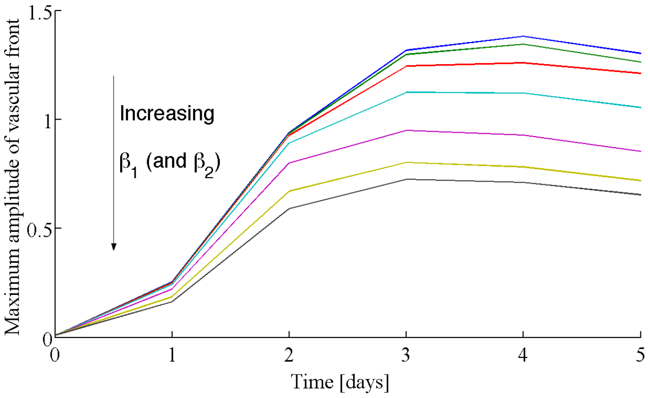

(a) Maximum amplitude of the vascular wavefront.

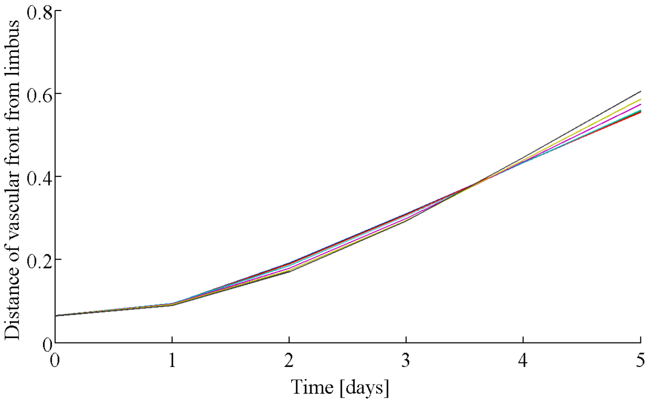

(b) Distance of the vascular wavefront from the limbus.

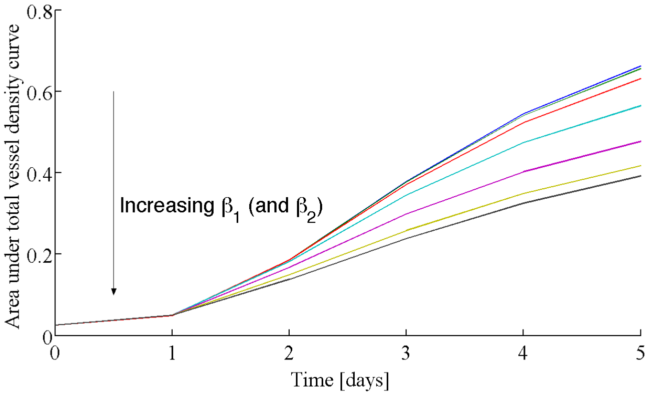

(c) Area under the total vascular density curve.

Figure 5.13.: Effect of varying β_1 and β_2 on model output summary statistics is shown. β_1 is varied from 1×10^{-11} to 1×10^{-8} in six steps, equally spaced in logspace, holding $\frac{\beta_1}{\beta_2}$ fixed. All other parameters are held fixed (Tables 5.3 and 5.4).

indirectly) in the same ways that VEGF-A does (see Chapter 2). Briefly, bFGF interacts primarily with FGFR-1 receptors on ECs, promoting their proliferation and migration, protease production, tubular morphogenesis (Javerzat *et al.* 2002) and, through more complex interactions, is believed to play a role in vessel (de-)maturation (Lieu *et al.* 2011; Murakami and Sakurai 2012) and EC survival (Cao *et al.* 2003). Thus, we model bFGF-induced angiogenesis using equations similar to

Parameter	Default dimensionless value	Fold increase in default parameter value when large anastomosis rates are adopted	Fold decrease in default parameter value when small anastomosis rates are adopted
β_1	0.3176	10	10
β_2	0.0238	10	10
α_0^v	2.1438	1.7	1.25
χ_v	3×10^{-4}	1.2	1.1
γ	1.99×10^{-2}	1.6	0.74
λ_1^v	0.3176	0.5	0.5
μ	2.779×10^{-4}	0.5	0.833
θ_v	50	1.1	1

Table 5.5.: Parameters varied in order to produce fit to experimental data as β_1 and β_2 are increased or decreased. Only parameters which vary from their default values (Tables 5.3 and 5.4) are shown.

those used to model VEGF-A$_{165}$-induced angiogenesis (Section 5.3.7), exchanging VEGF-A$_{165}$, $v(x,t)$, for bFGF, $f(x,t)$, and changing some of the parameter values to account for differences between the two molecules. The only revision made to the equations from Section 5.3.7 is to account for the competitive binding of bFGF to HSPGs.

In more detail, bFGF regulates EC behaviour by binding to FGFR-1 receptors. However, bFGF may also bind to HSPGs located on the surface of ECs. While the dynamics of bFGF capture and internalisation are very complex (Presta *et al.* 2005), here, we assume that both FGFR-1 and HSPG may bind and internalise bFGF, independent of one another and that it is the uptake via FGFR-1 only which stimulates EC activation. Thus, we model the evolution of bFGF concentration in our model using the equation:

$$\begin{aligned}\frac{\partial f(x,t)}{\partial t} &= \underbrace{D_f \frac{\partial^2 f(x,t)}{\partial x^2}}_{\text{diffusion}} - \underbrace{\lambda_f \; v(x,t)}_{\text{natural decay}} - \underbrace{2\,\pi\,\bar{R}\,P_f\,(\rho(x,t)+m(x,t))\,(f(x,t)-f_{blood})}_{\text{drainage into vascular system}} \\ &\quad \underbrace{- K_{EC}^{FGFR}\,(n(x,t)+\nu\,(\rho(x,t)+m(x,t)))\left(\frac{f(x,t)}{f(x,t)+f_{\frac{1}{2}}^{FGFR}}\right)}_{\text{uptake via FGFR}} \qquad (5.28) \\ &\quad \underbrace{- K_{EC}^{HSPG}\,(n(x,t)+\nu\,(\rho(x,t)+m(x,t)))\left(\frac{f(x,t)}{f(x,t)+f_{\frac{1}{2}}^{HSPG}}\right)}_{\text{uptake via HSPG}}.\end{aligned}$$

Here, $f_{\frac{1}{2}}^{FGFR}$ is the EC50 for EC activation through binding of bFGF to FGFR-1 receptors and $f_{\frac{1}{2}}^{HSPG}$ is the half saturation concentration of bFGF for cell-surface HSPGs. K_{EC}^{FGFR} and K_{EC}^{HSPG} represent the maximal rates of reduction in bFGF concentration due to cellular uptake via FGFR-1 and HSPG, respectively. Other parameters in Equation (5.28) parallel those defined in

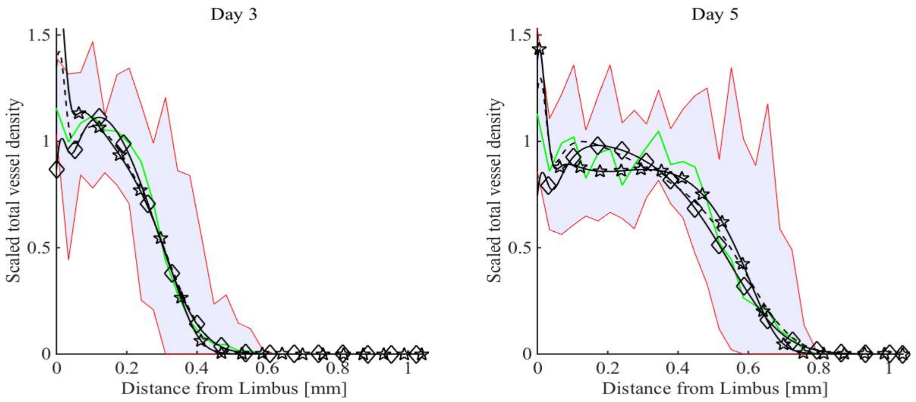

(a) Comparison of model outputs with VEGF-A$_{165}$-induced angiogenesis experimental data. As before, the solid green lines show the averaged experimental data and the shaded region the range in densities across all VEGF-A$_{165}$ experiments. Root mean squared error: $--$: 0.0738, $\star$: 0.0996, $\Diamond$: 0.0892.

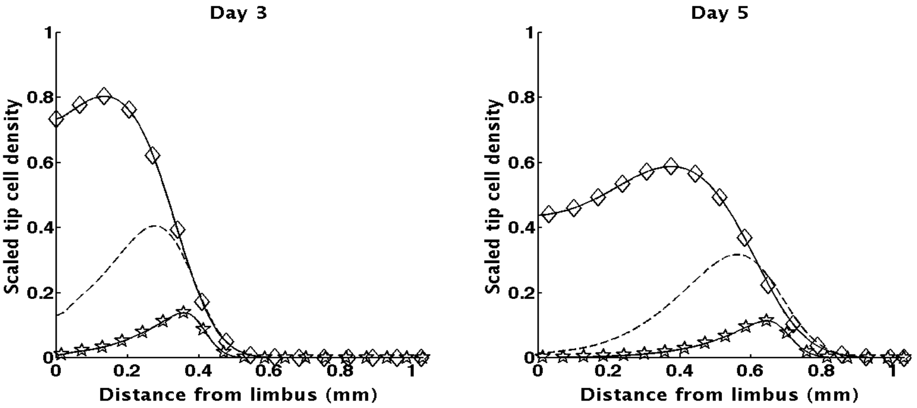

(b) Tip cell distributions. The larger the anastomosis rate the fewer tip cells are present at any one time and the more localised those tip cells are to the vascular wavefront.

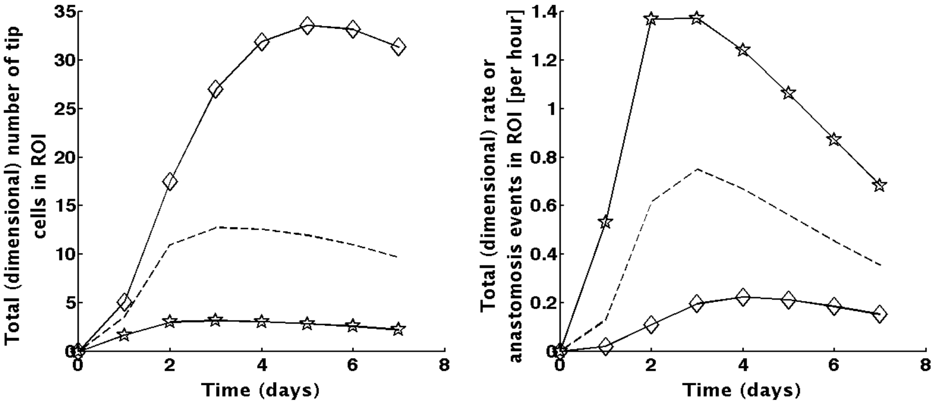

(c) Number of tip cells and total rate of anastomosis events (tip-to-tip and tip-to-vessel) in corneal region of interest (see main text for details).

Figure 5.14.: Effect of varying the rates of anastomosis on model system dynamics. β_1 is varied, holding $\frac{\beta_1}{\beta_2}$ constant. Other parameters are varied so that model outputs remain in good agreement with the experimental data (see (a) and Table 5.5). Default anastomosis rates $--$; ten-fold increase in anastomosis rates: $\star$; ten-fold decrease in anastomosis rates: $\Diamond$.

Section 5.3 for VEGF-A$_{165}$.

Since nondimensionalisation of the bFGF-induced angiogenesis model proceeds as in Section 5.3.7, the details are not repeated here. A value of $F_0 = 1 \times 10^{-9}\,$M is used as the reference value for bFGF

5.7. Parameter value estimation for bFGF-induced angiogenesis

Parameters pertinent to bFGF-induced angiogenesis that can be estimated from experimental data principally involve extracellular transport and uptake by cells. Bikfalvi *et al.* (1989) estimate $f_{\frac{1}{2}}^{FGFR} = 42.2 \pm 3.8\,$pM and $f_{\frac{1}{2}}^{HSPG} = 0.922 \pm 0.27\,$nM. They also estimate the number of FGFR and HSPG binding sites per human omental microvascular EC to be 70000 ± 6000 and 630000 ± 170000 sites per cell, respectively. Roghani and Moscatelli (1992) estimate the dissociation constant for HSPG receptors to be 20 nM and the number of HSPG sites per Chinese hamster ovary cell to be $\sim 5 \times 10^6$. Meanwhile, Moscatelli (1988) estimate $6000 - 17000$ FGFR receptors per bovine capillary EC and the number of HSPG receptors per bovine capillary EC to be approximately 1000000. Moscatelli (1988) also finds the dissociation constant of FGFR to be $\sim 20\,$pM and that of HSPG to be $\sim 2\,$nM. The internalisation rate of the bFGF/FGFR complex is $4.68\,\text{h}^{-1}$ (Fannon *et al.* 2003; Filion and Popel 2004) and that of the bFGF/HSPG complex is $0.3\,\text{h}^{-1}$ (Sperinde and Nugent 1998; Filion and Popel 2004). We use the estimates given by Bikfalvi *et al.* (1989) to parametrise our model. Thus we take $f_{\frac{1}{2}}^{FGFR} = 4.22\,$pM and $f_{\frac{1}{2}}^{HSPG} = 0.922\,$nM. We assume that there are approximately 630000 HSPG binding sites per EC and 70000 FGFR-1 binding sites per EC. Maximally, therefore, 1.16×10^{-19} and 10.45×10^{-19} moles of bFGF, respectively, can bind to FGFR and HSPG receptors on ECs at any one time. Thus, assuming that the number of receptors on the surface of a cell remains constant, a cell can uptake maximally 5.4×10^{-19} moles of bFGF per hour via FGFR-1 molecules and 3.1×10^{-19} moles of bFGF per hour via HSPGs. Accordingly, we assume $K_{EC}^{HSPG} = 3.1 \times 10^{-19}$. We fix $K_{EC}^{FGFR} = 1.8 \times 10^{-19}$ since this provides a better fit to experimental data than $K_{EC}^{FGFR} = 5.4 \times 10^{-19}$ whilst still being consistent with values found in the literature.

Filion and Popel (2004) estimate the diffusion coefficient for bFGF to be $7.92 \times 10^{-7}\,\text{m}^2\text{h}^{-1}$ at 37^oC using the Einstein-Stokes formula. Meanwhile, we follow Tong and Yuan (2008b) and Boyer and Hsu (1992) by fixing $D_f = 1.92 \times 10^{-7}\,\text{m}^2\text{h}^{-1}$. Westall *et al.* (1983) estimate the half-life of FGF, λ_f, to vary between a few hours and a day (or so) and Sperinde and Nugent (1998) provide an estimate for the half-life of bFGF inside the cell of 18-24 hours. We fix $\lambda_f = 0.04\,\mathrm{h}^{-1}$, corresponding to a half-life of approximately 18 hours. Fu and Shen (2003) estimate the permeability of vessels to α-lactalbumin to be $(1.98 \pm 0.216) \times 10^{-4}\,\mathrm{m\,h}^{-1}$. Since α-lactalbumin has a similar Stokes' radius (20.1 Angstroms) to bFGF (14.5 Angstroms, Dowd *et al.*, 1999), we fix $P_f = 3 \times 10^{-4}\,\mathrm{m\,h}^{-1}$ for the permeability of vessels to bFGF.

Default simulations mimic experiments involving cylindrical pellets of radius 0.3 mm and thickness 0.06 mm which contain 15 ng bFGF (18 kDa). Thus, we estimate the initial molar concentration of bFGF in the pellet to be $[F_t]_{init} = 4.92 \times 10^{-5}\,\mathrm{M}$. Other parameters, for which experimental data are not available, are modified to ensure a good fit of model results to experimental data. Values of parameter used for the simulation of bFGF-induced angiogenesis which differ from those used for VEGF-A_{165} are recorded in Table 5.6.

5.8. Numerical results: bFGF-induced angiogenesis

A comparison between the results of bFGF-induced angiogenesis simulation, using the default parameters provided above, and the experimental data is presented in Figure 5.15. We observe good quantitative agreement with the data. Our image analysis, presented in Chapter 4, revealed that, while the vasculature travels further towards bFGF pellets than VEGF-A_{165} pellets, the mean density of newly vascularised regions is transiently greater when VEGF-A_{165} pellets are used[4]. Our results also suggest that bFGF pellets induce a more sustained angiogenic response than their VEGF-A_{165} counterparts. In Figure 5.16 we compare the summary statistics extracted from model simulations with those estimated from the experimental data for both VEGF-A_{165}- and bFGF-induced angiogenesis. With regards to model parametrisation, our simulations suggest that the more sustained angiogenic response observed in bFGF experiments may be largely explained by bFGF having a longer half-life than VEGF-A_{165} ($\lambda_f = 0.04\,\mathrm{h}^{-1}$ vs $\lambda_v = 0.8\,\mathrm{h}^{-1}$). That is, bFGF remains stable inside the pellet and cornea for longer than VEGF-A_{165} and, thus, may elicit an angiogenic response for a longer period of time.

---

[4] Maximum amplitudes of experimental vascular density profiles were estimated by fitting a smoothing spline to the noisy vascular density profiles from individual experiments. To test whether the amplitudes are significantly different in VEGF-A_{165} and bFGF experiments we use the MATLAB function *ttest2* to perform the two-sample t-test. We assume that the two samples come from normal distributions with unknown and unequal variances. Day 3 maximum densities for VEGF-A_{165} experiments were significantly greater than those for bFGF experiments ($p < 0.01$), while day 5 maximum densities were not significantly different. This is as reflected in Figure 5.16.

Parameter	Description	Default value and units	Non-dimensional value	Sources
D_f	Diffusion constant for bFGF in cornea.	1.92×10^{-7} [m^{2}h^{-1}]	0.7622	(Boyer and Hsu 1992; Filion and Popel 2004; Tong and Yuan 2008b)
λ_f	Natural decay constant of bFGF.	0.04 [h^{-1}]	0.1588	(Westall *et al.* 1983; Sperinde and Nugent 1998)
K_{EC}^{FGFR}	Maximum rate of reduction in molar bFGF concentration per unit EC density due to FGFR binding.	1.8×10^{-22} [moles of bFGF h^{-1}cell^{-1} litre^{-1} m^3]	0.7146	(Fannon *et al.* 2003; Filion and Popel 2004; Bikfalvi *et al.* 1989).
$f_{\frac{1}{2}}^{FGFR}$	Concentration of bFGF at which occupation of FGFR receptors is half-maximal.	4.22×10^{-11} $[M]$	0.0422	(Bikfalvi *et al.* 1989).
K_{EC}^{HSPG}	Maximum rate of reduction in molar bFGF concentration per unit EC density due to HSPG binding.	3.1×10^{-22} [moles of bFGF h^{-1}cell^{-1} litre^{-1} m^3]	1.2307	(Sperinde and Nugent 1998; Filion and Popel 2004; Bikfalvi *et al.* 1989).
$f_{\frac{1}{2}}^{HSPG}$	Concentration of bFGF at which occupation of HSPG receptors is half-maximal.	9.22×10^{-10} [M]	0.9220	(Bikfalvi *et al.* 1989).
P_f	Permeability of corneal vasculature to bFGF.	3×10^{-4} [m h^{-1}]	1.1910	(Fu and Shen 2003).
f_{blood}	Concentration of bFGF in the blood.	0 [M]	0	-
θ_f	Binding constant.	55	55	-
k_p^f	Effective permeability of the cornea-pellet boundary to bFGF.	2.75×10^{-7} [m h^{-1}]	1.092×10^{-3}	-
λ_p^f	Natural decay constant of bFGF in the pellet.	0.04 [h^{-1}]	0.1588	Assume $\lambda_p^f = \lambda_f$.
$[F_t]_{init}$	Initial concentration of bFGF in pellet.	4.92×10^{-5} [M]	4.92×10^4	Roche, Penzberg.
λ_1^f	Maximal rate of bFGF-induced dematuration.	0.02 [h^{-1}]	0.0794	(Zheng *et al.* 2013).
χ_f	Chemotactic sensitivity of tip cells to bFGF.	4 [m^2 h^{-1} M^{-1}]	0.0159	As in Table 5.3.
α_0^f	Maximal rate of bFGF-induced tip cell production per unit vessel length.	1000 [tips h^{-1} per m of vessel]	0.794	-
γ	Maximal rate of regression of ECs (vessels) in low bFGF.	1.67×10^{-3} [h^{-1}]	6.62×10^{-3}	(Cao *et al.* 2003)
L	Average distance of pellets from limbal vessels in bFGF experiments.	1.1×10^{-3} [m]	1.1	Image analysis (Chapter 4)

Table 5.6.: Default parameter values relating to the bFGF-induced angiogenesis model. Parameters listed in this table relate to those whose values we assume may differ to those detailed in Tables 5.3 and 5.4. The most significant change in parameter value from those used in the VEGF-A$_{165}$ model, (5.19)-(5.23), is for λ_f (highlighted red), whose nondimensionalised value is 20-fold lower than that used in the VEGF-A$_{165}$ model.

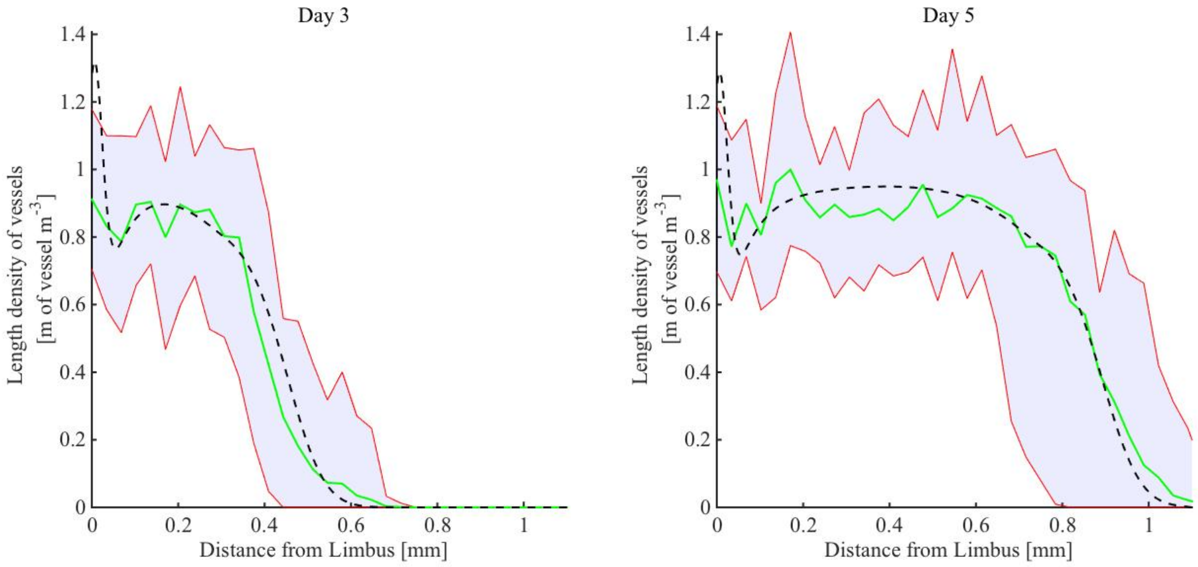

Figure 5.15.: Comparison of bFGF model results with experimental data when default parameters are used (Table 5.6). The black dashed lines show model predictions, the solid green lines show averaged experimental data and the shaded region (bounded by solid red lines) shows the range in densities across experimental data sets.

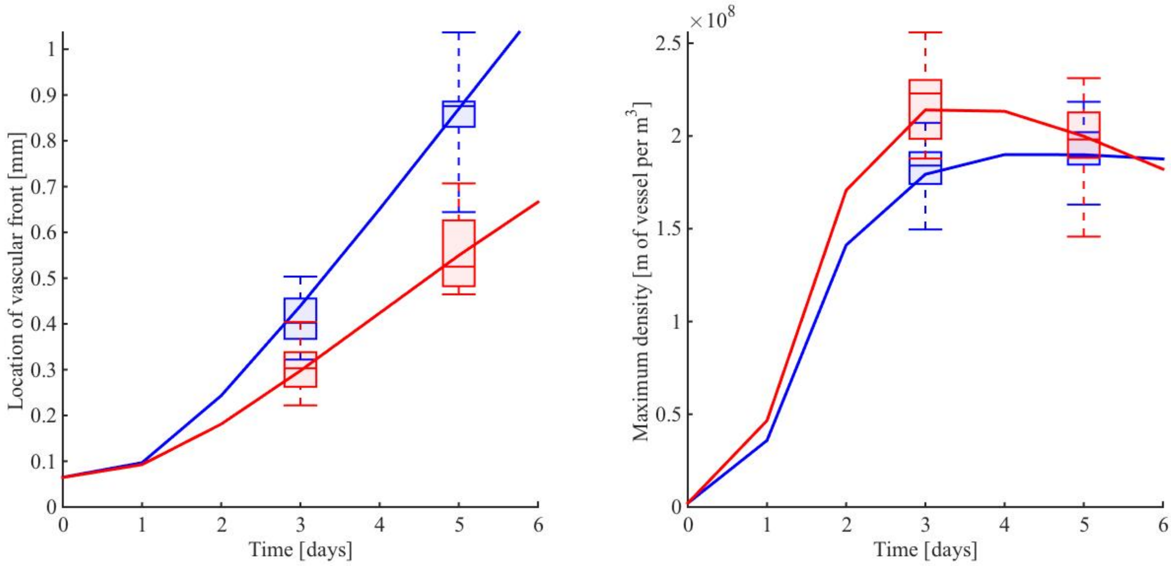

Figure 5.16.: Summary statistics extracted from model simulations and estimated from experimental data are compared for VEGF-A$_{165}$-induced angiogenesis (red) and bFGF-induced angiogenesis (blue). Continuous lines represent model predictions. The overlaid box plots represent experimental data (first, second and third quartile with maxima and minima are shown).

5.9. Model extension to account for tip cell-ECM interactions

From the results presented in Sections 5.5 and 5.8, it is clear that a model which incorporates only chemotaxis and random motion as mechanisms for tip cell motion is sufficient to describe the data extracted from the experimental images in Chapter 4. However, ECs *in vitro* also exhibit directed migration up gradients of immobilised ECM components, such as fibronectin and collagen (Smith *et al.* 2006; Bennet 2012), independently of chemotactic agents. Although the significance of such haptotactic movement in *in vivo* angiogenesis remains to be established, it is plausible that high concentration gradients of, for example, collagen may enhance tip cell migration (Davis 2005). Thus, in this section we extend the models of VEGF-A$_{165}$- and bFGF-induced angiogenesis presented in Sections 5.3-5.8 to investigate the possible roles of the ECM in regulating tip cell motility.

In more detail, following Machado *et al.* (2011) and Watson *et al.* (2012), we extend our model to incorporate key interactions between MMPs (e) and the ECM (c). We suppose that the exposure of tip cells to VEGF-A$_{165}$ (or bFGF) stimulates the release of MMPs (Rundhaug 2005), which degrade ECM proteins as they diffuse through the surrounding matrix. ECM degradation creates spatial gradients between regions occupied by the tip cells and those areas directly in front of them, up which tip cells may migrate. The equations we adopt to capture this behaviour in our extended model are:

$$\begin{aligned}
\frac{\partial c}{\partial t} &= -\underbrace{Bec}_{\text{degradation by MMPs}} + \underbrace{C(C_{max} - c)}_{\text{remodelling}}, && (5.29)\\
\frac{\partial e}{\partial t} &= \underbrace{D_e \frac{\partial^2 e}{\partial x^2}}_{\text{diffusion}} + \underbrace{Fn\frac{v}{v + v_{\frac{1}{2}}}}_{\text{production by tip cells}} - \underbrace{Ee}_{\text{removal}}. && (5.30)
\end{aligned}$$

In (5.29) we have also included a term which accounts phenomenologically for remodelling of the ECM. The parameter C quantifies the rate of ECM remodelling, while C_{max} is the equilibrium ECM density and B quantifies the rate at which MMPs degrade the ECM. In (5.30), the maximal rate of MMP production per unit tip cell density is F, and D_e is the diffusion constant for MMPs, which are removed from the system at rate E.

The ECM density is everywhere initialised to C_{max} and the MMP concentration is initialised to zero:

$$c(x, 0) = C_{max}; \quad e(x, 0) = 0, \tag{5.31}$$

and, for simplicity, we assume no flux boundary conditions for MMPs at both $x = 0$ and $x = L$:

$$\left. D_e \frac{\partial e}{\partial x} = 0, \right\} \quad x = 0; \quad x = L. \tag{5.32}$$

As noted above, spatial gradients of ECM proteins will stimulate haptotactic movement of tip cells. ECs may also alter their migration speed in response to the ECM density. Typically, the dependence of cell speed on ECM density is biphasic; the cell migration rate is maximal at intermediate levels of ECM density and reduced at both low and high densities (Palecek *et al.* 1997; Cox *et al.* 2001; Zaman *et al.* 2006). These phenomena are incorporated into our model by updating the tip cell flux as follows:

$$J_{tip} = - \underbrace{\mu(c)\,\frac{\partial n}{\partial x}}_{\text{random motion}} + \underbrace{\chi_v(c)\,n\,\frac{\partial v}{\partial x}}_{\text{chemotaxis}} + \underbrace{\Upsilon(c)\,n\,\frac{\partial c}{\partial x}}_{\text{haptotaxis}}, \tag{5.33}$$

where $\Upsilon(c)$ is the haptotaxis coefficient. In contrast to models presented earlier in this chapter, where the random motility coefficient, μ, and the chemotaxis coefficient χ_v were constant, here, μ, χ_v and Υ depend on the local ECM density, c. In this way, we aim to capture how permissive the ECM is to ECs as a function of ECM density. Most generally, in our extended model we will therefore assume a functional dependence of μ, χ_v and Υ on c of the form:

$$\ln\left(\frac{\mu(c)}{\mu_0}\right) = \ln\left(\frac{\chi_v(c)}{\chi_{v0}}\right) = \ln\left(\frac{\Upsilon(c)}{\Upsilon_0}\right) = \frac{-(\ln(c)-\eta)^2}{2\,\Gamma^2}. \tag{5.34}$$

This dependence is plotted in Figure 5.17. The parameters Γ and η determine the shape of the curve. To discern the effect that incorporating such functional dependence of taxis coefficients has on model predictions, in Section 5.11.2 we will also consider the use of constant taxis coefficients, i.e.:

$$\frac{\mu(c)}{\mu_0} = \frac{\chi_v(c)}{\chi_{v0}} = \frac{\Upsilon(c)}{\Upsilon_0} = 1. \tag{5.35}$$

Nondimensionalisation of our extended model proceeds as in Section 5.3.7, where distance is rescaled with the approximate pellet-limbus distance, $\hat{L}$, and time with $\tau = \frac{\hat{L}^2}{D_v}$, so that

$$x^* = \frac{x}{\hat{L}} \quad \text{and} \quad t^* = \frac{t}{\tau}. \tag{5.36}$$

We also rescale the dependent variables as

$$n^* = \frac{n}{n_0}, \quad \rho^* = \frac{\rho}{\rho_0}, \quad m^* = \frac{m}{\rho_0}, \quad v^* = \frac{v}{V_0} \quad c^* = \frac{c}{c_0}, \quad e^* = \frac{e}{e_0}, \quad \text{and} \quad [V_T]^* = \frac{[V_T]}{V_0}, \tag{5.37}$$

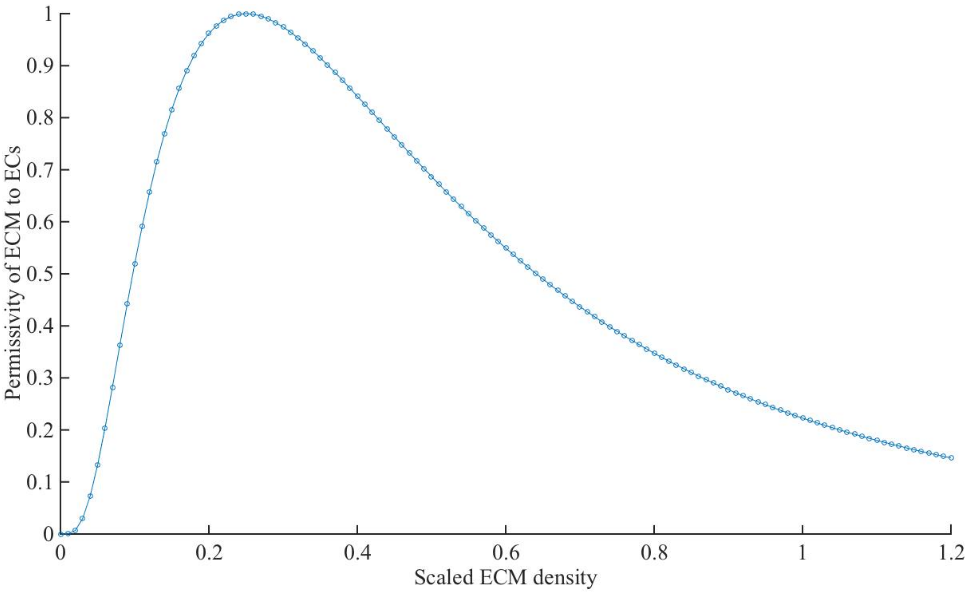

Figure 5.17.: The permissivity of the ECM to tip cells, i.e. $\frac{\mu(c)}{\mu_0}$, is assumed to vary with ECM density. Here, $\eta = -1.4$ and $\Gamma = 0.8$, as in default simulations (see Section 5.10).

and introduce the following dimensionless parameters in addition to those outlined in Section 5.3.7:

$$B^* = (B \tau e_0)\,, \quad C^*_{max} = \left(\frac{C_{max}}{c_0}\right), \quad C^* = (C\tau)\,,$$

$$D^*_e = \left(\frac{D_e}{D_v}\right), \quad F^* = \left(\frac{F n_0 \tau}{e_0}\right), \quad E^* = (E\tau)\,, \quad \Upsilon^*_0 = \left(\frac{\Upsilon_0 c_0}{D_v}\right).$$

The full system of dimensionless equations for our extended model of VEGF-A$_{165}$-induced angiogenesis (omitting asterisks for clarity of presentation) is given by:

$$\frac{\partial m}{\partial t} = -\lambda_1^v \left(\frac{v}{v + v_{\frac{1}{2}}}\right) m + \lambda_2^v \left(\frac{v_{\frac{1}{2}}}{v + v_{\frac{1}{2}}}\right) H\left(\nu\,(m+\rho) + n - N_{min}\right)\rho, \tag{5.38}$$

$$\begin{aligned}\frac{\partial n}{\partial t} = {} & \frac{\partial}{\partial x}\left(\mu(c)\,\frac{\partial n}{\partial x} - \chi_v(c)\; n\; \frac{\partial v}{\partial x} - \Upsilon(c)\; n\; \frac{\partial c}{\partial x}\right) + \alpha_0^v\; \rho\; \left(\frac{v}{v + v_{\frac{1}{2}}}\right) \\ & - \beta_1\; n\; (\rho + m) - 2\; \beta_2\; n^2 - \gamma\; n\; \left(\frac{v_{\frac{1}{2}}}{v + v_{\frac{1}{2}}}\right),\end{aligned} \tag{5.39}$$

$$\begin{aligned}\frac{\partial \rho}{\partial t} = {} & \kappa \left| \mu(c)\, \frac{\partial n}{\partial x} - \chi_v(c)\, n\, \frac{\partial v}{\partial x} - \Upsilon(c)\, n\, \frac{\partial c}{\partial x} \right| - \gamma\, \rho \left(\frac{v_{\frac{1}{2}}}{v + v_{\frac{1}{2}}} \right) + \bar{l}_\rho\, \beta_1\, n\, (\rho + m)^{\frac{1}{2}} \\ & + \bar{l}_n \beta_2\, n^{\frac{5}{3}} + \lambda_1^v \left(\frac{v}{v + v_{\frac{1}{2}}} \right) m - \lambda_2^v \left(\frac{v_{\frac{1}{2}}}{v + v_{\frac{1}{2}}} \right) H\left(\nu\,(m + \rho) + n - N_{min}\right) \rho, \end{aligned} \tag{5.40}$$

$$\begin{aligned}\frac{\partial v}{\partial t} = {} & D_v \frac{\partial^2 v}{\partial x^2} - \lambda_v\, v - 2\, \pi\, \bar{R}\, P_v\, (\rho + m)\, (v - v_{blood}) \\ & - K_{EC}^v\, (n + \nu\, (\rho + m)) \left(\frac{v}{v + v_{\frac{1}{2}}} \right), \end{aligned} \tag{5.41}$$

$$\frac{d[V_T]}{dt} = -\frac{\lambda_p^v}{\theta_v}[V_T] - \frac{\zeta_p k_p^v}{\Omega_p} \left(\frac{[V_T]}{\theta_v} - v(L,t) \right), \tag{5.42}$$

$$\frac{\partial c}{\partial t} = -B\ e\ c + C\ \left(C_{max} - c\right), \tag{5.43}$$

$$\frac{\partial e}{\partial t} = D_e\ \nabla^2 e + F\ n\ \frac{v}{v + v_{\frac{1}{2}}} - E\ e. \tag{5.44}$$

The red terms indicate extensions to the model presented in Section 5.3.7. The initial conditions are

$$v(x,0) = 0,\ \rho(x,0) = 0,\ n(x,0) = 0,\ m(x,0) = m_L\ exp\left[-\frac{x^2}{2\sigma^2} \right], \tag{5.45}$$

$$[V_T]\,(0) = [V_T]_{init}\,,\ c(x,0) = C_{max},\ e(x,0) = 0. \tag{5.46}$$

and the boundary conditions are

$$\left.\begin{aligned} & \mu(c)\, \frac{\partial n}{\partial x} - \chi_v(c)\, n\, \frac{\partial v}{\partial x} - \Upsilon(c)\, n\, \frac{\partial c}{\partial x} = 0, \\ & -D_v\, \frac{\partial v}{\partial x} = -P_v(v - v_{blood}), \\ & D_e \frac{\partial e}{\partial x} = 0 \end{aligned}\right\} \quad x = 0, \tag{5.47}$$

$$\left.\begin{aligned} & \mu(c)\, \frac{\partial n}{\partial x} - \chi_v(c)\, n\, \frac{\partial v}{\partial x} - \Upsilon(c)\, n\, \frac{\partial c}{\partial x} = 0, \\ & -D_v \frac{\partial v}{\partial x} = -k_p^v \left(\frac{[V_T]}{\theta_v} - v \right), \\ & D_e \frac{\partial e}{\partial x} = 0 \end{aligned}\right\} \quad x = L. \tag{5.48}$$

The dependence of μ, χ_v and Υ on c is given by (5.34). The updated equations for bFGF-induced angiogenesis follow directly, as outlined in Section 5.6.

5.10. Parameter value estimation for the extended model

Unless otherwise stated, we use the default parameter values from Sections 5.4 and 5.7. By extending our model to incorporate tip cell-ECM interactions we have introduced several new parameters. We proceed by first estimating their values.

Recent experiments have attempted to quantify the haptotactic motility of individual ECs (Smith *et al.* 2006). However, haptotaxis coefficients are not directly available from such experiments and, as with experimental estimates for the random motility and chemotactic sensitivity for isolated ECs, we would not expect these values to correspond to the haptotactic sensitivity of tip cells, which undergo interactions with trailing ECs. A number of mathematical models have considered tip cell movement subject to both haptotaxis and chemotaxis. In such cases the relative values of chemotaxis and haptotaxis coefficients are important. Thus, this is where we focus our discussion here. Orme and Chaplain (1997) were the first to include the effect of the ECM in a model of tumour-induced angiogenesis and to examine the response of ECs to spatial gradients in the ECM density. In the absence of reliable empirical data they chose (through simulation) a nondimensionalised value for the haptotaxis coefficient of 0.5. This is similar to the value they used for the chemotaxis coefficient, 0.65. Anderson and Chaplain (1998) also used a dimensionless haptotaxis coefficient (0.34) of similar magnitude to their chemotaxis coefficient (0.38). Meanwhile, Watson *et al.* (2012) adopted a nondimensionalised value of 0.0125 for their haptotaxis coefficient, which is ~ 30 times less than the nondimensionalised value they used for the maximum chemotactic sensitivity. We adopt a default value of $\Upsilon_0 = 1.25 \times 10^{-4}\,\mathrm{m}^2\mathrm{h}^{-1}\mathrm{M}^{-1}$. The default nondimensionalised value of Υ_0 is 40-fold and ~ 65-fold lower than the default values of χ_{v0} and χ_{f0} used to simulate VEGF-A$_{165}$- and bFGF-induced angiogenesis, respectively. However, in Section 5.11.2.1, we investigate how changing the balance between chemotaxis and haptotaxis (changing the ratio $\frac{\chi_{v0}}{\Upsilon_0}$) affects the angiogenic response predicted by our model when VEGF-A$_{165}$ is inhibited.

The parameter C_{max} is the equilibrium density of the ECM in the corneal stroma. Since collagen is the major solid component of the corneal stroma, we focus on its density when estimating C_{max}. A single collagen molecule (also known as tropocollagen) is used to make up larger collagen aggregates, such as fibrils. These fibrils are approximately 300 nm long, $30-35$ nm in diameter and, in the cornea are separated by distances of about 67 nm (Holmes *et al.* 2001). Using these figures we estimate that there are 7.43×10^{17} collagen aggregates per litre, equating to a molar concentration of $1.23 \times 10^{-6}\,\mathrm{M}$. Accordingly, we estimate $C_{max} = 1 \times 10^{-6}\,\mathrm{M}$.

Gioia *et al.* (2007) estimate $\frac{k_{cat}}{K_m}$ for the rate of enzymatic cleavage of collagen by MMP-2 and MMP-8 to be 1.44×10^{9} - $8.28 \times 10^{9}\,\mathrm{M}^{-1}\mathrm{h}^{-1}$ and 1.04×10^{8} - $2.02 \times 10^{8}\,\mathrm{M}^{-1}\mathrm{h}^{-1}$, respectively[5]. These values serve as a good approximation for the degradation rate of the ECM by MMPs, for which we take a default value of $B = 1 \times 10^{9}\,\mathrm{M}^{-1}\mathrm{h}^{-1}$.

Estimates of the diffusion constant of MMPs are sparse. However, some research has indicated that MMPs undergo biased diffusion along the surface of collagen fibrils; for example, Collier *et al.* (2011) experimentally find the diffusion coefficient of MMPs along collagen fibrils to be $D_e \approx 3 \times 10^{-8}\,\mathrm{m}^2\mathrm{h}^{-1}$. In the modelling literature, a range of values for MMP diffusion coefficients have been used: in their hybrid model of angiogenesis, Daub and Merks (2013) fix $D_e = 3.6 \times 10^{-9}\,\mathrm{m}^2\mathrm{h}^{-1}$, while Milde *et al.* (2008) take $D_e = 2.16 \times 10^{-7}\,\mathrm{m}^2\mathrm{h}^{-1}$. In the absence of more appropriate data we assume an unbiased (isotropic) diffusion coefficient of $D_e = 3 \times 10^{-8}\,\mathrm{m}^2\mathrm{h}^{-1}$.

To the best of our knowledge, estimates for the remaining parameters introduced in this section, η, Γ, C, F and E, are not available. We therefore selected values from plausible regimes in order to provide a good fit to the available data. The default values for η and Γ, which determine the shape of the function which describes the permissivity of the ECM to tip cells (see Equation (5.34)) are -1.4 and 0.8, respectively. We choose C, the rate constant for ECM remodelling, to be $0.05\,\mathrm{h}^{-1}$, since permanent ECM remodelling due to fibroblasts has been observed to occur over a period of several days (Petroll *et al.* 2004). We choose the maximal MMP production rate, F, to be $1 \times 10^{-19}\,\mathrm{M\,h}^{-1}\,(\mathrm{tip\,cell\,m}^{-3})^{-1}$ and the natural decay rate of MMPs, E, to be $25\,\mathrm{h}^{-1}$. The relatively high value for E reflects the fact that the natural decay term in (5.30) is assumed to encompass all processes involved in inhibiting ECM proteolysis by MMPs, as in Daub and Merks (2013). Taken together with the other parameter estimates, adopting these values for E and F leads to a level of ECM degradation which results in an ECM density around the vascular front which is close to that assumed to be optimal for EC migration (~ 0.25; see Figure 5.17).

For nondimensionalisation, appropriate values for the new scaling parameters are $c_0 = C_{max}$ and $e_0 = 1 \times 10^{-9}\,\mathrm{M}$. Default values for the new parameters introduced in this section (and sources where available) are summarised in Table 5.7. Several other parameter values have

---

[5] Here, k_{cat} is a constant describing the turnover rate of an enzyme-substrate complex to product and enzyme and K_m is the Michaelis-Menten constant, describing the amount of substrate needed for the enzyme to obtain half of its maximum rate of reaction.

Parameter	Description	Default value and units	Non-dimensional value	Sources
D_e	MMP diffusion constant.	3×10^{-8} [$\mathrm{m^2h^{-1}}$]	0.0119	(Milde *et al.* 2008; Collier *et al.* 2011; Daub and Merks 2013)
C_{max}	Maximum ECM concentration in cornea in absence of MMPs.	1×10^{-6} [M]	1	(Holmes *et al.* 2001)
B	Rate of ECM degradation by MMPs.	1×10^{9} [$\mathrm{M^{-1}h^{-1}}$]	3.97	(Gioia *et al.* 2007)
C	Rate constant for ECM remodelling.	0.05 [$\mathrm{h^{-1}}$]	0.1985	(Petroll *et al.* 2004)
E	MMP natural decay rate.	25 [$\mathrm{h^{-1}}$]	99.25	-
F	MMP production rate per unit tip cell density.	1×10^{-19} [$\mathrm{M\,h^{-1}}$ $(\mathrm{tip\,cell\,m^{-3}})^{-1}$]	397	-
Υ_0	Tip cell haptotaxis coefficient	1.25×10^{-4} [$\mathrm{m^2h^{-1}M^{-1}}$]	4.946×10^{-4}	(Orme and Chaplain 1997; Anderson and Chaplain 1998; Watson *et al.* 2012)
η	Shape parameter for function which determines the permissivity of the ECM to tip cells. See (5.34).	-	-1.4	
Γ	Shape parameter for function which determines the permissivity of the ECM to tip cells. See (5.34).	-	0.8	

Table 5.7.: Default parameter values used to model tip cell-ECM interactions for both VEGF-A$_{165}$- and bFGF-induced angiogenesis.

been modified to ensure that the model results are consistent with the experimental data from Chapter 4. These parameters are summarised in Tables 5.8 and 5.9.

5.11. Numerical results: extended model

In this section we present results generated from numerical simulations of our extended model (Equations (5.38) - (5.48)), obtained using the method of lines, as outlined in Section 5.5. We discuss the effect of varying parameter values on these results and investigate the effect of two anti-angiogenic therapies.

Figure 5.18 summarises results from VEGF-A$_{165}$-induced angiogenesis simulations when default parameter values are used (see Tables 5.3, 5.4, 5.7 and 5.8). Such simulations of the extended model commence as described in Section 5.5 for the original model (Equations (5.19) - (5.25)): VEGF-A$_{165}$ released from the pellet diffuses across the cornea, towards the limbal vessels, where it stimulates vessel dematuration and the production of tip cells. Initially these tip cells are unable to migrate rapidly since the local ECM density is high (and the ECM is most permissive

Parameter	Description	Default dimensional value and units	Non-dimensional value
λ_1^v	Maximal rate of VEGF-A$_{165}$-induced dematuration.	0.072 [h^{-1}]	0.286.
χ_{v0}	Maximal chemotactic sensitivity of tip cells to VEGF-A$_{165}$.	1.53 [m^{2}h^{-1}M^{-1}]	0.0198
μ_0	Maximal random motility coefficient for tip cells.	1.68×10^{-10} [m^{2}h^{-1}]	6.67×10^{-4}
α_0^v	Maximum rate of VEGF-A$_{165}$-induced tip cell production per unit vessel length.	3944 [tips h^{-1} per m of vessel]	3.13
γ	Maximal rate of regression of ECs (vessels) in low VEGF-A$_{165}$.	1.12×10^{-2} [h^{-1}]	0.0445
κ	Parameter quantifying the length of vessel left behind in a unit volume after a tip cell moves out of that unit volume.	6 [m of vessel cells^{-1} m^{-1}]	30

Table 5.8.: Default parameter values used to model VEGF-A$_{165}$-induced angiogenesis in extended model (including tip cell haptotaxis). Only parameters which differ in value from those in Table 5.3 are listed here.

Parameter	Description	Default dimensional value and units	Non-dimensional value
χ_{f0}	Maximal chemotactic sensitivity of tip cells to bFGF.	8.36 [m^{2}h^{-1}M^{-1}]	0.0332
μ_0	Maximal random motility coefficient for tip cells.	1.68×10^{-10} [m^{2}h^{-1}]	6.67×10^{-4}
α_0^f	Maximum rate of bFGF-induced tip cell production per unit vessel length.	618 [tips h^{-1} per m of vessel]	0.490
γ	Maximal rate of regression of ECs (vessels) in low bFGF.	2.67×10^{-3} [h^{-1}]	0.0106

Table 5.9.: Default parameter values used to model bFGF-induced angiogenesis in extended model (including tip cell haptotaxis). Only parameters which differ in value from those in Table 5.6 are listed here.

to tip cells at intermediate densities; see Figure 5.17). Tip cells exposed to VEGF-A$_{165}$ produce MMPs, which degrade the surrounding ECM as they diffuse through the tissue. This degradation has two direct effects. First, it lowers the ECM density near the tip cells, enabling them to migrate more freely. Second, it creates a spatial gradient in ECM density up which tip cells migrate via haptotaxis. At the vascular front, the tip cells then migrate towards the pellet via both chemotaxis and haptotaxis, leaving behind them a trail of vessels. As for the original model (see Section 5.5), since vessels and ECs are VEGF-A$_{165}$ sinks, continued vascular growth creates a barrier to the VEGF-A$_{165}$, preventing it from reaching the limbal vasculature. Consequently, because tip cell production depends on VEGF-A$_{165}$ levels, tip cell production at the limbus halts and is localised instead around the leading edge of the vascular front. As the simulation proceeds, and VEGF-A$_{165}$ levels decline, the rates of tip cell production and migration decrease. Moreover, as in the original model, decreased VEGF-A$_{165}$ levels, particularly in the tail-end of

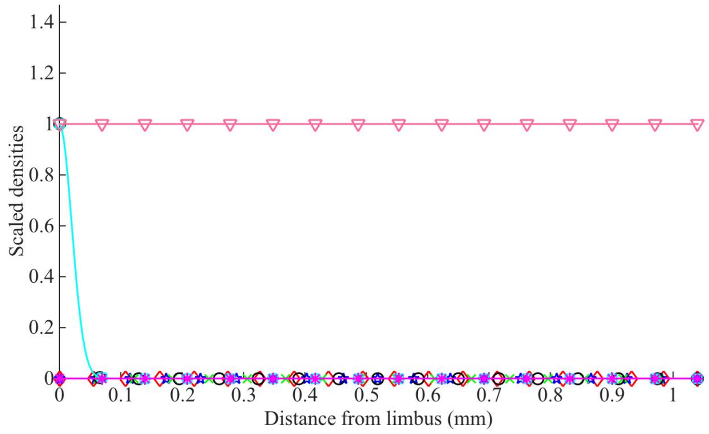

(a) Initial conditions. The cornea is initially avascular and contains no VEGF-A$_{165}$ or MMPs. Mature limbal vessels border the cornea. The ECM density is at its equilibrium concentration.

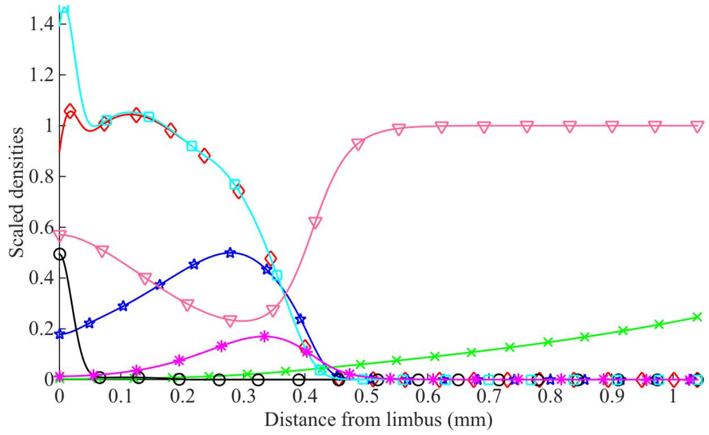

(b) Day 3 results. VEGF-A$_{165}$ is released from the pellet and diffuses towards the limbus where it stimulates vessel dematuration and tip cell production. The tip cells produce MMPs which degrade the ECM, establishing a local gradient in ECM density. They subsequently migrate by chemotaxis and haptotaxis towards the pellet, leaving behind them a trail of immature vessels.

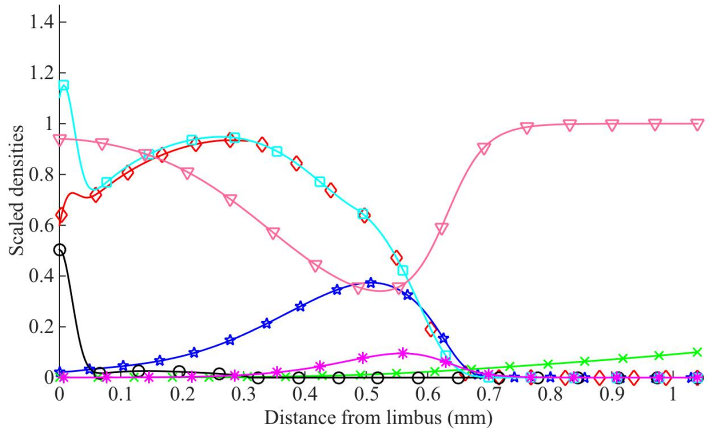

(c) Day 5 results. As VEGF-A$_{165}$ levels in the pellet decline, vascular growth slows and vessel regression occurs near the limbus.

Figure 5.18.: Results from a typical numerical simulation of our mathematical model, Equations (5.38) - (5.48), showing the angiogenic response of the limbal vessels to a VEGF-A$_{165}$ pellet implanted in the cornea. Scaled distributions of all state variables are overlaid for three time-points. Total vessel density (mature + immature): □; mature vessel density: ○; immature vessel density: ◇; tip cell density: ⋆; VEGF-A$_{165}$ concentration: ×; ECM density: ▽; MMP density: ∗. Parameter values are given in Tables 5.3, 5.4, 5.7 and 5.8.

the neovasculature, lead to significant vessel regression.

A potentially interesting consequence of including haptotaxis in our model is that it contributes to the movement of tip cells towards the limbus in the main body of the neovasculature, behind the vascular front. In more detail, at later times ($t > 2$ days), we observe decreases in the VEGF-A$_{165}$ concentrations and gradients in the tail-end and main body of the neo-vasculature, as discussed above. At the same time, the ECM density in this region begins to increase back to equilibrium levels (C_{max}), establishing a gradient in ECM density which is positive moving from the vascular front to the limbus. In the main body of the neo-vasculature, therefore, both random motion and haptotaxis contribute to the movement of tip cells backwards, towards the limbus. Since chemotaxis is negligible in this region we observe net migration of tip cells towards the limbus. This may suggest that, in higher spatial dimensions, haptotaxis has a role to play in establishing cross-linking between vessel sprouts behind the vascular front, where chemotaxis is no longer the dominant mechanism of tip cell motility. Considering the parametrisation of our extended model, such backward movement of tip cells increases the vascular density in the main body of the neo-vasculature. To counteract such increases (and maintain consistency with the experimental data) the rate of vessel regression, γ, was increased from its default value adopted in the original model, 5×10^{-3} [h^{-1}], to 1.12×10^{-2} [h^{-1}].

In Figure 5.19 we compare the results from simulations where default parameters have been used with experimental data for both VEGF-A$_{165}$- and bFGF-induced angiogenesis. Once again, while no formal fitting of the models to the data was attempted, in both cases, we observe good quantitative agreement. The behaviour of our extended model of bFGF-induced angiogenesis is qualitatively similar to that described above for VEGF-A$_{165}$-induced angiogenesis.

5.11.1. Parameter sensitivity analysis

We perform one at a time parameter sensitivity analysis for our extended model, Equations (5.38) - (5.48), following the procedure outlined in Section 5.5.2.1. Local sensitivity analysis is again performed around the point in parameter space representing VEGF-A$_{165}$-induced angiogenesis (Tables 5.3, 5.4, 5.7 and 5.8). In Figure 5.20 the normalised sensitivities of the vascular front location, the maximum amplitude of the vascular wavefront and the area under the vessel density curve, to changes in parameter values are presented for days 1, 3 and 5 of simulation time.

The behaviours of both the original and extended models upon varying most parameters (which the models have in common) are qualitatively similar. Noticeably, changing L, the distance

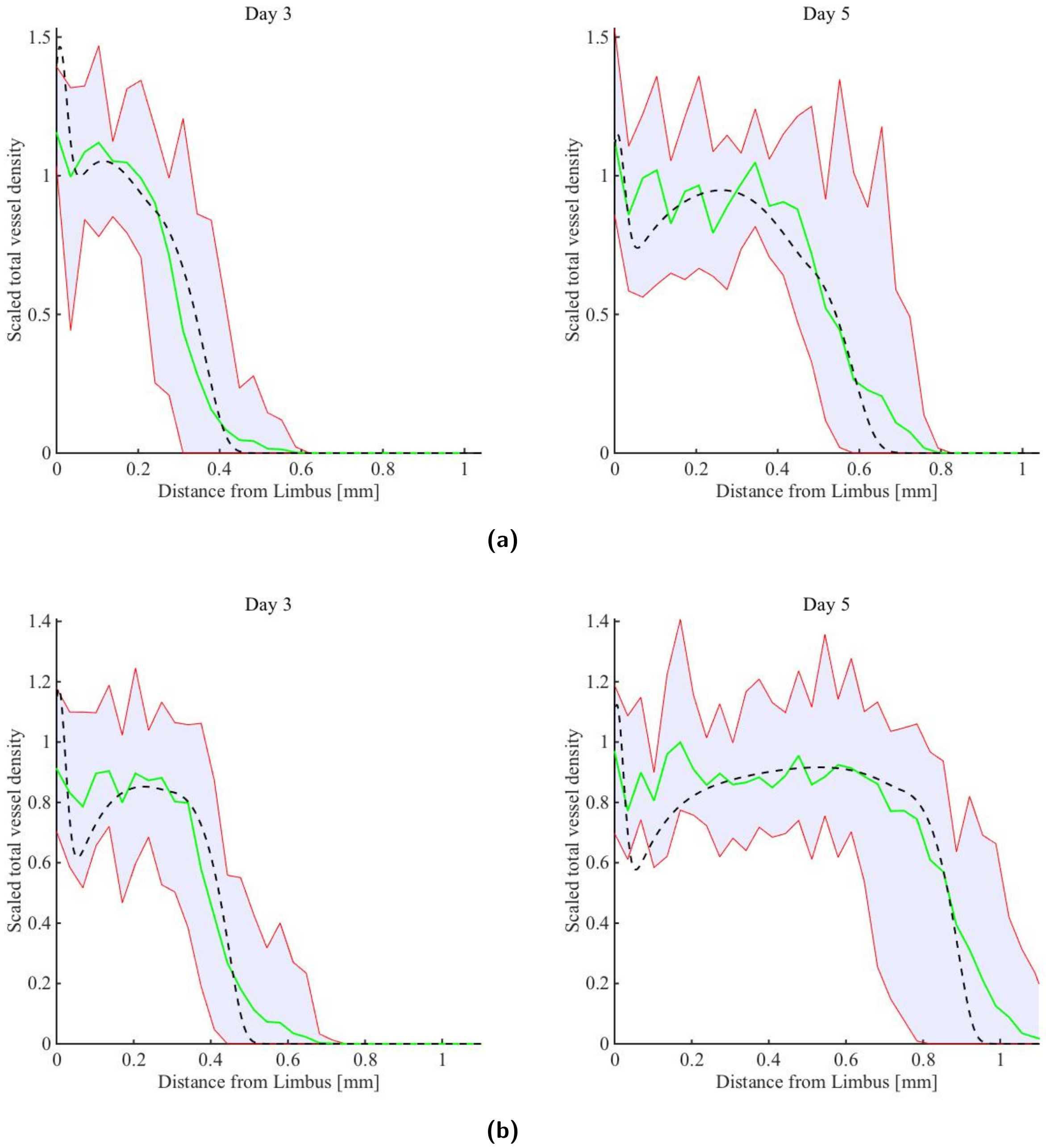

Figure 5.19.: Comparison of results from simulation of our extended model, Equations (5.38) - (5.48), with experimental data. (a) The fit of model results to the data for VEGF-A$_{165}$-induced angiogenesis when default parameters are used. (b) The fit of model results to the data for bFGF-induced angiogenesis when default parameters are used. Default parameters for VEGF-A$_{165}$- and bFGF-induced angiogenesis are provided in Tables 5.7, 5.9 and 5.8. The dashed black lines show model predictions, the solid green lines show averaged experimental data and the shaded region (bounded by solid red lines) shows the range in densities across experimental data sets.

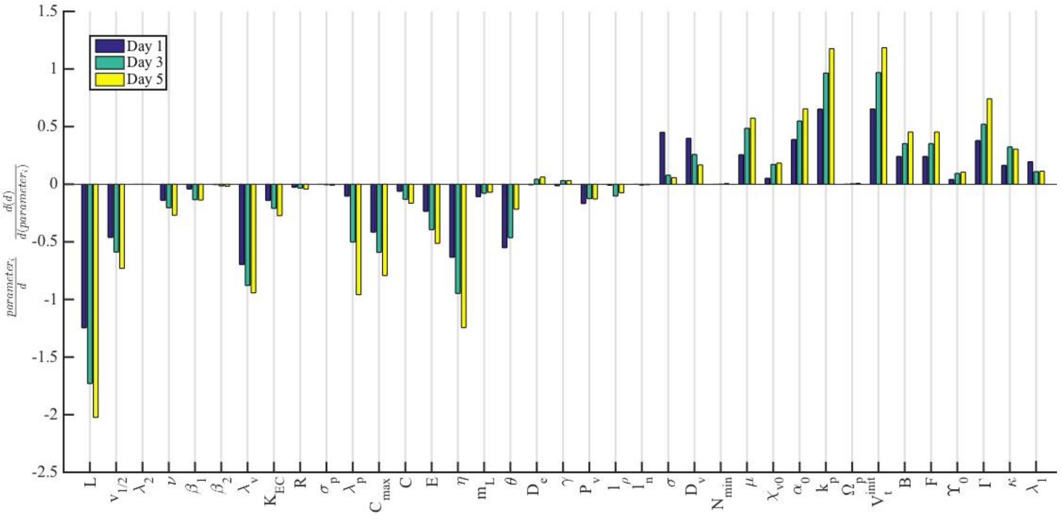

(a) Normalised sensitivity of the location of the advancing vascular wavefront, d.

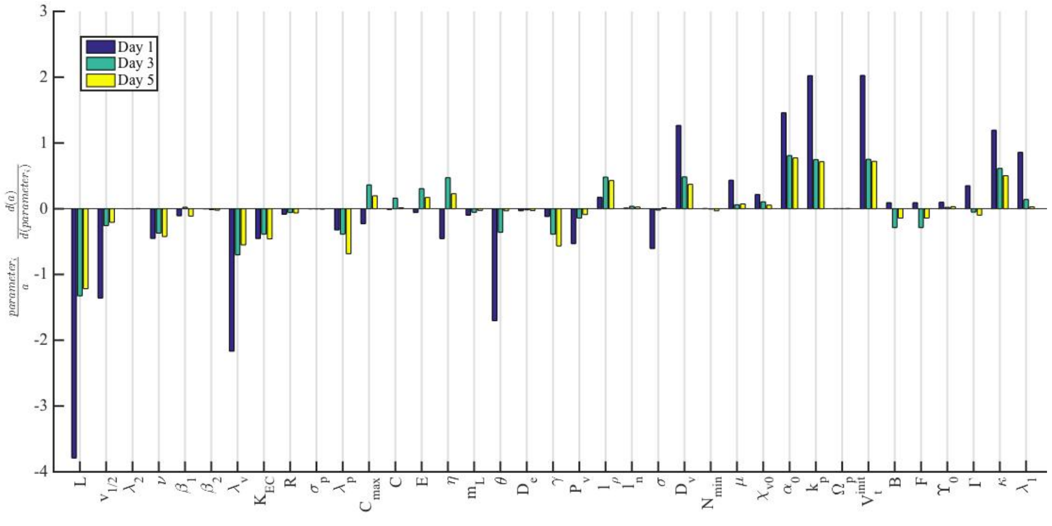

(b) Normalised sensitivity of the amplitude of the advancing vascular wavefront, a.

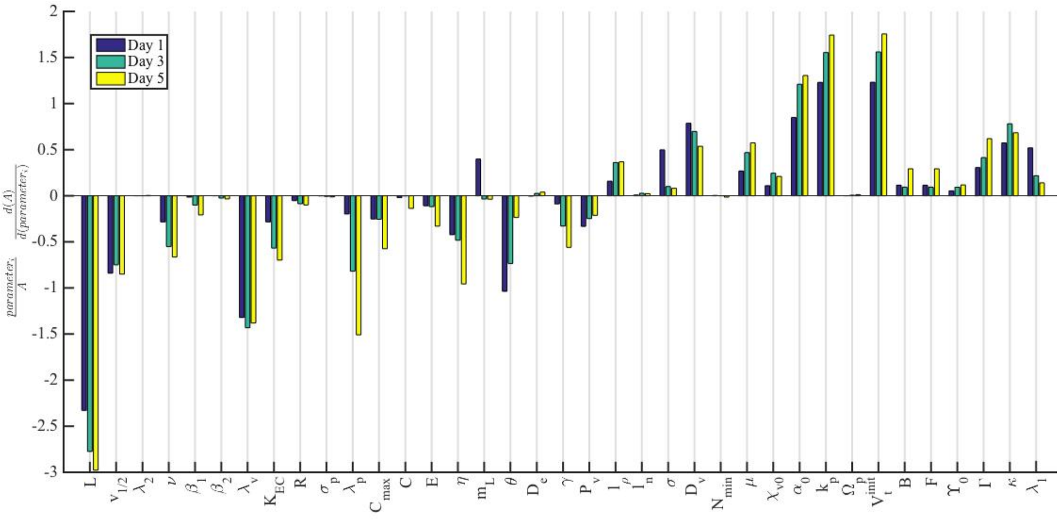

(c) Normalised sensitivity of the area under the vascular density curve, A.

Figure 5.20.: Normalised sensitivity of the extended model's output summary statistics in response to local changes in parameter values.

between the pellet and the limbus, once again has a pronounced effect on model simulations. Meanwhile, significant differences in behaviour between the two models are discernible when other parameters are modulated. In particular, consider the diffusion coefficient for VEGF-A$_{165}$, D_v. For the original model, as explained in Section 5.5.2.1, when D_v is increased the maximum amplitude of the vessel density also increases at each time point of interest (Figure 5.8b), while the location of the vascular front decreases (Figure 5.8a). This is principally because increases in D_v increase VEGF-A$_{165}$ levels across the model domain and decrease its spatial gradient, promoting tip cell production and reducing the chemotactic stimulus, respectively. However, when D_v is increased in our extended model (and default parameter values are adopted) we find that the location of the vascular front, and the maximum amplitude of the vessel density, increase significantly at all time points of interest. This difference may be explained by the fact that in the extended model, the increased VEGF-A$_{165}$ levels caused by increased D_v also promote MMP production, which increases ECM degradation. This, in turn, makes it easier for the tip cells to migrate through the ECM, compensating for the reduced chemotactic stimulus to the extent that tip cell migration is actually increased.

Of the new parameters introduced in the extended model, simulation results appear to be most sensitive to the values of the parameters which determine the permissivity of the ECM to tip cells: η, Γ and C_{max}. Notably, there are little data with which to estimate these parameters. This may, therefore, suggest an important direction of future experimental work: to establish precisely how the permissivity of the ECM to tip cells varies with ECM density.

5.11.2. Simulating anti-angiogenic therapies

In this section we use our extended model to investigate the effect of anti-VEGF-A and (anti-)MMP therapies on the angiogenic response of the corneal vasculature.

To delineate the effect of introducing various tip cell-ECM interactions into our model, here, for each therapy we consider two variants of our extended model:

M1: where the taxis coefficients are independent of the local ECM density, as summarised in Equation (5.35) (and as in the original model, (5.19)-(5.25)); and

M2: where the taxis coefficients depend on the local ECM density, as in Equation (5.34).

For each variant, we also investigate alternate model parametrisations in which the relative importance of haptotaxis and chemotaxis is modified. In more detail, we consider parametrisations for which:

1. $\frac{\chi_{v0}}{\Upsilon_0} = \infty$ (i.e. chemotaxis only).
2. $\frac{\chi_{v0}}{\Upsilon_0} = 40$ (default parametrisation).
3. $\frac{\chi_{v0}}{\Upsilon_0} = 15$.
4. $\frac{\chi_{v0}}{\Upsilon_0} = 1$.
5. $\frac{\chi_{v0}}{\Upsilon_0} = 0$ (i.e. haptotaxis only).

In what follows, we will refer to a specific variant as either M1 or M2, and to each parametrisation by a number (1-5), as per the itemised lists above. For example, the model M1.1 corresponds to a model in which the taxis coefficients are independent of the local ECM density, and in which tip cells move via chemotaxis and random motion only ($\Upsilon_0 = 0$). Note that, this model, M1.1, effectively reduces to the original model ((5.19)-(5.25)) since the equations for MMPs and the ECM do not affect the behaviour of tip cells.

For each model (M1 and M2) and for each parametrisation (1-5), several parameter values were modified from their default values so that simulations remain quantitatively consistent with the data from VEGF-A$_{165}$-induced angiogenesis experiments. Tables summarising these modifications are presented in Appendix A. In general, the fits of M2 to the data ($\times$, Figure 5.21), in which the taxis coefficients depend on the local ECM density, exhibit a steeper gradient at the vascular front than the fits of M1 to the data ($\circ$, Figure 5.21). A major contributing factor here is that, for M2, the optimal ECM density for migration is concentrated around the centre of the vascular front. Those tip cells at the leading edge of the front then experience increased ECM density and thus migrate more slowly than those tip cells in the middle of the front. This has a focussing effect on the distribution of tip cells, increasing the tip cell gradient. Additionally, for both M1 and M2, as Υ_0 is increased relative to χ_{v0}, a kink in the vascular front emerges. However, the experimental data are not of sufficient quality to confirm the presence or absence of such a kink *in vivo*. In fact, Figure 5.21 shows that all model parametrisations fit well to the experimental data; in each case the root mean square error between simulation results and experimental data is less than 0.11. Importantly, then, these data are not sufficient to rule out a model which incorporates only haptotaxis (M1.5 and M2.5) or only chemotaxis (M1.1 and M2.1).

5.11.2.1. Simulating anti-VEGF-A therapy

In this section we simulate the effect of an anti-VEGF-A drug on the angiogenic response of the corneal vasculature. To simulate the application of anti-VEGF-A therapy we increase λ_v, the rate of natural decay of VEGF-A$_{165}$. As alluded to above, of particular interest is the impact

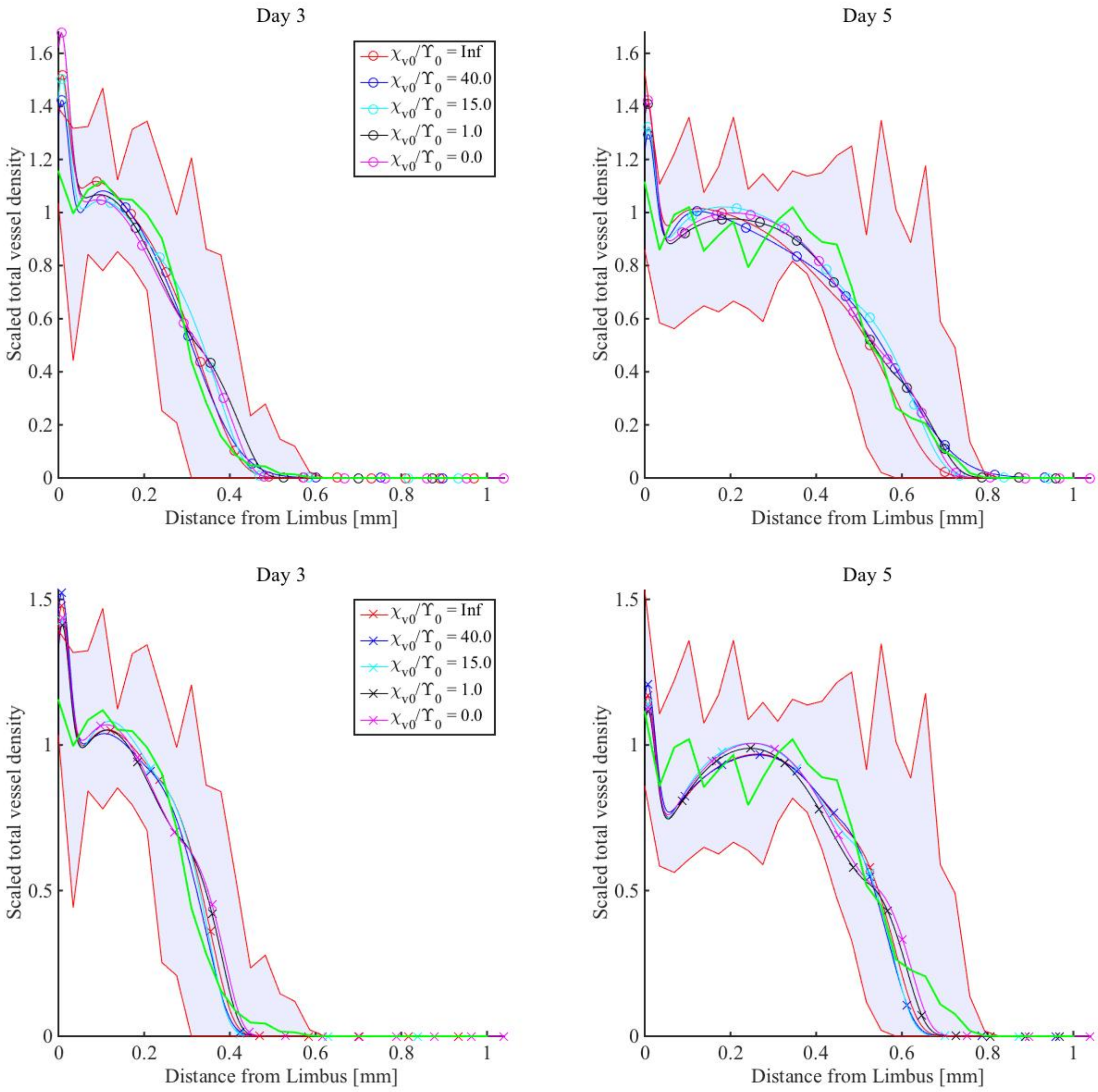

Figure 5.21.: Comparison of experimental data with the results from simulations of VEGF-A$_{165}$-induced angiogenesis. We simulate VEGF-A$_{165}$-induced angiogenesis for the cases where the taxis coefficients are independent of (M1 - $\circ$), and dependent on (M2 - $\times$), the local ECM density, and for different values of $\frac{\chi_{v0}}{\Upsilon_0}$. The solid green lines show averaged experimental data and the shaded region (bounded by solid red lines) shows the range in densities across experimental data sets.

of tip cell-ECM interactions on model predictions. Thus, we compare predictions made by the alternate parametrisations (1-5) of the two model variants (M1 and M2).

In Figure 5.22 we show the results of anti-VEGF-A therapy predicted by the models. We plot both the maximum amplitude of the vascular wavefront and the location of the vascular wavefront on day 5 of simulations for increasing values of λ_v, representing increasing VEGF-A$_{165}$ inhibition. Also plotted for the default value of λ_v (zero inhibition) is the range of values of our chosen metrics extracted from the experimental data. This serves to contextualise the magnitude

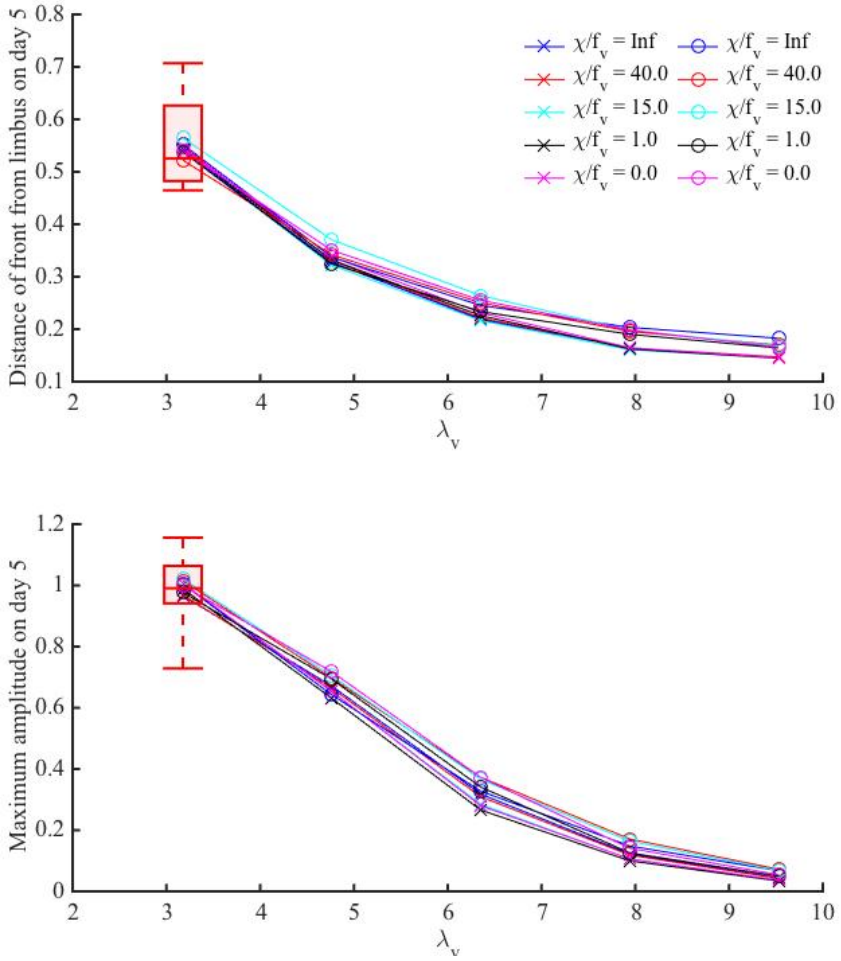

Figure 5.22.: The effect of anti-VEGF-A therapy on the model variants M1 (○) and M2 (×) are shown. We increase the value of λ_v to simulate the effect of anti-VEGF-A therapy. Continuous lines represent model predictions, while the overlaid box plots represent experimental data (first, second and third quartile with maxima and minima are shown).

of any differences in predictions made by the alternate model variants/parametrisations. As expected, for each model and for each parametrisation, administration of an anti-VEGF-A drug reduces the angiogenic response of the corneal vasculature; the location of the vascular wavefront and the amplitude of the vascular wavefront on day 5 both decrease with increasing λ_v.

Evidently, given this small number of points in parameter space (5), significant differences between predictions generated by the two model variants are not obvious. A small systematic increase in inhibition is evident when the taxis coefficients are assumed to depend on ECM density (M2 - ×). However, the difference between predictions made by each variant are small compared to the anticipated spread in *in vivo* experimental results.

5.11.2.2. Simulating (anti-)MMP therapy

A significant advantage of including the ECM and MMPs in our model is that it may be used to investigate the effect of (anti-)MMP therapies, as discussed in Rundhaug (2005). In this section we use our extended model, (5.38)-(5.48), to investigate the potential for modulating MMP activity as an anti-angiogenic treatment strategy. As in Section 5.11.2.1, we compare predictions made by the alternate parametrisations (1-5) of the two model variants (M1 and M2). To simulate the administration of an anti-MMP drug we increase E, the rate of removal of MMPs from the system. Given the non-monotonic dependence of motility parameters on ECM density in our extended model (M2), we also investigate the effect of decreasing E on the angiogenic response. We assume that decreasing E might, for example, represent a drug which increases the stabililty of MMPs in the extra-cellular space.

In Figures 5.23 and 5.24 we present results for simulations of MMP therapies. The maximum amplitude of the vascular wavefront and the location of the vascular wavefront on day 5 of simulations are plotted for increasing values of $\frac{E}{E_0}$, where E_0 represents the default value of E for a given parametrisation. Also plotted for the default value of E are the ranges of values of our chosen metrics extracted from the experimental data. Figures 5.23 and 5.24 show predictions made by model variants M1 and M2, respectively. Notably, clear qualitative differences are evident between predictions made by M1 and M2. We will discuss the response of each variant to changes in the value of E in turn.

For M1 (Figure 5.23), the values of the parameters χ_{v0} and Υ_0 strongly influence the predicted neovascular response as E is varied. As expected, when haptotaxis is absent (M1.1 - ○), the neovascular response is independent of the value of E. Meanwhile, for $\frac{\chi_{v0}}{\Upsilon_0} < \infty$ (i.e. when haptotaxis is introduced), increasing E reduces the migration rate of tip cells. This is because as E is increased fewer MMPs are available to degrade the ECM and the gradient of ECM at the front decreases, reducing the haptotactic force experienced by tip cells. As E is decreased relative to the default value, the migration rate of the tip cells initially increases because more MMPs are available to degrade the ECM locally, increasing the ECM gradient and thus the haptotactic force experienced by tip cells. However, decreasing E further acts to decrease the migration rate of tip cells since more MMPs are able to diffuse throughout the whole domain, significantly reducing the ECM density non-locally, and thus decreasing the ECM gradient to which tip cells are exposed. In general, the amplitude of the wavefront is directly influenced by the speed at

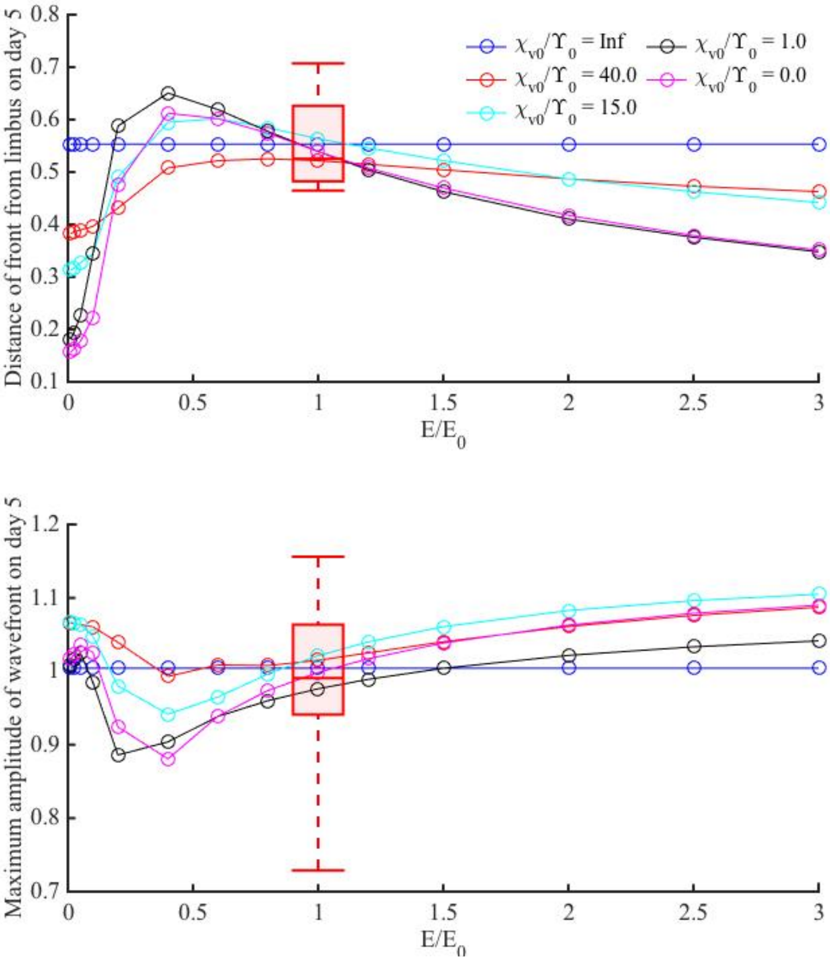

Figure 5.23.: The effect of modulating MMP activity for the model variant M1 is shown. We increase the value of E to simulate the effect of anti-MMP therapy. Meanwhile, decreasing E represents the administration of a drug which acts to stabilise MMPs in the extracellular space. Continuous lines represent model predictions, while the overlaid box plots represent experimental data (first, second and third quartile with maxima and minima are shown).

which the vascular front travels. An increased rate of migration also decreases the time during which the vasculature behind the migrating front is exposed to significant levels of VEGF-A$_{165}$, decreasing sprouting behind the front and making regression in the absence of VEGF-A$_{165}$ more likely. A reduced migration rate has the opposite effect, as depicted in Figure 5.23. As expected, as haptotaxis becomes more important (as $\frac{\chi_{v0}}{\Upsilon_0}$ decreases), changing E has a more pronounced effect on the neovascular response.

For M2 (Figure 5.24), variation in the values of the parameters χ_{v0} and Υ_0 has a less marked effect on the predicted neovascular response as E is varied. We see that for $E > E_0$ the rate of migration of the vascular front decreases for increasing E, whilst its amplitude increases. This behaviour is explained as follows. Inhibition of MMP activity decreases the amount of ECM degradation around the vascular front. When tip cells are exposed to higher densities of ECM

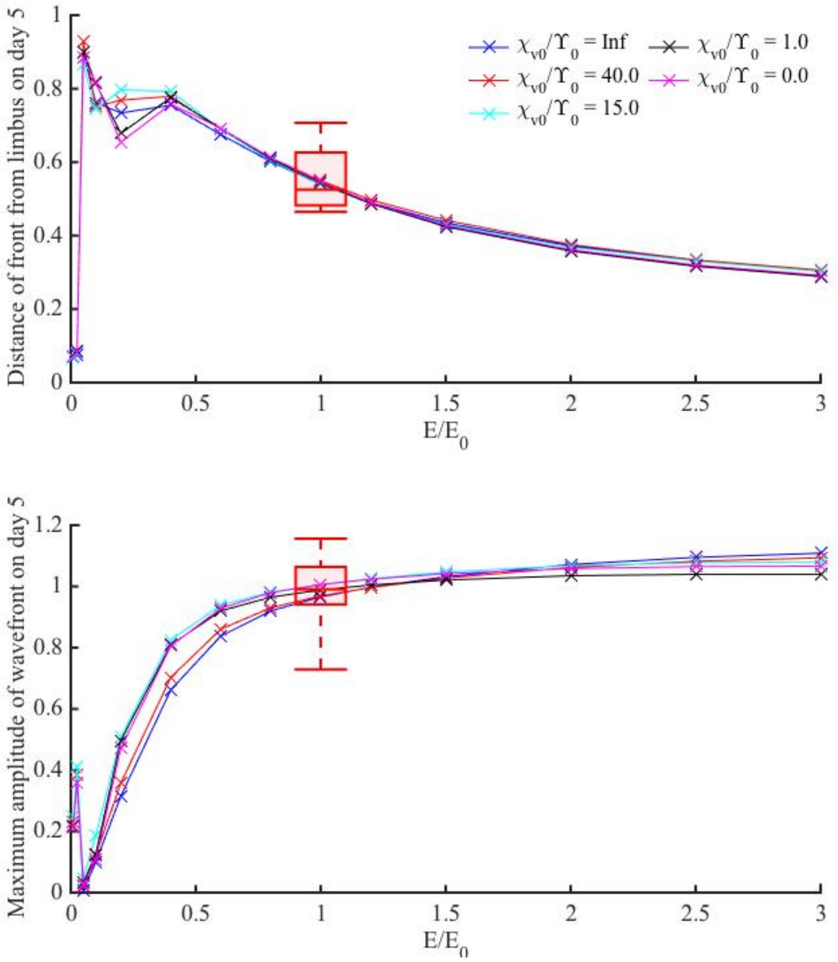

Figure 5.24.: The effect of modulating MMP activity for the model variant M2 is shown. We increase the value of E to simulate the effect of anti-MMP therapy. Meanwhile, decreasing E represents the administration of a drug which acts to stabilise MMPs in the extracellular space. Continuous lines represent model predictions, while the overlaid box plots represent experimental data (first, second and third quartile with maxima and minima are shown).

their rate of migration decreases, thus explaining the decrease in the rate of front migration. As above, as the rate of front migration decreases, the vasculature behind the front is exposed to increased levels of VEGF-A$_{165}$ for longer time periods, stimulating additional tip cell production and reducing regression. This, in turn, leads to modest increases in vascular density. We see that modest decreases in E below the default value increase the rate of migration of the vascular front whilst decreasing its amplitude. What is perhaps surprising about this result is that such a trend is evident even when the density of the ECM to which the majority of the vascular front is exposed is far below that which is optimal for tip cell migration (~ 0.25; see Figure 5.17). Evidently, increasing MMP activity and thus increasing the overall degradation of ECM around the vascular front enables a few tip cells at the very front of the vascular wave (where ECM levels remain near optimal) to travel quickly and efficiently towards the pellet. This increased rate of migration of just a few tip cells comes at the expense of having a far less dense vascular network (note the sharp decrease in maximum amplitude of the vascular front in Figure 5.24 between $\frac{E}{E_0} = 0.5$ and 0.05). For $\frac{E}{E_0} < 0.05$, ECM degradation becomes so great that all tip cells are exposed to negligible ECM densities and thus no discernible travelling wave emerges from the corneal vasculature. In this parameter regime, the increase in amplitude observed in Figure 5.24 is an artefact of how the amplitude of the wavefront is calculated[6].

These results suggest that, even though the permissivity of the ECM to tip cells is a non-monotonic function of ECM density (being low at both low and high ECM densities, and high at intermediate levels), the inhibition of MMP activity (leading to increased ECM levels overall) represents a more reliable strategy for reducing the angiogenic response than enhancing MMP activity (leading to decreased ECM levels overall).

5.12. Model simplification

Thus far, we have shown that detailed models, representing significant extensions to Byrne and Chaplain's (1995) model, when parametrised appropriately, can reproduce results from VEGF-A$_{165}$ experiments. Further, with only minor changes, the models can be used to simulate bFGF-induced angiogenesis. In all cases it is possible to achieve excellent quantitative agreement between model results and experimental data. However, this result raises the question of whether a simpler (mechanistic) model could also reproduce the experimental results in a quantitative manner. If so, it is natural to question the utility of formulating detailed mechanistic models. To address these issues, in this section we simplify the model from Section 5.3.7 and investigate whether it can fit to our experimental data. In this section, for clarity, we refer to the model from Section 5.3.7, (5.19)-(5.23), as our *detailed* model.

In our simplified model we ignore vessel maturity so that all vessels in the cornea represent immature vessels, $\rho(x, t)$. In the absence of mature vessels, we assume that the limbus is composed of immature vessels and that the initial distribution of vessels is Gaussian distributed about $x = 0$, with width σ. We also simplify the pellet dynamics; we no longer model directly the concentration of TAF inside the pellet. Instead we suppose that the initial concentration of TAF, $a(x, t)$, adjacent to the pellet is given by a_p and that the concentration of TAF on $x = L$ decays at a constant rate, λ_p. In addition, we neglect EC uptake of the TAF ($K^v_{EC} = 0$), tip-to-tip anastomosis ($\beta_2 = 0$) and vessel production due to anastomosis ($\bar{l}_\rho = \bar{l}_n = 0$). Moreover, we

---

[6] I.e., by ignoring the limbal vasculature.

assume that vessel and tip cell regression occur at a constant rate, independent of the local concentration of TAF. In summary, the non-dimensional equations associated with our simplified model are given by:

$$\frac{\partial n}{\partial t} = \frac{\partial}{\partial x}\left(\mu\,\frac{\partial n}{\partial x} - \chi_a\,n\,\frac{\partial a}{\partial x}\right) + \alpha_0^a\,\rho\,\left(\frac{a}{a + a_{\frac{1}{2}}}\right) - \beta_1\,n\,\rho - \gamma\,n, \tag{5.49}$$

$$\frac{\partial \rho}{\partial t} = \kappa\left|\mu\,\frac{\partial n}{\partial x} - \chi_a\,n\,\frac{\partial a}{\partial x}\right| - \gamma\,\rho, \tag{5.50}$$

$$\frac{\partial a}{\partial t} = D_a\frac{\partial^2 a}{\partial x^2} - \lambda_a\,a - 2\,\pi\,\bar{R}\,P_a\,\rho\,a. \tag{5.51}$$

These equations are subject to the boundary conditions

$$\left.\begin{aligned}\mu\frac{\partial n}{\partial x} - \chi n\frac{\partial a}{\partial x} &= 0,\\ -D_a\frac{\partial a}{\partial x} &= -P_a\rho a,\end{aligned}\right\}\quad x = 0, \qquad \left.\begin{aligned}&\mu\frac{\partial n}{\partial x} - \chi n\frac{\partial a}{\partial x} = 0,\\ &a = a_p\,e^{-\lambda_p t},\end{aligned}\right\}\quad x = L, \tag{5.52}$$

and the initial conditions

$$\rho(x,0) = \rho_L exp\left(-\frac{x^2}{2\sigma^2}\right), \quad n(x,0) = 0, \quad a(x,0) = a_p\,\delta(L). \tag{5.53}$$

Note that our simplified model is similar in complexity (number of parameters and dependent variables) to that proposed by Byrne and Chaplain (1995) (see Section 3.2.1). Table 5.10 summarises the default parameter values used in our simplified model to simulate VEGF-A$_{165}$- and bFGF-induced angiogenesis. The most significant difference in parameter values between the detailed and simplified models relates to P_a, the permeability of the vessels to the TAF. P_a was increased by a factor of approximately 10 for both VEGF-A$_{165}$- and bFGF-induced angiogenesis in moving from the detailed to the simplified model. This compensates for the removal of other sources of TAF uptake by ECs in Equation (5.51). Only modest changes in other model parameters were required to provide a good fit of the simplified model to the experimental data for both VEGF-A$_{165}$ and bFGF experiments. The scaling parameters used for nondimensionalisation here (for both VEGF-A$_{165}$- and bFGF-induced angiogenesis) are those presented in Table 5.2.

In Figure 5.25 we compare numerical results with experimental data for both VEGF-A$_{165}$- and bFGF-induced angiogenesis experiments. We see that our simplified model, when parametrised appropriately (see Table 5.10), reproduces quantitatively the dynamics of our experimental

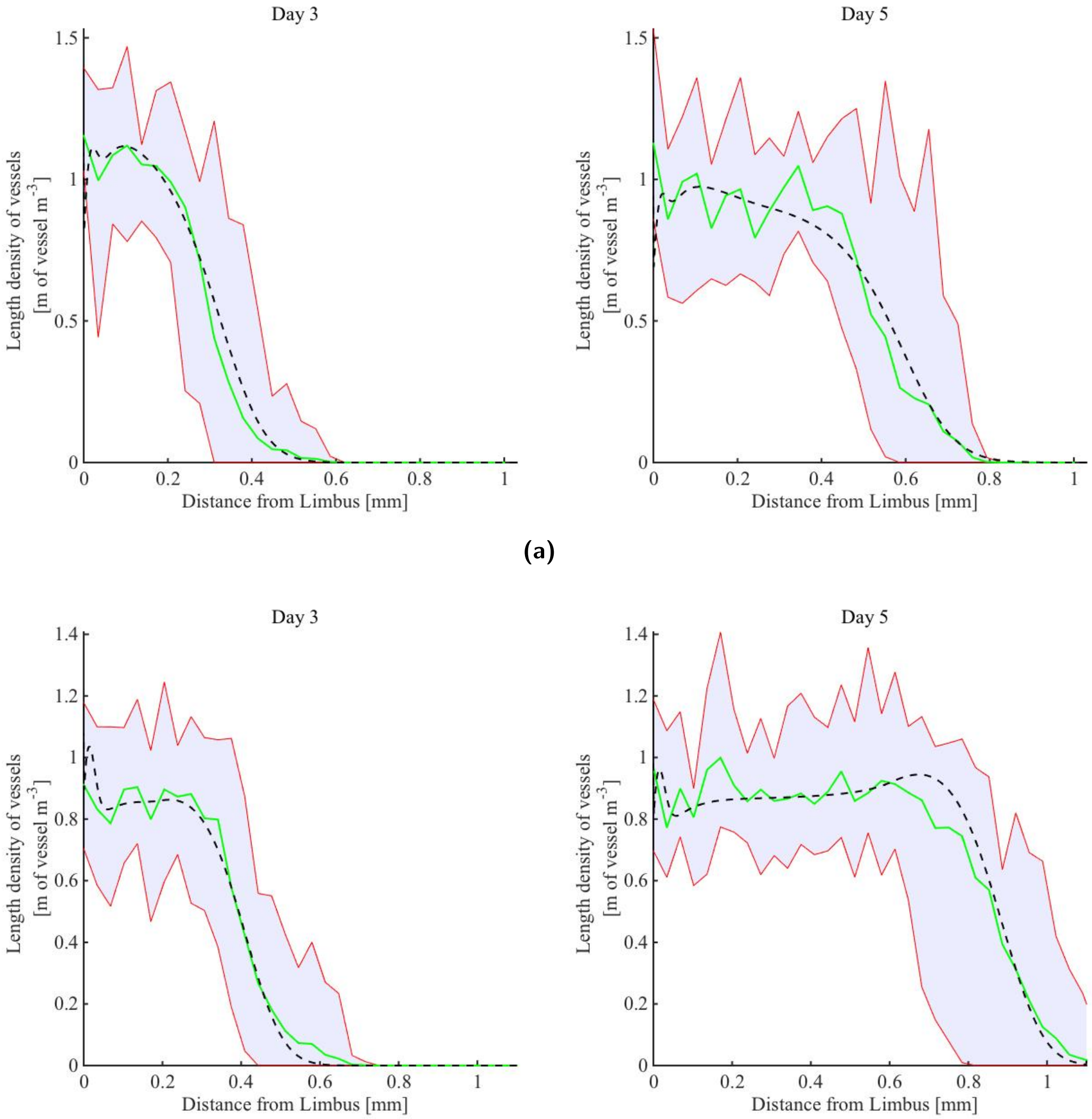

(a)

(b)

Figure 5.25.: Comparison of simplified model results with experimental data. (a) The fit of model results to the data for VEGF-A$_{165}$-induced angiogenesis when default parameters are used. (b) The fit of model results to the data for bFGF-induced angiogenesis when default parameters are used. Default parameters for both VEGF-A$_{165}$- and bFGF-induced angiogenesis are provided in Table 5.10. The dashed black lines show model predictions, the solid green lines show averaged experimental data and the shaded region (bounded by solid red lines) shows the range in densities across experimental data sets.

system (once again, no formal fitting of the model to the data was attempted). Evidently, a model significantly simpler than the one developed earlier in this chapter is capable of fitting well to the available experimental data. Table 5.11 summarises the root mean square error values for the fits of simulation results to experimental data when default parameter values are used.

		VEGF-A$_{165}$		**bFGF**	
Parameter	**Description**	**Default value**	**Non-dimensional value**	**Default value**	**Non-dimensional value**
D_a	Diffusion constant for TAF	2.52×10^{-7} [m^{2}h^{-1}]	1	1.92×10^{-7} [m^{2}h^{-1}]	0.762
μ	Tip cell random motility coefficient	7×10^{-11} [m^{2}h^{-1}]	2.78×10^{-4}	7×10^{-11} [m^{2}h^{-1}]	2.78×10^{-4}
χ	Tip cell chemotaxis coefficient	2.2 [m^{2}h^{-1}M^{-1}]	0.0284	2.1 [m^{2}h^{-1}M^{-1}]	0.0271
γ	Rate at which vessels regress	0.0035 [h^{-1}]	0.0139	0.002 [h^{-1}]	0.0079
λ_p	Rate at which TAF supply decays	0.016 [h^{-1}]	0.0635	0.0041 [h^{-1}]	0.0163
α_0	Coefficient characterising rate of tip cell production	3200 [tips h^{-1} M^{-1} (m of vessel)$^{-1}$]	2.5408	1200 [tips h^{-1} M^{-1} (m of vessel)$^{-1}$]	0.9528
P_a	Permeability of vessels to TAF	1×10^{-3} [m h^{-1}]	3.97	5×10^{-3} [m h^{-1}]	19.85
λ_a	Natural decay constant for TAF	0.8 [h^{-1}]	3.176	0.04 [h^{-1}]	0.1588
β	Coefficient characterising rate of tip-to-vessel anastomosis	0.4×10^{-9} [anastomosis events h^{-1}m^3 (m of vessels)$^{-1}$ (cell)$^{-1}$]	0.3176	0.4×10^{-9} [anastomosis events h^{-1}m^3 (m of vessels)$^{-1}$ (cell)$^{-1}$]	0.3176
a_p	Initial concentration of TAF at pellet	3.39×10^{-9} [M]	1.0431	2×10^{-9} [M]	0.6154
$a_{\frac{1}{2}}$	EC50 for EC activation by TAF.	6.5×10^{-10} [M]	0.2	4.22×10^{-11} [M]	0.013
ρ_L	Initial concentration of tip-cells at limbus	2×10^{8} [m of vessel m^{-3}]	1	2×10^{8} [m of vessel m^{-3}]	1
κ	Coefficient characterising amount of vessel left behind as a tip cell migrates.	3 [m of vessel cell^{-1} m^{-1}]	15	3 [m of vessel cell^{-1} m^{-1}]	15
σ	Width of initial distribution of vessels at limbus	2×10^{-5} [m]	0.02	2×10^{-5} [m]	0.02
$\bar{R}$	Average radius of vessels in cornea.	5×10^{-6} [m]	1	5×10^{-6} [m]	1
L	Pellet limbus distance.	1.04×10^{-3} [m]	1.04	1.1×10^{-3} [m]	1.1

Table 5.10.: Table of parameters for our simplified model. Parametrisations for VEGF-A$_{165}$- and bFGF-induced angiogenesis are shown. Rows highlighted green contain parameters whose values differ from those used in the detailed model. Those highlighted red contain parameters which were fixed at the same values as those used for the detailed model. Uncoloured rows contain parameters which do not have a direct analogue in the detailed model.

	VEGF-A$_{165}$ experiments	**bFGF experiments**
Detailed model	0.0738	0.0792
Simplified model	0.0661	0.0559

Table 5.11.: Root mean square errors between simulation results and experimental data for our detailed model, (5.19)-(5.25), and simplified model, (5.49)-(5.53), when default parameters used.

We postpone further discussion about the utility of developing a model which is more detailed than perhaps needed to describe the available experimental data until the end of this chapter.

5.12.1. Parameter sensitivity analysis

We perform one at a time parameter sensitivity analysis for our simplified model, following the procedure outlined in Section 5.5.2.1. Local sensitivity analysis is performed around the point in parameter space representing VEGF-A_{165}-induced angiogenesis (Table 5.10). The normalised sensitivity of the vascular front location, the maximum amplitude of the vascular wavefront and the area under the vessel density curve to changes in parameter values are presented in Figure 5.26. As in Figure 5.8, sensitivities are presented for days 1, 3 and 5 of simulation time to illustrate how the sensitivity of the system to different parameters changes over time.

Since many of the parameters in our simplified model have direct analogues in our detailed model it is possible to directly compare the results of our local sensitivity analysis for each model. Those parameters which do not have direct analogues, a_p and λ_p, can still be compared to parameters from the more complex model. a_p can be compared to $[V_T]_{init}$ since they both determine the amount of VEGF-A_{165} initially available at the pellet-side boundary of our model domain, and λ_p can be compared to λ_p^v since these parameters determine the rate at which the concentration of VEGF-A_{165} at the pellet-side boundary decreases.

Encouragingly, the behaviours of both models upon varying system parameters are similar (in a qualitative sense). A significant difference in behaviour between the models only occurs when the diffusion coefficient for the TAF is modulated. For the detailed model, as explained in Section 5.5.2.1, when the VEGF-A_{165} diffusion constant, D_v, is increased the maximum amplitude of the vessel density also increases at each time point of interest (Figure 5.8b), while the location of the vascular front decreases (Figure 5.8a). This is principally because increases in D_v increase VEGF-A_{165} levels across the model domain and decrease its spatial gradient, promoting tip cell production and reducing the chemotactic stimulus, respectively. However, when the diffusion constant of VEGF-A_{165} in our simplified model is increased we find that the location of the vascular front, as well as the maximum amplitude of the vessel density, increases significantly at all time points of interest. This difference may be explained by the fact that in the simplified model significant tip cell production and migration occur as soon as the TAF meets the limbal vasculature since the vessels located there are assumed immature. Thus, as D_a is increased, the TAF arrives at the limbal vasculature earlier giving tip cells the opportunity to begin migrating earlier. This effect could feasibly dominate other effects associated with changes in D_a. By contrast, in the detailed model the need for dematuration prior to tip cell production and migration may act as a buffer against effects related to the earlier arrival at the limbus of a TAF with greater diffusivity. A small detail which was disregarded earlier is that the location of the vascular front on day one of simulations does not change if D_v is increased in the detailed model. This is consistent with our hypothesis that vessel maturity and dematuration buffer against early effects associated with increasing the diffusivity of a TAF.

The detailed and simplified models do not always agree with respect to how the sensitivity of our summary statistics change over the duration of a simulation. For example, the sensitivity of the maximum amplitude of the vascular density to changes in P_v in the detailed model decreases monotonically over time, whereas in the simplified model a similar monotonic decrease is not observed. However, in a different region of parameter space the simplified model may agree more closely with the detailed model whilst still fitting to the data. More important, is that, for instance, increases in vessel permeability decrease the maximum amplitude of the vascular density for all times in both models.

Sensitivity analysis of our simplified model reveals again that changing L, the distance between the pellet and the limbus, has a pronounced effect on model simulations. The fact that this prediction appears to be robust across models with different structures adds credence to it.

5.12.1.1. Simulating anti-VEGF-A therapy

In this section we use our simplified model to simulate the effect of an anti-VEGF-A drug on the angiogenic response of the corneal vasculature. As in Section 5.11.2.1, we simulate anti-VEGF-A therapy by increasing λ_v, the rate of natural decay of VEGF-A$_{165}$. The results are plotted in Figure 5.27, together with the corresponding results for our original and extended models, Equations (5.19)-(5.25) and (5.38)-(5.48), respectively. While all results are in good qualitative agreement, those for the simple model are quantitatively different. A far more extensive search of parameter space is necessary to ascertain whether the simplified model is indeed capable of making predictions which agree quantitatively with our more detailed models.

5.13. Discussion

In this chapter we have developed several deterministic, continuum models of corneal angiogenesis. The first model (summarised in Section 5.3.7) extended previous models (Balding and McElwain 1985; Byrne and Chaplain 1995), principally by accounting for vessel maturation and the controlled release of a TAF from a pellet. While initially developed and parametrised for VEGF-A$_{165}$, the

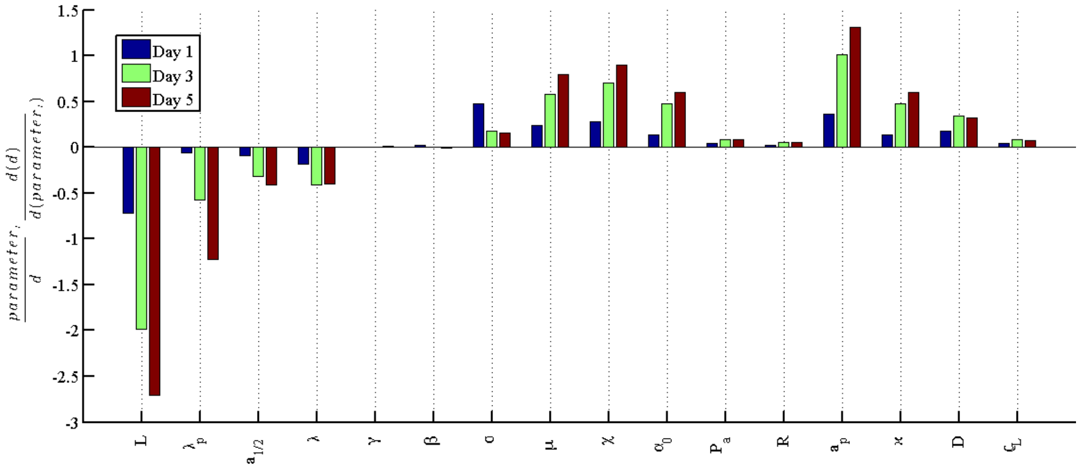

(a) Normalised sensitivity of the location of the advancing vascular wavefront, d.

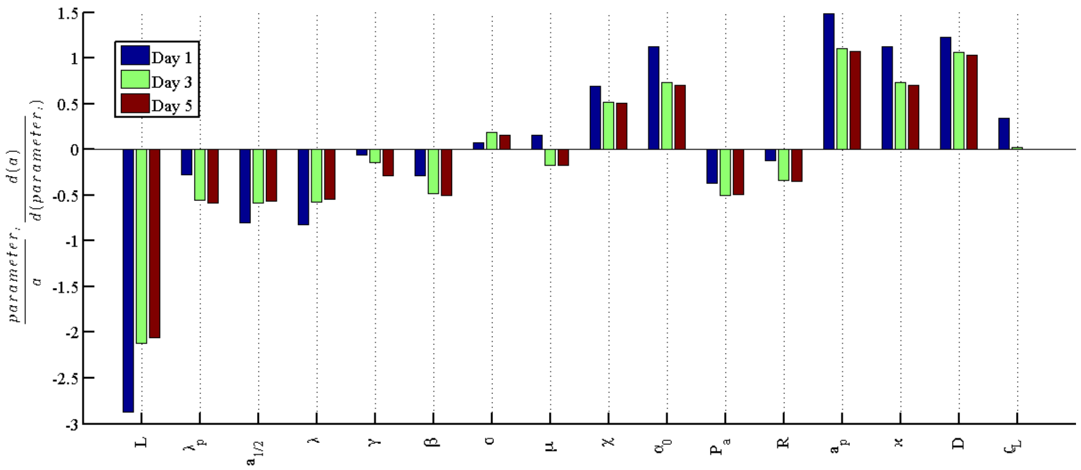

(b) Normalised sensitivity of the amplitude of the advancing vascular wavefront, a.

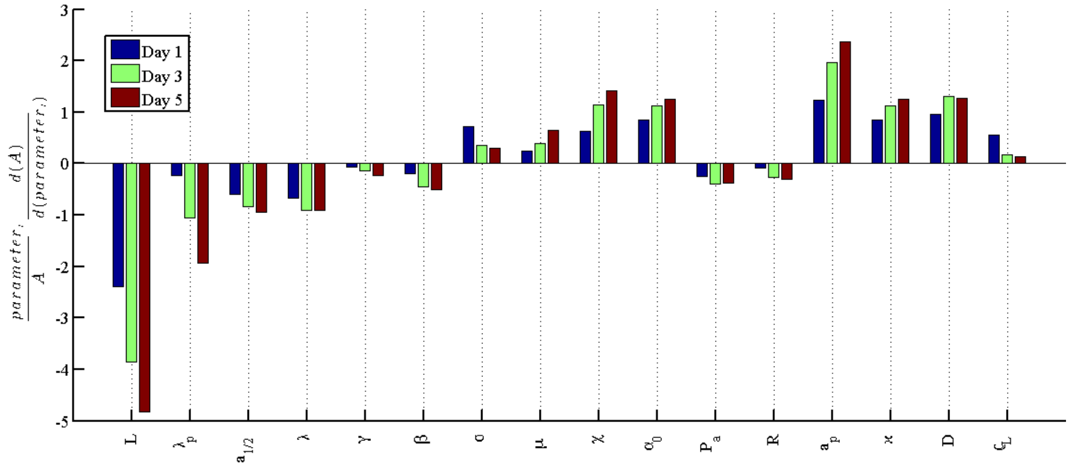

(c) Normalised sensitivity of the area under the vascular density curve, A.

Figure 5.26.: Normalised sensitivities of the simplified model, (5.49)-(5.51), output summary statistics in response to local changes in parameter values.

model proved sufficiently general and robust that, largely through variation of parameter values, it could also simulate angiogenesis in response to bFGF.

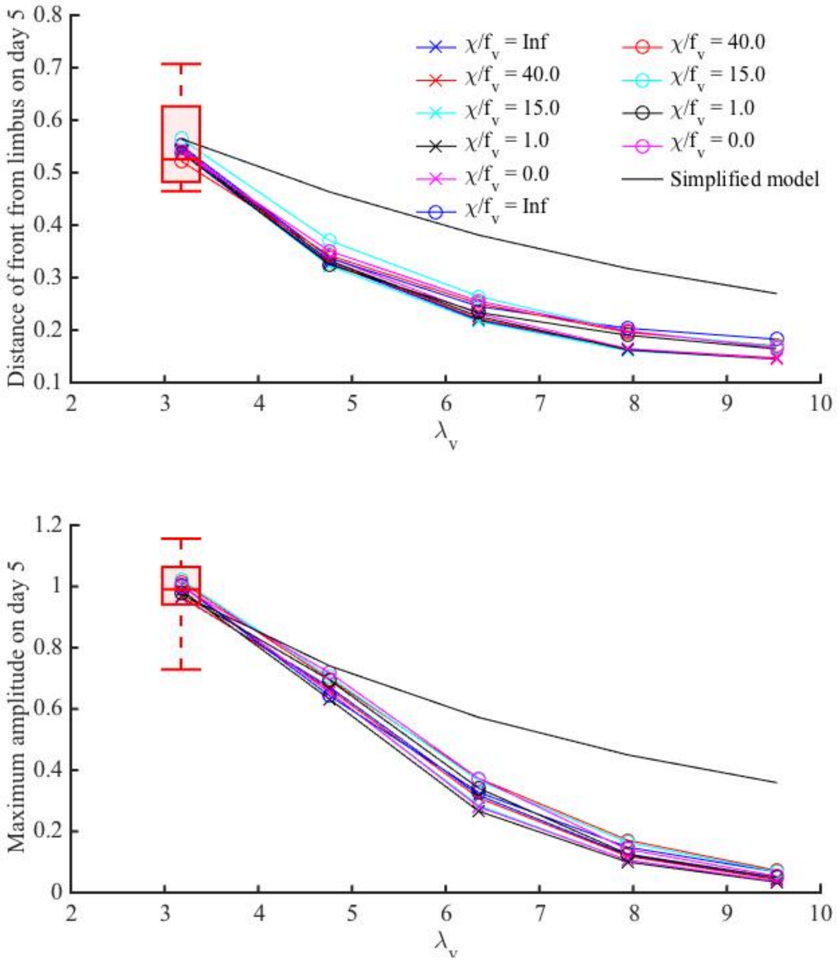

Figure 5.27.: The effect of anti-VEGF-A therapy on the original (−○−), simplified (—) and extended model (other keys - see Figure 5.22 for further details) is shown. As in Figure 5.22, continuous lines represent model predictions, while the overlaid box plots represent experimental data (first, second and third quartile with maxima and minima are shown).

A focus of the work in this chapter has been to integrate our mathematical model with quantitative data which are spatially and temporally resolved. These data were extracted from images of cornea micropocket experiments (for details see Chapter 4). While recent modelling efforts have attempted to link quantitative experimental data with tissue scale simulations of angiogenesis (Tong and Yuan 2008b; Watson *et al.* 2012), experimental images and image analysis techniques have not previously been fully exploited. Crucially, our image analysis provides a more detailed description of angiogenesis than has previously been used for continuum model development, parametrisation and validation. Thus, we are further able to constrain the parameter values which our model may take to exhibit biologically realistic behaviour. This then provides us with increased confidence in the predictions made by our mathematical model.

We also extended the model to incorporate tip cell-ECM interactions. In more detail, we included tip cell movement due to haptotaxis, and accounted for experimental evidence suggesting that ECs move most rapidly when exposed to intermediate ECM densities. To discern the effect that such tip cell-ECM interactions have on model predictions, we considered two variants of our extended model: one in which the tip cell taxis coefficients depended on the local ECM density and one in which they did not. We also compared several parametrisations of each model variant, in which the balance between chemotaxis and haptotaxis was varied. That all model variants and parametrisations fit acceptably to the experimental data (Figure 5.21) serves to highlight the level of structural and parameter uncertainty present, even when spatio-temporal data are available. Upon simulation of anti-VEGF-A therapy, the differences between predictions made by each variant (and for each parametrisation) were small compared to the anticipated spread in *in vivo* experimental results. However, upon modulation of MMP activity, we observe clear qualitative differences between predictions made by the two model variants. These results suggest that while the inclusion of ECM dependence of taxis coefficients is likely to be important for predicting the effect of MMP modulation on the angiogenic response of the corneal vasculature, it is much less important for predicting the effect of anti-VEGF-A therapies. Meanwhile, accurate estimation of the relative contributions of chemotaxis and haptotaxis to tip cell motion appear to be less important, yet they do effect results quantitatively. Clearly, more data are needed to discriminate between possible models. Moreover, to further discern whether haptotaxis and other tip cell-ECM interactions are indeed important phenomena to include in such a model of angiogenesis requires a more extensive (and much more time-consuming) exploration of parameter space.

We were careful to incorporate important aspects of TAF delivery to the vasculature within our original and extended models. Thus, with further work regarding parametrisation and corroboration with experimental data, our models could be used to investigate the dose dependence of the angiogenic response in cornea micropocket experiments. To the best of our knowledge, only one other model of corneal angiogenesis accounts explicitly for the controlled release of a TAF from a pellet (Tong and Yuan 2008b). And, while this model provided valuable insight into bFGF-induced angiogenesis in the cornea, it was hybrid and stochastic in nature and thus, given the computational time required to run simulations, was unsuitable for performing parameter sensitivity analyses. By contrast, the relatively simple and deterministic models developed here allows for efficient exploration of parameter space. Like existing mathematical models, our models suggest that successful and biologically realistic angiogenesis relies upon the striking of a delicate balance between the rate of tip cell production and the response of those tip cells to gradients in growth factors. Moreover, the availability of those growth factors to the vasculature, both at and behind the vascular front, clearly plays an important part in the dynamics of our system. This is consistent with experimental evidence suggesting that the delivery and dosage of VEGF-A, in particular, must be 'exquisitely regulated in [a] spatial, temporal and quantitative manner to avoid vascular disaster' (Yancopoulos *et al.* 2000). Our parameter sensitivity analysis further suggests that a significant proportion of the variability in experimental results could be due to differences in where the pellet was placed in the cornea, with the extent of neovascularisation varying by up to ±25 % with only a 10 % variation (±0.1 mm) in pellet placement. Thus, our sensitivity analysis corroborates what has long been a concern of the experimental community, that accurate pellet placement is critical if one is to obtain reproducible and reliable results using this assay (Bicknell *et al.* 1997). That all of the models presented in this chapter corroborate this finding provides us with additional confidence in the prediction.

We note here that the local sensitivity analyses performed in Sections 5.5.2.1, 5.11.1 and 5.12.1, for our original, extended and simplified models, respectively, are primarily useful for exploring the qualitative behaviour of our models, and do not account for physiological variation in parameter values. To estimate the impact of true physiological variation on system behaviour requires knowledge of the distribution of values which a parameter may take *in vivo*. A more powerful test of local parameter sensitivity is then to change the input parameters individually by a factor of its standard deviation (instead of by a fixed percentage of its value, as we have done) and to measure the effect of such a change on model outputs (Hamby 1994). This sensitivity measure then takes into account a parameter's physiological variability and the associated effect on model outputs. In theory, this procedure represents a simple extension to that which we have employed, however, at present we have little knowledge of physiological variation for most biologically derived parameter values in our models. In particular, whilst we may estimate reliably the variability in L, the distance between pellet and the limbus, and parameters such as $[V_T]_{init}$, the initial concentration of VEGF-A$_{165}$ in pellet, we have little data with which to estimate the physiological variability in values of χ_v, the chemotactic sensitivity, for example. Even so, our conclusions regarding pellet placement still stand, given that the major experimentally controllable inputs for the cornea micropocket experiments are $[V_T]_{init}$ and L, which can be estimated with some confidence. For example, if we assume that a reasonable estimate for the error in the mass of VEGF-A$_{165}$ in a pellet is 1% (3 ng), and that skilled lab technicians can place a pellet within 10% (0.1 mm) of its intended location (supported by our image analysis), it is clear that experimental variation in pellet placement will have a far greater effect on model predictions than dosage error (for which the sensitivity of model outputs is also smaller). To better capture the impact of physiological variation of parameter values on model outputs global sensitivity analysis techniques may also be employed. We discuss briefly the future use of such techniques in Chapter 8.

Throughout this chapter we have assumed that the vasculature detected in experimental images is identifiable with that in our model. However, experimental images show only perfused vessels whereas our model implicitly accounts for both perfused and unperfused vessels, i.e. immature vessels could be perfused or unperfused but our model does not differentiate between these two sub-populations. In the biological system, when sprouts first form, they are not perfused. In order to become perfused, it is reasonable to assume that vessels must first anastomose to form a closed loop, allowing blood to flow. Thus, in practice, there is a lag-time between tip cell production, subsequent migration and the emergence of a perfused vessel, which is identifiable with vessels in the experimental images. Since we do not model individual vessels, modelling the transition of a vessel from an unperfused to a perfused state in a mechanistic way is particularly challenging in a continuum framework. To overcome this challenge, in Chapter 7 we formulate a hybrid model of corneal angiogenesis which differentiates between perfused and unperfused vessels in a mechanistic way. We use this hybrid model, in part, to investigate how the relative distributions of perfused and unperfused vessels evolve over time and in response to changes in parameter values. Such a model will therefore allow us to put into context the comparison that we make between experimental images (Chapter 4) and results from continuum model simulations presented in this chapter.

Numerous subtleties underlie fitting models to data and making predictions based on models which have been fit to data. In this chapter, we have not attempted to rigorously fit our models to data by minimising, for example, the root mean squared error. Instead we opted to establish parameter values by a thorough review of the experimental literature and subsequent manual fine-tuning until our model outputs were quantitatively consistent with the experimental data presented in Chapter 4. By taking this approach we have shown that our models are able to capture quantitatively the available experimental data when model parameters are chosen within an acceptable physical range. An advantage of our approach is that it is easy to take into account other qualitative experimental evidence, for example, that tip cells should be largely confined to the vascular front throughout simulations (Gerhardt 2003). This qualitative constraint would be less straightforward to incorporate into an automated parameter fitting algorithm. It should also be noted that it is unlikely that our model parameters are globally (or even locally) identifiable with respect to the experimental data available to us. That is, given the high dimensional parameter space and relative paucity of the available experimental data, acceptable fits to the experimental data are likely to be achievable (a) in distinct and separate parts of parameter space, and/or (b) over extended connected regions of parameter space. Thus, any parameter fitting problem is likely to be ill-posed. Fitting our models to the data, then, by solving the optimisation problem (minimising the root mean square error) would not yield parameter values which are any more useful than those which we have arrived at through manual tuning. We postpone further discussion on the topics of parameter identifiability and uncertainty until the concluding chapter of this thesis, where we also discuss model validation.

We demonstrated in Section 5.12 that a model representing a significant simplification of our detailed models of corneal angiogenesis can fit the experimental data as well as our detailed models. This raises an important question: if a more simple model can fit the available experimental data as well as our detailed models, then why formulate models which are more detailed? The most pertinent answer to this question concerns the fact that our models are mechanistic. While both statistical and mechanistic models can be used to make predictions, the main advantage of using a mechanistic model over a statistical one is that it can be used to provide insight into the mechanisms underlying a phenomenon, and to make predictions based on our understanding of the underlying mechanisms. In particular, mechanistic models are more likely to work correctly and provide insightful predictions than statistical models when extrapolating beyond observed experimental conditions. However, we can only confidently extrapolate beyond currently observed conditions if we can trust that we have faithfully captured the most important phenomena and interactions underlying a system within our mechanistic model. That is, mechanistic models which more faithfully represent the underlying biology allow us to test that model in a setting other than the one in which our observed experiments are based and have some confidence in the prediction of that model. Consider the following illustrative example. In Section 5.12 we demonstrated that a model which does not address the concept of vessel maturity is capable of fitting well to our experimental data (Figure 5.25). However, if we test this model, administering no TAF, we see that this is ultimately a flaw in the model. In such experimental conditions the limbal vessels remain stable and no vascular growth or regression occurs. This is as observed in

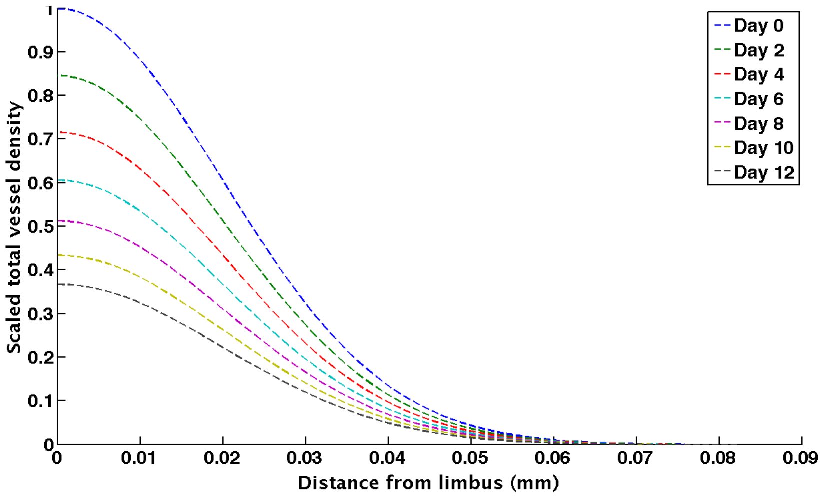

Figure 5.28.: When no TAF is administered ($a_p = 0$) in our simplified model, (5.49)-(5.51), the limbal vasculature regresses. This conflicts with what is known about our experimental system.

our detailed model, since in the absence of a TAF limbal vessels remain mature and stable. By contrast, for our simplified model, when no TAF is present the limbal vessels regress since they are unstable (see Figure 5.28). Thus, by testing our simplified model in the most simple experimental environment, we reveal a major flaw. Similarly, maturation is known to be an important factor in intra-tumoural angiogenesis and when considering the effects of anti-angiogenic therapies on tumour-associated vasculature. Thus, we conclude in this case that a robust model of angiogenesis must account for vessel maturation. The fact that our detailed models reproduce quantitatively the dynamics of vascular growth in both control (no TAF) and experimental (with VEGF-A$_{165}$ or bFGF) scenarios suggests that they capture the key physical and biological mechanisms underlying angiogenesis in cornea micropocket experiments. Related to the above, the 'more mechanistic' a model is the more likely it is that parameters will have biological definitions that can be estimated from existing experimental data, using physical arguments, or directly measured independently of the data used to compare against model output. Thus, parameters in detailed models may sometimes be fixed or heavily constrained. By contrast, models which are more phenomenological may have loose bounds on their allowed parameter values since they attempt to capture complex mechanisms using very simple terms. Perhaps counter- intuitively, then, models which are more mechanistic can be advantageous when fitting to experimental data since some model parameters may be fixed, decreasing the total number of parameters to fit.

In adapting our model of VEGF-A$_{165}$-induced angiogenesis to represent bFGF- induced angiogenesis in Section 5.6, we assumed that differences between the action of the two TAFs could be captured largely by changes in model parameter values. However, in reality, as noted in Chapter 2, the relationship between VEGF-A- and FGF-induced angiogenesis is more complicated. In particular, it is widely believed that bFGF induces angiogenesis upstream of VEGF-A, partly via the VEGF-A/VEGFR-2 pathway (Murakami and Sakurai 2012). To address this short-fall, in the next chapter we extend our model of bFGF-induced angiogenesis presented in Section 5.6 to incorporate downstream VEGF-A-induced angiogenesis. We use this model to determine the impact of VEGF-A/bFGF crosstalk on the angiogenic response of the corneal vasculature when it is exposed to VEGF-A_{165} and bFGF in combination.

CHAPTER 6

A Combined Model of VEGF-A_{165}- and bFGF-induced Angiogenesis

6.1. Overview

The models developed in Chapter 5 aimed to capture quantitatively the angiogenic response of the corneal vasculature to a single AF, either VEGF-A_{165} or bFGF. There, differences between the two AFs were captured primarily by changing model parameters. In practice, however, the relationship between VEGF-A and FGF is more complex: experimental evidence suggests that FGF induces angiogenesis partially via the VEGF-A/VEGFR-2 pathway (Murakami and Sakurai 2012). Thus, in this chapter we formulate a model in which the corneal vasculature responds to simultaneous administration of VEGF-A_{165} and bFGF, incorporating crosstalk between the two factors as suggested experimentally. The model is first developed in Section 6.2 and then parametrised in Section 6.3 using the experimental data presented in Chapter 4. Simulation results are presented in Sections 6.4 and 6.5, where we first demonstrate the consistency of simulation results with data from experiments in which vascular growth occurs in response to VEGF-A_{165} and bFGF alone. Having shown consistency with these data, we then use the model to characterise the impact of VEGF-A/bFGF crosstalk on the angiogenic response of the corneal vasculature when VEGF-A_{165} and bFGF are administered in combination. The model is also used to generate experimentally testable predictions regarding the effect of anti-VEGF-A therapies on bFGF-induced angiogenesis. We conclude in Section 6.6 by discussing the results presented in this chapter and directions for further work.

A paper based on the work presented in this chapter (and on the precursory work presented in Chapters 4 and 5) has been published in the Journal of the Royal Society Interface (Connor *et al.* 2015).

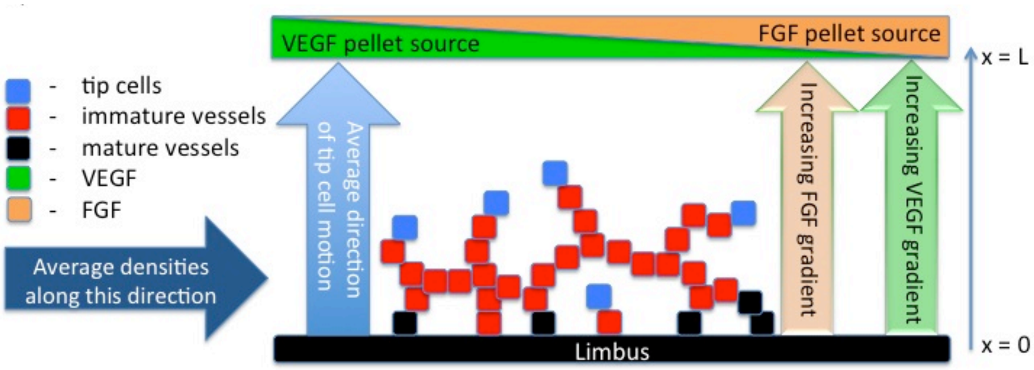

Figure 6.1.: Updated model schematic. Tip cells are assumed to migrate (and thus vessels grow), on average, in the direction of increasing AF concentration(s), i.e. towards the pellet(s). For simplicity, our model is again formulated in terms of dependent variables which represent quantities averaged in the plane perpendicular to the average direction of tip cell motion. The corneal vasculature now grows in response to VEGF-A$_{165}$ and bFGF simultaneously. Both bFGF and VEGF-A$_{165}$ pellets are assumed to be located at $x = L$.

6.2. Model development

In this section we combine the models of VEGF-A$_{165}$- and bFGF-induced angiogenesis presented in the previous chapter (see Sections 5.3 and 5.6 for details) into a single mathematical model. Figure 6.1 shows an updated model schematic. As before, we consider a 1-D Cartesian domain, $0 \leq x \leq L$, in which dependent variables represent averages over the plane perpendicular to the average direction of tip cell motion. Since the corneal vasculature now grows in response to VEGF-A$_{165}$ and bFGF simultaneously, our model consists of equations for the average density of tip cells, $n(x,t)$, the average length density of immature vessels, $\rho(x,t)$, the average length density of mature vessels, $m(x,t)$, the average concentration of VEGF-A$_{165}$, $v(x,t)$, and the average concentration of bFGF, $f(x,t)$. Again, we also model the mean concentration of VEGF-A$_{165}$ and bFGF in the pellets, denoted $[V_t](t)$ and $[F_t](t)$, respectively. See Table 6.1 for a summary of the dependent variables.

As noted in Chapter 2, bFGF is thought to induce angiogenesis upstream of VEGF-A, and partly via the VEGF-A/VEGFR-2 pathway (Murakami and Sakurai 2012). More specifically, exposure to bFGF upregulates the expression of VEGFR-2 (Murakami *et al.* 2011) and stimulates ECs to produce VEGF-A (Seghezzi *et al.* 1998). This may explain why blocking the VEGF-A/VEGFR-2 pathway inhibits FGF-induced angiogenesis (Seghezzi *et al.* 1998). By contrast, blockade of FGF/FGFR signalling appears to have a less marked effect on VEGF-A-induced angiogenesis (Murakami and Sakurai 2012). In our combined model of VEGF-A$_{165}$- and bFGF-induced angiogenesis, we incorporate these mechanisms of crosstalk.

Variable	Description	Units
n	Number of tip cells per unit volume, averaged along directions perpendicular to direction of tip migration.	tip cells m^{-3}
ρ	Length of immature vessels per unit volume, averaged along directions perpendicular to direction of tip migration.	m of vessel m^{-3}
m	Length of mature vessels per unit volume, averaged along directions perpendicular to direction of tip migration.	m of vessel m^{-3}
v	Mean molar concentration of VEGF-A$_{165}$ across cross-sectional area of cornea.	M
f	Mean molar concentration of bFGF across cross-sectional area of cornea.	M
$[V_t]$	Mean concentration of VEGF-A$_{165}$ inside pellet.	M
$[F_t]$	Mean concentration of bFGF inside pellet.	M

Table 6.1.: Table of dependent variables for our extended model.

Since we do not model VEGFR-2 density explicitly, increases in VEGFR-2 density are reflected in the transient modulation of a number of parameter values. In more detail, we assume that exposure to bFGF leads to increased uptake of VEGF-A$_{165}$ by ECs, increased VEGF-A$_{165}$-induced sprouting and increased dematuration in the presence of VEGF-A$_{165}$; i.e. increases in K^v_{EC}, α^v_0 and λ^v_1, respectively. Given that significant changes in expression happen on relatively short time-scales ($<$ 4 hours) (Pepper and Mandriota 1998), to simplify our model, we assume that the upregulation of VEGFR-2 expression (and thus modulation of parameter values) and the production of VEGF-A$_{165}$ are instantaneous. In particular, we suppose that VEGFR-2 expression is upregulated according to:

$$\Lambda(f) = \Lambda_0 \left(1 + \frac{sf}{f + f^{FGFR}_{\frac{1}{2}}} \right), \tag{6.1}$$

where s determines the maximal fold-increase in VEGFR-2 expression levels and Λ_0 is the level of VEGFR-2 expression in the absence of bFGF. In particular, here, we have assumed that the number of VEGFR-2 molecules per EC increases linearly with the fraction of bound FGFR-1 receptors. In the presence of bFGF, then, K^v_{EC}, α^v_0 and λ^v_1, are modified w.r.t. their definitions in our previous model, (5.19)-(5.23), as follows:

$$K^v_{EC} \longmapsto K^v_{EC} \frac{\Lambda(f)}{\Lambda_0}, \tag{6.2}$$

$$\alpha^v_0 \longmapsto \alpha^v_0 \frac{\Lambda(f)}{\Lambda_0}, \tag{6.3}$$

$$\lambda^v_1 \longmapsto \lambda^v_1 \frac{\Lambda(f)}{\Lambda_0}. \tag{6.4}$$

To account for bFGF-induced VEGF-A$_{165}$ production by ECs, we include an additional source term in the VEGF-A$_{165}$ equation, in which ECs release VEGF-A$_{165}$ at a rate proportional to the bound fraction of FGFR-1 molecules.

In our extended model we assume that tip cell chemotaxis and production, and vessel dematuration due to VEGF-A$_{165}$ and bFGF combine additively, whereas the dependence of vessel maturation and regression on VEGF-A$_{165}$ and bFGF are modelled using multiplicative terms. These decompositions ensure that in the absence of either factor the dependence of each process on the remaining AF is consistent with the relevant model from Chapter 5.

In summary, we propose the following system of equations to model combined VEGF-A$_{165}$- and bFGF-induced angiogenesis (terms highlighted in red are those associated with VEGF-A/bFGF crosstalk):

$$
\begin{aligned}
\frac{\partial m}{\partial t} &= -\left[\overbrace{\left(1+\frac{sf}{f+f_{\frac{1}{2}}^{FGFR}}\right)}^{\substack{\uparrow \text{VEGFR}-2 \rightarrow \uparrow \text{VEGF}-\text{A}_{165}- \\ \text{induced dematuration}}}\left(\frac{\lambda_1^v v}{v+v_{\frac{1}{2}}}\right)+\left(\frac{\lambda_1^f f}{f+f_{\frac{1}{2}}^{FGFR}}\right)\right] m \\
&\quad +\lambda_2\left(\frac{v_{\frac{1}{2}}}{v+v_{\frac{1}{2}}}\right)\left(\frac{f_{\frac{1}{2}}^{FGFR}}{f+f_{\frac{1}{2}}^{FGFR}}\right) H\left(\nu\,(m+\rho)+n-N_{min}\right)\rho,
\end{aligned} \tag{6.5}
$$

$$
\begin{aligned}
\frac{\partial n}{\partial t} &= \frac{\partial}{\partial x}\left(\mu\,\frac{\partial n}{\partial x}-\chi_f\, n\,\frac{\partial f}{\partial x}-\chi_v\, n\,\frac{\partial v}{\partial x}\right) \\
&\quad +\alpha_0^v \overbrace{\left(1+\frac{sf}{f+f_{\frac{1}{2}}^{FGFR}}\right)}^{\substack{\uparrow \text{VEGFR}-2 \rightarrow \uparrow \text{VEGF}-\text{A}_{165}- \\ \text{induced sprouting}}}\left(\frac{v}{v+v_{\frac{1}{2}}}\right)\rho+\alpha_0^f\left(\frac{f}{f+f_{\frac{1}{2}}^{FGFR}}\right)\rho \\
&\quad -\beta_1\,(\rho+m)\,n-2\,\beta_2\,n^2-\gamma\,n\left(\frac{v_{\frac{1}{2}}}{v+v_{\frac{1}{2}}}\right)\left(\frac{f_{\frac{1}{2}}^{FGFR}}{f+f_{\frac{1}{2}}^{FGFR}}\right),
\end{aligned} \tag{6.6}
$$

$$
\begin{aligned}
\frac{\partial \rho}{\partial t} &= \kappa\left|\mu\,\frac{\partial n}{\partial x}-\chi_f\, n\,\frac{\partial f}{\partial x}-\chi_v\, n\,\frac{\partial v}{\partial x}\right|+\beta_1\,\bar{l}_\rho\, n\,\,(m+\rho)^{\frac{1}{2}}+\beta_2\,\bar{l}_n\, n^{\frac{5}{3}} \\
&\quad -\gamma\,\rho\left(\frac{v_{\frac{1}{2}}}{v+v_{\frac{1}{2}}}\right)\left(\frac{f_{\frac{1}{2}}^{FGFR}}{f+f_{\frac{1}{2}}^{FGFR}}\right) \\
&\quad +\left[\left(1+\frac{sf}{f+f_{\frac{1}{2}}^{FGFR}}\right)\left(\frac{\lambda_1^v v}{v+v_{\frac{1}{2}}}\right)+\left(\frac{\lambda_1^f f}{f+f_{\frac{1}{2}}^{FGFR}}\right)\right] m \\
&\quad -\lambda_2\left(\frac{v_{\frac{1}{2}}}{v+v_{\frac{1}{2}}}\right)\left(\frac{f_{\frac{1}{2}}^{FGFR}}{f+f_{\frac{1}{2}}^{FGFR}}\right) H\left(\nu\,(m+\rho)+n-N_{min}\right)\rho,
\end{aligned} \tag{6.7}
$$

$$
\begin{aligned}
\frac{\partial f}{\partial t} &= D_f \frac{\partial^2 f}{\partial x^2} - \lambda_f \, v - 2\,\pi\,\bar{R}\,P_f\,(\rho + m)\,(f - f_{blood}) \\
&\quad - \left(\frac{K_{EC}^{FGFR}\, f}{f + f_{\frac{1}{2}}^{FGFR}} + \frac{K_{EC}^{HSPG} f}{f + f_{\frac{1}{2}}^{HSPG}} \right) \, (n + \nu\,(\rho + m)), \qquad (6.8)
\end{aligned}
$$

$$
\begin{aligned}
\frac{\partial v}{\partial t} &= D_v \frac{\partial^2 v}{\partial x^2} - \lambda_v \, v - 2\,\pi\,\bar{R}\,P_v\,(\rho + m)\,(v - v_{blood}) \\
&\quad - K_{EC}^{v} \, \overbrace{\left(1 + \frac{s f}{f + f_{\frac{1}{2}}^{FGFR}} \right)}^{\substack{\uparrow \text{VEGFR}-2 \to \uparrow \text{binding} \\ \text{of VEGF}-\text{A}_{165}}} \left(\frac{v}{v + v_{\frac{1}{2}}} \right) \, (n + \nu\,(\rho + m)) \qquad (6.9) \\
&\quad \underbrace{+ \, \phi\,(n + \nu\,(\rho + m)) \left(\frac{f}{f + f_{\frac{1}{2}}^{FGFR}} \right)}_{\substack{\text{bFGF stimulates ECs to} \\ \text{produce VEGF}-\text{A}_{165}}},
\end{aligned}
$$

$$
\frac{d[F_t]}{dt} = -\frac{\lambda_p^f}{\theta_f}[V_t] - \frac{\zeta_p k_p^f}{\Omega_p} \left(\frac{[F_t]}{\theta_f} - f(1,t) \right), \qquad (6.10)
$$

$$
\frac{d[V_t]}{dt} = -\frac{\lambda_p^v}{\theta_v}[V_t] - \frac{\zeta_p k_p^v}{\Omega_p} \left(\frac{[V_t]}{\theta_v} - v(1,t) \right). \qquad (6.11)
$$

Once more, these equations are subject to the boundary conditions

$$
\left.
\begin{array}{r}
\mu \, \dfrac{\partial n}{\partial x} - \chi_v \, n \, \dfrac{\partial v}{\partial x} - \chi_f \, n \, \dfrac{\partial f}{\partial x} = 0, \quad -D_f \dfrac{df}{dx} = -P_f \, (f - f_{blood}), \\
-D_v \dfrac{dv}{dx} = -P_v \, (v - v_{blood}),
\end{array}
\right\} \quad x = 0, \qquad (6.12)
$$

$$
\left.
\begin{array}{r}
\mu \, \dfrac{\partial n}{\partial x} - \chi_v \, n \, \dfrac{\partial v}{\partial x} - \chi_f \, n \, \dfrac{\partial f}{\partial x} = 0, \quad -D_f \dfrac{df}{dx} = -k_p^f \left(\dfrac{[F_t]}{\theta_f} - f \right), \\
-D_v \dfrac{dv}{dx} = -k_p^v \left(\dfrac{[V_t]}{\theta_v} - v \right),
\end{array}
\right\} \quad x = L, \qquad (6.13)
$$

and to the initial conditions

$$
m(x,0) = m_L exp\left[-\frac{x^2}{2\sigma^2} \right], \quad n(x,0) = 0, \quad \rho(x,0) = 0, \quad v(x,0) = 0, \quad f(x,0) = 0,
$$

$$
[F_t](0) = [F_t]_{init}, \quad [V_t](0) = [V_t]_{init}. \qquad (6.14)
$$

6.2.1. Nondimensionalisation

Nondimensionalisation of (6.5)-(6.14) proceeds as in Section 5.3.7 of Chapter 5. Distance is rescaled with a typical pellet-limbus spacing, $\hat{L}$, and time with $\tau = \frac{\hat{L}^2}{D_v}$, so that

$$x^* = \frac{x}{\hat{L}} \quad \text{and} \quad t^* = \frac{t}{\tau}, \tag{6.15}$$

where the $^*s$ denote dimensionless quantities. The dependent variables are rescaled as follows

$$n^* = \frac{n}{n_0}, \quad \rho^* = \frac{\rho}{\rho_0}, \quad m^* = \frac{m}{\rho_0}, \quad v^* = \frac{v}{V_0}, \quad [V_t]^* = \frac{[V_t]}{V_0}, \quad f^* = \frac{f}{F_0} \quad \text{and} \quad [F_t]^* = \frac{[F_t]}{F_0}.$$

Adopting these scalings, (6.5)-(6.14) transform as in Section 5.3.7. Therefore, for brevity, a full statement of the dimensionless model is omitted and we refer henceforth to the dimensional equations. We merely note here that our nondimensionalised extended model contains two new dimensionless parameters:

$$\phi^* = \left(\frac{\phi \tau n_0}{V_0}\right), \quad \text{and} \quad s^* = s.$$

6.3. Parameter value estimation

Unless otherwise stated we use the default parameter values from Chapter 5. Only two new parameters, ϕ and s, have been introduced in our combined model of VEGF-A$_{165}$- and bFGF-induced angiogenesis. We proceed by first estimating their default values.

Pepper and Mandriota (1998) report a fold-increase in total protein levels of VEGFR-2 when ECs are exposed to bFGF ($5.3 \times 10^{-4}\,\mathrm{M} \ggg f^{FGFR}_{\frac{1}{2}}$) of between 2 and 3.5. Thus, here, we set $s = 1$, assuming a maximal fold-increase of 2. In the absence of appropriate experimental data, initially we set ϕ, the maximal rate of increase in VEGF-A$_{165}$ concentration per unit EC density, to 1×10^{-22} moles m^3 l^{-1} per cell per hour, which is the same order of magnitude as K^v_{EC}, the maximum rate of VEGF-A$_{165}$ removal due to its binding with VEGFR-2 on ECs. In Section 6.5 we investigate how changes in the values of s and ϕ affect model predictions.

In Chapter 5, different values of γ, the maximal rate of regression of vessels, were used to simulate VEGF-A$_{165}$- and bFGF-induced angiogenesis ($\gamma = 5 \times 10^{-3}\,\mathrm{h}^{-1}$ vs $\gamma = 1.67 \times 10^{-3}\,\mathrm{h}^{-1}$, respectively). The default value of γ used here is identical to that used for VEGF-A$_{165}$-induced angiogenesis in Chapter 5 (all other parameters associated with VEGF-A$_{165}$-induced angiogenesis also remain unchanged from Chapter 5). The values of parameters associated with bFGF-induced angiogenesis, λ_1^f, χ_f and α_0^f, differ from those used in the previous chapter to ensure a good fit of the model to the data arising from bFGF experiments (see Figure 5.15). Retuning these parameters was necessary because, in our extended model, vascular growth occurs partly via the VEGF-A$_{165}$ submodel. In particular, dematuration, sprouting and chemotaxis are in part mediated by VEGF-A$_{165}$, even in the absence of a VEGF-A$_{165}$ pellet. In the absence of a VEGF-A$_{165}$ pellet, VEGF-A$_{165}$ is still produced by ECs, primarily around the vascular wavefront which is exposed to significant levels of bFGF. Initially, this leads to increased dematuration. To ensure that model results are consistent with the experimental data from Chapter 4 this additional dematuration due to VEGF-A$_{165}$ must be balanced by a reduction in the rate of dematuration due to bFGF. Thus, the value of λ_1^f is reduced compared to that used in the previous chapter. Similarly, VEGF-A$_{165}$ production at the front causes increased sprouting, which must be compensated for with a reduction in the sprouting rate due to bFGF, α_0^f. The VEGF-A$_{165}$ produced by ECs around the vascular front diffuses, decays and is taken up by the vasculature, producing a small negative VEGF-A$_{165}$ gradient moving from the front to the pellet (and from the front to the limbus). Thus, tip cells closest to the leading edge experience a chemotactic force directed away from the pellet, reducing the speed of migration of the vascular front. To compensate for this χ_f is increased w.r.t. its value in the previous chapter. For a consolidated list of scaling factors and default parameter values used for numerical simulation of our extended model see Appendix B.

6.4. Numerical results

Our mathematical model was solved using the method of lines, executed in MATLAB (see Chapter 5, Section 5.5, for further details). When generating numerical simulations we focused on four different *in vivo* scenarios (**S1-S4**):

S1. Control experiments: $[V_t]_{init} = [F_t]_{init} = 0$;

S2. VEGF-A$_{165}$ experiments: $[V_t]_{init}$ at its default value, $[F_t]_{init} = 0$;

S3. bFGF experiments: $[V_t]_{init} = 0$, $[F_t]_{init}$ at its default value;

S4. bFGF+VEGF-A$_{165}$ experiments: $[V_t]_{init}$ and $[F_t]_{init}$ are set to the default values.

Simulations of VEGF-A$_{165}$ experiments (S2) and bFGF experiments (S3) were used for model parametrisation; thereafter we used our model to predict the effect of combining bFGF and VEGF-A$_{165}$ (S4).

S1. Control experiments

As in Chapter 5, for control experiments, no AFs are administered and the dependent variables remain unchanged from their initial values: the limbal vessels remain mature and no angiogenic response is stimulated, consistent with *in vivo* experiments.

S2. VEGF-A$_{165}$-induced angiogenesis experiments

Simulations of angiogenesis in response to VEGF-A$_{165}$ are identical to those in Section 5.5 of Chapter 5 since our model simplifies to that presented in Section 5.3.7 when bFGF is absent, and the parameter values are identical. As such, for a comparison of experimental and simulated results of VEGF-A$_{165}$-induced angiogenesis one may consult Figure 5.4 from the previous chapter. For our extended model, demonstrating consistency of simulation results with these data allows us to fix model parameters associated with VEGF-A$_{165}$-induced angiogenesis (Tables B.2 and B.3).

S3. bFGF-induced angiogenesis experiments

To determine the impact of VEGF-A/bFGF interactions on the angiogenic response of the corneal vasculature we performed *in silico* knock-out experiments, in which different crosstalk terms were eliminated. The four model variants we consider are summarised in Table 6.2. Simulations in which bFGF-induced VEGF-A$_{165}$ production is neglected correspond to parametrisations where $\phi = 0$. For those in which bFGF-induced VEGFR-2 upregulation is neglected we fix $s = 0$. For each variant, other parameter values were manually tuned so that simulations of that variant are quantitatively consistent with the data from bFGF-induced angiogenesis experiments (as per Figure 4.9b). Modifying λ_1^f, α_0^f and χ_f was sufficient to provide good fits to the experimental data[1] (all other parameter values were held fixed at the values given in Tables B.2-B.4). For each variant, the fold changes in these parameter values (w.r.t. those stated in Table B.4) are shown in Table 6.3. A comparison between experimental data and results for all four model variants when bFGF is administered alone is shown in Figure 6.2. In each case there is good quantitative agreement between model results and the experimental data. Indeed, all four model variants are almost indistinguishable when tested using bFGF only. Demonstrating consistency of simulation results with the data in Figure 6.2 allows us to fix model parameters related to bFGF-induced angiogenesis for each variant. Because VEGF-A$_{165}$ acts downstream of bFGF it is not necessary to re-parametrise each model variant with respect to the VEGF-A$_{165}$ experiments and parameters associated with VEGF-A$_{165}$-induced angiogenesis can be considered fixed.

---

[1] Arguments for why we vary these parameter values only follow those presented in Section 6.3.

	Variant 1	Variant 2	Variant 3	Variant 4
bFGF-induced VEGF-A165 production	−	+	−	+
bFGF-induced VEGFR-2 upregulation	−	−	+	+

Table 6.2.: We formulate four variants of our mathematical model, (6.5)-(6.14), in which two documented mechanisms of crosstalk between VEGF-A$_{165}$ and bFGF are either included or excluded.

Parameter	**Fold increase in parameter value w.r.t. default values**			
	Variant 1	**Variant 2**	**Variant 3**	**Variant 4 (Default)**
λ_1^f	1.76	1.38	1.76	1
α_0^f	1.90	1.06	1.90	1
χ_f	0.86	1.03	0.86	1

Table 6.3.: Table of parameter modifications for the four variants of our model, (6.5)-(6.14). For each variant λ_1^f, α_0^f and χ_f are changed w.r.t. their default values (Table B.4) to ensure that the simulation results remain faithful to the data arising from experiments in which angiogenesis is induced by bFGF pellets only.

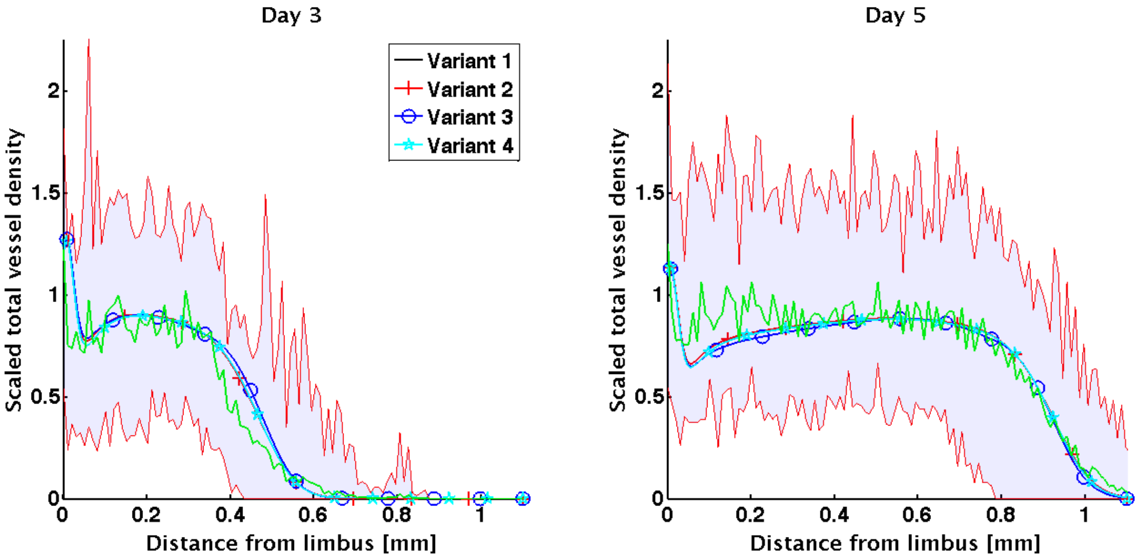

Figure 6.2.: Comparison of experimental data with the results from simulations of bFGF-induced angiogenesis for our four model variants (Table 6.2). The solid green lines show averaged experimental data and the shaded region (bounded by solid red lines) shows the range in densities across experimental data sets.

S4. Predicting the angiogenic response of corneal vasculature to VEGF-A$_{165}$ *and bFGF in combination*

We now use the model variants to predict the angiogenic response when VEGF-A$_{165}$ and bFGF are administered together. Figure 6.3 shows the scaled total vascular density on day three of such *in silico* experiments. We also show how the location of the vascular front evolves until it reaches

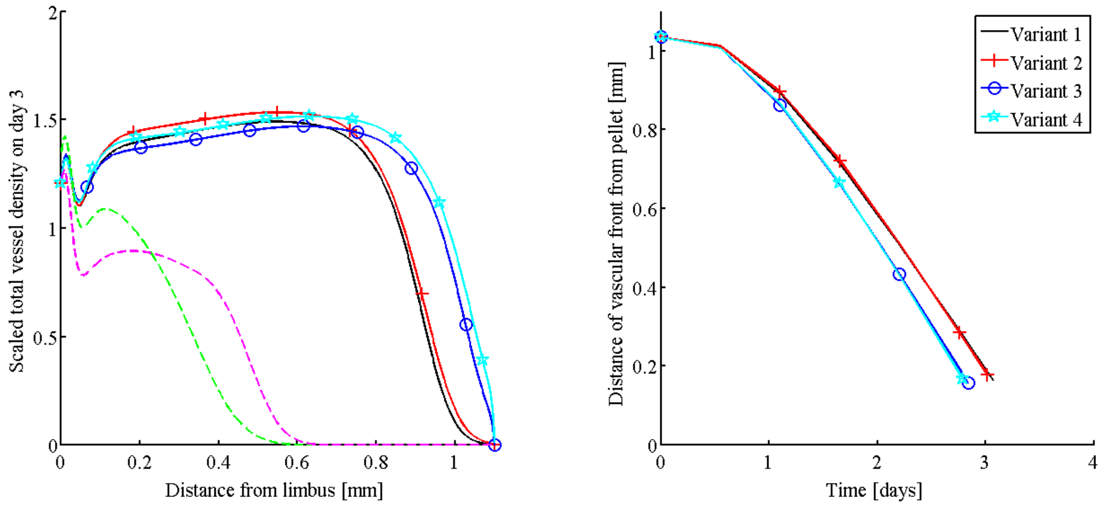

(a) **(b)**

Figure 6.3.: All four model variants (Table 6.2) are compared when vascular growth is stimulated by VEGF-A$_{165}$ and bFGF in combination. The angiogenic response at day three is presented in (a), while the distance moved is plotted in (b). For convenience, the angiogenic responses induced by each factor in isolation are shown in (a); - -: bFGF, - -: VEGF-A$_{165}$.

the pellet and our model ceases to be valid[2]. The special cases (variants) of our general model considered here provide insight into the likely effects of the two mechanisms of VEGF-A/bFGF crosstalk under consideration.

The results presented in Figure 6.3 suggest that bFGF-dependent VEGF-A$_{165}$ production (+ and ⋆) typically increases vascular density and marginally increases the front migration speed, whereas bFGF-dependent VEGFR-2 upregulation (○ and ⋆) increases the speed of migration of the front. In Figure 6.4 we compare summary statistics extracted from model simulations. In particular, we focus on the distance of the vascular front from the limbal vessels and the maximum amplitude of the vascular wavefront on day three. For each model variant, summary statistics extracted from simulated VEGF-A$_{165}$ experiments (S2), bFGF experiments (S3) and bFGF + VEGF-A$_{165}$ experiments (S4) are presented. Also shown are the expected values of the summary statistics for bFGF + VEGF-A$_{165}$ experiments if we were to assume that the effects of bFGF and VEGF-A$_{165}$ on the angiogenic response of the corneal vasculature are additive. Clearly, even in the simplest case, where no direct crosstalk between VEGF-A$_{165}$ and bFGF is included in the model (variant 1, Table 6.2), the effects of bFGF and VEGF-A$_{165}$ on the

---

[2] The validity of our model becomes questionable when the vasculature reaches the pellet(s) because we do not model the movement of tip cells into or around the pellet(s).

angiogenic response are nonlinear. In particular:

- The maximum amplitude of the vascular wavefront is less than would be expected from an additive response.
- The extent of neovascularisation towards the pellet is greater than would be expected from an additive response.

These observations may be explained as follows. Vessels and ECs are sinks of VEGF-A$_{165}$ and bFGF. Thus, vascular growth creates a moving barrier to the AFs, preventing them from penetrating parts of the neovasculature closest to the limbus, and inhibiting further vascular growth there. The more dense the vascular network (i.e. the higher the amplitude of the vascular wavefront) the more pronounced this effect will be. Thus, while administering VEGF-A$_{165}$ and bFGF in combination causes increases in vascular density (amplitude), this negative feedback loop limits the additive effect of the two factors on vascular density. The increased vascular density, and thus increased uptake of AFs at the vascular wavefront, also increases the local gradient of AFs to which tip cells are exposed. Thus, the chemotactic forces experienced by the tip cells due to VEGF-A$_{165}$ and bFGF are independently increased when the two factors are administered in combination. The effect of crosstalk between VEGF-A$_{165}$ and bFGF on the neovascular response may also be explained in similar terms. For instance, the observation that bFGF-induced upregulation of VEGFR-2 expression ($s \neq 0$) increases the rate of tip cell migration in the presence of VEGF-A$_{165}$ can be attributed to increased VEGF-A$_{165}$ uptake by ECs (since upregulation of VEGFR-2 increases K^v_{EC} and α^v_0), which increases the local gradient of VEGF-A$_{165}$ and hence the chemotactic force experienced by tip cells.

Predicting the effect of anti-VEGF-A therapy on bFGF-induced angiogenesis

A major advantage of including VEGF-A/bFGF crosstalk in our model is that we can study the effect of anti-VEGF-A drugs on bFGF-induced angiogenesis. Figure 6.5 shows the effect of removing VEGF-A$_{165}$ production from the full model (variant 4, Table 6.2) when bFGF only is administered (S3). In this figure, the dashed curve represents a control experiment in which bFGF-induced angiogenesis occurs partially via the VEGF-A/VEGFR-2 pathway, while the solid curve depicts the predicted response when an anti-VEGF-A drug is added to the system. This drug may, for example, sequester VEGF-A$_{165}$ in the extracellular space or block VEGF-A$_{165}$ binding to VEGFR-2. Our results are consistent with experiments in which fewer, thinner vessels, with decreased branching points were observed when an anti-VEGF-A monoclonal antibody was administered systemically to mice participating in bFGF-induced

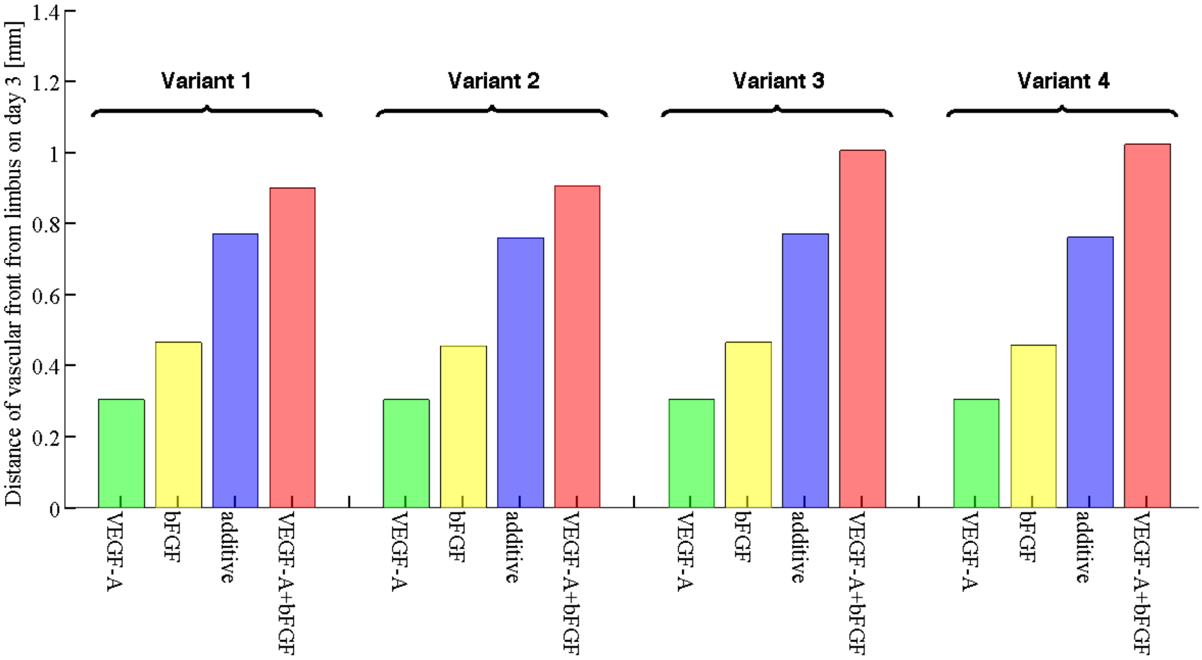

(a)

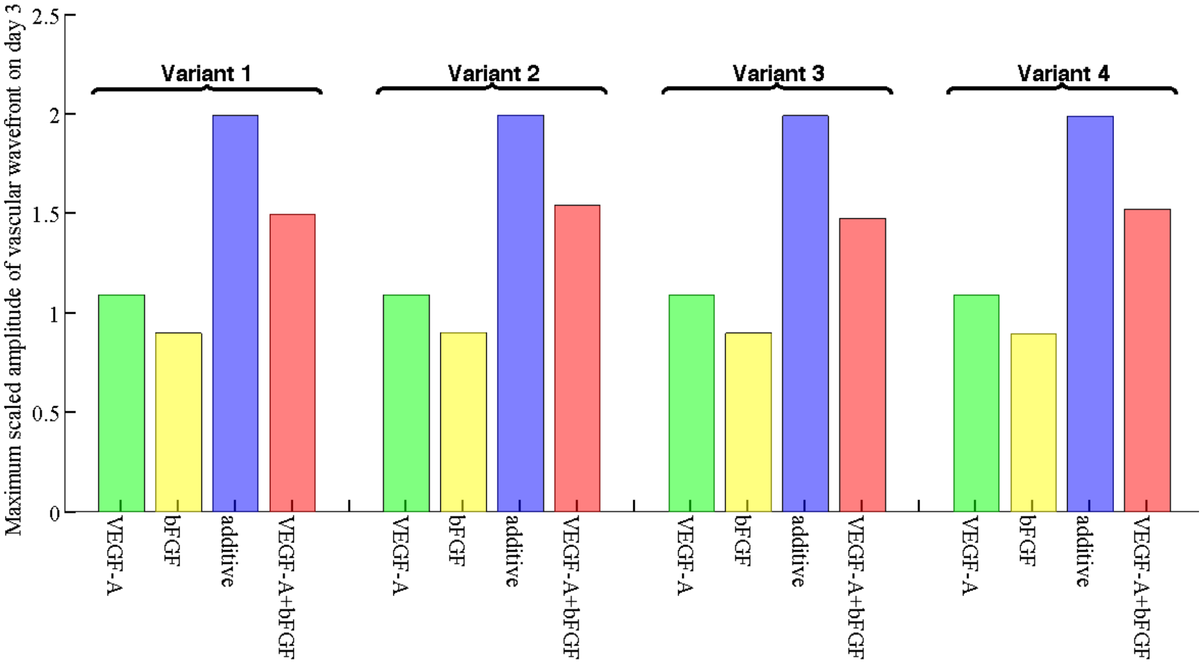

(b)

Figure 6.4.: Comparison of summary statistics extracted from simulations of four model variants (Table 6.2). (a) Distance of the vascular front from the limbal vessels on day three. (b) Maximum amplitude of the vascular wavefront on day three. Green bars: VEGF-A$_{165}$ experiments (S2); yellow bars: bFGF experiments (S3); red bars: bFGF + VEGF-A$_{165}$ experiments (S4). Also compared, blue bars, are the additive values of the summary statistics taken from VEGF-A$_{165}$ experiments (S2) and bFGF experiments (S3). Considering these two summary statistics, the effects of bFGF and VEGF-A$_{165}$ are not additive (compare blue and red bars) even when no crosstalk (synergy) between the two factors is included in the model (variant 1).

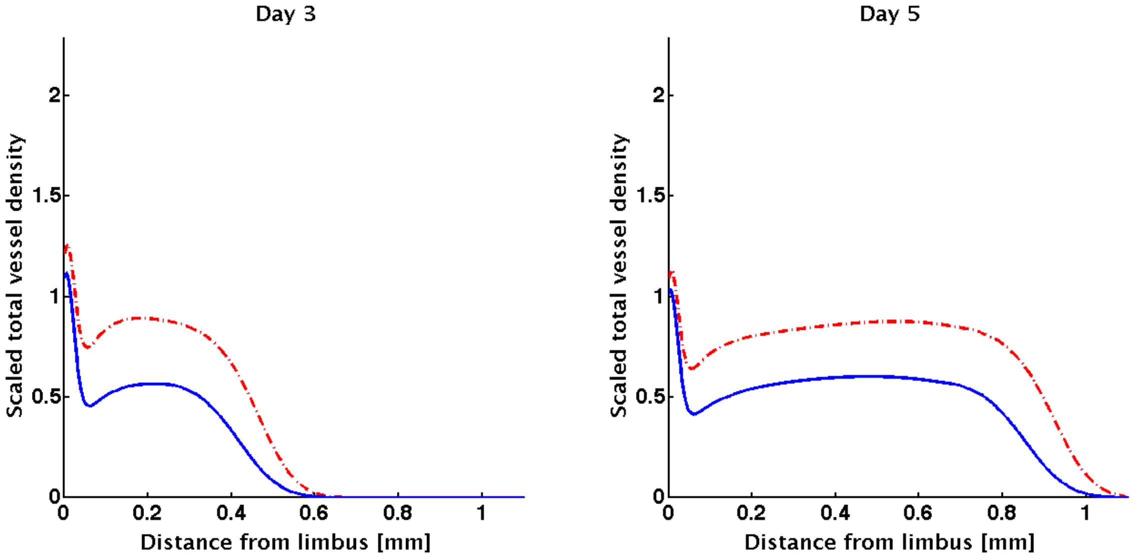

Figure 6.5.: Complete sequestration of VEGF-A$_{165}$ in the extra-cellular space diminishes the angiogenic response of limbal vessels exposed to bFGF alone. Dashed lines represent the results from *in silico* experiments in which our full model (variant 4, Table 6.2) was simulated. Solid lines are results from numerical simulations in which VEGF-A$_{165}$-induced angiogenesis is completely inhibited.

corneal angiogenesis experiments (Seghezzi *et al.* 1998). In our model, fewer vessels correspond to a reduced amplitude in the advancing vascular wavefront. Similar reductions in the angiogenic response induced by bFGF are observed when model variant 2 (Table 6.2) is considered. Naturally, when bFGF-induced VEGF-A$_{165}$ production is neglected (variants 1 and 3) the addition of an anti-VEGF-A drug does not affect the bFGF-induced angiogenic response. Another noteworthy model prediction is that the extent of neovascularisation towards the pellet is not significantly altered by the addition of an anti-VEGF-A drug. This result also appears to be consistent with the findings of Seghezzi *et al.* (1998).

6.5. Parameter sensitivity analysis

In this section, we consider the effect that parameter changes have on predictions (Figures 6.3 and 6.5) made by our extended model (variant 4, Table 6.2). In particular, we focus on the sensitivity of our predictions to changes in ϕ or s, doubling and halving these parameter values one at a time. Each time ϕ or s is changed, other parameters are altered so that a good fit of the model to the experimental data is maintained. As in Section 6.4, modifying α_0^f, λ_1^f and χ_f is sufficient in each case to provide good fits. The fold change in parameter values for changes in ϕ or s (w.r.t. their default values in Table B.4) are shown in Table 6.4.

Parameter	Fold increase in parameter value w.r.t. default values			
	$\phi \to \frac{\phi}{2}$	$\phi \to \phi \times 2$	$s \to \frac{s}{2}$	$s \to s \times 2$
λ_1^f	1.65	0.59	1	1
α_0^f	1.47	0.069	1	0.95
χ_f	0.91	1.21	1.03	0.97

Table 6.4.: Table of parameter modifications. Each time s or ϕ is changed λ_1^f, α_0^f and χ_f are changed w.r.t. their default values (Table B.4) to ensure that the simulation results remain faithful to the data arising from experiments in which angiogenesis is induced by bFGF pellets only.

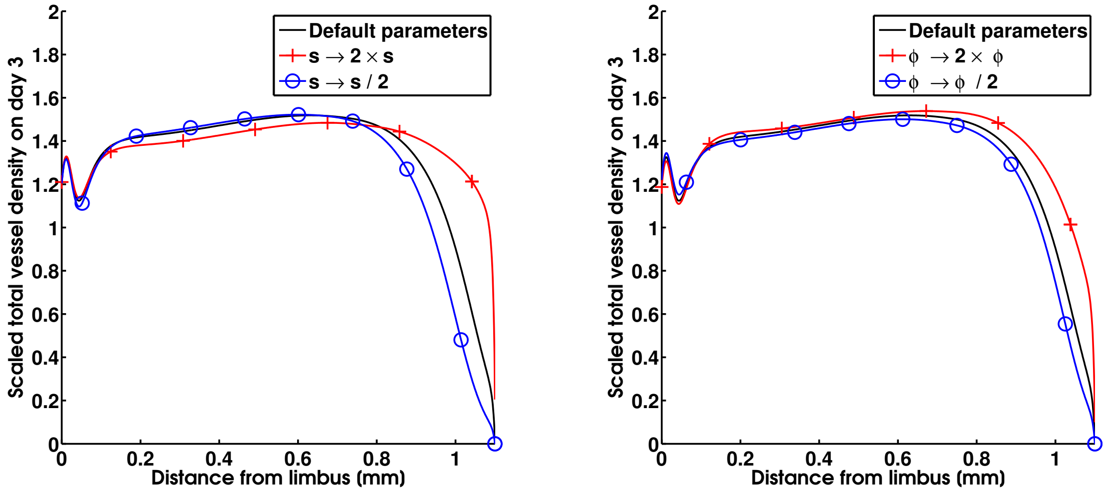

(a)

(b)

Figure 6.6.: Angiogenesis in response to VEGF-A$_{165}$ and bFGF (S4) is simulated using our full extended model (variant 4, Table 6.2). We explore how the model predictions change as ϕ and s are doubled/halved w.r.t. their default values (Table B.4). The vascular density profiles on day three of simulation time are compared as s is varied (a) and as ϕ is varied (b).

In Figure 6.6 we simulate vascular growth stimulated by both VEGF-A$_{165}$ and bFGF (S4) and note how the vascular density profile on day three changes as s and ϕ are varied. Corroborating the conclusions drawn from our *in silico* knock-out experiments in the previous section, the figure indicates that increases in s increase the rate of migration of the vascular wavefront, while decreasing the vascular density. By contrast, increases in ϕ cause small increases in front migration speed while increasing vascular density. These two observations may be explained as follows:

1. Increases in s (Figure 6.6a, + vs ○) increase the effective values of K_{EC}^v and α_0^v immediately behind the vascular wavefront, as in (6.2) and (6.3). Increases in the effective value of K_{EC}^v reduce sprouting due to VEGF-A$_{165}$ (and thus vascular density) because increasing K_{EC}^v reduces the penetration depth of VEGF-A$_{165}$ behind the vascular wavefront. Increases in

K^v_{EC} also increase the local gradient of VEGF-A$_{165}$ at the front, increasing the chemotactic force felt by tip cells and thus increasing the front migration speed. An increased rate of migration also decreases the time during which the vasculature behind the migrating front is exposed to significant levels of VEGF-A$_{165}$, further decreasing sprouting behind the front and making regression in the absence of AFs more likely. These effects appear to dominate over the increase in the effective value of α^v_0, which acts to promote sprouting behind the front.

2. Increases in ϕ (Figure 6.6b, + vs ○) increase the rate of VEGF-A$_{165}$-induced sprouting behind the vascular wavefront. Thus, as ϕ is increased, the vascular density increases. This increased vascular density then drives the increased rate of migration of tip cells; increased vascular density increases the rate of uptake of VEGF-A$_{165}$ at the vascular wavefront, increasing the local gradient of VEGF-A$_{165}$ and thus the chemotactic force experienced by tip cells. The increase in wavefront speed due to increased vascular density is self-limiting since, as discussed above, increasing the speed of migration decreases sprouting (and hence vascular growth) behind the wavefront. This negative feedback may explain why increases in ϕ have a less marked effect on front migration speeds than increases in s.

In Figure 6.7 we present simulation results for bFGF-induced angiogenesis, with strong VEGF-A$_{165}$ inhibition (as in Figure 6.5). Evidently, doubling/halving s with respect to its default value has little effect on the results of simulated VEGF-A$_{165}$ inhibition (Figure 6.7, ⋆ and ○). Meanwhile, doubling/halving ϕ is sufficient to explore almost the entire range of possible angiogenic responses to strong VEGF-A$_{165}$ inhibition (Figure 6.7, □ and +). That is, doubling ϕ results in almost no angiogenic response when simulating bFGF-induced angiogenesis with strong VEGF-A$_{165}$ inhibition. By contrast, the same experiment performed when ϕ is halved results in an angiogenic response which is almost identical to that predicted when bFGF-induced angiogenesis without VEGF-A$_{165}$ inhibition is simulated.

6.6. Discussion

In this chapter we have extended the 1-D continuum model presented in Chapter 5 to describe the response of the corneal vasculature to VEGF-A$_{165}$ and bFGF when administered in combination, incorporating two important mechanisms of crosstalk between VEGF-A and bFGF. Although crosstalk between VEGF-A and bFGF pathways in angiogenesis has been hypothesised for a number of years, this is the first time, to the best of our knowledge, that these hypotheses have

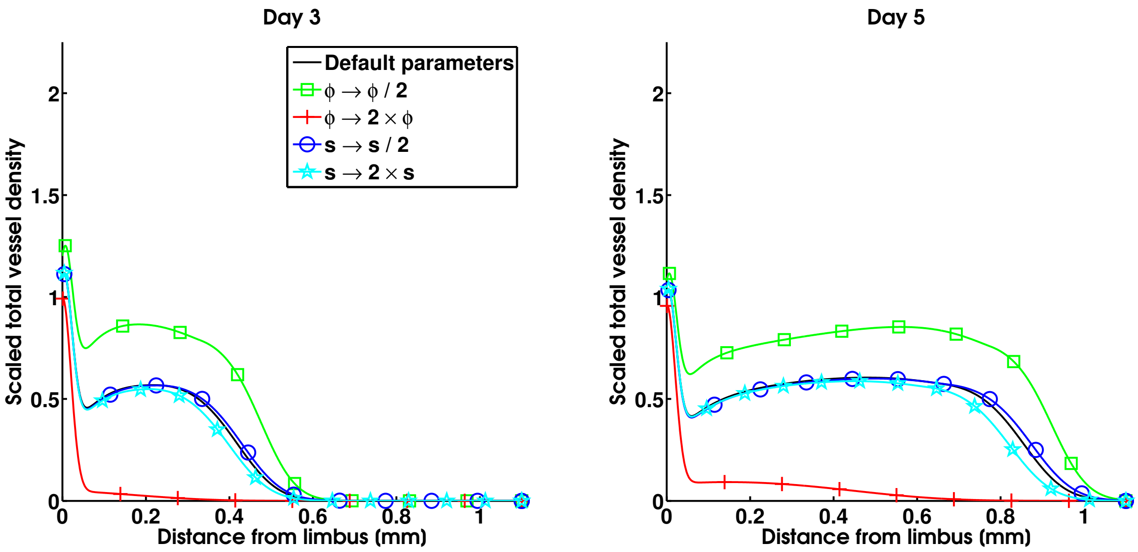

Figure 6.7.: bFGF-induced angiogenesis with strong VEGF-A inhibition is simulated using our full extended model (variant 4, Table 6.2). We explore how the simulation results change as ϕ and s are doubled/halved w.r.t. their default values (Table B.4). While modifying s results in little change to the model prediction, doubling/halving ϕ is sufficient to explore almost the entire range of possible responses to strong VEGF-A-inhibition.

been formalised within the context of a mathematical model.

As in Chapter 5, our model was parametrised using the data extracted from pertinent experimental images in Chapter 4. In particular, two data sets arising from VEGF-A$_{165}$ and bFGF experiments were used to parametrise the VEGF-A$_{165}$- and bFGF-induced angiogenesis submodels, respectively. The model was then used to generate experimentally testable predictions (Figures 6.3 and 6.5) and to study the impact of VEGF-A/bFGF crosstalk on the angiogenic response of the corneal vasculature. In our model, bFGF-induced upregulation of VEGFR-2 expression primarily increases the rate of tip cell migration in the presence of VEGF-A$_{165}$. Meanwhile, VEGF-A$_{165}$ production in ECs due to bFGF exposure appears to affect simulation results less drastically, causing small increases in tip cell migration speed and overall vessel density in the presence of VEGF-A$_{165}$. These observations may be explained in relatively simple terms, as in Section 6.5. Our model also predicts that strong anti-VEGF-A therapy can cause a reduction in vascular density similar to that seen in experiments performed by Seghezzi *et al.* (1998). Moreover, the model provides insight into the self-regulatory mechanisms which prevent run-away vascular growth *in vivo*, where multiple AFs are usually present (see Section 6.4, *S4. Predicting the angiogenic response of corneal vasculature to VEGF-A*$_{165}$ *and bFGF in combination*).

We believe that our model contains the crucial components which allow us to investigate the impact of VEGF-A$_{165}$ and bFGF on the angiogenic response of the corneal vasculature when administered individually and in combination. A number of simplifying assumptions have been made in developing our model. For instance, crosstalk between the VEGF-A$_{165}$ and bFGF pathways have been incorporated in a simplistic way; upregulation of VEGFR-2 expression and VEGF-A$_{165}$ production was assumed to be instantaneous. Whilst simple, our approach allows us to gain insight into the impact of each avenue of crosstalk on the angiogenic response of the corneal vasculature at the tissue scale. Such simplifying assumptions could be relaxed, however, this would be at significant expense to the relative simplicity of our model.

In Section 6.5, we explored how the model predictions change as ϕ (the maximum rate of bFGF-induced VEGF-A production) and s (the maximum bFGF-induced fold increase in VEGFR-2 expression) are doubled/halved w.r.t. their default values. Each time we doubled/halved ϕ or s we varied a number of other parameters to ensure that model results remain in good agreement with the available experimental data. The parameter sensitivity analysis performed here, then, further serves to highlight that the parameters of our models are only partially constrained by the experimental data that we have extracted from experimental images, as discussed in Chapter 5. Additionally, we note that this type of parameter sensitivity analysis was performed as a means of exploring model behaviour only, and not as a means for quantifying the impact of physiological variation in parameter values on the behaviour of the system (as discussed in Chapter 5 also).

Further experimental work is needed to validate the predictions made in this chapter (Figures 6.3 and 6.5 in particular) and to allow us to further constrain model parameters. However, we note that discriminating between models or establishing tight bounds on parameter values is likely to be particularly challenging using the cornea micropocket assay due to the sensitivity of experimental results to L, the distance that pellets are placed from the limbus. In the longer term, the model presented in this chapter could be extended to simulate vascular tumour growth, allowing us to predict the efficacy of anti-VEGF-A drugs in a tumour micro-environment where vascular remodelling occurs in response to multiple AFs. Such a model may also provide insight into FGF-resistance to anti-VEGF-A therapies and the potential efficacy of combined anti-FGF and anti-VEGF-A therapies. The work presented here provides a solid foundation for the development of such a model as it allows us to demonstrate consistency of simulation results with detailed quantitative data emerging from a simple and tractable experimental system.

CHAPTER 7

A Composite Hybrid Model of Corneal Angiogenesis

7.1. Overview

In the preceding chapters we have developed PDE models of angiogenesis in the cornea. We showed that these relatively simple models were able to capture quantitatively the dynamics of corneal angiogenesis in response to different growth factors. What is more, their simple and deterministic nature allowed us to explore parameter space efficiently and perform parameter sensitivity analyses with relative ease. However, as discussed in Chapter 5, some aspects of vascular growth, such as vessel perfusion, are difficult to incorporate in PDE models because individual vessels are not distinguished. Such models also do not address the highly unorganised and spatially heterogeneous nature of tumour vasculature. By contrast, discrete or composite hybrid models in which individual vessels are modelled allow us to explore spatial heterogeneities and interrogate the morphology and properties of individual vessels. Thus, in the penultimate chapter of this thesis we focus on composite hybrid models of angiogenesis and vascular tumour growth. More specifically, in this chapter we describe a 3-D composite hybrid model of VEGF-A_{165}-induced angiogenesis in the cornea which develops the 3-D model of angiogenesis implemented by Perfahl *et al.* (2011). Initially, we extend Perfahl *et al.*'s (2011) model by integrating with it an abstract representation of tip cell filopodia which enables tip cells to sense nearby vessels (or other tip cells) and facilitates the formation of anastomoses. We then further extend the model to include key tip cell-ECM interactions. The models developed in this chapter draw on the models of VEGF-A_{165}-induced angiogenesis developed in Chapter 5. However, in contrast to the models developed earlier in this thesis, our hybrid models distinguish between perfused and unperfused vessels, and, in so doing, provide greater insight into the dynamics of the *in vivo* system.

The remainder of this chapter is structured as follows. In Section 7.2 we introduce the submodels which comprise our first (most basic) discrete model. We also present the computational algorithm used to integrate those submodels into a fully multiscale composite hybrid model. We discuss the parametrisation of the model in Section 7.3. As with the models presented earlier in this thesis, we use the data extracted from experimental images in Chapter 4 for parametrisation. However, the discrete, 3-D nature of our model allows for a more rigorous comparison of simulation results with the experimental data than was possible with the earlier continuum models. Most significantly, because we now distinguish unperfused and perfused vessels, we compare only the perfused vasculature from numerical simulations with the experimentally derived vascular density profiles, which only show perfused vessels. The main results section, Section 7.4, is split into several parts, which address different aspects of our hybrid model's utility. In Section 7.4.1 we explain how we compare our hybrid model results with the experimental data of Chapter 4. Then, in Section 7.4.2 we use our model to investigate how accurately one may estimate the *in vivo* corneal vascular density from 2-D images, given that the neovasculature is actually a 3-D structure. Having shown that our model can capture quantitatively the dynamics of the *in vivo* system, we present representative results of 3-D simulations in Section 7.4.3 and compare the dynamics of the perfused vasculature with that of the vasculature as a whole (unperfused and perfused vessels) in Section 7.4.4. This provides insight into the validity of the comparison that we make in Chapters 5 and 6 between our continuum models of angiogenesis and the experimental data of Chapter 4. In Sections 7.4.5 and 7.4.6 we investigate, via a one at a time parameter sensitivity analysis, our abstract model of tip cell filopodia, and focus on the effect that dissecting the functionality of filopodia from tip cells has on the angiogenic response of the limbal vasculature when exposed to VEGF-A_{165}. We further extend our model to include key tip cell-ECM interactions in Sections 7.5- 7.7, and in Section 7.8 we simulate VEGF-A_{165} inhibition using our models. Finally, in Section 7.9 we summarise our results, discuss their implications and outline areas of future work.

7.2. Model development

The models presented in this chapter are composite hybrid models. As such, they utilise the advantages of both discrete and continuum modelling methodologies. Following Perfahl *et al.* (2011), we use an on-lattice, agent-based approach to model the evolution of vasculature. However, in contrast to Perfahl *et al.* (2011), who study angiogenesis in the context of a growing tumour, we study angiogenesis in a simpler and more controllable environment, the mouse cornea micropocket assay, for which quantitative data are available. In our hybrid models, as with the continuum models presented earlier in this thesis, angiogenesis, then, occurs in response to VEGF-A_{165} supplied by a slow-release pellet. The vasculature submodel incorporates vessel dematuration,

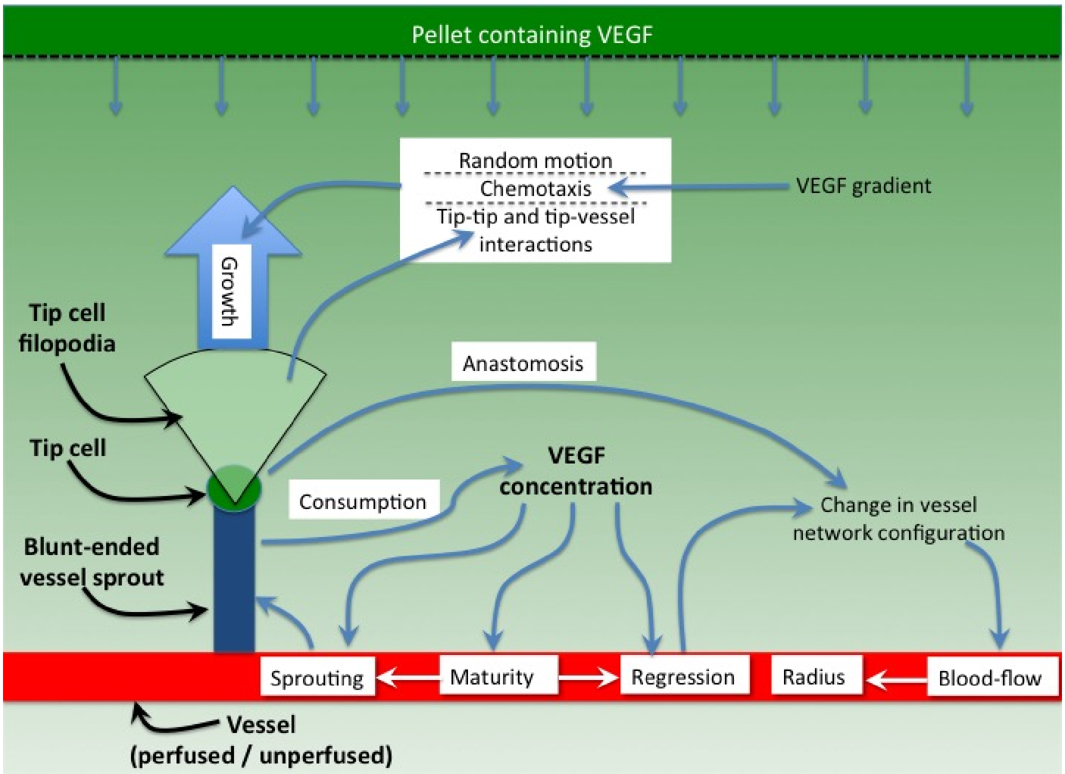

Figure 7.1.: Hybrid model overview and interactions diagram. VEGF-A is released from a pellet into the cornea, where it decays naturally and is consumed by vessels. Extracellular VEGF-A promotes vessel dematuration and sprouting. Tip cells at the leading front of new sprouts migrate up gradients of VEGF-A and undergo a small amount of random motion. A tip cell's motion is also also influenced by other nearby tip cells and vessels, which it senses by protruding filopodia into its local environment. Anastomoses form if tip cells collide with other tip cells or vessels. Additionally, immature vessels regress in low concentrations of VEGF-A. Both the formation of anastomoses and vessel regression affect blood-flow through the network, which, in turn, influences vessel diameters.

sprouting, growth and anastomosis. We also incorporate a simple model for the structural adaptation of the evolving vascular network in which flow through the network is calculated. This allows us to distinguish perfused and unperfused vessels. At the tissue level, initially we model the distribution of VEGF-A$_{165}$ via a reaction-diffusion equation.

In the remainder of this section we describe the model geometry and introduce the submodels which constitute our first discrete model of corneal angiogenesis: the vascular submodel and the VEGF-A$_{165}$ submodel. Additionally, we describe how the model is implemented computationally. A schematic of the major processes and interactions in our model is also presented in Figure 7.1. Emboldened in this figure are the biological entities included in our model: VEGF-A$_{165}$, tip cells, tip cell filopodia, vessels (perfused and unperfused) and sprouts. Vessels and sprouts both exist on a sliding scale of maturity.

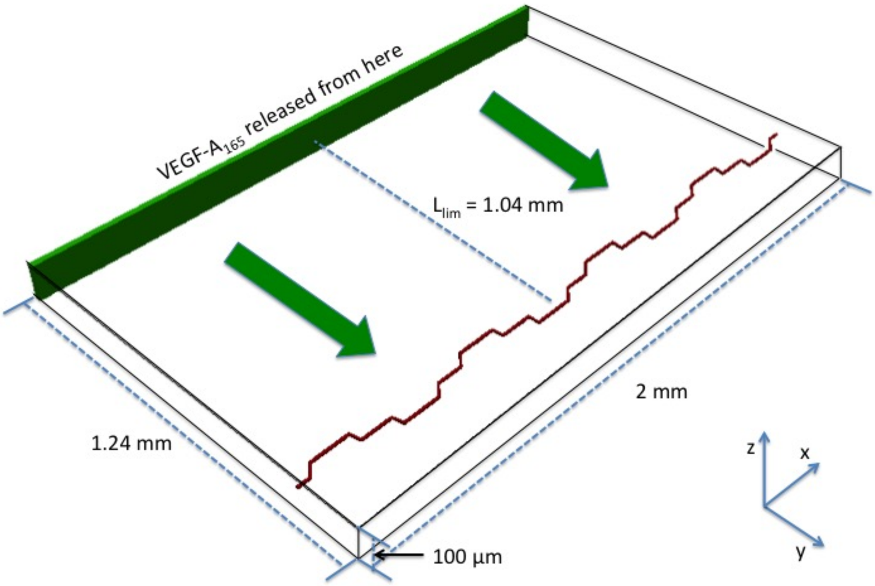

Figure 7.2.: Model geometry and initial configuration of the vascular network.

7.2.1. Model geometry

We consider a simplified 3-D Cartesian geometry; our model cornea is a cuboid in which $0 \leq x \leq 2\,\text{mm}$, $0 \leq y \leq 1.24\,\text{mm}$ and $0 \leq z \leq 100\,\mu\text{m}$. The boundary at $y = 1.24\,\text{mm}$ is identified with the edge of a VEGF-A$_{165}$-containing pellet (see Figure 7.2). The domain comprises locations as defined by a regular Cartesian lattice with lattice spacing $\Delta x = \Delta y = \Delta z = 20\,\mu\text{m}$. Associated with each location is a concentration of extracellular VEGF-A$_{165}$, which is dictated by the submodel presented in Section 7.2.3. Each location may also contain up to three vessel segments (each belonging to a different vessel) or a single tip cell. This permits the formation of bifurcations in simulated vascular networks, i.e. junctions between three vessels. For simplicity, vessel trifurcations are not permitted. For tip cell motion, we consider a Moore neighbourhood in three dimensions, i.e. a tip cell may move from its present location to any one of its twenty-six connected neighbouring locations (including diagonally connected neighbours). Tip cells may not pass though the domain boundaries, i.e. $x = 0$, $x = 1.24\,\text{mm}$, etc.

7.2.2. Vascular submodel

The model domain initially contains a single, mature limbal vessel which extends from $x = 0$ to $x = 2\,\text{mm}$. The location of segments along the vessel varies approximately sinusoidally in y and z with amplitude Δx. More explicitly, the coordinates of the limbal vessel segments, $(x_l,\, y_l,\, z_l)$, are given by the parametric equations

$$y_l = y_0 + A_y sin(2\pi f_y x_l), \tag{7.1}$$

$$z_l = z_0 + A_z sin(2\pi f_z x_l), \tag{7.2}$$

where $0 \leq x_l \leq 2\,\mathrm{mm}$. On average the vessel is located $40\,\mu\mathrm{m}$ from $z = 0$ ($z_0 = 40\,\mu\mathrm{m}$) and $1.04\,\mathrm{mm}$ from $y = y_{max} = 1.24\,\mathrm{mm}$ ($y_0 = 0.2\,\mathrm{mm}$). We fix $A_y = A_z = 16\,\mu\mathrm{m}$ and $f_y = f_z = 2\,\mathrm{mm}^{-1}$. When these co-ordinates are snapped to our on-lattice grid, this results in a vessel with tortuosity 1.12 (see Figure 7.2). The distance of the pellet to the limbus, L_{lim}, 1.04 mm, matches that estimated from experimental images in Chapter 4.

A pressure difference is prescribed across the limbal vessel and thus it is initially perfused. We denote the (arterial) input pressure by P_{in} and the (venous) output pressure by P_{out}. These pressures are maintained at fixed values throughout simulations. In the remainder of this section we describe separately the various elements of the vascular submodel which dictate how this simple vascular network evolves in response to VEGF-A$_{165}$.

7.2.2.1. Vessel maturity

Our model of vessel maturation and dematuration is similar to that adopted in Chapter 5: vessels demature in high VEGF-A$_{165}$ conditions and mature in low VEGF-A$_{165}$ conditions. However, instead of modelling maturity as a binary state, wherein a vessel segment is either mature or immature, maturity, m, is treated as a continuous variable between $m = 0$ (fully immature) and $m = 1$ (fully mature). The maturity of each vessel segment evolves according to the following ODE:

$$\frac{\partial m}{\partial t} = -\lambda_1^v \frac{v}{v + v_{\frac{1}{2}}} m + \lambda_2^v \frac{v_{\frac{1}{2}}}{v + v_{\frac{1}{2}}} (1 - m). \tag{7.3}$$

As in Chapter 5, v is the local extracellular concentration of VEGF-A$_{165}$, $v_{\frac{1}{2}}$ is the concentration of VEGF-A$_{165}$ at which VEGFR-2 receptors on ECs are half occupied, λ_1^v is the maximal rate of dematuration and λ_2^v is the maximal rate of maturation. Assuming Michaelis-Menten reaction-kinetics, dematuration occurs at a rate proportional to the fraction of bound VEGFR-2 receptors, while maturation occurs at a rate proportional to the fraction of unbound VEGFR-2 receptors. As stated above, we assume that initially ($t = 0$) the limbal vessel is fully mature ($m = 1$). New sprouts, forming after $t = 0$, are initially immature ($m = 0$).

7.2.2.2. Angiogenesis

As noted above, we adapt and extend the model of angiogenesis proposed by Perfahl *et al.* (2011). Our model incorporates the stochastic production of new vessel sprouts in the presence of VEGF-A_{165}, the growth of those sprouts and the formation of anastomoses. As in Perfahl *et al.* (2011), we employ a discrete version of the snail-trail approach, described in Chapter 3, to model the growth of a sprout. Thus, the dynamics of tip cells dictate the growth of vessel sprouts; stalk cells are not modelled explicitly but are assumed to proliferate, migrate and elongate at a rate sufficient to maintain a sprout which is contiguous with the parent vessel.

Sprouting New vessels may sprout from lattice sites occupied by a vessel segment. The probability that a new sprout emerges from an occupied lattice site in the time interval $[t,\, t+\Delta t]$ is given by P_{sprout}, where

$$P_{sprout} \quad = \quad P_{sprout}^{max} \triangle t\, L\, (1-m) \left(\frac{v}{v + v_{\frac{1}{2}}} \right). \tag{7.4}$$

P_{sprout}^{max} is the maximum probability of sprouting per minute per metre of vessel, and v, m and $v_{\frac{1}{2}}$ are as defined in (7.3). The length of the vessel segment under consideration, L, is variable since a vessel segment may have length Δx, $\sqrt{2}\Delta x$ or $\sqrt{3}\Delta x$ depending on its local orientation. As for vessel dematuration, the dependence of the sprouting rate on VEGF-A_{165} concentration is of Michaelis-Menten type.

We also impose several additional constraints on the probabilistic rule, (7.4). For example, sprout production from vessel network nodes is suppressed; sprouts may not form from arterial input nodes, venous output nodes, or those which belong to a network bifurcation. Additionally, we define an exclusion radius, R_{ex}, around each tip cell, inside which the formation of another sprout is not permitted. This rule accounts for the way in which Delta-Notch mediated lateral inhibition controls sprout spacing (see Chapter 2). When a new sprout forms the associated tip cell immediately moves from the location from which the sprout emerged, i (x_i, y_i, z_i), to a neighbouring location, j (x_j, y_j, z_j). The tip cell may not, however, move into a location already occupied by the vessel from which it has just emerged; it must move away from its parent vessel. It may also only move into a location, j, if there is sufficient space for it to move there[1]. While diagonal tip cell movement is allowed, a tip cell can not move diagonally if that would cause it to cross another vessel or sprout. Given that these three conditions are satisfied, the probability that

---

[1] As noted in Section 7.2.1, page 159, each lattice site may contain up to three vessel segments.

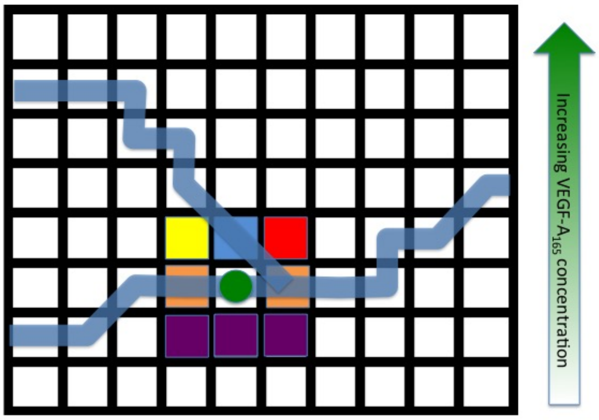

Figure 7.3.: Prohibited moves of a newly formed tip cell (green) are coloured purple, red and orange. See main text for details. Should the tip cell move into the blue square, occupied by another vessel, an anastomosis forms.

a new tip cell will move into a neighbouring site, j, is proportional to the magnitude of the local gradient of VEGF-A$_{165}$ in the direction $i \to j$, $\nabla_{i \to j} v$, if $\nabla_{i \to j} v > 0$ and zero otherwise. If the cumulative probability of a newly formed tip cell moving into a neighbouring site, j, is zero then the sprout fails to form. Figure 7.3 further illustrates the rules dictating sprout production in two dimensions. Sites highlighted in colour are those which constitute the Moore neighbourhood of a newly formed tip cell (green). The tip cell may not move into the purple sites since this would involve the tip cell moving down the VEGF-A$_{165}$ concentration gradient. It cannot move into the red site since it would cross another vessel, and may not move into the orange sites because the new sprout's parent vessel occupies these sites. Moves into the yellow and blue sites are permitted. If the tip cell moves into the blue site then an anastomosis forms. In this particular instance the tip cell is restricted in terms of where it can move, however, in a 3-D lattice there is greater flexibility.

Tip cell migration An empty lattice site only becomes occupied if a tip cell moves into that site. Tip cells perform a random walk, biased towards regions of high VEGF-A$_{165}$ concentration. As they move they leave behind them a vessel segment of length L in the site they previously occupied. Tip cell motion is also influenced by nearby vessels and nearby tip cells. In more detail, in the time interval $[t, t + \Delta t]$, the probability that a tip cell will move from site i (x_i, y_i, z_i) to site j (x_j, y_j, z_j), in the Moore neighbourhood of i, is given by

$$P_{ij} = \underbrace{\frac{\Delta t\, \mu}{k\, d_{ij}^2}}_{\text{random motion}} + \underbrace{\frac{\Delta t\, \chi}{k\, d_{ij}^2} \overbrace{\mathbb{R}\left(v_j - v_i\right)}^{\text{ramp function}}}_{\text{chemotaxis}} + \underbrace{\frac{\Delta t}{d_{ij}} \max\left(\delta_{ij}^{T-T}, \delta_{ij}^{T-V}\right)}_{\substack{\text{movement due to} \\ \text{tip}-\text{tip and tip}-\text{vessel} \\ \text{interactions}}}. \tag{7.5}$$

Here, d_{ij} is the distance between sites i and j, μ is the random motility coefficient and χ is the chemotaxis coefficient. $\mathbb{R}(v_j - v_i)$ is the ramp function defined as

$$\mathbb{R}(v_j - v_i) = \begin{cases} v_j - v_i & \text{if} \quad v_j - v_i > 0 \\ 0 & \text{otherwise.} \end{cases} \tag{7.6}$$

In (7.5), k is a constant, discussed further in Section 7.3. δ_{ij}^{T-T} and δ_{ij}^{T-V} are phenomenological interaction terms which account for the attraction tip cells feel towards nearby tip cells and vessels, respectively (details below).

The terms δ_{ij}^{T-T} and δ_{ij}^{T-V} are motivated primarily by the observation that, during angiogenesis *in vivo*, tip cells extend filopodia in their direction of migration allowing them to sense gradients in chemoattractants like VEGF-A$_{165}$ (Gerhardt 2003). Filopodia also allow tip cells to sense nearby cells and vessels, and, as such, facilitate EC migration and the formation of anastomoses (Phng *et al.* 2013). In our model, we focus on how filopodia facilitate anastomoses. We suppose that each tip cell, T_i, extends filopodia within a spherical sector, S_i, of radius r_f ahead of them. We further assume that each spherical sector, S_i, has a cone angle of θ_f. θ_f then corresponds to the range of angles over which tip cells extend filopodia. In what follows, we refer to S_i as a tip cell's *region of interaction* (see Figure 7.4 for an illustration in three dimensions).

We assume that tip cells tend to increase their rate of migration in the direction of vessel segments, ρ_k, which fall within its region of interaction by an amount F_{ρ_k}. For a vessel segment located a distance of r_{ρ_k} and at an angle of θ_{ρ_k} from the direction in which the tip cell last moved, we suppose that F_{ρ_k} is given by

$$F_{\rho_k} = K_\rho \left(1 - \frac{\theta_{\rho_k}}{\theta_f}\right) \left(1 - \frac{r_{\rho_k}^2}{r_f^2}\right), \tag{7.7}$$

where the constant K_ρ quantifies the maximum increase in migration rate due to tip-vessel interactions. For simplicity, we assume that such tip-vessel interactions bias tip cells to move

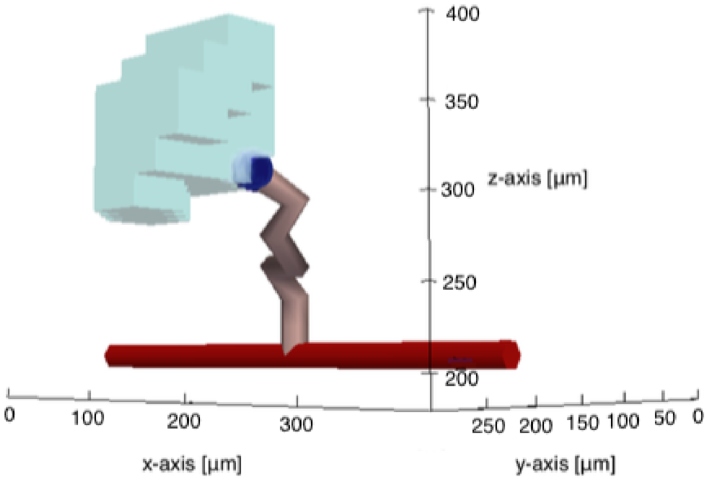

Figure 7.4.: A region of interaction (depicted in green) surrounding a tip cell (blue), representing the region of space explored by filopodia. Tip cells are attracted to vessels falling within this interaction volume. Tip cells are also attracted towards each other if their regions of interaction overlap. Here, $r_f = 100\,\mu m$ and $\theta_f = 60^o$.

into the neighbouring site, j, which minimises the distance between the tip cell and the vessel segment to which the tip cell is attracted. Thus, vessel segments within a well-defined volume of the region of interaction, Ω_j, contribute to the probability that a tip cell will move in a particular direction, $i \rightarrow j$. Figure 7.5a shows an example of such a tip-vessel interaction in two dimensions. The tip cell, (green) is attracted to the vessel segment (orange) which falls within its region of interaction (pale green). On our discrete lattice, the tip cell feels an attraction towards the red site. We assume that a tip cell's filopodia can not reach through or around vessels. Thus, if multiple vessels, ρ_k, fall within the same volume, Ω_j, only the vessel segment which is closest to the tip cell (in a particular direction) influences its motion. In summary, δ_{ij}^{T-V} is given by

$$\delta_{ij}^{T-V} = \max_{\rho_k \in \Omega_j} \left(F_{\rho_k}\right). \tag{7.8}$$

Ω_j contains the locations $\mathbf{x} \in S_i$ for which

$$\min_{\mathbf{x_s} \in nbhd} \left(|\mathbf{x} - \mathbf{x_s}|\right) = |\mathbf{x} - \mathbf{x_j}|, \tag{7.9}$$

where $nbhd$ contains the sites, $\mathbf{x_s}$, belonging to the Moore neighbourhood of the tip cell, T_i, and $\mathbf{x_j} \in nbhd$.

Tip cells are also able to sense each other; they are attracted to each other if their regions of interaction overlap (see Figure 7.5b). We consider the motion of one tip cell, T_i, at a time for simplicity. If T_i's region of interaction overlaps with the region of interaction of another tip cell, say T_k, then the tip cell tends to increase its rate of migration towards the centre of the region of

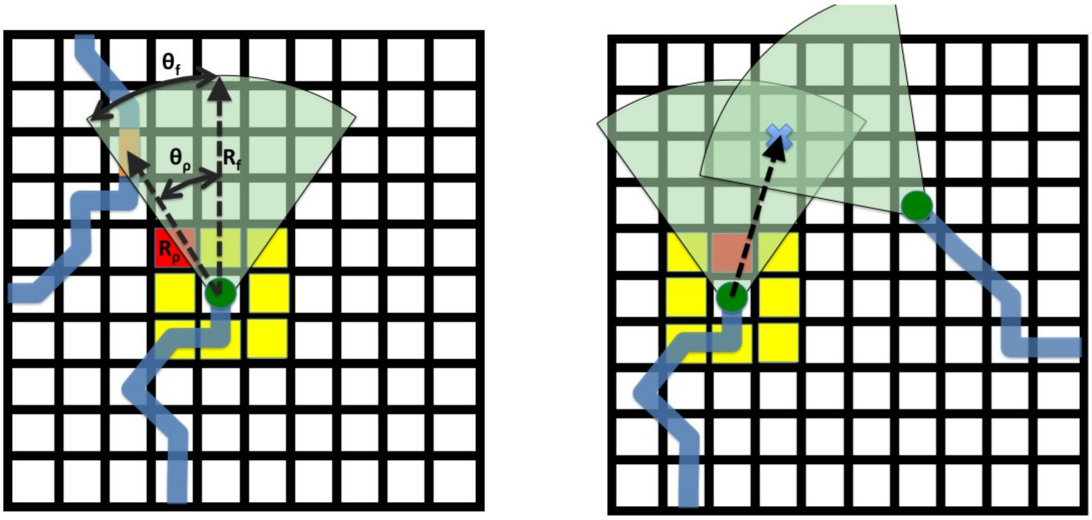

(a)

(b)

Figure 7.5.: Simplified 2-D schematics of tip-vessel and tip-tip interactions. Tip cells are green; coloured sites highlight the Moore neighbourhood of the tip cell of interest; regions of interaction are pictured in light green. (a) Vessel segments which fall within a tip cell's region of interaction (e.g. the orange segment, here) contribute to the probability that the tip cell will move into the neighbouring site which minimises the distance between the tip cell and the segment (highlighted red). (b) Tip cells whose regions of interaction overlap attract each other. Such interactions contribute to the probability that the tip cell of interest will move into the neighbouring site which minimises the distance between the tip cell of interest and the centre of the overlapping region (again highlighted red).

overlap, c_{ik}. The increase in the rate of migration towards c_{ik} is given by F_{T_k}, which we assume is proportional to the volume of the region of overlap between the two regions of interaction. More explicitly,

$$F_{T_k} = K_T \frac{\sum \phi_i \phi_k}{\sum \phi_i}, \tag{7.10}$$

where K_T is a constant quantifying the maximum increase in migration rate due to tip-tip interactions and where we define

$$\phi_i = \begin{cases} 1 & \text{inside } S_i, \\ 0 & \text{otherwise.} \end{cases} \tag{7.11}$$

In our on-lattice model, for simplicity, tip-tip interactions bias a tip cell's motion towards the neighbouring site, j, which minimises its distance to the centre of the region of overlap, c_{ik}. As for tip-vessel interactions, only the tip cell, T_k, which imparts the change in migration rate on T_i

in a given direction, $i \to j$, influences its motion. Finally, δ_{ij}^{T-T} is given by

$$\delta_{ij}^{T-T} = \max_{c_{ik} \in \Omega_j} \left(F_{T_k} \right). \tag{7.12}$$

As with the rules for sprouting, several constraints are appended to the probabilistic rule for tip cell motion, (7.5). As before, a tip cell can not move diagonally if that would cause it to cross another vessel or sprout, nor can it move into a location in which there is not sufficient room for it to move. Additionally, tip cells may not move back into the location from whence they directly came. Figure 7.6 exhibits such prohibited moves in two dimensions.

Formation of anastomoses In order for blood to flow in a newly formed vessel it must first form a connection with another vessel and, in so doing, establish a pressure difference across its two ends. As stated above, an anastomosis event occurs when a tip cell moves into a location which is already occupied by a vessel segment or another tip cell.

7.2.2.3. Vessel regression

Immature vessels are pruned from the network when exposed to low concentrations of VEGF-A$_{165}$. The probability that a vessel is removed from the network in the time interval $[t,\, t + \Delta t]$ is given by:

$$P_R = (1 - \bar{m})\, \Delta t \, \frac{v_{\frac{1}{2}}}{\bar{v} + v_{\frac{1}{2}}}, \tag{7.13}$$

where $\bar{m}$ and $\bar{v}$ are the mean maturity and concentration of VEGF-A$_{165}$ along the vessel, respectively.

7.2.2.4. Structural adaptation and blood flow

Structural adaptation refers to an acute, as opposed to chronic, form of vascular remodelling whereby the radius of each vessel changes in response to various stimuli. This is a complex process, whose details are not yet fully understood. As noted in Section 3.3.1.2, several models of angiogenesis and vascular tumour growth account for this phenomenon by adapting the model of structural adaptation formulated by Pries *et al.* (1990; 1994; 1998; 2001). Our preliminary investigations highlighted several issues with simple versions of this model which make them inappropriate for our present model. Primarily, in the absence of long-distance up- and down-stream stimuli, the algorithm is unstable for some configurations of vascular networks, and leads to the formation of vascular shunts.

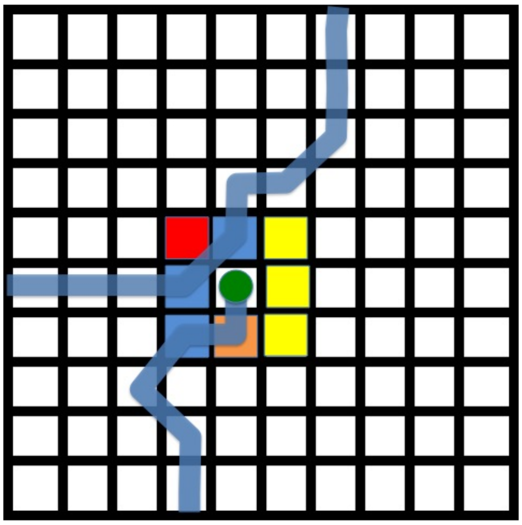

Figure 7.6.: Prohibited moves of a tip cell (green) are coloured red and orange. Sites highlighted in colour constitute the Moore neighbourhood of the tip cell (green) on a 2-D regular lattice. The tip cell may not move into the red site since it would cross another vessel, and it may not move into the orange site because it just moved out of that site. Moves into the yellow and blue sites are permitted and if the tip cell moves into one of the blue sites then an anastomosis forms.

In the absence of appropriate experimental data against which to compare our model simulations, we employ a simplified structural adaptation algorithm in which vessel radii take one of two values, R_{min} or R_{max}. Vessels which support blood flow have radius R_{max} whereas those in which blood flow is absent (e.g. blunt ended sprouts), have radius R_{min}. Once vessel radii have been prescribed, blood flow through the network is calculated using the Poiseuille approximation and conservation of mass at each node in the vessel network. The boundary inflow and outflow pressures are P_{in} and P_{out}, respectively. Following Owen *et al.* (2011), those vessels sustaining flow possess haematocrit levels equal to the inflow haematocrit, $H = H_{in}$, while vessels lacking flow have $H = 0$. After the flow and haematocrit levels have been calculated the vessel radii are updated. In general, the updated vessel radii and haematocrit levels affect the flow rates of plasma through the vessels. Thus, following Pries *et al.* (1990; 1994; 1998; 2001), at each time-step the calculation of flow rates, haematocrit levels and radii are iterated until the maximum proportional change in vessel radius is less than a pre-defined tolerance level, $RELTOL$. In practice, for sensible values of $RELTOL$ ($RELTOL < 1 - \frac{R_{min}}{R_{max}}$), the simplicity of our algorithm means that calculations are iterated at most twice at each time-step. This ensures that the flow rates correlate with the newly prescribed vessel radii, given our assumption of Poiseuille flow. Note, however, that since we do not model shear stress mediated vessel regression, the magnitudes of the flow rates do not affect model results. We adhere to the iterative structure proposed by

Pries *et al.* primarily to ensure model extensibility. It is trivial within our modelling framework (Chapter C) to use Pries *et al.*'s (1990; 1994; 1998; 2001) more detailed algorithm to calculate vessel radii. Alarcón *et al.* (2003) present further details of the original Pries *et al.* algorithm, including details of how to calculate blood flow through the network.

7.2.3. VEGF-A$_{165}$ release and transport submodel

In our hybrid model, VEGF-A$_{165}$ release and transport are modelled by extending the model presented in Chapter 5. The evolution of the VEGF-A$_{165}$ concentration in our computational domain depends on diffusion, natural decay, uptake by ECs and drainage through the vasculature. Using these assumptions, we propose the following PDE for the evolution of the VEGF-A$_{165}$ concentration, $v(x, y, z, t)$:

$$\frac{\partial v}{\partial t} = \underbrace{D_v \nabla^2 v}_{\text{diffusion}} - \underbrace{\lambda_v v}_{\substack{\text{natural}\\\text{decay}}} \underbrace{- \sum_{\substack{\text{perfused}\\\text{vessels}}} 2\,\pi\, R_p \overbrace{\frac{L_p}{\Delta x^3}}^{\substack{\text{perfused vessel}\\\text{length density}}} P_v (v - v_{blood})}_{\text{uptake by pefused vessels}} - \underbrace{\sum_{\text{vessels}} K^v_{EC} \overbrace{\frac{\nu\, L}{\Delta x^3}}^{\substack{\text{EC}\\\text{density}}} \frac{v}{v + v_{\frac{1}{2}}}}_{\text{uptake by ECs}} . \quad (7.14)$$

Here, D_v is the assumed constant diffusion coefficient for VEGF-A$_{165}$ in the corneal stroma, λ_v is the assumed constant rate of natural decay, P_v is the permeability of the vessels to VEGF-A$_{165}$ and K^v_{EC} is the maximal rate at which ECs uptake VEGF-A$_{165}$. As above, L is the length of a vessel segment (perfused or unperfused) within a given voxel. $\sum \frac{L}{\Delta x^3}$ is then the local vessel length density. Defining ν as the number of ECs per metre of vessel, $\sum \frac{\nu L}{\Delta x^3}$ is the local density of ECs. Note that, in contrast to the model outlined in Chapter 5, VEGF-A$_{165}$ is only drained by perfused vessels. That is, R_p and L_p are, respectively, the radius and length of perfused vessel segments within a given voxel.

Initially our model cornea contains no VEGF-A$_{165}$, so that:

$$v(x, y, z, 0) \quad = \quad 0, \qquad (7.15)$$

for $0 \le x \le x_{max}$, $0 \le y \le y_{max}$ and $0 \le z \le z_{max}$, and VEGF-A$_{165}$ is released into the model domain via a time-dependent boundary condition at $y = y_{max}$ ($0 \le x \le x_{max}$ and $0 \le z \le z_{max}$), reflecting the release of a finite amount of VEGF-A$_{165}$ from a pellet. For simplicity, no flux boundary conditions for v are imposed on all other domain boundaries. In summary, the following boundary conditions are used to close (7.14):

$$D_v \left.\frac{\partial v}{\partial x}\right|_{x=0} = 0, \quad D_v \left.\frac{\partial v}{\partial x}\right|_{x=x_{max}} = 0, \quad D_v \left.\frac{\partial v}{\partial z}\right|_{z=0} = 0, \quad D_v \left.\frac{\partial v}{\partial z}\right|_{z=z_{max}} = 0,$$

$$D_v \left.\frac{\partial v}{\partial y}\right|_{y=0} = 0, \quad -D_v \left.\frac{\partial v}{\partial y}\right|_{y=y_{max}} = -k_p^v \left(\frac{[V_T]}{\theta_v} - \bar{v}|_{y=y_{max}} \right), \tag{7.16}$$

where the evolution of $[V_T]$ is described by

$$\frac{d[V_T]}{dt} = -\lambda_p^v \frac{[V_T]}{\theta_v} - \frac{\zeta_p k_p^v}{\Omega_p} \left(\frac{[V_T]}{\theta_v} - \bar{v}|_{y=y_{max}} \right). \tag{7.17}$$

In (7.17) $\bar{v}|_{y=y_{max}}$ denotes the average concentration of VEGF-A$_{165}$ on $y = y_{max}$.

7.2.4. Computational algorithm

Simulations begin at time $t = 0$ and terminate at $t = t_{end} = 5$ days. The main steps involved in our simulation procedure can be summarised as follows (see also the flowchart in Figure 7.7):

1. Initialise system ($t = 0$):
   a) Stochastic components of our model include vessel sprouting, tip cell migration and vessel regression. We use a pseudo-random number generator to implement such stochastic behaviours; in particular, we use the Mersenne Twister algorithm (Matsumoto and Nishimura 1998). To ensure that different simulations do not produce identical results, the random number generator is initialised with a unique seed for each simulation.
   b) The vascular network is initialised as shown in Figure 7.2.
   c) The structural adaptation algorithm is executed, i.e. blood flow through the vascular network and the radii of the vessels are calculated.
   d) Our model cornea initially contains no VEGF-A$_{165}$.
2. The VEGF-A$_{165}$ distribution is calculated. The time-dependent problem, (7.14)-(7.17), is solved using the PETSC Time-Stepper (TS) library (Balay *et al.* 2012). We discretise (7.14)-(7.17) with respect to spatial variables, using (central) finite differences, reducing our PDE to a system of ODEs. We use the TS library's built-in backward Euler method to integrate the resulting ODEs over the time interval $[t, t + \Delta t]$.
3. The angiogenesis submodel is executed:

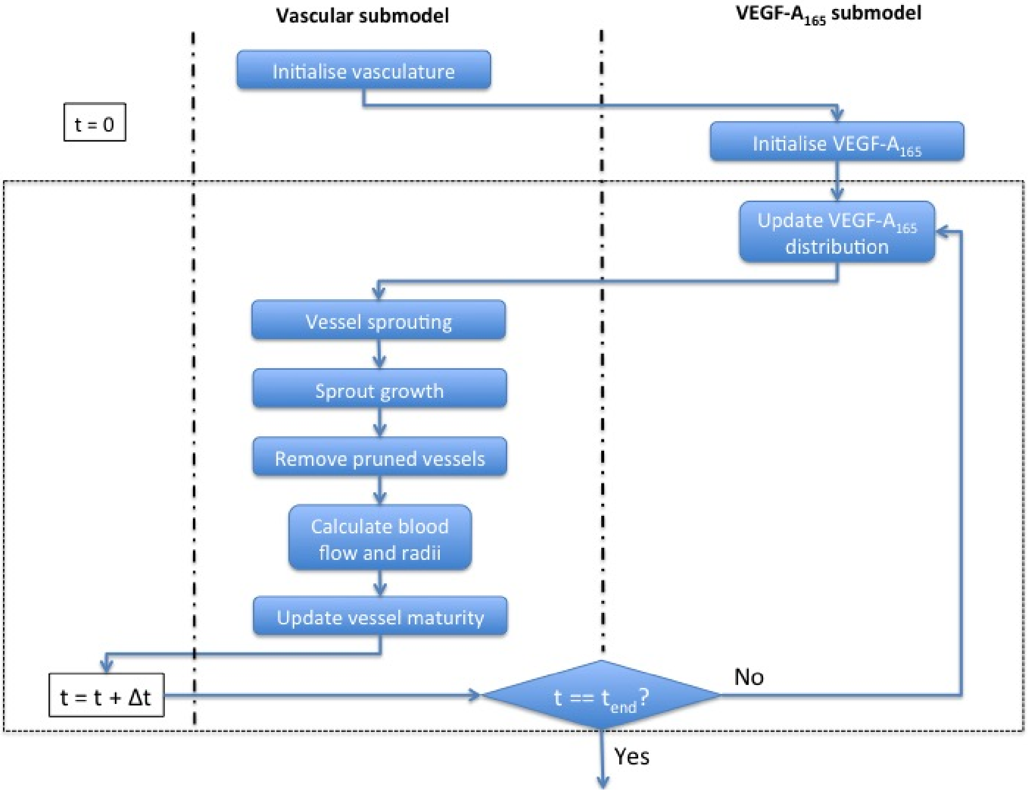

Figure 7.7.: Flowchart showing the sequence of computational steps used to simulate the hybrid model. See main text for details.

a) VEGF-A$_{165}$ entering the computational domain from $y = y_{max}$ stimulates the formation of new vessel sprouts. We loop over each location in our spatial lattice. New vessel sprouts may form at lattice sites containing a vessel segment according to the rules outlined in Section 7.2.2. If a tip cell moves into a lattice site which already contains a vessel then an anastomosis forms. We check for these instances whenever a new sprout is formed. Newly formed sprouts are not allowed to further extend in the time-step in which they are created.

b) We iterate through each pre-existing vessel sprout which is attached to an actively migrating tip cell. Tip cells move and thus sprouts grow according to the rules defined in Section 7.2.2. We check for anastomosis formation whenever a tip cell migrates.

4. The vessel regression model is executed. Immature vessels exposed to low levels of VEGF-A$_{165}$ are removed from the network.
5. Blood flow through the new network configuration is calculated and the vessel radii are updated using our simplified structural adaptation algorithm.
6. The maturity of each vessel segment is updated using (7.3). We solve the ODE over the time interval $[t, t + \Delta t]$ using the SUNDIALS CVODE solver (Cohen and Hindmarsh 1996).

7. The simulation time, t, is incremented by Δt.
8. Steps 2 - 7 are repeated until $t = t_{end}$.

7.2.5. Model implementation

It was clear from our review in Chapter 3 that existing hybrid models of tumour-induced angiogenesis are often extended or adapted to investigate new hypotheses or mechanisms. However, extending the code which implements these models has generally been done in an *ad hoc* way, since code is rarely developed with extensibility (or understandability) in mind. Recognising that this is a problem within the angiogenesis modelling community, which is only likely to get worse as these models become more detailed, significant efforts were devoted to code development in the course of this thesis. Specifically, we built an object-oriented modelling framework to facilitate the extensibility and adaptability of hybrid models of angiogenesis and vascular tumour growth. Its design was motivated by the family of related hybrid models to which the model of Perfahl *et al.* (2011) belongs (Alarcón *et al.* 2003; Alarcón *et al.* 2005; Alarcón *et al.* 2006; Betteridge *et al.* 2006; Owen *et al.* 2009; Perfahl *et al.* 2011) since they employ a range of interchangeable algorithms to model various behaviours associated with tumour-induced angiogenesis at multiple biological scales. The models presented in this chapter are implemented in our object-oriented modelling framework.

In Appendix C we present our framework in full and outline how object-orientation and object-oriented design patterns have been used to facilitate code understandability, adaptability and maintainability. Another useful by-product of the modular way in which the modelling framework has been implemented is that it is easy to deconstruct models into their component parts so that they may be individually tested, analysed, further developed and validated. In Appendix E we present the results of a number of tests performed within our framework which verify that important elements of the model presented above are correctly and accurately implemented.

7.3. Parameter value estimation

Since our hybrid model is based on the continuum model of Chapter 5, we use parameter values from the continuum model parameters as a starting point for estimating parameters in our hybrid model. Parameter values were then subsequently tuned so that simulation results were consistent with data extracted from VEGF-A$_{165}$ experiments in Chapter 4. This significantly reduced the number of simulations performed to identify parameter values which reveal that our hybrid model can capture quantitatively the dynamics of the *in vivo* system.

Table 7.1 lists parameters associated with the model geometry. As in Chapter 5, the distance between the pellet (at $y = y_{max}$) and the limbus, L_{lim}, was estimated by analysing the experimental images (Chapter 4). The thickness of our model domain, z_{max}, corresponds to the thickness of the corneal stroma, which in mice is approximately $100\,\mu$m (Zhang *et al.* 1996; Song *et al.* 2003). We choose $x_{max} = 2\,$mm so that sufficient sprouts form along the length of the limbus to provide results representative of the *in vivo* system. L_{lim} imposes a lower bound on y_{max} (see Figure 7.2). Further to that, y_{max} is chosen such that the no-flux boundary conditions imposed on the VEGF-A$_{165}$ distribution at the $y = 0$ boundary do not significantly effect simulation results. Decreasing y_{max} to, say, $y_{max} = L_{lim} + \Delta x$ increases the concentration of VEGF-A$_{165}$ at the limbus. Choosing $y_{max} > L_{lim} + \Delta x$ better approximates the situation *in vivo*, in which VEGF-A$_{165}$ diffuses past the limbus and into the sclera. $\Delta t = 10\,$minutes was chosen such that the cumulative probability that a tip cell moves to one of its neighbouring sites is never greater than 1 (see Equation (7.5)).

Parameters in (7.14), which dictate the distribution of VEGF-A$_{165}$ inside the model domain, were estimated from published data in Chapter 5. Estimates for λ_p^v, Ω_p, ζ_p and $[V_T]_{init}$ are also as stated in Chapter 5. In the absence of suitable experimental data, we manually tuned other parameters associated with the controlled release of VEGF-A$_{165}$ from the pellet so that simulation results were in good agreement with the VEGF-A$_{165}$ data in Chapter 4. In particular, we fixed $\theta_v = 30$ and $k_p^v = 1.12 \times 10^{-7}\,h^{-1}$. These values are lower than those used in the continuum model (we discuss this briefly in Section 7.4). Table 7.2 summarises the default values used for parameters associated with the VEGF-A$_{165}$ submodel (Section 7.2.3).

The maximal rate of maturation, λ_2^v, is fixed at $0.0005\,\mathrm{h}^{-1}$, as in Chapter 5. This ensures that numerical results are consistent with the observation that little maturation occurs in VEGF-A$_{165}$ experiments. The value of λ_1^v, the maximal rate of dematuration, is marginally smaller than that used in the continuum model: $\lambda_1^v = 0.07\,\mathrm{h}^{-1}$ (vs $0.08\,\mathrm{h}^{-1}$ in Chapter 5).

Following Owen *et al.* (2011), we fix $P_{in} = 25\,\mathrm{mm\,Hg}$ and $P_{out} = 15\,\mathrm{mm\,Hg}$, noting that simulation results are independent of these values (as long as $P_{in} > P_{out}$ so that a pressure difference exists across the network). As in Chapter 5, we assume a value of $5\,\mu m$ for the radius of perfused vessels, R_{max}, and since simulation results are insensitive to the value taken by R_{min}, the radius of unperfused vessels, we fix $R_{min} = 2\,\mu m$. Without loss of generality, we also fix

Parameter	Description	Default value and units	Sources
L_{lim}	Distance of pellet from limbal vessels.	1.04×10^{-3} [m]	Image analysis (Chapter 4)
Δt	Time step.	10 [mins]	–
Δx	Lattice spacing.	20×10^{-6} [m]	–
x_{max}	Width of model domain.	2×10^{-3} [m]	–
y_{max}	Length of model domain.	1.24×10^{-3} [m]	–
z_{max}	Thickness of model domain; thickness of cornea.	100×10^{-6} [m]	(Zhang *et al.* 1996; Song *et al.* 2003)

Table 7.1.: List of parameters associated with model geometry and running simulations.

$RELTOL = 1 \times 10^{-4}$ $(< 1 - \frac{R_{min}}{R_{max}})$, as in Owen *et al.* (2009). We also fix $H_{in} = 0.45$ as in Owen *et al.* (2011); the structure of our model dictates that simulation results are not sensitive to changes in H_{in}.

The dynamics of vessel sprouting in our hybrid model are much more complex than in our continuum model of Chapter 5. Thus, we relied on manually tuning P^{max}_{sprout} and R_{ex} to estimate their values. We found that fixing $P^{max}_{sprout} = 590$ sprouts per minute per metre of vessel and $R_{ex} = 60\,\mu m$ yielded results which are consistent with the experimental data from Chapter 4.

Isolated tip cells (ones not attached to a vessel sprout or in the vicinity of other tip cells or vessels) move according to a modified set of rules. That is, (7.5) simplifies to

$$P_{ij} = \frac{\Delta t\,\mu}{k\,d_{ij}^2} + \frac{\Delta t\,\chi}{k\,d_{ij}^2}\,\mathbb{R}\left(v_j - v_i\right). \tag{7.18}$$

In the continuum limit (Δt, $\Delta x \to 0$), for this probability of movement on a Moore neighbourhood in three dimensions, taking $k = \frac{26}{6}$, tip cells move according to the diffusion-chemotaxis equation:

$$\frac{\partial n}{\partial t} = \mu \nabla^2 n - \chi \nabla.\left(n \nabla v\right), \tag{7.19}$$

where $n = n(x, y, z, t)$ denotes the tip cell density. In one dimension, (7.19) describes the movement of tip cells in our continuum model of Chapter 5, where μ and χ are the macroscopic random motility coefficient and chemotactic sensitivity, respectively. Thus, to simplify the definition of χ and μ in our hybrid model, we fix $k = \frac{26}{6}$. The value of k depends on the number of dimensions in which a tip cell is moving and the type of neighbourhood, which dictates the number of different directions in which a tip cell may move. We explain how we derive (7.19) from (7.18) in Appendix D. In our continuum model, random motion ($\mu > 0$) was introduced to account for the fact that chemotaxis is not the only mechanism driving tip cell motion, and may account for some of the apparent randomness associated with tip cell motion;

Parameter	**Description**	**Default value and units**	**Sources**
D_v	Diffusion constant for VEGF-A$_{165}$ in cornea.	2.52×10^{-7} [m^{2}h^{-1}]	(Chen *et al.* 2006; MacGabhann 2005; Ambrosi *et al.* 2005; Swabb *et al.* 1974).
λ_v	Natural decay constant of VEGF-A$_{165}$.	0.8 [h^{-1}]	(Serini *et al.* 2003; Chen *et al.* 2006).
K^v_{EC}	Maximum rate of reduction in molar VEGF-A$_{165}$ concentration per unit EC density due to VEGFR-2 binding.	4×10^{-22} [moles of VEGF$_{165}$ h^{-1}cell^{-1} litre^{-1} m^3]	(Wang *et al.* 2002; MacGabhann and Popel 2003; Bikfalvi *et al.* 1991).
$v_{\frac{1}{2}}$	Concentration of VEGF-A$_{165}$ at which VEGFR-2 receptors are half occupied.	6.5×10^{-10} [M]	(Akeson *et al.* 2010; Wang *et al.* 2002)
ν	Number of ECs per metre of vessel.	1.2×10^{-5} [cells m^{-1}]	(Tong and Yuan 2008a)
P_v	Permeability of corneal vasculature to VEGF-A$_{165}$.	3×10^{-4} [m h^{-1}]	(Fu and Shen 2003; Stefanini *et al.* 2008).
v_{blood}	Concentration of VEGF-A$_{165}$ in the blood.	0 [M]	-
θ_v	Binding constant.	30	-
k^v_p	Effective permeability of the cornea-pellet boundary.	1.12×10^{-7} [m h^{-1}]	-
Ω_p	Volume of pellet.	1.7×10^{-11} [m^3]	Roche, Penzberg.
ζ_p	Surface area of pellet.	6.79×10^{-7} [m^2]	Roche, Penzberg.
λ^v_p	Natural decay constant of VEGF-A$_{165}$ in the pellet.	0.8 [h^{-1}]	Assume $\lambda_p = \lambda_v$.
$[V_T]_{init}$	Initial concentration of VEGF-A$_{165}$ in the pellet.	3.93×10^{-4} [M]	Roche, Penzberg.

Table 7.2.: List of parameters associated with the VEGF-A$_{165}$ submodel. All parameters listed here correspond directly to the parameters used in the continuum model of Chapter 5 (see Table 5.4). Rows highlighted red contain parameters whose values differ from those used in the continuum model.

$\mu = 7 \times 10^{-11}\,\mathrm{m}^2\,\mathrm{h}^{-1} = 1.1\dot{6} \times 10^{-12}\,\mathrm{m}^2\,\mathrm{min}^{-1}$ provided a good fit of numerical simulations to the data. In our hybrid model, the randomness associated with tip cell motion is partly accounted for by the model's stochastic nature. Additionally, tip-vessel and tip-tip interactions, in part, drive tip cell migration. Thus, the value of μ used in our hybrid model was reduced from $\mu = 1.1\dot{6} \times 10^{-12}\,\mathrm{m}^2\,\mathrm{min}^{-1}$ (in Chapter 5) to $\mu = 3 \times 10^{-15}\,\mathrm{m}^2\,\mathrm{min}^{-1}$. The default value of χ, the chemotactic sensitivity of tip cells, was also reduced. It is approximately five times smaller than that used in the equivalent continuum model: $\chi = 9.5 \times 10^{-9}\,\mathrm{m}^2\,\mathrm{min}^{-1}\,\mu\mathrm{M}^{-1}$ (versus $\chi = 5.75 \times 10^{-8}\,\mathrm{m}^2\,\mathrm{min}^{-1}\,\mu\mathrm{M}^{-1}$ in Chapter 5).

To produce results in good agreement with the experimental data we fixed $\gamma = 1.08 \times 10^{-4}\,\mathrm{min}^{-1}$. This value is 1.3−fold greater than that used in Chapter 5. Again we briefly discuss this change in parameter value in Section 7.4.

The parameter r_f represents the maximum probing distance of tip cell filopodia. The longest observed length of filopodia observed by Gerhardt (2003) was "$> 100\,\mu$m". Thus, we fixed $r_f = 120\,\mu$m. We assume that a tip cell extends filopodia in directions up to $\theta_f = 60^o$ away

Parameter	Description	Default value and units	Sources
λ_1^v	Maximal rate of vessel dematuration.	0.07 [h^{-1}]	–
λ_2^v	Maximal rate of vessel maturation.	0.0005 [h^{-1}]	–
R_{max}	Radius of perfused vessels.	5×10^{-5} [m]	(Tsai *et al.* 2009; Peebo *et al.* 2011)
R_{min}	Radius of unperfused vessels.	2×10^{-5} [m]	–
P_{in}	Arterial input pressure.	25 [mmHg]	(Owen *et al.* 2011)
P_{out}	Venous output pressure.	15 [mmHg]	(Owen *et al.* 2011)
H_{in}	Haematocrit level in perfused vessels.	0.45	(Owen *et al.* 2011)
$RELTOL$	Termination of the structural adaptation algorithm occurs when the maximum relative change in radii from one iteration to the next is less than $RELTOL$.	1×10^{-4}	(Owen *et al.* 2009)
P_{sprout}^{max}	Maximum probability of sprout formation per unit time per unit metre of vessel.	590 [min^{-1} (metre of vessel)$^{-1}$]	– .
R_{ex}	Radius of exclusion around tip cells.	60 [μm]	– .
χ	Chemotaxis coefficient for tip cells.	9.5×10^{-9} [m^2 min^{-1} μM^{-1}]	(Stokes and Lauffenburger 1991; Stokes *et al.* 1990; Balding and McElwain 1985; Byrne and Chaplain 1995; Addison-Smith 2010).
μ	Random motility coefficient for tip cells.	3×10^{-15} [m^2 min^{-1}]	(Sherratt and Murray 1990; Stokes *et al.* 1991; Kouvroukoglou *et al.* 2000; Addison-Smith 2010; Owen *et al.* 2011; Byrne and Chaplain 1995)
k	Constant dependent on the dimensionality of the model and the type of neighbourhood considered.	$\frac{26}{6}$	-
r_f	Maximum probing distance of tip cell filopodia.	120×10^{-6} [m]	(Gerhardt 2003)
θ_f	Maximum sensing angle of filopodia.	60 [°]	-
K_ρ	Constant quantifying maximum increase in tip cell migration rate due to tip-vessel interactions.	2.375×10^{-7} [m min^{-1}]	-
K_T	Constant quantifying maximum increase in tip cell migration rate due to tip-tip interactions.	1.615×10^{-7} [m min^{-1}]	-
γ	Maximal rate of regression of vessels in low VEGF-A$_{165}$.	1.08×10^{-4} [min^{-1}]	(Cao *et al.* 2003)

Table 7.3.: List of parameters relating to the vasculature submodel.

from the direction in which it is migrating. We found that vascular growth most accurately represents that seen *in vivo* if tip-tip and tip-vessel interactions are dominant in determining a tip cell's motion. Thus, K_ρ and K_t are given large values, $K_\rho = 2.375 \times 10^{-7}\,\mathrm{m\,min}^{-1}$ and $K_t = 1.615 \times 10^{-7}\,\mathrm{m\,min}^{-1}$, so that tip cells are strongly attracted to nearby vessels and each other. Typically, if the chemotactic sensitivity of tip cells, χ, is too high relative to the values of

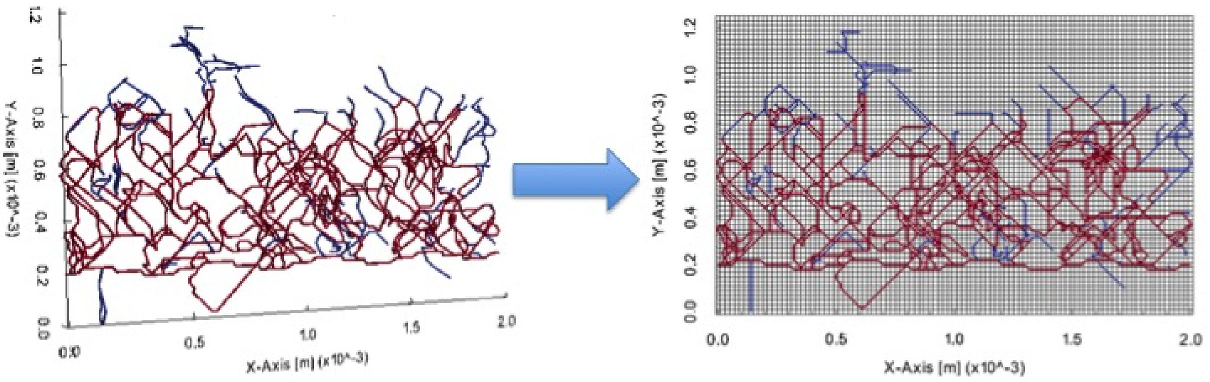

Figure 7.8.: Projection of a 3-D vascular network onto a 2-D grid for comparison with experimental data. Red vessels are perfused. Blue vessels are unperfused.

K_ρ and K_t then tip cells tend to migrate away from other vessels and up gradients in VEGF-A$_{165}$, resulting in relatively few anastomoses forming and the formation of underperfused vascular networks. Interestingly, in the total absence of chemotaxis, $\chi = 0$, we found that directed sprouting and tip-tip, tip-vessel interactions are sufficient to drive vascular growth towards the source of VEGF-A$_{165}$. This contrasts results presented by Stokes and Lauffenburger (1991), for example, whose model suggested that chemotaxis was an essential component of tip cell motion, which ensured that directed growth occurred towards the source of a chemoattractant. Table 7.3 summarises the parameter values associated with the vasculature submodel (Section 7.2.2).

7.4. Numerical results

In this section we present numerical results from simulations in which default parameter values were used (Tables 7.1-7.3). First, however, we describe how a fair comparison between experimental and simulated results was conducted for model parametrisation.

7.4.1. Comparison with experimental results

In Chapter 4 we estimated the vascular density at all locations between the limbus and the pellet from images captured during VEGF-A$_{165}$-induced angiogenesis experiments. The experimental images show a projection of a 3-D vascular network onto a 2-D plane. In such projections not all vessels are observable since some are obscured by vessels which are closer to the camera. Therefore, to perform a fair comparison, we project our computationally generated vessel networks onto the $x - y$ plane (see Figure 7.8). For each simulation, at each time point of interest ($t = 3\,$days and $t = 5\,$days), we count the number of lattice sites which are occupied by a vessel segment in our 2-D projections. We record the distance, y', of each occupied site from $y = 0.2\,$mm (the location

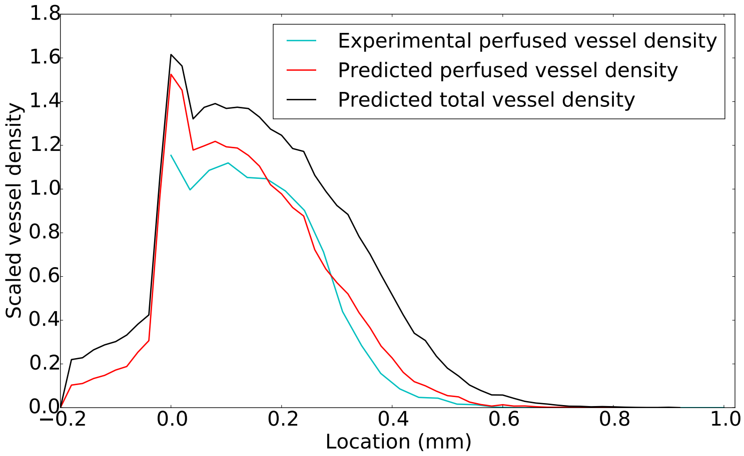

(a)

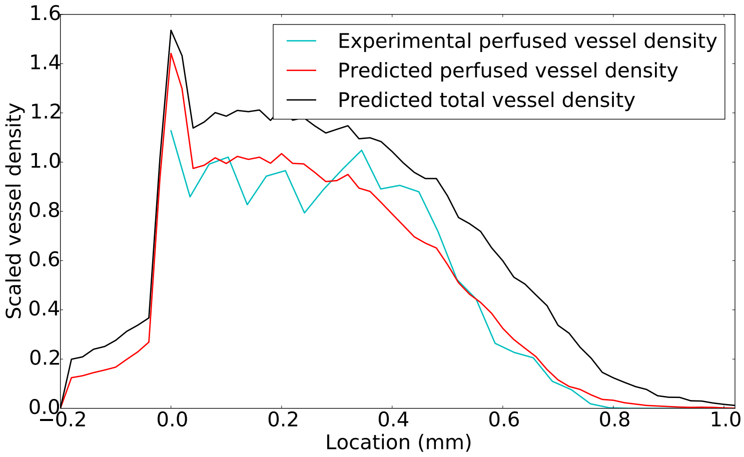

(b)

Figure 7.9.: 3-D vascular networks, resulting from simulations in which default parameters are used (Tables 7.1-7.3), are projected onto the $x-y$ plane and the average vessel density profiles from such projections are plotted against experimentally derived vessel density profiles. See main text for details. (a) Day 3 results. (b) Day 5 results. The vascular densities shown here are scaled ($\times 2 \times 10^8$ metre of vessel m^{-3}).

of the limbus) and also note whether each segment is perfused or not. For clarity, if the lattice sites at (x_1,y_1,z_1) and (x_1,y_1,z_2) in a 3-D simulated network are both occupied only one vessel segment is counted at the location (x_1,y_1) in our $x-y$ projection. We sum the contributions of occupied lattice sites along the x-direction in our projected networks. Consistent with our experimental analysis, since we do not know the true orientation of vessels in our projected networks, we ignore the orientation of vessel segments and assume that each occupied lattice site contributes a length Δx to the average vessel density at y'. As with our experimental analysis, we assume a thickness of $z_{max} = 100\,\mu m$. Figure 7.9 shows a comparison of the averaged vessel density profiles extracted from 2-D projections of simulated vessel networks ($N = 50$) and

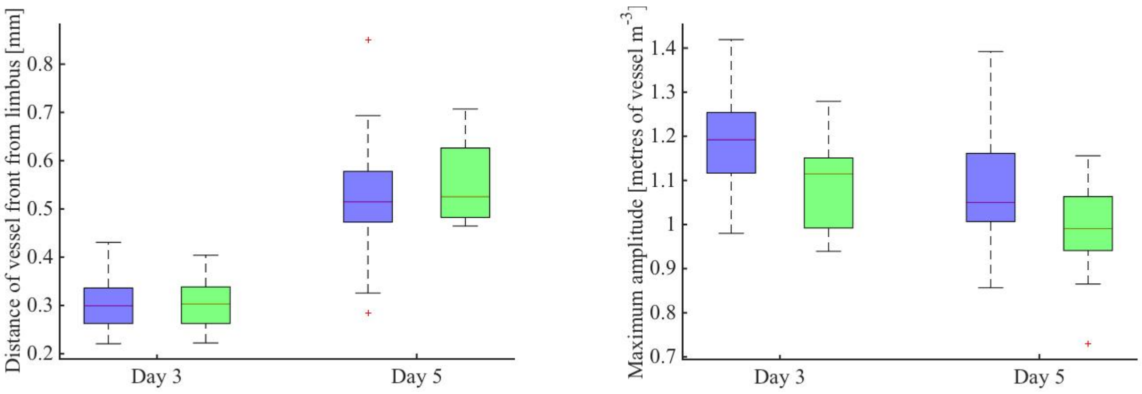

(a) (b)

Figure 7.10.: Summary statistics are extracted from individual simulations and experiments and compared. Blue bars show the distributions of summary statistics for simulated vascular networks, while green bars show those extracted from experimental images. (a) Distance of the perfused vascular front from the limbus. (b) Scaled maximum amplitude of the perfused vascular front ($\times 2 \times 10^8$ metre of vessel m^{-3}).

images of VEGF-A_{165} experiments ($N = 9$). We observe good quantitative agreement between experimental and simulated perfused vascular density profiles when default parameter values are used (Tables 7.1-7.3).

We also extracted summary statistics from 2-D projections of simulated vascular networks. In Figure 7.10 the location of the perfused vascular wavefront and the maximum amplitude of the perfused neovascular density at $t = 3$, 5 days are compared for experiments and simulations where default parameter values were used. For our default parameter values we observe good agreement between the summary statistics extracted from simulations and experiments when they are compared using the two-sample t-test and two-sample Kolmogorov-Smirnov test. When compared using the Kolmogorov-Smirnov test, for example, the amplitude of the perfused vascular density on day 5 and the location of the perfused vascular front on days 3 and 5 show excellent agreement ($p \gg 0.1$), while the other metric also shows reasonable agreement ($p > 0.04$). With further parameter tuning better agreement between simulations and experiments could likely be established. However, additional experimental data would be desirable before model parameters are tuned further. Note also that the stochastic nature of our model is sufficient to reproduce the variability in the summary statistics used to characterise the experimental data (see also Figure 7.13, which shows the range of perfused vessel densities observed across 50 simulations).

7.4.2. Recovery of 3-D density data

As noted in Section 7.4.1, some details of the 3-D *in vivo* vascular networks are lost when 2-D images of such structures are captured. For experimental images, these details are not recoverable. However, the 3-D structures from our simulated networks are available. Thus, our simulation results may provide insight into how much information is lost when we attempt to estimate the vascular density in cornea experiments using a 2-D image (and naively assume that each pixel contains a vessel segment of constant length, regardless of actual orientation). Figure 7.11 once again shows averaged vascular density profiles extracted from experimental images ($N = 9$) and simulations when default parameter values are used ($N = 50$). We show three alternate perfused vascular density profiles extracted from simulations:

1. A profile extracted from simulated networks which have been processed as outlined in Section 7.4.1.
2. A profile extracted from simulated networks which have been projected onto a 2-D plane, but where the orientation of vessel segments in that 2-D plane has been taken into account. For the 2-D projections each vessel segment may have length $L = \Delta x$ or $L = \sqrt{2}\Delta x$, depending on the segment's orientation in the projection.
3. A profile extracted from the unprojected, 3-D networks. In 3-D vessel segments may have length, $L = \Delta x$, $L = \sqrt{2}\Delta x$ or $L = \sqrt{3}\Delta x$, depending on the segment's local orientation.

When vascular density profiles are calculated from the 3-D networks, as well as recovering information about vessel segments which were hidden in the 2-D projections, we also recover information about the true orientation of vessel segments. For simulations in which default parameters are used, the perfused neovascular density (i.e. the density in regions of the vasculature which exclude the limbus) is almost two-fold greater (×1.8) when the 3-D networks are used rather than the 2-D projected networks where vessel orientation is ignored. If the orientation of vessels (as they appear in a 2-D projection) is considered only, then the discrepancy is less marked (×1.25 rather than ×1.8). Thus, our results suggest that estimating vascular density using 2-D images (and ignoring the local orientation of vessel segments) may result in a significant loss of information regarding the *in vivo* vascular density. The location of the vascular front is not significantly affected by whether projected or unprojected networks are used to assess vascular density.

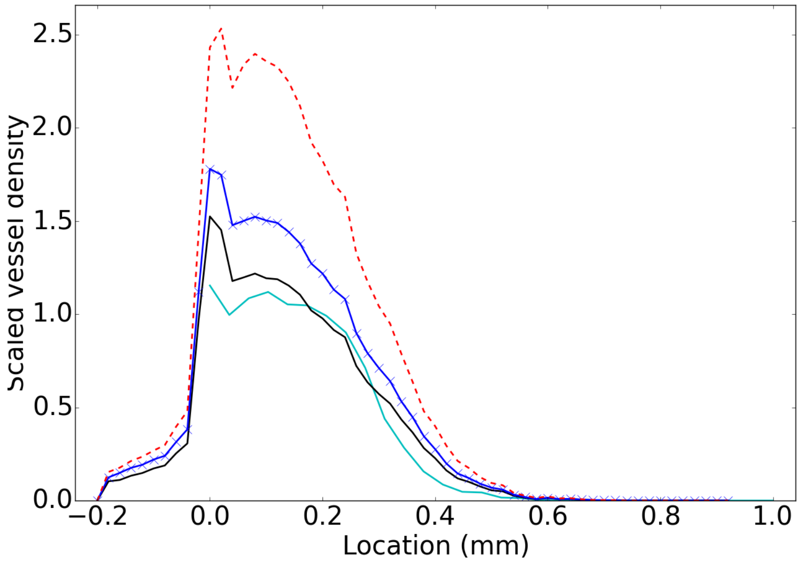

(a)

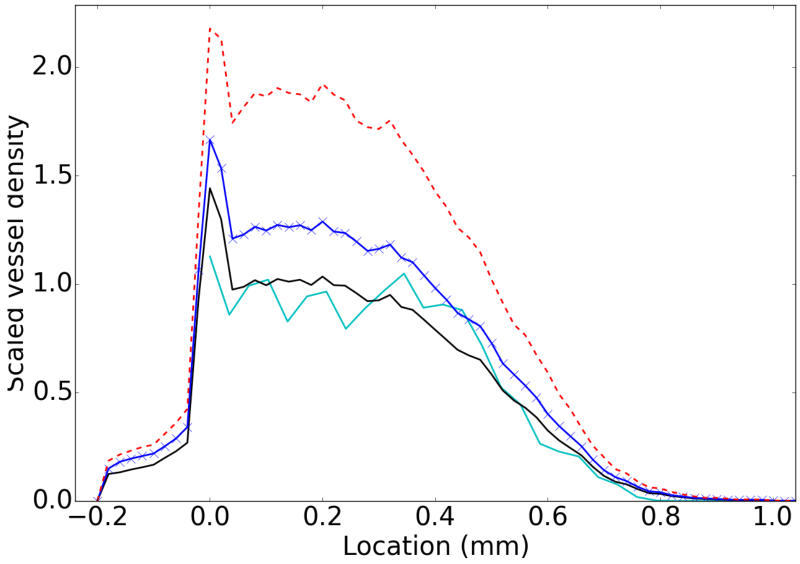

(b)

Figure 7.11.: Projected and unprojected vessel density profiles are compared with the experimental data. See main text for details. (a) Day 3 results. (b) Day 5 results. −: experimental (projected) perfused vessel density; −: simulated (projected) perfused vessel density (vessel segment orientation in the plane of the network projection is not taken into account in calculating the vascular density); − × −: simulated (projected) perfused vessel density (vessel segment orientation in the plane of the network projection is taken into account in calculating the vascular density); - -: simulated (unprojected) perfused vessel density (true vessel segment orientation is taken into account in calculating the vascular density). The vascular densities shown here are scaled ($\times 2 \times 10^8$ metre of vessel m^{-3}).

7.4.3. 3-D simulation results

Presented in Figure 7.12 are representative results from simulations where default parameter values have been used (Tables 7.1-7.3). Plots showing how the densities of each model species

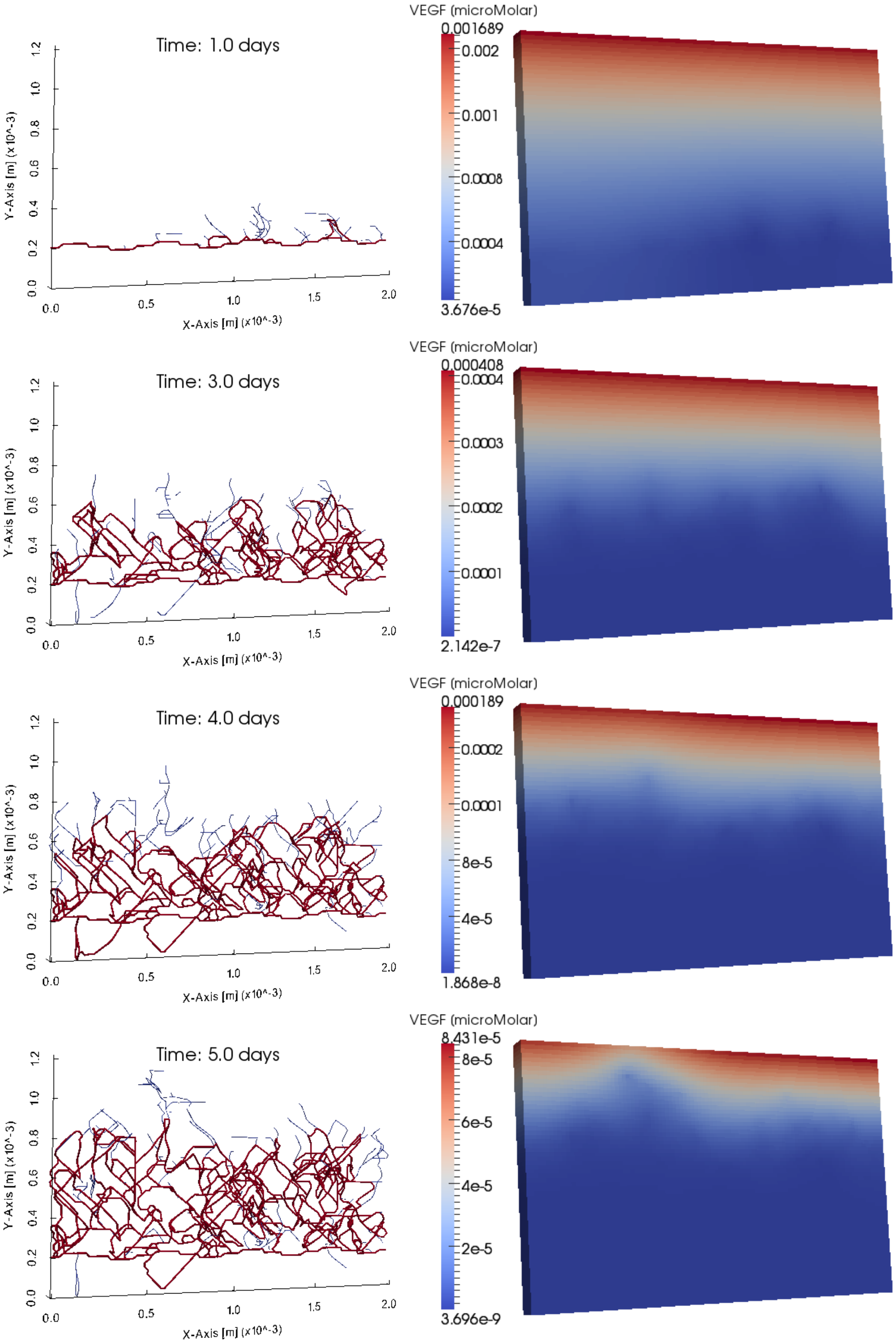

Figure 7.12.: Representative results from our model of angiogenesis in three dimensions when default parameter values are used (Tables 7.1-7.3). The evolving vascular network is shown in panels on the left while the VEGF-A$_{165}$ distribution is shown on the right. Red vessels are perfused; blue vessels are unperfused. In the panels on the right, the scale has been altered at each time-point to maximise the contrast in VEGF-A$_{165}$ concentrations throughout the computational domain at that time.

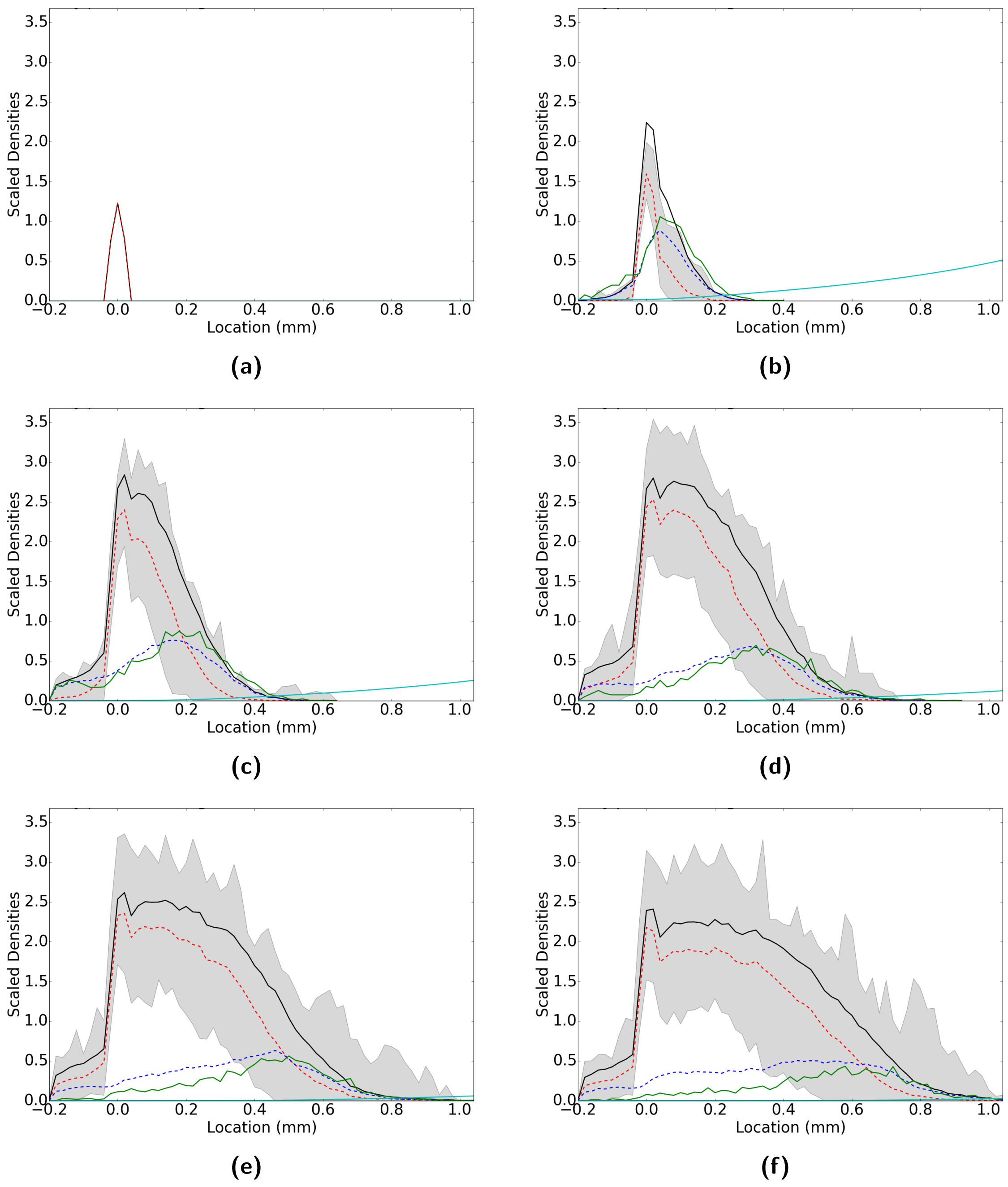

(a) **(b)**

(c) **(d)**

(e) **(f)**

Figure 7.13.: 3-D results, as in Figure 7.12, are averaged over the x- and z-directions and over many simulations ($N = 50$). Results are from simulations in which default parameter values were used (Tables 7.1-7.3). (a) Initial conditions. (b) Day 1 results. (c) Day 2 results. (d) Day 3 results. (e) Day 4 results. (f) Day 5 results. −: total vessel density ($\times 2 \times 10^8$ metres of vessel m^{-3}); - -: unperfused vessel density ($\times 2 \times 10^8$ metres of vessel m^{-3}); - -: perfused vessel density ($\times 2 \times 10^8$ metres of vessel m^{-3}); −: tip cell density ($\times 1 \times 10^{12}$ cells m^{-3}); −: VEGF-A$_{165}$ concentration ($\times 3.25 \times 10^{-9}$ M). The shaded area shows the range of perfused vascular densities across simulations.

(averaged over 50 simulations) varies with distance from the limbus and over time are shown in Figure 7.13. Such profiles provide useful summaries of simulation data, allowing us to gauge the expected behaviour of the various model species. Such averaged densities may also be compared directly with the averaged densities which constitute the state variables of our continuum model of Chapter 5.

The behaviour of our hybrid model matches that of the continuum model of VEGF-A$_{165}$-induced angiogenesis developed in Chapter 5 when default parameter values are used. However, processes such as the formation of anastomoses and the transition of vessels from an unperfused to a perfused state are now modelled explicitly. Typical model simulations proceed as follows. VEGF-A$_{165}$ is released from the pellet, initially increasing the concentration of VEGF-A$_{165}$ inside the model cornea. The VEGF-A$_{165}$ diffuses towards the limbus, where it stimulates vessel dematuration and the formation of unperfused, immature vessel sprouts at about $t = 5$ hours. Tip cells at the leading edge of these sprouts migrate, on average, towards the pellet, leaving behind them a trail of immature and unperfused vessel segments. Tip cells actively seek out vessels and other tip cells as they migrate. The first anastomoses usually occur between $t = 10$ hours and $t = 24$ hours, after which time perfused vessels are observable. As the vascular density increases, anastomosis events become more prevalent and perfused vessels start to dominate unperfused ones, particularly close to the limbus. As for the continuum model of Chapter 5, the growing vessels take up VEGF-A$_{165}$, forming a moving barrier through which little VEGF-A$_{165}$ can pass. Thus, since vessel sprouting depends on an adequate supply of VEGF-A$_{165}$, it is primarily confined to regions of neovasculature which are closest to the pellet. At later times, as VEGF-A$_{165}$ levels decrease, vascular sprouting and growth rates decline. Moreover, as elements of the vasculature closest to the limbus become starved of VEGF-A$_{165}$, the vascular density behind the migrating vascular front decreases.

7.4.4. Comparing the dynamics of the perfused vasculature and the vasculature as a whole

In Chapter 5 we compared the total vascular density predicted by our model to the density of perfused vessels estimated from experimental images, assuming that the dynamics of the total vasculature (unperfused and perfused vessels) serves as a good approximation to that of the perfused vasculature. Our hybrid model enables us to test the validity of this assumption. Presented in Figure 7.14 are summary statistics extracted from the averaged perfused and total vascular density profiles shown in Figure 7.13. Once more, we focus on the distance that the vascular front has travelled towards the pellet and the maximum amplitude of the averaged vascular density profiles. When default parameter values are used, the behaviour of the vasculature taken as a whole is in good agreement with that of the perfused vascular density,

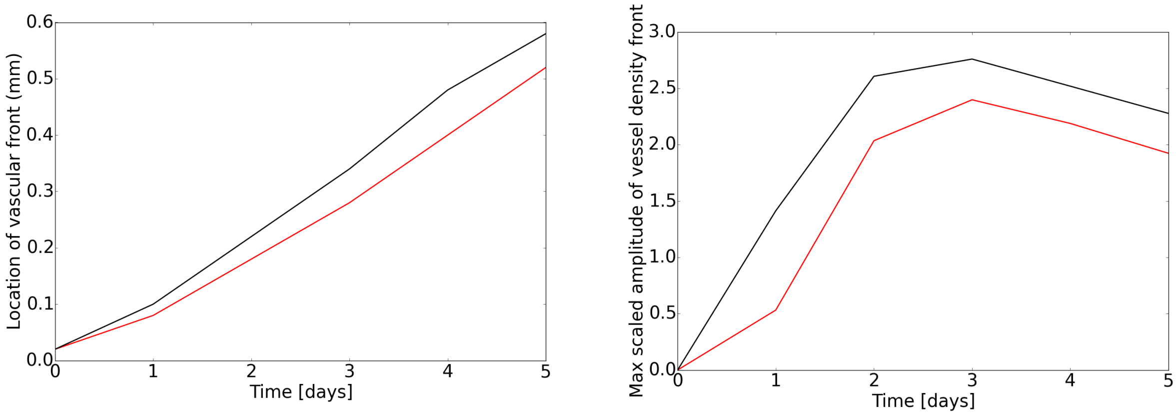

(a) **(b)**

Figure 7.14.: Summary statistics are extracted from the spatially averaged simulation results (Figure 7.13) and plotted over time. Parameter values are as in Tables 7.1-7.3. (a) The distance that vascular front has travelled towards the pellet. (b) The maximum amplitude of the vascular wavefront ($\times 2 \times 10^8$ metres of vessel m^{-3}). —: total vessel density; —: perfused vessel density.

especially at later time-points, including those at $t = 3$ days and $t = 5$ days. In particular, the position of the wavefront of the perfused vasculature follows closely behind that of the total vasculature and after $t \approx 2$ days the two vascular fronts are separated by a fixed characteristic distance of approximately 0.06 mm. The amplitude of the total vascular density profile does not approximate well the amplitude of the perfused vascular density profile at early times ($t < 1$ day) since few anastomoses have occurred at this early stage. However, at later times ($3\,\text{days} \leq t \leq 5\,\text{days}$) the ratio between the maximum amplitude of the total vascular density and that of the perfused vascular density asymptotes to approximately 1.15. Evidently, in our model, not all vessels become perfused; unperfused vessels remain present in the tail end of the vasculature (nearest the limbus) for several reasons. First, some vessels form self-loops which, by their nature, remain unperfused (see Figure 7.15). Second, some tip cells become stranded in regions in which there is a negligible VEGF-A$_{165}$ gradient and no nearby vessels to attract the tip cell. In the absence of such stimuli, the tip cells stagnate and fail to form anastomoses. Finally, regression of vessels in the tail-end of the neovasculature may cause other vessels to revert to an unperfused state.

The difference between the behaviour of the vasculature as a whole and that of the perfused vasculature at early-time points is explained by considering the lag-time between the emergence of a tip cell and the formation of an anastomosis leading to vessel perfusion. Such emergent delay dynamics also help to explain why the values of γ, θ_v and k_p^v differ from those used in

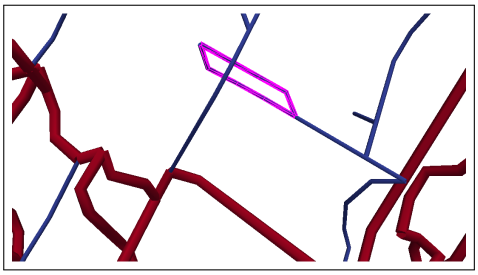

Figure 7.15.: A self-loop (highlighted in pink) formed during a simulation in which default parameter values were used (Tables 7.1-7.3).

the continuum model. The more detailed dynamics of the hybrid model dictate that a stronger angiogenic response is required initially (compared to our continuum model) to reproduce the perfused vascular densities observed on day three of experiments. This stronger angiogenic response, however, must be tempered at later times. Reducing θ_v (by 40%) and k_p^v (by 30%) with respect to their values used in Chapter 5 produces the required angiogenic response[2]. The stronger total angiogenic response induced by a faster release of VEGF-A$_{165}$ from the pellet must be balanced by a faster rate of vessel regression in regions where VEGF-A$_{165}$ levels are too low to sustain vessels so that simulation results remain consistent with the experimental data. Thus, we increased γ with respect to its value in our continuum model of Chapter 5. Note that differences in parameter values may also arise because in the hybrid model the vasculature is denser than that predicted by the continuum model. This is because the hybrid model, through a more rigorous comparison, aims to capture the true 3-D vascular density whilst the continuum model was able to capture only the perceived vascular density from 2-D images.

In summary, the results presented in this section suggest that comparing the total vascular density output from our continuum model and the perfused vascular density estimated from experimental images is valid to a first approximation. Our results may also suggest that the use of snail-trail based continuum models of angiogenesis in models of vascular tumour growth, as in Panovska *et al.* (2007), is reasonable (at least for reproducing simple behaviours). In vascular tumour growth, it is the perfused vasculature which performs a functional role, delivering oxygen and nutrients to cancer cells and normal tissue. While the snail-trail model of angiogenesis adopted in Panovska *et al.* (2007) does not distinguish perfused and unperfused vessels, our results suggest that assuming that oxygen and nutrients are provided by all vessels, rather than just perfused ones, may serve as a good first approximation. However, we note that the total vascular density in such simple continuum models is unlikely to approximate well the behaviour

---

[2] The default value of P_{sprout}^{max} also likely plays a role in inducing a stronger angiogenic response.

of the perfused vasculature when vascular growth is dysregulated or anti-angiogenic therapies are considered.

7.4.5. Parameter sensitivity analysis

In this section we investigate the effect of varying those model parameters associated with our tip cell sensing model: r_f, θ_f, K_T and K_ρ. This allows us to investigate the effect of filopodia dysregulation on VEGF-A$_{165}$-induced angiogenesis. We vary one parameter at a time, keeping all other parameters fixed at their default values (Tables 7.1-7.3). We increase/decrease the value of each parameter by 25% and simulate the model 50 times for each choice of parameter values. We are interested in the effect of such variations in parameter values on the average behaviour of both the total vasculature (unperfused and perfused vessels) and the perfused vasculature, in particular, and focus on how the location of the vascular wavefronts and the maximum vascular densities on days three and five vary with changes in parameter values. Since our simulations are stochastic, it is important to determine whether the mean summary statistics extracted from simulations with different parameter values differ from those extracted from default simulations in a statistically significant manner. To test for statistically significant differences we use the two-sample t-test, considering test statistics with $p < 0.001$ as significant. The summary statistics (the location of the vascular wavefronts and the maximum vascular densities on days three and five) extracted from individual simulations are presented in Figures 7.16-7.19. In Appendix F we also present the averaged total and perfused vascular density profiles for $t = 3\,\text{days}$ and $t = 5\,\text{days}$ for each choice of parameter values (Figures F.1-F.4). The results of the sensitivity analysis are consolidated in Table 7.4.

Varying the strength with which tip cells attract other tip cells - K_T (Equation 7.10): Since tip cells are most prevalent around the vascular front, most tip-tip interactions occur in this region. Tip cells located at the vascular front which are migrating towards the pellet experience an increased rate of migration in the direction of the pellet due to tip-tip interactions. The magnitude of this increase is proportional to K_T. Both increases and decreases in K_T significantly affect the speed of vascular growth towards the pellet (Figure 7.16a). However, changes in K_T do not significantly affect maximum amplitude of the vascular wavefront, particularly in the long-time limit (Figure 7.16b). For smaller times, e.g. $t \leq 3$ days, reductions in K_T result in small but significant reductions in the amplitude of the perfused vascular wavefront. This is likely due to a reduction in lateral motion of tip cells and hence a reduction in the rate at which

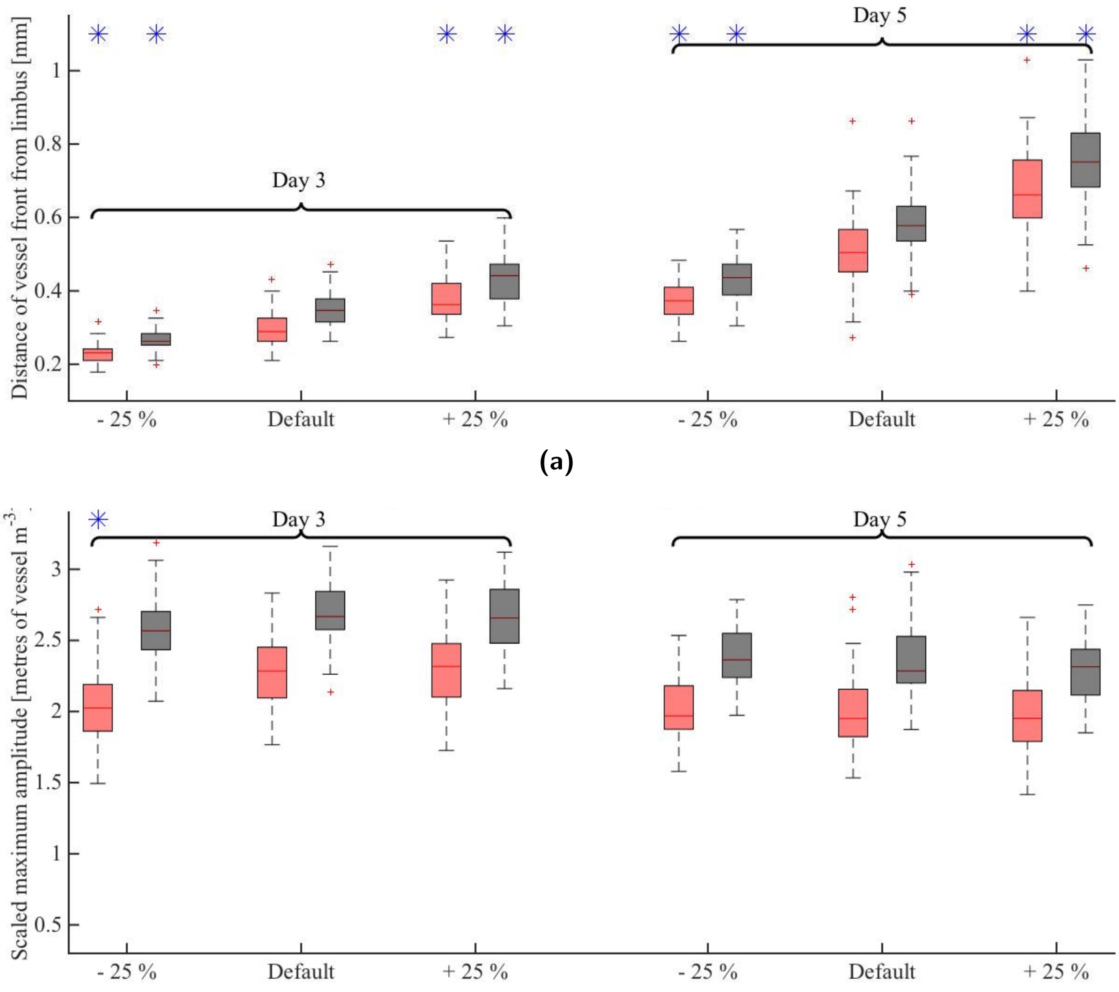

(a)

(b)

Figure 7.16.: Summary statistics extracted from hybrid model simulations in which the strength of tip-tip interactions, K_T, was varied about its default value. All other parameters were held fixed at their default values (Tables 7.1-7.3). (a) The distance of the vascular wavefront from the limbus. (b) The maximum amplitude of the vascular wavefront. The bars show the maximum, minimum, interquartile range and median values of our chosen summary statistics for each set of parameter values. Those quantities which are significantly different to the results obtained from default simulations are identified with an asterisk, $\ast$. Red bars: perfused vasculature; grey bars: perfused + unperfused vasculature.

anastomoses form.

Varying the strength with which vessels attract tip cells - K_ρ (Equation 7.7): Neither the maximum amplitude nor the speed of migration of the vascular front are greatly affected by increases or decreases in K_ρ (Figure 7.17 and Figure F.2). A more in-depth analysis of the simulated network topologies would likely elucidate quantitative differences between the networks produced when K_ρ is varied, however, such analysis is beyond the scope of this thesis.

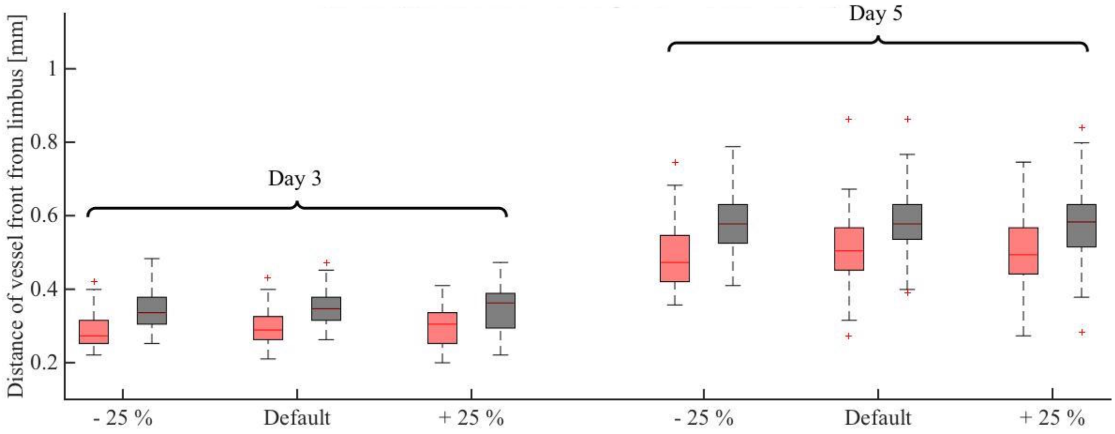

(a)

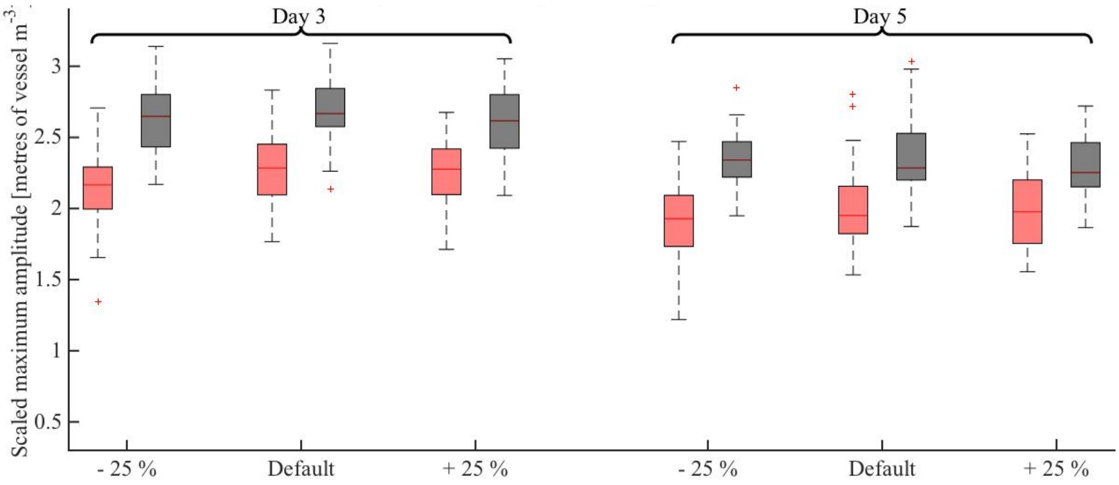

(b)

Figure 7.17.: Summary statistics extracted from hybrid model simulations in which the strength of tip-vessel interactions, K_ρ, was varied about its default value. All other parameters were held fixed at their default values (Tables 7.1-7.3). (a) The distance of the vascular wavefront from the limbus. (b) The maximum amplitude of the vascular wavefront. Those quantities which are significantly different to the results obtained from default simulations are identified with an asterisk, $\ast$. Red bars: perfused vasculature; grey bars: perfused + unperfused vasculature.

Varying the sensing angle of filopodia - θ_f (Equation 7.7): Decreasing the angle over which tip cell filopodia explore their local neighbourhood decreases the frequency with which tip cells form anastomoses. This is because tip cells are less efficient at sensing nearby vessels situated laterally. Reducing a tip cell's ability to sense vessels and form crosslinks with those vessels leads to a significant reduction in total as well as perfused vascular densities (Figure 7.18b). Importantly, the fraction of the vasculature which is perfused is greatly decreased when θ_f is decreased (see Figures 7.18b and F.3).

Reductions in θ_f also reduce the rate of migration towards the pellet (Figure 7.18a) for two main reasons. First, as θ_f decreases tip-tip interactions around the vascular front decrease. Given

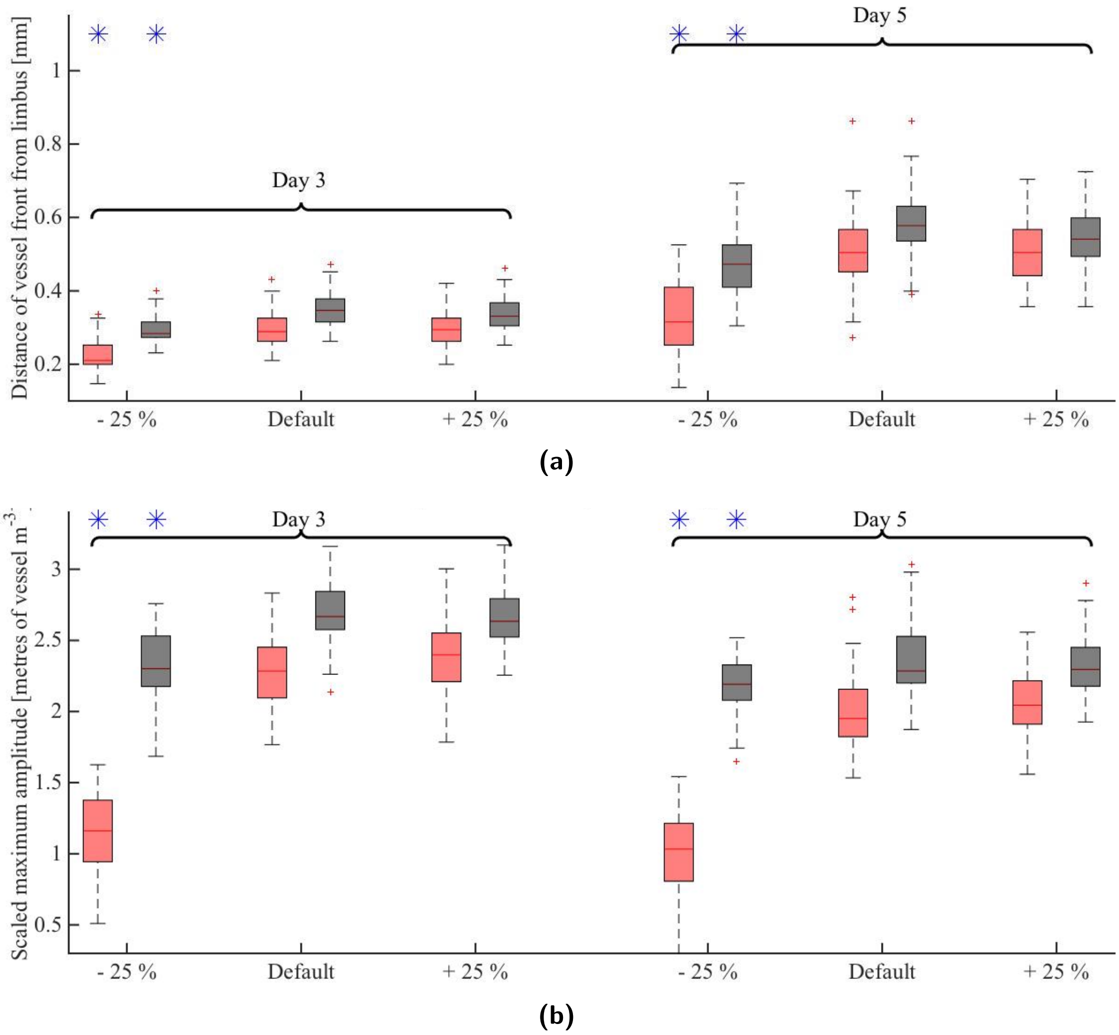

Figure 7.18.: Summary statistics extracted from hybrid model simulations in which θ_f was varied about its default value. All other parameters were held fixed at their default values (Tables 7.1-7.3). (a) The distance of the vascular wavefront from the limbus. (b) The maximum amplitude of the vascular wavefront. Those quantities which are significantly different to the results obtained from default simulations are identified with an asterisk, $\ast$. Red bars: perfused vasculature; grey bars: perfused + unperfused vasculature.

the sensitivity of front migration speed to the strength of tip-tip interactions (Figure 7.16a), the reduced frequency of tip-tip interactions is likely to be responsible for the reduction in migration speed observed here. Further, if fewer perfused vessels form then the uptake of VEGF-A$_{165}$ by the vasculature also declines (since it is the perfused vessels which drain the vasculature) and tip cells experience a reduced chemotactic force towards the pellet.

Varying the maximum probing distance of filopodia - r_f (Equation 7.7): Decreasing r_f induces small but significant decreases in the amplitude of the perfused vascular wavefront (Figures 7.19b and F.4). This is likely a result of decreasing levels of tip-tip and tip-vessel

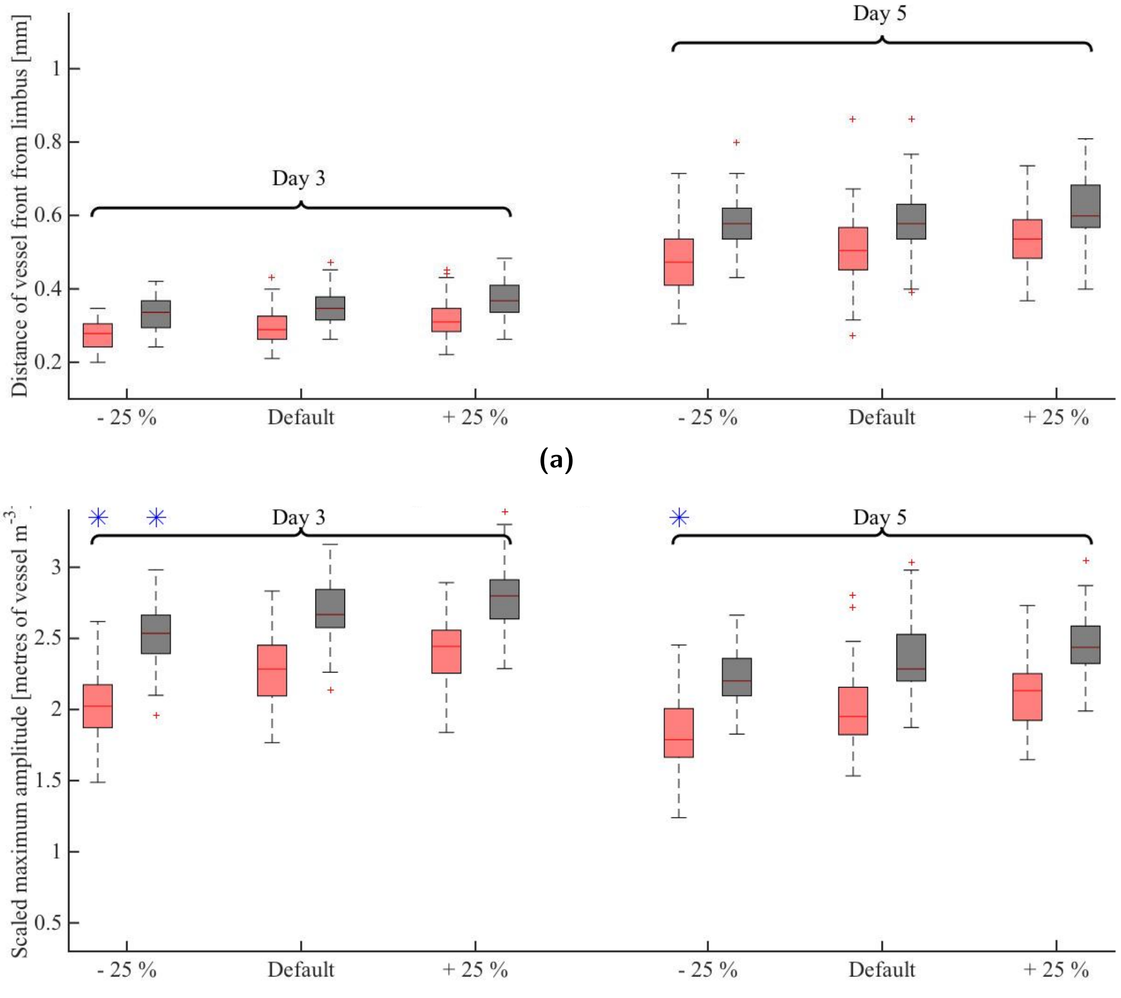

(a)

(b)

Figure 7.19.: Summary statistics extracted from hybrid model simulations in which the maximum probing distance of filopodia, r_f, was varied about its default value. All other parameters were held fixed at their default values (Tables 7.1-7.3). (a) The distance of the vascular wavefront from the limbus. (b) The maximum amplitude of the vascular wavefront. Those quantities which are significantly different to the results obtained from default simulations are identified with an asterisk, $\ast$. Red bars: perfused vasculature; grey bars: perfused + unperfused vasculature.

interactions and, thus, anastomoses and the associated decrease in lateral motion. By contrast, increasing r_f above the default value does not significantly increase the amplitude of the vascular wavefront. Changes in the front migration speed are not significant (Figure 7.19a).

Summary The sensitivity analysis presented here indicates that, via manipulation of parameters, our tip cell sensing model can be used to regulate the level of perfusion in the developing neovasculature. In particular, we have identified θ_f, the angle over which tip cells project filopodia, as an important parameter for determining the degree of perfusion in simulated vascular networks. Meanwhile, the strength of tip-tip interactions, K_T, was found to play a

	$\uparrow K_T$	$\downarrow K_T$	$\uparrow K_\rho$	$\downarrow K_\rho$	$\uparrow \theta_f$	$\downarrow \theta_f$	$\uparrow r_f$	$\downarrow r_f$
Day 3 - Amplitude of perfused vessel density		🟦				🟦		🟦
Day 3 - Amplitude of total vessel density						🟦		🟦
Day 5 - Amplitude of perfused vessel density						🟦		🟦
Day 5 - Amplitude of total vessel density						🟦		
Day 3 - Location of perfused vessel density front	🟥	🟦				🟦		
Day 3 - Location of total vessel density front	🟥	🟦				🟦		
Day 5 - Location of perfused vessel density front	🟥	🟦				🟦		
Day 5 - Location of total vessel density front	🟥	🟦				🟦		

Table 7.4.: Summary of results from tip sensing model sensitivity analysis. Rows show the summary statistics extracted from simulations, while columns show the changes in parameter values. The cells of the table show the effect of the parameter change (given in the column title) on a given summary statistic (row title). A blue or red cell denotes that the change in parameter value caused a statistically significant decrease or increase in the summary statistic, respectively. White cells denote no statistically significant change.

dominant role in determining the speed of migration of the vascular front.

The one-at-a-time sensitivity analysis performed here shares similarities with that performed for our continuum models in Chapter 5. As such it suffers from the same shortcomings. Another shortcoming of such a simplified approach to sensitivity analysis is particularly evident here. It is well known that local sensitivity analyses cannot be used as a robust measure of sensitivity unless the response of a model to the value of a parameter is linear (Saltelli and Annoni 2010)[3]. Clearly, our model does not respond linearly to changes in the parameter values of our tip cell sensing model. Most obviously, r_f features non-linearly in (7.7), whereas the same equation depends linearly on K_ρ, for example. Equation (7.7), taken alone, dictates the value of F_{ρ_k}, the amount by which a tip cell tends to increase its rate of migration towards a vessel. Then, considering an individual tip cell located a distance r_v from a vessel, if $r_v \approx r_f$ then a 25 % increase in r_f has a much greater effect on the value of F_{ρ_k} than does a 25 % increase in the value of K_ρ. Meanwhile, if $r_v \ll r_f$ then a 25 % increase in r_f has a much lesser effect on the value of F_{ρ_k} than does a 25 % increase in the value of K_ρ. Similar statements apply regarding the relative effects of changes in the value of θ_f vs K_ρ. Given that whether F_{ρ_k} is most sensitive to K_ρ or r_f (or θ_f) is a function of the relative locations of a tip cell and a nearby vessel it is difficult to interpret the amount by which such changes will affect the more global properties of a simulation (e.g. front

---

[3] Note that our main aim is not to quantify the sensitivity of model results to changes in parameter values, but rather to explore qualitatively changes in the behaviour of our model.

location), and to which parameter such global properties are likely to be most sensitive. We further note that the dependence of tip cell behaviour on r_f and θ_f is more complex than that presented above since the frequency of tip-tip and tip-vessel interactions, a major determinant of tip cell migration speed and the rate at which they form anastomoses, depends on the volume swept out by each region of interaction, which also depends on r_f and θ_f. Such complex and non-linear dependencies motivate both the numerical study of parameter sensitivity performed here and more global sensitivity studies (see Chapter 8). However, a clear barrier to performing such global studies here is the computational expense of our discrete model.

7.4.6. Simulating the dissection of filopodia formation

In this section we investigate the effect of inhibiting filopodia formation on the neovascular response of the limbus. Phng *et al.* (2013) performed experiments in which zebrafish embryos were exposed to low levels of Latrunculin B, which inhibits actin polymerisation in ECs. They found that:

1. Exposure to low concentrations of Latrunculin B decreases the frequency of filopodia protrusions from tip cells.
2. Filopodia are not required for sprout formation.
3. Filopodia facilitate the formation of anastomoses.
4. Filopodia are not required for tip cell guidance. ECs can migrate, albeit at a reduced rate; ECs lacking filopodia migrate at approximately half the rate of ECs with filopodia.
5. In low concentrations of Latrunculin B, where filopodia formation is inhibited, tip cells continue to produce lamallipodia, which guide tip cell migration and generate the forces required for tip cell migration, albeit at a reduced speed.

Guided by Phng *et al.*'s observations, we simulate the impact of low concentrations of Latrunculin B on tip cells by decreasing K_T and K_ρ (at equal rates); sprouting is not affected by a reduction in filopodia formation. Our results are summarised in Figure 7.20. Reducing K_T and K_ρ results in an approximately linear decrease in the rate of vascular growth towards the pellet. The amplitude of the total and perfused vascular wavefront is not greatly affected by small to moderate reductions (25% - 50%) in K_T and K_ρ at late time points ($t = 5$ days). However, much greater reductions in wavefront amplitudes are observed at early time points as K_T and K_ρ are decreased towards 50% of their default value. Moreover, the proportion of perfused vessels in the neovasculature decreases, reflecting the decreased rate at which anastomoses form. When K_T

and K_ρ are 25% of their default values the amplitude of the perfused vascular density approaches half that of the total vascular density. For $K_T = K_\rho = 0$, vascular growth is negligible and few anastomoses form. This level of inhibition is unlikely to occur in practice, however; such levels of inhibition would probably be fatal, as in Phng *et al.* (2013).

Our model exhibits behaviours consistent with the experimental results of Phng *et al.* (2013) for moderate inhibition of actin polymerisation. When filopodia formation is decreased tip cells continue to migrate, however, at a reduced rate. Additionally, the rate at which anastomoses form is reduced. In our model, the effect of filopodia on vascular growth and network formation is a collective phenomenon. That is, the effect of filopodia on tip cell migration is wholly reliant on the presence of other tip cells or vessels. This represents a substantial simplification of the situation *in vivo*. In particular, the presence or absence of filopodia (and lamallipodia) does not affect the ability of tip cells to migrate via chemotaxis in our model. Our model could, however, be extended to include the effect of filopodia formation on the chemotactic force generated by a tip cell.

As noted in Section 7.3, chemotaxis is not required to produce networks which are consistent in density and extent with experimental networks; at the level of sprouting produced in default simulations, directed sprouting, and tip-tip and tip-vessel interactions are sufficient to drive vascular growth towards the pellet at an appropriate rate. Despite the relative insensitivity of our simulation results to the presence or absence of tip cell chemotaxis, both the neovascular density and the speed of migration of the vascular front towards the pellet are affected by changes in the dose of VEGF-A$_{165}$ administered via the pellet. Figure 7.21 (and Figure F.5) show how model results vary when the initial concentration of VEGF-A$_{165}$, $[V_T]_{init}$, is reduced (by 25% and 50%). The rate of migration towards the pellet for both the perfused vasculature and the vasculature as a whole decreases as $[V_T]_{init}$ is reduced (Figure 7.21a). Yet more significant is the reduction in both total vascular density and the proportion of the vasculature which is perfused as $[V_T]_{init}$ is decreased (Figure 7.21b). The dose response observed here is likely a result of decreasing VEGF-A$_{165}$ levels stimulating the production of fewer tip cells. Fewer tip cells, in turn, results in a reduced vascular density and a reduction in tip-vessel and tip-tip interactions, which are the primary drivers of vascular growth towards the pellet in our model.

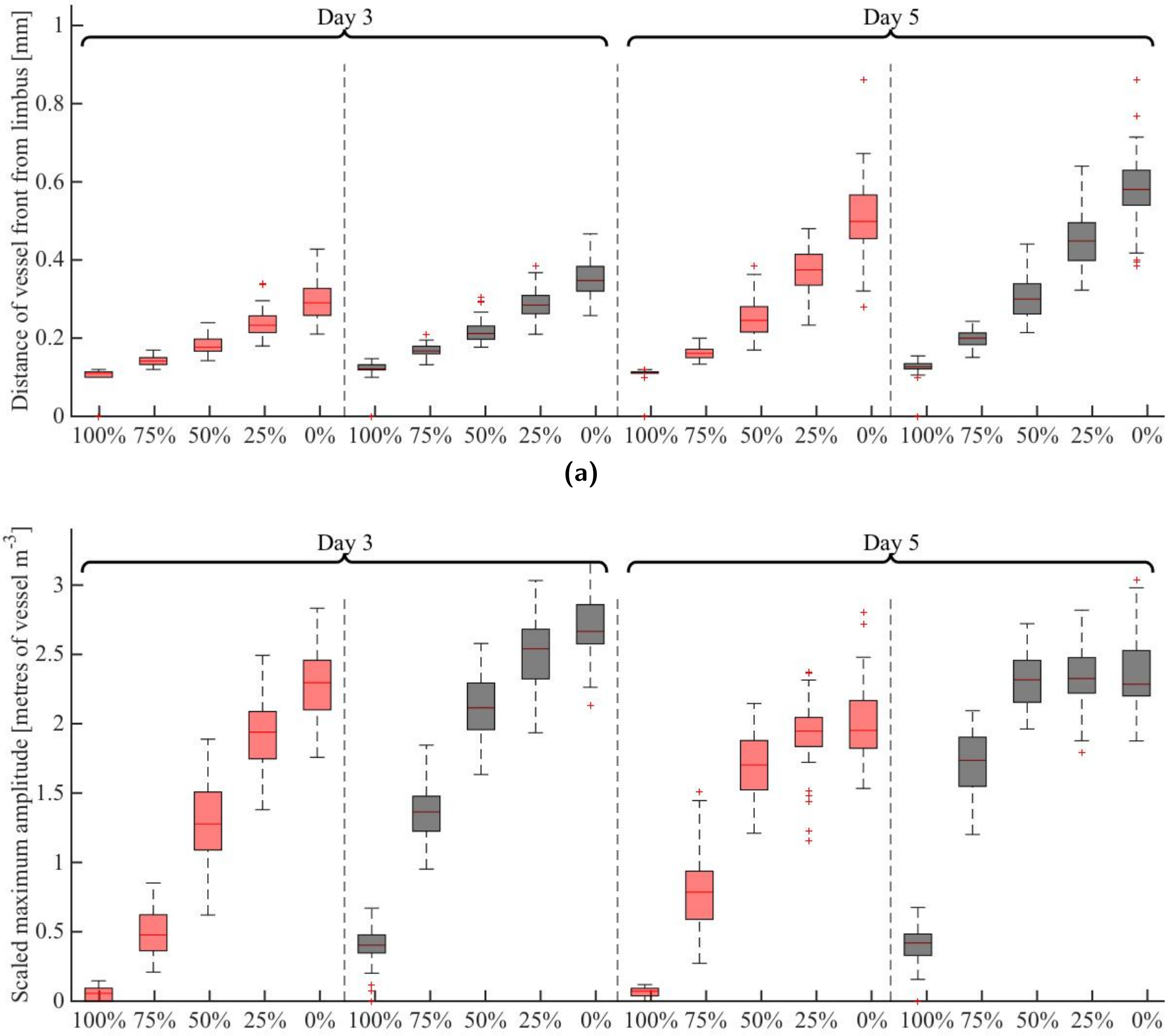

(a)

(b)

Figure 7.20.: Summary statistics extracted from hybrid model simulations in which the formation of filopodia is inhibited. To simulate the inhibition of filopodia formation, K_T and K_ρ were decreased from their default value. On the x-axis of the bar charts are the percentages by which K_T and K_ρ were decreased for a given set of simulations. All other parameters were held fixed at their default values (Tables 7.1-7.3). (a) The distance of the vascular wavefront from the limbus. (b) The maximum amplitude of the vascular wavefront ($\times 2 \times 10^8$ metres of vessel m^{-3}). Red bars: perfused vasculature; grey bars: perfused + unperfused vasculature.

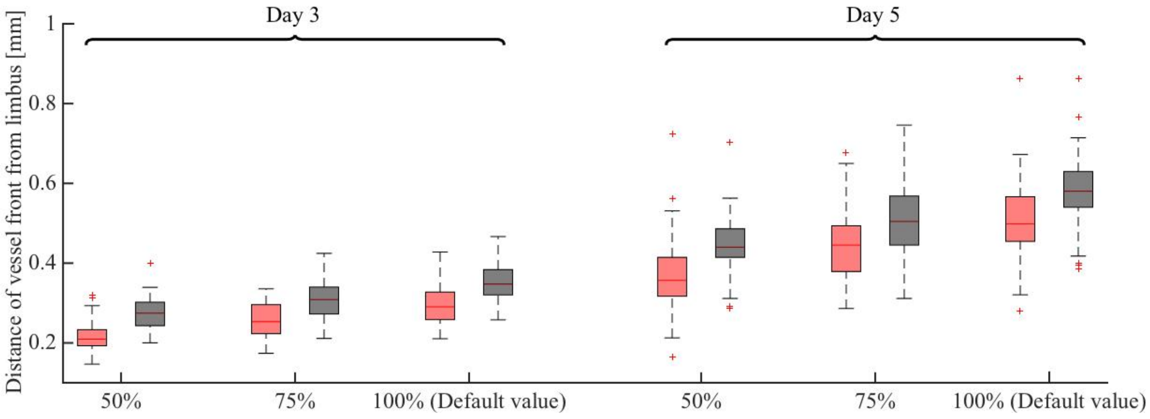

(a)

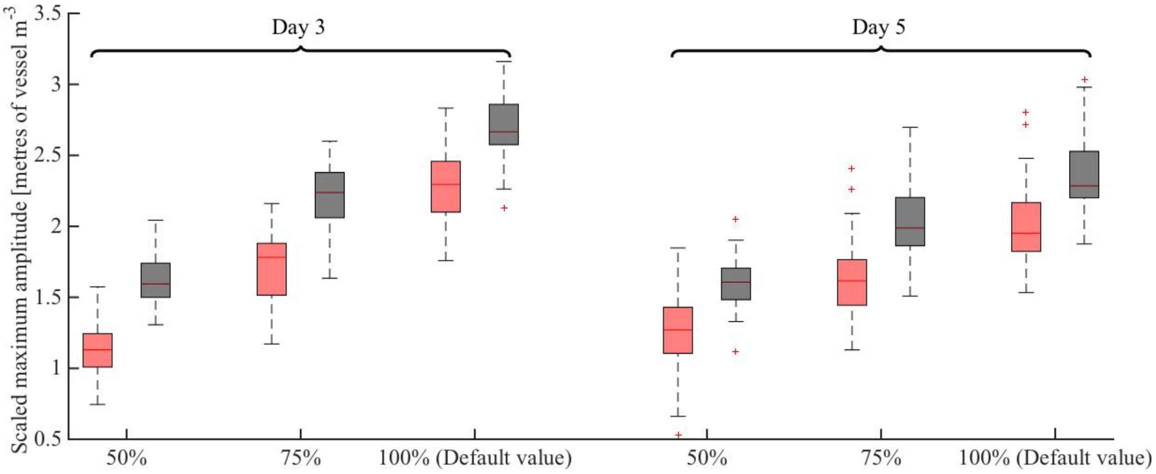

(b)

Figure 7.21.: Summary statistics extracted from hybrid model simulations in which the initial concentration of VEGF-A$_{165}$ in the pellet, $[V_T]_{init}$, is decreased by 25% and then by 50% from its default value. All other parameters are held fixed at their default values (Tables 7.1-7.3). (a) The distance of the vascular wavefront from the limbus. (b) The maximum amplitude of the vascular wavefront.

7.5. Model extension to account for tip cell-ECM interactions

In this section we extend the model presented above to include key tip cell-ECM interactions. As in Chapter 5 (Section 5.9), we suppose that the exposure of tip cells to VEGF-A$_{165}$ stimulates the release of MMPs (e) (Rundhaug 2005), which degrade ECM proteins (c) as they diffuse throughout the surrounding matrix. The degradation of the ECM creates a gradient between the area occupied by the tip cells and the area immediately in front of them, up which tip cells may migrate. The equations we adopt to capture this behaviour in our extended model are:

$$\frac{\partial c}{\partial t} = -\underbrace{Bec}_{\substack{\text{degradation}\\ \text{by MMPs}}} + \underbrace{C(C_{max} - c)}_{\text{remodelling}}, \tag{7.20}$$

$$\frac{\partial e}{\partial t} = \underbrace{D_e \nabla^2 e}_{\text{diffusion}} + \underbrace{Fn\frac{v}{v + v_{\frac{1}{2}}}}_{\substack{\text{production by}\\ \text{tip cells}}} - \underbrace{Ee}_{\text{removal}}, \tag{7.21}$$

where $n = n(x, y, z)$ is the local tip cell density:

$$n(x, y, z) = \begin{cases} \frac{1}{\Delta x^3} & \text{if tip cell at (x, y, z),} \\ 0 & \text{otherwise.} \end{cases} \tag{7.22}$$

Equations (7.20) and (7.21) are 3-D analogues of the equations used to model tip cell-ECM interactions in Chapter 5 (Equations 5.29 and 5.30) which have been further adapted to account for the fact that tip cells are now modelled as discrete entities. As in Chapter 5, the parameter C quantifies the rate of ECM remodelling, while C_{max} is the equilibrium ECM density and B quantifies the rate of degradation of the ECM by MMPs. In (7.21), the maximal rate of MMP production per unit tip cell density is F, and D_e is the diffusion constant for MMPs, which are removed from the system at rate E.

The ECM density is everywhere initialised to C_{max} and the MMP concentration is initialised to zero:

$$c(x, y, z, 0) = C_{max}; \quad e(x, y, z, 0) = 0, \tag{7.23}$$

for $0 \leq x \leq x_{max}$, $0 \leq y \leq y_{max}$ and $0 \leq z \leq z_{max}$. For simplicity, no flux boundary conditions for e are imposed on all domain boundaries.

Following the reasoning presented in Chapter 5, we update the tip cell transition probabilities (Equation 7.5) to include a haptotactic term and a multiplicative factor which accounts for how the permissivity of the ECM to tip cells changes with the local ECM density, c. The probability that a tip cell will move from site i (x_i, y_i, z_i) to site j (x_j, y_j, z_j), in the Moore neighbourhood of i, is now given by:

$$P_{ij} = \Xi(c_i)\Big(\underbrace{\frac{\Delta t\, \mu}{k\, d_{ij}^2}}_{\substack{\text{random}\\ \text{motion}}} + \underbrace{\frac{\Delta t\, \chi}{k\, d_{ij}^2} \overbrace{\mathbb{R}\left(v_j - v_i\right)}^{\text{ramp function}}}_{\text{chemotaxis}} + \underbrace{\frac{\Delta t\, \Upsilon}{2\, k\, d_{ij}^2} \left(c_j - c_i\right)}_{\text{haptotaxis}} + \underbrace{\frac{\Delta t}{d_{ij}} \max\left(\delta_{ij}^{T-T}, \delta_{ij}^{T-V}\right)}_{\substack{\text{movement due to}\\ \text{tip}-\text{tip and tip}-\text{vessel}\\ \text{interactions}}} \Big), \tag{7.24}$$

where μ, χ, k, d_{ij}, δ_{ij}^{T-T} and δ_{ij}^{T-V} are as defined previously (see Section 7.2.2) and Υ is the

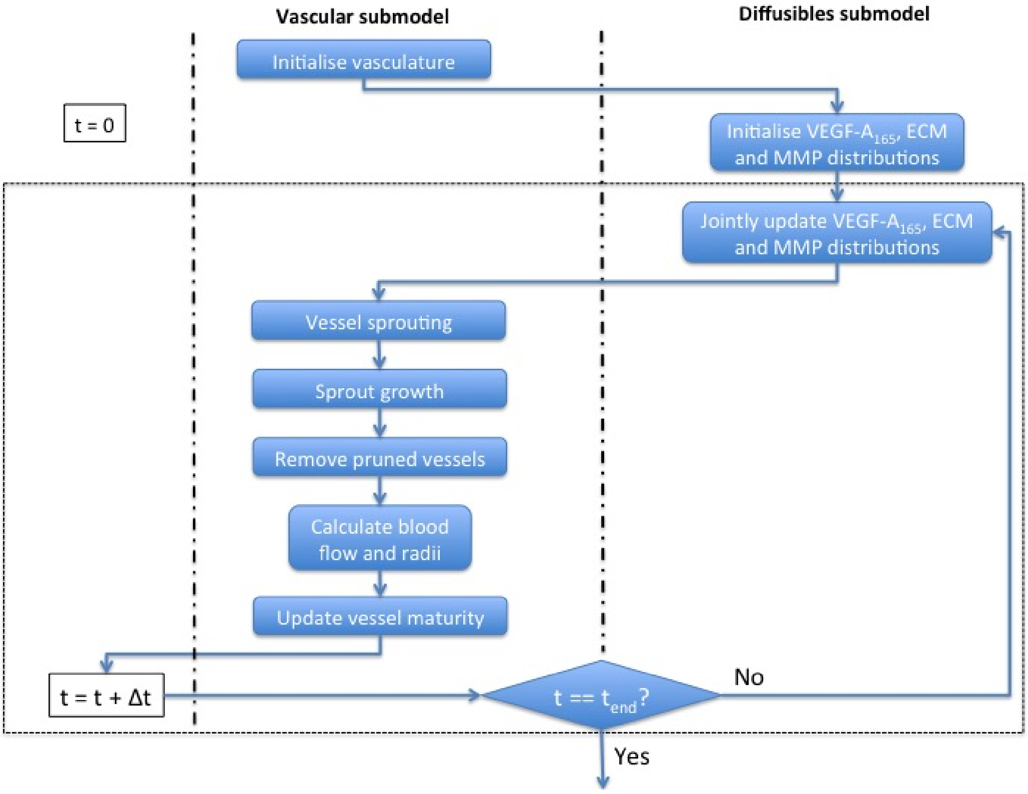

Figure 7.22.: Flowchart showing the sequence of computational steps used to simulate the extended model. See main text for details.

haptotaxis coefficient. $\Xi(c_i)$ captures how a tip cell's migration speed is modulated in response to local changes in ECM density and is given by:

$$\ln\left(\Xi(c_i)\right) = \frac{-(\ln(c_i) - \eta)^2}{2\,\Gamma^2}. \tag{7.25}$$

We note that, while we have captured the same phenomena in our discrete model of tip cell movement as we did in our continuum model of Chapter 5, in the continuum limit (Δt, $\Delta x \to 0$), for this probability of movement on a Moore neighbourhood in three dimensions (and taking $k = \frac{26}{6}$, as before), tip cells move with a macroscopic flux which is different to that presented in Chapter 5 (Equation 5.33).

The only update that must be made to our simulation procedure is that the more complex system of coupled equations, (7.14)-(7.17), (7.20) and (7.21) must now be solved simultaneously (whereas previously only Equations 7.14-7.17 were solved). The new system of equations is solved as previously described in Section 7.2.4; the equations are discretised with respect to spatial variables using (central) finite differences, reducing the PDEs to a coupled system of ODES which are integrated over the time interval $[t, t + \Delta t]$ using the backward Euler method. The updated simulation procedure is shown in Figure 7.22.

7.6. Parameter value estimation for the extended model

Estimation of the parameters introduced in our extended model follows that presented in Chapter 5 and thus the details are not repeated here. Table 7.5 summarises the default values of new parameters introduced in our extended model. As for the default value of the chemotactic sensitivity parameter, χ, in the model presented earlier in this chapter, the default value of Υ, the haptotaxis coefficient, is approximately 4 times smaller than that used in our continuum model of Chapter 5 (5×10^{-7} here vs. $\sim 2 \times 10^{-6}\,\mathrm{m}^2\mathrm{min}^{-1}\mathrm{M}^{-1}$ in the continuum model). Other parameters associated with tip cell-ECM interactions were also modified relative to their default values in our continuum model to ensure that the results of the extended model are consistent with the experimental data. In more detail, the value of C is half that used in the continuum model, and F is approximately one sixth of the value used in the continuum model. The shape parameter, Γ, which determines how the permissivity of the ECM to tip cells changes with the ECM density also differs from that used in our continuum model. Here, we fix $\Gamma = 1.4$ (vs 0.8 in the continuum model). Increasing Γ has the effect of broadening the range of ECM densities in which tip cells can migrate most effectively through the ECM.

A number of other parameter values are also modified with respect to their values used as default in the model presented earlier in this chapter. These are presented in Table 7.6. In particular, χ has been decreased by a factor of ~ 5 to compensate for the fact that tip cells now move in response to an additional cue (i.e. they now move via haptotaxis). Meanwhile, K_T and K_ρ have been increased each by a factor of ~ 1.2 principally to compensate for the fact that tip cells are not always in an optimum environment for migration. θ_v and k_p^v have also been increased slightly in order to bring simulation results in line with those from experiments.

7.7. Numerical results: extended model

In this section we present the results generated from numerical simulations of our extended model in which default parameter values (see Section 7.6) are adopted. Figure 7.23 shows representative results from such simulations. Further to the evolving vascular networks and VEGF-A$_{165}$ distributions which were shown in Figure 7.12 for our original discrete model, we include in this figure images of the ECM densities (right hand side panels) at the various time-points of interest, exhibiting the additional level of detail included in our extended model.

Clearly evident from the inspection of individual simulations (as in Figure 7.23) is the short

Parameter	Description	Default value and units	Sources
D_e	MMP diffusion constant.	3×10^{-8} [m^{2}h^{-1}]	(Milde *et al.* 2008; Collier *et al.* 2011; Daub and Merks 2013)
C_{max}	Maximum ECM concentration in cornea in absence of MMPs.	1×10^{-6} [M]	(Holmes *et al.* 2001)
B	Rate of ECM degradation by MMPs.	1×10^{9} [M^{-1}h^{-1}]	(Gioia *et al.* 2007)
C	Rate constant for ECM remodelling.	0.025 [h^{-1}]	(Petroll *et al.* 2004)
E	MMP natural decay rate.	25 [h^{-1}]	-
F	MMP production rate per unit tip cell density.	1.6×10^{-20} [M h^{-1} (tip cell m^{-3})$^{-1}$]	-
Υ	Tip cell haptotaxis coefficient	5×10^{-7} [m^{2}min^{-1}M^{-1}]	(Orme and Chaplain 1997; Anderson and Chaplain 1998; Watson *et al.* 2012)
η	Shape parameter for function which determines the permissivity of the ECM to tip cells. See (7.25).	-6.6 [ln(M)]	
Γ	Shape parameter for function which determines the permissivity of the ECM to tip cells. See (7.25).	1.4	

Table 7.5.: Default parameter values used to model tip cell-ECM interactions for VEGF-A$_{165}$-induced angiogenesis.

Parameter	Description	Default dimensional value and units
θ_v	Binding constant.	40
k_p^v	Effective permeability of the cornea-pellet boundary.	1.28×10^{-7} [m h^{-1}]
χ	Chemotactic sensitivity of tip cells to VEGF-A$_{165}$.	2×10^{-9} [m^{2}min$^{-1}\mu$M^{-1}]
K_ρ	Constant quantifying maximum increase in tip cell migration rate due to tip-vessel interactions.	2.8×10^{-7} [m min^{-1}]
K_T	Constant quantifying maximum increase in tip cell migration rate due to tip-tip interactions.	1.904×10^{-7} [m min^{-1}]

Table 7.6.: Default parameter values used to model VEGF-A$_{165}$-induced angiogenesis in extended model (including tip cell haptotaxis). Only parameters which differ in value from those presented in Section 7.3 are listed here.

range action of MMPs in our model. That is, those tip cells at the vascular front in particular are largely responsible for clearing their own path through the ECM. The extracellular legacy left by those tip cells nearest the front is also clearly evident from individual simulations; those tip cells nearest the front leave a trail of reduced ECM density in their wake which facilitates the migration of other tip cells behind the front. Notably, the level of ECM degradation at

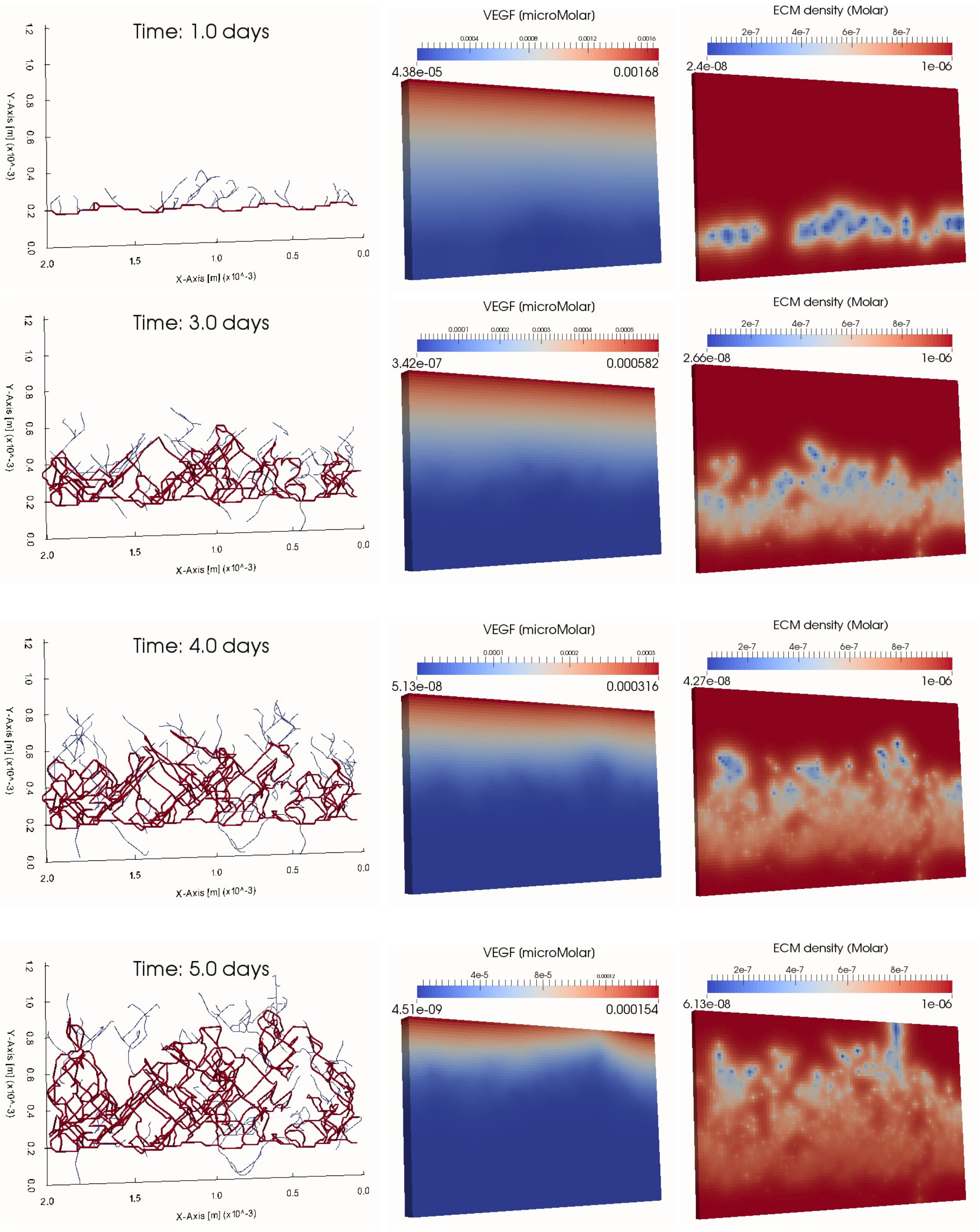

Figure 7.23.: Representative results from our extended discrete model of angiogenesis in which default parameter values are used (see Section 7.6). The evolving vascular network is shown in the panels on the left, VEGF-A$_{165}$ distributions are shown in the central panels, and ECM densities are shown on the right (right panels show a slice cut through the centre of the domain, $z = 60\,\mu\text{m}$). Red vessels are perfused; blue vessels are unperfused. In the central and right panels, the scale has been altered at each time-point to maximise the contrast in VEGF-A$_{165}$ concentrations and ECM densities throughout the computational domain at that time.

the vascular front, where the VEGF-A$_{165}$ levels, and thus MMP production, are highest leads to ECM densities which are sub-optimal for tip cell migration. For example, on day 3 of the exemplar simulation shown in Figure 7.23 some tip cells at the vascular front are exposed to ECM densities of $\sim 2.7 \times 10^{-8}$ M (right panels), far below the optimum level of 2.5×10^{-7} M. These tip cells then move approximately 70% less efficiently than they would in an optimum environment (see Equation 7.25). Meanwhile, those tip cells occupying locations further from the vascular front are exposed to ECM levels which are closer to the optimum level because these tip cells are exposed to lower levels of VEGF-A$_{165}$, and thus produce fewer MMPs, and the ECM degraded by leading tip cells has begun to recover back to equilibrium levels (see Equation 7.20).

As for our original discrete model we present plots showing how the densities of each model species (averaged over 50 simulations) vary with distance from the limbus and over time (see Figure 7.24). This allows us to compare directly the average behaviour of our hybrid model with the behaviour of the analogous continuum model from Chapter 5 (Section 5.9). As for our original discrete model, the behaviour of our extended hybrid model broadly matches that of the extended continuum model when default parameter values are used. However, of particular note is that in discrete simulations the averaged concentrations of MMPs are roughly an order of magnitude smaller than those observed in default simulations of our analogous continuum model, and ECM densities are much higher on average. Even so, tip cells in our discrete model are exposed locally to much lower ECM densities than is suggested by interrogation of ECM densities averaged over the $x - z$ plane (as in Figure 7.24). This is because, as noted above, degradation of the ECM by MMPs produced by tip cells in our discrete model is a local phenomenon, and the ECM in regions not occupied by tip cells remains at roughly equilibrium levels (C_{max}).

For default simulations of our extended model, the behaviour of the vasculature and the VEGF-A$_{165}$ distributions are very similar to that of the original discrete model. This is perhaps not surprising given that both models were parametrised against the same experimental data. As for the original model, initially, VEGF-A$_{165}$ released from the pellet diffuses across the cornea, towards the limbal vessels, where it stimulates vessel dematuration and the production of tip cells. Initially these tip cells are unable to migrate rapidly since the local ECM density is high (and the ECM is most permissive to tip cells at intermediate densities). Tip cells exposed to VEGF-A$_{165}$ produce MMPs, which locally degrade the ECM as they diffuse through the tissue. This degradation lowers the ECM density near the tip cells, enabling them to migrate more freely, and it creates a spatial gradient in ECM density up which tip cells migrate via haptotaxis.

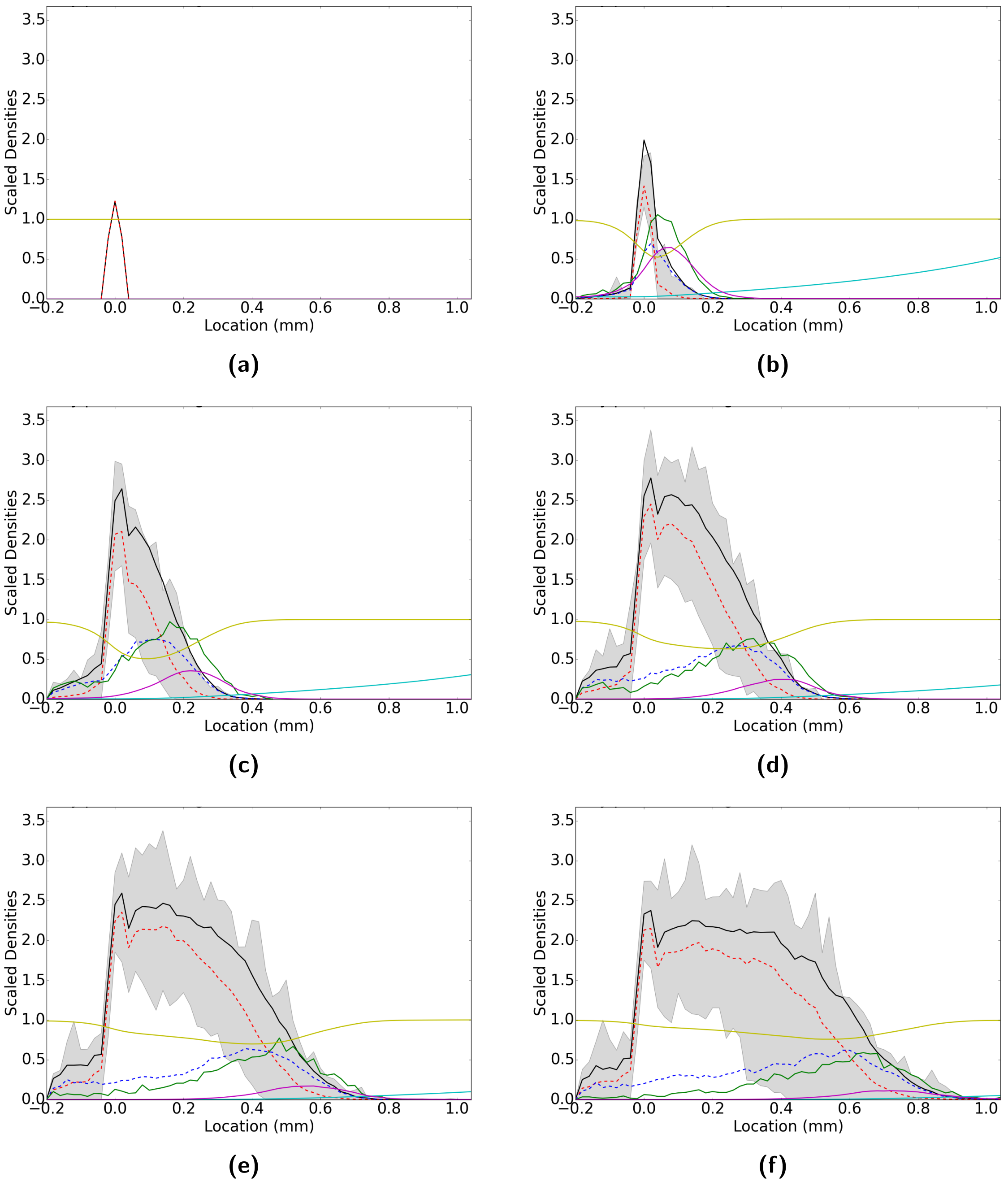

(a) **(b)** **(c)** **(d)** **(e)** **(f)**

Figure 7.24.: 3-D results, as in Figure 7.23, are averaged over the x- and z-directions and over many simulations ($N = 50$). Results are from simulations of our extended model in which default parameter values were used (see Section 7.6). (a) Initial conditions. (b) Day 1 results. (c) Day 2 results. (d) Day 3 results. (e) Day 4 results. (f) Day 5 results. —: total vessel density ($\times 2 \times 10^8$ metres of vessel m^{-3}); - -: unperfused vessel density ($\times 2 \times 10^8$ metres of vessel m^{-3}); - -: perfused vessel density ($\times 2 \times 10^8$ metres of vessel m^{-3}); —: tip cell density ($\times 1 \times 10^{12}$ cells m^{-3}); —: VEGF-A$_{165}$ concentration ($\times 3.25 \times 10^{-9}$ M); —: ECM density ($\times 1 \times 10^{-6}$ M); —: MMP concentration ($\times 1 \times 10^{-10}$ M). The shaded area shows the range of perfused vascular densities across simulations.

Tip cells then migrate towards the pellet via both chemotaxis and haptotaxis and by interacting with each other, leaving behind them a trail of vessels. As noted above, tip cells also leave

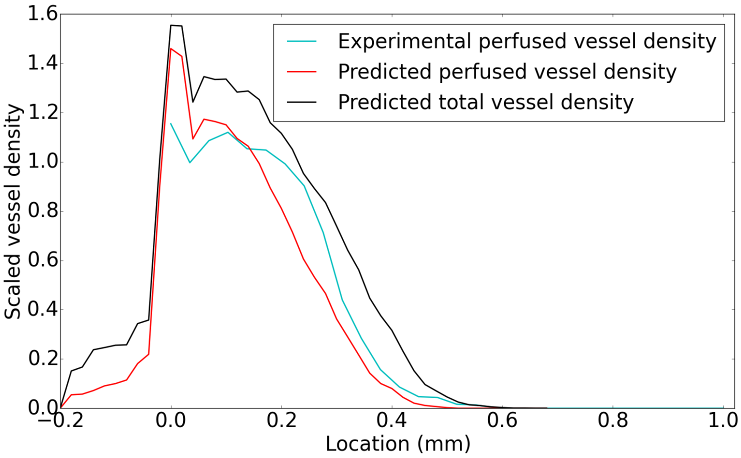

(a)

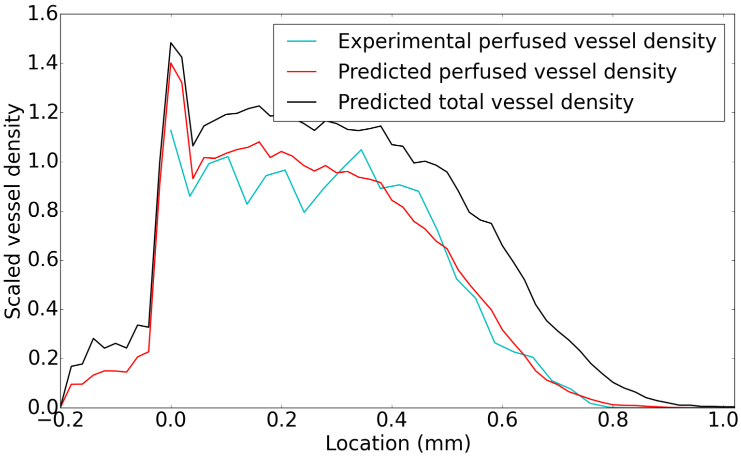

(b)

Figure 7.25.: 3-D vascular networks, resulting from simulations of our extended model in which default parameters are used (see Section 7.6), are projected onto the $x - y$ plane and the average vessel density profiles from such projections are plotted against experimentally derived vessel density profiles. See main text for details. (a) Day 3 results. (b) Day 5 results. The vascular densities shown here are scaled ($\times 2 \times 10^8$ metre of vessel m^{-3}).

behind them a trail of reduced ECM density through which other tip cells, which do not produce as many MMPs, can migrate. As before, tip cell production is localised around the leading edge of the vascular front and as the simulation proceeds, and VEGF-A$_{165}$ levels decline, the rates of tip cell production and migration decrease, and significant vessel regression occurs, particularly in the tail-end of the neovasculature. In the absence of VEGF-A$_{165}$, and thus MMPs produced by tip cells, ECM densities behind the vascular front recuperate, increasing towards equilibrium levels (C_{max}). In the *in vivo* system, the deposition of new ECM may be be due to fibroblasts, for example. However, in our model we incorporate such regeneration of the ECM phenomenologically, as we did in our extended continuum model of Chapter 5.

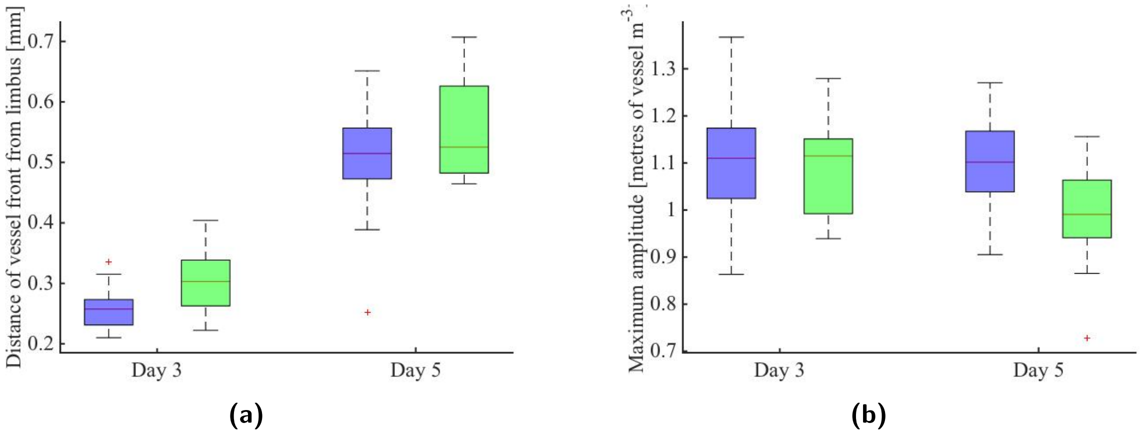

Figure 7.26.: Summary statistics are extracted from individual simulations of our extended model and experiments, and compared. Blue bars show the distributions of summary statistics for simulated vascular networks, while green bars show those extracted from experimental images. (a) Distance of the perfused vascular front from the limbus. (b) Scaled maximum amplitude of the perfused vascular front ($\times 2 \times 10^8$ metre of vessel m^{-3}).

The vascular networks resulting from simulations of our extended model (using default parameters) are compared with those from experiments in Figures 7.25 and 7.26. Figure 7.25 shows a comparison of the averaged vessel density profiles extracted from 2-D projections of simulated vessel networks ($N = 50$) and images of VEGF-A$_{165}$ experiments ($N = 9$). We observe good quantitative agreement between the averaged experimental and simulated perfused vascular density profiles when default parameter values are used. In Figure 7.26 the location of the perfused vascular wavefront and the maximum amplitude of the perfused neovascular density at $t = 3, 5$ days are compared for experiments and simulations where default parameter values were used. As for the original discrete model, the summary statistics compared to experiments are those extracted from 2-D projections of simulated vascular networks. We again observe good agreement between the summary statistics extracted from simulations and experiments when they are compared using the two-sample t-test and two-sample Kolmogorov-Smirnov test. The amplitude of the perfused vascular density on day 3 and the location of the perfused vascular front on day 5 show excellent agreement ($p \gg 0.1$), while the other metrics also show reasonable agreement ($p > 0.025$). With further parameter tuning better agreement between simulations and experiments could likely be established. However, given the computational time taken to run simulations, as before, additional experimental data would be desirable before model parameters are further tuned.

For our extended model, we have again compared the behaviour of the perfused and total

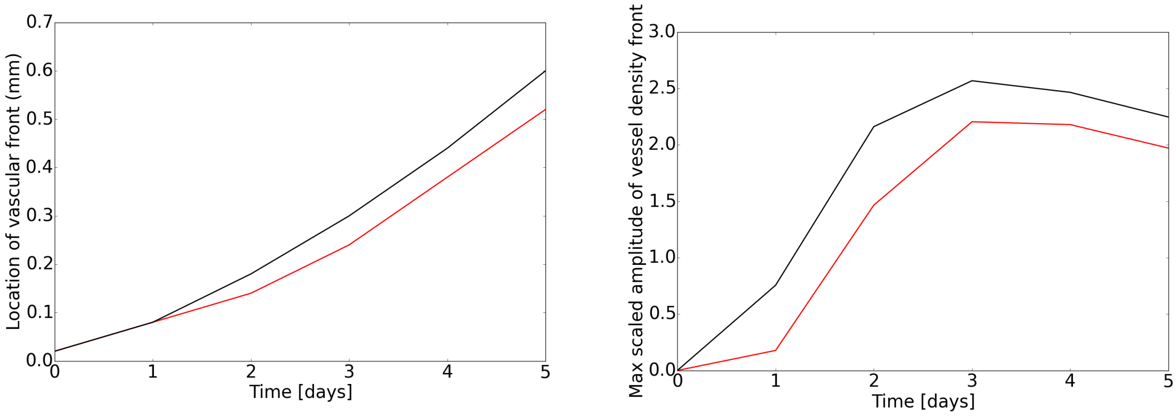

(a)

(b)

Figure 7.27.: Summary statistics are extracted from the spatially averaged simulation results (Figure 7.24) and plotted over time. (a) The distance that vascular front has travelled towards the pellet. (b) The maximum amplitude of the vascular wavefront ($\times 2 \times 10^8$ metres of vessel m^{-3}). —: total vessel density; —: perfused vessel density.

(unperfused + perfused) vasculature. In Figure 7.27 we present the summary statistics extracted from the averaged perfused and total vascular density profiles shown in Figure 7.24. The results in Figure 7.24 closely resemble those presented in Figure 7.14 for the original model[4]. On closer inspection, we see that for our extended model, as for our original model, after $t \approx 2$ days the two vascular fronts are separated by a distance of approximately 0.06 mm and that, at later times ($3\,\text{days} \leq t \leq 5\,\text{days}$), the proportion of the vasculature that is perfused is $85 - 90\,\%$.

7.8. Simulating anti-VEGF-A therapy

In this section we simulate the effect of an anti-VEGF-A drug on the angiogenic response of the corneal vasculature, comparing the predicted responses from our original and extended models (presented in Sections 7.2 and 7.5, respectively). To simulate the application of anti-VEGF-A therapy we increase λ_v, the rate of natural decay of VEGF-A$_{165}$.

In Figure 7.28 we show the results of anti-VEGF-A therapy predicted by the models. We plot both the maximum amplitude of the vascular wavefront and the location of the vascular wavefront on days 3 and 5 of simulations for increasing values of λ_v, representing increasing VEGF-A$_{165}$ inhibition. Both our original and extended models exhibit the same qualitative behaviour: administration of an anti-VEGF-A drug reduces the angiogenic response of the corneal vasculature. On average the location of the vascular wavefront (Figure 7.28a) and the

---

[4] Once again this is unsurprising, given that both the original and extended models were parametrised against the same experimental data

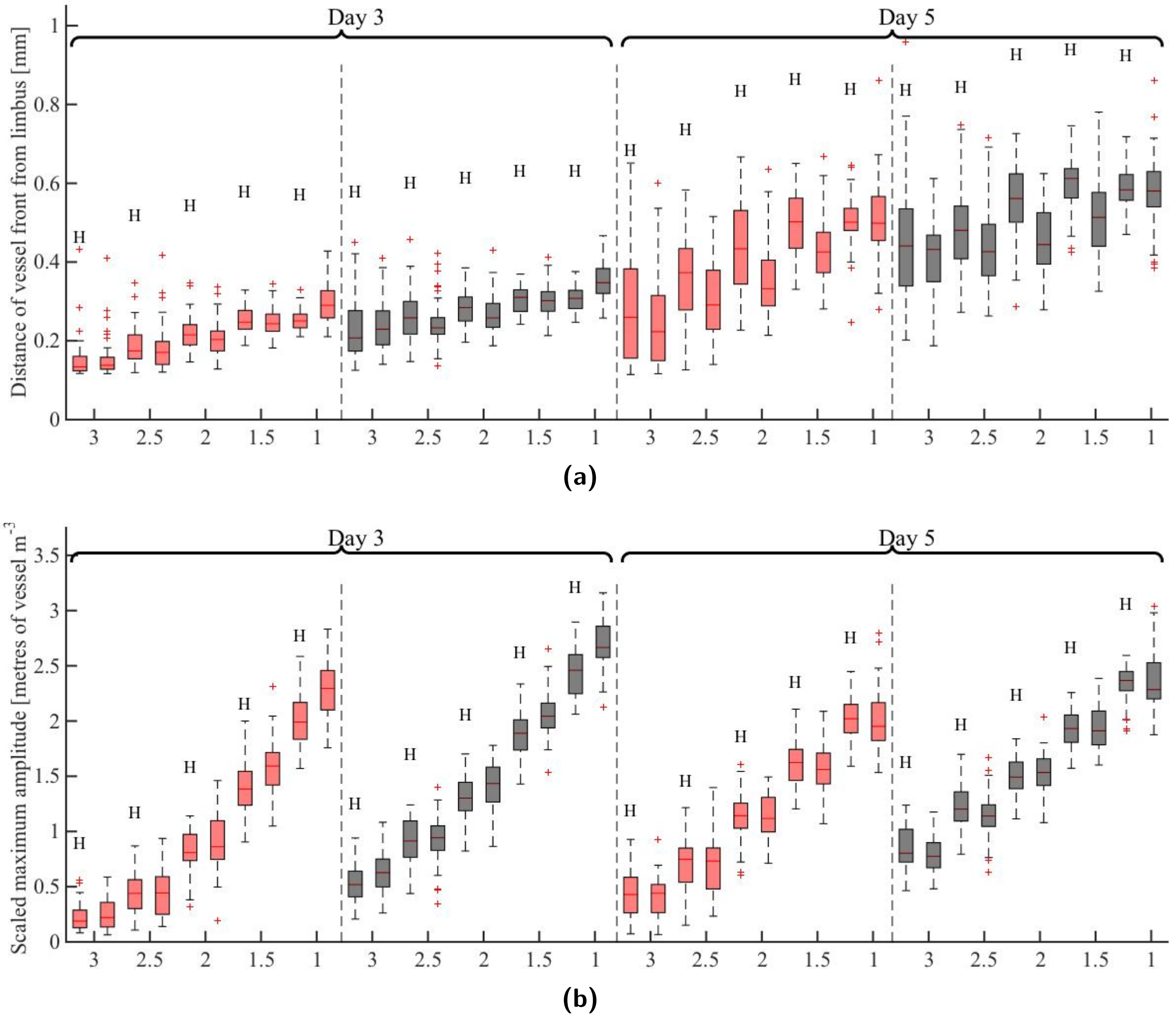

Figure 7.28.: Summary statistics extracted from hybrid model simulations in which VEGF-A$_{165}$ is inhibited. To simulate the inhibition of VEGF-A$_{165}$, λ_v was increased from its default value. On the x-axis of the box and whisker plots are the fold changes in λ_v for a given set of simulations. We compare the original and extended model where default parameter values are used. All other parameters were held fixed at their default values (Tables 7.1-7.3). (a) The distance of the vascular wavefront from the limbus. (b) The maximum amplitude of the vascular wavefront ($\times 2 \times 10^8$ metres of vessel m^{-3}). Red bars: perfused vasculature; grey bars: perfused + unperfused vasculature. Those box and whiskers labelled with a 'H' denote results from our extended model.

amplitude of the vascular wavefront (Figure 7.28b) on days 3 and 5 decrease with increasing λ_v for both models. For our extended model, the location of the vascular front on day 5 in particular decreases at a lower rate than that of the original model. A central reason for this is as follows. As VEGF-A$_{165}$ inhibition is increased tip densities decrease and thus tip-tip interactions, one of the primary drivers of vascular growth in our model, are also reduced. This acts to reduce the migration speed of tip cells. However, reduced VEGF-A$_{165}$ levels permit some tip cells to produce MMPs at a rate which leads to local ECM levels which are near optimal for migration.

Then, occasionally a few tip cells may be able to migrate (if close enough in proximity) more efficiently towards the pellet. Thus there are two competing effects of VEGF-A$_{165}$ inhibition in our extended model. That significant migration of tip cells only occurs if they happen to be close enough in proximity also serves to explain the large increase in the variance of vascular front location as VEGF-A$_{165}$ is inhibited in our extended model. Note that this difference in behaviour between the two models is likely to be dependent on the parameters adopted in the extended model.

7.9. Discussion

In this chapter we have presented two 3-D hybrid models of angiogenesis in the cornea which incorporate vessel dematuration, angiogenic sprouting, tip cell migration, anastomosis and a simple description of structural adaptation. As in Chapter 5, angiogenesis is stimulated by VEGF-A$_{165}$ which diffuses from a slow-release pellet. We initially extended an existing model of vessel sprouting and tip cell migration implemented in three dimensions by Perfahl *et al.* (2011). Perfahl *et al.* (2011) sought to extend the 2-D model of vascular tumour growth developed by Owen *et al.* (2009) to three dimensions. In the model of Owen *et al.* (2009), as in our model, anastomoses form when tip cells move into a location which is already occupied by another vessel or tip cell. In two dimensions, tip cells intersect with vessels or other tip cells relatively frequently. However, when moving from two to three dimensions, in the absence of signals which guide tip cells towards vessels or other tip cells, anastomoses tend not to occur unless the surrounding vasculature is dense. Thus, when moving from two to three dimensions, Perfahl *et al.* (2011) changed various (three) model parameter values in order to increase the vascular density in their 3-D domain, and thereby increase the likelihood that anastomoses would form. This approach yielded insight into the behaviour of tumours growing in three dimensions and, in particular, the influence of domain size and boundary conditions on simulated vascular tumour growth in three dimensions. However, in practice their approach generates 3-D vascular networks which contain a significant proportion of unperfused vessels. *In vivo*, tip cells extend lamellipodia and filopodia up to distances of "$> 100\,\mu$m" (Gerhardt 2003), allowing them to sense nearby cells and vessels, and facilitating the formation of anastomoses. This process is believed to be essential for the formation of vascular networks in three dimensions. In our model we assume that tip cells can sense nearby vessels and other tip cells and bias their motion towards them in order to facilitate anastomosis and thus the formation of well-perfused, functional vascular networks.

We note that our approach shares similarities with that adopted by Secomb *et al.* (2013). They too assume that a tip cell may sense nearby vessels and bias their motion in the direction of those vessels. Their approach, however, did not take into account tip-tip interactions and tip cell motion was restricted to a 2-D plane. We also note that, while we have assumed that it is a tip cell's filopodia which are responsible for such sensing, other chemical or mechanical signals may also facilitate tip cell guidance towards other vessels or tip cells. Our model could be extended to include these alternative guidance signals (see discussion in Chapter 8).

Composite hybrid models, such as the ones considered here, are difficult to parametrise, particularly if accurate data are not available; the complexity and time taken to run simulations limits our ability to search high dimensional parameter spaces within reasonable time-frames. For the same reasons, establishing the sensitivity of model outputs to changes in parameter values is also difficult. This motivates studies of simpler continuum models (in parallel with such hybrid models) for which simulations are usually less computationally intensive. For example, consider that the time required to run a simulation of our original hybrid model (adopting default parameter values, as in Tables 7.1-7.3) is approximately one hour on a single core of a laptop with a 4-core Intel Core i7 @ 2.7 GHz processor and 16 GB RAM. By contrast, the run-time of a single simulation of our 1-D continuum model of VEGF-A_{165}-induced angiogenesis (Chapter 5, (5.19)-(5.25)) on the same desktop is less than a minute. A further barrier to establishing parameter values is that our hybrid models are stochastic. Thus, many simulations must be performed to establish the average behaviour of our models when a given set of parameter values is adopted. However, since our hybrid models are based on the continuum models of Chapter 5, we were able to base preliminary estimates for several parameters on parameter values used in those continuum models. One at a time sensitivity analysis of our continuum models, presented in Chapter 5, also indicated how our hybrid model outputs would change in response to changes in parameter values. This allowed us to tune hybrid model parameter values in a more informed way than would have been possible otherwise. Simplified models, or *meta models*, are often employed in engineering to relieve the computational burden of running complex model simulations many times (Zadeh *et al.* 2008). We have found that studying complementary continuum and multiscale hybrid models of angiogenesis in parallel may aid the parametrisation of computationally expensive multiscale hybrid models.

With the aid of the continuum models, the hybrid model was parametrised so that the averaged perfused vascular density profiles extracted from default simulations are in good agreement with data on perfused vessels extracted from experimental images. This contrasts how the models developed in Chapters 5 and 6, which did not distinguish perfused and unperfused vessels, were parametrised. Furthermore, due to the 3-D nature of our model, we could compare our model to the experimental data in a way which was consistent with how the vascular density data was extracted from the experimental images: we compared the averaged vascular density profiles generated from simulated vascular networks which had been projected on to a 2-D plane with those extracted from 2-D experimental images.

It is common for pharmaceutical companies to use 2-D images or slices from 3-D vascular network structures to gain insight in to the action of a drug, for example. Mathematical models, such as ours, provide an inexpensive method by which to assess whether the metrics extracted from 2-D slices or projections of 3-D network structures provide an accurate description of the 3-D structures. Our analysis suggests that it depends on the metrics of interest. In particular, analysis of our simulated 3-D vascular networks provided insight into how accurately measurements of vascular density from 2-D experimental images approximate *in vivo* vascular density. Our simulation results suggested that, while the vascular density estimated from 2-D images may underestimate the *in vivo* vascular density by up to $40 - 50\%$, the location of the vascular front may be accurately estimated from the analysis of 2-D images.

As with our continuum models of Chapter 5, when parametrised against available experimental data, our hybrid model exhibits some desirable features, including a self-adaptive regulatory behaviour similar to that noted previously by Tong and Yuan (2008b). That is, since vessels are VEGF-A_{165} sinks, continued vascular growth creates a barrier to the VEGF-A_{165}, preventing it from reaching the limbal vasculature. Consequently, because tip cell production depends on VEGF-A_{165} levels, it is localised around the leading edge of the vascular front. The fact that our hybrid model distinguishes perfused and unperfused vessels also allows us to examine the relationship between the dynamics of the perfused vasculature and the vasculature as a whole (perfused and unperfused vessels). Our default simulations predict that, for the experimental time-points of interest ($t = 3\,\mathrm{days}$ and $t = 5\,\mathrm{days}$), the behaviour of the perfused vasculature approximates well the behaviour of the vasculature as a whole. After $t \approx 2\,\mathrm{days}$ the distance between the migrating fronts of perfused and unperfused vessels stabilises at a value of approximately $0.06\,\mathrm{mm}$, and after $t \approx 3\,\mathrm{days}$ approximately 85% of the vasculature is perfused. An interesting extension of the work presented here would be to characterise the distance between perfused and unperfused vascular fronts in terms of its dependence on system parameters using analytical methods, i.e. in a continuum framework, or via further numerical studies.

That the behaviour of the perfused vasculature approximates well the behaviour of the vasculature as a whole for the experimental time-points of interest provides us with convincing evidence that comparing the total vascular density predicted by simple mathematical models (such as those presented earlier in this thesis) with the perfused vascular density extracted from experimental images is a reasonable approximation. However, whether the perfused vascular density extracted from experimental images accurately estimates the *in vivo* vascular density is another issue which, given the results presented in this chapter, we may call into question.

We demonstrated that, by manipulating parameter values in our tip cell sensing model, we could control the level of perfusion in the developing neovasculature. In particular, through one at a time sensitivity analysis, we identified θ_f, the angle over which tip cells project filopodia, as an important parameter for determining the degree of perfusion in simulated vascular networks. Additionally, the strength of tip-tip interactions, K_T, was found to play a dominant role in determining the speed of migration of the vascular front. Other parameters associated with our tip cell sensing model affect simulation results less markedly. Our model also highlights the role of filopodia (and potentially other signals) in facilitating the formation of anastomoses, as a driver of vascular growth in the cornea, and, thus, as a potential therapeutic target against angiogenesis.

In Section 7.5 we further extended the model of Perfahl *et al.* (2011) to include important tip cell-ECM interactions, largely following the approach adopted by Machado *et al.* (2011) and Watson *et al.* (2012). This extended model was also parametrised by rigorously comparing simulation results with those from complementary experiments, and in Section 7.8 we compared how both our extended and original discrete models behave when VEGF-A$_{165}$ is inhibited. Both discrete models behave qualitatively as expected: the angiogenic response is reduced as VEGF-A$_{165}$ is further inhibited. Quantitatively there were some discrepancies in model results under VEGF-A$_{165}$ inhibition. However, this is likely to be sensitive to the particular sets of parameter values adopted for our models. We note here that the extra detail afforded by the extension of our discrete model to include the effects of the ECM on tip cells came at the cost of significantly increased computational expense; simulations of our extended model (using default parameter values) take roughly twice as long as simulations of our original model.

Both the initiation of angiogenesis (i.e. vessel dematuration and sprouting) and tip cell migration are complex processes which have been greatly simplified in our models. However, having implemented our models inside a computational framework designed to facilitate extensibility, it should be relatively easy to extend them to investigate biological phenomena, such as maturation, in greater detail and also the response of the emerging vasculature to multiple AFs. Our computational framework also makes it straightforward to integrate our hybrid models of angiogenesis with models of vascular tumour growth such as those developed by Alarcón and co-workers (Alarcón *et al.* 2003; Alarcón *et al.* 2005; Alarcón *et al.* 2006; Betteridge *et al.* 2006; Owen *et al.* 2009; Perfahl *et al.* 2011). This will form the focus of future work, as discussed in Chapter 8. Additionally, we aim to incorporate a more detailed model of structural adaptation, similar to that of Pries *et al.* (1990; 1994; 1998; 2001), and with it a model of shear stress mediated vessel regression. A more challenging extension, not currently possible in our computational framework, would be to investigate the use of off-lattice techniques to model vascular growth. Such off-lattice techniques would also facilitate a move towards more complex tissue domains; we could perhaps model the cornea as a spherical (or hemispherical) shell.

CHAPTER 8

Summary and Future Directions

8.1. Overview

In this chapter we summarise the contributions of the work presented in this thesis (Section 8.2) and discuss possible directions for further research (Section 8.3).

8.2. Summary of research contributions

Mathematical modelling of tumour-induced angiogenesis has become a popular field of research within the theoretical biology community over the past few decades, and an eclectic array of mathematical models have been developed to investigate phenomena associated with vascular growth in cancer. Early continuum models of angiogenesis were developed with simplicity in mind and aimed to establish qualitative agreement with experimental studies, while subsequent models have dealt with the cellular and sub-cellular phenomena that lead to angiogenesis in increasing levels of detail. Recently the trend in the modelling of tumour-induced angiogenesis has been towards the development of hybrid models, which aim to address the multiscale nature of cancer and angiogenesis, and investigate cross-scale coupling mechanisms. However, the parametrisation and validation of such models have been largely neglected. For mathematical models of intra-tumoural angiogenesis to be truly useful in the future, we must devote significant resources towards developing techniques which will allow us to rigorously compare experimental and simulated results in a quantitative way. This will allow us to develop models which not only look like the system they are trying to model but are in quantitative agreement with it. Moreover, these models must develop in terms of the biology that they describe so that they can address questions at the forefront of clinical angiogenesis research.

To advance the state of theoretical approaches towards tumour-induced angiogenesis we have focused on integrating quantitative spatiotemporal data depicting the growth of vasculature in the cornea with existing mathematical techniques for modelling angiogenesis. State-of-the-art image processing methods designed to (semi-)automatically extract vascular networks from images were first reviewed and quantitatively compared in Chapter 4. Such image processing algorithms are evidently capable of extracting vessels from images to a high level of accuracy. We used one such image processing technique — the Gaussian matched filter approach — to extract vascular network data from 2-D images of corneal angiogenesis. The data that we extracted provide quantitative estimates for how the perfused vasculature behind the invading front of tip cells evolves in space and time in response to VEGF-A_{165} or bFGF, two AFs which are known to play key roles in tumour-induced angiogenesis. By using computer-aided techniques to obtain quantitative data from images, rather than manual vessel annotation, we aimed to reduce the subjectivity associated with vessel identification and provide a method which is fast and relatively effortless, and, thus, scalable to large numbers of images.

In Chapters 5 and 6, we developed 1-D continuum models of angiogenesis in the cornea. The first model developed in Chapter 5 aimed to capture quantitatively the response of the corneal vasculature to VEGF-A_{165} supplied from a slow-release pellet. Comparison with the quantitative spatiotemporal data of Chapter 4, revealed that our model can capture quantitatively the dynamics of the *in vivo* system when parameters are chosen from a biologically plausible range. A one at a time parameter sensitivity analysis revealed that the angiogenic response of the corneal vasculature was extremely sensitive to the distance that the pellet is placed away from the limbus, corroborating what has long been a concern of the experimental community, that accurate pellet placement is critical if one is to obtain reproducible and reliable results using this assay (Bicknell *et al.* 1997). By making minimal changes to the model we adapted it to simulate bFGF-induced angiogenesis, again showing that the model can capture quantitatively the dynamics of bFGF-induced angiogenesis in the cornea when bFGF-specific parameters are chosen from a biologically plausible range. Comparison of our VEGF-A_{165} and bFGF model parametrisations suggested that the more sustained angiogenic response observed in bFGF experiments may be explained by bFGF having a longer half-life than VEGF-A_{165} ($\lambda_f = 0.04\,\mathrm{h}^{-1}$ vs $\lambda_v = 0.8\,\mathrm{h}^{-1}$). bFGF's longer half-life means that it remains stable inside the pellet and cornea for longer than VEGF-A_{165} and, thus, may elicit a stronger angiogenic response for a longer period of time. The model was then further extended to account for tip cell-ECM interactions and we investigated the impact that such interactions have on model predictions of anti-angiogenic therapies.

Building on the models presented in Chapter 5, in Chapter 6 we developed a continuum model in which the corneal vasculature evolved in response to bFGF and VEGF-A_{165} when administered either alone or in combination, incorporating documented regions of cross-talk between the two factors. To the best of our knowledge this represents the first mathematical model in which angiogenesis may occur in response to bFGF and VEGF-A$_{165}$ simultaneously. The model was used to investigate the impact of bFGF/VEGF-A$_{165}$ cross-talk on the angiogenic response, and to generate experimentally testable predictions regarding the angiogenic response of the limbal vasculature when exposed to both bFGF and VEGF-A$_{165}$, and the effect of anti-VEGF-A therapy on bFGF-induced angiogenesis. Our model predicts that strong anti-VEGF-A therapy administered during bFGF-induced angiogenesis can cause a reduction in vascular density, in qualitative agreement with experiments performed by Seghezzi *et al.* (1998).

The last results chapter of this thesis (Chapter 7) focused on the development of a hybrid model of tumour-induced angiogenesis, which was implemented in a modelling framework built specifically to facilitate the extensibility and adaptability of hybrid models of angiogenesis and vascular tumour growth. We initially adapted and extended the model of VEGF-A$_{165}$-induced angiogenesis developed by Perfahl *et al.* (2011) to include a biologically motivated model of tip cell sensing which allowed tip cells to sense vessels and other tip cells in 3-D space and to bias their motion towards them. A mutually symbiotic relationship between our continuum and hybrid models was clearly demonstrated. First, because of the similarities between our continuum model of VEGF-A$_{165}$-induced angiogenesis of Chapter 5 and the hybrid model, we were able to use the continuum model to aid the parametrisation of our hybrid model. This substantially reduced the number of simulations and, hence, the time required to establish parameter values for which our hybrid model produces simulation results which are quantitatively consistent with the available data. Equally, we used the parametrised hybrid model to investigate the relative behaviours of the total and perfused vessel populations, our simulations suggesting that comparing the total vascular density predicted by the continuum models with the perfused vascular density extracted from experimental images is acceptable as a first approximation. We also used our hybrid model to provide insight into how accurately the measurements of vascular density from 2-D experimental images may estimate the *in vivo* vascular density, given that it is a 3-D structure. Our simulations suggested that the vascular densities extracted from 2-D images may underestimate the *in vivo* vascular density by a factor of approximately two.

Interestingly, we found that vascular growth in our hybrid model most accurately represents that seen *in vivo* if tip-tip and tip-vessel interactions are dominant over chemotaxis in determining a tip cell's motion. Moreover, in the absence of chemotaxis, we found that directed sprouting and the tip-tip and tip-vessel interactions included within our model are sufficient to drive vascular growth towards the source of VEGF-A_{165}. This contrasts with results presented by Stokes and Lauffenburger (1991), for example, whose model suggested that chemotaxis was essential for ensuring directed growth towards the source of a chemoattractant. By changing the tip cell sensing model parameters we were able to tune the extent to which tip cells are attracted to nearby vessels or other tip cells and, thus, control the rate at which anastomoses form and the level of perfusion in the evolving neovasculature. Additionally we investigated the effect of removing filopodia formation on the results of model simulations, our results suggesting that inhibiting filopodia formation as part of a mono- or combination therapy may help to inhibit pathological angiogenesis *in vivo*. Finally, as for our continuum models of Chapter 5, we further extended our hybrid model to include key tip cell-ECM interactions, and evaluated how such interactions affect predictions of the effect of anti-VEGF-A therapies.

In summary, this thesis clearly demonstrates the benefits of adopting an integrated approach to modelling tumour-induced angiogenesis. By exploiting a close link with quantitative data we have been able to extend the predictive and hypothesis-testing capabilities of our models. Moreover, by developing complementary hybrid and continuum models of angiogenesis we have been able to offer increased insight into the results of experimental angiogenesis assays and the mechanisms underlying angiogenesis.

8.3. Future directions

A number of extensions to the work presented in this thesis have been suggested in the preceding chapters. In this section we elaborate on some of these extensions. We also discuss issues that have been highlighted by attempting to integrate the results of model simulations with quantitative data throughout the course of this thesis.

8.3.1. Extension of mathematical models

The model of VEGF-A- and bFGF-induced angiogenesis of Chapter 6 provides a solid foundation for the development of a model of vascular tumour growth in which the tumour vasculature remodels in response to multiple factors. Extending the model to simulate vascular tumour growth may allow us to predict the efficacy of anti-VEGF-A drugs in a tumour micro-environment where vascular remodelling occurs in response to multiple AFs, and provide insight into bFGF-resistance to anti-VEGF-A therapies. Such a model could also be used to provide insight into the potential efficacy of combined anti-bFGF and anti-VEGF-A therapies. The model could also be extended to include more detailed models of the biochemistry underlying angiogenesis. For example, maturity has been incorporated into our continuum models in a simple way. To extend the model of maturation, angiopoietins, PDGF, pericytes, etc, could be introduced (as in Jackson and Zheng, 2010, for example). This would allow us to model vessel maturation and dematuration in a more mechanistic way, and to explore a wide array of combination anti-angiogenic therapies.

The hybrid models of Chapter 7 could also be further developed to incorporate more biological detail. For example, having already introduced ECM degradation by tip cells into our model, the model could be further extended to account for VEGF-A_{165} (or bFGF) sequestration by and cleavage from the ECM. Furthermore, we are in a good position to integrate the model of structural adaptation developed by Pries *et al.* (1990; 1994; 1998; 2001) into our hybrid model. This would allow us to more accurately predict vessel diameters, flow rates and shear stresses inside vessels, and so implement more accurate models of vessel regression which take into account flow-induced shear stress.

While the tip cell sensing model presented in Chapter 7 has been developed to capture tip cells mechanically sensing vessels or other tips using filopodia, experimental evidence also points towards other mechanisms of tip cell guidance towards other vessels. Song and Munn (2011), for instance, hypothesise that the motion of tip cells against the direction of interstitial fluid flow may guide those tip cells towards vessels that have higher microvascular pressure than their own. This followed experiments in which tip cells moving against the flow of interstitial fluid produced more filopodia than those tip cells moving with the direction of flow. This phenomenon could be integrated into our hybrid model of angiogenesis to test, explore and extend Song and Munn's hypothesis. Recent work by Soltani and co-workers (Soltani and Chen 2013; Sefidgar *et al.* 2014) has seen the model of tumour-induced angiogenesis of Anderson and Chaplain (1998) integrated with a model of interstitial fluid flow. Their model of interstitial fluid flow provides a basis for integrating such a phenomenon into our own model, thereby offering a mechanism by which to explore tip cell guidance due to interstitial fluid flow within our modelling framework.

We anticipate that extending our hybrid model to incorporate these additional biological details will be relatively straightforward, since our model has been developed inside a framework designed to facilitate the implementation of such extensions. Our framework also makes easy the re-integration of such hybrid models of angiogenesis into larger models of vascular tumour growth. This will also form the focus of future work.

8.3.2. Further development of modelling framework

Fully integrating the vascular growth functionality implemented in our modelling framework into Chaste (Pitt-Francis *et al.* 2009; Mirams *et al.* 2013) (see Appendix C) in a way which is understandable and extensible represents a fruitful direction for further research. Incorporating the vascular growth functionality fully into Chaste would allow us to exploit Chaste's existing on- and off-lattice mesh classes. This could allow for the implementation of off-lattice cell and vascular growth models, facilitating a move towards modelling tumour-induced angiogenesis in irregular-shaped geometries. There is also scope for further developing our code base so that other network structures could easily be modelled using similar techniques. For example, classes which are similar to those used to implement models of vascular growth could be used to implement models of neuronal growth (neurogenesis) or the growth of lymph vessels inside a tumour (lymphangiogenesis). This would then allow for the development of models of tumour growth which include both angiogenesis and lymphangiogenesis.

8.3.3. Further experiments and additional experimental data

In order to validate our models and to further constrain model parameter values, additional experiments and data are required. First, further experimental work is required in order to test the predictions made by our models. For example, simulations of the continuum model of Chapter 6 predict that strong anti-VEGF-A therapy administered during bFGF-induced angiogenesis can cause a reduction in vascular density, a result in qualitative agreement with experiments performed by Seghezzi *et al.* (1998). To further validate our model, we would like to compare our model prediction (Figure 6.5) with quantitative data from complementary *in vivo* experiments. To further constrain parameter values and to validate our models, experimental data which describe the spatiotemporal distribution of unperfused vessels, and tip cells should also be acquired. In particular, we showed in Chapter 5 that additional spatiotemporal data which details the locations of tip cells would be useful for further constraining model parameter values.

If the models in this thesis are to be further increased in complexity, as suggested in Section 8.3.1, further quantitative, spatiotemporal data would be required to keep the models grounded in experimental observation. For example, data detailing the location of pericytes (and whether they are associated with a vessel or not) would be beneficial, particularly if pericytes were to be included within the models. Meanwhile, data describing the radii of vessels, would be very useful if a detailed model of structural adaptation is to be integrated into our hybrid model.

The discrete model offers an opportunity to perform even more detailed comparisons between simulation results and data. For example, armed with appropriate images, we could examine the model's ability to capture experimentally observable branching point distributions, vessel length distributions, and other metrics which aptly describe the topology of the neovasculature. Unfortunately, the 2-D images available to us were not appropriate for extracting such data reliably. High resolution 3-D images are required to obtain such statistics with reliability. Given the provision of such data, this may prove a fruitful direction of research in the future.

We note that discriminating between models or establishing tight bounds on parameter values to ensure that our models accurately capture new experimental data is likely to be particularly challenging using the cornea assay. We anticipate that this will be difficult because of the apparent sensitivity of experimental results to the distance that pellets are placed from the limbus. As noted in Chapter 4, to help improve the accuracy of data arising from cornea experiments, images should include a scale bar. Future work could also entail investigating additional image processing techniques that might enable us to extract vascular networks more robustly and in a way which requires less human intervention.

8.3.4. Formally evolving tighter constraints on parameter values

The spatially and temporally resolved data used to parametrise the models presented in this thesis allow us to constrain model parameter values to a greater extent than would be possible if, for example, only the location of the vascular wavefront were used. Moreover, by incorporating this additional data we ensure that our models more accurately capture the observed biological behaviour. However, the amount and quality of data currently available to parametrise dynamic, spatially-resolved models, such as ours, do not allow one to completely constrain model parameters. In fact, in Chapter 6, for example, we showed explicitly that the parameters ϕ (the maximum rate of bFGF-induced VEGF-A production) and s (the maximum bFGF-induced fold increase in VEGFR-2 expression) are quite loosely constrained by the available experimental data.

Throughout this thesis, aware of this limitation of our data, we opted to establish parameter values by a thorough review of the experimental literature and subsequent manual fine-tuning until our model outputs were quantitatively consistent with the experimental data presented in Chapter 4. By taking this approach we were able to demonstrate that our models can capture quantitatively the available experimental data when parameters are chosen within acceptable physical ranges. An alternative approach would have been to rigorously fit our models to the data by minimising, for example, the root mean squared error. Such classical inverse analysis aims to establish which model parameter values permit best agreement between a model and experimental observations. However, this type of analysis fails to take into account the uncertainty in experimental observations. Moreover, most inverse problems within the biological modelling arena are ill-posed and a range of parameter values may provide adequate fits to the data (as we have shown). Thus, there is also some uncertainty in the value of parameters which classical inverse analysis fails to account for.

Yet another approach to parameter estimation is based in the Bayesian framework. In Bayesian inverse analysis, both the experimental observations and model parameter values are represented by probability density functions (PDFs), which quantify the uncertainty in their values. Then, the solution to an inverse problem in the Bayesian framework is a PDF which characterises how uncertain one is about the value of various model parameters given the experimental observations available to constrain those parameters[1]. Bayesian approaches to parameter estimation could be used to integrate the spatiotemporal data from Chapter 4 with the models presented in this thesis. By adopting this approach, and since parameter estimates in the Bayesian framework are PDFs, we could then formally quantify the extent to which the values of the parameters in our models are constrained by our data. Within such an approach, as more data become available, they too could be used to further refine the PDFs of model parameters. That is, as more data become available, the parameter values could be further constrained since only a subset of the parameter values which allow our model to fit to the original experimental data are likely to permit the model to fit to any new data also. Furthermore, with additional data, it may be possible to formally rule out a model given some new data if a model cannot capture that data. A good introduction to the use of Bayesian techniques within the tumour modelling arena is provided in Hawkins-Daarud *et al.* (2012).

8.3.5. Parameter identifiability, global sensitivity analysis and uncertainty analysis

Parameter identifiability analysis attempts to establish whether the parameter set which generates the solution to a given parameter fitting problem is unique (either locally or globally) (Little *et al.* 2010). Additionally, it may provide insight into what new experiments are required, and

---

[1] Such Bayesian techniques also take into account prior information about the values of parameters, i.e. estimates from the literature.

what new data should be acquired, so that model parameters may be fully constrained (uniquely identifiable with respect to the available data) (Quaiser *et al.* 2011). Identifiability analysis is a large and ever-expanding field within biological modelling, and we have not the space to give a vast amount of detail here. However, we note that establishing whether parameters are identifiable in models which contain more than ten unfixed parameters is typically difficult, and most work has focused on developing methods to prove *a priori* identifiability of parameters in systems of linear coupled ODEs. Research into the identifiability of parameters in simple, dynamic, spatially-resolved biological models has received some attention (see, for example, Fister and McCarthy, 2007) but has not been as widely explored. For such complex systems as we consider, brute force Monte Carlo methods (potentially based in a Bayesian framework) are likely to be required to establish whether model parameters are identifiable with respect to the available data. These brute force methods usually involve performing many thousands or millions of simulations across expansive regions of parameter space.

It is likely that parameter values from complex models of tumour-induced angiogenesis will, in general, not be uniquely identifiable with respect to the available experimental data. In such instances, to take into account the uncertainty associated with parameter values one may simulate the model over a wide area of multi-dimensional parameter space to ascertain many sets of plausible parameter values for which the model outputs match the currently available experimental data. For instance, in a Bayesian framework, sophisticated sampling algoithms, such as Markov Chain Monte Carlo methods (Andrieu and Thoms 2008) permit efficient exploration of parameter space in such a way that (in the long time limit) the amount of ‘time’ spent in a particular region of parameter space is proportional to the probability that a particular set of parameter values is the ‘true’ one. When making a prediction with such a model, it is then possible to take into account the uncertainty in parameter values by simulating the model using all (or many) sets of parameters for which the model is in quantitative agreement with the data (i.e. we select parameter values by sampling from the posterior distribution of parameter values obtained via Bayesian inference). This then allows one to establish confidence bounds on model predictions (given the uncertainty associated with parameter values). Such a procedure could be extremely important when a clinical decision is to be made based on a model prediction. For example, in the future, mathematical models may be used to predict tumour growth inside an individual and their response to different therapies. For such applications, uncertainty analyses would have to be carried out to discern the range of possible predicted treatment outcomes due to uncertainty in model parameter values. In such situations, in which models could be used to suggest treatment strategies, it would also be important to take into account the impact of structural uncertainty on model predictions. That is, different models may contain different mechanisms and thus make different predictions.

In the short term, it is clear that more effort must be focused on exploring parameter space more broadly and globally (i.e. not around a single point in parameter space). The models developed in this thesis would certainly benefit from a more detailed, global parameter sensitivity analysis. Global sensitivity analyses, such as those reviewed in Marino *et al.* (2008), can be used to rank parameters in terms of their significance, that is, in terms of the magnitude with which changes in parameter values affect simulation results. These ranking data can be used to provide informative feedback to experimental collaborators that details which parameters should be known to a greater degree of accuracy in order to reduce the uncertainty associated with model predictions. This, in turn, should stimulate the conduction of additional experiments which attempt to pin-down those significant parameters.

At present a major obstacle to exploring large parameter spaces with complex models of tumour-induced angiogenesis is their computational expense, i.e. the time taken to evaluate simulation runs. However, with continued improvements in computer hardware and software (algorithms) in the future, which should enable substantial speed-ups in the evaluation of model simulations, brute-force methods for assessing the identifiability, the global sensitivity and the uncertainty in predictions of models of tumour-induced angiogenesis are likely to become more plausible. A particularly exciting prospect involves the use of model emulators (National Research Council. 2012), which may be used to enable faster exploration of parameter space and thus perform faster quantification of uncertainty and sensitivity analysis (particularly for computationally expensive models). Emulation techniques have thus far been largely neglected by the tumour and angiogenesis modelling community and should be further developed and adopted in the future.

8.3.6. An alternative approach to integrating the models with experimental data

In Chapters 5, 6 and 7 models were parametrised by comparing simulation results to spatiotemporal data which had been averaged across a number of different experiments involving different animals. However, whether parametrising our models according to data averaged over a number of similar experiments is the most appropriate approach to take moving forwards is an open question. An alternative approach would be to fit the models to data arising from each individual experiment. Consider, for example, using data from experiments which included a cohort of 30 mice. From each mouse, one obtains a different vascular density profile. To parametrise a model of corneal angiogenesis, one would then ‘fit’ it 30 times to the 30 different vascular density profiles, providing 30 model parametrisations. Then, when, for example, predicting the impact of anti-VEGF-A therapy on bFGF-induced angiogenesis (as in Chapter 6), one would actually make 30 predictions with the model using the 30 different model parametrisations. Then, instead of comparing a single model prediction with the mean response from, say, 30 complementary experiments designed to test the prediction, one would aim to compare statistically the results of the 30 new experiments against the 30 model predictions. Provided the results of the ensemble of model predictions are not statistically different to those of the new complementary experiments, one then might conclude that the model is consistent with the new set of experimental data. Such an ensemble of predictions might also provide insight into the degree of inter-individual variability expected in experiments designed to test the model predictions. Methods to capture inter-individual variability for predictive purposes are used within the pharmaceutical industry (Ribba *et al.* 2014) and are being investigated within the cardiac modelling community (see, for example, Britton *et al.*, 2013).

Our hybrid model results suggest that vascular densities extracted from 2-D cornea images may underestimate the *in vivo* vascular density by approximately 50%. To facilitate the more accurate parametrisation of our continuum models, for each experiment, the discrete model could be used to estimate the true vascular density of the 3-D *in vivo* structure. The vascular density profiles from our parametrised hybrid model could subsequently be used to parametrise our continuum models.

8.4. Final comments

We conclude by re-iterating a point made at the end of Chapter 4. We are beginning to see the emergence of high quality, time-lapse images of the cellular processes underlying cancer and vascular development. In addition, image processing algorithms designed to extract useful data from such images continue to improve. In the future, more work needs to be done to merge the two complementary fields of image analysis and mathematical modelling in angiogenesis and cancer research. The successful merging of the two fields, together with the materialisation of quality quantitative data, which are spatially and temporally resolved, will allow for improved parametrisation of mathematical models of angiogenesis. This, in turn, will allow us to extend the hypothesis generating and testing capabilities of such models, and to begin making reliable quantitative predictions. The work contained in the thesis illustrates the potential benefits of fostering a closer integration between mathematical modelling and image analysis within tumour-induced angiogenesis research.

Appendices

APPENDIX A

Alternate Parametrisations of the Model of Corneal Angiogenesis from Section 5.11.2

Tables A.1 and A.2 display the fold changes in parameter values used to obtain alternate fits to the experimental data for the model variants M1 and M2, respectively, as shown in Figure 5.21.

Parameter	**Default non-dimensionalised parameter value**	**Fold increase in parameter value w.r.t. default value**			
	M1.2	**M1.1**	**M1.3**	**M1.4**	**M1.5**
$\frac{\chi_0}{f_{v0}}$	40	∞	15	1	0
μ	2.14×10^{-4}	1.3	1	1	1
χ_0	3.12×10^{-2}	1.43	0.769	0.139	0
α_0	2.57	0.833	1	0.976	1
β_1	0.318	1	1	1.89	1.79
γ	2.58×10^{-2}	0.769	1	1	1
θ	47	1.04	1.09	0.993	1.04
C_{max}	1	1	1	0.875	1
C	0.199	1	1	1.79	1
E	133	0.745	1.45	1.49	1.49
f_{v0}	7.79×10^{-4}	0	2.05	5.54	4.11

Table A.1.: Table of parameter modifications for the five variants of our model, (5.38) - (5.48). For each variant various parameter values have been changed w.r.t. their default values to ensure that the simulation results remain faithful to the data arising from experiments in which angiogenesis is induced by VEGF-A$_{165}$ pellets only. All values are shown to three significant figures.

Parameter	**Default non-dimensionalised parameter value**	**Fold increase in parameter value w.r.t. default value**			
	M2.2	**M2.1**	**M2.3**	**M2.4**	**M2.5**
$\frac{\chi_0}{f_{v0}}$	40	∞	15	1	0
χ_0	1.98×10^{-2}	1	0.997	0.144	0
α_0	3.13	1.06	0.96	0.84	0.86
θ	53.8	1.03	1.06	0.951	0.94
E	98.2	0.907	1.25	1.32	1.27
f_{v0}	4.95×10^{-4}	0	2.66	5.76	5.76

Table A.2.: Table of parameter modifications for the five variants of our model, (5.38) - (5.48). For each variant various parameter values have been changed w.r.t. their default values to ensure that the simulation results remain faithful to the data arising from experiments in which angiogenesis is induced by VEGF-A$_{165}$ pellets only. All values are shown to three significant figures.

APPENDIX B

Extended Continuum Model Parameter Values

Most of the default parameter values used for simulation of the extended model presented in Chapter 6 are the same as those used in Chapter 5 (summarised in Tables 5.2-5.6). Only three parameter values were modified in Chapter 6, while two new parameters were introduced, s and ϕ. For convenience, here, we consolidate the default parameters used to simulate our extended PDE model of angiogenesis from Chapter 6 (see Tables B.1-B.4).

Scaling parameter	**Description**	**Value [units]**
$\hat{L}$	Length scale. Approximate distance between limbal vessels and pellet.	0.001 [m]
τ	Time scale. Time for VEGF-A$_{165}$ to diffuse from the pellet to limbal vessels.	3.97 [h]
V_0	Reference value for VEGF-A$_{165}$ concentration.	3.25×10^{-9} [M]
F_0	Reference value for bFGF concentration.	1×10^{-9} [M]
n_0	Reference value for tip cell density.	1×10^{12} [tips m^{-3}]
ρ_0	Reference value for (mature and immature) vessel length density.	2×10^{8} [m of vessels m^{-3}]

Table B.1.: Table of scaling parameters for the extended model of angiogenesis in which vascular growth occurs in response to both bFGF and VEGF-A$_{165}$ (Chapter 6).

Parameter	Description	Default value and units	Non-dimensional value	Sources
λ_2	Maximal rate of vessel maturation.	0.0005 [h^{-1}]	0.002	(Zheng *et al.* 2013)
ν	Average number of ECs contained in a metre of vessel.	1.2×10^5 [cells (m of vessel)$^{-1}$]	24	(Tong and Yuan 2008b)
N_{min}	Local density of ECs required for maturation.	$0.95 \times m_L \times \nu$ [cells m^{-3}]	22.8	-
σ	Initial width of limbal vessel density distribution.	20×10^{-6} [m]	0.02	-
m_L	Maximum density of mature vessel length density at the limbus initially.	2×10^8 [m of vessel m^{-3}]	1	-
μ	Random motility coefficient for tip cells.	7×10^{-11} [m^2 h^{-1}]	2.779×10^{-4}	(Sherratt and Murray 1990; Stokes *et al.* 1991; Kouvroukoglou *et al.* 2000; Addison-Smith 2010; Owen *et al.* 2011; Byrne and Chaplain 1995).
β_1	Rate of tip-to-vessel anastomosis per unit vessel length density per unit tip density per unit volume.	0.4×10^{-9} [anastomosis events h^{-1} m^{-3} (m of vessels m^{-3})$^{-1}$ (cells m^{-3})$^{-1}$]	0.3176	-
β_2	Rate of tip-to-tip anastomosis per unit tip density squared per unit volume.	0.6×10^{-14} [anastomosis events h^{-1} m^{-3} (cells m^{-3})$^{-2}$]	0.0238	-
γ	Maximal rate of regression of ECs (vessels).	5×10^{-3} [h^{-1}]	1.99×10^{-2}	(Cao *et al.* 2003)
κ	Parameter quantifying the length of vessel left behind in a unit volume after a tip cell moves out of that unit volume.	5 [m of vessel cells^{-1} m^{-1}]	25	-
$\bar{l}_\rho$	Constant of proportionality which quantifies the inter vessel distances.	1	0.3536	-
$\bar{l}_n$	Constant of proportionality which quantifies the inter tip cell distances.	1	0.5	-
s	Maximal fold increase in VEGFR-2 receptors induced by bFGF binding to FGFR-1.	1	1	(Pepper and Mandriota 1998)
ϕ	Maximal rate of increase in VEGF-A_{165} concentration due to bFGF binding to FGFR-1 per unit EC density.	1×10^{-22} [moles of $VEGF_{165}$ $h^{-1}cell^{-1}l^{-1}m^3$]	0.4605	-
$\bar{R}$	Average radius of vessels in cornea.	5×10^{-6} [m]	1	(Tsai *et al.* 2009; Peebo *et al.* 2011)
Ω_p	Volume of pellet.	1.7×10^{-11} [m^3]	1.7×10^{-2}	Roche, Penzberg.
ζ_p	Surface area of pellet.	6.79×10^{-7} [m^2]	0.679	Roche, Penzberg.
L	Pellet-limbus distance.	1.1×10^{-3} [m]	1.1	Assumed

Table B.2.: List of parameters which span both submodels of VEGF-A_{165}- and bFGF-induced angiogenesis, (6.5)-(6.14).

Parameter	Description	Default value and units	Non-dimensional value	Sources
λ_1^v	Maximal rate of VEGF-A$_{165}$-induced dematuration.	0.08 [h^{-1}]	0.3176	(Zheng *et al.* 2013)
χ_v	Chemotactic sensitivity of tip cells to VEGF-A$_{165}$.	3.45 [m^2 h^{-1} M^{-1}]	0.0445	(Stokes and Lauffenburger 1991; Stokes *et al.* 1990; Balding and McElwain 1985; Byrne and Chaplain 1995; Addison-Smith 2010).
α_0^v	Maximum rate of VEGF-A$_{165}$-induced production of tip cells per unit vessel length.	2700 [tips h^{-1} per m of vessel]	2.1438	-
D_v	Diffusion constant for VEGF-A$_{165}$ in cornea.	2.52×10^{-7} [m^{2}h^{-1}]	1	(Chen *et al.* 2006; MacGabhann 2005; Ambrosi *et al.* 2005; Swabb *et al.* 1974).
λ_v	Natural decay constant of VEGF-A$_{165}$.	0.8 [h^{-1}]	3.176	(Serini *et al.* 2003; Chen *et al.* 2006).
K_{EC}^v	Maximum rate of reduction in molar VEGF-A$_{165}$ concentration per unit EC density due to VEGFR-2 binding.	4×10^{-22} [moles of $\mathrm{VEGF-A_{165}}$ h^{-1}cell^{-1} l^{-1} m^3]	0.4886	(Wang *et al.* 2002; MacGabhann and Popel 2003; Bikfalvi *et al.* 1991).
$v_{\frac{1}{2}}$	Concentration of VEGF-A$_{165}$ at which VEGFR-2 receptors are half occupied.	6.5×10^{-10} [M]	0.02	(Akeson *et al.* 2010; Wang *et al.* 2002)
P_v	Permeability of corneal vasculature to VEGF-A$_{165}$.	3×10^{-4} [m h^{-1}]	1.191	(Fu and Shen 2003; Stefanini *et al.* 2008).
v_{blood}	Concentration of VEGF-A$_{165}$ in the blood.	0 [M]	0	-
θ_v	Binding constant.	50	50	-
k_p^v	Effective permeability of the cornea-pellet boundary.	1.6×10^{-7} [m h^{-1}]	6.352×10^{-4}	-
λ_p^v	Natural decay constant of VEGF-A$_{165}$ in the pellet.	0.8 [h^{-1}]	3.176	Assume $\lambda_p = \lambda_v$.
$[V_t]_{init}$	Initial concentration of VEGF-A$_{165}$ in pellet.	3.93×10^{-4} [M]	1.2092×10^5	Roche, Penzberg.

Table B.3.: List of parameters associated with the VEGF-A$_{165}$-induced angiogenesis submodel only.

Parameter	Description	Default value and units	Non-dimensional value	Sources
λ_1^f	Maximal rate of bFGF-induced dematuration.	0.017 [h^{-1}]	0.0675	(Zheng *et al.* 2013).
χ_f	Chemotactic sensitivity of tip cells to bFGF.	4.64 [$\mathrm{m}^2\ \mathrm{h}^{-1}\ \mathrm{M}^{-1}$]	0.01844	As in Table B.3.
α_0^f	Maximal rate of bFGF-induced tip cell production per unit vessel length.	580 [tips h^{-1} per m of vessel]	0.4605	-
D_f	Diffusion constant for bFGF in cornea.	1.92×10^{-7} [$\mathrm{m}^2\mathrm{h}^{-1}$]	0.7622	(Boyer and Hsu 1992; Filion and Popel 2004; Tong and Yuan 2008b)
λ_f	Natural decay constant of bFGF.	0.04 [h^{-1}]	0.1588	(Westall *et al.* 1983; Sperinde and Nugent 1998)
K_{EC}^{FGFR}	Maximum rate of reduction in molar bFGF concentration per unit EC density due to FGFR binding.	1.8×10^{-22} [moles of bFGF $\mathrm{h}^{-1}\mathrm{cell}^{-1}$ $\mathrm{litre}^{-1}\ \mathrm{m}^3$]	0.7146	(Fannon *et al.* 2003; Filion and Popel 2004; Bikfalvi *et al.* 1989).
$f_{\frac{1}{2}}^{FGFR}$	Concentration of bFGF at which occupation of FGFR receptors is half-maximal.	4.22×10^{-11} [M]	0.0422	(Bikfalvi *et al.* 1989).
K_{EC}^{HSPG}	Maximum rate of reduction in molar bFGF concentration per unit EC density due to HSPG binding.	3.1×10^{-22} [moles of bFGF $\mathrm{h}^{-1}\mathrm{cell}^{-1}$ $\mathrm{litre}^{-1}\ \mathrm{m}^3$]	1.2307	(Sperinde and Nugent 1998; Filion and Popel 2004; Bikfalvi *et al.* 1989).
$f_{\frac{1}{2}}^{HSPG}$	Concentration of bFGF at which occupation of HSPG receptors is half-maximal.	9.22×10^{-10} [M]	0.9220	(Bikfalvi *et al.* 1989).
P_f	Permeability of corneal vasculature to bFGF.	3×10^{-4} [$\mathrm{m\ h}^{-1}$]	1.1910	(Fu and Shen 2003).
f_{blood}	Concentration of bFGF in the blood.	0 [M]	0	-
θ_f	Binding constant.	55	55	-
k_p^f	Effective permeability of the cornea-pellet boundary to bFGF.	2.75×10^{-7} [$\mathrm{m\ h}^{-1}$]	1.09e-03	-
λ_p^f	Natural decay constant of bFGF in the pellet.	0.04 [h^{-1}]	0.1588	Assume $\lambda_p^f = \lambda_f$.
$[F_t]_{init}$	Initial concentration of bFGF in pellet.	4.92×10^{-5} [M]	4.92×10^4	Roche, Penzberg.

Table B.4.: List of additional parameters required for the simulation of bFGF-induced angiogenesis. Highlighted in green are those parameters whose value has changed from that presented in Chapter 5. See Section 6.3 for details.

APPENDIX C

A Computational Framework for the Implementation of Composite Hybrid Models of Angiogenesis and Vascular Tumour Growth

C.1. Overview

At present, mathematical models of cancer and angiogenesis are often implemented by hand, in the language of choice of a modeller, with the emphasis being on producing simulation results rather than on code design. Priority is not given to how code may be made understandable, or be reused or extended at a later date. This means that, in order to move forwards, modellers new to the field must often either reimplement models completely anew or spend lots of time becoming familiar with existing code in order to manipulate and evaluate simulation runs. Additionally, modellers are met with significant issues when they wish to reuse, extend, or maintain existing model code. As such, the development of cancer models and the success of the cancer modelling community as a whole are severely hindered.

Recognising the importance of good code design, we have devoted considerable effort to developing an object-oriented computational framework for developing and implementing composite hybrid models of angiogenesis and vascular tumour growth. Our focus has been to apply software engineering techniques that allow models developed in our framework to be highly reusable, adaptable and extensible. In Sections C.2-C.4, we present our computational framework and elaborate upon its design, which has been primarily motivated by an existing family of related hybrid multiscale models (Alarcón *et al.* 2003; Alarcón *et al.* 2005; Alarcón *et al.* 2006; Betteridge *et al.* 2006; Owen *et al.* 2009; Perfahl *et al.* 2011). In developing our framework, we have exploited object-oriented design principles, describing the models abstractly and decoupling the framework design from model implementations. Sections C.3 and C.4, in particular, draw attention to the elements of object-oriented programming (OOP) which make it appropriate for developing models of complex biological systems, using the models on which our design is based as a case-study. In

Section C.5 we present an exemplar simulation of vascular tumour growth implemented within the framework. Most promisingly, by decomposing models into collaborating classes of biological entities and behavioural algorithms, our framework aims to facilitate the rigorous validation of multiscale models of angiogenesis and tumour growth, and enable comprehensive testing, or verification (see, for example, Pathmanathan and Gray, 2013), of model code. In Section C.6, we describe the testing strategy that we employ and the current level of testing in our framework. Finally, in Section C.7 we discuss the utility of our modelling framework and directions in which it could be extended in the future.

The work presented here is an extension of that presented at The Fourth International Conference on Advances in System Simulation (SIMUL) in Lisbon in November 2012. The paper which accompanied the presentation appeared in the conference proceedings (Connor *et al.* 2012). The work presented here has also contributed to the production of three other publications (Johnson *et al.* 2012; McKeever *et al.* 2013; Johnson *et al.* 2014).

C.2. Functional scope of the modelling framework

As noted in Chapter 3, the trend in angiogenesis modelling over the past decade and a half has been towards the development of multiscale hybrid models. Many such models share common features and utilise common modelling methodologies to represent various components of angiogenesis models. For example, coupled systems of ODEs are often used to describe subcellular processes and protein interaction networks, and PDEs are used to describe the diffusion of nutrients or chemical signals through tissues. Meanwhile, cell-cell interactions are commonly modelled discretely using on- or off-lattice techniques. Multiscale models allow modellers to capture the interdependence of biological phenomena which occur at different biological scales. Moreover, due to their modular nature, multiscale hybrid models also lend themselves well to incremental extension and/or modification. The computational framework presented here has been developed so as to facilitate the development and extension of the code underlying the implementations of such models.

The development strategy adopted has been to reverse-engineer a family of related models published by Tomás Alarcón and collaborators (Alarcón *et al.* 2003; Alarcón *et al.* 2005; Alarcón *et al.* 2006; Betteridge *et al.* 2006; Owen *et al.* 2009; Perfahl *et al.* 2011) in order to extract and abstract the common methodologies and data structures involved in the development and implementation of vascular tumour growth models. The framework was then implemented based on these abstractions. The nature of our development strategy dictates that, at present, the functionality of our framework is focused around the modelling methodologies that have been employed by Alarcón and co-workers. However, having employed an object-oriented framework, and having designed it with reusability and extensibility in mind, our framework can be extended to allow for additional functionality and novel model features with relative ease. For example, in Chapter 7 we extended the model of angiogenesis implemented in Perfahl *et al.* (2011) to incorporate MMP-mediated haptotaxis as in Stephanou *et al.* (2006) and Watson *et al.* (2012). The models could also be further adapted to study angiogenesis in the retina, as Watson *et al.* (2012) have.

In the remainder of this section we summarise the key features of the models implementable in our framework, while details regarding the implementation of these features are provided in subsequent sections. We do not elaborate upon specifics of the particular models implemented as full details may be found in the original papers.

C.2.1. On-lattice simulations

All biological entities in our simulations, namely cells and vessels, occupy locations in discrete space. In terms of model implementation this means that cells and vessels occupy sites on a lattice-based spatial mesh. Most generally, our spatial mesh allows for multiple occupancy. That is, we may allow more than one cell and/or vessel to occupy each location in the lattice simultaneously. Moreover, normal cells, cancerous cells and vessels may occupy different volume fractions of a lattice site, thus allowing for different levels of crowding for different biological entities. Lattice sites may also be empty.

The spatial lattice defines the extent of our model domain and, once created, is immutable. All model domains are regular (most generally, cuboid) in shape and may extend in two or three dimensions. The models implemented in our framework require the definition of a lattice neighbourhood. We implement both von Neumann and Moore type neighbourhoods in our framework (Packard and Wolfram 1985). Again, these neighbourhoods are implemented in both two and three dimensions.

C.2.2. Vascular networks

Vascular networks are composed of vessels and nodes, at which vessels connect. Vessels are biological entities which span multiple sites in our spatial lattice. They, themselves, are composed of vessel segments, each of which occupy a single lattice site. Properties of discrete vessel segments, e.g. maturity, may be prescribed by simple rules or via the evolution of systems of ODEs representing molecular or cell-level behaviour. Vessels may adapt their radii according to a structural adaptation algorithm, like that devised by Pries *et al.* (1998). Such structural adaptation algorithms also determine the rate of blood flow in a vessel and the flow-induced wall shear stress exerted on a vessel. In turn, this allows us to calculate explicitly which vessels are perfused and which are unperfused. Vessels may be removed from a vascular network, simulating vessel regression, and new sprouts may form from existing vessels. These sprouts are able to grow in response to stimuli (for example, via chemotaxis) and the blunt-ended tips of those sprouts may anastomose with other vessels. There is also scope for modelling vessel collapse due to tumour-induced mechanical pressures, as in Alarcón *et al.* (2006).

Initial vessel network structures may be hard-coded inside our modelling framework or may be described in an external file and imported when required. Such files may describe arbitrary artificial vascular networks or real vascular networks derived from imaging data. Thus, our framework allows for the import and simulation of the evolution of realistic vascular geometries taken from imaging data.

C.2.3. Cell populations

Most generally, we model two types of cells, cancerous and normal, which compete for nutrients and space within our model domain. These cells are each associated with a single lattice site and are permitted to move, divide and die throughout the duration of a simulation. Death and division are related to the removal and addition of cells, respectively, from and to the cell population and, hence, the spatial lattice. Meanwhile, movement simply relates to the translocation of a cell from one lattice site to another. How and when cells perform such actions are prescribed by appropriate user-defined rule-sets.

Cell division is generally controlled via a subcellular model. We have implemented both simple rule-based and ODE-based subcellular models, which dictate the time-evolution of various cell-cycle protein concentrations. Subcellular models are also responsible for prescribing what state a cell is in. Generally, cells may occupy proliferative, quiescent or apoptotic states.

C.2.4. Diffusibles

PDEs are used to model the distribution of diffusible chemicals. Through the use of existing numerical libraries, there is considerable scope for the types and complexity of PDEs which may be solved: time-dependent or -independent, linear or non-linear, coupled or uncoupled. Here, vessels or cells may act as sources or sinks for diffusible chemicals. The concentration of each diffusible chemical of interest is calculated at the location of each lattice site. Locally, these concentrations may then be used to influence cell and/or vessel behaviour.

C.3. Object-orientation for composite hybrid models of vascular tumour growth

The way in which we think about and describe the world usually involves looking at it in terms of objects and the interactions between those objects. Object-oriented programming (OOP) strives to describe systems in terms of objects and their interactions computationally. Objects in OOP may represent real world objects, such as those found in biology, or more abstract notions like mathematical concepts, constructs and algorithms. Thus, OOP may be used to facilitate the mathematical modelling and analysis of complex biological systems. By describing systems in a way with which we are familiar, OOP promotes both an understanding of the system which we are trying to model and also an understanding of the model code itself. That is, OOP helps us to manage the *essential* complexity associated with real-world modelling (Brooks 1987).

Object-orientation was originally heralded as a ‘silver bullet’ (Brooks 1987) for dealing with the software crisis, which was characterised by, amongst other things, the high complexity, low productivity, and poor reliability of software systems. OOP promised to encourage code reuse, maintainability, understandability and extensibility for systems amenable to object-oriented design (Page-Jones 2002). However, producing an object-oriented system or program with long term re-usability, extensibility and maintainability requires considerable investment of time and effort at the start of the project, for what at first may seem like little return; it is an art-form, often requiring years of experience and/or a time-consuming trial and error approach. Nevertheless, the potential benefits of a good object-oriented design are worth the time and effort spent.

OOP is one of the most popular programming paradigms worldwide and is used extensively by software engineers in large software projects (Louden and Adams 2011). However, OOP is often used poorly or inappropriately by mathematical modellers, who may not have a background in computer science and little experience with OOP. Further, since academics are under pressure to publish results from implemented models quickly, typically little time or effort is invested in design of model code, which might ensure that a model implementation would be more understandable and could be more easily maintained and extended at a later date. By contrast, we have carefully considered the design of our model code in order to facilitate its reusability, extensibility and understandability. In large part, these attributes have been acquired through the application of object-oriented techniques and design patterns, which we describe in the remainder of this section and in Section C.4.

Many of the object-oriented techniques described in this section help modellers to accurately describe the world in a way which is natural and understandable to others. This is particularly important within the field of biological modelling. Not only is it desirable for other modellers and programmers to understand our code, so that they may easily use, reuse and extend our models, but it is extremely desirable for experimentalists to be able to understand the system described through the code. This is because systems biology and the development of accurate and validated complex multiscale models rely heavily on co-operation between experimentalists and modellers. Making computational models easier to understand for experimentalists, who may have little programming experience, will promote closer collaboration of experimentalists and modellers.

C.3.1. Objects, classes and modularity

Objects in the context of OOP are complex data structures which contain data fields (attributes) and a set of operational methods to which that object may respond (its interface). In this way, objects represent a convenient data-centric way of decomposing systems into understandable and manageable sets of modules. In OOP, one usually designs *classes*, not objects. Classes then form the templates from which multiple objects can be instantiated; these objects may then exist concurrently inside a program at run-time. For example, our framework contains a `Cell` class. From this class many `Cell` objects are instantiated and exist concurrently in each simulation of vascular tumour growth. Classes may be developed and tested individually before being integrated into larger systems being developed by a team or, in our case, a larger community of programmers (or modellers). Designing classes appropriately makes possible their reuse in other applications.

By enforcing boundaries and structure on a program or model, objects as modules increase the maintainability of code. In software design, *low coupling* and *high cohesion* are often highlighted as desirable qualities which a re-usable, extensible and maintainable piece of software should possess (Hitz and Montazeri 1995). Broadly, coupling refers to the interdependencies between different modules and cohesion refers to how strongly related the functions within a module are. High cohesion is an important quality because it increases the understandability of code. Low coupling, where one module interacts with another through a stable and well-defined interface and independently of the internal structure of the other module, increases maintainability, reuse and extensibility of code. Designing a library of classes with these properties is technically demanding and time-consuming but the benefits are invaluable, especially later in the life-cycle of a project.

C.3.2. Encapsulation, and information and implementation hiding

The wrapping up of operations and attributes into a class, so that those attributes may only be manipulated through, or accessed via, the operations provided by the class, is an example of encapsulation. Good encapsulation hides the details of an object's internal attributes and the implementation of operations from modellers using that object (Page-Jones 2002). These techniques are known as information and implementation hiding, respectively, and their use is essential for promoting code understandability in our framework.

Many complex algorithms are employed in the models implementable in our framework, none more so than the structural adaptation algorithms used to determine the pseudo-steady-state radii of vessels and haematocrit distribution in a vessel network (see Alarcón *et al.*, 2003, for details). However, by packaging the operations and parameters required by this algorithm into a single `StructuralAdaptationAlgorithm` class and providing a single operation by which the entire algorithm may be invoked, we ensure that modellers may easily run the structural adaptation algorithm on a simulated vessel network without necessarily knowing the detailed mathematics involved in the algorithm. By encapsulating all parameters associated with the structural adaptation algorithm in this class, we also reduce the possibility of introducing errors into model implementation. This is established by ensuring that these parameters may only be accessed from a single point in the code and thus may not inadvertently affect other parts of the model implementation. In this way, encapsulation facilitates model code maintainability and changeability as well as understandability.

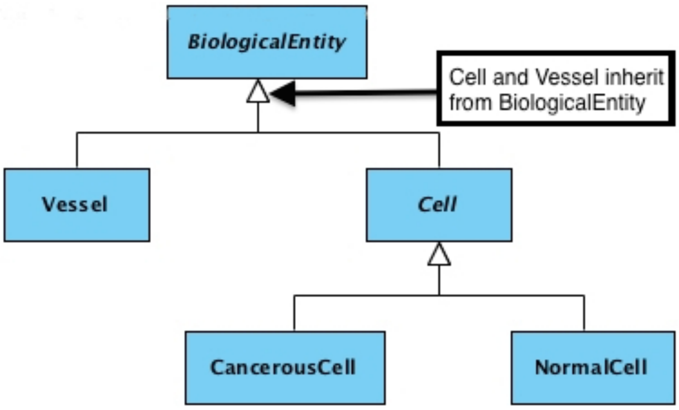

Figure C.1.: UML diagram illustrating the class hierarchy for biological entities in our framework.

C.3.3. Class and containment hierarchies

In the real world, objects are often related by *is-a* type relationships. This type of relationship is realisable in OOP languages, such as C++ and Java, through the use of inheritance. For instance, in the models which motivate our work, *vessels* and *cells* are the primary *biological entities* of interest. Additionally, we usually consider two types of cells: *cancerous* and *normal*. These relationships are represented in OOP using inheritance to define class hierarchies. In Figure C.1 we present a UML (Unified modelling language) (Fowler 2006) class diagram which depicts the relationships between the various biological entities within our framework[1]. The classes `CancerousCell` and `NormalCell` inherit from the class `Cell`, which in turn inherits from the `BiologicalEntity` class. Within this context, the `BiologicalEntity` class is known as the *superclass*, *parent class* or *base class* of the `Cell` class. Conversely, `Cell` is the *subclass*, *child class* or *derived class* of `BiologicalEntity`. The class of `Vessel` also inherits from the `BiologicalEntity` class. In this way, appropriate relationships, which mimic real-world relationships, are defined between some classes of objects in our modelling domain. Furthermore, class inheritance provides a powerful mechanism by which code may be reused. By inheriting from an existing class, such as our `Cell` class, the subclasses (`CancerousCell` and `NormalCell`) automatically obtain all of the functionality (operations) and attributes defined in the `Cell` class. Moreover, new operations and attributes may be defined in the subclasses. In this way, inheritance allows programmers to define classes as incremental variations of more basic and abstract classes.

In OOP, inheritance also enables *substitutability*. In our example, this means that objects

---

[1] UML is a standard notation for documenting object-oriented systems.

of type `CancerousCell` or `NormalCell` may be provided at run-time in any context where an object of type `Cell` is expected without affecting the correctness of the model implementation. This property of an object-oriented system imposes strict rules on class inheritance, namely that any class inheritance hierarchy must follow the principle of type conformance (Page-Jones 2002). Similarly, the Liskov substitution principle (Liskov 1987) defines the appropriate use of subtyping relationships. Unfortunately, modellers using OOP often exploit inheritance for code reuse only, without understanding proper type (or class) design or the concept of substitutability. The ability to substitute classes dynamically at run-time is hugely advantageous and we expand on this idea in Sections C.3.4 and C.4.

OOP also allows objects to be contained within other objects. This is known as a containment hierarchy. A simple example implemented in our framework is shown in Figure C.2. This hierarchy reflects the fact that simulations contain, amongst other things (see Figure C.4), a vessel network and a cell population. Vessel networks, themselves, comprise many vessels which are connected at nodes in that vessel network. Vessels, in turn, are composed of vessel segments, each of which may contain chemicals. Separately, a cell population contains cells, each of which contains a set of intra-cellular chemicals, whose concentrations may dictate that cell's behaviour.

The construction of containment hierarchies is a useful technique, particularly for multiscale modelling. Objects contained within other objects may be used to represent nested levels of organisation, naturally mimicking the biologists' view of their systems. This technique also provides an intuitive mechanism for simplifying the implementation of individual submodels at the specific biological scale(s) with which that submodel is concerned. More complex containment hierarchies may be constructed to model biology at increasing levels of detail, as demonstrated in Webb and White (2005).

Class composition and inheritance may be combined effectively in order to promote further reuse and extensibility of model code. This is best exemplified by the strategy pattern, explained in Section C.4.2.

C.3.4. Polymorphism

There are two distinct types of polymorphism in OOP: *static polymorphism* and *dynamic polymorphism*. Static polymorphism is also known as *overloading* and involves defining operations with the same name, but which take different types and/or numbers of input arguments. An example of overloading would be when requesting that a `CellPopulation` provide access to a

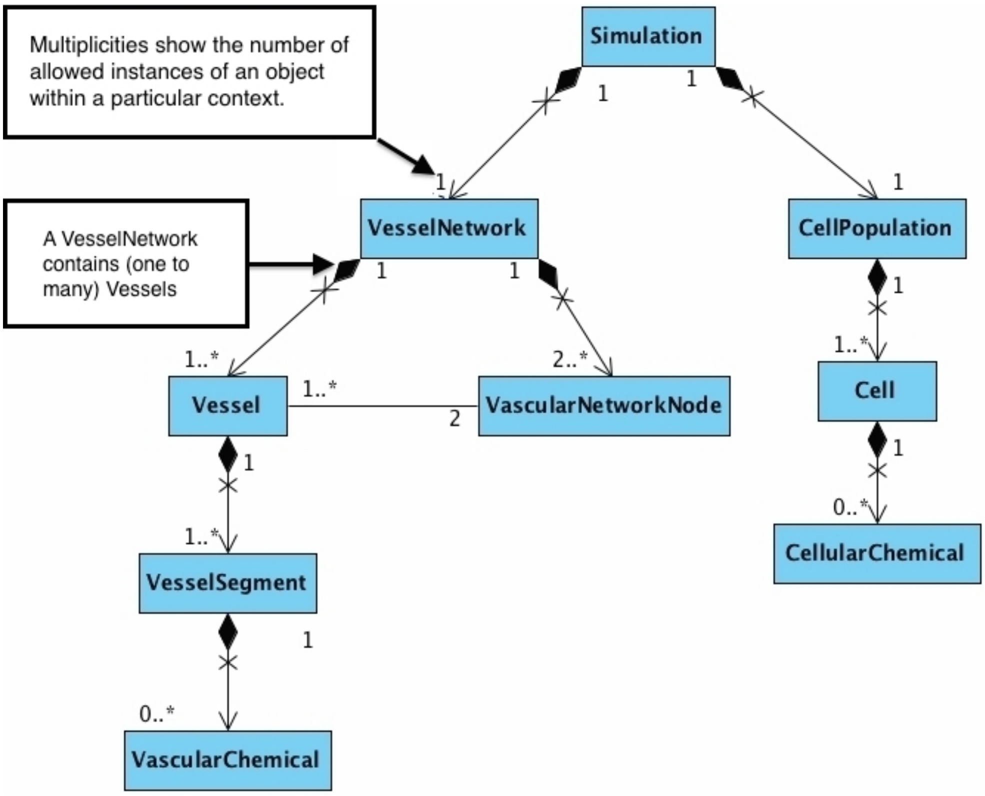

Figure C.2.: UML diagram depicting the containment hierarchy for major biological classes in our modelling framework.

`Cell` contained within that population. We may wish to access a `Cell` object by providing the `CellPopulation` object with either a unique id number, which each cell possesses, or with the location of the cell. In order to implement these requirements we define two operations inside the `CellPopulation` class, each called `GetCell`, which each return a `Cell` object of interest:

1. `GetCell( int idNumber )` returns the `Cell` with `id` equal to `idNumber`.
2. `GetCell( coordinate cellLocation )` returns the `Cell` with `location` equal to `cellLocation`.

This technique aids program design and model implementation by providing a uniform and intuitive interface by which object attributes may be accessed or manipulated (Gupta *et al.* 2003).

Dynamic polymorphism, or *overriding*, is closely related to the concepts of inheritance and substitutability (Section C.3.3). We have already noted that inheritance guarantees that a subclass will contain at least the same operations that are defined in that class's superclass and sometimes more. OOP also allows the implementation of inherited operations to be redefined in a subclass: this is overriding. Calls to an operation which have been overridden in a subclass generally perform a slightly modified function. The functionality executed by a program then depends on what type of object the method is actually called on at run-time. This technique empowers modellers to create implementations which are very malleable and extensible by allowing interchangeable classes within a class hierarchy to perform moderately different functions in response to the same operation call. The primary use of this type of polymorphism within our framework is in the implementation of the strategy design pattern, discussed in Section C.4.2.

C.4. Design patterns

Design patterns represent elegant and re-usable solutions to problems commonly encountered in software design (Gamma *et al.* 2003). Simply using a design pattern can improve code readability and understandability, especially for programmers and modellers who are familiar with the pattern used. Utilising these tried and tested solutions to software development problems may prevent subtle issues that may not have been anticipated but which could cause problems at a later stage in the life-cycle of a development process. From a biological modelling perspective, certain design patterns, for example the visitor pattern (Section C.4.1), enable programmers to separate out biological structure from algorithms which determine the behaviour of the biological entities in a modelling domain. Such design patterns may further promote the understandability of model code for biologists.

We do not intend to explain or provide an exhaustive list of design patterns here, but instead present two behavioural design patterns that are used extensively throughout our framework: the visitor pattern and strategy pattern. We have also made use of the factory pattern, the template method pattern and the null object pattern in our code but do not present full descriptions of these additional patterns here (see Gamma *et al.*, 2003, for details).

C.4.1. Visitor pattern

The main appeal of using the visitor pattern is that it allows programmers to add new algorithms which operate over a class hierarchy without having to modify that class hierarchy. If not using this pattern, one would have to add operations specific to an algorithm to each member of the hierarchy. Implementation of this pattern involves defining two class hierarchies: one for the classes of objects being operated on (*elements*) and one for *visitors* which define the operations on elements. A dynamically polymorphic `accept` operation is defined in the element hierarchy which accepts a visitor object as an argument. A visited element responds to an `accept` operation call by calling the `visit` operation on the provided visitor, giving itself as an argument.

Generic `visit` operations defined in the visitor hierarchy are overridden and overloaded in each member of the hierarchy, in order to define the behaviour of each algorithm on each element class, respectively. By grouping together related operations on one class hierarchy within a separate class hierarchy, we simplify both the class of objects carrying out a specific behaviour (elements) and the implementations of the various algorithms which determine that behaviour. In our framework, this pattern is used extensively to implement models for the behaviour of the vasculature, diffusible substances and cells. We will describe the visitor pattern as implemented in the context of modelling cell behaviour to better illustrate its use.

In our framework, populations of cells are modelled using an agent-based approach, where the behaviours of the cells are modelled by the application of rules, which may differ according to the type of cell to which the rule is being applied. We model three aspects of cell behaviour: movement, death, and proliferation. In addition we also model subcellular events. Models for subcellular processes include rules which dictate how the cell-cycle progresses, when cells should undergo apoptosis, when they should enter a quiescent state, when they should divide and how and when chemicals, such as VEGF, are produced and released. A number of subcellular models have been implemented in our framework, including a model in which division occurs after a fixed period of time (Alarcón *et al.* 2003), a simple oxygen dependent phase model (Owen *et al.* 2011), and a more complex subcellular model, first introduced in Alarcón *et al.* (2005), involving the solution of seven coupled ODEs which represent how various intra-cellular chemicals evolve in time and account for the effect of local oxygen concentrations on cell-cycle progression. Similarly, different submodels dictate how cells should move and proliferate and also how and when a cell should die, e.g. in response to the presence of a drug (Alarcón *et al.* 2006).

Following the template outlined above, we define a `Cell` class hierarchy and a `CellVisitor` class hierarchy, whose members define the algorithms which determine various aspects of a `Cell` object's behaviour (Figure C.3a). Dynamic polymorphism allows the different types of `CellVisitor` classes to modulate the type of cell behaviour which the visitor executes by responding to the same `visit` operation calls. Static polymorphism allows the same `CellVisitor` to implement slightly modified behaviours depending on what type of `Cell` object that visitor is operating. In this way, an algorithm used to determine the behaviour of multiple cell types may be encapsulated inside a single class. Additionally, algorithm specific data structures and parameters are encapsulated within the visitor classes thus making the code more understandable and maintainable.

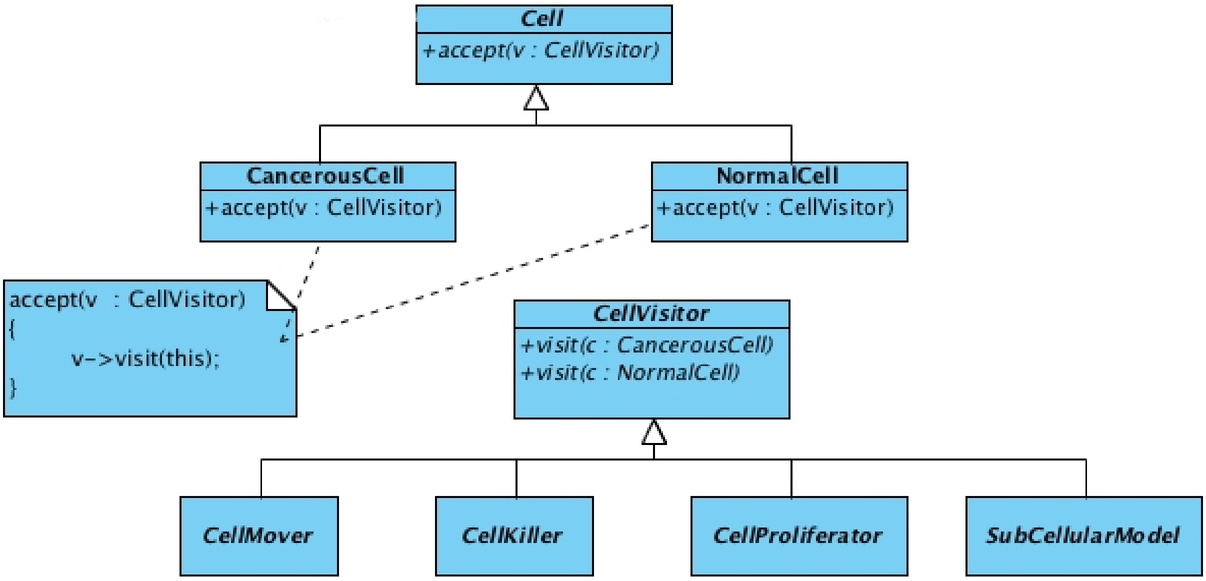

(a) `Cell` and `CellVisitor` hierarchies.

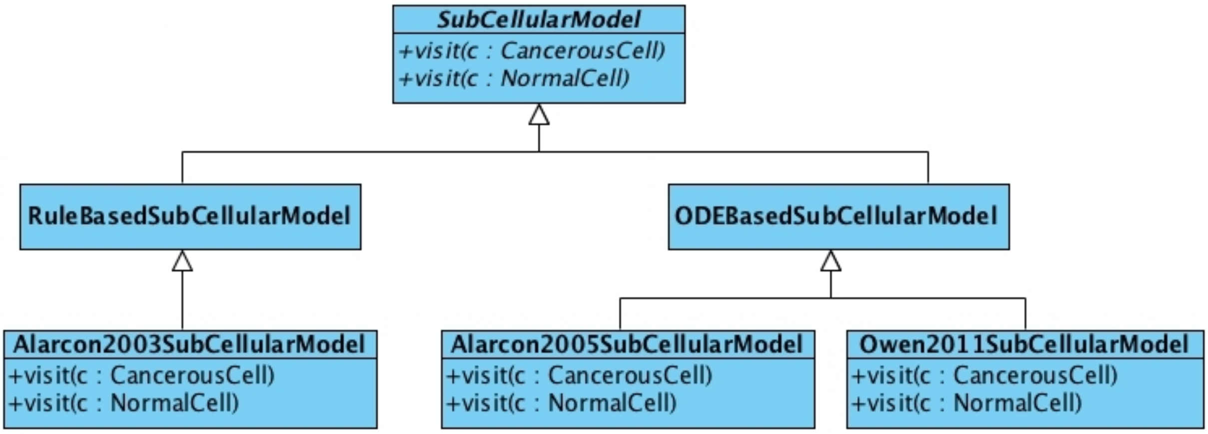

(b) Hierarchy of classes that encapsulate the various subcellular models used in our framework.

Figure C.3.: Visitor pattern as implemented within the context of modelling discrete cell behaviour.

We build the `CellVisitor` hierarchy in order to account for the different algorithms which may be used to model the same aspects of cell behaviour. For example, since we use several different types of subcellular model in our framework, we construct a hierarchy of `SubCellularModel` classes, each of which encapsulates a particular submodel, as shown in Figure C.3b. At run-time, we may then choose which model we would like to simulate with ease. We expand upon this idea in Section C.4.2, where we present the strategy pattern.

To implement different types of cell behaviour in our framework one calls the `accept` method of a `Cell` object providing a `CellVisitor` object as an argument. The behaviour invoked by such a method call depends on the run-time type of both the `Cell` object on which the method is called and the `CellVisitor` object provided as an argument. It is clear to see, therefore, why the visitor pattern is often used in many mainstream languages, including C++ and Java, to compensate for the lack of double (or multiple) dispatch in those languages, as discussed in detail by Bettini *et al.* (2006)[2].

It is particularly easy to vary and add functionality to our framework using this pattern. A new type of cell behaviour or a modified algorithm for, for instance, cell movement may be added to the framework by simply creating a new concrete class in the `CellVisitor` hierarchy. In this regard, this pattern makes extending certain aspects of the framework extremely easy and intuitive. In general, the visitor pattern is applied only when the element class hierarchy is unlikely to change. Adding a new class to this hierarchy means that a new concrete implementation of the `visit` operation, which takes an instance of the new class as an argument, must be added to each concrete `CellVisitor` with an appropriate implementation. Thus, extending model code in this way can prove difficult. This issue may be partially negated by defining appropriate default implementations in the abstract `CellVisitor` class, however, this opens the door for potential bugs to creep in to model implementations. Nonetheless, this pattern is both adequate and appropriate for our purposes since we are currently interested primarily in changing the algorithms that determine the behaviour of biological entities rather than changing the types of biological entities that are present. More complex variants of the visitor pattern have also been implemented, which aim to increase the ease with which both the element and visitor class hierarchies may be extended at the expense of having a less comprehensible underlying structure. For example, see Alexandrescu's implementation of a generic cyclic and acyclic visitor library (Alexandrescu 2001).

C.4.2. Strategy pattern

As well as modelling the behaviour of biological entities using the visitor pattern, we have also utilised the strategy pattern, which allows us to vary the precise algorithms which determine the various aspects of biological entity behaviour at run-time. Again, we clarify this statement with an example. At the highest level, for the running of simulations we utilise this pattern by defining a `Simulation` class. This class co-ordinates the events which occur during a model

---

[2] In languages supporting double (or multiple) dispatch, methods may be dynamically selected based on the run-time type of both the owner of the method (the class in which the method is defined) and the method argument(s). By contrast, single dispatch is where methods are dynamically selected based on the run-time type of the owner of the method only.

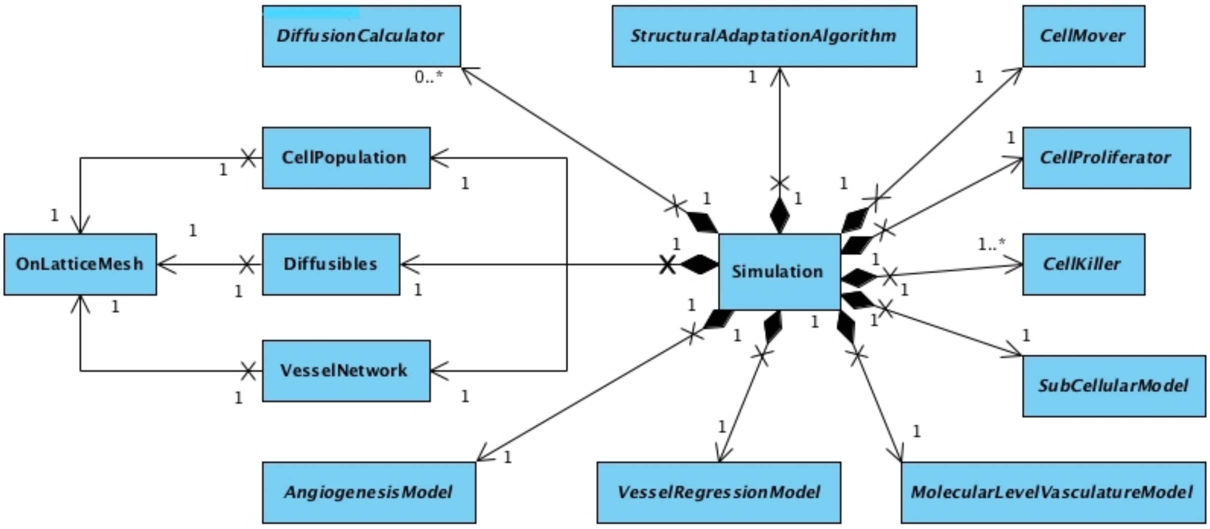

Figure C.4.: Class diagram showing the major classes involved in a simulation of vascular tumour growth in our modelling framework.

simulation, whilst delegating the responsibility of carrying out specific tasks to other classes. For example, a `Simulation` has a reference to the abstract `SubCellularModel` class. Different algorithms for this particular aspect of the system's behaviour are implemented as concrete subclasses of the `SubCellularModel` class, as shown in Figure C.3b. Due to substitutability, an instance of one such subclass may be assigned to the `SubCellularModel` reference at run-time, providing the implementation as desired by a modeller for a particular realisation of a model. Figure C.4 displays a class diagram which illustrates how a model simulation is constructed in our framework. Given that some simulations may not require a particular behaviour to be modelled, we complement the implementation of this design pattern by additionally implementing the *null object pattern* (an instance of this pattern involves defining an additional class within a class hierarchy which has an appropriate interface but possesses neutral behaviour). An example showing how we construct a simulation in our framework using this pattern is presented in the next section.

In summary, the strategy pattern promotes the understanding of model code by factoring out common functionality of algorithms into a suitable superclass, and promotes code maintainability and extensibility, allowing us to implement a large range of different models within our framework in an intuitive way.

C.5. Model realisation

Due to its strongly object-oriented nature, a language supporting object-orientation is required to implement our framework. The nature of the models we consider also requires a language which supports pseudorandom number generation and multi-dimensional arrays. We chose C++ as our programming language because it fits these requirements, is relatively fast and is well-known and familiar to the scientific community. A wide range of reliable open-source C++ libraries are also available which provide relevant trusted functionality and optimised algorithms. Several Boost (Gurtovoy and Abrahams 2002) libraries are used extensively throughout our code, as is the Standard Template Library. We also employ the PETSc (Balay *et al.* 1997) library to solve large, sparse linear systems of equations and the SUNDIALS CVODE solver (Cohen and Hindmarsh 1996) to solve systems of ODEs. The most recent implementation of our framework is as a user project inside Chaste (Pitt-Francis *et al.* 2009; Mirams *et al.* 2013). Chaste is another object-oriented mathematical modelling and simulation framework whose development to date has focused on cardiac physiology and multi-cell models of tissue growth and carcinogenesis in the intestinal crypt. Chaste provides intuitive and easy-to-use interfaces to several numerical libraries, such as CVODE and PETSc, which we use throughout our code. We also utilise other select Chaste classes, designed to, for example, help solve linear elliptic PDEs and systems of ODEs, or maintain a consistent time-step in the different submodels of a hybrid multiscale model. In addition to the libraries used above for running model simulations, simulations are visualised using Paraview[3].

Running a complex multiscale simulation of angiogenesis or vascular tumour growth requires the co-ordinated interactions of many objects. One of the aims of our framework was to make the construction and running of simulations intuitive and simple. Figure C.5 shows a simulation which demonstrates a considerable portion of the framework's functionality. In this simulation, an initially small avascular tumour grows in a 3-D vascularised domain. We allow three cancerous cells to occupy a lattice site maximally while only one normal cell may occupy each lattice site, exploiting the fact that our on-lattice mesh allows for multiple occupancy. As the tumour grows, some cancer cells become starved of oxygen and become quiescent (grey cells). These quiescent cells release VEGF which diffuses throughout the model domain and stimulates the sprouting and growth of new vessels. Vessels may be perfused (shown in red) or unperfused (blue), depending

---

[3] `http://www.paraview.org`

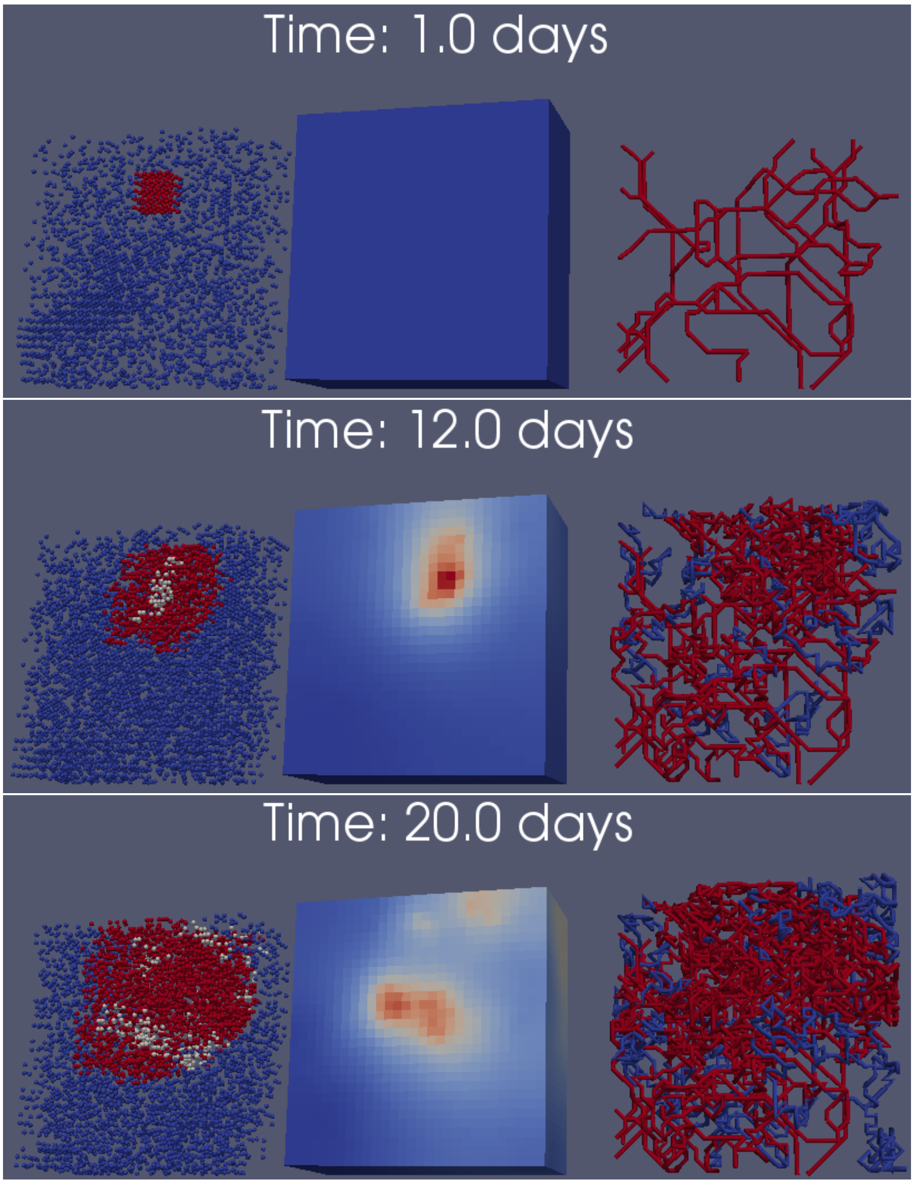

Figure C.5.: Snapshots from a 3-D model of tumour-induced angiogenesis. Cell distributions are shown on the left-hand-side panels. Normoxic cancerous cells are red, hypoxic cancerous cells are grey and normal cells blue. The VEGF distributions, in terms of dimensionless concentrations, are shown in the middle panels and vessel networks in the panels on the right. Red vessels are those which are perfused and blue vessels are those which are unperfused.

on the connectivity of the vascular network, with only perfused vessels delivering oxygen to the model domain. In this exemplar simulation all cells are immotile and a mechanism for vessel regression has not been included. The initial vascular network was imported from a file external to the modelling framework. The file describes a real vascular network, the details of which were extracted from a mammary carcinoma in a rat dorsal skin flap preparation[4]. This example, therefore, exhibits the potential for importing and simulating the evolution of realistic vascular geometries taken from imaging data within our framework. To illustrate how such a simulation is set up in our framework we provide a walk-through in pseudocode of the main steps involved in Algorithm 1. The first step is to initialise the spatial mesh. The spatial mesh is then used to initialise a `Diffusibles` object, a `VesselNetwork` object and a `CellPopulation` object. Diffusible species of interest are added to the `Diffusibles` object and the `CellPopulation` object is populated with cells, each of which contains intracellular chemicals (proteins involved in the cell-cycle and species which diffuse throughout the model domain). Other objects which dictate the biological object behaviours, the simulation submodels, are then created and customised appropriately. Finally, a `Simulation` object is instantiated to which the various submodels are added before the simulation is run.

There is considerable scope for changing parameters in submodels and for removing and adding submodels to simulations. A significant advantage offered by our object-oriented framework is the ease with which submodels at the various biological scales may be analysed, tested and validated in isolation (see Section C.6 for further discussion). Figure C.6 illustrates an example of data extracted from a simulation which considered only the progression of the Alarcón *et al.* (2005) cell-cycle model. This functionality also facilitates the customisation of submodels to experimental and/or patient-specific data and the further development of those models.

C.6. Testing strategy

As alluded to above, the object-based structure of our framework is particularly amenable to component-wise testing, allowing the output from individual methods which implement simple submodels or calculations to be easily tested against the expected outcome from such a submodel or calculation. Such testing gives us confidence that our model implementation is correct, and that no mistakes have been made. This process, then, forms an important part of model verification (Pathmanathan and Gray 2013).

As noted in Section C.5, our framework is implemented inside the Chaste framework (as a user project). This allows us to take advantage of the various open-source tools which have been integrated into Chaste's build system to aid in the analysis and testing of its constitutive code. In particular, Chaste makes use of the C++ library CxxTest[5], a testing framework which, if used properly, may facilitate the automatic verification of model code. The aim, in Chaste, is to test every line of code to make sure that it does what it was written to do. The Chaste development

---

[4] Original data available from `http://www.physiology.arizona.edu/people/secomb/network`. The preparation and imaging method can be found in Secomb *et al.* (1998).

[5] `http://cxxtest.tigris.org`.

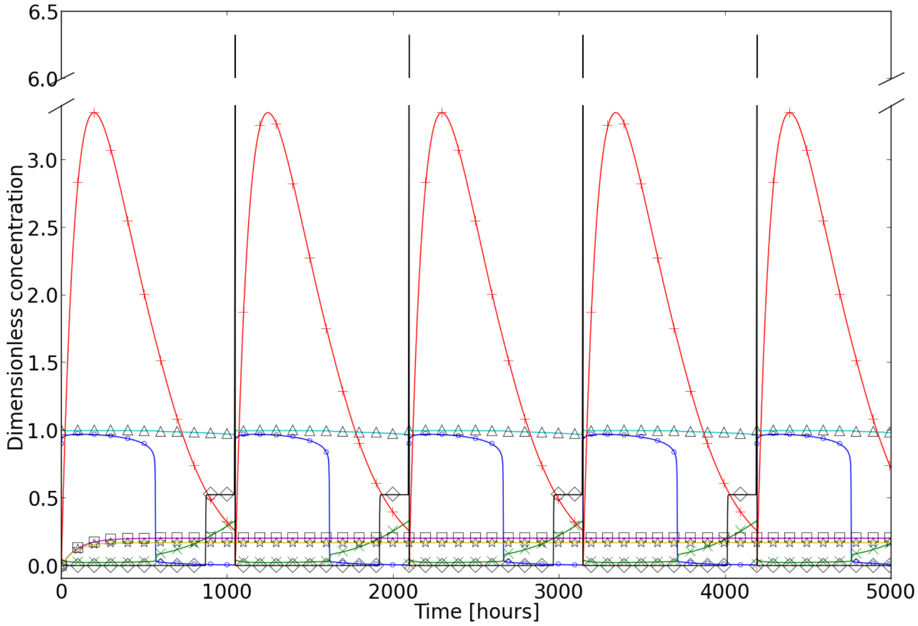

Figure C.6.: Plot showing the time-evolution of intra-cellular chemical concentrations involved in the Alarcón *et al.* 2005 cell-cycle model for a normal cell exposed to a dimensionless oxygen concentration of one. Cdh1: ∘; CycCDK: ×; p27: +; npRB: △; p53: □; VEGF: ⋆; Cell-cycle phase: ♢. The cell-cycle phase periodically rises to 2π, denoting the completion of a full cycle.

team achieve this by implementing a test-driven development strategy (see Pitt-Francis *et al.* (2009) for details). All functional code developed in Chaste, then, has an associated test suite, written using the CxxTest library. A typical test suite file for a C++ class in Chaste will include a number of individual test methods, which instantiate and set up relevant classes, check that no exceptions are thrown and then implement a number of methods which check that any output is correct (to within some tolerance level). As such, the elements of code used within our framework which come from the core Chaste modelling framework are fully tested.

While a test-driven development strategy has not been adopted for the implementation of the vascular tumour growth modelling framework presented here, significant efforts have been devoted to ensuring that important classes and important elements of the functionality of the framework are well tested. To do this a number of CxxTest test suites have been written. For example, the `VesselNetwork` class is tested using a test suite, `TestVesselNetwork.hpp`. This test ensures that 77% of the lines in the `VesselNetwork` class are correctly executed and that outputs from the execution of important `VesselNetwork` class methods are tested against what is expected. Meanwhile, the `Vessel` class is 92% covered by the `TestVessel.hpp` test suite. Other elements of the framework, such as those classes which encapsulate the sub cellular model classes implemented in our framework (see Figure C.3b) are equally well tested; the test coverage of these classes are on average 81%. In the future, the extent of testing in our framework will be further increased, particularly as it is further integrated with Chaste's code-base (see discussion in Section C.7).

Finally, here, we note that the ability to interrogate individual calculations and submodels is particularly advantageous in multiscale modelling of complex biological systems, since the correctness of a model implementation is almost never obvious from observation of the emergent behaviour of a complex biological model. As such, in Appendix E we present the results of a number of tests performed within our framework which verify that important elements of the hybrid model presented in Chapter 7 are correctly and accurately implemented.

C.7. Discussion

Over a number of decades, many computational models of cancer have been developed to account for phenomena occurring at various individual biological scales. In recent years, attempts have been made to integrate and extend these models across the different biological scales, forming so-called composite hybrid multiscale models. From our review of such multiscale models in Chapter 3, it is evident that existing models are often extended to incorporate novel biological details. However, such extensions are generally difficult to implement as the existing model code has not been developed with understandability and extensibility in mind. This means that code is often added on to existing implementations in an *ad hoc* way, over an extended period of time, often making that code less understandable. As multiscale models of cancer further increase in complexity in the coming years the task of further extending or modifying those models is only going to become more difficult. Thus, in the current absence of a coding standard for angiogenesis and cancer modelling, it is imperative that we, as computational biologists, begin to think carefully about how to structure our model code carefully so that it is understandable to others, and may be easily maintained and extended in an intuitive way.

Motivated by the multiscale models of vascular tumour growth developed by Alarcón and co-workers we have built an object-oriented framework for developing and implementing multiscale models of vascular tumour growth, which is both flexible and intuitive to use. Object-orientation has been used to describe elements of the application domain in a way which should be understandable to both experimental biologists and mathematical modellers with relatively little programming experience. Furthermore, by exploiting various object-oriented techniques and via the application of several well-known design patterns, in particular, the visitor and strategy patterns, we have ensured that code in our framework is maintainable, and that models implementable in our framework are easily extensible. Since very little literature exists relating to the application of object-oriented techniques to modelling complex biological systems, biological modellers have little reference material to guide them in the construction of complex biological model systems using the powerful tool-kit that object-orientation provides. Thus, a major contribution of our work here is to exhibit the adoption of various object-oriented techniques and patterns in a context with which many modellers will be familiar.

Our framework primarily comprises a hierarchy of biologically-based classes, which model populations of cells and vasculature, and several physics- and rule-based class hierarchies which describe how those biological entities behave and interact. At the highest level, this library of classes may be thought of as a domain specific embedded language (Mernik *et al.* 2005) in which data types and commands specific to the angiogenesis and cancer modelling domain have been defined and may be invoked at will. In this language, models are composed and executed using declarative statements, as shown in Algorithm 1, while lower level implementations of classes handle the interpretation of a user's wishes. Thus, we enable high-level assembly and simulation of models by non-expert users. Meanwhile, the underlying structure of our class library allows users with more modelling and computational experience to further develop models and submodels with relative ease. Thus, our framework satisfies the requirements of two separate categories of users.

The development of our core modelling framework has been use-case driven, the primary use-cases being that the models of Alarcón and co-workers should be implementable in our framework. Importantly, by basing our design around these models, we ensure that it will be more useful than a purely abstract design. Additionally, this family of models has employed a diverse range of interchangeable algorithms for modelling various types of behaviour at multiple biological scales. This has enabled us to explore the extensibility of model code in the context of existing models. We have found that, by employing our design, we are able to move from one model implementation to another simply by defining a few new classes in pre-existing class hierarchies. This drastically reduces the development time required to produce a novel model implementation.

The framework provides a convenient plug-and-play environment in which a variety of different models may be implemented. Furthermore, models may be easily deconstructed into their component submodels, which may be individually tested, analysed, validated and further developed before being re-integrated into the larger models of vascular tumour growth. Thus, our framework simultaneously addresses what we consider to be two major challenges in cancer modelling: it facilitates the verification and validation of complex multiscale models of cancer, and their extension to incorporate novel data and new functionality. On a related note, utilising the same piece of model code in different *in silico* experiments allows us to investigate the robustness of a model, whilst ensuring that the underlying implementation of that model does not vary from experiment to experiment.

In Chapter 7 we use elements of our framework to develop a hybrid model of angiogeneis in the cornea and compare the results of hybrid model simulation with the quantitative data extracted from experimental images in Chapter 4. With further development, parametrisation and comparison with experimental data, we believe that our model of angiogenesis could be re-integrated within larger models of vascular tumour growth as a partially validated submodel. Due to the modular nature of our framework and the design patterns utilised in its construction, the re-integration of such a validated submodel is likely to be as simple as changing a single line of code in, for example, Algorithm 1.

To date, the functionality of our framework focuses around the methodologies employed by Alarcón and co-workers. However, having employed an object-oriented approach, and having designed the framework with re-usability and extensibility in mind, it can be extended to allow for additional functionality with relative ease. While we currently utilise parts of Chaste's code, in particular making use of the Chaste interfaces to various numerical libraries, in the future we aim to further integrate our code base with Chaste's in order to further promote the extensibility of the models implemented within our framework. In particular, by making use of Chaste's on- and off-lattice mesh classes we could permit the implementation of off-lattice cell and vascular growth models. This would facilitate a move towards modelling irregular-shaped tissue geometries. By integrating our code with Chaste we also aim to increase its visibility to potential users, and its adoption.

Our current study addresses the reuse and extensibility of model code for a set of hybrid models of vascular tumour growth. Whilst we have focused on describing the models abstractly, we have not attempted to provide a standard for describing or implementing models of this type. Thus, the models implementable in our framework are not interoperable with similar models from the wider modelling community. The issue of interoperability has been identified by other members of the modelling community. Most recently, CHIC (Computational horizons in cancer;

Stamatakos 2014) is a European funded project, the major goal of which is to establish the technological infrastructure required to facilitate the reuse and integration of cancer models originating from different research groups. Integrating models from different research groups represents a far greater challenge than the extension and reuse of a family of related models, as presented here. For instance, one must ensure that models are linked only in a way which is semantically meaningful, that programs developed in different languages are able to interface with one another, that integrated models are numerically stable and simulations converge, and that models and their submodels are rigorously tested and validated. The complexities of establishing such an infrastructure whilst ensuring the aforementioned issues are dealt with in a satisfactory way are substantial. Thus, we believe that such issues are destined to remain at the forefront of *in silico* oncology research efforts for years to come.

Algorithm 1 Example simulation pseudocode. Brief explanatory comments are shown in blue.

```
// Create and customise spatial mesh.
  spatialMesh = OnLatticeMesh(latticeSiteSize,domainSize_X,domainSize_Y,domainSize_Z)
                    ⋮
  spatialMesh.SetTypeOfNeighbourhood(‘Moore’)
// Create diffusibles structure which contains the diffusible species of interest.
  diffusibles = Diffusibles(spatialMesh)
  diffusibles.AddDiffusibleSpecies(‘Oxygen’)
  diffusibles.AddDiffusibleSpecies(‘VEGF’)
// Create an initial vessel network.
// A prototype vessel is used as a template to create all other vessels in the network.
// In this case the vessel network is described in a file external to our framework.
  prototypeVessel = Vessel()
  prototypeVessel.AddIntraVascularChemical(‘VEGF’)
  prototypeVessel.AddIntraVascularChemical(‘Oxygen’)
  vesselNetworkFactory = DataFromFileVesselNetworkFactory(spatialMesh,prototypeVessel,file)
  vesselNetwork = vesselNetworkFactory.CreateVesselNetwork()
// Create a cell population and populate it with normal and cancerous cells.
  cellPopulation = CellPopulation(OnLatticeMesh)
  for i = 1 .. numberOfCells

          if (location is inside tumour region)
                  newCell = CancerousCell(location)
          else
                  newCell = NormalCell(location)
          end if

          newCell.AddIntraCellularChemical(‘p53’)
          newCell.AddIntraCellularChemical(‘VEGF’)
          newCell.AddIntraCellularChemical(‘Oxygen’)

          cellPopulation.AddCell(newCell)

  end for
// Create and customise modules which dictate cell behaviour.
  subCellularModel = Owen2011SubCellularModel(cellPopulation)
                    ⋮
  cellProliferator = OxygenBasedCellProliferator(cellPopulation,diffusibles)
                    ⋮
// Create and customise modules which will calculate the distributions of diffusible species.
  oxygenCalculator = Owen2011OxygenCalculator(cellPopulation,vesselNetwork)
                    ⋮
  vegfCalculator = Owen2011VEGFCalculator(cellPopulation,vesselNetwork)
                    ⋮
// Create and customise modules which dictate vascular network behaviour.
  structuralAdaptationAlgorithm = SimpleStructuralAdaptationAlgorithm()
                    ⋮
  angiogenesisModel = Owen2009AngiogenesisModel()
                    ⋮
// Create a simulation, customise the simulation with the submodels as defined above then run the simulation for the desired duration.
  simulation = Simulation(cellPopulation,vesselNetwork,diffusibles)
  simulation.AddSubCellularModel(subCellularModel)
  simulation.AddCellProliferator(cellProliferator)
                    ⋮
  simulation.AddAngiogenesisModel(angiogenesisModel)
  simulation.AddStructuralAdaptationAlgorithm(structuralAdaptationAlgorithm)
  simulation.SetDuration(simulationRunTime)
  simulation.SetTimestep(timestep)
  simulation.Run()
```

APPENDIX D

Derivation of (7.19) Using (7.18)

The derivation of (7.19) using (7.18) presented here follows the approach taken by Stevens and Othmer (1997) and Painter and Hillen (2002). That is, we visualise the motion of tip cells in terms of a continuous-time, discrete-space random walk on a regular lattice, with lattice spacing h. Initially, we focus on motion in one dimension only.

We define $n_i(t)$ to be the probability that a tip cell is located at the lattice site $i \in \mathbf{Z}$ at time, t, given that the cell is located at $i = 0$ at $t = 0$. Further, we assume that this quantity evolves according to the continuous-time discrete space equation:

$$\frac{\partial n_i}{\partial t} = \tau^{+}_{i-1}\, n_{i-1} + \tau^{-}_{i+1}\, n_{i+1} - (\tau^{+}_{i} + \tau^{-}_{i})\, n_i, \tag{D.1}$$

where $\tau^{\pm}_{i}$ are the probabilities per unit time that a tip cell will transition from site i to $i \pm 1$. We can equate the distribution described by $\{n_i\}$ with the distribution of tip cells in, for example, our continuum models of Chapter 5 and 6. Equation D.1 describes the changing density distribution as individual tip cells enter or leave the different sites in our discrete lattice.

In our discrete model of Chapter 7, the probability per unit time that an isolated tip cell moves from site i to $i \pm 1$ is of the form

$$\tau^{\pm}_{i} = \underbrace{\alpha}_{\substack{\text{random}\\ \text{motion}}} + \underbrace{\beta\, \mathbb{R}\,(v_{i\pm1} - v_i)}_{\text{chemotaxis}}, \tag{D.2}$$

where $\mathbb{R}(x)$ is the ramp function[1] and v_i is the concentration of VEGF-A$_{165}$ at i. Then, substituting (D.2) into (D.1), we find that:

$$\begin{aligned}\frac{\partial n_i}{\partial t} &= \alpha\ (n_{i+1} - 2n_i + n_{i-1}) + \beta\, n_{i-1}\, \mathbb{R}(v_i - v_{i-1}) + \beta\, n_{i+1}\, \mathbb{R}(v_i - v_{i+1}) \\ &\quad -\beta\, n_i\, \mathbb{R}(v_{i+1} - v_i) - \beta\, n_i\, \mathbb{R}(v_{i-1} - v_i).\end{aligned} \tag{D.3}$$

---

[1] The ramp function, $\mathbb{R}(x)$ is related to the Heaviside step function, $H(x)$, via $\mathbb{R}(x) = x\, H(x)$. Thus, $\mathbb{R}(x)$ is equal to x where $x \geq 0$ and equal to zero elsewhere.

Following Painter and Hillen's argumentation, as the spatial scale, h, is changed, the transition probabilities per unit time must also change accordingly; the transition probabilities should scale according to $\tau_h^{\pm} = \frac{q}{h^2}\tau^{\pm}$, for some constant q:

$$\tau_h^{\pm} = \frac{q}{h^2}\tau^{\pm} = \underbrace{\frac{\alpha q}{h^2}}_{\substack{\text{random}\\ \text{motion}}} + \underbrace{\frac{\beta q}{h^2}\,\mathbb{R}\left(v_{i+1} - v_i\right)}_{\text{chemotaxis}}, \tag{D.4}$$

Then, setting $i = \frac{x}{h}$ we can interpret each lattice site as a point in continuous space, x, so that (D.3) becomes:

$$\begin{aligned} \frac{\partial n(x,t)}{\partial t} &= \frac{\alpha q}{h^2}\,\left(n(x+h,t) - 2n(x,t) + n(x-h,t)\right) \\ &\quad + \frac{\beta q}{h^2}\,n(x-h,t)\,\mathbb{R}(v(x,t) - v(x-h,t)) \\ &\quad + \frac{\beta q}{h^2}\,n(x+h,t)\,\mathbb{R}(v(x,t) - v(x+h,t)) \\ &\quad - \frac{\beta q}{h^2}\,n(x,t)\,\mathbb{R}(v(x+h,t) - v(x,t)) \\ &\quad - \frac{\beta q}{h^2}\,n(x,t)\,\mathbb{R}(v(x-h,t) - v(x,t)). \end{aligned} \tag{D.5}$$

Using the expansions

$$n(x+h,t) \approx n(x,t) + h\,\frac{\partial n(x,t)}{\partial x} + \frac{h^2}{2}\,\frac{\partial^2 n(x,t)}{\partial x^2} + \frac{h^3}{6}\,\frac{\partial^3 n(x,t)}{\partial x^3} + \frac{h^4}{24}\,\frac{\partial^4 n(x,t)}{\partial x^4} + \mathcal{O}(h^5) \tag{D.6}$$

and

$$n(x-h,t) \approx n(x,t) - h\,\frac{\partial n(x,t)}{\partial x} + \frac{h^2}{2}\,\frac{\partial^2 n(x,t)}{\partial x^2} - \frac{h^3}{6}\,\frac{\partial^3 n(x,t)}{\partial x^3} + \frac{h^4}{24}\,\frac{\partial^4 n(x,t)}{\partial x^4} + \mathcal{O}(h^5) \tag{D.7}$$

we find that the first term on the RHS of (D.5) is given by

$$\frac{\alpha q}{h^2}\,\left(n(x+h,t) - 2n(x,t) + n(x-h,t)\right) \;\approx\; \alpha q \frac{\partial^2 n}{\partial x^2} + \mathcal{O}(h^2). \tag{D.8}$$

To find continuum approximations to the last 4 terms on the RHS of (D.5), we must find appropriate expansions for $\mathbb{R}(v(x,t) - v(x-h,t))$, $\mathbb{R}(v(x,t) - v(x+h,t))$, $\mathbb{R}(v(x+h,t) - v(x,t))$ and $\mathbb{R}(v(x-h,t) - v(x,t))$. To do so, we use the expansion

$$\mathbb{R}(y + dy) \;=\; \mathbb{R}(y) + dy\,\frac{\partial \mathbb{R}(y)}{\partial y} + \frac{dy^2}{2}\,\frac{\partial^2 \mathbb{R}(y)}{\partial y^2} + \mathcal{O}(dy^3), \tag{D.9}$$

and the following relationships

$$\mathbb{R}(a\,y) = a\,\mathbb{R}(y), \tag{D.10}$$

$$H(a\,y) = H(y), \tag{D.11}$$

$$\frac{\partial \mathbb{R}(y)}{\partial y} = H(y), \tag{D.12}$$

$$\frac{\partial H(y)}{\partial y} = \delta(y). \tag{D.13}$$

Using the expansion, (D.9), and the relationships, (D.10)-(D.13), we find that:

$$\begin{aligned}
\mathbb{R}\left(v(x,t)-v(x-h,t)\right) &\approx \mathbb{R}\left(h\,\frac{\partial v(x,t)}{\partial x} - \frac{h^2}{2}\,\frac{\partial^2 v(x,t)}{\partial x^2} + \frac{h^3}{6}\,\frac{\partial^3 v(x,t)}{\partial x^3} - \frac{h^4}{24}\,\frac{\partial^4 v(x,t)}{\partial x^4}\right) \\
&\approx h\,\mathbb{R}\left(\frac{\partial v(x,t)}{\partial x}\right) \\
&\quad + H\left(\frac{\partial v(x,t)}{\partial x}\right)\left(-\frac{h^2}{2}\,\frac{\partial^2 v(x,t)}{\partial x^2} + \frac{h^3}{6}\,\frac{\partial^3 v(x,t)}{\partial x^3} - \frac{h^4}{24}\,\frac{\partial^4 v(x,t)}{\partial x^4}\right) \\
&\quad + \frac{\delta}{2}\left(\frac{\partial v(x,t)}{\partial x}\right)\left(\frac{h^2}{2}\,\frac{\partial^2 v(x,t)}{\partial x^2}\right)^2 + \mathcal{O}(h^5),
\end{aligned} \tag{D.14}$$

$$\begin{aligned}
\mathbb{R}\left(v(x,t)-v(x+h,t)\right) &\approx \mathbb{R}\left(-h\,\frac{\partial v(x,t)}{\partial x} - \frac{h^2}{2}\,\frac{\partial^2 v(x,t)}{\partial x^2} - \frac{h^3}{6}\,\frac{\partial^3 v(x,t)}{\partial x^3} - \frac{h^4}{24}\,\frac{\partial^4 v(x,t)}{\partial x^4}\right) \\
&\approx h\,\mathbb{R}\left(-\frac{\partial v(x,t)}{\partial x}\right) \\
&\quad + H\left(-\frac{\partial v(x,t)}{\partial x}\right)\left(-\frac{h^2}{2}\,\frac{\partial^2 v(x,t)}{\partial x^2} - \frac{h^3}{6}\,\frac{\partial^3 v(x,t)}{\partial x^3} - \frac{h^4}{24}\,\frac{\partial^4 v(x,t)}{\partial x^4}\right) \\
&\quad + \frac{\delta}{2}\left(-\frac{\partial v(x,t)}{\partial x}\right)\left(\frac{h^2}{2}\,\frac{\partial^2 v(x,t)}{\partial x^2}\right)^2 + \mathcal{O}(h^5),
\end{aligned} \tag{D.15}$$

$$\begin{aligned}
\mathbb{R}\left(v(x-h,t)-v(x,t)\right) &\approx \mathbb{R}\left(-h\,\frac{\partial v(x,t)}{\partial x} + \frac{h^2}{2}\,\frac{\partial^2 v(x,t)}{\partial x^2} - \frac{h^3}{6}\,\frac{\partial^3 v(x,t)}{\partial x^3} + \frac{h^4}{24}\,\frac{\partial^4 v(x,t)}{\partial x^4}\right) \\
&\approx h\,\mathbb{R}\left(-\frac{\partial v(x,t)}{\partial x}\right) \\
&\quad + H\left(-\frac{\partial v(x,t)}{\partial x}\right)\left(\frac{h^2}{2}\,\frac{\partial^2 v(x,t)}{\partial x^2} - \frac{h^3}{6}\,\frac{\partial^3 v(x,t)}{\partial x^3} + \frac{h^4}{24}\,\frac{\partial^4 v(x,t)}{\partial x^4}\right) \\
&\quad + \frac{\delta}{2}\left(-\frac{\partial v(x,t)}{\partial x}\right)\left(\frac{h^2}{2}\,\frac{\partial^2 v(x,t)}{\partial x^2}\right)^2 + \mathcal{O}(h^5),
\end{aligned} \tag{D.16}$$

$$\begin{aligned}
\mathbb{R}\left(v(x+h,t)-v(x,t)\right) &\approx \mathbb{R}\left(h\,\frac{\partial v(x,t)}{\partial x} + \frac{h^2}{2}\,\frac{\partial^2 v(x,t)}{\partial x^2} + \frac{h^3}{6}\,\frac{\partial^3 v(x,t)}{\partial x^3} + \frac{h^4}{24}\,\frac{\partial^4 v(x,t)}{\partial x^4}\right) \\
&\approx h\,\mathbb{R}\left(\frac{\partial v(x,t)}{\partial x}\right) \\
&\quad + H\left(\frac{\partial v(x,t)}{\partial x}\right)\left(\frac{h^2}{2}\,\frac{\partial^2 v(x,t)}{\partial x^2} + \frac{h^3}{6}\,\frac{\partial^3 v(x,t)}{\partial x^3} + \frac{h^4}{24}\,\frac{\partial^4 v(x,t)}{\partial x^4}\right) \\
&\quad + \frac{\delta}{2}\left(\frac{\partial v(x,t)}{\partial x}\right)\left(\frac{h^2}{2}\,\frac{\partial^2 v(x,t)}{\partial x^2}\right)^2 + \mathcal{O}(h^5).
\end{aligned} \tag{D.17}$$

Inserting (D.14)-(D.17) into the last 4 terms on the RHS of (D.5), we find that

$$\begin{aligned}
&n(x-h,t)\;R(v(x,t)-v(x-h,t))\\
&+n(x+h,t)\;R(v(x,t)-v(x+h,t))\\
&-n(x,t)\;R(v(x-h,t)-v(x,t))\\
&-n(x,t)\;R(v(x+h,t)-v(x,t)) \;\approx\; -n(x,t)\;H\left(\frac{\partial v(x,t)}{\partial x}\right)\;\frac{\partial^2 v(x,t)}{\partial x^2}\;h^2 \qquad \text{(D.18)}\\
&\qquad -n(x,t)\;H\left(-\frac{\partial v(x,t)}{\partial x}\right)\;\frac{\partial^2 v(x,t)}{\partial x^2}\;h^2\\
&\qquad -\frac{\partial n(x,t)}{\partial x}\;\mathbb{R}\left(-\frac{\partial v(x,t)}{\partial x}\right)\;h^2\\
&\qquad +\frac{\partial n(x,t)}{\partial x}\;\mathbb{R}\left(\frac{\partial v(x,t)}{\partial x}\right)\;h^2+\mathcal{O}(h^3).
\end{aligned}$$

Given that

$$H\left(\frac{\partial v(x,t)}{\partial x}\right)+H\left(-\frac{\partial v(x,t)}{\partial x}\right)=1, \qquad \text{(D.19)}$$

and

$$\mathbb{R}\left(\frac{\partial v(x,t)}{\partial x}\right)-\mathbb{R}\left(-\frac{\partial v(x,t)}{\partial x}\right)=\frac{\partial v(x,t)}{\partial x}, \qquad \text{(D.20)}$$

in the limit of $h \to 0$ we find the continuum limit of Equation (D.5):

$$\frac{\partial n}{\partial t}=\alpha q\frac{\partial^2 n}{\partial x^2}-\beta q\frac{\partial}{\partial x}\left(n\frac{\partial v}{\partial x}\right)=-\frac{\partial}{\partial x}\left(-\mu\frac{\partial n}{\partial x}+\chi n\frac{\partial v}{\partial x}\right), \qquad \text{(D.21)}$$

where the macroscopic random motility coefficient, μ, and chemotactic sensitivity, χ, are related to the microscopic model parameters in (D.4) via the relationships

$$\mu = q\alpha, \quad \text{and} \quad \chi = q\beta. \qquad \text{(D.22)}$$

For tip cells moving on a 3-D lattice, on which locations are denoted $(i,\,j,\,k)=(\frac{x}{h},\,\frac{y}{h},\,\frac{z}{h})$, the relationships between the microscopic model parameters in (D.4) and the macroscopic parameters, χ and μ, are readily generalisable. The motion of tip cells which are only permitted to move along the three orthogonal lattice directions $(x,\,y,\,z)$, is described in the continuum limit by the following equation:

$$\frac{\partial n}{\partial t}=-\nabla\cdot\left(-\mu\nabla n+\chi n\nabla v\right), \qquad \text{(D.23)}$$

where, again,

$$\mu = q\alpha, \quad \text{and} \quad \chi = q\beta. \tag{D.24}$$

If diagonal movement is permitted in 3-D, as we allow in our discrete model of Chapter 7, then tip cell motion is again described by (D.23), however, to account for the extra degrees of freedom, μ and χ are now given by:

$$\mu = \frac{26}{6}q\alpha, \quad \text{and} \quad \chi = \frac{26}{6}q\beta. \tag{D.25}$$

APPENDIX E

Hybrid Model Verification

In this section we aim to establish confidence in the implementation of the hybrid model of corneal angiogenesis presented in Chapter 7. Specifically, we present results which verify that the calculation of the VEGF-A_{165} distribution has been implemented correctly and that the emergent behaviour of migrating tip cells within our computational model conforms to that expected from theory in simple environments. We have also implemented other lower level tests which check, for example, that anastomosis events change the topology of a vascular network in the correct way.

E.1. VEGF-A_{165} distribution calculation

The VEGF-A_{165} submodel, (7.14)-(7.17), does not have a closed form analytical solution, even in the absence of vasculature. Thus, to establish confidence in the implementation of this submodel, we compare its numerical solution with the output from an equivalent 1-D problem, implemented independently in MATLAB. To compare the model outputs we average the 3-D model solution over the plane perpendicular to the y-direction.

We test the VEGF-A_{165} submodel for the case where the model domain contains a single, static tortuous vessel (see Figure 7.2), which does not evolve in time. We fix $x_{max} = 1\,\mathrm{mm}$. All other model parameters associated with the VEGF-A_{165} submodel are as in the default model parametrisation (Table 7.2). Figure E.1a shows the spatially averaged results over a seven day period. VEGF-A_{165} enters the model domain uniformly from the boundary at $y = y_{max} = 1.24\,\mathrm{mm}$, diffuses, decays and is taken up by the vasculature which is positioned around $y = 0.2\,\mathrm{mm}$.

The 1-D model, which we use as a benchmark against which to check our 3-D model implementation, is based on the continuum model presented in Chapter 5. In summary, the 1-D model

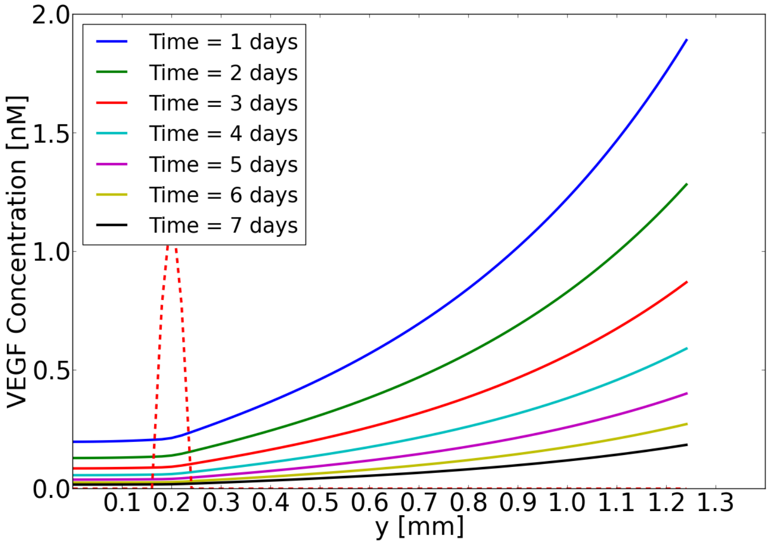

(a)

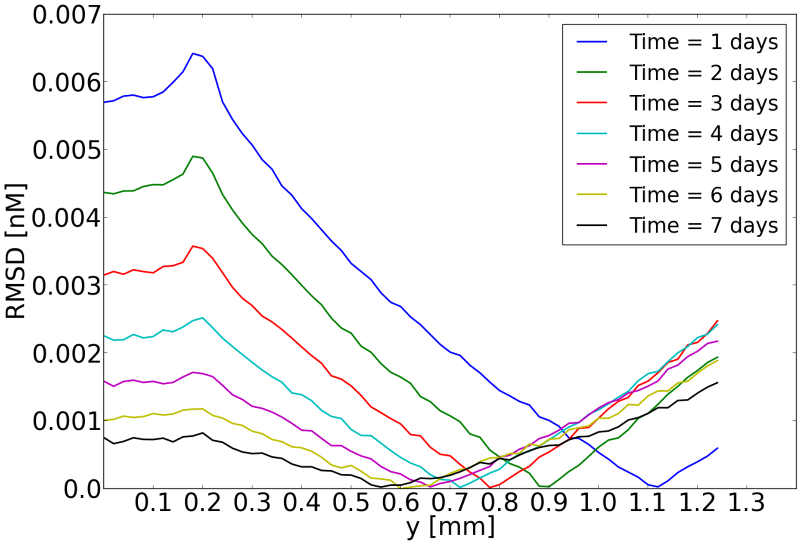

(b)

Figure E.1.: The numerical solution of (7.14)-(7.17) in our 3-D hybrid model formulation is compared to numerical results from an equivalent 1-D model, (E.1)-(E.3), implemented in MATLAB. (a) The results from simulation in our hybrid formulation are averaged in the plane perpendicular to the y-direction and plotted over time. --: scaled vascular density ($\times 2 \times 10^8$ metre of vessel m^{-3}). (b) Root mean squared difference between spatially averaged results from the 3-D hybrid model and results from the 1-D model.

is

$$\frac{\partial v}{\partial t} = \underbrace{D_v \frac{\partial^2 v}{\partial y^2}}_{\text{diffusion}} - \underbrace{\lambda_v\, v}_{\text{natural decay}} - \underbrace{2\,\pi\,\bar{R}\,P_v\,\rho\,(v - v_{blood})}_{\text{drainage through vessels}}$$

$$\underbrace{- K^v_{EC}\,\nu\,\rho\left(\frac{v}{v + v_{\frac{1}{2}}}\right)}_{\text{uptake by endothelial cells}}. \tag{E.1}$$

$$D_v \frac{\partial v}{\partial y}\bigg|_{y=0} = 0, \quad - D_v \frac{\partial v}{\partial y}\bigg|_{y=0} = -k^v_p \left(\frac{[V_T]}{\theta_v} - v|_{y=y_{max}}\right) \tag{E.2}$$

$$\frac{d[V_T]}{dt} = -\lambda^v_p \frac{[V_T]}{\theta_v} - \frac{\zeta_p k^v_p}{\Omega_p}\left(\frac{[V_T]}{\theta_v} - v|_{y=y_{max}}\right). \tag{E.3}$$

ρ is the vessel length density averaged along the plane perpendicular to the y-direction. The spatially averaged vessel density in the 3-D model provides us with values for ρ:

$$\rho = \begin{cases} 0.7732 \ \text{ metres of vessel m}^{-3} & y = 0.2 \pm \Delta y\,\text{mm}, \\ 1.1964 \ \text{ metres of vessel m}^{-3} & y = 0.2\,\text{mm}, \\ 0 & \text{otherwise.} \end{cases} \tag{E.4}$$

Other parameters in (E.1)-(E.3) correspond directly to the parameters used in our hybrid model, (7.14)-(7.17). Thus, for this test, parameters in our 1-D model take values equal to those used to generate the results in Figure E.1a.

We solved (E.1)-(E.4) using the method of lines in MATLAB, taking the node spacing to be $\Delta y = 20\,\mu$m to ensure consistency with our 3-D calculation, in which Δx, the lattice spacing, is $20\,\mu$m. In more detail, (E.1)-(E.3) were discretised in space using (central) finite differences. We then solved the resulting system of ODEs using MATLAB's inbuilt ODE solver, ode15s, as in Chapter 5.

We plot the root mean squared error between the spatially averaged 3-D model results and the 1-D model results in Figure E.1b. Good agreement between the two models suggests that our 3-D model is likely to be correctly implemented.

As we did for our continuum models in Chapter 5 (Section 5.5.1), we also confirmed that the numerical solution of (7.14)-(7.17) converges at the rate predicted by theory as the time discretisation parameter, Δt, is decreased. This was achieved by solving the equations for successively smaller Δt and comparing how the solution converges. As predicted by theory, the error in solution decreases as $O(\Delta t)$ in the L^{∞}-norm. Meanwhile, convergence of the solution error as the space discretisation parameter, Δx, decreases is not demonstrable since our discrete problem contains non-smooth source-sink terms and Δx is predicated by size of cells/vessels. Finally, we have confirmed the absence of unphysical, negative values.

E.2. Tip cell motion and vascular growth

We perform two tests to confirm that our model of tip cell motion is correctly implemented. Both tests involve the migration of isolated ECs, which move according to the modified probabilistic rule, (7.18). Our first test confirms that the random (diffusive) motion of tip cells is accurately implemented. We set $\mu = 1 \times 10^{-13}\,\mathrm{m}^2\mathrm{min}^{-1}$, $\Delta t = 5\,\mathrm{mins}$ and $\Delta x = 20\,\mu\mathrm{m}$ and consider a single isolated EC in the absence of VEGF-A$_{165}$, measuring the cell's displacement from its initial location, $d(0)$ over time. Theory predicts a root mean squared displacement of

$$|d(t) - d(0)| = \sqrt{6 \times \mu \times t}, \tag{E.5}$$

for an EC undergoing random motion in three dimensions. Figure E.2 shows the displacement of an isolated EC within our modelling framework undergoing random motion, averaged over 5000 realisations. Excellent agreement between our numerical results and theory indicate that the random motion element of our tip cell movement model is correctly implemented.

Our second test focuses on our implementation of the chemotactic element of tip cell motion. We expose isolated ECs to a constant gradient of VEGF-A$_{165}$ in the y-direction. We fix $\mu = 1 \times 10^{-13}\,\mathrm{m}^2\mathrm{min}^{-1}$, $\Delta t = 5\,\mathrm{mins}$ and $\Delta x = 20\,\mu\mathrm{m}$ and vary the gradient of VEGF-A$_{165}$ to which cells are exposed. We time how long it takes the cell to move, according to the probabilistic rule, (7.18), a distance of 1 mm in the y-direction. The cell moves unimpeded in the x- and z-directions. Theory (Codling *et al.* 2008) predicts that ECs should travel on average at speed

$$s_y = \chi \frac{\partial v}{\partial y} \tag{E.6}$$

in the y-direction. Figure E.3 shows how the speed of migration of isolated ECs within our modelling framework varies with the chemotaxis coefficient, χ, and with the gradient of VEGF-A$_{165}$ to which a cell is exposed. Results are averaged over 100 realisations for each value of χ and

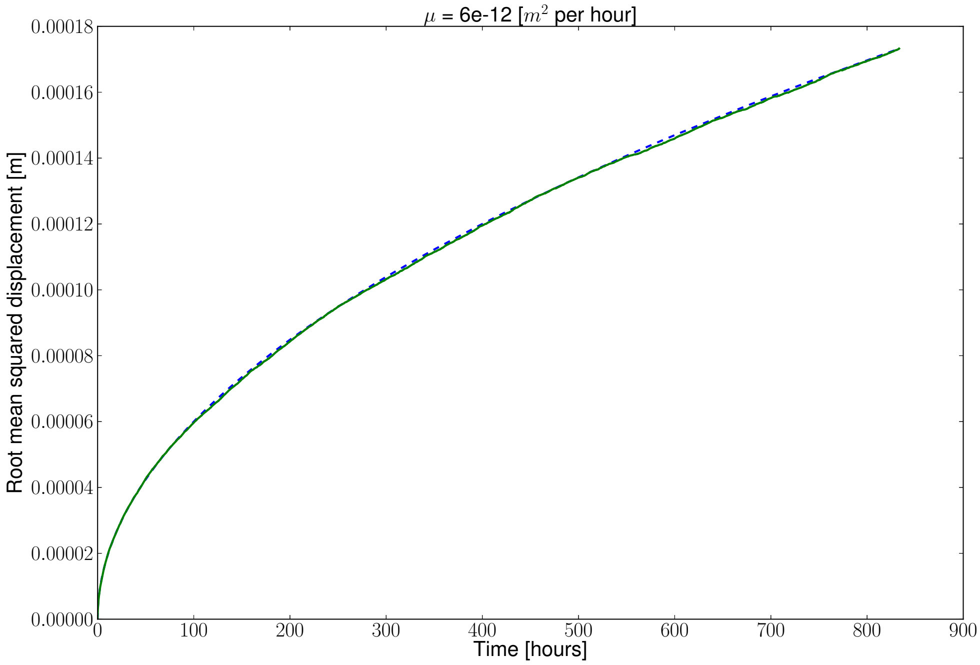

Figure E.2.: Simulated random motion of isolated ECs. The root mean squared displacement of isolated ECs over time is plotted. - -: theory; –: simulated ($n = 5000$).

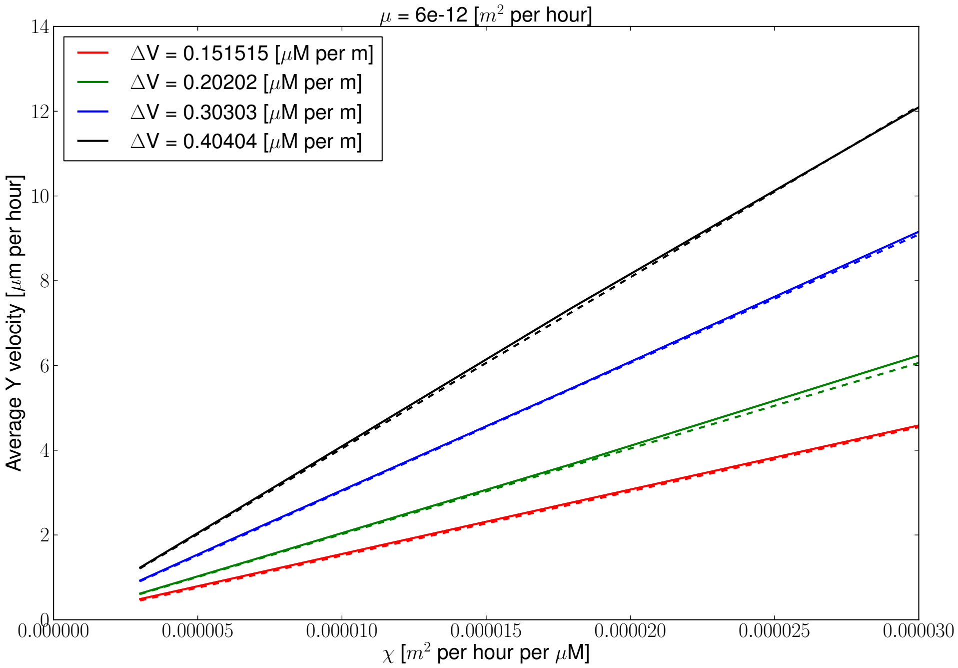

Figure E.3.: Simulated migration of isolated ECs. The chemotactic sensitivity, χ, is varied, as is the gradient of VEGF-A$_{165}$ to which tip cells are exposed in the y-direction. - -: theory; –: simulated ($n = 100$).

each gradient. The close agreement between numerical results and theory suggests that the chemotactic element of tip cell motion has been correctly implemented. We repeated this test for tip cells attached to the end of a growing sprout, setting $K_\rho = K_T = 0$ (see Figure E.4). While the results from simulated tip cell migration and theory are still in good agreement, for $\mu > 0$ the average speed of tip cell migration in the y-direction exceeds that predicted by theory. This is because tip cells in our full model can not move back into the site from whence they directly came. This additional constraint further biases tip cell motion in the direction of increasing y, increasing the tip cell's speed of migration. For $\mu = 0$, no such bias exists and the rate of vascular growth (the tip cell migration speed) is accurately predicted by (E.6). Note also that, as $\frac{\mu}{\chi}$ is increased, the likelihood of a vessel anastomosing with itself or its parent vessel becomes increasingly likely, even in the absence of tip-tip and tip-vessel interactions ($K_\rho = K_T = 0$). In Figure E.4 the average speed was calculated using tip cells which successfully traversed 1 mm in the y-direction, i.e. those which did not anastomose. All 100 tip cells anastomosed with either the growing sprout's parent vessel or the growing sprout itself when $\chi = 1 \times 10^{-8}\, m^2\, min^{-1}\, \mu M^{-1}$ and $\mu = 1 \times 10^{-13}\, m^2\, min^{-1}$.

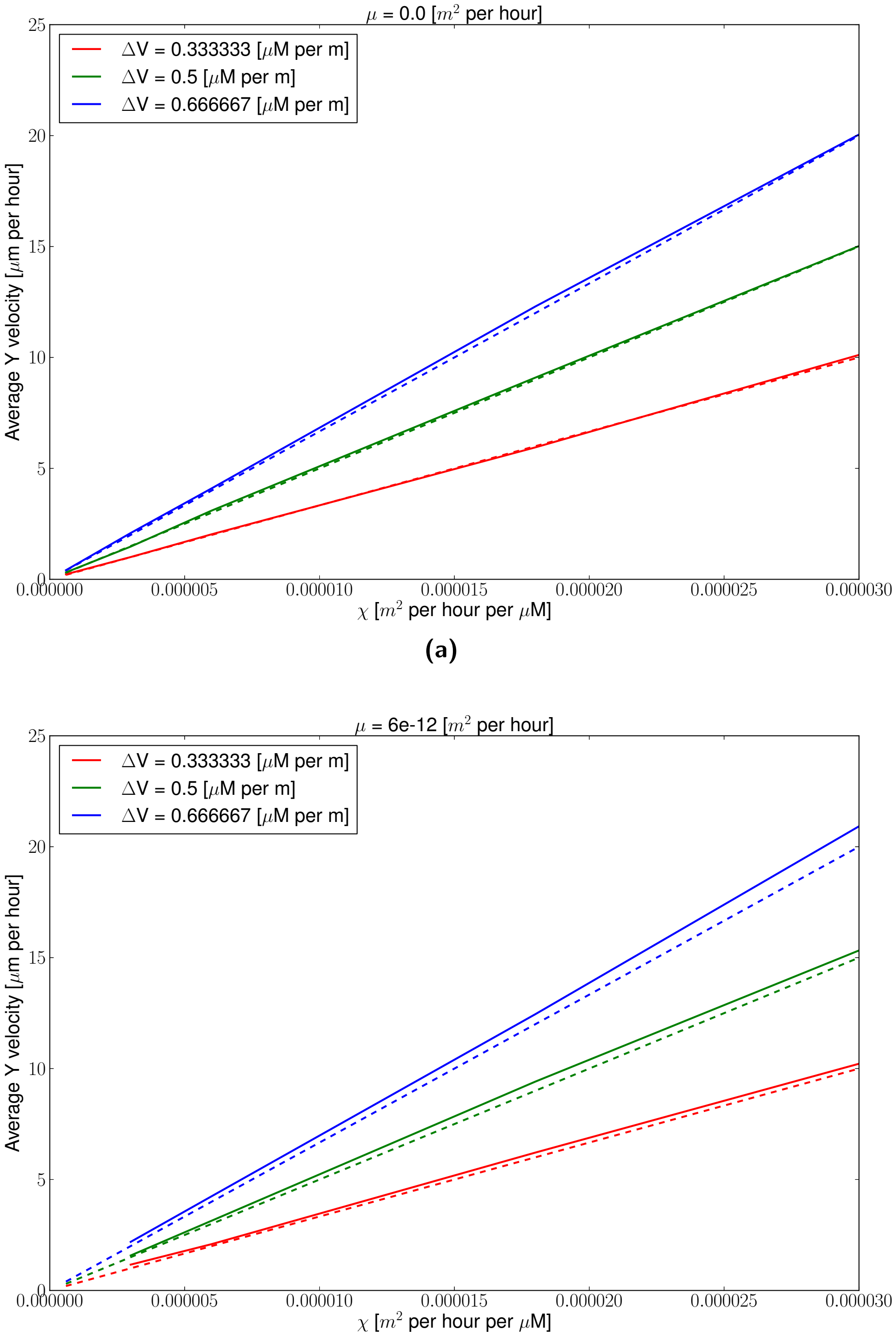

(a)

(b)

Figure E.4.: Simulated migration of tip cells which are attached to growing vessel sprouts. The chemotactic sensitivity, χ is varied as is the gradient of VEGF-A$_{165}$ to which tip cells are exposed in the y-direction. - -: theory; $-$: simulated (n = 100) (a) The random motility coefficient, μ, is set to zero. The rate of vascular growth agrees well with that predicted by theory. (b) For $\mu > 0$, tip cell migration is biased in the direction of increasing VEGF-A$_{165}$ concentration, increasing the rate of vascular growth.

APPENDIX F

Supplementary Figures from Chapter 7

In Sections 7.4.5 and 7.4.6 we studied the sensitivity of simulation results to changes in parameters associated with the tip cell sensing model incorporated into our hybrid model. Here, we present supplementary figures to accompany those sections.

In Figures F.1-F.4 the total and perfused vascular density profiles (averaged over 50 simulations) are plotted for $t = 3\,$days and $t = 5\,$days as the parameters r_f, θ_f, K_T and K_ρ are increased/decreased by 25% one at a time. All other parameters are fixed at their default values (Tables 7.1-7.3). Meanwhile, Figure F.5 shows how the total and perfused vascular density profiles (averaged over 50 simulations) vary as the initial concentration of VEGF-A$_{165}$, $[V_T]_{init}$, is reduced (by 25% and 50%). All other parameters are fixed at their default values (Tables 7.1-7.3)

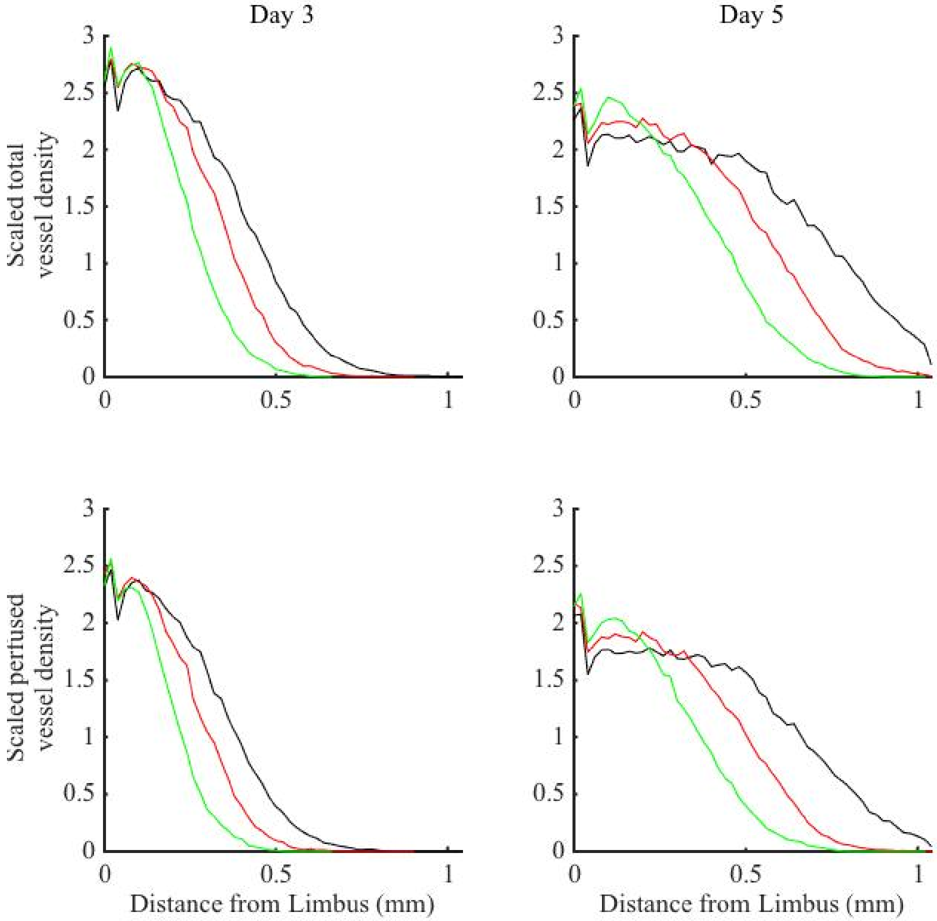

Figure F.1.: The strength of tip-tip interactions, K_T, is increased/decreased by 25% from its default value. All other parameters are held fixed at their default values (Tables 7.1-7.3). The total and perfused vascular density profiles on days three and five are plotted for each choice of parameter values. $-$: default parameters; $-$: $+25\%$; $-$: -25%.

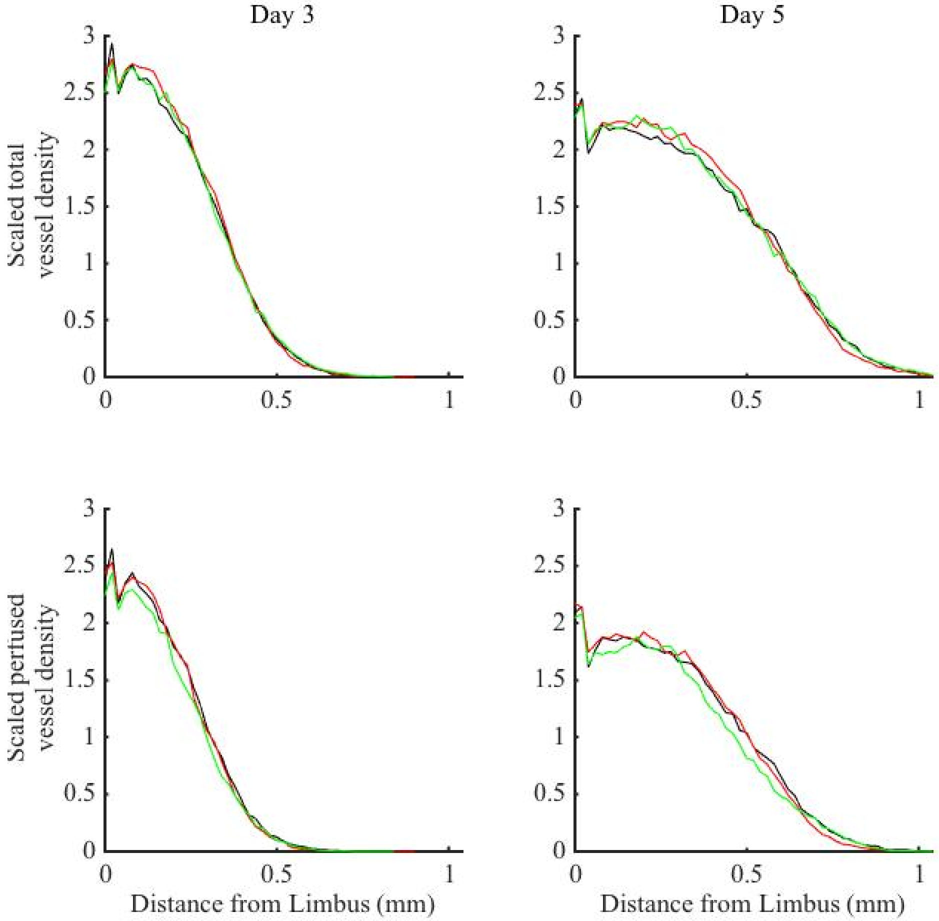

Figure F.2.: The strength of tip-vessel interactions, K_ρ, is increased/decreased by 25% from its default value. All other parameters are held fixed at their default values (Tables 7.1-7.3). The total and perfused vascular density profiles on days three and five are plotted for each choice of parameter values. −: default parameters; −: +25%; −: −25%.

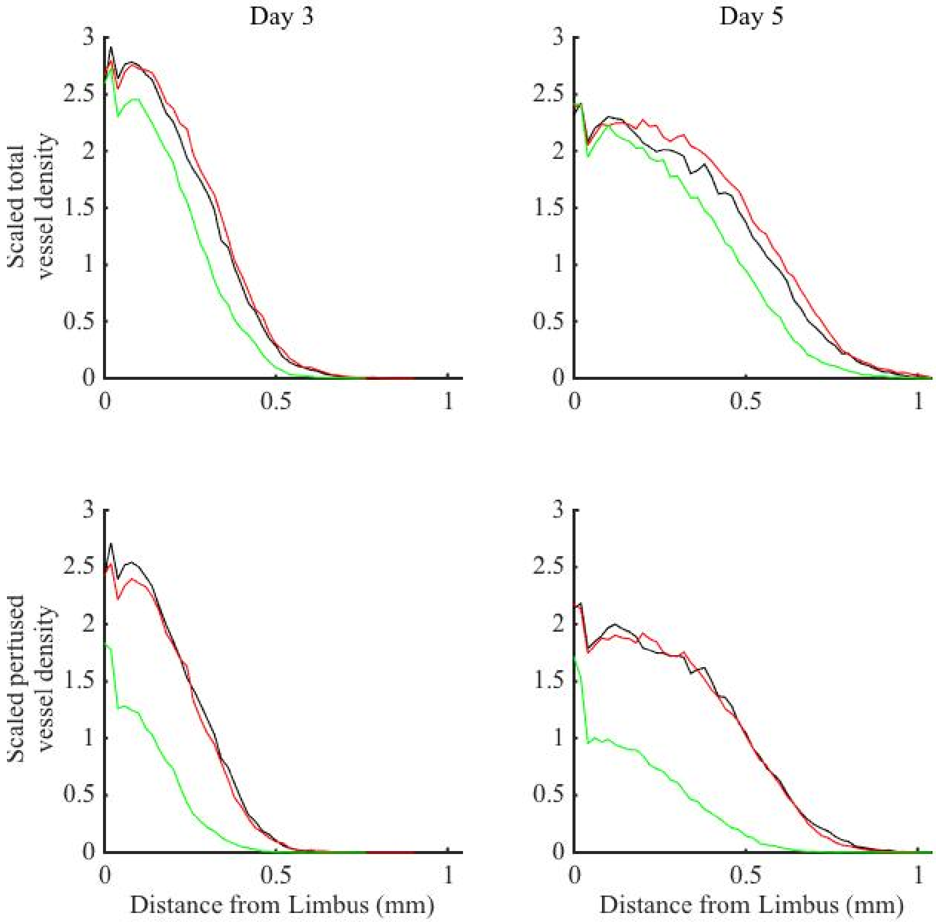

Figure F.3.: The angle over which filopodia explore their local environment, θ_f, is increased/decreased by 25%. All other parameters are held fixed at their default values (Tables 7.1-7.3). The total and perfused vascular density profiles on days three and five are plotted for each choice of parameter values. –: default parameters; –: +25%; –: −25%.

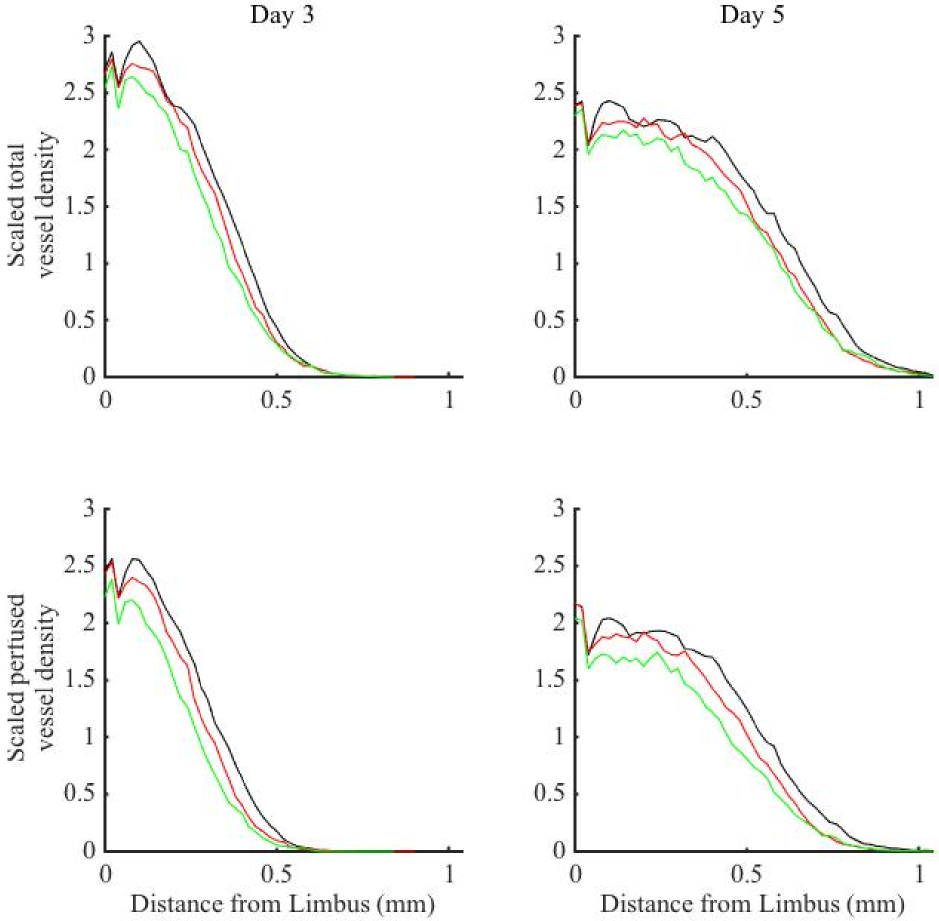

Figure F.4.: The maximum probing distance of filopodia, r_f, is increased/decreased by 25% from its default value. All other parameters are held fixed at their default values (Tables 7.1-7.3). The total and perfused vascular density profiles on days three and five are plotted for each choice of parameter values. −: default parameters; −: +25%; −: −25%.

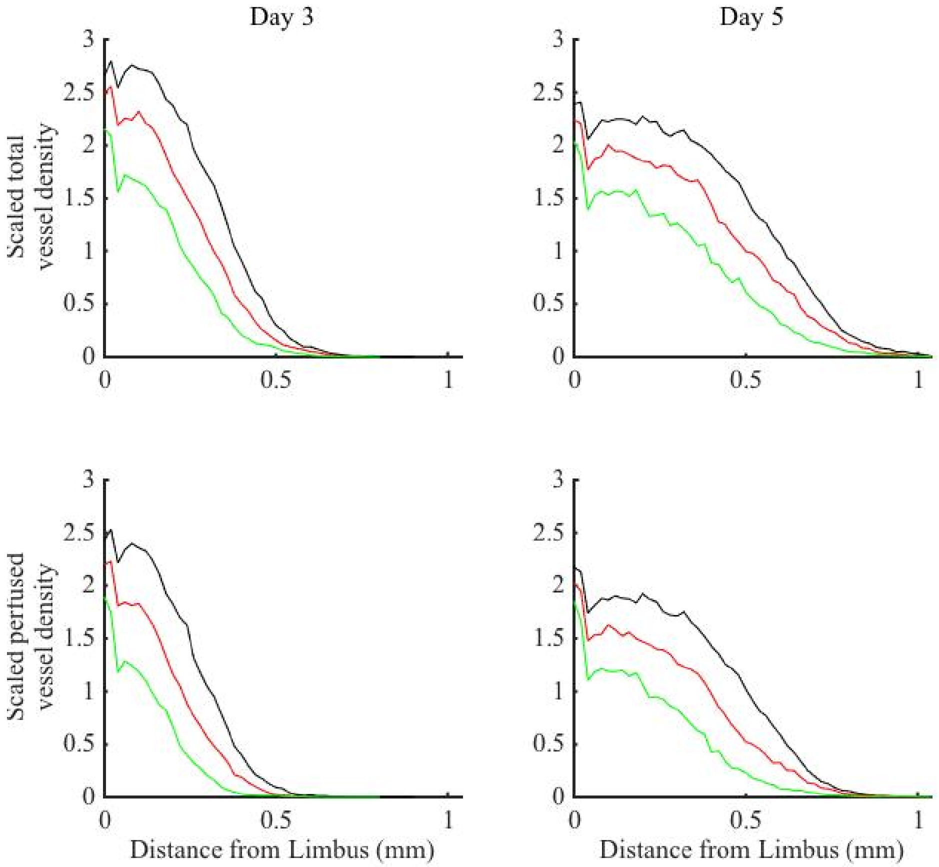

Figure F.5.: Hybrid model results from simulations in which the initial concentration of VEGF-A$_{165}$ in the pellet, $[V_T]_{init}$, is decreased by 25% and 50% from its default value. All other parameters are held fixed at their default values (Tables 7.1-7.3). The total and perfused vascular density profiles on days three and five are plotted for each choice of parameter values. $-$: default parameters; $-$: -25%; $-$: -50%.

Bibliography

B Addison-Smith (2010). "Mathematical Modelling of Tumour-Induced Angiogenesis". PhD thesis. Queensland University of Technology (cit. on pp. 82, 84, 175, 4, 5).

A. Akeson, A. Herman, D. Wiginton, and J. Greenberg (2010). "Endothelial cell activation in a VEGF-A gradient: relevance to cell fate decisions". *Microvasc. Res.* 80.1, pp. 65–74. doi: `10.1016/j.mvr.2010.02.001` (cit. on pp. 80, 84, 174, 5).

M. Al-Rawi, M. Qutaishat, and M. Arrar (2007). "An improved matched filter for blood vessel detection of digital retinal images". *Comput. Biol. Med.* 37.2, pp. 262–267. doi: `10.1016/j.compbiomed.2006.03.003` (cit. on pp. 47, 52, 56, 57, 64).

T. Alarcón, H. M. Byrne, and P. K. Maini (2003). "A cellular automaton model for tumour growth in inhomogeneous environment". *J. Theor. Biol.* 225.2, pp. 257–274. doi: `10.1016/S0022-5193(03)00244-3` (cit. on pp. 25, 39, 40, 168, 171, 211, 7, 8, 13, 18).

– (2005). "A multiple scale model for tumor growth". *Multiscale Model Sim.* 3.2, pp. 440–475. doi: `10.1111/j.1742-4658.2012.08572.x` (cit. on pp. 25, 33, 39, 40, 171, 211, 7, 8, 18, 24).

T. Alarcón, M. R. Owen, H. M. Byrne, and P. K. Maini (2006). "Multiscale modelling of tumour growth and therapy: the influence of vessel normalisation on chemotherapy". *Comput. Math. Method. M.* 7.2-3, pp. 85–119. doi: `10.1080/10273660600968994` (cit. on pp. 25, 40, 171, 211, 7, 8, 10, 18).

A. Alexandrescu (2001). *Modern C++ Designs.* Generic Programming and Design Patterns Applied. Addison-Wesley (cit. on p. 20).

E Allen, I. B. Walters, and D Hanahan (2011). "Brivanib, a dual FGF/VEGF inhibitor, is active both first and second line against mouse pancreatic neuroendocrine tumors developing adaptive/evasive resistance to VEGF inhibition". *Clin. Cancer Res.* 17.16, pp. 5299–5310. doi: `10.1158/1078-0432.CCR-10-2847` (cit. on p. 20).

D Ambrosi, F Bussolino, and L Preziosi (2005). "A review of vasculogenesis models". *J. Theor. Med.* 6.1, pp. 1–19. doi: `10.1080/1027366042000327098` (cit. on pp. 83, 86, 174, 5).

A. R. A. Anderson and M. A. J. Chaplain (1998). "Continuous and discrete mathematical models of tumour-induced angiogenesis". *B. Math. Biol.* 60, pp. 857–900 (cit. on pp. 34–36, 39–41, 110, 112, 199, 216).

C. Andrieu and J. Thoms (2008). "A tutorial on adaptive mcmc". *Statistics and Computing* 18.4, pp. 343–373. doi: `10.1007/s11222-008-9110-y` (cit. on p. 220).

H. G. Augustin, G. Young Koh, G. Thurston, and K. Alitalo (2009). "Control of vascular morphogenesis and homeostasis through the angiopoietin–Tie system". *Nat. Rev. Mol. Cell Bio.* 10.3, pp. 165–177. doi: `10.1038/nrm2639` (cit. on pp. 9, 10, 81).

S Balay, J Brown, K Buschelman, V Eijkhout, W Gropp, D Kaushik, M Knepley, L Curfman McInnes, B Smith, and H Zhang (2012). *PETSc Users Manual* (cit. on p. 169).

S. Balay, W. D. Gropp, L. C. McInnes, and B. F. Smith (1997). "Efficient management of parallelism in object-oriented numerical software libraries". *Modern software tools for scientific computing.* Springer, pp. 163–202 (cit. on p. 22).

D Balding and D. McElwain (1985). "A mathematical model of tumour-induced capillary growth". *J. Theor. Biol.* 114.1, pp. 53–73. doi: `10.1016/S0022-5193(85)80255-1` (cit. on pp. 2, 5, 27, 34, 70, 72, 73, 82, 84, 130, 175).

K Bartha and H Rieger (2006). "Vascular network remodelling via vessel cooption, regression and growth in tumours". *J. Theor. Biol.* 241.4, pp. 903–918. doi: `doi:10.1016/j.jtbi.2006.01.022` (cit. on pp. 33, 40, 41).

D. O. Bates and S. J. Harper (2002). "Regulation of vascular permeability by vascular endothelial growth factors". *Vasc. Pharmacol.* 39.4-5, pp. 225–237. doi: `10.1016/S1537-1891(03)00011-9` (cit. on p. 14).

P. M. Becker (2005). "Neuropilin-1 regulates vascular endothelial growth factor-mediated endothelial permeability". *Circ. Res.* 96.12, pp. 1257–1265. doi: `10.1161/01.RES.0000171756.13554.49` (cit. on p. 14).

L. E. Benjamin, D Golijanin, A Itin, D Pode, and E Keshet (1999). "Selective ablation of immature blood vessels in established human tumors follows vascular endothelial growth factor withdrawal". *J. Clin. Invest.* 103, pp. 159–166 (cit. on pp. 14, 70, 72, 73).

B. E. Bennet (2012). “The Haptotactic Motility of Angiogenic Endothelial Cells”. PhD thesis. University of Maine (cit. on p. 106).

K. Bentley, G. Mariggi, H. Gerhardt, and P. A. Bates (2009). “Tipping the balance: robustness of tip cell selection, migration and fusion in angiogenesis”. *PLoS Comp. Biol.* 5.10, e1000549. DOI: `10.1371/journal.pcbi.1000549.t004` (cit. on p. 82).

K. Bentley, M. Jones, and B. Cruys (2013). “Predicting the future: towards symbiotic computational and experimental angiogenesis research”. *Exp. Cell Res.* Pp. 1–7. DOI: `10.1016/j.yexcr.2013.02.001` (cit. on p. 43).

G. Bergers and D. Hanahan (2008). “Modes of resistance to anti-angiogenic therapy”. *Nat. Rev. Cancer* 8.8, pp. 592–603. DOI: `10.1038/nrc2442` (cit. on p. 20).

R Betteridge, M. R. Owen, H. M. Byrne, T. Alarcón, and P. K. Maini (2006). “The impact of cell crowding and active cell movement on vascular tumour growth”. *Netw. Heterog. Media* 1.4, pp. 515–535. DOI: `10.3934/nhm.2006.1.515` (cit. on pp. 25, 40, 171, 211, 7, 8).

L. Bettini, S. Capecchi, and B. Venneri (2006). “Double dispatch in C++”. *Software: Practice and Experience* 36.6, pp. 581–613. DOI: `10.1002/spe.709` (cit. on p. 20).

R. Bicknell, C. E. Lewis, and N. Ferrara, eds. (1997). *Tumour angiogenesis.* Oxford Univ Press (cit. on pp. 134, 213).

A Bikfalvi, E Dupuy, A. L. Inyang, N Fayein, G Leseche, Y Courtois, and G Tobelem (1989). “Binding, internalization, and degradation of basic fibroblast growth factor in human microvascular endothelial cells”. *Exp. Cell Res.* 181.1, pp. 75–84 (cit. on pp. 102, 104, 6).

A Bikfalvi, C Sauzeau, H Moukadiri, J Maclouf, N Busso, M Bryckaert, J Plouet, and G Tobelem (1991). “Interaction of vasculotropin/vascular endothelial cell growth factor with human umbilical vein endothelial cells: binding, internalization, degradation, and biological effects”. *J. Cell Physiol.* 149.1, pp. 50–59 (cit. on pp. 85, 86, 174, 5).

P. M. Boyer and J. T. Hsu (1992). “Experimental studies of restricted protein diffusion in an agarose matrix”. *AIChE J.* 38.2, pp. 259–272 (cit. on pp. 102, 104, 6).

O. J. Britton, A Bueno-Orovio, K Van Ammel, H. R. Lu, R Towart, D. J. Gallacher, and B Rodríguez (2013). “Experimentally calibrated population of models predicts and explains intersubject variability in cardiac cellular electrophysiology”. *Proc. Natl. Acad. Sci.* 110.23, E2098–E2105. DOI: `10.1073/pnas.1304382110` (cit. on p. 222).

F. Brooks Jr (1987). “No silver bullet: essence and accidents of software engineering”. *Computer* 20.4, pp. 10–19. DOI: `10.1109/MC.1987.1663532` (cit. on p. 11).

A. S. Brown (2005). “Quantitation of hemodynamic function during developmental vascular regression in the mouse eye”. *Invest. Ophth. Vis Sci* 46.7, pp. 2231–2237. DOI: `10.1167/iovs.04-0848` (cit. on p. 72).

P. H. Burri, R. Hlushchuk, and V. Djonov (2004). “Intussusceptive angiogenesis: its emergence, its characteristics, and its significance”. *Dev. Dynam.* 231.3, pp. 474–488. DOI: `10.1002/dvdy.20184` (cit. on p. 11).

H. M. Byrne and M. A. J. Chaplain (1995). “Mathematical models for tumour angiogenesis: numerical simulations and non-linear wave solutions”. *B. Math. Biol.* 57, pp. 461–486 (cit. on pp. 2, 5, 27, 28, 30–32, 68, 70, 72, 73, 79, 82, 84, 125, 126, 130, 175, 4).

H. M. Byrne, M. A. J. Chaplain, D. L. Evans, and I Hopkinson (2000). “Mathematical modelling of angiogenesis in wound healing: comparison of theory and experiment”. *Comput. Math. Method. M.* 2.3, pp. 175–197 (cit. on pp. 27, 32).

R. Cao, E. Bråkenhielm, R. Pawliuk, D. Wariaro, M. J. Post, E. Wahlberg, P. Leboulch, and Y. Cao (2003). “Angiogenic synergism, vascular stability and improvement of hind-limb ischemia by a combination of PDGF-BB and FGF-2”. *Nat. Med.* 9.5, pp. 604–613. DOI: `10.1038/nm848` (cit. on pp. 15, 16, 23, 81, 82, 84, 99, 104, 175, 4).

R. Cao, S. Lim, H. Ji, Y. Zhang, Y. Yang, J. Honek, E.-M. Hedlund, and Y. Cao (2011). “Mouse corneal lymphangiogenesis model”. *Nat. Protoc.* 6.6, pp. 817–826. DOI: `10.1038/nprot.2011.359` (cit. on p. 66).

P. Carmeliet (2000). “Mechanisms of angiogenesis and arteriogenesis.” *Nat. Med.* 6.4 (cit. on p. 9).

– (2005). “Angiogenesis in life, disease and medicine”. *Nature* 438, pp. 932–936 (cit. on p. 1).

P. Carmeliet and R. K. Jain (2011). “Molecular mechanisms and clinical applications of angiogenesis”. *Nature* 473.7347, pp. 298–307. DOI: `10.1038/nature10144` (cit. on pp. 1, 8, 20).

Y. S. Chang, E. di Tomaso, D. M. McDonald, R. Jones, R. K. Jain, and L. L. Munn (2000). “Mosaic blood vessels in tumors: frequency of cancer cells in contact with flowing blood”. *P. Nat. Acad. Sci. USA.* 97.26, pp. 14608–14613 (cit. on p. 8).

T Chanwimaluang and G. Fan (2003). “An efficient blood vessel detection algorithm for retinal images using local entropy thresholding”. *Proceedings of the 2003 International Symposium on Circuits and Systems. ISCAS ’03.* DOI: `10.1109/ISCAS.2003.1206162` (cit. on p. 60).

M. A. J. Chaplain and A. M. Stuart (1993). “A model mechanism for the chemotactic response of endothelial cells to tumour angiogenesis factor”. *Math. Med. Biol.* (Cit. on p. 27).

S. Chaudhuri, S. Chatterjee, N. Katz, M. Nelson, and M. Goldbaum (1989). “Detection of blood vessels in retinal images using two-dimensional matched filters”. *IEEE T. Med. Imaging* 8.3, pp. 263–269 (cit. on pp. 46, 47, 52, 56, 57, 64).

L. Chen, B. Hann, and L. Wu (2011). “Experimental models to study lymphatic and blood vascular metastasis”. *J. Surg. Oncol.* 103.6, pp. 475–483. DOI: `10.1002/jso.21794` (cit. on p. 23).

R. R. Chen, E. A. Silva, W. W. Yuen, and D. J. Mooney (2006). “Spatio–temporal VEGF and PDGF delivery patterns blood vessel formation and maturation”. *Pharm. Res.* 24.2, pp. 258–264. DOI: `10.1007/s11095-006-9173-4` (cit. on pp. 83, 85, 86, 174, 5).

A. S. Chung and N. Ferrara (2011). “Developmental and pathological angiogenesis”. *Annu. Rev. Cell. Dev. Bi.* 27.1, pp. 563–584. DOI: `10.1146/annurev-cellbio-092910-154002` (cit. on p. 44).

K. P. Claffey, K. Abrams, S.-C. Shih, L. F. Brown, A. Mullen, and M. Keough (2001). “Fibroblast growth factor 2 activation of stromal cell vascular endothelial growth factor expression and angiogenesis”. *Lab. Invest.* 81.1, pp. 61–75 (cit. on p. 16).

E. A. Codling, M. J. Plank, and S Benhamou (2008). “Random walk models in biology”. *J. R. Soc. Interface.* 5.25, pp. 813–834. DOI: `10.1016/j.jtbi.2007.03.026` (cit. on p. 39).

S. D. Cohen and A. C. Hindmarsh (1996). “CVODE, a stiff/nonstiff ODE solver in C”. *Comput. Phys.* 10.2, pp. 138–143 (cit. on pp. 170, 22).

I. E. Collier, W. Legant, B. Marmer, O. Lubman, S. Saffarian, T. Wakatsuki, E. Elson, and G. I. Goldberg (2011). “Diffusion of mmps on the surface of collagen fibrils: the mobile cell surface – collagen substratum interface”. *PLoS ONE* 6.9, e24029. DOI: `10.1371/journal.pone.0024029.t001` (cit. on pp. 111, 112, 199).

A. J. Connor, J. Cooper, H. M. Byrne, P. K. Maini, and S. McKeever (2012). “Object-oriented paradigms for modelling vascular tumour growth: a case study”. *Proceedings of The Fourth International Conference on Advances in System Simulation (SIMUL 2012)*, pp. 1–10 (cit. on p. 8).

A. J. Connor *et al.* (2015). “An integrated approach to quantitative modelling in angiogenesis research”. *J. R. Soc. Interface.* Pp. 1–22 (cit. on p. 139).

J. Cooper, J. O. Vik, and D. Waltemath (2014). “A call for virtual experiments: accelerating the scientific process”. *Prog. Biophys. Mol. Biol.* Pp. 1–6. DOI: `10.7287/peerj.preprints.273v1` (cit. on p. vi).

E. A. Cox, S. K. Sastry, and A. Huttenlocher (2001). “Integrin-mediated adhesion regulates cell polarity and membrane protrusion through the rho family of gtpases”. *Mol. Biol. Cell* 12.2, pp. 265–277 (cit. on p. 107).

C. Daly, E. Pasnikowski, E. Burova, V. Wong, T. H. Aldrich, J. Griffiths, E. Ioffe, T. J. Daly, J. P. Fandl, and N. Papadopoulos (2006). “Angiopoietin-2 functions as an autocrine protective factor in stressed endothelial cells”. *P. Nat. Acad. Sci. USA.* 103.42, pp. 15491–15496 (cit. on p. 17).

J. T. Daub and R. M. H. Merks (2013). “A cell-Based model of extracellular-matrix-guided endothelial cell migration during angiogenesis”. *Bull. Math. Biol.* 75.8, pp. 1377–1399. DOI: `10.1007/s11538-013-9826-5` (cit. on pp. 111, 112, 199).

G. E. Davis (2005). “Endothelial extracellular matrix: biosynthesis, remodeling, and functions during vascular morphogenesis and neovessel stabilization”. *Circ. Res.* 97.11, pp. 1093–1107. DOI: `10.1161/01.RES.0000191547.64391.e3` (cit. on p. 106).

F De Smet, I Segura, K De Bock, P. J. Hohensinner, and P. Carmeliet (2009). “Mechanisms of vessel branching: filopodia on endothelial tip cells lead the way”. *Arterioscl. Throm. Vasc.* 29.5, pp. 639–649. DOI: `10.1161/ATVBAHA.109.185165` (cit. on p. 10).

A. S. Deakin (1976). “Model for initial vascular patterns in melanoma transplants”. *Growth* 40, pp. 191–201 (cit. on p. 27).

M. T. Dehkordi, S. Sadri, and A. Doosthoseini (2011). “A review of coronary vessel segmentation algorithms”. *Journal of Medical Signals and Sensors* 1.1, p. 49 (cit. on p. 45).

T. S. Deisboeck, Z. Wang, P. Macklin, and V. Cristini (2011). “Multiscale cancer modeling”. *Annu. Rev. Biomed. Eng.* 13.1, pp. 127–155. DOI: `10.1146/annurev-bioeng-071910-124729` (cit. on p. 33).

E. Dejana, E. Tournier-Lasserve, and B. M. Weinstein (2009). "The control of vascular integrity by endothelial cell junctions: molecular basis and pathological implications". *Dev. Cell.* 16.2, pp. 209–221. DOI: `10.1016/j.devcel.2009.01.004` (cit. on p. 8).

P. V. Dickson, J. B. Hamner, T. L. Sims, C. H. Fraga, C. Y. C. Ng, S Rajasekeran, N. L. Hagedorn, M. B. McCarville, C. F. Stewart, and A. M. Davidoff (2007). "Bevacizumab-induced transient remodeling of the vasculature in neuroblastoma xenografts results in improved delivery and efficacy of systemically administered chemotherapy". *Clin. Cancer Res.* 13.13, pp. 3942–3950. DOI: `10.1158/1078-0432.CCR-07-0278` (cit. on p. 19).

V Djonov, M Schmid, S. A. Tschanz, and P. H. Burri (2000). "Intussusceptive angiogenesis: its role in embryonic vascular network formation". *Circ. Res.* 86.3, pp. 286–292. DOI: `10.1161/01.RES.86.3.286` (cit. on p. 9).

C. J. Dowd, C. L. Cooney, and M. A. Nugent (1999). "Heparan sulfate mediates bFGF transport through basement membrane by diffusion with rapid reversible binding". *J. Biol. Chem* 274.8, pp. 5236–5244 (cit. on p. 103).

H. F. Dvorak (2002). "Vascular permeability factor/vascular endothelial growth factor: a critical cytokine in tumor angiogenesis and a potential target for diagnosis and therapy". *J. Clin. Oncol.* 20.21, pp. 4368–4380. DOI: `10.1200/JCO.2002.10.088` (cit. on p. 14).

J. M. L. Ebos, C. R. Lee, W. Cruz-Munoz, G. A. Bjarnason, J. G. Christensen, and R. S. Kerbel (2009). "Accelerated metastasis after short-term treatment with a potent inhibitor of tumor angiogenesis". *Cancer Cell* 15.3, pp. 232–239. DOI: `10.1016/j.ccr.2009.01.021` (cit. on p. 20).

Q. Ebrahem, S. S. Chaurasia, A. Vasanji, J. H. Qi, P. A. Klenotic, A. Cutler, K. Asosingh, S. Erzurum, and B. Anand-Apte (2010). "Cross-talk between vascular endothelial growth factor and matrix metalloproteinases in the induction of neovascularization in vivo". *Am. J. Pathol.* 176.1, pp. 496–503. DOI: `10.2353/ajpath.2010.080642` (cit. on p. 18).

L. Edelstein (1982). "The propagation of fungal colonies: a model for tissue growth". *J. Theor. Biol.* 98.4, pp. 679–701 (cit. on p. 27).

M. Fannon, K. Forsten-Williams, C. J. Dowd, D. A. Freedman, J. Folkman, and M. A. Nugent (2003). "Binding inhibition of angiogenic factors by heparan sulfate proteoglycans in aqueous humor: potential mechanism for maintenance of an avascular environment". *FASEB J.* 17.8, pp. 902–904 (cit. on pp. 102, 104, 6).

T. Fawcett (2004). "ROC graphs: notes and practical considerations for researchers". *Mach. Learn.* 31, pp. 1–38 (cit. on p. 54).

N Ferrara, H. P. Gerber, and J LeCouter (2003). "The biology of VEGF and its receptors". *Nat. Med.* 9.6, pp. 669–676 (cit. on p. 14).

R. J. Filion and A. S. Popel (2004). "A reaction-diffusion model of basic fibroblast growth factor interactions with cell surface receptors". *Ann. Biomed. Eng.* 32.5, pp. 645–663 (cit. on pp. 102, 104, 6).

K. R. Fister and M. L. McCarthy (2007). "Identification of a chemotactic sensitivity in a coupled system". *Math. Med. Biol.* arXiv: `0707.2417v1` (cit. on p. 220).

J. Folkman and M. Klagsbrun (1975). "Fundamental aspects of neoplasia". *Springer, Berlin* (cit. on p. 82).

J. Folkman, M Bach, J. W. Rowe, F Davidoff, P Lambert, C Hirsch, A Goldberg, H. H. Hiatt, J Glass, and E Henshaw (1971). "Tumor angiogenesis: therapeutic implications". *New Engl. J. Med.* 285.21, pp. 1182–1186. DOI: `10.1056/NEJM197111182852108` (cit. on pp. 1, 8, 9).

M Fowler (2006). *UML Distilled.* 3rd. Addison-Wesley (cit. on p. 14).

A. F. Frangi, W. J. Niessen, K. L. Vincken, and M. A. Viergever (1998). "Multiscale vessel enhancement filtering". *Proceedings of the First International Conference on Medical Image Computing and Computer-Assisted Intervention - MICCAI'98.* Springer, pp. 130–137 (cit. on p. 48).

H. B. Frieboes, J. S. Lowengrub, S Wise, X Zheng, P Macklin, E. L. Bearer, and V Cristini (2007). "Computer simulation of glioma growth and morphology". *Neuroimage* 37, S59–S70 (cit. on p. 41).

P. Friedl and D. Gilmour (2009). "Collective cell migration in morphogenesis, regeneration and cancer". *Nat. Rev. Mol. Cell Bio.* 10.7, pp. 445–457. DOI: `10.1038/nrm2720` (cit. on p. 82).

B. M. Fu and S. Shen (2003). "Structural mechanisms of acute VEGF effect on microvessel permeability". *Am. J .Physiol-Heart C.* 284.6, H2124–H2135. DOI: `10.1152/ajpheart.00894.2002` (cit. on pp. 85, 86, 103, 104, 174, 5, 6).

T. Fujii and H. Kuwano (2010). "Regulation of the expression balance of angiopoietin-1 and angiopoietin-2 by Shh and FGF-2". *In Vitro Cell Dev.-An.* 46.6, pp. 487–491. DOI: `10.1007/s11626-009-9270-x` (cit. on p. 16).

K Gaengel, G Genove, A Armulik, and C Betsholtz (2009). "Endothelial-mural cell signaling in vascular development and angiogenesis". *Arterioscl. Throm. Vasc.* 29.5, pp. 630–638. DOI: `10.1161/ATVBAHA.107.161521` (cit. on p. 10).

E. A. Gaffney, K Pugh, P. K. Maini, and F Arnold (2002). "Investigating a simple model of cutaneous wound healing angiogenesis". *J. Math. Biol.* 45.4, pp. 337–374. DOI: `10.1007/s002850200161` (cit. on p. 27).

N. W. Gale, G. Thurston, S. F. Hackett, R. Renard, Q. Wang, J. McClain, C. Martin, C. Witte, M. H. Witte, and D. Jackson (2002). "Angiopoietin-2 is required for postnatal angiogenesis and lymphatic patterning, and only the latter role is rescued by angiopoietin-1". *Dev. Cell.* 3.3, pp. 411–423 (cit. on p. 17).

E. Gamma, R. Helm, R. Johnson, and J. Vlissides (2003). *Design patterns: elements of reusable object-oriented software.* Addison-Wesley (cit. on p. 17).

H. P. Gerber, V Dixit, and N Ferrara (1998). "Vascular endothelial growth factor induces expression of the antiapoptotic proteins Bcl-2 and A1 in vascular endothelial cells". *J. Biol. Chem.* 273.21, pp. 13313–13316. DOI: `10.1074/jbc.273.21.13313` (cit. on p. 14).

H Gerhardt (2003). "VEGF guides angiogenic sprouting utilizing endothelial tip cell filopodia". *J. Cell. Biol.* 161.6, pp. 1163–1177. DOI: `10.1083/jcb.200302047` (cit. on pp. 9, 87, 136, 163, 174, 175, 207).

J. L. Gevertz and S. Torquato (2006). "Modelling the effects of vasculature evolution on early brain tumour growth". *J. Theor. Biol.* 243.4, pp. 517–531. DOI: `10.1016/j.jtbi.2006.07.002` (cit. on p. 81).

M. A. Gimbrone, R. S. Cotran, S. B. Leapman, and J. Folkman (1974). "Tumour growth and neovascularization: an experimental model using the rabbit cornea". *J. Natl. Cancer Inst.* 52, pp. 413–427 (cit. on p. 21).

M. Gioia, S. Monaco, G. F. Fasciglione, A. Coletti, A. Modesti, S. Marini, and M. Coletta (2007). "Characterization of the mechanisms by which gelitinase A, neutrophil collagenase, and membrane-type metalloproteinase MMP-14 recognize collagen I and enzymatically process the two α-chains". *Journal of Molecular Biology* 368.4, pp. 1101–1113. DOI: `10.1016/j.jmb.2007.02.076` (cit. on pp. 111, 112, 199).

S Goel, D. G. Duda, L Xu, L. L. Munn, Y Boucher, D Fukumura, and R. K. Jain (2011). "Normalization of the vasculature for treatment of cancer and other diseases". *Physiol. Rev.* 91.3, pp. 1071–1121. DOI: `10.1152/physrev.00038.2010` (cit. on pp. 10, 19).

D. Gospodarowicz (1974). "Localisation of a fibroblast growth factor and its effect alone and with hydrocortisone on 3T3 cell growth". *Nature* 249, pp. 123–127 (cit. on p. 15).

A Gupta, S Chempath, M. J. Sanborn, A Clark, and R. Q. Snurr (2003). "Object-oriented programming paradigms for molecular modeling". *Mol. Simulat.* 29.1, pp. 29–46. DOI: `10.1080/0892702031000065719` (cit. on p. 16).

A. Gurtovoy and D. Abrahams (2002). "The Boost C++ metaprogramming library" (cit. on p. 22).

A. Hall (2006). "Review of the pericyte during angiogenesis and its role in cancer and diabetic retinopathy". *Toxicol. Pathol.* 34.6, pp. 763–775. DOI: `10.1080/01926230600936290` (cit. on p. 71).

D. M. Hamby (1994). "A review of techniques for parameter sensitivity analysis of environmental models". *Environ. Monit. Assess.* 32.2, pp. 135–154 (cit. on p. 134).

D. Hanahan and R. A. Weinberg (2011). "Hallmarks of cancer: the next generation". *Cell* 144.5, pp. 646–674. DOI: `10.1016/j.cell.2011.02.013` (cit. on p. 7).

A. Hawkins-Daarud, S. Prudhomme, K. G. van der Zee, and J. T. Oden (2012). "Bayesian calibration, validation, and uncertainty quantification of diffuse interface models of tumor growth". *J. Math. Biol.* 67.6-7, pp. 1457–1485. DOI: `10.1007/s00285-012-0595-9` (cit. on p. 219).

A. Hawkins-Daarud, R. C. Rockne, A. R. A. Anderson, and K. R. Swanson (2013). "Modeling tumor-associated edema in gliomas during anti-angiogenic therapy and its impact on imageable tumor". *Frontiers In Oncology* 3. DOI: `10.3389/fonc.2013.00066/abstract` (cit. on p. 28).

A Hegen (2004). "Expression of angiopoietin-2 in endothelial cells is controlled by positive and negative regulatory promoter elements". *Arterioscl. Throm. Vasc.* 24.10, pp. 1803–1809. DOI: `10.1161/01.ATV.0000140819.81839.0e` (cit. on pp. 14, 16).

A. Hegen, S. Koidl, K. Weindel, D. Marmé, H. G. Augustin, and U. Fiedler (2004). "Expression of angiopoietin-2 in endothelial cells is controlled by positive and negative regulatory promoter elements". *Arterioscl. Throm. Vasc.* 24.10, pp. 1803–1809. DOI: `10.1161/01.ATV.0000140819.81839.0e` (cit. on p. 9).

M. Hitz and B. Montazeri (1995). "Measuring coupling and cohesion in object-oriented systems". *Proc Int'l Symp Applied Corporate Computing.* na, pp. 1–10 (cit. on p. 13).

R. Hlushchuk, O. Riesterer, O. Baum, J. Wood, G. Gruber, M. Pruschy, and V. Djonov (2008). “Tumor recovery by angiogenic switch from sprouting to intussusceptive angiogenesis after treatment with PTK787/ZK222584 or ionizing radiation”. *Am. J. Pathol.* 173.4, pp. 1173–1185. DOI: `10.2353/ajpath.2008.071131` (cit. on p. 11).

R. Hlushchuk, A. N. Makanya, and V. Djonov (2011). “Escape mechanisms after antiangiogenic treatment, or why are the tumors growing again?” *Int. J. Dev. Biol.* 55.4-5, pp. 563–567. DOI: `10.1387/ijdb.103231rh` (cit. on pp. 9, 19).

J Holash (1999). “Vessel cooption, regression, and growth in tumors mediated by angiopoietins and VEGF”. *Science* 284.5422, pp. 1994–1998. DOI: `10.1126/science.284.5422.1994` (cit. on p. 7).

D. F. Holmes, C. J. Gilpin, C. Baldock, U. Ziese, A. J. Koster, and K. E. Kadler (2001). “Corneal collagen fibril structure in three dimensions: structural insights into fibril assembly, mechanical properties, and tissue organization”. *P. Nat. Acad. Sci. USA.* 98.13, pp. 7307–7312 (cit. on pp. 110, 112, 199).

H Honda and K Yoshizato (1997). “Formation of the branching pattern of blood vessels in the wall of the avian yolk sac studied by computer simulation.” *Dev. Growth Differ.* 39, pp. 581–589 (cit. on p. 40).

S. R. Hubbard (1999). “Structural analysis of receptor tyrosine kinases”. *Progress In Biophysics and Molecular Biology* 71.3, pp. 343–358 (cit. on p. 13).

W. Hundsdorfer (2000). “Numerical solution of advection-diffusion-reaction equations”. *Lecture Notes* (cit. on p. 86).

T. Jackson and X. Zheng (2010). “A cell-based model of endothelial cell migration, proliferation and maturation during corneal angiogenesis”. *Bull. Math. Biol.* 72.4, pp. 830–868. DOI: `10.1007/s11538-009-9471-1` (cit. on pp. 37, 216).

R. K. Jain (2001). “Delivery of molecular and cellular medicine to solid tumors”. *Adv. Drug. Deliver. Rev.* (Cit. on pp. 10, 19).

– (2003). “Molecular regulation of vessel maturation”. *Nat. Med.* 9.6, pp. 685–693 (cit. on p. 2).

S. Javerzat, P. Auguste, and A. Bikfalvi (2002). “The role of fibroblast growth factors in vascular development”. *Trends. Mol. Med.* 8.10, pp. 483–489 (cit. on pp. 15, 99).

J. Jeon, V. Quaranta, and P. T. Cummings (2010). “An off-lattice hybrid discrete-continuum model of tumor growth and invasion”. *Biophysj* 98.1, pp. 37–47. DOI: `10.1016/j.bpj.2009.10.002` (cit. on p. 32).

D. Johnson, A. J. Connor, and S. McKeever (2012). “Modular markup for simulating vascular tumour growth”. *The 5th International Advanced Research Workshop on In Silico Oncology and Cancer Investigation (5th IARWISOCI) – The TUMOR Workshop*, pp. 1–4 (cit. on p. 8).

D. Johnson, D. Johnson, A. connor, S. McKeever, Z. Wang, T. Deisboeck, T. Quaiser, and E. Shochat (2014). “Semantically linking in silico cancer models”. *Cancer Informatics*, p. 133. DOI: `10.4137/CIN.S13895` (cit. on p. 8).

R. Kalluri (2003). “Basement membranes: structure, assembly and role in tumour angiogenesis”. *Nat. Rev. Cancer* 3.6, pp. 422–433. DOI: `10.1038/nrc1094` (cit. on p. 18).

M. R. Kano, Y. Morishita, C. Iwata, S. Iwasaka, T. Watabe, Y. Ouchi, K. Miyazono, and K. Miyazawa (2005). “VEGF-A and FGF-2 synergistically promote neoangiogenesis through enhancement of endogenous PDGF-B-PDGFRβ signaling”. *J. Cell Sci.* 118.16, pp. 3759–3768. DOI: `10.1242/jcs.02483` (cit. on p. 16).

B. M. Kenyon, E. E. Voest, C. C. Chen, E Flynn, J. Folkman, and R. J. D’Amato (1996). “A model of angiogenesis in the mouse cornea”. *Investigative Opthalmology and Visual Science* 37.8, pp. 1625–1632 (cit. on pp. 21, 36).

B. A. Keyt, L. T. Berleau, H. V. Nguyen, H. Chen, H. Heinsohn, R. Vandlen, and N. Ferrara (1996). “The carboxyl-terminal domain (111165) of vascular endothelial growth factor is critical for its mitogenic potency”. *J. Biol. Chem* 271.13, pp. 7788–7795. DOI: `10.1074/jbc.271.13.7788` (cit. on p. 13).

Y Kienast *et al.* (2013). “Ang-2-VEGF-A crossmab, a novel bispecific human IgG1 antibody blocking VEGF-A and Ang-2 functions simultaneously, mediates potent antitumor, antiangiogenic, and antimetastatic efficacy”. *Clin. Cancer Res.* 19.24, pp. 6730–6740. DOI: `10.1158/1078-0432.CCR-13-0081` (cit. on pp. 20, 44).

W. W. Kilarski, B. Samolov, L. Petersson, A. Kvanta, and P. Gerwins (2009). “Biomechanical regulation of blood vessel growth during tissue vascularization”. *Nat. Med.* 15.6, pp. 657–664. DOI: `10.1038/nm.1985` (cit. on p. 9).

C. Kirbas and F. Quek (2004). “A review of vessel extraction techniques and algorithms”. *Comput. Surv.* 36.2. DOI: `10.1145/1031120.1031121` (cit. on p. 45).

A. E. Koch, P. J. Polverini, S. L. Kunkel, L. A. Harlow, L. A. DiPietro, V. M. Elner, S. G. Elner, and R. M. Strieter (1992). “Interleukin-8 as a macrophage-derived mediator of angiogenesis”. *Science* 258, pp. 1798–1801 (cit. on p. 21).

S Kouvroukoglou, K. C. Dee, R Bizios, L. V. McIntire, and K Zygourakis (2000). “Endothelial cell migration on surfaces modified with immobilized adhesive peptides”. *Biomaterials* 21.17, pp. 1725–1733 (cit. on pp. 82, 84, 175, 4).

P. Kovesi (1999). “Image features from phase congruency”. *VIDERE: Journal of Computer Vision Research* 1.3, pp. 1–26 (cit. on p. 49).

– (2000). “Phase congruency: a low-level image invariant”. *Psychol. Res.* 64.2, pp. 136–148 (cit. on pp. 49–51).

– (2003). “Phase congruency detects corners and edges”. *Proceedings of the Australian Pattern Recognition Society Conference: DICTA 2003* (cit. on p. 49).

D. S. Lee, H Rieger, and K Bartha (2006). “Flow correlated percolation during vascular remodeling in growing tumors”. *Phys. Rev. Lett.* 96.5, p. 058104. DOI: `10.1103/PhysRevLett.96.058104` (cit. on pp. 40, 41).

C Lieu, J Heymach, M Overman, H Tran, and S Kopetz (2011). “Beyond VEGF: inhibition of the fibroblast growth factor pathway and antiangiogenesis”. *Clin. Cancer Res.* 17.19, pp. 6130–6139. DOI: `10.1158/1078-0432.CCR-11-0659` (cit. on pp. 15, 99).

B. Liskov (1987). “Data abstraction and hierarchy”. *ACM Sigplan Notices* 23.5, pp. 17–34. DOI: `10.1145/62138.62141` (cit. on p. 15).

M. P. Little, W. F. Heidenreich, and G. Li (2010). “Parameter identifiability and redundancy: theoretical considerations”. *PLoS ONE* 5.1, e8915 (cit. on pp. v, 219).

K. C. Louden and P. Adams (2011). *Programming Languages: Principles and Practice.* Cengage (cit. on p. 11).

J Lowell, A Hunter, D Steel, A Basu, R Ryder, and R. L. Kennedy (2004). “Measurement of retinal vessel widths from fundus images based on 2-D modeling”. *IEEE T. Med. Imaging* 23.10, pp. 1196–1204. DOI: `10.1109/TMI.2004.830524` (cit. on p. 46).

F. MacGabhann and A. S. Popel (2003). “Model of competitive binding of vascular endothelial growth factor and placental growth factor to VEGF receptors on endothelial cells”. *Am. J. Physiol.-Heart C.* 286.1, 153H–164. DOI: `10.1152/ajpheart.00254.2003` (cit. on pp. 85, 86, 174, 5).

F. MacGabhann (2005). “Differential binding of VEGF isoforms to VEGF receptor 2 in the presence of neuropilin-1: a computational model”. *Am. J. Physiol.-Heart C.* 288.6, H2851–H2860. DOI: `10.1152/ajpheart.01218.2004` (cit. on pp. 83, 86, 174, 5).

M. J. C. Machado, M. G. Watson, A. H. Devlin, M. A. J. Chaplain, S. R. McDougall, and C. A. Mitchell (2011). “Dynamics of angiogenesis during wound healing: a coupled in vivo and in silico study”. *Microcirculation* 18.3, pp. 183–197. DOI: `10.1111/j.1549-8719.2010.00076.x` (cit. on pp. 39, 106, 210).

P Macklin, S McDougall, A. R. A. Anderson, M. A. J. Chaplain, V Cristini, and J Lowengrub (2008). “Multiscale modelling and nonlinear simulation of vascular tumour growth”. *J. Math. Biol.* 58.4-5, pp. 765–798. DOI: `10.1007/s00285-008-0216-9` (cit. on p. 39).

P. Macklin and J. S. Lowengrub (2008). “A new ghost cell/level set method for moving boundary problems: application to tumor growth”. *J. Sci. Comput.* 35.2-3, pp. 266–299. DOI: `10.1007/s10915-008-9190-z` (cit. on p. 39).

A. J. Maniotis, R. Folberg, A. Hess, E. A. Seftor, L. M. Gardner, J. Pe’er, J. M. Trent, P. S. Meltzer, and M. J. Hendrix (1999). “Vascular channel formation by human melanoma cells in vivo and in vitro: vasculogenic mimicry”. *Am. J. Pathol.* 155.3, pp. 739–752. DOI: `10.1016/S0002-9440(10)65173-5` (cit. on p. 8).

N. V. Mantzaris, S. Webb, and H. G. Othmer (2004). “Mathematical modeling of tumor-induced angiogenesis”. *J. Math. Biol.* 49.2, pp. 111–187 (cit. on pp. 18, 26).

S. Marino, I. B. Hogue, C. J. Ray, and D. E. Kirschner (2008). “A methodology for performing global uncertainty and sensitivity analysis in systems biology”. *J. Theor. Biol.* 254.1, pp. 178–196. DOI: `10.1016/j.jtbi.2008.04.011` (cit. on p. 221).

M. Matsumoto and T. Nishimura (1998). “Mersenne twister: a 623-dimensionally equidistributed uniform pseudo-random number generator”. *ACM T. Model. Comput. S.* 8.1. DOI: `10.1145/272991.272995` (cit. on p. 169).

S. R. McDougall, A. R. A. Anderson, M. A. J. Chaplain, and J. A. Sherratt (2002). “Mathematical modelling of flow through vascular networks: implications for tumour-induced angiogenesis and chemotherapy strategies”. *Bull. Math. Biol.* 64.4, pp. 673–702. DOI: `10.1006/bulm.2002.0293` (cit. on pp. 38, 39).

S. R. McDougall, A. R. A. Anderson, and M. A. J. Chaplain (2006). “Mathematical modelling of dynamic adaptive tumour-induced angiogenesis: clinical implications and therapeutic targeting strategies”. *J. Theor. Biol.* 241.3, pp. 564–589. DOI: `10.1016/j.jtbi.2005.12.022` (cit. on pp. 38, 39).

S. McKeever, M. Gill, A. J. Connor, and D. Johnson (2013). “Abstraction in physiological modelling languages”. *Proceedings of the Symposium on Theory of Modeling & Simulation - DEVS Integrative M&S Symposium (Mod4Sim) 2013*, pp. 1–8 (cit. on p. 8).

A Meeson, M Palmer, M Calfon, and R Lang (1996). “A relationship between apoptosis and flow during programmed capillary regression is revealed by vital analysis”. *Development* 122, pp. 3929–3938 (cit. on p. 71).

M Mernik, J Heering, and A. M. Sloane (2005). “When and how to develop domain-specific languages”. *ACM Comput. Surv.* 37.4, pp. 316–344. DOI: `doi:10.1145/1118890.1118892` (cit. on p. 27).

F. Milde, M. Bergdorf, and P. Koumoutsakos (2008). “A hybrid model for three-dimensional simulations of sprouting angiogenesis”. *Biophysj* 95.7, pp. 3146–3160. DOI: `10.1529/biophysj.107.124511` (cit. on pp. 111, 112, 199).

G. R. Mirams *et al.* (2013). “Chaste: an open source C++ library for computational physiology and biology”. *PLoS Comp. Biol.* 9.3, e1002970. DOI: `10.1371/journal.pcbi.1002970.s006` (cit. on pp. 217, 22).

G. Morgan (2003). “Chemotherapy and the cell cycle”. *Cancer Nursing Practice*, pp. 1–4 (cit. on p. 18).

D. Moscatelli (1988). “Metabolism of receptor-bound and matrix-bound basic fibroblast growth factor by bovine capillary endothelial cells.” *J. Cell Biol.* 107.2, pp. 753–759 (cit. on p. 102).

L Moserle, G Jimenez-Valerio, and O Casanovas (2014). “Antiangiogenic therapies: going beyond their limits”. *Cancer Discovery* 4.1, pp. 31–41. DOI: `10.1158/2159-8290.CD-13-0199` (cit. on p. 20).

M. Murakami and T. Sakurai (2012). “Role of fibroblast growth factor signaling in vascular formation and maintenance: orchestrating signaling networks as an integrated system”. *Wiley Interdisciplinary Reviews: Systems Biology and Medicine* 4.6, pp. 615–629. DOI: `10.1002/wsbm.1190` (cit. on pp. 15, 17, 99, 138–140).

M. Murakami and M. Simons (2008). “Fibroblast growth factor regulation of neovascularization”. *Curr. Opin. Hematol.* 15.3, pp. 215–220. DOI: `10.1097/MOH.0b013e3282f97d98` (cit. on pp. 16, 44).

M. Murakami, L. T. Nguyen, K. Hatanaka, W. Schachterle, P.-Y. Chen, Z. W. Zhuang, B. L. Black, and M. Simons (2011). “FGF-dependent regulation of VEGF receptor 2 expression in mice”. *J. Clin. Invest.* 121.7, pp. 2668–2678. DOI: `10.1172/JCI44762DS1` (cit. on pp. 16, 140).

V. R. Muthukkaruppan, L Kubai, and R Auerbach (1982). “Tumor-induced neovascularization in the mouse eye”. *J. Natl. Cancer I.* 69.3, pp. 699–708 (cit. on pp. 28, 31, 82).

National Research Council. (2012). *Assessing the Reliability of Complex Models: Mathematical and Statistical Foundations of Verification, Validation, and Uncertainty Quantification.* Tech. rep. (cit. on pp. 91, 221).

R. D. Nelson, P. G. Quie, and R. L. Simmons (1975). “Chemotaxis under agarose: a new and simple method for measuring chemotaxis and spontaneous migration of human polymorphonuclear leukocytes and monocytes”. *J. Immunol.* 115.6, pp. 1650–1656 (cit. on p. 82).

M Nguyen, Y Shing, and J. Folkman (1994). “Quantification of angiogenesis and antiangiogenesis in the chick embryo chorioallantoic membrane”. *Microvasc. Res.* 47, pp. 31–40 (cit. on p. 21).

L. J. Nissen, R. Cao, E.-M. Hedlund, Z. Wang, X. Zhao, D. Wetterskog, K. Funa, E. Bråkenhielm, and Y. Cao (2007). “Angiogenic factors FGF2 and PDGF-BB synergistically promote murine tumor neovascularization and metastasis”. *J. Clin. Invest.* 117.10, pp. 2766–2777. DOI: `10.1172/JCI32479DS1` (cit. on p. 16).

B Obara, M Fricker, D Gavaghan, and V Grau (2012). “Contrast-independent curvilinear structure detection in biomedical images”. *IEEE T. Image Process.* 21.5, pp. 2572–2581. DOI: `10.1109/TIP.2012.2185938` (cit. on pp. 49, 51, 52, 56–58).

B. Olofsson, E. Korpelainen, M. S. Pepper, S. J. Mandriota, K. Aase, V. Kumar, Y. Gunji, M. M. Jeltsch, M. Shibuya, and K. Alitalo (1998). “Vascular endothelial growth factor B (VEGF-B) binds to VEGF receptor-1 and regulates plasminogen activator activity in endothelial cells”. *P. Nat. Acad. Sci. USA.* 95.20, pp. 11709–11714 (cit. on p. 14).

M. E. Orme and M. A. J. Chaplain (1997). “Two-dimensional models of tumour angiogenesis and anti-angiogenesis strategies.” *Ima J. Math. Appl. Med. Biol.* 14.3, pp. 189–205 (cit. on pp. 110, 112, 199).

M. R. Owen, T. Alarcón, P. K. Maini, and H. M. Byrne (2009). “Angiogenesis and vascular remodelling in normal and cancerous tissues”. *J. Math. Biol.* 58.4-5, pp. 689–721. DOI: `10.1007/s00285-008-0213-z` (cit. on pp. 25, 32, 33, 40, 171, 173, 175, 207, 211, 7, 8).

M. R. Owen, I. J. Stamper, M Muthana, G. W. Richardson, J Dobson, C. E. Lewis, and H. M. Byrne (2011). “Mathematical modelling predicts synergistic antitumor effects of combining a macrophage based, hypoxia-targeted gene therapy with chemotherapy”. *Cancer Res.* 71.8, pp. 2826–2837. DOI: `10.1158/0008-5472.CAN-10-2834` (cit. on pp. 33, 40, 72, 82, 84, 167, 172, 173, 175, 4, 18).

N. H. Packard and S. Wolfram (1985). “Two-dimensional cellular automata”. *J. Stat. Phys.* 38.5-6, pp. 901–946 (cit. on p. 9).

M. Page-Jones (2002). *Fundamentals of object-oriented design in UML.* Addison-Wesley (cit. on pp. 11, 13, 15).

K. J. Painter and T Hillen (2002). “Volume-filling and quorum-sensing in models for chemosensitive movement”. *Can. Appl. Math. Quart* 10.4, pp. 501–543 (cit. on pp. 31, 32).

S. P. Palecek, J. C. Loftus, M. H. Ginsberg, D. A. Lauffenburger, and A. F. Horwitz (1997). “Integrin-ligand binding properties govern cell migration speed through cell-substratum adhesiveness.” *Nature* 385.6616, pp. 537–540. DOI: `10.1038/385537a0` (cit. on p. 107).

J Panovska, H. M. Byrne, and P. K. Maini (2007). “Mathematical modelling of vascular tumour growth and implications for therapy”. *Model. Simul. Sci. Eng.* Pp. 205–216 (cit. on pp. 27, 185).

J. E. Park, H. H. Chen, J. Winer, K. A. Houck, and N. Ferrara (1994). “Placenta growth factor. Potentiation of vascular endothelial growth factor bioactivity, in vitro and in vivo, and high affinity binding to Flt-1 but not to Flk-1/KDR.” *J. Biol. Chem* 269.41, pp. 25646–25654 (cit. on p. 14).

P. Pathmanathan and R. A. Gray (2013). “Verification of computational models of cardiac electrophysiology”. *Int. J. Numer. Meth. Biomed. Eng.* 30.5, pp. 525–544. DOI: `10.1002/cnm.2615` (cit. on pp. 8, 24).

B. B. Peebo (2008). “Angiogenesis from a new perspective”. PhD thesis. Linköping University (cit. on pp. 9, 11).

B. B. Peebo, P Fagerholm, C Traneus-Rockert, and N Lagali (2011). “Time-lapse in vivo imaging of corneal angiogenesis: the role of inflammatory cells in capillary sprouting”. *Invest. Ophth. Vis Sci* 52.6, pp. 3060–3068. DOI: `10.1167/iovs.10-6101` (cit. on pp. 85, 86, 175, 4).

S. M. Peirce (2008). “Computational and mathematical modeling of angiogenesis”. *Microcirculation* 15.8, pp. 739–751. DOI: `10.1080/10739680802220331` (cit. on pp. v, vi, 26).

M. S. Pepper and S. J. Mandriota (1998). “Regulation of vascular endothelial growth factor receptor-2 (Flk-1) expression in vascular endothelial cells”. *Exp. Cell Res.* 241.2, pp. 414–425 (cit. on pp. 141, 144, 4).

H Perfahl *et al.* (2011). “Multiscale modelling of vascular tumour growth in 3D: the roles of domain size and boundary conditions”. *PLoS ONE* 6.4, (17 pages). DOI: `10.1371/journal.pone.0014790` (cit. on pp. 6, 25, 40, 41, 156, 157, 161, 171, 207, 210, 211, 214, 7–9).

W. M. Petroll, H. D. Cavanagh, and J. V. Jester (2004). “Dynamic threedimensional visualization of collagen matrix remodeling and cytoskeletal organization in living corneal fibroblasts”. *Scanning* (cit. on pp. 111, 112, 199).

G. J. Pettet, H. M. Byrne, D. McElwain, and J Norbury (1996a). “A model of wound-healing angiogenesis in soft tissue”. *Math. Biosci.* 136.1, pp. 35–63 (cit. on p. 27).

G. J. Pettet, M. A. J. Chaplain, D. L. S. McElwain, and H. M. Byrne (1996b). “On the role of angiogenesis in wound healing”. *P. Roy. Soc. B.-Biol. Sci.* 263.1376, pp. 1487–1493. DOI: `10.1098/rspb.1996.0217` (cit. on p. 27).

L. K. Phng and H. Gerhardt (2009). “Angiogenesis: a team effort coordinated by Notch”. *Dev. Cell.* 16.2, pp. 196–208. DOI: `10.1016/j.devcel.2009.01.015` (cit. on pp. 17, 18).

L. K. Phng, F Stanchi, and H Gerhardt (2013). “Filopodia are dispensable for endothelial tip cell guidance”. *Development* 140.19, pp. 4031–4040. DOI: `10.1242/dev.097352` (cit. on pp. 163, 192, 193).

J Pitt-Francis *et al.* (2009). “Chaste: a test-driven approach to software development for biological modelling”. *Comput. Phys. Commun.* 180.12, pp. 2452–2471. DOI: `10.1016/j.cpc.2009.07.019` (cit. on pp. 217, 22, 25).

M. J. Plank and B. D. Sleeman (2004). “Lattice and non-lattice models of tumour angiogenesis”. *Bull. Math. Biol.* 66.6, pp. 1785–1819. DOI: `10.1016/j.bulm.2004.04.001` (cit. on p. 41).

M. J. Plank, B. D. Sleeman, and P. F. Jones (2004). “A mathematical model of tumour angiogenesis, regulated by vascular endothelial growth factor and the angiopoietins”. *J. Theor. Biol.* 229.4, pp. 435–454. DOI: `10.1016/j.jtbi.2004.04.012` (cit. on pp. 37, 81).

P. J. Polverini, N. P. Bouck, and F Rastinejad (1991). “Assay and purification of naturally occurring inhibitor of angiogenesis”. *Method. Enzymol.* 198, pp. 440–450 (cit. on p. 36).

M Presta, D Moscatelli, J Joseph-Silverstein, and D. B. Rifkin (1986). “Purification from a human hepatoma cell line of a basic fibroblast growth factor-like molecule that stimulates capillary endothelial cell plasminogen activator production, DNA synthesis, and migration.” *Mol. Cell Biol.* 6.11, pp. 4060–4066 (cit. on p. 15).

M. Presta, P. Dell’Era, S. Mitola, E. Moroni, R. Ronca, and M. Rusnati (2005). “Fibroblast growth factor/fibroblast growth factor receptor system in angiogenesis”. *Cytokine Growth F. R.* 16.2, pp. 159–178. DOI: `10.1016/j.cytogfr.2005.01.004` (cit. on pp. 15–17, 44, 100).

A. R. Pries, T. W. Secomb, P Gaehtgens, and J. F. Gross (1990). “Blood flow in microvascular networks”. *Circ. Res.* 67.4, pp. 826–834. DOI: `doi:10.1161/01.RES.67.4.826` (cit. on pp. 38–41, 166–168, 211, 216).

A. R. Pries, T. W. Secomb, T Gessner, M. B. Sperandio, J. F. Gross, and P Gaehtgens (1994). “Resistance to blood flow in microvessels in vivo”. *Circ. Res.* 75.5, pp. 904–915. DOI: `doi:10.1161/01.RES.75.5.904` (cit. on pp. 38–41, 166–168, 211, 216).

A. R. Pries, T. W. Secomb, and P Gaehtgens (1998). “Structural adaptation and stability of microvascular networks: theory and simulations”. *Am. J .Physiol-Heart C.* 275.2, H349–H360 (cit. on pp. 38–41, 166–168, 211, 216, 10).

A. R. Pries, B Reglin, and T. W. Secomb (2001). “Structural adaptation of microvascular networks: functional roles of adaptive responses”. *Am. J .Physiol-Heart C.* 281.3, H1015–H1025 (cit. on pp. 166–168, 211, 216).

A. R. Pries, M. Höpfner, F. le Noble, M. W. Dewhirst, and T. W. Secomb (2010). “The shunt problem: control of functional shunting in normal and tumour vasculature”. *Nat. Rev. Cancer* 10.8, pp. 587–593. DOI: `10.1038/nrc2895` (cit. on pp. 12, 13).

T. Quaiser (2012). “Data- and model-based identification of biochemical processes”. PhD thesis. Ruhr University Bochum (cit. on p. v).

T. Quaiser, A. Dittrich, F. Schaper, and M. Mönnigmann (2011). “A simple work flow for biologically inspired model reduction - application to early JAK-STAT signaling”. *BMC Syst. Biol.* 5.1, p. 30. DOI: `10.1186/1752-0509-5-30` (cit. on pp. v, 220).

A. A. Qutub, F Mac Gabhann, E. D. Karagiannis, P Vempati, and A. S. Popel (2009). “Multiscale models of angiogenesis”. *IEEE Eng. Med. Biol.* 28.2, pp. 14–31. DOI: `10.1109/MEMB.2009.931791` (cit. on p. 26).

M. Ramsauer and P. A. D’Amore (2002). “Getting Tie(2)d up in angiogenesis”. *J. Clin. Invest.* 110.11, pp. 1615–1617. DOI: `10.1172/JCI17326` (cit. on p. 10).

K. A. Rejniak and A. R. A. Anderson (2010). “Hybrid models of tumor growth”. *Wiley Interdisciplinary Reviews: Systems Biology and Medicine* 3.1, pp. 115–125. DOI: `10.1002/wsbm.102` (cit. on pp. 32, 33).

N Resnick, H Yahav, A Shay-Salit, M Shushy, S Schubert, L. C. M. Zilberman, and E Wofovitz (2003). “Fluid shear stress and the vascular endothelium: for better and for worse”. *Prog. Biophys. Mol. Biol.* 81, pp. 177–199 (cit. on p. 71).

B. Ribba, N. H. Holford, P Magni, I Trocóniz, I Gueorguieva, P Girard, C Sarr, M Elishmereni, C Kloft, and L. E. Friberg (2014). “A review of mixed-effects models of tumor growth and effects of anticancer drug treatment used in population analysis”. *CPT Pharmacometrics Syst. Pharmacol.* 3.5, e113. DOI: `10.1038/psp.2014.12` (cit. on p. 222).

M. S. Rogers, A. E. Birsner, and R. J. D’Amato (2007). “The mouse cornea micropocket angiogenesis assay”. *Nat. Protoc.* 2.10, pp. 2545–2550. DOI: `10.1038/nprot.2007.368` (cit. on pp. 21, 22, 59).

M. Roghani and D Moscatelli (1992). “Basic fibroblast growth factor is internalized through both receptor-mediated and heparan sulfate-mediated mechanisms.” *J. Biol. Chem.* 267.31, pp. 22156–22162 (cit. on p. 102).

R. Roskoski Jr. (2007). “Vascular endothelial growth factor (VEGF) signaling in tumor progression”. *Crit. Rev. Oncol. Hemat.* 62.3, pp. 179–213. DOI: `10.1016/j.critrevonc.2007.01.006` (cit. on pp. 8, 13, 15).

A. L. Rubinstein (2003). “Zebrafish: from disease modeling to drug discovery”. *Curr. Opin. Drug Discovery Dev.* 6.2, pp. 218–223 (cit. on p. 21).

J. E. Rundhaug (2005). "Matrix metalloproteinases and angiogenesis". *J. Cell. Mol. Med.* 9.2, pp. 267–285 (cit. on pp. 18, 106, 122, 195).

A. Saltelli and P. Annoni (2010). "Environmental modelling & software". *Environ. Model. Softw.* 25.12, pp. 1508–1517. DOI: `10.1016/j.envsoft.2010.04.012` (cit. on p. 191).

R. C. Schugart, A Friedman, R Zhao, and C. K. Sen (2008). "Wound angiogenesis as a function of tissue oxygen tension: a mathematical model". *P. Nat. Acad. Sci. USA.* 105.7, pp. 2628–2633 (cit. on p. 27).

M Scianna, C. G. Bell, and L Preziosi (2013). "A review of mathematical models for the formation of vascular networks". *J. Theor. Biol.* 333.C, pp. 174–209. DOI: `10.1016/j.jtbi.2013.04.037` (cit. on pp. 26, 28).

T. W. Secomb, R Hsu, R. D. Braun, J. R. Ross, J. F. Gross, and M. W. Dewhirst (1998). "Theoretical simulation of oxygen transport to tumors by three-dimensional networks of microvessels". *Adv. Exp. Med. Biol.* Pp. 629–634 (cit. on p. 24).

T. W. Secomb, J. P. Alberding, R. Hsu, M. W. Dewhirst, and A. R. Pries (2013). "Angiogenesis: an adaptive dynamic biological patterning problem". *PLoS Comp. Biol.* 9.3, e1002983. DOI: `10.1371/journal.pcbi.1002983.s001` (cit. on p. 208).

M Sefidgar, K Raahemifar, H Bazmara, M Bazargan, S. M. Mousavi, and M Soltani (2014). "Effect of remodeled tumor-induced capillary network on interstitial flow in cancerous tissue". *Biomedical Engineering (MECBME), 2014 Middle East Conference on*, pp. 212–215. DOI: `10.1109/MECBME.2014.6783242` (cit. on p. 216).

G. Seghezzi, S. Patel, C. J. Ren, A. Gualandris, G. Pintucci, E. S. Robbins, R. L. Shapiro, A. C. Galloway, D. B. Rifkin, and P. Mignatti (1998). "Fibroblast growth factor-2 (FGF-2) induces vascular endothelial growth factor (VEGF) expression in the endothelial cells of forming capillaries: an autocrine mechanism contributing to angiogenesis". *J. Cell Biol.* 141.7, pp. 1659–1673 (cit. on pp. 15, 16, 140, 151, 154, 214, 217).

D. R. Senger, S. J. Galli, A. M. Dvorak, C. A. Perruzzi, V. S. Harvey, and H. F. Dvorak (1983). "Tumor cells secrete a vascular permeability factor that promotes accumulation of ascites fluid". *Science* 219.4587, pp. 983–985 (cit. on p. 14).

G Serini, D Ambrosi, E Giraudo, A Gamba, L Preziosi, and F Bussolino (2003). "Modelling the early stages of vascular network assembly". *EMBO J.* 22.8, pp. 1771–1779 (cit. on pp. 85, 86, 174, 5).

L. F. Shampine and M. W. Reichelt (1997). "The MATLAB ODE suite". *SIAM J. Sci. Comp.* 18.1, pp. 1–22 (cit. on p. 87).

J. A. Sherratt and J. D. Murray (1990). "Models of epidermal wound healing". *P. Roy. Soc. Lond. B Bio.* 241.1300, pp. 29–36 (cit. on pp. 81, 84, 175, 4).

A. Shirinifard, J. S. Gens, B. L. Zaitlen, N. J. Popławski, M. Swat, and J. A. Glazier (2009). "3D multi-cell simulation of tumor growth and angiogenesis". *PLoS ONE* 4.10, e7190. DOI: `10.1371/journal.pone.0007190.t002` (cit. on p. 32).

M. M. Sholley, G. P. Ferguson, H. R. Siebel, J. L. Montour, and J. D. Wilson (1984). "Mechanisms of neovascularization. Vascular sprouting can occur without proliferation of endothelial cells." *Lab. Invest.* 51.6, pp. 624–634 (cit. on pp. 38, 82).

D Shweiki, M Neeman, A Itin, and E Keshet (1995). "Induction of vascular endothelial growth factor expression by hypoxia and by glucose deficiency in multicell spheroids: implications for tumour angiogenesis." *Proc. Natl. Acad. Sci. Usa* 3, pp. 768–772 (cit. on p. 7).

J. T. Smith, J. T. Elkin, and W. M. Reichert (2006). "Directed cell migration on fibronectin gradients: effect of gradient slope". *Exp. Cell Res.* 312.13, pp. 2424–2432. DOI: `10.1016/j.yexcr.2006.04.005` (cit. on pp. 106, 110).

M Soltani and P Chen (2013). "Numerical modeling of interstitial fluid flow coupled with blood flow through a remodeled solid tumor microvascular network". *PLoS ONE* 8.6, e67025. DOI: `10.1371/journal.pone.0067025.t002` (cit. on pp. 33, 216).

J Song, Y.-G. Lee, and J Houston (2003). "Neonatal corneal stromal development in the normal and lumican-deficient mouse". *Invest. Ophth. Vis Sci* 44.2, pp. 548–557. DOI: `10.1167/iovs.02-0592` (cit. on pp. 22, 61, 65, 80, 98, 172, 173).

J. W. Song and L. L. Munn (2011). "Fluid forces control endothelial sprouting". *P. Nat. Acad. Sci. USA.* 108.37, pp. 15342–15347. DOI: `10.1073/pnas.1105316108/-/DCSupplemental` (cit. on p. 216).

J. Sottile (2004). "Regulation of angiogenesis by extracellular matrix". *Biochimica et Biophysica Acta (BBA) - Reviews on Cancer* 1654.1, pp. 13–22. DOI: `10.1016/j.bbcan.2003.07.002` (cit. on p. 18).

G. V. Sperinde and M. A. Nugent (1998). "Heparan sulfate proteoglycans control intracellular processing of bFGF in vascular smooth muscle cells". *Biochemistry* 37.38, pp. 13153–13164 (cit. on pp. 102, 104, 6).

F. Spill, P. Guerrero, T. Alarcón, P. K. Maini, and H. M. Byrne (2014). "Mesoscopic and continuum modelling of angiogenesis". *J. Math. Biol.* Pp. 1–48 (cit. on p. 31).

J Staal, M. D. Abramoff, M Niemeijer, M. A. Viergever, and B van Ginneken (2004). "Ridge-based vessel segmentation in color images of the retina". *IEEE T. Med. Imaging* 23.4, pp. 501–509. DOI: `10.1109/TMI.2004.825627` (cit. on pp. 47, 51).

G. Stamatakos (2014). "Computational horizons in cancer (CHIC)". *The Parliament*, pp. 1–1 (cit. on p. 29).

C. A. Staton, M. W. R. Reed, and N. J. Brown (2009). "A critical analysis of current in vitro and in vivo angiogenesis assays". *Int. J. Exp. Pathol.* 90.3, pp. 195–221. DOI: `10.1111/j.1365-2613.2008.00633.x` (cit. on p. 21).

M. O. Stefanini, F. T. Wu, F. Mac Gabhann, and A. S. Popel (2008). "A compartment model of VEGF distribution in blood, healthy and diseased tissues". *BMC Syst. Biol.* 2.1, p. 77. DOI: `10.1186/1752-0509-2-77` (cit. on pp. 85, 86, 174, 5).

A Stephanou, S. R. McDougall, A. R. A. Anderson, and M. A. J. Chaplain (2005). "Mathematical modelling of flow in 2D and 3D vascular networks: applications to anti-angiogenic and chemotherapeutic drug strategies". *Math. Comput. Modelling* 41, pp. 1137–1156 (cit. on pp. 36, 38, 39).

– (2006). "Mathematical modelling of the influence of blood rheological properties upon adaptative tumour-induced angiogenesis". *Math. Comput. Modelling* 44.1-2, pp. 96–123. DOI: `10.1016/j.mcm.2004.07.021` (cit. on pp. 33, 39, 9).

A. Stevens and H. G. Othmer (1997). "Aggregation, blowup, and collapse: the abc's of taxis in reinforced random walks". *SIAM J. Appl. Math.* 57.4, pp. 1044–1081 (cit. on p. 31).

C. L. Stokes, M. A. Rupnick, S. K. Williams, and D. A. Lauffenburger (1990). "Chemotaxis of human microvessel endothelial cells in response to acidic fibroblast growth factor." *Lab. Invest.* (Cit. on pp. 82, 84, 175, 5).

C. L. Stokes, D. A. Lauffenburger, and S. K. Williams (1991). "Migration of individual microvessel endothelial cells: stochastic model and parameter measurement". *J. Cell Sci.* 99.2, pp. 419–430 (cit. on pp. 81, 84, 175, 4).

C. L. Stokes and D. A. Lauffenburger (1991). "Analysis of the roles of microvessel endothelial cell random motility and chemotaxis in angiogenesis". *J. Theor. Biol.* 152.3, pp. 377–403. DOI: `10.1016/S0022-5193(05)80201-2` (cit. on pp. 33, 35, 36, 84, 175, 176, 215, 5).

J. C. Strikwerda (2004). *Finite difference schemes and partial differential equations.* SIAM (cit. on p. 35).

B Styp-Rekowska, R Hlushchuk, A. R. Pries, and V Djonov (2011). "Intussusceptive angiogenesis: pillars against the blood flow". *Acta Physiologica* 202.3, pp. 213–223. DOI: `10.1111/j.1748-1716.2011.02321.x` (cit. on p. 11).

E. A. Swabb, J. Wei, and P. M. Gullino (1974). "Diffusion and convection in normal and neoplastic tissues". *Cancer Res.* 34.10, pp. 2814–2822 (cit. on pp. 83, 86, 174, 5).

B. D. Thackray and A. C. Nelson (1993). "Semi-automatic segmentation of vascular network images using a rotating structuring element (ROSE) with mathematical morphology and dual feature thresholding". *IEEE T. Med. Imaging* 12.3, pp. 385–392 (cit. on p. 37).

M. Thomas, Y. Kienast, W. Scheuer, M. Bähner, K. Kaluza, C. Gassner, F. Herting, U. Brinkmann, S. Seeber, and A. Kavlie (2013). "A novel angiopoietin-2 selective fully human antibody with potent anti-tumoral and anti-angiogenic efficacy and superior side effect profile compared to pan-angiopoietin-1/-2 inhibitors". *PLoS ONE* 8.2 (cit. on pp. 23, 44).

G. Thurston, J. S. Rudge, E. Ioffe, H. Zhou, L. Ross, S. D. Croll, N. Glazer, J. Holash, D. M. McDonald, and G. D. Yancopoulos (2000). "Angiopoietin-1 protects the adult vasculature against plasma leakage". *Nat. Med.* 6.4, pp. 460–463 (cit. on p. 17).

R. J. Tomanek and G. C. Schatteman (2000). "Angiogenesis: new insights and therapeutic potential". *Anat. Rec.* 261.3, pp. 126–135 (cit. on p. 10).

S Tong and F. Yuan (2001). "Numerical simulations of angiogenesis in the cornea". *Microvasc. Res.* 61.1, pp. 14–27. DOI: `10.1006/mvre.2000.2282` (cit. on p. 36).

S. Tong and F. Yuan (2008a). "Dose response of angiogenesis to basic fibroblast growth factor in rat corneal pocket assay: I. Experimental characterizations". *Microvasc. Res.* 75.1, pp. 10–15. DOI: `10.1016/j.mvr.2007.06.002` (cit. on pp. 80, 174).

– (2008b). "Dose response of angiogenesis to basic fibroblast growth factor in rat corneal pocket assay: II. Numerical simulations". *Microvasc. Res.* 75.1, pp. 16–24. DOI: `10.1016/j.mvr.2007.09.005` (cit. on pp. 36, 37, 42, 68, 76, 77, 80, 84, 87, 102, 104, 132, 133, 209, 4, 6).

Trisilowati and D. G. Mallet (2012). "In silico experimental modeling of cancer treatment". *ISRN Oncology* 2012, pp. 1–8. DOI: `10.5402/2012/828701` (cit. on p. 2).

P. S. Tsai, J. P. Kaufhold, P Blinder, B Friedman, P. J. Drew, H. J. Karten, P. D. Lyden, and D Kleinfeld (2009). "Correlations of neuronal and microvascular densities in murine cortex revealed by direct counting and colocalization of nuclei and vessels". *J. Neurosci.* 29.46, pp. 14553–14570. DOI: `10.1523/JNEUROSCI.3287-09.2009` (cit. on pp. 85, 86, 175, 4).

S. Tsunoda, T. Nakamura, H. Sakurai, and I. Saiki (2007). "Fibroblast growth factor-2-induced host stroma reaction during initial tumor growth promotes progression of mouse melanoma via vascular endothelial growth factor A-dependent neovascularization". *Cancer Sci.* 98.4, pp. 541–548. DOI: `10.1111/j.1349-7006.2007.00432.x` (cit. on p. 16).

K. A. Vermeer, F. M. Vos, H. G. Lemij, and A. M. Vossepoel (2004). "A model based method for retinal blood vessel detection". *Comput. Biol. Med.* 34.3, pp. 209–219. DOI: `10.1016/S0010-4825(03)00055-6` (cit. on p. 46).

J. Waltenberger, L. Claesson-Welsh, A. Siegbahn, M. Shibuya, and C.-H. Heldin (1994). "Different signal transduction properties of KDR and Flt1, two receptors for vascular endothelial growth factor." *J. Biol. Chem* 269.43, pp. 26988–26995 (cit. on p. 14).

A Walter (2009). "A Comparison of Continuum and Cell-based Models of Colorectal Cancer". PhD thesis. University of Nottingham (cit. on p. 32).

D. Wang, R. E. Lehman, D. B. Donner, M. R. Matli, R. S. Warren, and M. L. Welton (2002). "Expression and endocytosis of VEGF and its receptors in human colonic vascular endothelial cells". *Am. J. Physiol.-Gastr. L.* 282.6, G1088–G1096. DOI: `10.1152/ajpgi.00250.2001` (cit. on pp. 75, 80, 84–86, 174, 5).

L. Wang, A. Bhalerao, and R. Wilson (2007). "Analysis of retinal vasculature using a multiresolution hermite model". *IEEE T. Med. Imaging* 26.2, pp. 137–152. DOI: `10.1109/TMI.2006.889732` (cit. on p. 46).

M. G. Watson, S. R. McDougall, M. A. J. Chaplain, A. H. Devlin, and C. A. Mitchell (2012). "Dynamics of angiogenesis during murine retinal development: a coupled in vivo and in silico study". *J. R. Soc. Interface.* 9.74, pp. 2351–2364. DOI: `10.1074/jbc.271.7.3877` (cit. on pp. 39, 42, 68, 106, 110, 112, 132, 199, 210, 9).

K Webb and T White (2005). "UML as a cell and biochemistry modeling language". *Biosystems* 80.3, pp. 283–302. DOI: `10.1016/j.biosystems.2004.12.003` (cit. on p. 15).

M Welter, K Bartha, and H Rieger (2008). "Emergent vascular network inhomogeneities and resulting blood flow patterns in a growing tumor". *J. Theor. Biol.* 250.2, pp. 257–280. DOI: `10.1016/j.jtbi.2007.09.031` (cit. on pp. 40, 41).

– (2009). "Vascular remodelling of an arterio-venous blood vessel network during solid tumour growth". *J. Theor. Biol.* 259.3, pp. 405–422. DOI: `10.1016/j.jtbi.2009.04.005` (cit. on pp. 33, 40, 41).

F. C. Westall, R. Rubin, and D. Gospodarowicz (1983). "Brain-derived fibroblast growth factor: a study of its inactivation". *Life Sci.* 33.24, pp. 2425–2429 (cit. on pp. 102, 104, 6).

D. Wu, M. Zhang, J.-C. Liu, and W. Bauman (2006). "On the adaptive detection of blood vessels in retinal images". *IEEE T. Bio. Med. Eng* 53.2, pp. 341–343 (cit. on p. 46).

G. D. Yancopoulos, S. Davis, N. W. Gale, J. S. Rudge, S. J. Wiegand, and J. Holash (2000). "Vascular-specific growth factors and blood vessel formation". *Nature* 407.6801, pp. 242–248 (cit. on p. 134).

P. M. Zadeh, V. V. Toropov, and A. S. Wood (2008). "Metamodel-based collaborative optimization framework". *Struct. Multidiscip. O.* 38.2, pp. 103–115. DOI: `10.1007/s00158-008-0286-8` (cit. on p. 208).

M. H. Zaman, L. M. Trapani, A. L. Sieminski, D. MacKellar, H. Gong, R. D. Kamm, A. Wells, D. A. Lauffenburger, and P. Matsudaira (2006). "Migration of tumor cells in 3D matrices is governed by matrix stiffness along with cell-matrix adhesion and proteolysis". *P. Nat. Acad. Sci. USA.* 103.29, pp. 10889–10894 (cit. on p. 107).

E Zhang, S Schrunder, and F Hoffmann (1996). "Orthotopic corneal transplantation in the mouse: a new surgical technique with minimal endothelial cell loss". *Graef. Arch. Clin. Exp.* 243, pp. 714–719 (cit. on pp. 22, 61, 65, 80, 98, 172, 173).

X Zheng, S Wise, and V Cristini (2005). “Nonlinear simulation of tumor necrosis, neo-vascularization and tissue invasion via an adaptive finite-element/level-set method”. *Bull. Math. Biol.* 67.2, pp. 211–259. DOI: `10.1016/j.bulm.2004.08.001` (cit. on p. 41).

X. Zheng, G. Y. Koh, and T. Jackson (2013). “A continuous model of angiogenesis: initiation, extension, and maturation of new blood vessels modulated by vascular endothelial growth factor, angiopoietins, platelet-derived growth factor-B, and pericytes”. *Discrete and Continuous Dynamical Systems-Series B (DCDS-B)* 18.4, pp. 1109–1154. DOI: `10.3934/dcdsb.2013.18.1109` (cit. on pp. 38, 81, 84, 104, 4–6).